WYDZIAŁ BIOLOGII
i OCHRONY ŚRODOWISKA
Uniwersytet Łódzki

Szkoła Doktorska Nauk Ścisłych i Przyrodniczych
Uniwersytetu Łódzkiego

Mateusz Paweł Kciuk

NUMER ALBUMU: 6158

Komórkowe mechanizmy aktywności biologicznej sulfonamidów, pochodnych układu pirazolo[4,3-*e*][1,2,4]triazyny w prawidłowych i nowotworowych komórkach człowieka *in vitro*

Cellular mechanisms of biological activity of sulfonamide derivatives of the pyrazolo[4,3-*e*][1,2,4]triazine ring system in normal and tumor human cells *in vitro*

Praca doktorska
wykonana w Katedrze Biotechnologii Molekularnej i Genetyki,
Wydział Biologii i Ochrony Środowiska UŁ

Promotor
dr hab. Renata Kontek, prof. UŁ
Katedra Biotechnologii Molekularnej i Genetyki,
Wydział Biologii i Ochrony Środowiska UŁ

Drugi Promotor
prof.dr hab. Mariusz Mojzych
Instytut Nauk Chemicznych,
UPH w Siedlcach

Łódź, 2023

Podziękowania

Pragnę serdecznie podziękować moim promotorom
dr hab. Renacie Kontek oraz **dr hab. Mariuszowi Mojzychowi**
za okazane wsparcie, zaangażowanie i merytoryczną pomoc
podczas realizacji niniejszej pracy doktorskiej.

Dziękuję
Pracownikom i **Doktorantom**
Katedry Biotechnologii Molekularnej i Genetyki
za otwartość, życzliwość, zaufanie i możliwość współpracy.

Dziękuję mojej **Rodzinie** i **Bliskim**
za nieustające wsparcie, cierpliwość i wiarę we mnie
podczas przygotowywania rozprawy doktorskiej.

Spis treści

Wykaz skrótów:

ABC – ang. *ATP-binding cassette transporters*

ABL – białkowa kinaza tyrozynowa ABL (ang. *tyrosine-protein kinase ABL*)

ADMET – absorpcja, dystrybucja, metabolizm, wydalanie oraz toksyczność leku (ang. *absorption, distribution, metabolism, excretion and toxicity*)

AKT – białkowa kinaza serynowo/treoninowa AKT (ang. *serine/threonine-protein kinase AKT*)

AO – oranż akrydyny (ang. *acridine orange*)

APE1 – endonukleaza DNA miejsc apurynowych/apirymidynowych (ang. *DNA-(apurinic or apyrimidinic site) endonuclease*)

ATM – białkowa kinaza serynowa ATM (ang. *ATM serine protein kinase*)

ATR – białkowa kinaza serynowo-treoninowa ATR (ang. *ATR serine/threonine kinase*)

BBB – bariera krew-mózg (ang. *blood–brain barrier*)

BCR – ang. *breakpoint cluster region protein*

BMI – wskaźnik masy ciała (ang. *body mass index*)

BrdU – bromodeoksyurydyna (ang. *bromodeoxyuridine/5-bromo-2′-deoxyuridine*)

BTK – kinaza tyrozynowa Brutona (ang. *Bruton's tyrosine kinase*)

CADD – wspomagane komputerowo projektowanie leków (ang. *computer-aided drug design*)

CARD – ang. *caspase activation and recruitment domain*

CAs – anhydrazy węglanowe (ang. *carbonic anhydrases*)

CDKs – kinazy zależne od cyklin (ang. *cyclin-dependent kinases*)

CHARMM – ang. *chemistry at harvard molecular mechanics*

CHK1/CHK2 – białkowe kinazy serynowo-treoninowe CHK1/2 (ang. *serine/threonine-protein kinase CHK1/CHK1*)

CLL – przewlekła białaczka limfocytowa (ang. *chronic lymphocytic leukemia*)

DCF – 2′,7′-dichlorofluoresceina (ang. *2′,7′-dichlorofluorescein*)

DCFH2 – 2',7'-dichlorodihydrofluoresceina (ang. *2′,7′-dichlorodihydrofluorescein*)

DCFH-DA – dioctan dihydrodichlorofluoresceiny (ang. *2,7-dichlorodihydrofluorescein diacetate*)

DDR – szlak odpowiedzi na uszkodzenia DNA (ang. *DNA damage response*)

DFT – teoria funkcjonału gęstości (ang. *density functional theory*)

EB – bromek etydyny (ang. *ethidium bromide*)

FADD – ang. *Fas (TNFRSF6)-associated via death domain*

FITC – izotiocyjanian fluoresceiny (ang. *fluorescein isothiocyanate*)

GROMOS – ang. *groningen molecular simulation*

HIA – absorpcja bierna w przewodzie pokarmowym człowieka (ang. *human gastrointestinal absorption*)

HR – rekombinacja homologiczna (ang. *homologous DNA repair*)

IARC – międzynarodowa agencja ds. badań nad rakiem (ang. *International Agency for Research on Cancer*)

MCL – chłoniak z komórek płaszcza (ang. *mantle cell lymphoma*)

MESP – ang. *molecular electrostatic potential*

MLKL – ang. *mixed lineage kinase domain like pseudokinase*

MM-GBSA – ang. *molecular mechanics-generalized born surface area*

MMP – (transbłonowy) potencjał błony mitochondrialnej (ang. *mitochondrial membrane potential*)

mTOR – białkowa kinaza serynowo/treoninowa mTOR (ang. *serine/threonine-protein kinase mTOR*)

NF-κB – jądrowy czynnik transkrypcyjny kappaB (ang. *nuclear factor NF-kappa-B*)

NMR – magnetyczny rezonans jądrowy (ang. *nuclear magnetic resonance*)

PARP-1 – polimeraza poli(ADP-rybozy)-1 (ang. *poly [ADP-ribose] polymerase 1*)

PD-1 – receptor programowanej śmierci 1 (ang. *programmed death receptor 1*)

PD-L1 – ligand dla receptora programowanej śmierci (ang. *programmed death ligand 1*)

P-gp – glikoproteina P

PI – jodek propidyny (ang. *propidium iodide*)

RFT – reaktywne formy tlenu

RIPK1/2/3 – ang. *receptor interacting serine/threonine kinase 1/2/3*

RMSD – ang. *root mean square deviation*

RMSF – ang. *root mean square fluctuation*

RPA70 – ang. *replication protein A 70 kDa*

RT-PCR – łańcuchowa reakcja polimerazy DNA w czasie rzeczywistym (ang. *real-time polymerase chain reaction*)

sICAM-1 – rozpuszczalna międzykomórkowa cząsteczka adhezyjna-1 (ang. *soluble intercellular adhesion molecule-1*)

TNF – czynnik martwicy nowotworów (ang. *tumor necrosis factor*)

TNFRSF1A/TNF-R1 – ang. *tumor necrosis factor receptor superfamily member 1A*

TNFSF10/TRAIL/APO-2L – ang. *tumor necrosis factor ligand superfamily member 10*

TOP1 – ang. *topoisomerase 1*

TOP2B – ang. *topoisomerase 2β*

TP53 – ang. *cellular tumor antigen p53*

TRADD – ang. *TNFRSF1A associated via death domain*

TRAIL – ang. *tumor necrosis factor ligand superfamily member 10*

WEE1 – kinaza białkowa podobna do WEE1 (ang. *Wee1-like protein kinase*)

1. Współpraca naukowa

Niniejsza praca doktorska została zrealizowana w ramach współpracy z następującymi ośrodkami badawczymi:

- **Instytut Nauk Chemicznych, Wydział Nauk Ścisłych i Przyrodniczych, Uniwersytet Przyrodniczo-Humanistyczny w Siedlcach**

Sulfonamidowe pochodne układu pirazolo[4,3-*e*][1,2,4]triazyny zostały zsyntetyzowane, scharakteryzowane w Instytucie Nauk Chemicznych, Uniwerystetu Przyrodniczo-Humanistycznego w Siedlcach.

- **Chitkara College of Pharmacy, Chitkara University, Rajpura, Punjab, Indie**

Wsparcie w badaniach komputerowych (*in silico*): **dr Somdutt Mujwar** z Uniwersytetu Chitkara w Indiach oraz:

dr Ismail Celik	Department of Pharmaceutical Chemistry, Faculty of Pharmacy, Erciyes University, Kayseri, Turcja
dr Enfale Zerroug	Group of Computational and Pharmaceutical Chemistry, LMCE Laboratory, University of Biskra, Algieria
dr Amit Dubey	Computational Chemistry and Drug Discovery Division, Quanta Calculus, Greater Noida, Uttar Pradesh, Indie. Department of Pharmacology, Saveetha Dental College and Hospital, Saveetha Institute of Medical and Technical Sciences, Chennai, Tamil Nadu, Indie
dr Rajamanikandan Sundaraj	Centre for Drug Discovery, Department of Biochemistry, Karpagam Academy of Higher Education, Coimbatore, Indie

2. Źródło finansowania badań

Badania przeprowadzone w niniejszej pracy zostały sfinansowane z subwencji Katedry Biotechnologii Molekularnej i Genetyki, dofinansowania dla doktorantów Szkoły Doktorskiej Nauk Ścisłych i Przyrodniczych Uniwersytetu Łódzkiego oraz dzięki realizacji projektu badawczego pt.: „***Aktywność biologiczna syntetycznych, sulfonamidowych pochodnych układu pirazolo[4,3,-e]tetrazolo[4,5,-b][1,2,4]triazyny w prawidłowych oraz nowotworowych komórkach człowieka in vitro***" w ramach konkursu grantowego UŁ **Doktoranckie Granty Badawcze** (Inicjatywa Doskonałości – Uczelnia Badawcza (IDUB))

3. Spis publikacji wchodzących w skład rozprawy doktorskiej

- **Praca przeglądowa:**

1. Bernat Z.; Szymanowska A.; **Kciuk M.**; Kotwica-Mojzych K.; Mojzych M. ***Review of the Synthesis and Anticancer Properties of Pyrazolo[4,3-e][1,2,4]Triazine Derivatives.*** Molecules 2020, 25, 3948, IF: 4,412; punkty MEiN: 140 pkt.

- **Prace oryginalne:**

1. **Kciuk M.**; Mujwar S.; Szymanowska A.; Marciniak B.; Bukowski K.; Mojzych M.; Kontek R. ***Preparation of Novel Pyrazolo[4,3-e]Tetrazolo[1,5-b][1,2,4]Triazine Sulfonamides and Their Experimental and Computational Biological Studies.*** Int. J. Mol. Sci. 2022, 23, IF: 5,6; punkty MEiN: 140 pkt.
2. **Kciuk M.**; Mujwar S.; Marciniak B.; Gielecińska A.; Bukowski K.; Mojzych M.; Kontek R. ***Genotoxicity of Novel Pyrazolo[4,3-e]Tetrazolo[1,5-b][1,2,4]Triazine Sulfonamides in Normal and Cancer Cells In Vitro.*** Int. J. Mol. Sci. 2023, 24, 4053, IF: 5,6; punkty MEiN: 140 pkt.
3. **Kciuk M.**; Marciniak B.; Celik I.; Zerroug E.; Dubey A.; Sundaraj R.; Mujwar S.; Bukowski K.; Mojzych M.; Kontek R. ***Pyrazolo[4,3-e]Tetrazolo[1,5-b][1,2,4]Triazine Sulfonamides as an Important Scaffold for Anticancer Drug Discovery—In Vitro and In Silico Evaluation.*** Int. J. Mol. Sci. 2023, 24, 10959, IF: 5,6; punkty MEiN: 140 pkt.

Sumaryczny IF: 21,212; **punkty MEiN:** 560.

4. Pozostały dorobek naukowy

Publikacje:

1. Bukowski K.; **Kciuk M.**; Kontek R. ***Mechanisms of Multidrug Resistance in Cancer Chemotherapy.*** Int. J. Mol. Sci. 2020, 21, 3233, IF: 5,924; punkty MEiN: 140 pkt.

2. **Kciuk M.**; Bukowski K.; Marciniak B.; Kontek R. ***Advances in DNA Repair-Emerging Players in the Arena of Eukaryotic DNA Repair.*** Int. J. Mol. Sci. 2020, 21, 3934, IF: 5,924; punkty MEiN: 140 pkt.

3. **Kciuk M.**; Kontek R. ***Rola Sirtuin w Naprawie DNA.*** Postępy Biochem. 2020, 66, 1–7, IF: 0,94; punkty MEiN: 70 pkt.

4. **Kciuk M.**; Marciniak B.; Kontek R. ***Irinotecan—Still an Important Player in Cancer Chemotherapy: A Comprehensive Overview.*** Int. J. Mol. Sci. 2020, 21, 4919, IF: 5,924; punkty MEiN: 140 pkt.

5. **Kciuk M.**; Marciniak B.; Mojzych M.; Kontek R. ***Focus on UV-Induced DNA Damage and Repair-Disease Relevance and Protective Strategies.*** Int. J. Mol. Sci. 2020, 21, E7264, IF: 5,924; punkty MEiN: 140 pkt.

6. **Kciuk M.**; Gielecińska A.; Mujwar S.; Mojzych M.; Kontek R. ***Cyclin-Dependent Kinases in DNA Damage Response.*** Biochim. Biophys. Acta Rev. Cancer 2022, 188716, IF: 11,2; punkty MEiN: 200 pkt.

7. **Kciuk M.**; Gielecińska A.; Mujwar S.; Mojzych M.; Kontek R. ***Cyclin-Dependent Kinase Synthetic Lethality Partners in DNA Damage Response.*** Int. J. Mol. Sci. 2022, 23, 3555, IF: 5,6; punkty MEiN: 140 pkt.

8. **Kciuk M.**; Gielecińska A.; Budzinska A.; Mojzych M.; Kontek R. ***Metastasis and MAPK Pathways.*** Int. J. Mol. Sci. 2022, 23, 3847, IF: 5,6; punkty MEiN: 140 pkt.

9. Fidan O.; Mujwar S.; **Kciuk M.** ***Discovery of Adapalene and Dihydrotachysterol as Antiviral Agents for the Omicron Variant of SARS-CoV-2 through Computational Drug Repurposing.*** Mol. Divers. 2022, 27, 463–475, IF: 3,8; punkty MEiN: 70 pkt.

10. **Kciuk M.**; Gielecińska A.; Kołat D.; Kałuzińska Ż.; Kontek R. ***Cancer-Associated Transcription Factors in DNA Damage Response.*** Biochim. Biophys. Acta Rev. Cancer 2022, 1877, 188757, IF: 11,2; punkty MEiN: 200 pkt.

11. Bukowski K.; Marciniak B.; **Kciuk M.**; Mojzych M.; Kontek R. ***Pyrazolo[4,3-e]Tetrazolo[1,5-b][1,2,4]Triazine Sulfonamides as Novel Potential Anticancer Agents: Cytotoxic and Genotoxic Activities In Vitro.*** Molecules 2022, 27, 3761, IF: 4.6; punkty MEiN: 140 pkt.

12. Kołat D.; **Kciuk M.**; Kłosiński K.; Kałuzińska Ż. ***Pyroptosis-Related Signatures in Bladder Cancer Prognosis and Treatment-Are We There Yet?*** Transl. Cancer Res. 2022, 11, 1861–1864, IF: 0,9; punkty MEiN: 40 pkt.

13. **Kciuk M.**; Mujwar S.; Rani I.; Munjal K.; Gielecińska A.; Kontek R.; Shah K. ***Computational Bioprospecting Guggulsterone against ADP Ribose Phosphatase of SARS-CoV-2.*** Molecules. 2022, 27, 8287, IF: 4,6; punkty MEiN: 140 pkt.

14. Kołat D.; Zhao L.-Y.; **Kciuk M.**; Płuciennik E.; Kałuzińska-Kołat Ż. ***AP-2δ Is the Most Relevant Target of AP-2 Family-Focused Cancer Therapy and Affects Genome Organization.*** Cells. 2022, 11, 4124, IF: 6; punkty MEiN: 140 pkt.

15. **Kciuk M.**; Gielecińska A.; Mujwar S.; Mojzych M.; Marciniak B.; Drozda R.; Kontek R. ***Targeting Carbonic Anhydrase IX and XII Isoforms with Small Molecule Inhibitors and Monoclonal Antibodies.*** J. Enzyme Inhib. Med. Chem. 2022, 37, 1278–1298, IF: 5,756; punkty MEiN: 140 pkt.

16. Kałuzińska-Kołat Ż.; **Kciuk M.**; Waszczykowska K.; Płuciennik E.; Kołat D. ***Penduletin - Yet Underestimated Flavonoid with a Potential Anti-Cancer Activity.*** Anticancer Agents Med. Chem. 2023, 23, 860–863, IF: 2,8; punkty MEiN: 70 pkt.

17. **Kciuk M.**; Kołat D.; Kałuzińska-Kołat Ż.; Gawrysiak M.; Drozda R.; Celik I.; Kontek R. ***PD-1/PD-L1 and DNA Damage Response in Cancer.*** Cells. 2023, 12, 530, IF: 6; punkty MEiN: 140 pkt.

18. **Kciuk M.**; Gielecińska A.; Mujwar S.; Kołat D.; Kałuzińska-Kołat Ż.; Celik I.; Kontek R. ***Doxorubicin-An Agent with Multiple Mechanisms of Anticancer Activity.*** Cells. 2023, 12, 659, IF: 6; punkty MEiN: 140 pkt.

19. Gielecińska A.; **Kciuk M.**; Mujwar S.; Celik I.; Kołat D.; Kałuzińska-Kołat Ż.; Kontek, R. ***Substances of Natural Origin in Medicine: Plants vs. Cancer.*** Cells. 2023, 12, 986, IF: 6; punkty MEiN: 140 pkt.

20. Mohamed Abdoul-Latif F.; Ainane A.; Houmed Aboubaker I.; Merito Ali A.; El Montassir Z.; **Kciuk M.**; Mohamed J.; Ainane T. ***Chemical Composition of the Essential Oil of Catha Edulis Forsk from Djibouti and Its Toxicological Investigations In Vivo and In Vitro.*** Processes. 2023, 11, 1324, IF: 3,5; punkty MEiN: 70 pkt.

21. Bukowski K.; Marciniak B.; **Kciuk M.**; Mujwar S.; Mojzych M.; Kontek R. ***Pyrazolo[4,3-e]Tetrazolo[1,5-b][1,2,4]Triazine Sulfonamides as Novel Potential Anticancer Agents: Apoptosis, Oxidative Stress, and Cell Cycle Analysis.*** Int. J. Mol. Sci. **2023**, 24, 8504, IF: 5,6; punkty MEiN: 140 pkt.

22. **Kciuk M.**; Yahya E.B.; Mohamed Ibrahim Mohamed M.; Rashid S.; Iqbal M.O.; Kontek R.; Abdulsamad M.A.; Allaq A.A. ***Recent Advances in Molecular Mechanisms of Cancer Immunotherapy.*** Cancers. 2023, 15, 2721, IF: 5,2; punkty MEiN: 140 pkt.

23. **Kciuk M.**; Yahya E.B.; Mohamed M.M.I.; Abdulsamad M.A.; Allaq A.A.; Gielecińska A.; Kontek R. ***Insights into the Role of LncRNAs and MiRNAs in Glioma Progression and Their Potential as Novel Therapeutic Targets.*** Cancers. **2023**, 15, 3298, IF: 5,2; punkty MEiN: 140 pkt.

24. **Kciuk M.**; Alam M.; Ali N.; Rashid S.; Głowacka P.; Sundaraj R.; Celik I.; Yahya E.B.; Dubey A.; Zerroug E.; Kontek R. ***Epigallocatechin-3-Gallate Therapeutic Potential in Cancer: Mechanism of Action and Clinical Implications.*** Molecules. 2023, 28, 5246, IF: 4,6; punkty MEiN: 140 pkt.

25. Kruczkowska W.; **Kciuk M.**; Pasieka Z.; Kłosiński K.; Płuciennik E.; Elmer J.; Waszczykowska K.; Kołat D.; Kałuzińska-Kołat Ż. ***The Artificial Oxygen Carrier Erythrocruorin—Characteristics and Potential Significance in Medicine.*** J Mol Med. 2023, IF: 4,7; punkty MEiN: 140 pkt.

Sumaryczny IF: 133,492; punkty MEiN: 3240

Bibliometria:

Całkowity IF = 154,704

Punktacja MEiN = 3800 pkt

Indeks Hirscha = 9 (wg Scopus oraz Web of Science)

Liczba cytowań (bez autocytowań) – 714 (wg Web of Science)

Monografie, udział w monografiach:

Szczerbiec D.; **Kciuk M**. ***Pęcherzyki błonowe bakterii Gram-ujemnych – rola oraz możliwości praktycznego zastosowania w przyszłości.*** Badania i Rozwój Młodych Naukowców w Polsce; Nauki Medyczne i nauki o zdrowiu. Część III. 2020.

Kciuk M. ***Biologia molekularna nowotworów głowy i szyi.*** Badania i Rozwój Młodych Naukowców w Polsce; Nauki Medyczne i nauki o zdrowiu. Część IV. 2020.

Kciuk M.; Szczerbiec D. ***Koewolucja: Mycobacterium tuberculosis i Homo sapiens.*** Badania i Rozwój Młodych Naukowców w Polsce; Nauki Medyczne i nauki o zdrowiu. Część IV. 2020.

Kciuk M.; Marciniak B.; Kontek R. ***Glejak – wyzwanie współczesnej medycyny.*** Badania i Rozwój Młodych Naukowców w Polsce (ISBN 978-83-66743-20-5). 2021.

Kciuk M.; Marciniak B.; Kontek R. ***Rola białek szoku cieplnego w naprawie DNA.*** Badania i Rozwój Młodych Naukowców w Polsce (ISBN 978-83-66743-20-5). 2021.

Orzechowska M.; **Kciuk M.** ***Śmierć komórkowa zależna od PARP-1.*** Badania i Rozwój Młodych Naukowców w Polsce (ISBN 978-83-66743-20-5). 2021.

Doniesienia konferencyjne

Orzechowska M.; **Kciuk M.** ***Znaczenie lipidomiki błon komórkowych w chorobach nowotworowych***. Młodzi Naukowcy w Polsce – Badania i Rozwój. Plakat. 22.03.2021.

Kciuk M. ***Cytotoksyczność pochodnych pirazolotriazyny w prawidłowych i nowotworowych komórkach człowieka in vitro***. VI Ogólnopolska Konferencja Doktorantów Nauk o Życiu BioOpen Plakat. 15-16.04.2021.

Gielecińska A.; **Kciuk M.** ***Wpływ NAD+ zależnych sirtuin na starzenie komórkowe C.elegans***. Nature. Polish Scientific Conference 2021. Plakat. 12.06.2021

Kciuk M. ***Biological activity of synthetic sulfonamide derivatives of pyrazolo[4,3-e]tetrazolo[4,5- b][1,2,4]triazine in normal and cancer cells in vitro***. 1st International Scientific Conference "Advances in biomedical research with the use of in vitro methods" Prezentacja ustna. 17.06.2021.

Kciuk M. ***Sulfonamidowe pochodne pirazolo[4,3-e][1,2,4]triazyny, jako potencjalne inhibitory szlaku AKT-mTOR oraz PD-L1, o aktywności przeciwnowotworowej – badania in silico oraz in vitro***. VI Ogólnopolska Konferencja Genetyczna „Genomica" Plakat 20-22.05.

Szkolenia:

- qPCR – profilowanie ekspresji genów. MBS szkolenia. 11-12.09.2020 r.
- Zakażenia hodowli mykoplazmą – zapobieganie oraz detekcja, Online 19.03.2021 r.
- Analiza interakcji DNA-białko, Poznań 11.04.2021 r.
- Zastosowanie nowatorskich metod cytometrycznych w wieloparametrycznej analizie komórek, Online 12.04.2021 r.
- Research Project Management: Getting Started, Online 17.04.2021 r.
- Hodowle komórek w 3D, Online 23.04.2021 r.
- Ekstrakcja i oczyszczanie białka z materiału biologicznego, Online 30.04.2021 r.
- Jak zdobyć granty na badania?, Warszawa 13.05.2021 r.
- Basic principles of Regulatory Affairs for medicinal products, veterinary products with elements of pharmacovigilance, Warszawa 22.05.2021 r.
- Case Study Regulatory and PV Documentation for medicinal and veterinary products, Warszawa 23.05.2021 r.
- Western blotting – wskazówki i porady dotyczące optymalizacji procesu, Online 28.05.2021 r.

5. Wprowadzenie

5.1. Uzasadnienie podjętej tematyki

Liczba zachorowań na chorobę nowotworową stale wzrasta, a rozwój oporności komórek w odpowiedzi na zastosowane środki chemioterapeutyczne, przyczynia się do ograniczonej skuteczności jej leczenia. Według Międzynarodowej Agencji ds. Badań nad Rakiem (ang. *International Agency for Research on Cancer*; IARC) w 2020 roku, blisko 10 milionów ludzi zmarło z powodu chorób nowotworowych, będących obecnie jedną z głównych przyczyn zgonów na świecie. Dodatkowo, brak aktywności fizycznej, wysoki wskaźnik masy ciała (ang. *body mass index*; BMI), a także nadużywanie tytoniu i alkoholu, przyczyniają się do zwiększonego ryzyka transformacji nowotworowej u ludzi. Wśród najczęściej występujących nowotworów złośliwych wyróżnić można: raka piersi, płuc, okrężnicy i odbytnicy, prostaty, skóry, żołądka oraz szyjki macicy **(Rycina 1)** [1].

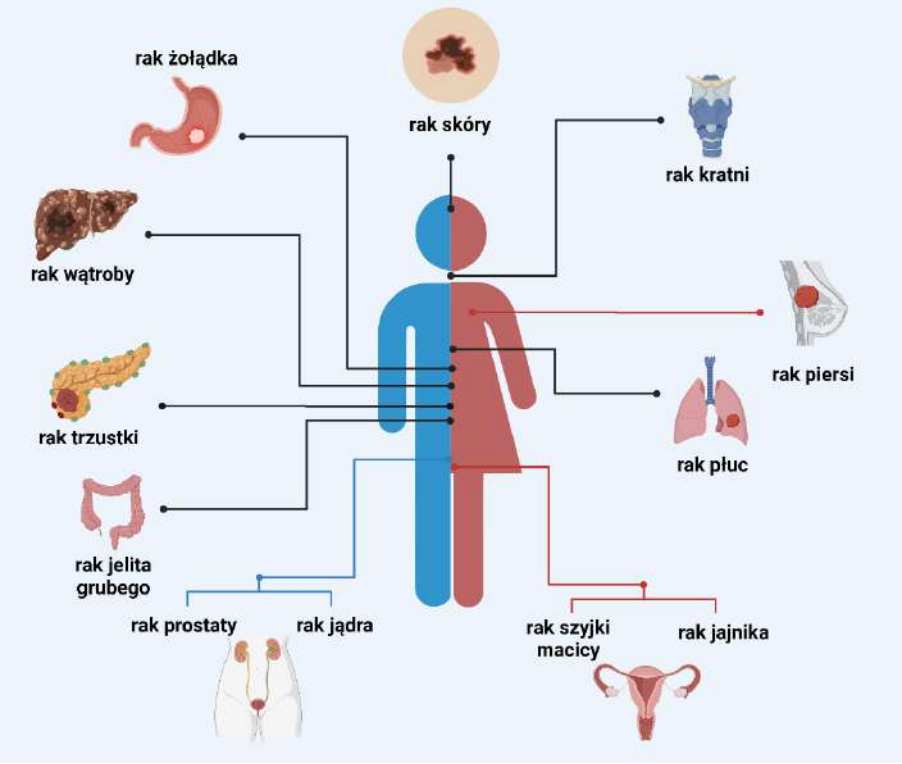

Rycina 1. Najczęściej występujące typy nowotworów u ludzi.

Pomimo znacznych postępów w leczeniu chorób nowotworowych, w tym rozwoju chirurgii, radioterapii, terapii hormonalnej, terapii genowej i immunoterapii, w wielu przypadkach pierwszym, a zarazem wiodącym sposobem leczenia pozostaje chemioterapia. Dlatego też, poszukiwanie nowych, skutecznych leków chemioterapeutycznych, stanowi jeden z wiodących tematów badań podejmowanych przez naukowców na całym świecie [2–5].

Szlaki sygnałowe w komórkach prawidłowych wykrywają zmiany zachodzące w środowisku i odpowiadają na nie, regulując aktywność komórkową. Komórki zawierają w swoich błonach liczne receptory, które umożliwiają przekazywanie sygnałów (np. czynników wzrostu) spoza komórki do jej wnętrza (szlaki sygnałowe). Zakłócenia funkcjonowania szlaków sygnałowych mają poważne konsekwencje i mogą prowadzić do transformacji nowotworowej. Identyfikacja nieprawidłowo działających szlaków zaangażowanych w karcynogenezę dostarcza informacji o celach molekularnych, które mogą zostać wykorzystane do projektowania nowych leków onkologicznych, a tym samym opracowania nowych terapii przeciwnowotworowych [2–5].

Powszechną strategią opracowywania leków przeciwnowotworowych jest synteza antymetabolitów. Związki te, strukturalnie podobne do naturalnie występujących substratów procesów komórkowych, hamują szlaki metaboliczne kluczowe dla podziałów komórkowych. Zablokowanie ww. procesów spowalnia proliferację komórek, powodując ich śmierć na drodze regulowanej śmierci komórkowej, tj. apoptozy (*apoptosis*, z gr. opadanie) [6,7]. Apoptoza jest genetycznie zaprogramowanym procesem, w którym, w sposób aktywny usuwane są uszkodzone, zbędne lub nowotworowo zmienione komórki. Proces ten odpowiada m.in. za wzrost i rozwój narządów, różnicowanie tkanek, prawidłowe funkcjonowanie układu odpornościowego, selekcję oraz odnowę komórek. Deregulacja procesu apoptozy ma charakter destrukcyjny i jest ściśle powiązana z etiologią i patogenezą wielu zespołów chorobowych, w tym chorób neurodegeneracyjnych, nowotworowych i zaburzeń autoimmunologicznych.

Komórki przechodzące apoptozę nie podlegają lizie, co pozwala na uniknięcie rozwoju stanu zapalnego, spowodowanego uwolnieniem zawartości komórek poza ich strukturę, w konsekwencji prowadząc do uszkodzenia komórek sąsiadujących. Zaburzenia sygnalizacji procesu apoptozy mogą przyczyniać się do rozwoju oporności komórek nowotworowych na powszechnie stosowane chemioterapeutyki. Leki cytotoksyczne, stanowiące podstawę systemowego leczenia nowotworów opartego na chemioterapii, oddziałują na mitochondrialny (wewnątrzpochodny) lub związany z aktywacją receptorów śmierci (ang. *death receptors*) (zewnątrzpochodny) szlak apoptozy [8,9]. Obecnie zdecydowana większość leków przeciwnowotworowych wykazuje właściwości proapoptotyczne. Ich terapeutyczne działanie opiera się głównie na blokowaniu zwiększonego tempa proliferacji komórek, co prowadzi do ich eliminacji m.in. na drodze apoptozy. Selektywność leków nie jest jednak wystarczająca, co powoduje wystąpienie efektów toksycznych, prowadzących do śmierci komórek prawidłowych oraz pojawienia się skutków ubocznych, często niebezpiecznych dla zdrowia i znacznie obniżających komfort życia pacjentów onkologicznych. Dlatego też, ocena skutków cytotoksyczności, genotoksyczności, jak i proapoptotycznych właściwości potencjalnych leków przeciwnowotworowych, w stosunku do komórek prawidłowych oraz nowotworowych, jest podstawą opracowania nowych, efektywniejszych chemioterapeutyków [9].

Wiele onkoterapuetyków, obecnie stosowanych w praktyce klinicznej, jak np.: 5-fluorouracyl, metotreksat, doksorubicyna czy winblastyna, zawiera w swej strukturze pierścienie heterocykliczne [10,11]. Dlatego też, włączenie struktur heterocyklicznych w chemiczną strukturę cząsteczek potencjalnych leków ma kluczowe znaczenie dla projektowania związków o wysokiej aktywności przeciwnowotworowej oraz selektywności. Jednocześnie umożliwia ich optymalizację pod kątem kluczowych właściwości fizykochemicznych, tj. lipofilowości, polarności i rozpuszczalności w wodzie [12]. Antymetabolity, o budowie chemicznej zbliżonej do naturalnie występujących heterocyklicznych

zasad azotowych DNA/RNA, stanowią jedną z głównych grup leków przeciwnowotworowych. Nie tylko zakłócają kluczowe dla utrzymania wzrostu komórek szlaki biosyntezy DNA/RNA, ale także wykazują działanie genotoksyczne związane z powstawaniem uszkodzeń DNA [7,10], prowadzące do aktywacji punktów kontrolnych cyklu komórkowego (ang. *cell-cycle checkpoints*), jego zatrzymania i/lub apoptotycznej śmierci komórek [13].

Liczne nukleozydy, zawierające w swoich pierścieniach atomy węgla i azotu, wykazują znaczny potencjał, jako antymetabolity. Związki „6-aza", tj. 6-azacytydyna i 6-azaurydyna, są dobrze znanymi przykładami analogów naturalnie występujących składników kwasów nukleinowych [14,15]. Do wspomnianej grupy należą również monocykliczne pochodne 1,2,4-triazyny, wykazujące szeroką aktywność biologiczną, w tym: przeciwnowotworową, przeciwdrobnoustrojową, przeciwgrzybiczą, przeciwzapalną, przeciwmalaryczną i przeciwwirusową [16,17]. 1,2,4-triazyny skondensowane z pięcioczłonowymi heterocyklami są uważane za bioizosteryczne z pierścieniem purynowym, przez co wzbudziły duże zainteresowanie wśród naukowców pracujących w obszarze chemii medycznej [18,19]. Cząsteczka 1,2,4-triazyny jest jednym z trzech potencjalnych izomerów sześcioczłonowego pierścienia, zawierającego trzy atomy azotu. Uważa się, że pierścień 1,2,4-triazynowy ma zasadnicze znaczenie dla farmakologicznej aktywności ww. związków, w tym właściwości przeciwnowotworowych. Pochodne układu pirolo[2,1-*c*][1,2,4]triazyny i pirolo[2,1-*f*][1,2,4]triazyny stanowią najliczniejszą grupę związków triazynowych o działaniu przeciwnowotworowym [16,17]. W przeciwieństwie do pirolo-triazyn, układ pierścieni pirazolo[4,3-*e*][1,2,4]triazyny pozostaje mniej zbadaną strukturą chemiczną. Wczesne badania nad szeregiem prostych, podstawionych pochodnych pirazolo-triazyny nie wykazały znacznej aktywności przeciwnowotworowej tych związków, dlatego też zdecydowano o połączeniu ich struktury z różnymi grupami farmakoforowymi, w tym ugrupowaniem sulfonamidowym. Związki należące do tej klasy heterocykli wykazują aktywność

przeciwnowotworową poprzez zahamowanie aktywności kinazy tyrozynowej ABL (ang. *tyrosine-protein kinase ABL*) [20], anhydraz węglanowych (ang. *carbonic anhydrases*; CAs) [21,22] oraz kinaz zależnych od cyklin (ang. *cyclin-dependent kinases*; CDKs) [20]. Szczególnie interesującą grupę związków o działaniu cytostatycznym stanowią również pirazolo[4,3-*e*][1,2,4]triazyny skondensowane z pierścieniem 1,2,4-triazolowym lub tetrazolowym, które wykazują aktywność cytostatyczną/cytotoksyczną w stężeniach nano- i mikromolarnych [18]. Powyższe dane wydają się być istotne w aspekcie stopnia nasilenia ewentualnych skutków ubocznych, które mogą wystąpić w organizmie pacjenta.

W niniejszej pracy poddano ocenie aktywność biologiczną nowych, syntetycznych, sulfonamidowych pochodnych pirazolo[4,3-*e*]tetrazolo[1,5-*b*][1,2,4]triazyny. Związki z tej grupy heterocykli, wykazują wysoką aktywność cytotoksyczną [23–25], genotoksyczną [23] oraz proapoptotyczną [24–26]. Wykazano m.in., że pochodna pirazolo[4,3-*e*]tetrazolo[1,5-*b*][1,2,4]triazyny, skutecznie ogranicza żywotność i indukuje apoptotyczną śmierć komórek poprzez hamowanie kinazy tyrozynowej Brutona (ang. *Bruton's tyrosine kinase*; BTK) [25]. BTK jest niereceptorową kinazą tyrozynową, zaangażowaną w rozwój limfocytów B, ich różnicowanie oraz przekazywanie sygnałów w komórce. W ciągu ostatniej dekady inhibitory BTK stały się alternatywą dla schematów leczenia chorób nowotworowych opartych na klasycznej chemioterapii, szczególnie u pacjentów cierpiących na przewlekłą białaczkę limfocytową (ang. *chronic lymphocytic leukemia*; CLL) oraz chłoniaka z komórek płaszcza (ang. *mantle cell lymphoma*; MCL), który należy do nowotworów układu chłonnego i stanowi jedno z większych wyzwań współczesnej onkologii [27,28]. Badana pochodna pirazolo-triazyny wykazywała również potencjał przeciwnowotworowy w badaniach *in vivo* w mysim modelu ksenoprzeszczepu (ksenotransplantacji) komórek raka okrężnicy. Efekt ten przypisano obniżonej ekspresji białkowej kinazy serynowo/treoninowej AKT (ang. *serine/threonine-protein kinase AKT*; AKT), CDK2, białkowej kinazy serynowo/treoninowej mTOR (ang. *serine/threonine-protein kinase mTOR*; mTOR)

oraz ligandu dla receptora programowanej śmierci PD-L1 (ang. *programmed death ligand 1*; PD-L1) w odpowiedzi na inkubację komórek z badanym związkiem [29].

AKT jest kinazą aktywowaną w odpowiedzi na bodźce, w tym czynniki wzrostu i składniki macierzy pozakomórkowej. Białko to reguluje wiele szlaków sygnalizacyjnych zaangażowanych w metabolizm, apoptozę oraz proliferację komórek [30]. Liczne badania [31] wykazały, że istnieje związek pomiędzy spadkiem aktywności AKT w odpowiedzi na inhibitory tego białka oraz zahamowaniem proliferacji komórek nowotworowych. Do tej pory opisano wiele obiecujących inhibitorów kinazy AKT, w tym: ipatasertib (RG7440), afuresertib (GSK2110183), uprosertib (GSK2141795) i capivasertib (AZD5363). Związki te wiążą się z miejscem aktywnym ATP enzymu, wykazując w ten sposób działanie cytotoksyczne i antyproliferacyjne [31]. Z kolei, mTOR jest jedną z kinaz aktywowanych przez AKT, która bierze udział w sygnalizacji komórkowej kontrolującej proliferację, wzrost oraz ruchliwość komórek. Badania przedkliniczne i kliniczne wykazały, że hamowanie szlaku AKT-mTOR prowadzi do regresji nowotworów u ludzi [32,33]. CDK2 jest kinazą białkową zaangażowaną w kontrolę przebiegu cyklu komórkowego. Jej selektywna inhibicja może przyczyniać się do zatrzymania cyklu komórkowego na granicy faz S (od ang. *synthesis*) oraz M (od ang. *mitosis*), prowadząc do zmniejszenia objętości i masy guza. Niskocząsteczkowe inhibitory kinazy CDK2 są przedmiotem intensywnych badań klinicznych. Jednakże do tej pory nie udało się wprowadzić na rynek farmaceutyczny wystarczająco specyficznej i skutecznej cząsteczki [34]. W przeciwieństwie do CDK2, zablokowanie interakcji pomiędzy receptorem programowanej śmierci 1 (ang. *programmed death receptor 1*; PD-1) oraz jego ligandem – PD-L1, uważane jest za podstawę nowoczesnej immunoterapii. Niektóre nowotwory potrafią unikać odpowiedzi układu odpornościowego poprzez aktywację i wykorzystanie punktów kontroli układu immunologicznego (ang. *immune checkpoint*), w tym PD-1/PD-L1, które działają na różnych etapach odpowiedzi odpornościowej i regulują czas trwania i nasilenia aktywności

limfocytów T. PD-1 stanowi punkt kontroli układu odpornościowego, który komórki nowotworowe mogą wykorzystać do ucieczki spod nadzoru układu immunologicznego. Ligandy PD-L1 i PD-L2 wiążą receptor PD-1 na limfocytach T i hamują ich aktywność. Poprzez ten mechanizm dochodzi do zablokowania odpowiedzi immunologicznej. Wyniki badań klinicznych sugerują wysoką skuteczność terapeutyczną przeciwciał monoklonalnych skierowanych przeciwko interakcji PD-1/PD-L1 [35,36]. Przeciwciała ukierunkowane na immunologiczny punkt kontrolny PD-1/PD-L1, prowadzą do poprawy skuteczności terapii nowotworowej w przypadku różnych typów nowotworów, w tym: czerniaka, drobnokomórkowego raka płuc, chłoniaka Hodgkina (ang. *Hodgkin's lymphoma*), raka płaskonabłonkowego głowy i szyi, czy raka wątrobowokomórkowego [37]. Wśród dopuszczonych do użytku klinicznego przeciwciał monoklonalnych, skierowanych przeciwko cząsteczce PD-1, wyróżnić można: pembrolizumab [38–40], niwolumab [41–43] i cemiplimab [44,45]. Ponadto, dostępne w leczeniu nowotworów są przeciwciała anty-PD-L1, w tym: atezolizumab [46–48], awelumab [49,50] oraz durwalumab [51,52]. Zdecydowana większość inhibitorów PD-1/PD-L1 stosowanych w warunkach klinicznych to przeciwciała monoklonalne, jednakże ich zastosowanie kliniczne jest ograniczone ze względu na niską biodostępność po podaniu doustnym oraz powodowane skutki uboczne. Dotychczas nie wprowadzono na rynek farmaceutyczny żadnych niskocząsteczkowych inhibitorów PD-1/PD-L1. Wykazano natomiast, że niektóre związki heterocykliczne zawierające azot, tj. pochodne 1,3,4-oksadiazolu, mają hamujący wpływ na interakcje PD-1/PD-L1 [53,54].

Inna sulfonamidowa pochodna pirazolo[4,3-*e*]tetrazolo[1,5-*b*][1,2,4]triazyny również wykazała obiecujący potencjał przeciwnowotworowy *in vitro*, wywierając hamujący wpływ na żywotność i proliferację ludzkich komórek nowotworowych jelita grubego (linia DLD-1 i HT-29) [24]. Wydaje się, że mechanizm molekularny działania związku, związany jest ze stymulacją zarówno wewnątrz-, jak i zewnątrzpochodnego szlaku apoptozy. Wiąże się to ze zwiększoną aktywnością

enzymów z grupy kaspaz, w tym kaspazy-8 oraz -9. Zaobserwowano również negatywną regulację syntezy kluczowych białek, biorących udział w progresji i przerzutowaniu raka jelita grubego człowieka, tj. rozpuszczalnej międzykomórkowej cząsteczki adhezyjnej-1 (ang. *soluble intercellular adhesion molecule-1*; sICAM-1), katepsyny B oraz kinazy mTOR, po inkubacji ww. komórek z badaną pochodną pirazolo-triazyny [24].

Aktywność cytotoksyczną, genotoksyczną, proapoptotyczną oraz prooksydacyjną związków będących pochodnymi pirazolo[4,3-*e*]tetrazolo[1,5-*b*][1,2,4]triazyny oceniono również w badaniach *in vitro,* przeprowadzonych na komórkach nowotworowych wyprowadzonych z tkanek innych narządów, tj. prostaty, szyjki macicy oraz trzustki. Ponownie, sulfonamidowe pochodne wykazywały wysoki potencjał przeciwnowotworowy, związany z indukcją uszkodzeń DNA, na co wskazały wyniki testu kometowego oraz znakowanie ufosforylowanego w pozycji Ser-139 histonu H2AX (γH2AX) [23,55].

W świetle powyższych danych, sulfonamidy z grupy pochodnych pirazolo[4,3-*e*][1,2,4]triazyny okazały się stanowić niezwykle interesującą grupę związków heterocyklicznych o zróżnicowanej aktywności biologicznej. Przeprowadzone, w ramach niniejszej rozprawy doktorskiej, zadania badawcze pozwoliły na ocenę stopnia, w jakim nowosyntetyzowane związki, będące pochodnymi pirazolo-triazyny, wykazują efektywne działanie przeciwnowotworowe w komórkach linii nowotworowych oraz prawidłowych człowieka, w różnych układach doświadczalnych oraz w aspekcie zróżnicowanych miejsc docelowych, poprzez analizę cyto- i genotoksyczności indukowanej przez badane związki i ich właściwości prooksydacyjnych i proapoptotycznych.

Poznanie mechanizmów działania badanych, nowych sulfonamidowych pochodnych pirazolo[4,3-*e*]tetrazolo[1,5-*b*][1,2,4]triazyny, a także ich potencjalnej aktywności przeciwnowotworowej związanej ze strukturą chemiczną, stanowi podstawę do dalszej optymalizacji farmakokinetycznej związków celem uzyskania

bardziej efektywnego działania onkoterapeutycznego i wyznaczenia kierunków kolejnych etapów badań na modelu *in vivo*.

5.2. Hipoteza badawcza

Hipotezą badawczą prezentowanej pracy doktorskiej było założenie, że badane związki wykazują wysoce efektywną aktywność przeciwnowotworową wobec komórek linii nowotworowych człowieka, osiągając jednocześnie niski profil toksyczności względem komórek prawidłowych, w układzie *in vitro*.

5.3. Główny cel pracy

Celem niniejszej pracy była ocena mechanizmów komórkowych, odpowiedzialnych za aktywność biologiczną nowych sulfonamidowych pochodnych pirazolo[4,3-*e*]tetrazolo[1,5-*b*][1,2,4]triazyny, w oparciu o analizy dotyczące stopnia ich cytotoksyczności i genotoksyczności, zdolności do indukowania apoptozy oraz stresu oksydacyjnego w komórkach linii nowotworowych i prawidłowych człowieka.

5.4. Cele szczegółowe pracy

1. Synteza sulfonamidowych pochodnych pirazolo[4,3-*e*]tetrazolo[1,5-*b*][1,2,4]triazyny.
2. Ocena właściwości cytotoksycznych oraz antyproliferacyjnych badanych związków w komórkach linii prawidłowych i nowotworowych człowieka.
3. Określenie stopnia genotoksyczności badanych związków w komórkach linii nowotworowych oraz prawidłowych człowieka.

4. Ocena zdolności nowych pochodnych pirazolo[4,3-*e*]tetrazolo [1,5-*b*][1,2,4]triazyny do indukcji apoptozy w komórkach linii nowotworowych człowieka.
5. Ocena zdolności prooksydacyjnych badanych związków w komórkach linii nowotworowych człowieka.
6. Analiza odpowiedzi komórek linii nowotworowych człowieka na testowane związki pod kątem zmian profilu ekspresji genów związanych z procesem apoptozy.

5.5. Materiały i metody badawcze

Linie komórkowe wykorzystane w badaniach

W badaniach wykorzystano następujące komórki linii nowotworowych człowieka:

- BxPC-3 (komórki gruczolakoraka trzustki, ang. *pancreas adenocarcinoma*, ATCC® CRL-1687™),
- HCT-116 (komórki raka jelita grubego, ang. *colorectal carcinoma*, ATCC® CCL-247 ™),
- PC-3 (komórki raka prostaty, ang. *prostate cancer*, ATCC® CRL-1435™).

Ponadto, w badaniach cytotoksyczności (*test MTT*), żywotności (*barwienie komórek błękitem trypanu*) oraz genotoksyczności (*wersja alkaliczna testu kometowego*) wykorzystano prawidłowe fibroblasty ludzkie - linia komórek WI-38 (ang. *human lung fibroblasts*, ATCC® CCL-75™) oraz prawidłowe fibroblasty mysie: linia komórek L929 (ang. *mouse fibroblasts*, ATCC® CCL-1™).

Charakterystyka badanych związków chemicznych

W prezentowanej pracy doktorskiej dokonano syntezy czterech syntetycznych sulfonamidowych pochodnych pirazolo[4,3-*e*]tetrazolo[1,5-

b][1,2,4]triazyny, które będą dalej nazywane związkami **MM**. Są one zbudowane z pierścienia tetrazolu, układu pirazolo[4,3-*e*][1,2,4]triazyny, ugrupowania fenylosulfonowego oraz heterocyklicznej reszty aminowej, którą jest: N-aminoetylolmorfolina (**MM134**), morfolina (**MM136**), N-metylopiperazyna (**MM137**) lub piperydyna (**MM139**) **(Rycina 2)**.

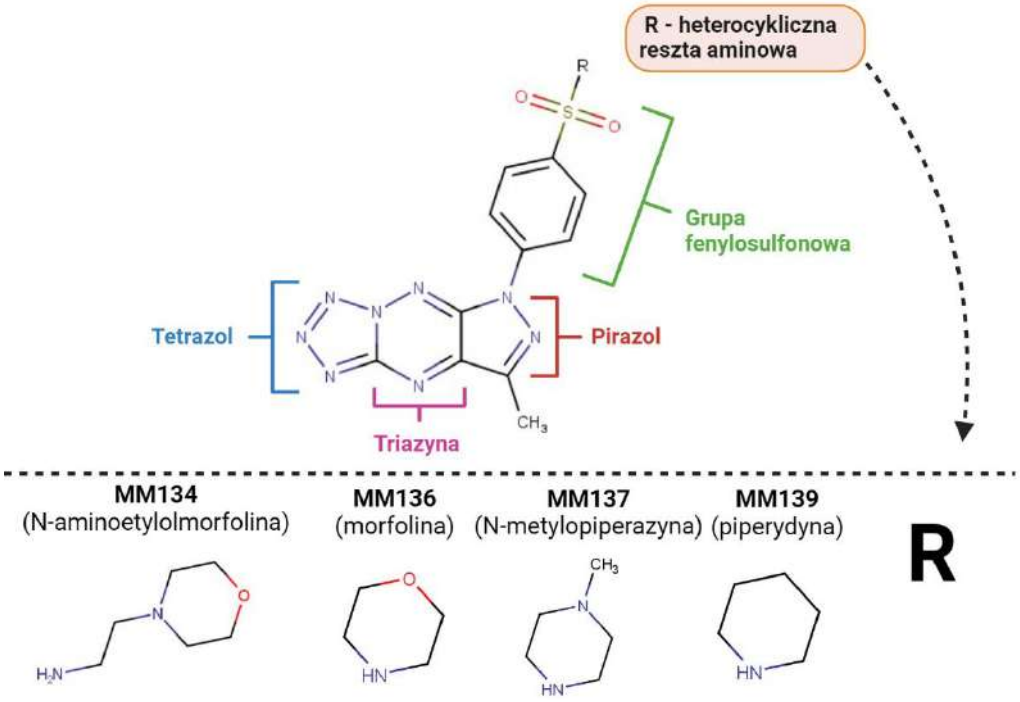

Rycina 2. Struktura chemiczna sufonamidowych pochodnych pirazolo[4,3-*e*]tetrazolo[1,5-*b*][1,2,4]triazyny użytych w badaniach: **MM134** (N-(2-morfolinoet-1-ylo)-4-[7-metylo-5H-pirazolo[4,3-*e*]tetrazolo[1,5-*b*][1,2,4]triazyn-5-yl)] benzenosulfonamid), **MM136** (N-(morfolin-1-ylo)-4-[7-metylo-5H-pirazolo[4,3-*e*]tetrazolo[1,5-*b*][1,2,4]triazyn-5-yl)] benzenosulfonamid), **MM137** (N-(morfolin-1-ylo)-4-[7-metylo-5H-pirazolo[4,3-*e*]tetrazolo[1,5-*b*][1,2,4]triazyn-5-yl)] benzenosulfonamid) oraz **MM139** (N-(morfolin-1-ylo)-4-[7-metylo-5H-pirazolo[4,3-*e*]tetrazolo[1,5-*b*][1,2,4]triazyn-5-yl)] benzenosulfonamid).

Metody badawcze wykorzystane w pracy

W pracy zastosowano następujące metody badawcze:

1. Synteza chemiczna związków oraz badania potwierdzające ich strukturę chemiczną:

- spektroskopia magnetycznego rezonansu jądrowego (ang. *nuclear magnetic resonance*; NMR).

2. Ocena właściwości cytotoksycznych oraz antyproliferacyjnych badanych związków:
    - test MTT (ang. *(3-(4,5-dimethylthiazol-2-yl)-2,5-diphenyltetrazolium bromide)*,
    - test wychwytu czerwieni obojętnej (ang. *neutral red uptake assay*),
    - test włączenia bromodeoksyurydyny (BrdU) (ang. *bromodeoxyuridine/5-bromo-2'-deoxyuridine incorporation assay*).
3. Ocena żywotności komórek:
    - barwienie komórek przy pomocy błękitu trypanu (ang. *trypan blue staining*),
    - test *Alamar Blue* (ang. *Alamar Blue assay*).
4. Określenie stopnia genotoksyczności indukowanej przez badane związki w komórkach linii nowotworowych oraz prawidłowych człowieka:
    A. Elektroforeza pojedynczych komórek, czyli test kometowy (ang. *comet assay/single cell gel electrophoresis assay*):
        - alkaliczna wersja testu kometowego (ang. *alkaline comet assay*),
        - neutralna wersja testu kometowego (ang. *neutral comet assay*).

    B. Immunofluorescencyjna detekcja ufosforylowanego histonu H2AX (γH2AX) (ang. *γH2AX staining*)
5. Ocena właściwości proapoptotycznych pochodnych pirazolo-triazyny w komórkach linii nowotworowych:
    - analiza cytometryczna poprzez identyfikację fosfatydyloseryny eksponowanej na powierzchni badanych komórek przy pomocy jodku propidyny oraz aneksyny V sprzężonej z izotiocyjanianem fluoresceiny (ang. *flow cytometry analysis with annexin V-FITC staining*),

- mikroskopowa ocena zmian w morfologii komórek przy zastosowaniu mieszaniny barwników fluorescencyjnych - oranżu akrydyny oraz bromku etydyny (ang. *dual acridine orange/ethidium bromide (AO/EB) fluorescent staining*),
- ocena zmian potencjału błony mitochondrialnej ($\Delta\Psi m$) za pomocą barwnika fluorescencyjnego *MitoTracker Red* (ang. *changes in transmembrane mitochondrial potential – MitoTracker Red*),
- oznaczenie aktywności kaspaz 3/7/8/9 przy pomocy sond fluorescencyjnych (ang. *caspase 3/7/8/9 detection*),
- analiza apoptotycznej fragmentacji DNA komórek (ang. *DNA laddering*).

6. Ocena zdolności prooksydacyjnych badanych związków w komórkach linii nowotworowych człowieka:
    - detekcja reaktywnych form tlenu (nadtlenku wodoru (H_2O_2), rodnika hydroksylowego (OH^-) oraz nadtlenoazotynu ($ONOO^-$)) przy pomocy dioctanu 2,7-dichlorodihydrofluoresceiny (ang. *2,7-dichlorodihydrofluorescein diacetate*; DCFH-DA).
7. Analiza przebiegu cyklu komórkowego oraz jego poszczególnych faz po inkubacji komórek linii nowotworowych z badanymi związkami:
    - cytometria przepływowa z wykorzystaniem barwienia DNA jodkiem propidyny.
8. Wpływ badanych związków na klonogenność komórek nowotworowych:
    - test klonogenny (ang. *clonogenic assay*).
9. Badanie zmian profilu ekspresji genów związanych z apoptozą:
    - łańcuchowa reakcja polimerazy DNA w czasie rzeczywistym (ang. *real-time polymerase chain reaction*; RT-PCR).

Metodologia została rozszerzona o badania obliczeniowe (*in silico*) realizowane we współpracy z ośrodkami zagranicznymi, w tym:

10. Ocenę parametrów ADMET (ang. *absorption, distribution, metabolism, excretion and toxicity*) badanych związków oraz określenie ich właściwości lekopodobnych (ang. *druglikeness*).
11. Identyfikację potencjalnych celów molekularnych badanych związków przy pomocy dokowania molekularnego (ang. *molecular docking*).
12. Ocenę stabilności kompleksów utworzonych pomiędzy badanymi związkami a celami molekularnymi przy zastosowaniu symulacji dynamiki molekularnej (ang. *molecular dynamics simulation*) oraz analiz post-dynamicznych.
13. Określenie właściwości elektronowych i strukturalnych cząsteczek przy wykorzystaniu teorii funkcjonału gęstości (ang. *density functional theory*; DFT).

6. Omówienie publikacji wchodzących w skład rozprawy doktorskiej

Choroby nowotworowe są jedną z najczęstszych przyczyn przedwczesnej umieralności ludzi w Polsce i na świecie. Wysoka zapadalność na schorzenia onkologiczne oraz towarzysząca im śmiertelność stwarzają pilną potrzebę opracowywania nowych onkoterapeutyków o wysokiej selektywności i bardziej efektywnych mechanizmach działania. W związku z tym, przeprowadzane są szeroko zakrojone badania, mające na celu opracowanie, syntezę oraz ocenę właściwości biologicznych wielu struktur chemicznych, mogących wykazywać potencjał przeciwnowotworowy. Podstawę strukturalną wielu powszechnie stosowanych w praktyce klinicznej leków, stanowią związki heterocykliczne [56,57]. Autorski artykuł przeglądowy [**publikacja nr 1 cyklu**] zwraca uwagę na 1,2,4-triazynę, jako chemiczną strukturę wiodącą, naturalnie występującą w związkach o różnorodnej aktywności biologicznej, która może stanowić podstawę do opracowania nowych związków, w tym hybryd z pierścieniem pirazolu. W **publikacji nr 1** opisano metody syntezy i funkcjonalizacji struktury pirazolo[4,3-*e*][1,2,4]triazyny, która z grupy związków skondensowanych pirazolotriazyn jest najsłabiej scharakteryzowana w literaturze naukowej. Właściwa funkcjonalizacja rdzenia heterocyklicznego jest kluczowym elementem projektowania nowych cząsteczek o potencjalnej aktywności biologicznej. W omawianej pracy przeglądowej dokonano podsumowania dotychczasowych wyników badań naukowców pracujących nad ww. układem heterocyklicznym. W **publikacji nr 1** przedstawione zostały metody otrzymywania pochodnych pirazolo[4,3-*e*][1,2,4]triazyny, w tym pochodnych sulfonamidowych oraz opisano ich aktywność cytotoksyczną/cytostatyczną względem komórek linii nowotworowych. Zwrócono również uwagę na potencjalne cele molekularne pirazolo[4,3-*e*][1,2,4]triazyn, których inhibicja mogłaby stanowić wyjaśnienie ich aktywności przeciwnowotworowej. Do ww. celów molekularnych należą anhydrazy węglanowe (CAIX i CAXII) oraz enzymy z rodziny kinaz, w tym kinaza

ABL oraz kinazy zależne od cyklin (CDK2). Wśród zaprezentowanych w **publikacji nr 1** przykładów, na szczególną uwagę zasługują trójcykliczne pirazolo[4,3-*e*][1,2,4]triazyny skondensowane z pierścieniem triazolowym lub tetrazolowym, które wykazują wyższą aktywność antyproliferacyjną niż stosowane klinicznie cytostatyki, tj. cisplatyna i 5-fluorouracyl.

Publikacja pt.: „*Preparation of Novel Pyrazolo[4,3-e]tetrazolo[1,5-b][1,2,4]triazine Sulfonamides and Their Experimental and Computational Biological Studies*" [**publikacja nr 2 cyklu**] stanowi pierwsze opracowanie wyników prac eksperymentalnych, mających na celu ocenę aktywności biologicznej nowych, sulfonamidowych pochodnych układu pirazolo[4,3-*e*][1,2,4]triazyny. W kolejnych sekcjach omawianej publikacji przedstawiona została metoda syntezy sulfonamidowych pochodnych pirazolo[4,3-*e*]tetrazolo[1,5-*b*][1,2,4]triazyny: **MM134**, **MM136**, **MM137** oraz **MM139**, uzupełniona badaniem z wykorzystaniem spektroskopii magnetycznego rezonansu jądrowego (ang. *nuclear magnetic resonance*; NMR), analizą ich cytotoksyczności oraz badaniami mającymi na celu ocenę proapoptotycznych właściwości związków **MM** wobec ludzkich komórek linii nowotworowych oraz prawidłowych.

Synteza sulfonamidowych pochodnych pirazolo[4,3-*e*]tetrazolo[1,5-*b*][1,2,4]triazyny [**publikacja nr 2; Figure 2**] została przeprowadzona zgodnie z metodologią opracowaną uprzednio przez **dr hab. Mariusza Mojzycha**, **prof. UPH w Siedlcach** i opisaną w pracy „*The Effect of Novel 7-methyl-5-phenyl-pyrazolo[4,3-e]tetrazolo[4,5-b][1,2,4]triazine Sulfonamide Derivatives on Apoptosis and Autophagy in DLD-1 and HT-29 Colon Cancer Cells*", w której poddano analizie również aktywność biologiczną (cytotoksyczność i zdolność do indukcji apoptozy oraz autofagii) dwóch związków, należących do grupy sulfonamidowych pochodnych pirazolo[4,3-*e*]tetrazolo[1,5-*b*][1,2,4]triazyn w komórkach linii nowotworowych jelita grubego [26]. Wcześniejsze badania wykazały, że w układach heterocyklicznych z końcowym pierścieniem tetrazolowym może występować tautomeria walencyjna, czyli stan równowagi pomiędzy pochodną

azydkową, a układem trójcyklicznym. Równowaga tautomeryczna jest ważnym i interesującym zjawiskiem chemicznym, ponieważ różne tautomery tego samego związku mogą wykazywać zróżnicowane właściwości fizykochemiczne, a nawet biologiczne, w zależności od przyjętej formy tautomerycznej. Dlatego przewidywanie składu mieszaniny tautomerycznej jest istotne dla projektowania nowych związków biologicznie czynnych [58–60]. Zjawisko tautomerii związków zostało również szerzej opisane w publikacji przeglądowej [**publikacja nr 1 cyklu**]. Analiza widm ^{1H} NMR badanych sulfonamidowych pochodnych [**publikacja nr 2; Figure 3**] wykazała, że forma tetrazolowa związków dominowała nad formą azydkową po ustaleniu równowagi tautomerycznej, co jest zgodne z wcześniejszymi wynikami badań i danymi literaturowymi [58,60–62].

W kolejnym etapie pracy poddano ocenie właściwości cytotoksyczne testowanych pochodnych. Zbadano wpływ 72-godzinnej inkubacji komórek linii nowotworowych (BxPC-3, HCT-116 i PC-3) oraz prawidłowych ludzkich (WI-38) i mysich (L929) fibroblastów z badanymi związkami **MM**. W oparciu o uzyskane dane, wyznaczono wartość IC_{50} (ang. *inhibitory concentration 50%*), odpowiadającą stężeniu związku pozwalającemu na zahamowanie aktywności metabolicznej komórek w 50% względem komórek stanowiących grupę kontrolną, dla której przyjmuje się wartość 100%. Badania potwierdziły wysoką (mikromolarną) cytotoksyczność związków **MM** oraz zależny od stężenia spadek żywotności komórek po ich uprzedniej inkubacji z badanymi pochodnymi pirazolo[4,3-*e*]tetrazolo[1,5-*b*][1,2,4]triazyny. Wyznaczone wartości IC_{50} mieściły się w zakresie 0,11–0,38 μM w przypadku komórek linii nowotworowych [**publikacja nr 2; Figure 4, Table 1**], oraz 0,18–0,58 μM dla prawidłowych komórek mysich linii L929 oraz 0,27–0,65 μM dla prawidłowych ludzkich fibroblastów płuc linii WI-38 [**publikacja nr 2; Figure 5, Table 1**]. Związki **MM** wykazywały wyższą aktywność cytotoksyczną względem komórek linii nowotworowych niż komórek prawidłowych, wskazując na potencjalnie selektywne działanie cytotoksyczne w stosunku do komórek zmienionych nowotworowo **(Tabela 1)**.

Tabela 1. Wartości IC_{50} wyznaczone po 72 godzinach inkubacji badanych komórek ze związkami **MM** (test MTT); ± SD.

Sulfonamidowe pochodne pirazolo[4,3-*e*]tetrazolo[1,5-*b*][1,2,4]triazyny	Linia komórkowa				
	IC_{50} ± SD [μM]				
	BxPC-3 (rak trzustki)	HCT-116 (rak jelita grubego)	PC-3 (rak prostaty)	L929 (linia prawidłowa)	WI-38 (linia prawidłowa)
MM134	0,32 ± 0,1	0,38 ± 0,03	0,16 ± 0,02	0,58 ± 0,005	0,65 ± 0,07
MM136	0,25 ± 0,08	0,25 ± 0,07	0,13 ± 0,01	0,22 ± 0,08	0,48 ± 0,09
MM137	0,16 ± 0,04	0,14 ± 0,02	0,11 ± 0,007	0,18 ± 0,0008	0,27 ± 0,04
MM139	0,33 ± 0,14	0,35 ± 0,05	0,17 ± 0,003	0,26 ± 0,02	0,54 ± 0,06

Najbardziej wrażliwe na cytotoksyczne działanie badanych pochodnych pirazolo[4,3-*e*]tetrazolo[1,5-*b*][1,2,4]triazyny były komórki raka prostaty (linia PC-3). Niższą wrażliwość wykazały komórki gruczolakoraka trzustki (linia BxPC-3) oraz komórki raka jelita grubego (linia HCT-116). Spośród testowanych związków **MM**, najwyższą aktywność cytotoksyczną względem badanych komórek wykazał związek **MM137**, na co wskazują wyznaczone wartości IC_{50}, mieszczące się w zakresie od 0,11–0,17 μM dla wykorzystanych w teście komórek linii nowotworowych [**publikacja nr 2**].

Kolejne zadanie badawcze obejmowało analizę aktywności proapoptotycznej związków **MM** względem komórek linii nowotworowych BxPC-3 oraz PC-3. Z uwagi na fakt, że wartości IC_{50} wyznaczone w teście MTT dla komórek linii HCT-116 i BxPC-3 były na bardzo zbliżonym poziomie, zdecydowano, że to linia komórkowa raka trzustki (BxPC-3), należąca do nowotworów o wysokiej śmiertelności i bardzo agresywnym przebiegu, zostanie wykorzystana do dalszych badań. W celu oceny zdolności pochodnych pirazolo-triazyn (związków **MM**) do indukcji apoptozy zostały zastosowane następujące metody badawcze: (a) cytometryczna analiza liczby komórek apoptotycznych i nekrotycznych poprzez identyfikację fosfatydyloseryny eksponowanej na powierzchni komórek apoptotycznych przy pomocy aneksyny V, sprzężonej z izotiocyjanianem fluoresceiny (ang. *fluorescein isothiocyanate*; FITC) oraz

jednoczesne barwienie DNA komórek jodkiem propidyny (ang. *propidium iodide*; PI), (b) mikroskopowa ocena morfologii komórek linii nowotworowych przy zastosowaniu mieszaniny barwników fluorescencyjnych - oranżu akrydyny (ang. *acridine orange*; OA) i bromku etydyny (ang. *ethidium bromide*; EB) oraz (c) ocena zmian potencjału błony mitochondrialnej ($\Delta\Psi m$) z użyciem barwnika fluorescencyjnego *MitoTracker Red*. Szczegółowy opis wybranych metod znajduje się w **sekcji 4.3. publikacji nr 2** prezentowanego cyklu. Po przeprowadzeniu badań z użyciem cytometru przepływowego, zaobserwowano istotny statystycznie ($p < 0,05$) wzrost liczby komórek apoptotycznych, po 24- i 48-godzinnej inkubacji komórek linii BxPC-3 z badanymi związkami **MM**, które w stężeniu odpowiadającym wyznaczonym wartościom $IC_{50,}$ indukowały apoptozę na poziomie 18,9–65,3% (24-godzinna inkubacja) oraz 40,8–86,9% (48-godzinna inkubacja). Najsilniejsze właściwości proapoptotyczne w komórkach linii BxPC-3 wykazywał związek **MM134**, który w stężeniu IC_{50} indukował ich apoptozę na poziomie 65,3 ± 9,1% po 24-godzinnej oraz 86,9 ± 1,16% po 48-godzinnej inkubacji z ww. związkiem [**publikacja nr 2; Figure 6**]. Natomiast w komórkach nowotworowych linii PC-3 nie zaobserwowano wzrostu liczby komórek apoptotycznych po 24-godzinnej inkubacji z testowanymi pochodnymi pirazolo-triazyny. Odnotowano natomiast, że związki **MM134**, **MM137** oraz **MM139** zastosowane przez 48 h w najwyższych stężeniach odpowiadających podwójnej wartości IC_{50} ($2xIC_{50}$), indukowały statystycznie istotny wzrost odsetka komórek apoptotycznych linii PC-3 w porównaniu z kontrolą negatywną. Wynosił on odpowiednio: 20,37 ± 2,5% (**MM134**), 38,93 ± 4% (**MM137)** oraz 15 ± 2,42% (**MM139**) [**publikacja nr 2; Figure 7**]. Jednocześnie, liczba komórek nekrotycznych po 24-godzinnej oraz 48-godzinnej inkubacji komórek linii PC-3 i BxPC-3 ze związkami **MM,** nie przekraczała poziomu 10% we wszystkich przeprowadzonych seriach doświadczalnych.

Podobna zależność została zaobserwowana przy zastosowaniu metody opartej na barwieniu komórek mieszaniną barwników fluorescencyjnych (OA/EB) [**publikacja nr 2; Figure 8–9**]. Związki **MM134** i **MM139** zastosowane w stężeniach IC_{50} oraz $2xIC_{50}$, indukowały statystycznie istotny wzrost frakcji komórek apoptotycznych linii BxPC-3, zarówno po ich 24-godzinnej, jak i 48-godzinnej inkubacji z ww. związkami. Nie zaobserwowano natomiast istotnego statystycznie ($p < 0,05$) wzrostu liczby komórek apoptotycznych po 24-godzinnej inkubacji ze związkami **MM136** i **MM137**. Podobnie jak w przypadku wyników uzyskanych w analizie cytometrycznej, nie odnotowano istotnego statystycznie wzrostu frakcji komórek apoptotycznych linii PC-3 po ich 24-godzinnej inkubacji z testowanymi pochodnymi pirazolo[4,3-*e*]tetrazolo[1,5-*b*][1,2,4]triazyny. Związki **MM134**, **MM137** i **MM139** indukowały statystycznie istotny wzrost frakcji komórek apoptotycznych linii PC-3 po 48-godzinnej inkubacji z ww. związkami w porównaniu z próbą kontrolną, w obu testowanych stężeniach, jednak ich średni udział w badanej populacji nie przekroczył 30% [**publikacja nr 2; Figure 8–9**].

W **Tabeli 2** zostały zestawione wyniki analizy cytometrycznej oraz podwójnego barwienia AO/EB, które potwierdzają podobny kierunek działania wszystkich badanych pochodnych pirazolo-triazyny. Rozbieżności w wielkościach poszczególnych frakcji apoptotycznych między zastosowanymi barwieniami mogą wynikać z różnic związanych z odmiennym mechanizmem liczenia komórek w próbach: w cytometrze przepływowym zliczana jest automatycznie większa liczba komórek w jednej próbie (10 000), z kolei w analizie mikroskopowej liczba analizowanych komórek w jednej próbie wynosi ≥ 200.

Tabela 2. Właściwości proapoptotyczne związków **MM134**, **-6**, **-7** oraz **-9** względem komórek nowotworowych linii BxPC-3 oraz PC-3 wykonane przy pomocy cytometru przepływowego oraz podwójnego barwienia AO/BE [63]. Wyniki przedstawiono, jako odsetek [%] komórek apoptotycznych w populacjach komórek linii BxPC-3 oraz PC-3 po ich ekspozycji na badane związki w stężeniu odpowiadającym uzyskanej w teście MTT **[Tabela 1]** wartości IC_{50}. Wyniki istotne statystycznie ($p < 0,05$) oznaczono pogrubioną czcionką; ± SD.

Zastosowana metoda	Linia komórkowa	Czas inkubacji	Kontrola negatywna	MM134	MM136	MM137	MM139
Detekcja fosfatydyloseryny przy pomocy kompleksu aneksyny V-FITC oraz jodku propidyny – cytometr przepływowy	BxPC-3	24 h	10,2 ± 2,09	**65,3 ± 9,1**	**41,7 ± 0,17**	18,9 ± 2,95	**59,6 ± 7,42**
		48 h	8,33 ± 1,13	**86,9 ± 1,16**	**56,3 ± 4,9**	**40,8 ± 1,36**	**85,4 ± 6,25**
	PC-3	24 h	6,5 ± 2,05	4,83 ± 0,94	5,23 ± 1,19	6,87 ± 0,58	4,53 ± 1
		48 h	8,37 ± 1,06	8,9 ± 0,26	7,23 ± 0,23	**22,5 ± 3,18**	8,9 ± 0,76
Barwienie OA/EB	BxPC-3	24 h	5 ± 4,24	**20,5 ± 0,7**	13,5 ± 3,6	15 ± 1,4	**25,5 ± 0,7**
		48 h	2,5 ± 0,7	**41,5 ± 0,7**	**43,2 ± 1,7**	**38,8 ± 13**	**57,3 ± 10,3**
	PC-3	24 h	5,1 ± 2,69	5 ± 1,4	5,5 ± 2,12	8,5 ± 2,12	5,5 ± 0,7
		48 h	1,5 ± 0,7	**8,5 ± 0,7**	6	**15 ± 2,83**	**13,5 ± 3,53**

Badania właściwości proapoptotycznych nowych pochodnych pirazolo[4,3-*e*]tetrazolo[1,5-*b*][1,2,4]triazyny zostały dopełnione o analizę transbłonowego potencjału mitochondrialnego (ang. *mitochondrial membrane potential*; MMP; $\Delta\Psi m$), przy pomocy fluorescencyjnego barwnika *MitoTracker Red*. Intensywność obserwowanej fluorescencji odzwierciedla prawidłową funkcję mitochondriów i zmienia się wraz ze zmianami w ich potencjale transbłonowym. Przeprowadzone badania wykazały, że związki **MM** zaburzały funkcjonowanie mitochondriów, czego efektem był zależny od dawki, spadek obserwowanej fluorescencji w badanych populacjach komórek nowotworowych linii BxPC-3 oraz PC-3 [**publikacja nr 2; Figure 11, Table 2**]. Uzyskane wyniki, sugerują aktywację

wewnątrzpochodnego szlaku apoptozy i są zgodne z wcześniejszymi doniesieniami Hermanowicz i wsp. [25] oraz Bukowskiego i wsp. [55], a dotyczącymi oceny aktywności biologicznej pochodnych pirazolo-triazyny.

Wyniki badań *in silico* przeprowadzone we współpracy z ośrodkami zagranicznymi, opublikowane w **publikacji nr 2** [**sekcja 2.4.**], **publikacji nr 3** [**sekcja 2.6.**] oraz **publikacji nr 4** [**sekcja 2.2.**], zostały omówione w ostatniej części niniejszego opracowania.

W **publikacji nr 3** zostały wykonane analizy potencjału genotoksycznego badanych pochodnych pirazolo[4,3-*e*]tetrazolo[1,5-*b*][1,2,4]triazyny przy pomocy trzech metod, różniących się specyficznością wykrywanych uszkodzeń. Z definicji przez genotoksyczność rozumiemy zdolność czynników chemicznych, fizycznych lub biologicznych do uszkadzania materiału genetycznego komórek [64,65]. Alkaliczna wersja testu kometowego (ang. *alkaline comet assay*) umożliwia wykrywanie szerokiego spektrum uszkodzeń DNA, w tym miejsc alkalicznie labilnych oraz pęknięć nici DNA [66–70]. Neutralna wersja tego testu (ang. *neutral comet assay*) pozwala na specyficzną detekcję dwuniciowych pęknięć w DNA (ang. *double-strand breaks; DSBs*) pojedynczych komórek [71]. Trzecią zastosowaną metodą było immunofluorescencyjne znakowanie skupisk ufosforylowanego histonu γH2AX, pozwalające na wizualizację uszkodzeń DNA również o charakterze dwuniciowych pęknięć. W porównaniu do poprzednich testów, charakteryzuje się on wyższą czułością, pozwalającą np. na wykrycie pęknięć DNA związanych z procesami naprawczymi w komórkach (niewykrywalnymi w teście kometowym), a które mają potencjał do indukcji szlaku odpowiedzi na uszkodzenia DNA (ang. *DNA damage response*; DDR) [72,73], który odpowiedzialny jest za aktywację mechanizmów naprawy DNA lub eliminację komórek na drodze śmieci apoptotycznej [74,75] **(Rycina 3)**.

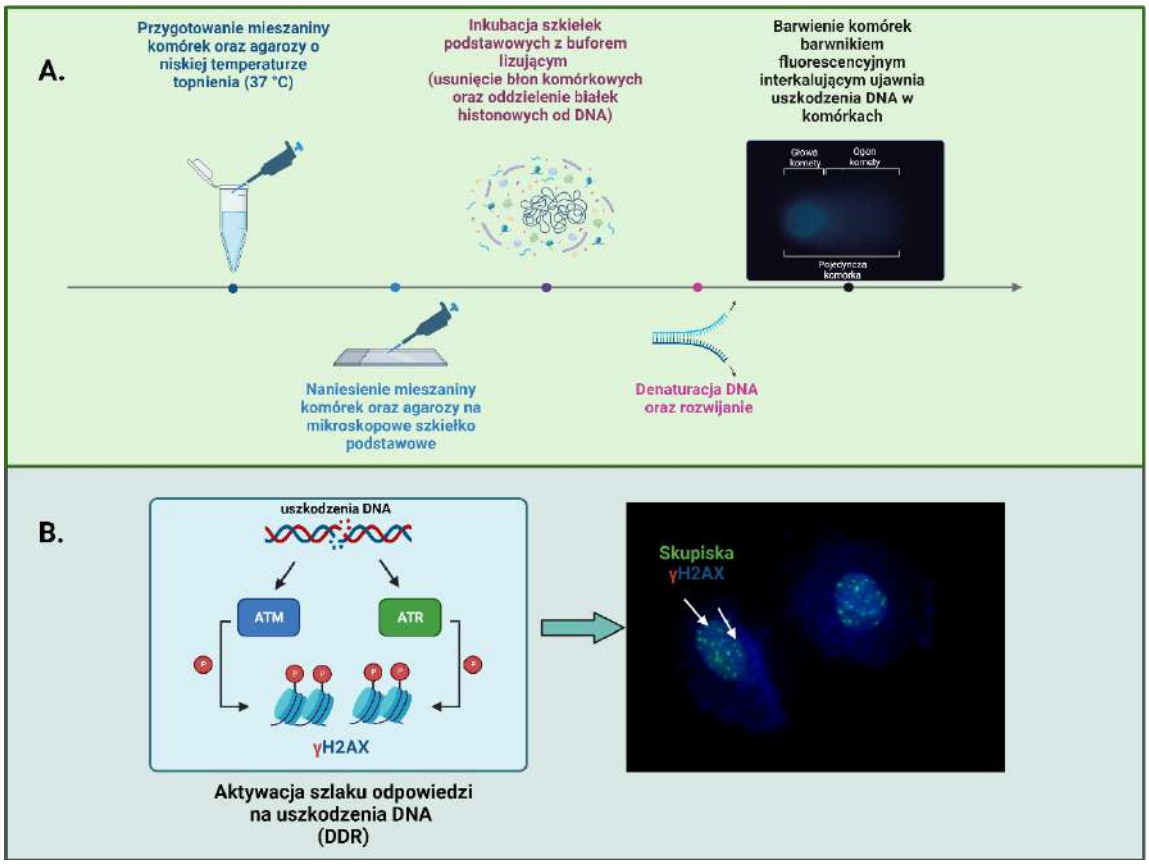

Rycina 3. **(A)** Etapy testu kometowego; (**B**) Detekcja ufosforylowanego histonu γH2AX (uszkodzenia DNA są bezpośrednią przyczyną indukcji szlaku DDR, w którym kinazy serynowo-treoninowe ATM oraz ATR fosforylują seryny 139 (Ser-139) histonów H2AX, prowadząc do powstawania skupisk γH2AX w miejscach pojawienia się dwuniciowych pęknięć DNA).

Ponadto, przed przystąpieniem do testów związanych z oznaczeniem stopnia genotoksyczności indukowanej przez związki **MM**, przeprowadzona została ocena żywotności komórek z użyciem błękitu trypanu oraz resazuryny (test Alamar Blue) [**publikacja nr 3, sekcja 4.4. oraz 4.5.**]. 24-godzinna inkubacja komórek linii nowotworowych BxPC-3 oraz PC-3 z testowanymi pochodnymi pirazolo[4,3-*e*]tetrazolo[1,5-*b*][1,2,4]triazyny, we wszystkich badanych stężeniach, nie spowodowała spadku żywotności komórek poniżej przyjętej w literaturze naukowej wartości granicznej [76–78], wynoszącej 70% [**publikacja nr 3; Figure 3 oraz Figure 4**].

W wyniku 24-godzinej inkubacji komórek linii nowotworowych linii BxPC-3 oraz PC-3 ze związkami **MM**, zaobserwowano, zależny od dawki wzrost

uszkodzeń DNA w obu wariantach testu kometowego [**publikacja nr 3**]. Wyniki alkalicznej wersji testu kometowego wykazały zróżnicowane działanie genotoksyczne związków **MM134**, **MM136**, **MM137** oraz **MM139** w komórkach linii nowotworowych BxPC-3 i PC-3 [**publikacja nr 3; Figure 5**]. Po 24-godzinnej inkubacji ze związkami **MM**, zastosowanymi w stężeniach równych wyznaczonej wartości IC_{50} dla danej linii komórkowej, najwyższy potencjał genotoksyczny został odnotowany dla związków **MM136** i **MM139** w komórkach linii BxPC-3. Z kolei, w komórkach linii PC-3 najefektywniej indukował uszkodzenia DNA związek **MM137** i **MM139**. Ponadto, komórki linii BxPC-3 wykazały wyższą wrażliwość na działanie związków **MM** niż komórki linii PC-3. Natomiast 24-godzinna inkubacja prawidłowych fibroblastów płuc człowieka (linia komórkowa WI-38) z badanymi związkami **MM**, nie spowodowała znaczącego wzrostu stopnia uszkodzeń DNA w badanych komórkach. Warto podkreślić, że komórki linii WI-38 poddano działaniu związków **MM** w stężeniach odpowiadających wyznaczonym wartościom IC_{50}, których zakres był wyższy (0,27–0,65 μM) niż w przypadku wartości IC_{50} otrzymanych dla komórek linii nowotworowych (0,11–0,33 μM) [**publikacja nr 3; Figure 6**]. Po przeprowadzeniu neutralnej wersji testu kometowego, wykazano, że po 24-godzinnej ekspozycji komórek nowotworowych linii BxPC-3 na działanie związków **MM** najwyższy poziom uszkodzeń DNA odnotowano dla związków **MM134** oraz **MM136**, podczas gdy związki **MM136** i **MM139** wykazywały najsilniejszą aktywność genotoksyczną w komórkach linii PC-3. W większości serii doświadczalnych zaobserwowano wzrost liczby pęknięć dwuniciowych DNA wraz ze wzrostem stężenia badanego związku [**publikacja nr 3; Figure 8**]. Wyniki alkalicznej oraz neutralnej wersji testu kometowego zostały podsumowane w **Tabeli 3**.

Tabela 3. Procent [%] uszkodzeń DNA w komórkach linii nowotworowych BxPC-3 i PC-3 oraz komórkach prawidłowych (WI-38) po 24-godzinnej inkubacji ze związkami **MM134**, **-6**, **-7** oraz **-9** użytymi w stężeniu równym wyznaczonej wartości IC_{50} oraz $2xIC_{50}$; 20 μM bleomycyna stanowiła kontrolę pozytywną eksperymentu. Dane przedstawiono, jako medianę parametru „% DNA w ogonie komety" wraz z rozstępem międzykwartylowym (nawias). Wyniki istotne statystycznie ($p < 0,05$) zaznaczono pogrubieniem czcionki.

Wersja testu kometowego	**Linia komórkowa**	**Kontrola negatywna**	**MM134**		**MM136**		**MM137**		**MM139**		**Bleomycyna**
			IC_{50}	**2x IC_{50}**	**IC_{50}**	**2xIC_{50}**	**IC_{50}**	**2xIC_{50}**	**IC_{50}**	**2xIC_{50}**	**(20 μM)**
Alkaliczna	BxPC-3	0,18 (0,01–1,4)	**2,5** (0,4–14,7)	**14,7** (3,3–31,7)	**8,26** (0,4–20,8)	**18,8** (2,5–38,5)	**3,28** (0,22–16,8)	**11,6** (1,7–28,7)	**4,74** (0,86–16,4)	**7,6** (1,4–16,9)	**50,7** (37,3–62)
	PC-3	0,9 (0,09–2,96)	**1,03** (0,14–5,8)	**1,6** (0,26–9,1	**1,63** (0,4–13,8)	**4,54** (0,72-23)	**2,32** (0,45–11,8)	**3,8** (0,9–18)	**3,35** (0,63–22)	**11,7** (2,4–28,7)	**19,3** (5,5–34,8)
	WI-38	0,05 (0,004–0,4)	**1,5** (0,17–5,2)	**0,99** (0,02–6,6)	0,01 (0,0008–0,2)	**1,06** (0,03–4,6)	0,09 (0,007–0,94)	**0,25** (0,01–2,6)	0,085 (0,005–1,32)	**0,23** (0,001–4,17)	**29,1** (16,5–50,4)
Neutralna	BxPC-3	2,5 (1,26–4,08)	**4,21** (2,45–6,6)	**8** (3,7–16,1)	**4,10** (1,63–6,8)	**5,06** (2,3–7,1)	2,86 (1,25–5,48)	**4,07** (1,9–8,1)	**3,72** (2,48–5,61)	**4,8** (2,3–11,2)	**9,7** (6,8–16,7)
	PC-3	1,5 (0,03–2,83)	**4,09** (2,22–7,26)	**5** (2,6–9,3)	**4,6** (0,63–10,9)	**5,3** (4–7,9)	**2,82** (1,7–5,53)	**5,2** (2–7,9)	**5** (3,19–7,24)	**6,5** (4,7–8,8)	**10,4** (5,5–16,4)

W celu dalszej oceny zdolności związków **MM** do indukcji pęknięć dwuniciowych DNA w badanych komórkach po 24-godzinnej inkubacji, wykorzystano immunofluorescencyjną detekcję ufosforylowanego histonu H2AX (γH2AX). Histon H2AX jest jednym z najważniejszych substratów kinaz ATM (ang. *serine-protein kinase*) oraz ATR (ang. *ATR serine/threonine kinase*), aktywowanych w odpowiedzi na uszkodzenia DNA. Skupiska (ang. *foci*) ufosforylowanego histonu γH2AX stanowią marker pojawiających się w materiale genetycznym komórki dwuniciowych pęknięć DNA oraz odpowiedzialne są za rekrutację białek, które pośredniczą i stabilizują szlak sygnalizacyjny DDR [79–81]. Ze względu na relatywnie duży rozmiar komórek, umożliwiający dokładną i wiarygodną analizę skupisk ufosforylowanego histonu γH2AX, w przeprowadzonym teście wykorzystano komórki linii PC-3. Pomimo podjętych prób optymalizacji procesu znakowania, w przypadku komórek linii BxPC-3 nie udało się uzyskać wystarczającej rozdzielczości, która pozwoliłaby na ilościową analizę skupisk histonu γH2AX. Po 24-godzinnej inkubacji ze związkami **MM** w stężeniach odpowiadającym wartościom IC_{50}, zaobserwowano istotny statystycznie ($p < 0,05$) wzrost liczby ognisk γH2AX w porównaniu z kontrolą negatywną [**publikacja nr 3; Figure 10**].

Przeprowadzone badania genotoksyczności związków **MM** wykazały, najwyższą aktywność związku **MM134**, nieco niższą związków **MM137**, **MM139** oraz najsłabszą związku **MM136** względem komórek linii BxPC-3 [**publikacja nr 3; Figure 10**].

Wiele leków przeciwnowotworowych, np. związki platyny (cisplatyna, oxaliplatyna) [82], doksorubicyna [83,84], bleomycyna [85] oraz kamptotecyna, działa poprzez indukowanie stresu oksydacyjnego w komórkach nowotworowych [86]. Badania właściwości prooksydacyjnych oraz proapoptotycznych związków **MM** poprzedzono wykonaniem testu wychwytu czerwieni obojętnej (ang. *neutral red uptake assay*). Test pozwala na ocenę przepuszczalności błony komórkowej i aktywności lizosomalnej komórek, umożliwiając detekcję oprócz komórek

żywych także i martwych [87,88]. Przeprowadzony test umożliwił weryfikację wyznaczonych w teście MTT wartości IC_{50} **(Tabela 4)**.

Tabela 4. Wartości IC_{50} [μM] oszacowane po 24-godzinnej inkubacji komórek nowotworowych linii BxPC-3 oraz PC-3 w dwóch niezależnych eksperymentach za pomocą testu wychwytu czerwieni obojętnej. Wartości IC_{50} ± SD zaprezentowano wraz z odpowiadającymi im współczynnikami determinacji (ang. *coefficients of determination* (R^2))

Pirazolo[4,3-*e*]tetrazolo[1,5-*b*][1,2,4]triazyna	**$IC_{50\ (1)}$ [μM]**	**$R^2_{(1)}$**	**$IC_{50\ (2)}$ [μM]**	**$R^2_{(2)}$**	**Średnie stężenie IC_{50} ± SD [μM]**
BxPC-3					
MM134	0,36	0,93	0,35	0,97	**0,35** ± 0,007
MM136	0,24	0,99	0,3	0,99	**0,27** ± 0,04
MM137	0,17	0,95	0,19	0,94	**0,18** ± 0,014
MM139	0,27	0,99	0,3	0,98	**0,28** ± 0,02
PC-3					
MM134	0,07	0,89	0,13	0,97	**0,1** ± 0,04
MM136	0,12	0,99	0,14	0,98	**0,13** ± 0,014
MM137	0,06	0,99	0,06	0,99	**0,06**
MM139	0,21	0,99	0,14	0,99	**0,17** ± 0,05

Obliczone w teście z czerwienią obojętną wartości IC_{50} mieściły się w zakresie 0,18–0,35 μM dla komórek linii BxPC-3 oraz 0,06–0,17 μM dla komórek linii PC-3 i były zbieżne z uzyskanymi wartościami w teście MTT. Linia komórek nowotworowych PC-3 wykazywała najwyższą wrażliwość na cytotoksyczne działanie związków **MM**, przy czym najbardziej efektywne działanie cytotoksyczne, odnotowano dla związku **MM137** IC_{50} = 0,18 μM dla komórek BxPC-3 oraz 0,06 μM dla komórek PC-3 [**publikacja nr 4; Tabela S1**].

Komórkowe poziomy reaktywnych form tlenu (RFT) zostały oznaczone przy użyciu sondy fluorescencyjnej dioctanu 2,7-dichlorodihydrofluoresceiny (ang. *2,7-dichlorodihydrofluorescein diacetate*; DCFH-DA), która dyfunduje przez błonę komórkową, gdzie przy udziale esteraz jest hydrolizowana do 2',7'-dichlorodihydrofluoresceiny (ang. *2',7'-dichlorodihydrofluorescein*; DCFH2)

i pozostaje w cytoplazmie. Utlenianie DCFH2 prowadzi do powstania fluorescencyjnej 2′,7′-dichlorofluoresceiny (ang. *2′,7′-dichlorofluorescein*; DCF) o widmie ekscytacji (λex = 503 nm) i emisji (λem = 523 nm). Sonda jest doskonałym czujnikiem ogólnego stresu oksydacyjnego, ponieważ reaguje z wieloma RFT, w tym nadtlenkiem wodoru, rodnikiem hydroksylowym i peroksyazotynem [89]. Indukcję RFT w komórkach linii BxPC-3 i PC-3 oszacowano po 1-godzinnej inkubacji z **MM134**, **-6**, **-7** oraz **-9** przy użyciu DCFH-DA [**publikacja nr 4; Figure 1**].

We wszystkich badanych stężeniach ($^1/_2IC_{50}$, IC_{50}, $2xIC_{50}$) związki **MM134**, **-6**, **-7** i **-9** indukowały istotny statystycznie (p < 0,05) wzrost produkcji RFT w komórkach linii BxPC-3 w porównaniu z kontrolą negatywną. Niemniej, obserwowane poziomy RFT spadały wraz ze wzrostem stężenia związków **MM134**, **MM136** i **MM139** [**publikacja nr 4; Figure 1A**]. Jak zilustrowano na Rycinie 1B [**Figure 1B**], badane związki **MM** wykazywały zróżnicowaną aktywność prooksydacyjną wobec komórek linii PC-3, w zależności od zastosowanego stężenia, np. związek **MM137** we wszystkich badanych stężeniach indukował stres oksydacyjny na poziomie wyższym od zaobserwowanego w kontroli negatywnej podczas gdy pochodna **MM136** w najwyższym z zastosowanych stężeń ($2xIC_{50}$), wykazywała najniższą aktywność prooksydacyjną.

W **publikacji nr 3** wykazano, że związki **MM134**, **MM136**, **MM137** oraz **MM139** charakteryzują się aktywnością genotoksyczną, czego odzwierciedleniem było powstawanie pęknięć DNA w komórkach nowotworowych. Ponadto, działają proapoptotycznie, zarówno w stosunku do komórek linii BxPC-3, jak i PC-3, na co wskazały zmiany transbłonowego potencjału mitochondrialnego, ekspozycja fosfatydyloseryny na powierzchni komórek oraz charakterystyczne dla apoptozy zmiany morfologii ich, w tym kondensacja chromatyny, czy tzw. „wrzenie" błony komórkowej [**publikacja nr 2**].

W **publikacji nr 4** cyklu zostały przeprowadzone ostatnie dedykowane procesowi apoptozy analizy aktywności kaspaz 3/7/8/9. Aktywność enzymatyczna

kaspaz w komórkach linii nowotworowych BxPC-3 oraz PC-3, została oznaczona po 24-godzinnej inkubacji z testowanymi pochodnymi pirazolo[4,3-*e*]tetrazolo[1,5-*b*][1,2,4]triazyny [**publikacja nr 4; Figure 2**]. Związki **MM134**, **MM136** oraz **MM139** użyte w stężeniu IC_{50} oraz $2xIC_{50}$ indukowały statystycznie istotny ($p < 0,05$) wzrost aktywności kaspaz efektorowych 3/7 w komórkach linii BxPC-3, w porównaniu z kontrolą negatywną, podczas gdy związek **MM137** wykazywał istotność statystyczną jedynie w najwyższym z zastosowanych stężeń [**publikacja nr 4; Figure 2A**].

Nie odnotowano wzrostu aktywności enzymatycznej kaspazy-3 oraz -7 w komórkach linii PC-3 po inkubacji ze związkami **MM** [**publikacja nr 4, Figure 2B**] w porównaniu z kontrolą negatywną. Podobnie, nie zaobserwowano zmian morfologicznych komórek, charakterystycznych dla procesu apoptozy podczas obrazowania metodą barwienia mieszaniną oranżu akrydyny oraz bromku etydyny, a także w czasie detekcji fosfatydyloseryny eksponowanej na powierzchni komórek [**publikacja nr 2; Figure 7, Figure 9**].

Ze względu na wcześniejszy brak aktywności proapoptotycznej związków **MM** w stosunku do komórek linii PC-3, do analizy aktywności kaspazy-8 i -9 wykorzystano komórki linii BxPC-3 [**publikacja nr 4; Figure 2C/D**]. W przeprowadzonych testach zaobserwowano stosunkowo niską aktywność kaspaz, co mogło być spowodowane m.in. hamującym działaniem związków **MM** na ich aktywność, a także tempo proliferacji komórek badanych linii nowotworowych.

W kolejnym etapie badań, został przeprowadzony test włączenia bromodeoksyurydyny (BrdU) [**publikacja nr 4; Figure 3**] oraz test klonogenności [**publikacja nr 4; Figure 4**] po inkubacji komórek z pochodnymi pirazolo[4,3-*e*]tetrazolo[1,5-*b*][1,2,4]triazyny.

Zahamowanie proliferacji komórek linii PC-3 pod wpływem związków **MM** zbadano przy pomocy immunofluorescencyjnej detekcji BrdU. Związki **MM** zastosowane w najwyższym stężeniu ($2xIC_{50}$) indukowały statystycznie istotny

(p < 0,05) spadek liczby komórek proliferujących w próbach badanych, w porównaniu z kontrolą negatywną (% proliferujących komórek = 88,5 ± 0,98). Związek **MM139** prowadził do najsilniejszego zahamowania proliferacji komórek (% proliferujących komórek = 46,8 ± 0,77; p = 0,0002) i wykazał wyższe działanie cytostatyczne niż zastosowana, jako kontrola pozytywna cisplatyna (10 μM) (% proliferujących komórek = 62 ± 2,8). Co ciekawe, inkubacja komórek linii PC-3 ze związkiem **MM137,** zastosowanym w stężeniu równym wartości IC_{50}, spowodowała statystycznie istotny spadek liczby komórek proliferujących w próbie (% proliferujących komórek = 65,6 ± 5,79; p = 0,04) [**publikacja nr 4; Figure 3, Table S2**]. Niestety, w przypadku komórek linii BxPC-3 nie udało się zoptymalizować metody detekcji BrdU, w sposób umożliwiający na ilościową ocenę preparatów.

Test klonogenny (ang. *clonogenic assay*), znany również, jako test tworzenia kolonii (ang. *colony formation assay*), jest rodzajem testu określającym stopień przeżywalności komórek *in vitro*, pozwalającym na ocenę potencjału pojedynczej komórki do tworzenia kolonii. Utworzone kolonie podlegają analizie ilościowej po utrwaleniu aldehydem glutarowym oraz barwieniem fioletem krystalicznym [**publikacja nr 4; Figure S2, Figure 4**]. Przeprowadzone oznaczenia wykazały, statystycznie istotny (p < 0,05) spadek zdolności tworzenia kolonii po 10-dniowej inkubacji ze związkami **MM**, zarówno w przypadku komórek linii BxPC-3, jak i PC-3. Związki **MM136** oraz **MM139** wykazywały najsilniejsze działanie hamujące powstawanie kolonii komórek BxPC-3. Z kolei, związki **MM137** oraz **MM139** wykazywały najsilniejsze działanie hamujące tworzenie kolonii komórek linii PC-3 [**publikacja nr 4; Figure 4**]. Wyniki przeprowadzonych testów (z BrdU oraz testu klonogenności) wskazują na silne działanie antyproliferacyjne oraz antyklonogenne badanych związków **MM**.

Kolejnym etapem badań wykonanych w ramach prezentowanej pracy doktorskiej, była analiza przebiegu cyklu komórkowego oraz jego poszczególnych faz w komórkach linii nowotworowych przy użyciu cytometru przepływowego.

Przeprowadzone badania nie wykazały istotnie statystycznych zmian w cyklu podziałowym po 24-godzinnej inkubacji badanych komórek linii nowotworowych ze związkami **MM**. Nie zaobserwowano również obecności populacji komórek w fazie sub-G1, która odpowiada fragmentacji DNA zachodzącej podczas procesu apoptozy [**publikacja nr 4; Figure 5**]. Jednak odnotowana nieobecność ww. frakcji komórek nie wyklucza możliwości inicjacji apoptozy przez związki **MM**, gdyż fragmenty DNA mogą być nadal zatrzymywane w jądrze komórkowym [90]. Może o tym świadczyć obecność pęknięć nici DNA po inkubacji badanych komórek ze związkami **MM**, która została potwierdzona w teście kometowym i immunofluorescencyjnym barwieniu histonu γH2AX [91].

Fragmentacja DNA jest jednym z charakterystycznych elementów apoptozy. Endonukleazy aktywowane w odpowiedzi na kaskadę kaspaz, rozkładają DNA komórki na fragmenty o długości 180-200 par zasad lub ich wielokrotności, co w trakcie analizy żelowej skutkuje pojawieniem się tzw. drabinki (ang. *ladder)* [92,93]. W badaniach skupiono się na komórkach linii BxPC-3, które podczas badań ekspozycji fosfatydyloseryny wykazywały większą wrażliwość na proapoptotyczne działanie związków [63]. Jednakże, podobnie jak w przypadku analizy cyklu komórkowego, w której nie zaobserwowano frakcji komórek subG1 odpowiadającej fragmentacji DNA, tutaj również nie stwierdzono drabinkowania (ang. *laddering*) DNA [**publikacja nr 4; Figure 6**] **(Rycina 4)**.

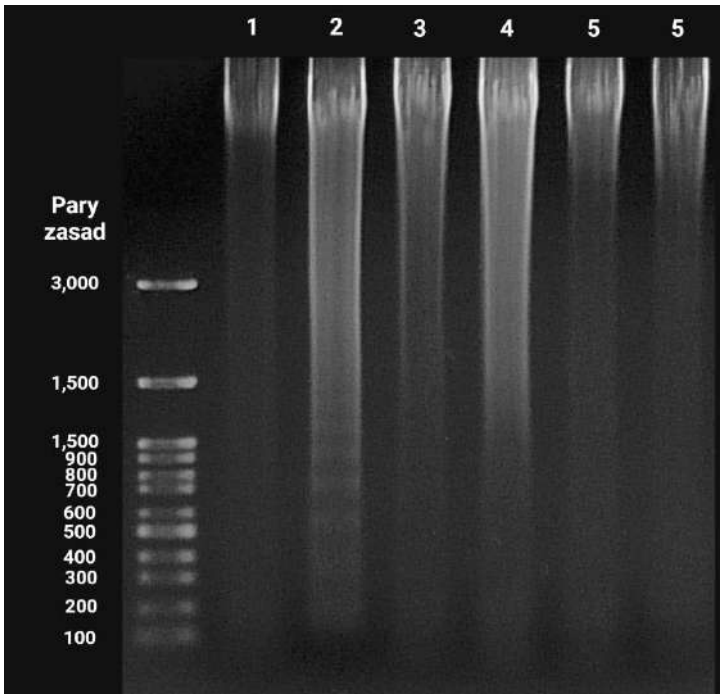

Rycina 4. Fragmentacja DNA komórek linii BxPC-3 poddanych 24-godzinnej ekspozycji na związki **MM134**, **-6**, **-7** oraz **-9**, użyte w stężeniach odpowiadających stężeniom IC_{50}, oszacowanym przy pomocy testu wychwytu czerwieni obojętnej: **(1)** kontrola negatywna (dimetylosulfotlenek; DMSO), **(2)** 2 μM 7-etylo-10-hydroksykamptotecyna (SN-38), **(3) MM134**, **(4) MM136**, **(5) MM137**, **(6) MM139**.

Przedstawione wyniki poziomu fragmentacji DNA wraz z ekspozycją fosfatydyloseryny na powierzchni komórek poddanych działaniu związków **MM**, mogą sugerować na indukcję wczesnego stadium apoptozy lub indukcję innego rodzaju śmierci komórkowej (np. nekroptozy).

Ostatecznych konkluzji dyskryminujących rodzaj śmierci komórkowej, indukowanej przez badane sulfonamidowe pochodne pirazolo[4,3-*e*]tetrazolo[1,5-*b*][1,2,4]triazyny, dostarczyły badania dotyczące zmiany ekspresji genów w komórkach, zachodzące po 24-godzinnej inkubacji komórek linii BxPC-3 ze związkiem **MM134**, w stężeniu IC_{50}, po zastosowaniu, którego odnotowano najwyższą aktywność proapoptotyczną podczas analizy cytometrycznej. Oceniono zmiany profilu ekspresyjnego 96 genów przy pomocy łańcuchowej reakcji polimerazy DNA w czasie rzeczywistym (ang. *real-time polymerase chain reaction*; RT-PCR). W celu określenia profilu ekspresji genów w badanych komórkach,

wykorzystano komercyjny zestaw *RT² Profiler PCR Array analysis of human apoptotic gene expression (PAHS-012Z)* firmy Qiagen [**publikacja nr 4; Figure 7**]. Różnice w ekspresji genów między próbą kontrolną (DMSO), a grupą poddaną działaniu związku **MM134** uznano za istotne dla $p < 0,05$.

W przeprowadzonych badaniach, jako wartość graniczną przyjęto absolutny współczynnik regulacji (ang. a*bsolute fold regulation*) > 2, który jest biologicznym odzwierciedleniem zmiany względnej ekspresji genu (ang. *fold change*). Współczynnik *fold change* ($2^{-\Delta\Delta Ct}$) jest znormalizowaną ekspresją ($2^{-\Delta Ct}$) genu w próbie badanej, podzieloną przez znormalizowaną ekspresję genu w próbie kontrolnej. Wartości współczynnika regulacji (*fold regulation*) powyżej jedności wskazują na zwiększenie ekspresji genu. Z kolei, poniżej jedności wskazują na zmniejszenie ekspresji genu. Uzyskane wyniki wykazały zróżnicowaną ekspresję 33 genów pomiędzy badanymi populacjami komórek ($p < 0,05$). Wyniki przedstawiono na **Rycinie 5** oraz w **Tabeli 5** [**publikacja nr 4; Figure 7, Table 1**]. Geny o zwiększonej ekspresji oznaczono kolorem czerwonym, natomiast geny o zmniejszonej ekspresji kolorem zielonym.

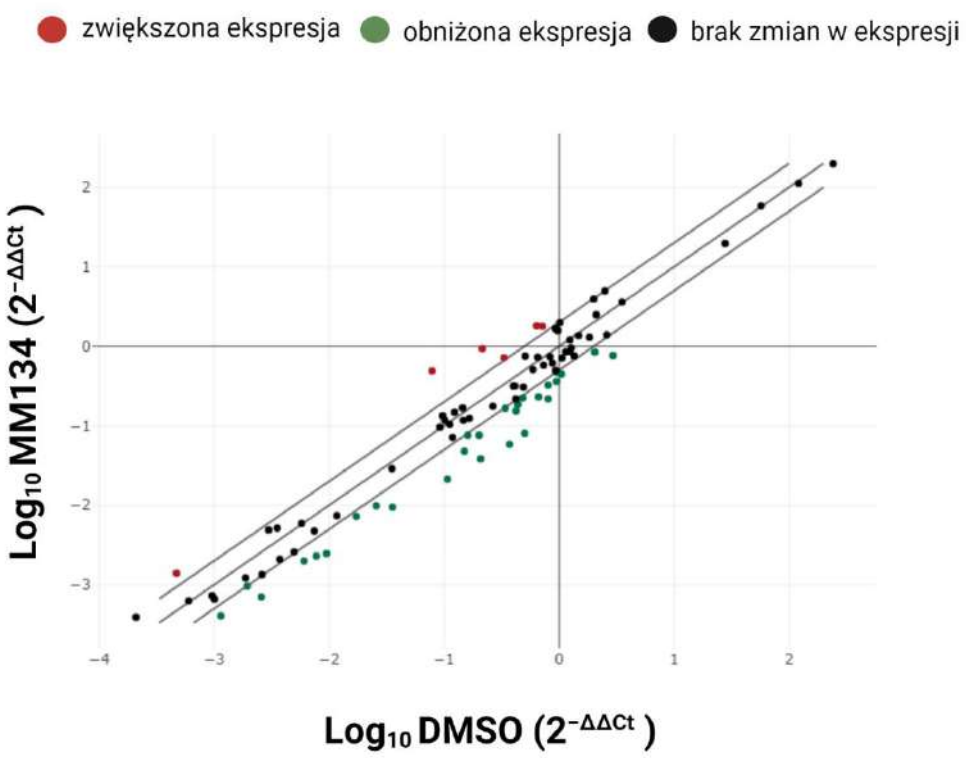

Rycina 5. Wykres obrazujący zróżnicowanie ekspresji (ang. *differential gene expression*) 96 genów w komórkach linii BxPC-3 po ich inkubacji ze związkiem **MM134** użytym w stężeniu odpowiadającym wartości IC_{50} oraz komórkami kontrolnymi poddanymi inkubacji z rozpuszczalnikiem w tym samym stężeniu (DMSO). Doświadczenie przeprowadzono w trzech powtórzeniach.

Tabela 5. Geny ulegające zmienionej ekspresji ($p < 0,05$) pomiędzy grupą komórek kontrolnych (DMSO) oraz badanych, poddanych inkubacji ze związkiem **MM134**, użytym w stężeniu odpowiadającym wartości IC_{50}. Kolorem **czerwonym** oznaczono geny ulegające zwiększonej ekspresji, natomiast kolorem **zielonym** geny ulegające zmniejszonej ekspresji. Doświadczenie przeprowadzono w trzech powtórzeniach. Wartości *p* zostały obliczone na podstawie testu t-Studenta dla wartości $2^{-\Delta Ct}$ dla każdego genu w grupie kontrolnej oraz w grupie badanej. Obliczenia wartości *p* oparte zostały na parametrycznym, niesparowanym, dwustronnym rozkładzie t o równych wariancjach dla dwóch prób.

Symbol genu	Pełna nazwa genu w języku angielskim	Współczynnik fold regulation	Wartość prawodopodobieństwa (*p*)
BCL10	B-cell CLL/lymphoma 10	2.50	0.019800
GADD45α	Growth arrest and DNA-damage-inducible, alpha	6.24	0.000393
RIPK2	Receptor-interacting serine-threonine kinase 2	2.83	0.002422
TNF	Tumor necrosis factor	2.96	0.042660
TNFRSF10B	Tumor necrosis factor receptor superfamily, member 10b	4.36	0.001260
TNFRSF1A	Tumor necrosis factor receptor superfamily, member 1A	2.18	0.018576
ABL1	C-abl oncogene 1, non-receptor tyrosine kinase	-2.65	0.006966
AIFM1	Apoptosis-inducing factor, mitochondrion-associated, 1	-2.48	0.001081
APAF1	Apoptotic peptidase activating factor 1	-2.74	0.002161
BAD	BCL2-associated agonist of cell death	-2.36	0.006358
BAG1	BCL2-associated athanogene	-2.11	0.006014
BCL2L10	BCL2-like 10 (apoptosis facilitator)	-2.38	0.019800
BIRC5	Baculoviral IAP repeat containing 5	-5.01	0.003025
BNIP3	BCL2/adenovirus E1B 19kDa interacting protein 3	-2.04	0.009433
BNIP3L	BCL2/adenovirus E1B 19kDa interacting protein 3-like	-2.01	0.005716
CASP1	Caspase 1, apoptosis-related cysteine peptidase (interleukin 1, beta, convertase)	-3.76	0.033341
CASP14	Caspase 14, apoptosis-related cysteine peptidase	-2.83	0.000610
CASP2	Caspase 2, apoptosis-related cysteine peptidase	-2.63	0.009949
CASP6	Caspase 6, apoptosis-related cysteine peptidase	-2.87	0.016235
CD27	CD27 molecule	-3.05	0.001928
CD70	CD70 molecule	-3.67	0.000879
CIDEA	Cell death-inducing DFFA-like effector a	-2.03	0.001025

CIDEB	Cell death-inducing DFFA-like effector b	-2.15	0.002795
CRADD	CASP2 and RIPK1 domain containing adaptor with death domain	-3.37	0.001127
DFFA	DNA fragmentation factor, 45kDa, alpha polypeptide	-2.34	0.020318
FADD	Fas (TNFRSF6)-associated via death domain	-3.68	0.000243
FAS	Fas (TNF receptor superfamily, member 6)	-5.41	0.000181
NAIP	NLR family, apoptosis inhibitory protein	-6.35	0.025237
NOD1	Nucleotide-binding oligomerization domain containing 1	-3.13	0.000604
PYCARD	PYD and CARD domain containing	-2.41	0.010219
TNFRSF11B	Tumor necrosis factor receptor superfamily, member 11b	-3.85	0.000160
TNFSF10	Tumor necrosis factor (ligand) superfamily, member 10	-6.25	0.000372
TP53	Tumor protein p53	-3.84	0.023076

W przeprowadzonej analizie zaobserwowano zwiększoną ekspresję 6 genów w komórkach linii BxPC-3 w odpowiedzi na związek **MM134**: *BCL10* (ang. *B-cell CLL/lymphoma 10*), *GADD45α* (ang. *growth arrest and DNA-damage-inducible, alpha*), *RIPK2* (ang. *receptor-interacting serine-threonine kinase 2*), *TNF* (ang. *tumor necrosis factor*), *TNFRSF10B* (ang. *tumor necrosis factor receptor superfamily, member 10b*) oraz *TNFRSF1A* (ang. *tumor necrosis factor receptor superfamily, member 1A*; *TNF-R1*) **(Tabela 5)**.

BCL10 jest białkiem regulatorowym apoptozy oraz szlaku sygnalizacyjnego jądrowego czynnika transkrypcyjnego kappaB (ang. *nuclear factor NF-kappa-B*; NF-κB), które zawiera w swojej strukturze domenę odpowiadającą za rekrutację kaspaz (ang. *caspase activation and recruitment domain*; CARD) [94]. Wykazano, że nadekspresja BCL10 w komórkach może sprzyjać indukcji apoptozy. Ponadto, uważa się, że domena CARD obecna w N-końcowej domenie białka BCL10 pośredniczy w wiązaniu cząsteczek adaptorowych i kaspaz. Białka zawierające domenę CARD oddziałują ze sobą w odpowiedzi na szereg czynników stresogennych, w tym uszkadzających DNA oraz ligandy śmierci komórkowej, tj. FAS oraz TNF. Powstałe wiązanie aktywuje sygnalizację proapoptotyczną [95]. Jednakże, białko BCL10 posiada dualistyczną naturę, przez co odgrywa podwójną

rolę w przebiegu procesu apoptozy, mogąc z jednej strony stymulować ten rodzaj śmierci komórkowej, a z drugiej brać udział w tworzeniu kompleksów hamujących ww. proces w odpowiedzi na uszkodzenia DNA. Obecne w cytoplazmie białko BLC10 ulega translokacji do jądra, gdzie sprzyja naprawie DNA poprzez wpływ na ubikwitynację histonów oraz rekrutację białek naprawy na drodze rekombinacji homologicznej (ang. *homologous DNA repair*; HR) [96].

Receptor TNFRSF10B (znany również, jako receptor śmierci 5 (ang. *death receptor 5*; DR5) należy do rodziny receptorów TNF posiadających w swojej strukturze wewnątrzkomórkową domenę śmierci. Głównym ligandem aktywującym ww. receptor jest TNFSF10 (ang. *tumor necrosis factor ligand superfamily member 10),* znany również, jako TRAIL lub APO-2L, którego wiązanie prowadzi do aktywacji sygnalizacji proapoptotycznej w wyniku, której dochodzi do składania kompleksu DISC, przyczyniając się do aktywacji kaspazy-8 oraz kaskady pozostałych kaspaz [97]. Wiązanie TRAIL z receptorem może wyzwalać również inne szlaki sygnalizacyjne, w tym prowadzące do aktywacji czynnika NF-κB lub procesu nekroptozy [98,99].

Proces apoptozy indukowany wiązaniem ligandu TNF z receptorem TNF-R1 prowadzi do rekrutacji białka adaptorowego FADD (ang. *Fas (TNFRSF6)-associated via death domain*) lub TRADD (ang. *TNFRSF1A associated via death domain*) oraz kaspazy-8. Natomiast utworzenie kompleksu pomiędzy aktywowanym receptorem TNF-R1 oraz białkami RIPK1 (ang. *receptor interacting serine/threonine kinase 1*) i RIPK3 (ang. *receptor interacting serine/threonine kinase 3*) rekrutuje białko MLKL (ang. *mixed lineage kinase domain like pseudokinase*), które migruje z cytozolu do błony komórkowej, prowadząc do utworzenia w niej porów. W konsekwencji dochodzi do uwolnienia zawartości komórki poza jej obręb, co powoduje wyzwolenie odpowiedzi prozapalnej [100,101]. Podczas nekroptozy nie dochodzi do drabinkowania DNA, wzrostu aktywności kaspaz, ani też zwiększonej ekspresji białek proapoptotycznych. Niemniej, jak w przypadku komórek apoptotycznych, w czasie nekroptozy reszty fosfatylydoseryny są eksponowane na zewnątrz błony

komórkowej. TNF należy do najpowszechniejszych cytokin wyzwalających szlak sygnalizacyjny prowadzący do indukcji śmierci nekroptotycznej [102–104].

Uzyskane wyniki sugerują, że badane komórki linii nowotworowych wykazują zróżnicowaną odpowiedź na zastosowane sulfonamidowe pochodne pirazolo[4,3-*e*]tetrazolo[1,5-*b*][1,2,4]triazyny. Przeprowadzone badania wykazały, że badane związki **MM** mogą indukować śmierć komórek, zarówno na drodze apoptotycznej, jak i nekroptotycznej **(Rycina 6)**.

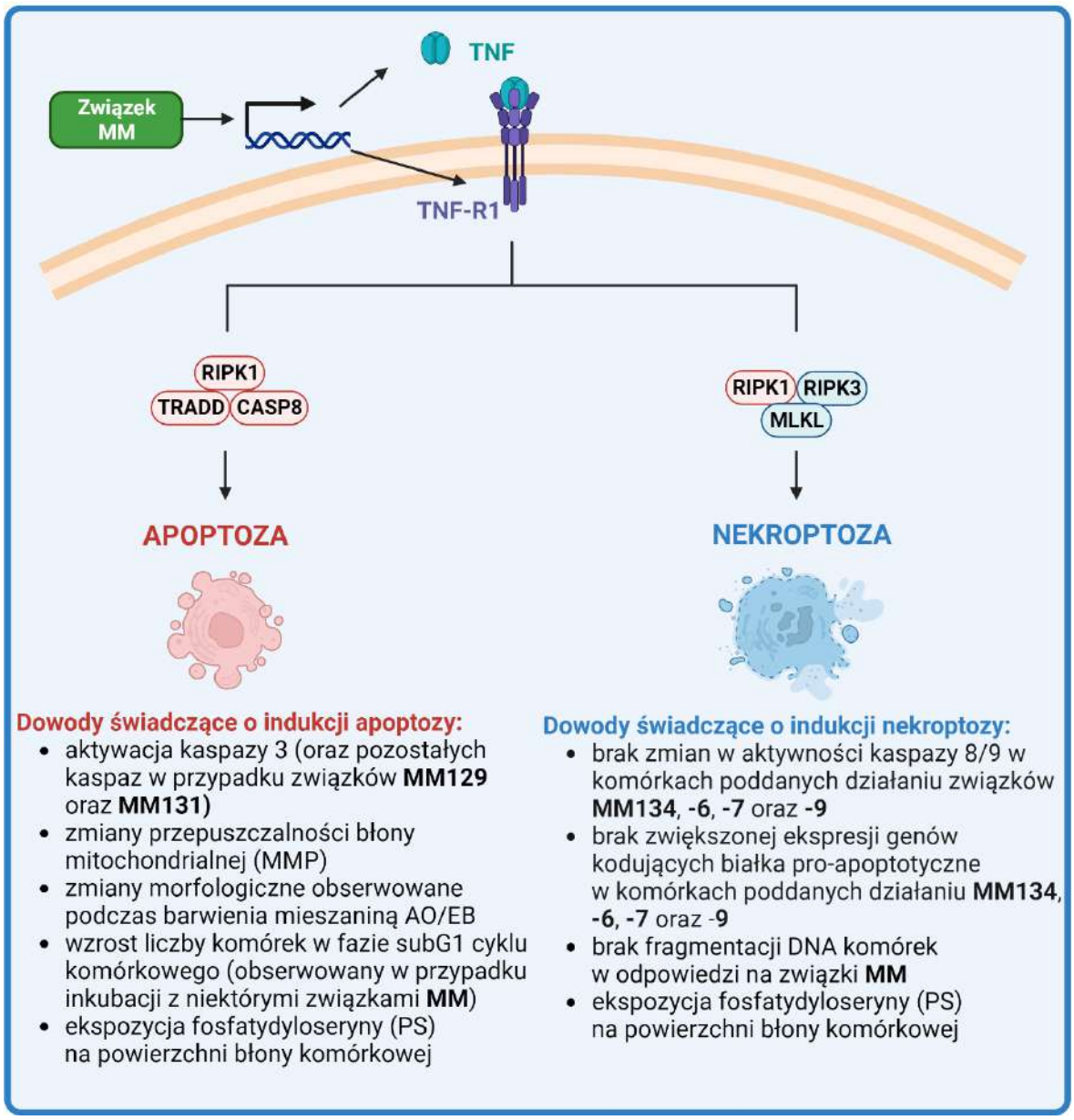

Rycina 6. Hipotetyczne rodzaje śmierci komórkowej wyzwalane w odpowiedzi na związki **MM**.

Ponadto, przeprowadzone analizy wykazały, zdecydowany wzrost ekspresji genu *GADD45α*, należącego do rodziny białek GADD45, których zwiększony poziom indukowany jest przez pojawiające się w komórce uszkodzenia DNA, w konsekwencji prowadząc do zatrzymania cyklu komórkowego, naprawy DNA i/lub śmierci komórki. Wzmożoną produkcję białek GADD45 obserwowano m.in. po eskpozycji komórek na chemioterapeutyki, co potwierdza stwierdzenie, że ich obecność jest kluczowa dla efektywnej eliminacji komórek nowotworowych [105].

Synteza białka GADD45*α* kontrolowana jest przez białko TP53 [106], chociaż może odbywać się niezależnie od niego, oraz być zmienna, w zależności od typu nowotworu oraz zastosowanego czynnika chemioterapeutycznego [107,108]. Wzrost poziomu białka GADD45*α* w komórce przyczynia się do zahamowania jej proliferacji, co może wynikać ze zdolności GADD45*α* do zakłócania interakcji pomiędzy CDK1 oraz cykliną B1, prowadząc do zahamowania aktywności kinazy oraz zatrzymania cyklu komórkowego na granicy faz G2/M [109,110]. Jednak zależność ta nie wpływa na apoptotyczną śmierć komórek [111,112].

Białko GADD45*α* może również powodować zatrzymanie cyklu komórkowego na granicy faz G1/S oraz G2/M w wyniku interakcji z białkiem P21 [105]. Zahamowanie aktywności kinazy AKT może prowadzić do niezależnej od TP53 nadprodukcji białka GADD45*α* w komórkach nowotworowych [113]. Wydaje się to być szczególnie interesujące, biorąc pod uwagę możliwość hamowania ww. kinazy przez sulfonamidowe pochodne pirazolo[4,3-*e*]tetrazolo[1,5-*b*][1,2,4]triazyny, na co wskazują wyniki badań *in silico* przeprowadzonych w ramach niniejszej pracy [**publikacja nr 4**] **(Rycina 7)**.

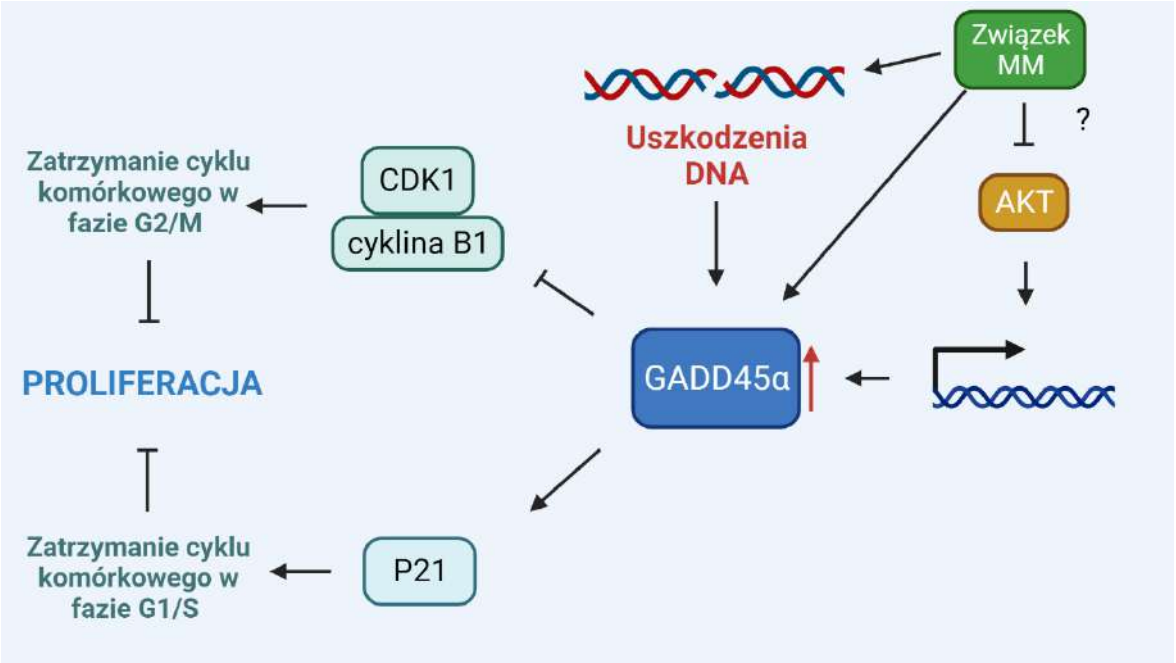

Rycina 7. Potencjalny mechanizm działania związków **MM** opracowany na podstawie przeprowadzonych badań *in vitro* oraz *in silico*.

Uzupełnienie badań eksperymentalnych stanowiły badania obliczeniowe (*in silico*), przeprowadzone we współpracy z ośrodkami zagranicznymi. Analizy oparte były na wspomaganym komputerowo projektowaniu nowych leków (ang. *computer-aided drug design*; CADD) z optymalizacją ich farmakokinetyki i farmakodynamiki poprzez wykorzystanie zarówno narzędzi obliczeniowych, jak i modelowanie molekularne oraz symulację dynamiki molekularnej. Multidyscyplinarne podejście CADD może pomóc także w identyfikacji i walidacji potencjalnych celów molekularnych, których zaburzenia związane są z patogenezą nowotworów. Co więcej, umożliwia przeszukiwanie ogromnych bibliotek chemicznych cząsteczek, mogących potencjalnie wchodzić w interakcje z określonym celem molekularnym, stanowiącym przedmiot badań. Metody stosowane w wirtualnych badaniach przesiewowych, w tym dokowanie molekularne (ang. *molecular docking*) oraz symulacje dynamiki molekularnej (ang. *molecular dynamics simulation*), ułatwiają przewidywanie powinowactwa wiązania cząsteczek i sposobu asocjacji z białkami docelowymi. Pozwala to na wybór najbardziej obiecujących związków do badań podstawowych. Ponadto, techniki

modelowania molekularnego i symulacji mogą pomóc poprawić powinowactwo wiązania, zdefiniować tzw. właściwości lekopodobne cząsteczek (ang. *druglikeness*) i prognozować właściwości substancji pod kątem ich wchłaniania, dystrybucji, metabolizmu, wydalania i toksyczności (ang. *absorption, distribution, metabolism, excretion, and toxicity*; ADMET) [114–118].

Pierwszym etapem badań *in silico* było określenie parametrów ADMET oraz właściwości lekopodobnych związków **MM** przy pomocy narzędzia internetowego - SwissADME (http://www.swissadme.ch, dostęp 1 maja 2022 r.). Właściwości lekopodobne badanych związków oszacowano w oparciu o regułę Lipińskiego, która zakłada, że substancja chemiczna jest prawdopodobnie przyswajalna przez układ pokarmowy, jeśli spełnia, co najmniej trzy z następujących kryteriów: (**1**) współczynnik rozpuszczalności związku w n-oktanolu/wodzie (logP) jest mniejszy niż 5; (**2**) masa cząsteczkowa związku nie przekracza 500 Da; (**3**) liczba donorów (ang. *hydrogen bond donors*) wiązań wodorowych w strukturze związku nie powinna przekraczać pięciu; oraz (**4**) liczba akceptorów wiązań wodorowych (ang. *hydrogen bond acceptors*) nie powinna przekraczać dziesięciu [119]. Zgodnie z powyższymi założeniami, związki **MM** charakteryzują się właściwościami lekopodobnymi. Jedynym naruszeniem reguły jest zbyt duża liczba atomów azotu lub tlenu w cząsteczce związków (>10) [**publikacja nr 2; Table 7**].

SwissADME umożliwia również łatwe oszacowanie głównych parametrów farmakokinetycznych, w tym absorpcji biernej w przewodzie pokarmowym człowieka (ang. *human gastrointestinal absorption*; HIA), przenikania cząsteczek przez barierę krew-mózg (ang. *blood–brain barier*; BBB), hamowania aktywności cytochromu P450 (CYP450) czy oceny prawdopodobieństwa zachowania się związków, jako substratów glikoproteiny P (P-gp) [120]. Na podstawie przeprowadzonych testów i analiz, odnotowano, że badane pochodne pirazolo[4,3-*e*]tetrazolo[1,5-*b*][1,2,4]triazyny, nie penetrują przez barierę krew-mózg oraz mogą stanowić substrat dla P-gp będącej transporterem błonowym należącym do nadrodziny białek ABC (ang. *ATP-binding cassette transporters*), które ograniczają

przedostawanie się związków chemicznych przez barierę krew-narząd i warunkują lekooporność nowotworów. Około 50–90% przebadanych cząsteczek terapeutycznych jest substratami dla izoform cytochromu P450, w tym CYP2D6 i CYP3A4. Spośród badanych związków **MM**, najlepsze parametry farmakokinetyczne, tj. wysoką wchłanialność z przewodu pokarmowego oraz brak aktywności hamującej względem enzymów z rodziny CYP, wykazywała cząsteczka związku **MM137** [**publikacja nr 2; Table 6**].

Badania *in silico* z użyciem dokowania molekularnego i dynamiki molekularnej są wykorzystywane w dziedzinie chemii i biologii do analiz struktury i właściwości molekuł oraz interakcji między nimi. Dokowanie molekularne to metoda komputerowego modelowania, która służy do przewidywania i analizowania oddziaływań między cząsteczkami [121,122]. Natomiast dynamika molekularna to metoda symulacji komputerowej, która służy do badania ruchu cząsteczek w czasie. Poprzez zastosowanie równań ruchu i praw fizyki, dynamika molekularna pozwala na symulację trajektorii ruchu cząsteczek przez ściśle zdefiniowany okres czasowy. Umożliwia także badanie struktury, elastyczności, zmian konformacyjnych i właściwości fizykochemicznych cząsteczek. Obie metody są nieodzowne dla zrozumienia mechanizmów biologicznych na poziomie molekularnym. Pozwalają zarówno na analizę, jak i predykcję interakcji molekularnych potencjalnych leków [123–125].

Pierwszym etapem badań z użyciem ww. metodologii był wybór potencjalnych celów molekularnych, który został dokonany w oparciu o najnowsze doniesienia literaturowe [20,24,25,29,126,127]. Do badań wybrano kinazy ABL (ang. *tyrosine-protein kinase* ABL), BCR (ang. *breakpoint cluster region protein*) oraz CDK ze względu na ich podobieństwo strukturalne do acylonukleozydów pirazolo[4,3-*e*][1,2,4]triazyny, które zostały wcześniej przebadane pod kątem aktywności hamującej wobec ww. kinaz. [20,127]. Ponadto, badania enzymatyczne dowiodły, że sulfonamidowe pochodne pirazolo[4,3-*e*][1,2,4]triazyny mogą działać, jako nanomolarne inhibitory enzymów z grupy anhydraz węglanowych,

w szczególności izoformy IX oraz XII (CAIX/XII) [21,22,128,129]. CAXI oraz XII zwróciły uwagę wielu badaczy zainteresowanych projektowaniem leków przeciwnowotworowych, ze względu na kluczowe funkcje, jakie pełnią podczas przerzutowania komórek czy w odpowiedzi na niedobór tlenu w mikrośrodowisku guza (hipoksję). Co więcej, ich synteza ograniczona jest tylko do komórek nowotworowych, co daje możliwość opracowania nowych terapii celowanych o zmniejszonym profilu toksyczności. Należy zauważyć, że sulfonamidy stanowią obecnie najliczniejszą grupę inhibitorów CAIX/XII [130–132]. Udział pozostałych celów molekularnych wybranych do badań *in silico,* tj. AKT, BTK, mTOR, PD-1, PD-L1, czy sICAM oraz ich zaangażowanie w proces patogenezy nowotworów został opisany we wprowadzeniu do niniejszej rozprawy doktorskiej, a wybór uzasadniony był wynikami otrzymanymi przez innych autorów dla związków z tej samej grupy chemicznej [24,25,29,126].

Badania przesiewowe oparte na symulacji dokowania molekularnego sulfonamidowych pochodnych pirazolo[4,3-*e*]tetrazolo[1,5-*b*][1,2,4]triazyny, wykazały, że cząsteczki **MM136** i **MM139** są najsilniejszymi inhibitorami dla wszystkich wytypowanych celów molekularnych [**publikacja nr 2; Table 4**].

Uzyskane w badaniach *in silico* wyniki wykazały, że związek **MM134** przejawia aktywność hamującą wobec AKT2. Zaobserwowano również silne oddziaływanie związku **MM136** z AKT1, mTOR1, mTOR2 i PD-L1. **MM137** okazał się być najskuteczniejszym inhibitorem kinazy ABL2, natomiast **MM139** wykazywał silne właściwości hamujące wobec dziewięciu spośród siedemnastu badanych makrocząsteczkowych celów molekularnych leków przeciwnowotworowych, tj.: ABL1, AKT3, BTK, CA-IX, CA-XII, CDK2, CDK4, CDK7 i ICAM-1. Dwuwymiarowe interakcje pomiędzy związkiem **MM136** oraz AKT1 i PD-L1 zaprezentowano w **publikacji nr 2** [**Figure 12**]. Wiązanie związku **MM139** z białkami AKT1 i PD-L1 przedstawione zostały w **publikacji nr 2** [**Figure 13**].

Kolejnym etapem badań *in silico* była ocena dynamiki molekularnej kompleksów utworzonych przez związki **MM136** oraz **MM139** z białkami AKT1 oraz PD-L1. Do oceny stabilności ww. asocjacji posłużyły parametry RMSD (ang. *root mean square deviation*) oraz RMSF (ang. *root mean square fluctuation*). RMSD jest miarą średniego odchylenia struktury cząsteczki od struktury referencyjnej w trakcie symulacji dynamiki molekularnej. Parametr ten służy do monitorowania zmian konformacyjnych cząsteczki w czasie oraz porównania jej różnych konformacji. Im większa wartość RMSD, tym większe odchylenie od struktury referencyjnej. RMSD może być używane do oceny stabilności strukturalnej, jakości dopasowania do struktur eksperymentalnych lub porównywania różnych konformacji cząsteczki. Jest również miarą fluktuacji atomów wokół ich średniej pozycji w trakcie trwania symulacji. Parametr ten wyznacza elastyczność i ruchliwość poszczególnych atomów w cząsteczce, a jego wysoka wartość wskazuje na dużą zmienność położenia atomów, co odpowiada obszarom o wysokiej elastyczności lub aktywności [133,134].

Badania potwierdziły, że utworzone kompleksy są wystarczająco stabilne, aby testowane związki mogły wywierać działanie przeciwnowotworowe na drodze oddziaływania z wytypowanymi białkami. Ponadto, określono reszty aminokwasowe celów molekularnych, kluczowe w kontekście wiązania związków **MM**. Szczegóły dotyczące symulacji zamieszono w sekcji 2.4.2 **publikacji nr 2**.

Analogiczne badania [**publikacja nr 3, Sekcja 2.6.**] przeprowadzono w celu wyjaśnienia potencjalnego mechanizmu genotoksyczności badanych związków. W tym przypadku, wybrano cele molekularne, których inhibicja mogłaby prowadzić do pojawienia się uszkodzeń DNA w materiale genetycznym komórki. Wśród nich znalazły się m.in. endonukleaza DNA miejsc apurynowych/apirymidynowych (ang. *DNA-(apurinic or apyrimidinic site) endonuclease*; APE1), kinazy ATR oraz ATM, kinazy punktu kontrolnego CHK1/CHK2 (ang. *serine/threonine-protein kinase CHK1/CHK1*; CHK1/CHK2), polimeraza poli(ADP-rybozy)-1 (ang. *poly [ADP-ribose] polymerase 1*; PARP-1),

białko RPA70 (ang. *replication protein A 70 kDa*; RPA70), topoziomerazy: topoizomeraza I (ang. *topoisomerase 1*; TOP1) oraz topoizomeraza II beta (ang. *topoisomerase 2β*; TOP2B) oraz kinaza białkowa podobna do WEE1 (ang. *Wee1-like protein kinase*; WEE1).

Wyniki uzyskane z użyciem dokowań molekularnych wskazały, że związki **MM** posiadają wysokie powinowactwo wiązania się z celami makrocząsteczkowymi, w tym APE1, CHK1 oraz TOPI, co było warunkowane zwiększoną liczbą obserwowanych interakcji chemicznych dla ich kompleksów [**publikacja nr 3; Figure 12**]. W toku analizy wykazano, że związek **MM137** wykazuje najsilniejsze powinowactwo do pięciu spośród wytypowanych celów molekularnych, jednakże w przypadku ATR oraz WEE1 różnice energii wymagane do konkurencyjnego hamowania docelowych enzymów były stosunkowo niewielkie w porównaniu z energiami otrzymanymi dla ich referencyjnych ligandów. Dlatego do badań dynamiki molekularnej wybrano białka APE1, CHK1 oraz TOP1. Najwyższą stabilność zaobserwowano w przypadku kompleksów uformowanych między związkiem **MM137** oraz CHK1 [**publikacja nr 3; sekcja 2.6.2.**].

Przeprowadzone badania pozwoliły na ustalenie wiodących celów molekularnych związków **MM** do dalszych badań *in silico*. W **publikacji nr 4** dokonano ponownej walidacji celów molekularnych z zastosowaniem dodatkowego oprogramowania, pozwalającego na dokowanie oraz analizę dynamiki molekularnej najlepiej rokujących kompleksów. Wykorzystanie zróżnicowanej metodologii w badaniach *in silico* ma wiele zalet. Programy wykorzystują odmienne algorytmy, funkcje oceny (ang. *scoring functions*) [135,136] oraz pola siłowe (ang. *force fields*) [137,138], co może powodować różnice w predykcji trybów wiązania oraz energii wiązań. Funkcje oceny są matematycznym modelem, który przypisuje ocenę, nazywaną *score'em*, do każdego możliwego kompleksu ligand-białko. W zależności od wybranego algorytmu dokowania, *scoring function* może uwzględniać różne czynniki i parametry w tym

energię wiązania, komplementarność kształtu lub interakcje elektrostatyczne między ligandem, a białkiem [135,136]. Natomiast pola siłowe, nazywane również funkcjami siłowymi, są matematycznymi modelami opisującymi interakcje między atomami w cząsteczkach. Stosowane do symulacji ruchu i dynamiki molekularnej, mają na celu zrozumienie zachowań cząsteczek w skali atomowej lub molekularnej [137,138]. Spójne wyniki uzyskane podczas analiz wieloprogramowych, zapewniają większą rzetelność predykcji. Pojedyncze oprogramowanie często nie jest w stanie uchwycić wszystkich aspektów dokowania i dynamiki molekularnej. Należy również pamiętać, że narzędzia chemiinformatyczne mają unikalne funkcje, możliwości i ograniczenia, a ich połączenie może prowadzić do bardziej kompleksowych oraz wiarygodnych wyników.

Dokowania molekularne zostały przeprowadzone z dla następujących celów molekularnych: AKT1 [139], AKT2 [140], BTK [141], CHK1, [142], mTOR1 [143] oraz PD-L1 [144], które wytypowano na podstawie energii wiązania oraz stabilności otrzymanych we wcześniejszych badaniach kompleksów. Do oceny wiązania związków **MM** oraz ww. białek zastosowano siedem algorytmów funkcji oceny, w tym Jain [135], LigScore1, LigScore2 [145], PLP1, PLP2 [146], PMF i PMF04 [147]. Wybór potencjalnych celów molekularnych został zawężony w oparciu o energię wiązania związków **MM**, ograniczając się do białek AKT2, BTK, CHK1 i PD-L1 [**publikacja nr 4; Table 3**]. Wiązanie związków **MM134**, **-6** oraz **-7** z kinazą AKT2 zaprezentowano w **publikacji nr 4 [Figure 9**]. Szczegóły interakcji **MM139** z kinazą BTK przedstawiono na Rycinie 10 **publikacji nr 4 [Figure 10**]. Biorąc pod uwagę wyniki badań eksperymentalnych otrzymanych dla komórek linii nowotworowych raka prostaty (PC-3) i raka trzustki (BxPC-3) oraz deregulację ścieżki AKT-mTOR, obserwowaną w przypadku wielu nowotworów [148], zdecydowano się na dalszą analizę oddziaływania kinazy AKT2 ze związkami **MM**.

W kolejnym etapie badań wykorzystano metodę MM-GBSA (ang. *molecular mechanics-generalized born surface area*), która należy do metod obliczeniowych, stosowanych w celu oszacowania energii swobodnej wiązania w kompleksach

ligand-białko. W praktyce MM-GBSA polega na przeprowadzeniu serii obliczeń dla kompleksu ligand-białko oraz pojedynczych składników: ligandu, białka i rozpuszczalnika. Obliczona zostaje energia wewnętrzna, czyli energia wiązań i oddziaływań wewnątrz cząsteczkowych oraz energia swobodna solwatacyjna, obejmująca oddziaływania między cząsteczkami a rozpuszczalnikiem. Następnie dokonuje się pomiaru różnicy energii między kompleksem a składnikami, aby oszacować energię swobodną wiązania [149,150].

Cztery spośród badanych kompleksów wykazywały wartość energii wiązania z AKT2 w zakresie od -46,50 kcal/mol do -25,15 kcal/mol. Energia solwatacyjna niepolarna (ΔG-solv), solwatacyjna polarna (ΔGsolvlipo), siły van der Waalsa i energia kulombowska były siłą napędową wiązania liganda w miejscu aktywnym białka. Związek **MM139** nie sprzyjał wiązaniu kowalencyjnemu z białkiem, co wynikało z niskiej energii wiązania w porównaniu z innymi kompleksami [**publikacja nr 4; Table 4**].

Narzędzia dynamiki molekularnej wykorzystano także do oceny stabilności kompleksów utworzonych pomiędzy związkami **MM134**, **-6**, **-7** lub **-9** oraz AKT2. W tym celu użyto oprogramowania *Gromacs*, który w przeciwieństwie do wcześniej używanego oprogramowania *Desmond*, oferuje szeroki wybór pól siłowych, w tym OPLS-AA CHARMM (ang. *chemistry at harvard molecular mechanics*), AMBER (ang. *assisted model building with energy refinement*) oraz GROMOS (ang. *groningen molecular simulation*) [151]. W ten sposób Gromacs zapewnia większą elastyczność w wyborze pola siłowego i opcji parametryzacji dynamiki molekularnej. W niniejszej analizie oddziaływań wykorzystano pole siłowe AMBER99SB. Wyniki przedstawiono w postaci obrazu oraz charakterystyki trajektorii symulacyjnej [**publikacja nr 4; Figure 11**] (z wyznaczeniem zakresów RMSD oraz RMSF) oraz diagramów interakcji pomiędzy związkami **MM134**, **-6**, **-7**, **-9**, ligandem referencyjnym (ko-krystalizowanym z białkiem, w tym przypadku G39) i kinazą AKT2 które zaprezentowano na kolejnych Rycinach w **publikacji nr 4** [**Figure S4–S6**]. Istotnymi elementem badań dynamiki molekularnej jest określenie liczby

wiązań wodorowych pomiędzy ligandem, a receptorem (białkiem) w trakcie ich oddziaływań [152] oraz określenie tzw. promienia gyracji, który jest średnią odległością atomów od środka masy cząsteczki [153,154] [**publikacja nr 4; Figure S7**]. Oba parametry pozwalają na dokładniejsze poznanie struktury, dynamiki i zachowania cząsteczek badanych systemów. Udział poszczególnych oddziaływań w energię wiązania związków **MM** oraz ligandu referencyjnego z kinazą AKT2 przedstawiono w Tabeli 5 w **publikacji nr 4 [Table 5]**.

Odrębnym i niezależnym etapem analiz chemiinformatycznych związków **MM134**, **-6**, **-7** oraz **-9** były obliczenia w ramach teorii funkcjonału gęstości (ang. *density functional theory*; (DFT), będącą zaawansowaną metodą obliczeniową chemii kwantowej, mającą na celu opisanie elektronowej struktury molekuł. Obliczenia DFT służą do wyznaczania energetycznych, strukturalnych i spektralnych właściwości cząsteczek [155,156]. W tym przypadku, pozwoliły one na określenie reaktywności związków **MM** [**publikacja nr 4; Figure S3**]. Ponadto, przeprowadzono analizę molekularnego potencjału elektrostatycznego (ang. *molecular electrostatic potential*; MESP) w celu zbadania reaktywności i wzorców wiązań molekularnych w związkach **MM** [157]. Ulokowanie reaktywnych miejsc elektrofilowych oraz nukleofilowych w cząsteczkach związków **MM** przedstawione zostały na Rycinie 8 w **publikacji nr 4 [Figure 8**].

7. Dyskusja

Wyniki badań przeprowadzonych w ramach niniejszej pracy doktorskiej wskazują na wysoką cytotoksyczność badanych pochodnych układu pirazolo[4,3-*e*]tetrazolo[1,5-*b*][1,2,4]triazyny (**MM134**, **-6**, **-7** oraz **-9**) względem linii komórek nowotworowych gruczolakoraka trzustki (BxPC-3), raka jelita grubego (HCT-116) i raka prostaty (PC-3) [**publikacja nr 4; Table S3**] **(Tabela 6)**.

Tabela 6. Podsumowanie wyników testów cytotoksyczności nowych sulfonamidowych pochodnych układu pirazolo[4,3-*e*]tetrazolo[1,5-*b*][1,2,4]triazyny (związków **MM**). Działanie cytotoksyczne związków określono dla ludzkich komórek nowotworowych, wywodzących się z różnych tkanek: BxPC-3 (gruczolakorak trzustki), PC-3 (rak prostaty), HCT-116 (rak okrężnicy) oraz ludzkich komórek prawidłowych (fibroblasty płuc człowieka - linia WI-38). Wyniki uzyskane zostały po 24- lub 72-godzinnej inkubacji komórek ze związkami **MM** i zaprezentowane, jako wartości IC_{50} [μM] ± SD

Metoda	**Linia komórkowa**	**Pirazolo[4,3-*e*]tetrazolo[1,5-*b*][1,2,4]triazyna**			
		MM134	**MM136**	**MM137**	**MM139**
24-godzinna inkubacja					
IC_{50} [μM]					
Test wychwytu czerwieni obojętnej	BxPC-3	**0,35** ± 0,007	**0,27** ± 0,04	**0,18** ± 0,014	**0,28** ± 0,02
	PC-3	**0,1** ± 0,04	**0,13** ± 0,014	**0,06**	**0,17** ± 0,05
72-godzinna inkubacja					
IC_{50} [μM]					
Test MTT	BxPC-3	**0,32** ± 0,1	**0,25** ± 0,08	**0,16** ± 0,04	**0,33** ± 0,14
	PC-3	**0,16** ± 0,02	**0,13** ± 0,01	**0,11** ± 0,007	**0,17** ± 0,003
	WI-38	**0,65** ± 0,07	**0,48** ± 0,09	**0,27** ± 0,04	**0,54** ± 0,06

W porównaniu do pozostałych sulfonamidowych pochodnych pirazolo[4,3-*e*]tetrazolo[1,5-*b*][1,2,4]triazyny opisanych w literaturze [23–26], związki **MM134**, **-6**, **-7** oraz **-9,** będące przedmiotem niniejszych badań wykazały najefektywniejsze działanie cytotoksyczne względem komórek linii PC-3 oraz BxPC-3 **(Tabela 6)**.

Związki **MM** charakteryzowały się wyższą selektywnością działania względem komórek linii nowotworowych niż w przypadku komórek prawidłowych linii WI-38. Ponadto, związki **MM134**, **-6**, **-7** oraz **-9** odznaczały się wyższą aktywnością cytotoksyczną niż powszechnie stosowane chemioterapeutyki, tj. cisplatyna (wartości IC_{50} = 38 μM oraz >100 μM odpowiednio dla komórek linii DLD-1 (rak jelita grubego) oraz HT-29 (gruczolakorak jelita grubego) po 24-godzinnej inkubacji [158] lub doksorubicyna (wartości IC_{50} = 2,75 μM) po 72-godzinnej inkubacji komórek linii HT-29) [159].

Indukcja apoptozy jest pożądanym sposobem eliminacji komórek nowotworowych, która pozwala na ograniczenie niekorzystnych efektów (np. stanów zapalnych), związanych z uwolnieniem się zawartości komórek do środowiska, które są typowe dla innych mechanizmów śmierci komórkowej, w tym: nekrozy, nekroptozy czy pyroptozy.

Wyniki uzyskane podczas realizacji prezentowanej pracy wykazały, że związki **MM** z grupy sulfonamidowych pochodnych pirazolo[4,3-*e*]tetrazolo[1,5-*b*][1,2,4]triazyny charakteryzują się zróżnicowaną aktywnością proapoptotyczną [24,25,55,63]. Związki **MM134**, **-6**, **-7** oraz **-9** zastosowane w stężeniu IC_{50} wykazały wyższy potencjał proapoptotyczny wobec komórek linii BxPC-3 niż względem komórek linii PC-3.

Zaobserwowane w przeprowadzonych badaniach obniżenie potencjału błony mitochondrialnej komórek nowotworowych w odpowiedzi na związki **MM134**, **-6**, **-7** oraz **-9** wskazuje na zaburzenie struktury i funkcji mitochondriów, co może wynikać z zainicjowanego procesu apoptozy w badanych komórkach linii nowotworowych poddanych działaniu sulfonamidowych pochodnych pirazolo-triazyny [160].

Kolejnym kluczowym procesem w przebiegu apoptozy jest aktywacja kaspaz efektorowych, w tym kaspazy-3 oraz -7. Przeprowadzona analiza wykazała zróżnicowaną aktywację kaspaz 3/7 w komórkach BxPC-3 w zależności od rodzaju związku **MM** i zastosowanego stężenia. Jedynie związek **MM139** aktywował

efektywnie kaspazy 3/7 we wszystkich zastosowanych stężeniach. Nie zaobserwowano wzrostu aktywności kaspaz po inkubacji komórek linii PC-3 z testowanymi związkami.

Gornowicz i wsp. w swoich badaniach również zaobserwowali wzrost aktywności kaspaz-3, -7, -8 oraz -9 po inkubacji komórek linii DLD-1 oraz HT-29 z sulfonamidowymi pochodnymi pirazolo-triazyny [24, 26]. Pochodne indukowały także inne, charakterystyczne dla apoptozy zmiany, w tym eksternalizację fosfatydyloseryny na powierzchni komórek, czy typowy dla apoptozy obraz morfologiczny komórek. Podczas realizacji zadań badawczych zaplanowanych w niniejszej pracy, a dotyczących detekcji procesu apoptozy, nie wykazano wzrostu enzymatycznej aktywności kaspaz inicjatorowych tj. kaspazy-8 oraz -9 po inkubacji komórek linii BxPC-3 z badanymi związkami **MM134**, **-6**, **-7** oraz **-9**.

Kolejny etap badań dotyczył genotoksyczności indukowanej przez związki **MM**. Badane w niniejszej pracy pochodne charakteryzowały się podobnym potencjałem genotoksycznym, co zostało zaobserwowane również przez Bukowskiego i wsp. [23] dla innych pochodnych pirazolo-triazyny w stosunku do komórek linii BxPC-3. Wzrost poziomu uszkodzeń DNA w komórkach linii nowotworowych korelował ze wzrostem stężenia związków **MM**. Działaniu związków **MM** poddano także komórki prawidłowe linii WI-38 w stężeniach odpowiadających uzyskanym w teście MTT wartościom IC_{50}, które były wyższe (zakres IC_{50}: 0,27–0,65 μM) niż wyznaczone dla komórek nowotworowych (zakres IC_{50}: 0,11–0,33 μM). Pomimo tego, pochodne pirazolo-triazyny indukowały mniej uszkodzeń DNA w komórkach prawidłowych niż w komórkach nowotworowych, co może wskazywać na potencjalną selektywność działania związków **MM**.

Jednym z czynników predysponujących zarówno do powstawania uszkodzeń DNA, zatrzymania cyklu komórkowego, jak i indukcji procesu apoptozy jest wzmożona produkcja RFT, którą zaobserwowano po inkubacji komórek linii nowotworowych BxPC-3 i PC-3 ze związkami **MM134**, **-6**, **-7** oraz **-9**,

co również odnotował Bukowski i wsp. [55] w badaniach nad sulfonamidowymi pochodnymi pirazolo-triazyny.

Badania Bukowskiego i wsp. [55] oraz Gornowicz i wsp. [24], wykazały, że testowane przez nich związki należące do grupy sufonamidowych pochodnych pirazolo-triazyny wpływają na przebieg cyklu komórkowego i jego poszczególnych faz w sposób bardzo zróżnicowany w zależności od zastosowanej linii komórkowej. Pomimo negatywnych wyników, jakie dostarczyła analiza cyklu komórkowego przeprowadzona w ramach prezentowanej pracy nie można wykluczyć indukcji śmierci apoptotycznej komórek eksponowanych na działanie związków **MM134**, **-6**, **-7** oraz **-9**. Brak frakcji komórek w fazie sub-G1, która reprezentuje fragmentację materiału genetycznego, może wynikać z faktu, że fragmenty DNA są wciąż zatrzymywane w jądrze komórkowym [161].

Przeprowadzone badania ekspresji genów wskazały natomiast na mieszany charakter śmierci komórkowej indukowanej przez badane sulfonamidowe pochodne pirazolo[4,3-*e*]tetrazolo[1,5-*b*][1,2,4]triazyny i pojawienie się nekroptozy, jako komplementarnego mechanizmu działania związków **MM**. Chociaż uważa się, że apoptoza jest głównym i prawdopodobnie najważniejszym typem programowanej śmierci komórkowej wyzwalanej w odpowiedzi na działanie związków chemioterapeutycznych, to może być niewystarczająca do skutecznej walki z nowotworem. Komórki nowotworowe często wykształcają strategie pozwalające uniknąć apoptotycznej śmierci, przez co efektywność tego procesu jest ograniczona. Dlatego stopniowo rośnie zainteresowanie badaniem innych rodzajów śmierci komórkowej indukowanej w odpowiedzi na leki przeciwnowotworowe. Najnowsze badania wskazują, że wiele stosowanych klinicznie związków terapeutycznych samodzielnie lub w połączeniu z cząsteczkami modulacyjnymi ich działanie, może prowadzić do nekroptotycznej śmierci komórek nowotworowych. Wśród nich wyróżnić można cisplatynę [162–165], etopozyd [166–168], 5-fluorouracyl [169–171], gemcytabinę [172,173], paklitaksel [174,175] oraz winblastynę. [176]. Podczas nekroptozy dochodzi do

uwolnienia zawartości komórkowej do otaczającego mikrośrodowiska i stymulacji reakcji immunologicznej skierowanej przeciwko komórkom nowotworowym. Może mieć to kluczowe znaczenie ze względu na wyzwolenie trwałej odpowiedzi immunologicznej skierowanej przeciw komórkom nowotworowym oraz możliwość połączenia indukcji apoptozy z immunoterapią, w celu zwiększenia jej skuteczności. Z drugiej strony, nagłe pojawienie się i narastający w organizmie pacjenta proces zapalny prowadzić może do niekorzystnych efektów ubocznych, które ograniczyć mogą zastosowanie ww. kombinacji. Nekroptoza jest względnie nowo zidentyfikowanym procesem, którego zrozumienie jest obecnie ograniczone, a wpływ na organizm człowieka nieznany [168,177,178]. Indukcja tego alternatywnego szlaku śmierci komórkowej w odpowiedzi na badane pochodne pirazolo[4,3-*e*][1,2,4]triazyny powinna być potwierdzona dodatkowymi testami biochemicznymi oraz molekularnymi ukierunkowanymi na analizę ekspresji oraz detekcję ufosforylowanych białek RIPK3 oraz MLKL [179]. Nie można również wykluczyć indukcji innych form śmierci komórek nowotworowych tj. pyroptozy (ang. *pyroptosis*) [180,181], ferroptozy (ang. *ferroptosis*) [182] i innych, w odpowiedzi na badane związki. Efekt inkubacji komórek z badanym związkiem **MM** może, bowiem zależeć od „wewnętrznej zdolności" komórek do umierania wobec określonego schematu, zakodowanego w materiale genetycznym lub aktualnego stanu metabolicznego komórki [177].

Zahamowanie proliferacji komórek oraz utrata potencjału klonogennego mogą być związane ze zdolnością związków **MM** do zwiększenia produkcji białka GADD45α, które jest związane z tworzeniem kompleksów pomiędzy CDK1 oraz cykliną B1 (zahamowanie cyklu komórkowego na granicy faz G2/M) lub oddziałuje z białkiem P21 (zatrzymanie cyklu komórkowego na granicy faz G1/S) [105]. Wzrost syntezy białka GADD45α może również wynikać z zahamowania kinazy AKT [113], która została zidentyfikowana, jako prawdopodobny cel molekularny związków **MM134**, **-6** oraz **-7** w badaniach *in silico*.

Przedstawione w prezentowanej pracy doktorskiej wyniki badań wykazały zróżnicowaną aktywność cytotoksyczną i genotoksyczną, a także prooksydacyjną nowych pochodnych układu pirazolo[4,3-*e*][1,2,4]triazyny. Odnotowana aktywność proapoptotyczna badanych związków **MM** nie stanowiła jedynego mechanizmu, poprzez, który indukowana była śmierć badanych komórek. Prawdopodobnie mogła być ona także inicjowana poprzez proces nekroptozy. Wszystkie badane pochodne układu pirazolo[4,3-*e*][1,2,4]triazyny wykazały silny potencjał onkoterapeutyczny w przeprowadzonych testach komórkowych.

Rycina 8 przedstawia potencjalny mechanizm działania związków **MM** wykorzystanych w przeprowadzonych w ramach niniejszej pracy doktorskiej badaniach:

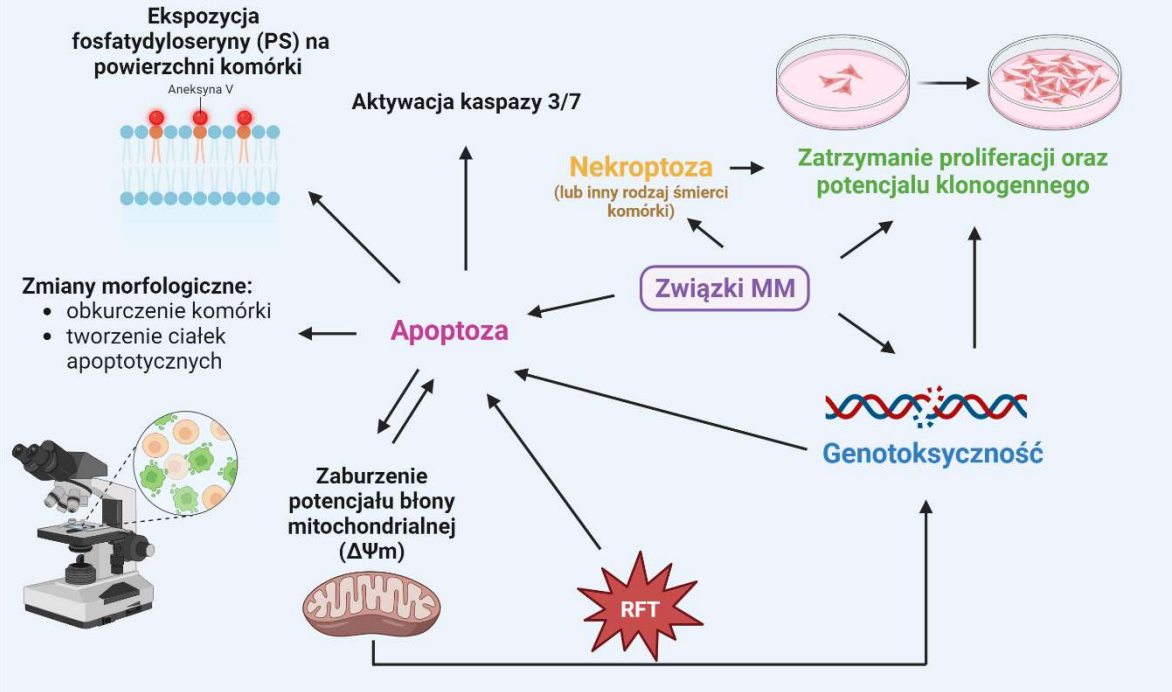

Rycina 8. Potencjalny mechanizm działania związków **MM** opracowany na podstawie przeprowadzonych badań *in vitro* oraz *in silico*.

Wykonane, w ramach niniejszej pracy, badania stanowią istotny wkład w wiedzę dotyczącą aktywności biologicznej nowych pochodnych z grupy pirazolo-triazyn, co może pozwolić na wskazanie dalszych kierunków syntez chemicznych celem optymalizacji działania terapeutycznego pochodnych układu

pirazolo[4,3-*e*][1,2,4]triazyny. Otrzymane wyniki badań umożliwią również ukierunkowanie dalszych, szczegółowych analiz, zarówno w zakresie badań podstawowych, jak i przedklinicznych. Włączenie badań *in silico* znacznie poszerzyło wiedzę dotyczącą potencjalnych celów molekularnych badanych związków **MM**, dzięki czemu może być znacznie doprecyzowany mechanizm ich działania w komórce. Uzyskane wyniki mogą stanowić źródło informacji do bardziej szczegółowych, molekularnych badań związków chemicznych należących do grupy pochodnych układu pirazolo[4,3-*e*][1,2,4]triazyny i pomóc w określeniu ich potencjalnej roli w onkoterapiach.

8. Wnioski

Wyniki przeprowadzonych w niniejszej pracy badań, pozwalają na sformułowanie następujących wniosków:

1. Sulfonamidowe pochodne oparte na strukturze trójpierścieniowej pirazolo[4,3-*e*]tetrazolo[1,5-*b*][1,2,4]triazyny wykazały wyższą aktywność cytotoksyczną wobec komórek nowotworowych gruczolakoraka trzustki (BxPC-3), raka jelita grubego (HCT-116) i raka prostaty (PC-3) niż komórek prawidłowych, w tym ludzkich (WI-38) oraz mysich (L929) fibroblastów. Najbardziej wrażliwe na działanie badanych pochodnych okazały się komórki linii PC-3, najmniej wrażliwe komórki linii HCT-116.
2. Najsilniejsze działanie cytotoksyczne wykazywał związek **MM137**.
3. Zaobserwowano zależny od dawki oraz specyficzny dla rodzaju komórek nowotworowych efekt genotoksyczny, wyrażony poprzez wzrost poziomu uszkodzeń DNA w komórkach poddanych inkubacji ze związkami **MM**.
4. Badane pochodne pirazolo-triazyny charakteryzowały się zróżnicowanym działaniem proapoptotycznym oraz prooksydacyjnym, szczególnie w komórkach linii BxPC-3.
5. Nie wykazano zmian w przebiegu cyklu komórkowego oraz jego poszczególnych faz w komórkach nowotworowych poddanych działaniu związków **MM**.
6. Wykazano antyproliferacyjne oraz antyklonogenne działanie związków **MM** w komórkach nowotworowych linii BxPC-3 oraz PC-3.
7. Analiza ekspresji genów wskazała na udział białka GADD45α w zahamowaniu proliferacji komórek nowotworowych w odpowiedzi na badane pochodne oraz potencjalną indukcję nekroptozy i apoptozy komórek nowotworowych.
8. Przeprowadzone badania *in silico* wykazały obiecujące właściwości farmakokinetyczne badanych związków oraz wskazują na kinazę AKT2,

jako główny cel molekularnego działania sulfonamidowych pochodnych pirazolo[4,3-*e*]tetrazolo[1,5-*b*][1,2,4]triazyny.

9. Literatura uzupełniająca

1. Ferlay, J.; Colombet, M.; Soerjomataram, I.; Parkin, D.M.; Piñeros, M.; Znaor, A.; Bray, F. Cancer Statistics for the Year 2020: An Overview. *Int. J. Cancer* **2021**, doi:10.1002/ijc.33588.
2. Wang, X.; Zhang, H.; Chen, X. Drug Resistance and Combating Drug Resistance in Cancer. *Cancer Drug Resist. Alhambra Calif* **2019**, *2*, 141–160, doi:10.20517/cdr.2019.10.
3. Majidinia, M.; Mirza-Aghazadeh-Attari, M.; Rahimi, M.; Mihanfar, A.; Karimian, A.; Safa, A.; Yousefi, B. Overcoming Multidrug Resistance in Cancer: Recent Progress in Nanotechnology and New Horizons. *IUBMB Life* **2020**, *72*, 855–871, doi:10.1002/iub.2215.
4. Nussinov, R.; Tsai, C.-J.; Jang, H. Anticancer Drug Resistance: An Update and Perspective. *Drug Resist. Updat. Rev. Comment. Antimicrob. Anticancer Chemother.* **2021**, *59*, 100796, doi:10.1016/j.drup.2021.100796.
5. Bhimani, J.; Philipps, L.; Simpson, L.; Lythgoe, M.; Soultati, A.; Webb, A.; Savage, P. The Impact of New Cancer Drug Therapies on Site Specialised Cancer Treatment Activity in a UK Cancer Network 2014-2018. *J. Oncol. Pharm. Pract. Off. Publ. Int. Soc. Oncol. Pharm. Pract.* **2020**, *26*, 93–98, doi:10.1177/1078155219839445.
6. Hatse, S.; De Clercq, E.; Balzarini, J. Role of Antimetabolites of Purine and Pyrimidine Nucleotide Metabolism in Tumor Cell Differentiation. *Biochem. Pharmacol.* **1999**, *58*, 539–555, doi:10.1016/s0006-2952(99)00035-0.
7. Parker, W.B. Enzymology of Purine and Pyrimidine Antimetabolites Used in the Treatment of Cancer. *Chem. Rev.* **2009**, *109*, 2880–2893, doi:10.1021/cr900028p.
8. Brunelle, J.K.; Zhang, B. Apoptosis Assays for Quantifying the Bioactivity of Anticancer Drug Products. *Drug Resist. Updat. Rev. Comment. Antimicrob. Anticancer Chemother.* **2010**, *13*, 172–179, doi:10.1016/j.drup.2010.09.001.
9. D'Arcy, M.S. Cell Death: A Review of the Major Forms of Apoptosis, Necrosis and Autophagy. *Cell Biol. Int.* **2019**, *43*, 582–592, doi:10.1002/cbin.11137.
10. Nussbaumer, S.; Bonnabry, P.; Veuthey, J.-L.; Fleury-Souverain, S. Analysis of Anticancer Drugs: A Review. *Talanta* **2011**, *85*, 2265–2289, doi:10.1016/j.talanta.2011.08.034.
11. Bukowski, K.; Kciuk, M.; Kontek, R. Mechanisms of Multidrug Resistance in Cancer Chemotherapy. *Int. J. Mol. Sci.* **2020**, *21*, doi:10.3390/ijms21093233.
12. Martins, P.; Jesus, J.; Santos, S.; Raposo, L.R.; Roma-Rodrigues, C.; Baptista, P.V.; Fernandes, A.R. Heterocyclic Anticancer Compounds: Recent Advances and the Paradigm Shift towards the Use of Nanomedicine's Tool Box. *Molecules* **2015**, *20*, 16852–16891, doi:10.3390/molecules200916852.
13. Swift, L.H.; Golsteyn, R.M. Genotoxic Anti-Cancer Agents and Their Relationship to DNA Damage, Mitosis, and Checkpoint Adaptation in Proliferating Cancer Cells. *Int. J. Mol. Sci.* **2014**, *15*, 3403–3431, doi:10.3390/ijms15033403.
14. Kabbaj, Y.; Lazrek, H.B.; Barascut, J.L.; Imbach, J.L. Synthesis and Biological Activity of Some Unsaturated 6-Azauracil Acyclonucleosides. *Nucleosides Nucleotides Nucleic Acids* **2005**, *24*, 161–172, doi:10.1081/NCN-55695.
15. Saad, H.A.; Moustafa, A.H. Synthesis and Anticancer Activity of Some New S-Glycosyl and s-Alkyl 1,2,4-Triazinone Derivatives. *Mol. Basel Switz.* **2011**, *16*, 5682–5700, doi:10.3390/molecules16075682.

16. Kumar, R.; Sirohi, T.S.; Singh, H.; Yadav, R.; Roy, R.K.; Chaudhary, A.; Pandeya, S.N. 1,2,4-Triazine Analogs as Novel Class of Therapeutic Agents. *Mini Rev. Med. Chem.* **2014**, *14*, 168–207, doi:10.2174/1389557514666140131111837.
17. Cascioferro, S.; Parrino, B.; Spanò, V.; Carbone, A.; Montalbano, A.; Barraja, P.; Diana, P.; Cirrincione, G. An Overview on the Recent Developments of 1,2,4-Triazine Derivatives as Anticancer Compounds. *Eur. J. Med. Chem.* **2017**, *142*, 328–375, doi:10.1016/j.ejmech.2017.08.009.
18. Bernat, Z.; Szymanowska, A.; Kciuk, M.; Kotwica-Mojzych, K.; Mojzych, M. Review of the Synthesis and Anticancer Properties of Pyrazolo[4,3-e][1,2,4]Triazine Derivatives. *Molecules* **2020**, *25*, doi:10.3390/molecules25173948.
19. Mojzych, M.; Rykowski, A.; Wierzchowski, J. Pyrazolo[4,3-e][1,2,4]Triazines: Purine Analogues with Electronic Absorption in the Visible Region. *Mol. Basel Switz.* **2005**, *10*, 1298–1306, doi:10.3390/10101298.
20. Mojzych, M.; Šubertová, V.; Bielawska, A.; Bielawski, K.; Bazgier, V.; Berka, K.; Gucký, T.; Fornal, E.; Kryštof, V. Synthesis and Kinase Inhibitory Activity of New Sulfonamide Derivatives of Pyrazolo[4,3-e][1,2,4]Triazines. *Eur. J. Med. Chem.* **2014**, *78*, 217–224, doi:10.1016/j.ejmech.2014.03.054.
21. Mojzych, M.; Ceruso, M.; Bielawska, A.; Bielawski, K.; Fornal, E.; Supuran, C.T. New Pyrazolo[4,3-e][1,2,4]Triazine Sulfonamides as Carbonic Anhydrase Inhibitors. *Bioorg. Med. Chem.* **2015**, *23*, 3674–3680, doi:10.1016/j.bmc.2015.04.011.
22. Mojzych, M.; Bielawska, A.; Bielawski, K.; Ceruso, M.; Supuran, C.T. Pyrazolo[4,3-e][1,2,4]Triazine Sulfonamides as Carbonic Anhydrase Inhibitors with Antitumor Activity. *Bioorg. Med. Chem.* **2014**, *22*, 2643–2647, doi:10.1016/j.bmc.2014.03.029.
23. Bukowski, K.; Marciniak, B.; Kciuk, M.; Mojzych, M.; Kontek, R. Pyrazolo[4,3-e]Tetrazolo[1,5-b][1,2,4]Triazine Sulfonamides as Novel Potential Anticancer Agents: Cytotoxic and Genotoxic Activities In Vitro. *Molecules 27*, doi:https://doi.org/10.3390/molecules27123761.
24. Gornowicz, A.; Szymanowska, A.; Mojzych, M.; Czarnomysy, R.; Bielawski, K.; Bielawska, A. The Anticancer Action of a Novel 1,2,4-Triazine Sulfonamide Derivative in Colon Cancer Cells. *Molecules* **2021**, *26*, 2045, doi:10.3390/molecules26072045.
25. Hermanowicz, J.M.; Szymanowska, A.; Sieklucka, B.; Czarnomysy, R.; Pawlak, K.; Bielawska, A.; Bielawski, K.; Kalafut, J.; Przybyszewska, A.; Surazynski, A.; et al. Exploration of Novel Heterofused 1,2,4-Triazine Derivative in Colorectal Cancer. *J. Enzyme Inhib. Med. Chem.* **2021**, *36*, 535–548, doi:10.1080/14756366.2021.1879803.
26. Gornowicz, A.; Szymanowska, A.; Mojzych, M.; Bielawski, K.; Bielawska, A. The Effect of Novel 7-Methyl-5-Phenyl-Pyrazolo[4,3-e]Tetrazolo[4,5-b][1,2,4]Triazine Sulfonamide Derivatives on Apoptosis and Autophagy in DLD-1 and HT-29 Colon Cancer Cells. *Int. J. Mol. Sci.* **2020**, *21*, 5221, doi:10.3390/ijms21155221.
27. Mohamed, A.J.; Yu, L.; Bäckesjö, C.-M.; Vargas, L.; Faryal, R.; Aints, A.; Christensson, B.; Berglöf, A.; Vihinen, M.; Nore, B.F.; et al. Bruton's Tyrosine Kinase (Btk): Function, Regulation, and Transformation with Special Emphasis on the PH Domain. *Immunol. Rev.* **2009**, *228*, 58–73, doi:10.1111/j.1600-065X.2008.00741.x.
28. Burger, J.A. Bruton Tyrosine Kinase Inhibitors: Present and Future. *Cancer J. Sudbury Mass* **2019**, *25*, 386–393, doi:10.1097/PPO.0000000000000412.
29. Hermanowicz, J.M.; Pawlak, K.; Sieklucka, B.; Czarnomysy, R.; Kwiatkowska, I.; Kazberuk, A.; Surazynski, A.; Mojzych, M.; Pawlak, D. MM-129 as a Novel Inhibitor

Targeting PI3K/AKT/MTOR and PD-L1 in Colorectal Cancer. *Cancers* **2021**, *13*, 3203, doi:10.3390/cancers13133203.
30. Nicholson, K.M.; Anderson, N.G. The Protein Kinase B/Akt Signalling Pathway in Human Malignancy. *Cell. Signal.* **2002**, *14*, 381–395, doi:10.1016/s0898-6568(01)00271-6.
31. Uko, N.E.; Güner, O.F.; Matesic, D.F.; Bowen, J.P. Akt Pathway Inhibitors. *Curr. Top. Med. Chem.* **2020**, *20*, 883–900, doi:10.2174/1568026620666200224101808.
32. Khan, K.H.; Yap, T.A.; Yan, L.; Cunningham, D. Targeting the PI3K-AKT-MTOR Signaling Network in Cancer. *Chin. J. Cancer* **2013**, *32*, 253–265, doi:10.5732/cjc.013.10057.
33. Alzahrani, A.S. PI3K/Akt/MTOR Inhibitors in Cancer: At the Bench and Bedside. *Semin. Cancer Biol.* **2019**, *59*, 125–132, doi:10.1016/j.semcancer.2019.07.009.
34. Tadesse, S.; Caldon, E.C.; Tilley, W.; Wang, S. Cyclin-Dependent Kinase 2 Inhibitors in Cancer Therapy: An Update. *J. Med. Chem.* **2019**, *62*, 4233–4251, doi:10.1021/acs.jmedchem.8b01469.
35. Akinleye, A.; Rasool, Z. Immune Checkpoint Inhibitors of PD-L1 as Cancer Therapeutics. *J. Hematol. Oncol.J Hematol Oncol* **2019**, *12*, 92, doi:10.1186/s13045-019-0779-5.
36. Liu, C.; Seeram, N.P.; Ma, H. Small Molecule Inhibitors against PD-1/PD-L1 Immune Checkpoints and Current Methodologies for Their Development: A Review. *Cancer Cell Int.* **2021**, *21*, 239, doi:10.1186/s12935-021-01946-4.
37. Lee, H.T.; Lee, S.H.; Heo, Y.-S. Molecular Interactions of Antibody Drugs Targeting PD-1, PD-L1, and CTLA-4 in Immuno-Oncology. *Mol. Basel Switz.* **2019**, *24*, E1190, doi:10.3390/molecules24061190.
38. Descourt, R.; Greillier, L.; Perol, M.; Ricordel, C.; Auliac, J.-B.; Falchero, L.; Gervais, R.; Veillon, R.; Vieillot, S.; Guisier, F.; et al. First-Line Single-Agent Pembrolizumab for PD-L1-Positive (Tumor Proportion Score ≥ 50%) Advanced Non-Small Cell Lung Cancer in the Real World: Impact in Brain Metastasis: A National French Multicentric Cohort (ESCKEYP GFPC Study). *Cancer Immunol. Immunother. CII* **2022**, doi:10.1007/s00262-022-03232-2.
39. Duan, H.; Shao, C.; Pan, M.; Liu, H.; Dong, X.; Zhang, Y.; Tong, L.; Feng, Y.; Wang, Y.; Wang, L.; et al. Neoadjuvant Pembrolizumab and Chemotherapy in Resectable Esophageal Cancer: An Open-Label, Single-Arm Study (PEN-ICE). *Front. Immunol.* **2022**, *13*, 849984, doi:10.3389/fimmu.2022.849984.
40. Wu, M.; Qin, S.; Wang, L.; Tan, C.; Peng, Y.; Zeng, X.; Luo, X.; Yi, L.; Wan, X. Cost-Effectiveness of Pembrolizumab Plus Chemotherapy as First-Line Therapy for Advanced Oesophageal Cancer. *Front. Pharmacol.* **2022**, *13*, 881787, doi:10.3389/fphar.2022.881787.
41. Miron, B.; Geynisman, D.M. Bempegaldesleukin/Nivolumab and Challenges in First-Line Treatment of Metastatic Urothelial Carcinoma. *Eur. Urol.* **2022**, S0302-2838(22)02399-5, doi:10.1016/j.eururo.2022.05.023.
42. Bennani, N.N.; Kim, H.J.; Pederson, L.D.; Atherton, P.J.; Micallef, I.N.; Thanarajasingam, G.; Nowakowski, G.S.; Witzig, T.; Feldman, A.L.; Ansell, S.M. Nivolumab in Patients with Relapsed or Refractory Peripheral T-Cell Lymphoma: Modest Activity and Cases of Hyperprogression. *J. Immunother. Cancer* **2022**, *10*, e004984, doi:10.1136/jitc-2022-004984.

43. Matsuo, M.; Yasumatsu, R.; Masuda, M.; Yamauchi, M.; Wakasaki, T.; Hashimoto, K.; Jiromaru, R.; Manako, T.; Nakagawa, T. Five-Year Follow-up of Patients With Head and Neck Cancer Treated With Nivolumab and Long-Term Responders for Over Two Years. *Vivo Athens Greece* **2022**, *36*, 1881–1886, doi:10.21873/invivo.12907.
44. Xiang, Z.; Li, J.; Zhang, Z.; Cen, C.; Chen, W.; Jiang, B.; Meng, Y.; Wang, Y.; Berglund, B.; Zhai, G.; et al. Comprehensive Evaluation of Anti-PD-1, Anti-PD-L1, Anti-CTLA-4 and Their Combined Immunotherapy in Clinical Trials: A Systematic Review and Meta-Analysis. *Front. Pharmacol.* **2022**, *13*, 883655, doi:10.3389/fphar.2022.883655.
45. Jiang, M.; Liu, C.; Ding, D.; Tian, H.; Yu, C. Comparative Efficacy and Safety of Anti-PD-1/PD-L1 for the Treatment of Non-Small Cell Lung Cancer: A Network Meta-Analysis of 13 Randomized Controlled Studies. *Front. Oncol.* **2022**, *12*, 827050, doi:10.3389/fonc.2022.827050.
46. Imai, H.; Nagai, Y.; Minemura, H.; Tsuda, T.; Yamada, Y.; Wasamoto, S.; Kishikawa, T.; Shiono, A.; Shiihara, J.; Yamaguchi, O.; et al. Efficacy and Safety of Amrubicin Monotherapy after Atezolizumab plus Carboplatin and Etoposide in Patients with Relapsed Small-Cell Lung Cancer. *Invest. New Drugs* **2022**, doi:10.1007/s10637-022-01269-9.
47. Kuwano, A.; Yada, M.; Narutomi, F.; Nagasawa, S.; Tanaka, K.; Kurosaka, K.; Ohishi, Y.; Masumoto, A.; Motomura, K. Therapeutic Efficacy of Atezolizumab plus Bevacizumab for Hepatocellular Carcinoma with WNT/β-Catenin Signal Activation. *Oncol. Lett.* **2022**, *24*, 216, doi:10.3892/ol.2022.13337.
48. Gürbüz, M.; Kutlu, Y.; Akkuş, E.; Köksoy, E.B.; Köse, N.; Öven, B.B.; Uluç, B.O.; Demiray, A.G.; Erdem, D.; Demir, B.; et al. Atezolizumab Combined with Chemotherapy in the First-Line Treatment of Extensive-Stage Small Cell Lung Cancer: A Real-Life Data of the Turkish Oncology Group. *J. Cancer Res. Clin. Oncol.* **2022**, doi:10.1007/s00432-022-04087-x.
49. Chan, D.L.; Rodriguez-Freixinos, V.; Doherty, M.; Wasson, K.; Iscoe, N.; Raskin, W.; Hallet, J.; Myrehaug, S.; Law, C.; Thawer, A.; et al. Avelumab in Unresectable/Metastatic, Progressive, Grade 2-3 Neuroendocrine Neoplasms (NENs): Combined Results from NET-001 and NET-002 Trials. *Eur. J. Cancer Oxf. Engl. 1990* **2022**, *169*, 74–81, doi:10.1016/j.ejca.2022.03.029.
50. Kim, E.S. Avelumab: First Global Approval. *Drugs* **2017**, *77*, 929–937, doi:10.1007/s40265-017-0749-6.
51. Kawanaka, Y.; Yasuda, Y.; Tanizaki, J.; Iwashima, D.; Nonagase, Y.; Uemasu, K.; Hirayama, Y.; Ogura, M.; Ozaki, T.; Takahashi, K.-I. The Safety and Efficacy of Durvalumab Consolidation Therapy in the Management of Patients with Stage III Non-Small-Cell Lung Cancer and Preexisting Interstitial Lung Disease. *Respir. Investig.* **2022**, S2212-5345(22)00059-4, doi:10.1016/j.resinv.2022.05.004.
52. Rosenberg, J.E.; Park, S.H.; Kozlov, V.; Dao, T.V.; Castellano, D.; Li, J.-R.; Mukherjee, S.D.; Howells, K.; Dry, H.; Lanasa, M.C.; et al. Durvalumab Plus Olaparib in Previously Untreated, Platinum-Ineligible Patients With Metastatic Urothelial Carcinoma: A Multicenter, Randomized, Phase II Trial (BAYOU). *J. Clin. Oncol. Off. J. Am. Soc. Clin. Oncol.* **2022**, JCO2200205, doi:10.1200/JCO.22.00205.
53. Fang, L.; Tian, J.; Zhang, K.; Zhang, X.; Liu, Y.; Cheng, Z.; Zhou, J.; Zhang, H. Discovery of 1,3,4-Oxadiazole Derivatives as Potential Antitumor Agents Inhibiting the Programmed Cell Death-1/Programmed Cell Death-Ligand 1 Interaction. *Bioorg. Med. Chem.* **2021**, *46*, 116370, doi:10.1016/j.bmc.2021.116370.

54. Kciuk, M.; Kołat, D.; Kałuzińska-Kołat, Ż.; Gawrysiak, M.; Drozda, R.; Celik, I.; Kontek, R. PD-1/PD-L1 and DNA Damage Response in Cancer. *Cells* **2023**, *12*, 530, doi:10.3390/cells12040530.
55. Bukowski, K.; Marciniak, B.; Kciuk, M.; Mujwar, S.; Mojzych, M.; Kontek, R. Pyrazolo[4,3-e]Tetrazolo[1,5-b][1,2,4]Triazine Sulfonamides as Novel Potential Anticancer Agents: Apoptosis, Oxidative Stress, and Cell Cycle Analysis. *Int. J. Mol. Sci.* **2023**, *24*, 8504, doi:10.3390/ijms24108504.
56. Dennison, S.R.; Whittaker, M.; Harris, F.; Phoenix, D.A. Anticancer Alpha-Helical Peptides and Structure/Function Relationships Underpinning Their Interactions with Tumour Cell Membranes. *Curr. Protein Pept. Sci.* **2006**, *7*, 487–499, doi:10.2174/138920306779025611.
57. Kumar, N.; Goel, N. Heterocyclic Compounds: Importance in Anticancer Drug Discovery. *Anticancer Agents Med. Chem.* **2022**, *22*, 3196–3207, doi:10.2174/1871520622666220404082648.
58. Mojzych, M.; Karczmarzyk, Z.; Wysocki, W.; Urbańczyk-Lipkowska, Z.; Żaczek, N. Valence Tautomerism of New Pyrazolo[4,3-e]Tetrazole[4,5-b][1,2,4]Triazines. *J Mol Struct* **2014**, *1067*, 147–153.
59. Cmoch, P. Multinuclear Magnetic Resonance Study of the Structure and Tautomerism of Azide and Iminophosphorane Derivatives of Chloropyridazines. *Magn. Reson. Chem.* **2002**, *40*, 507–516, doi:10.1002/mrc.1055.
60. Karczmarzyk, Z.; Mojzych, M.; Rykowski, A. Synthesis and Structure of a Novel Mesomeric Betaine 6,7-Dimethyl-2H-Pyrazolo[4,3-e]Tetrazolo[4,5-b][1,2,4]Triazine. *J. Mol. Struct.* **2007**, *829*, 22–28, doi:10.1016/j.molstruc.2006.06.003.
61. Mojzych, M.; Karczmarzyk, Z.; Rykowski, A. Synthesis and Structure of 7-Methyl-5-Phenyl-1H-Pyrazolo[4,3-e]Tetrazolo[4,5-b][1,2,4]Triazine. *J Chem Crystallogr* **2005**, *35*, 151–155.
62. Deev, S.L.; Shestakova, T.; Charushin, V.N.; Chupakhin, O.N. Synthesis and Azido-Tetrazole Tautomerism of 3-Azido-1,2,4-Triazin. *Chem Heterocycl Compd* **2017**, *53*, 963–975.
63. Kciuk, M.; Mujwar, S.; Szymanowska, A.; Marciniak, B.; Bukowski, K.; Mojzych, M.; Kontek, R. Preparation of Novel Pyrazolo[4,3-e]Tetrazolo[1,5-b][1,2,4]Triazine Sulfonamides and Their Experimental and Computational Biological Studies. *Int. J. Mol. Sci.* **2022**, *23*, doi:10.3390/ijms23115892.
64. Phillips, D.H.; Arlt, V.M. Genotoxicity: Damage to DNA and Its Consequences. *EXS* **2009**, *99*, 87–110, doi:10.1007/978-3-7643-8336-7_4.
65. Barabadi, H.; Najafi, M.; Samadian, H.; Azarnezhad, A.; Vahidi, H.; Mahjoub, M.A.; Koohiyan, M.; Ahmadi, A. A Systematic Review of the Genotoxicity and Antigenotoxicity of Biologically Synthesized Metallic Nanomaterials: Are Green Nanoparticles Safe Enough for Clinical Marketing? *Medicina (Mex.)* **2019**, *55*, 439, doi:10.3390/medicina55080439.
66. Czubaszek, M.; Szostek, M.; Wójcik, E.; Andraszek, K. [The comet assay as a method of identifying chromosomes instability]. *Postepy Hig. Med. Doswiadczalnej Online* **2014**, *68*, 695–700, doi:10.5604/17322693.1106384.
67. Horváthová, E.; Slamenová, D.; Gábelová, A. Use of Single Cell Gel Electrophoresis (Comet Assay) Modifications for Analysis of DNA Damage. *Gen. Physiol. Biophys.* **1999**, *18 Spec No*, 70–74.

68. Hartmann, A.; Agurell, E.; Beevers, C.; Brendler-Schwaab, S.; Burlinson, B.; Clay, P.; Collins, A.; Smith, A.; Speit, G.; Thybaud, V.; et al. Recommendations for Conducting the in Vivo Alkaline Comet Assay. 4th International Comet Assay Workshop. *Mutagenesis* **2003**, *18*, 45–51, doi:10.1093/mutage/18.1.45.
69. de Lapuente, J.; Lourenço, J.; Mendo, S.A.; Borràs, M.; Martins, M.G.; Costa, P.M.; Pacheco, M. The Comet Assay and Its Applications in the Field of Ecotoxicology: A Mature Tool That Continues to Expand Its Perspectives. *Front. Genet.* **2015**, *6*, 180, doi:10.3389/fgene.2015.00180.
70. Singh, N.P.; McCoy, M.T.; Tice, R.R.; Schneider, E.L. A Simple Technique for Quantitation of Low Levels of DNA Damage in Individual Cells. *Exp. Cell Res.* **1988**, *175*, 184–191, doi:10.1016/0014-4827(88)90265-0.
71. Fairbairn, D.W.; Olive, P.L.; O'Neill, K.L. The Comet Assay: A Comprehensive Review. *Mutat. Res.* **1995**, *339*, 37–59, doi:10.1016/0165-1110(94)00013-3.
72. Nagelkerke, A.; Span, P.N. Staining Against Phospho-H2AX (γ-H2AX) as a Marker for DNA Damage and Genomic Instability in Cancer Tissues and Cells. *Adv. Exp. Med. Biol.* **2016**, *899*, 1–10, doi:10.1007/978-3-319-26666-4_1.
73. Nikolova, T.; Marini, F.; Kaina, B. Genotoxicity Testing: Comparison of the ΓH2AX Focus Assay with the Alkaline and Neutral Comet Assays. *Mutat. Res. Genet. Toxicol. Environ. Mutagen.* **2017**, *822*, 10–18, doi:10.1016/j.mrgentox.2017.07.004.
74. Cheng, B.; Pan, W.; Xing, Y.; Xiao, Y.; Chen, J.; Xu, Z. Recent Advances in DDR (DNA Damage Response) Inhibitors for Cancer Therapy. *Eur. J. Med. Chem.* **2022**, *230*, 114109, doi:10.1016/j.ejmech.2022.114109.
75. Choi, W.; Lee, E.S. Therapeutic Targeting of DNA Damage Response in Cancer. *Int. J. Mol. Sci.* **2022**, *23*, 1701, doi:10.3390/ijms23031701.
76. Rr, T.; E, A.; D, A.; B, B.; A, H.; H, K.; Y, M.; E, R.; Jc, R.; Yf, S. Single Cell Gel/Comet Assay: Guidelines for in Vitro and in Vivo Genetic Toxicology Testing. *Environ. Mol. Mutagen.* **2000**, *35*, doi:10.1002/(sici)1098-2280(2000)35:3<206::aid-em8>3.0.co;2-j.
77. Burlinson, B.; Tice, R.R.; Speit, G.; Agurell, E.; Brendler-Schwaab, S.Y.; Collins, A.R.; Escobar, P.; Honma, M.; Kumaravel, T.S.; Nakajima, M.; et al. Fourth International Workgroup on Genotoxicity Testing: Results of the in Vivo Comet Assay Workgroup. *Mutat. Res. Toxicol. Environ. Mutagen.* **2007**, *627*, 31–35, doi:10.1016/j.mrgentox.2006.08.011.
78. A, A.; H, S.; B, Z.; M, D.; P, M. Do Cytotoxicity and Cell Death Cause False Positive Results in the in Vitro Comet Assay? *Mutat. Res. Genet. Toxicol. Environ. Mutagen.* **2022**, *881*, doi:10.1016/j.mrgentox.2022.503520.
79. Sirbu, B.M.; Cortez, D. DNA Damage Response: Three Levels of DNA Repair Regulation. *Cold Spring Harb. Perspect. Biol.* **2013**, *5*, a012724, doi:10.1101/cshperspect.a012724.
80. Kozlov, S.V.; Graham, M.E.; Jakob, B.; Tobias, F.; Kijas, A.W.; Tanuji, M.; Chen, P.; Robinson, P.J.; Taucher-Scholz, G.; Suzuki, K.; et al. Autophosphorylation and ATM Activation: Additional Sites Add to the Complexity. *J. Biol. Chem.* **2011**, *286*, 9107–9119, doi:10.1074/jbc.M110.204065.
81. Pilié, P.G.; Tang, C.; Mills, G.B.; Yap, T.A. State-of-the-Art Strategies for Targeting the DNA Damage Response in Cancer. *Nat. Rev. Clin. Oncol.* **2019**, *16*, 81–104, doi:10.1038/s41571-018-0114-z.
82. Romani, A.M.P. Cisplatin in Cancer Treatment. *Biochem. Pharmacol.* **2022**, *206*, 115323, doi:10.1016/j.bcp.2022.115323.

83. Zhang, Y.; Ding, C.; Zhu, W.; Li, X.; Chen, T.; Liu, Q.; Zhou, S.; Zhang, T.-C.; Ma, W. Chemotherapeutic Drugs Induce Oxidative Stress Associated with DNA Repair and Metabolism Modulation. *Life Sci.* **2022**, *289*, 120242, doi:10.1016/j.lfs.2021.120242.
84. Kciuk, M.; Gielecińska, A.; Mujwar, S.; Kołat, D.; Kałuzińska-Kołat, Ż.; Celik, I.; Kontek, R. Doxorubicin-An Agent with Multiple Mechanisms of Anticancer Activity. *Cells* **2023**, *12*, 659, doi:10.3390/cells12040659.
85. Allawzi, A.; Elajaili, H.; Redente, E.F.; Nozik-Grayck, E. Oxidative Toxicology of Bleomycin: Role of the Extracellular Redox Environment. *Curr. Opin. Toxicol.* **2019**, *13*, 68–73, doi:10.1016/j.cotox.2018.08.001.
86. Yokoyama, C.; Sueyoshi, Y.; Ema, M.; Mori, Y.; Takaishi, K.; Hisatomi, H. Induction of Oxidative Stress by Anticancer Drugs in the Presence and Absence of Cells. *Oncol. Lett.* **2017**, *14*, 6066–6070, doi:10.3892/ol.2017.6931.
87. Repetto, G.; del Peso, A.; Zurita, J.L. Neutral Red Uptake Assay for the Estimation of Cell Viability/Cytotoxicity. *Nat. Protoc.* **2008**, *3*, 1125–1131, doi:10.1038/nprot.2008.75.
88. Ates, G.; Vanhaecke, T.; Rogiers, V.; Rodrigues, R.M. Assaying Cellular Viability Using the Neutral Red Uptake Assay. *Methods Mol. Biol. Clifton NJ* **2017**, *1601*, 19–26, doi:10.1007/978-1-4939-6960-9_2.
89. Reiniers, M.J.; van Golen, R.F.; Bonnet, S.; Broekgaarden, M.; van Gulik, T.M.; Egmond, M.R.; Heger, M. Preparation and Practical Applications of 2′,7′-Dichlorodihydrofluorescein in Redox Assays. *Anal. Chem.* **2017**, *89*, 3853–3857, doi:10.1021/acs.analchem.7b00043.
90. Riccardi, C.; Nicoletti, I. Analysis of Apoptosis by Propidium Iodide Staining and Flow Cytometry. *Nat. Protoc.* **2006**, *1*, 1458–1461, doi:10.1038/nprot.2006.238.
91. Kciuk, M.; Mujwar, S.; Marciniak, B.; Gielecińska, A.; Bukowski, K.; Mojzych, M.; Kontek, R. Genotoxicity of Novel Pyrazolo[4,3-e]Tetrazolo[1,5-b][1,2,4]Triazine Sulfonamides in Normal and Cancer Cells In Vitro. *Int. J. Mol. Sci.* **2023**, *24*, 4053, doi:10.3390/ijms24044053.
92. Matassov, D.; Kagan, T.; Leblanc, J.; Sikorska, M.; Zakeri, Z. Measurement of Apoptosis by DNA Fragmentation. *Methods Mol. Biol. Clifton NJ* **2004**, *282*, 1–17, doi:10.1385/1-59259-812-9:001.
93. Majtnerová, P.; Roušar, T. An Overview of Apoptosis Assays Detecting DNA Fragmentation. *Mol. Biol. Rep.* **2018**, *45*, 1469–1478, doi:10.1007/s11033-018-4258-9.
94. Wang, L.; Guo, Y.; Huang, W.J.; Ke, X.; Poyet, J.L.; Manji, G.A.; Merriam, S.; Glucksmann, M.A.; DiStefano, P.S.; Alnemri, E.S.; et al. Card10 Is a Novel Caspase Recruitment Domain/Membrane-Associated Guanylate Kinase Family Member That Interacts with BCL10 and Activates NF-Kappa B. *J. Biol. Chem.* **2001**, *276*, 21405–21409, doi:10.1074/jbc.M102488200.
95. Yui, D.; Yoneda, T.; Oono, K.; Katayama, T.; Imaizumi, K.; Tohyama, M. Interchangeable Binding of Bcl10 to TRAF2 and CIAPs Regulates Apoptosis Signaling. *Oncogene* **2001**, *20*, 4317–4323, doi:10.1038/sj.onc.1204576.
96. Luo, Y.; Wu, J.; Zou, J.; Cao, Y.; He, Y.; Ling, H.; Zeng, T. BCL10 in Cell Survival after DNA Damage. *Clin. Chim. Acta Int. J. Clin. Chem.* **2019**, *495*, 301–308, doi:10.1016/j.cca.2019.04.077.
97. Micheau, O. Regulation of TNF-Related Apoptosis-Inducing Ligand Signaling by Glycosylation. *Int. J. Mol. Sci.* **2018**, *19*, 715, doi:10.3390/ijms19030715.
98. Nahacka, Z.; Svadlenka, J.; Peterka, M.; Ksandrova, M.; Benesova, S.; Neuzil, J.; Andera, L. TRAIL Induces Apoptosis but Not Necroptosis in Colorectal and

Pancreatic Cancer Cells Preferentially via the TRAIL-R2/DR5 Receptor. *Biochim. Biophys. Acta Mol. Cell Res.* **2018**, *1865*, 522–531, doi:10.1016/j.bbamcr.2017.12.006.
99. Shlyakhtina, Y.; Pavet, V.; Gronemeyer, H. Dual Role of DR5 in Death and Survival Signaling Leads to TRAIL Resistance in Cancer Cells. *Cell Death Dis.* **2017**, *8*, e3025, doi:10.1038/cddis.2017.423.
100. Dhuriya, Y.K.; Sharma, D. Necroptosis: A Regulated Inflammatory Mode of Cell Death. *J. Neuroinflammation* **2018**, *15*, 199, doi:10.1186/s12974-018-1235-0.
101. Park, M.Y.; Ha, S.E.; Vetrivel, P.; Kim, H.H.; Bhosale, P.B.; Abusaliya, A.; Kim, G.S. Differences of Key Proteins between Apoptosis and Necroptosis. *BioMed Res. Int.* **2021**, *2021*, 3420168, doi:10.1155/2021/3420168.
102. Zargarian, S.; Shlomovitz, I.; Erlich, Z.; Hourizadeh, A.; Ofir-Birin, Y.; Croker, B.A.; Regev-Rudzki, N.; Edry-Botzer, L.; Gerlic, M. Phosphatidylserine Externalization, "Necroptotic Bodies" Release, and Phagocytosis during Necroptosis. *PLoS Biol.* **2017**, *15*, e2002711, doi:10.1371/journal.pbio.2002711.
103. Shlomovitz, I.; Speir, M.; Gerlic, M. Flipping the Dogma - Phosphatidylserine in Non-Apoptotic Cell Death. *Cell Commun. Signal. CCS* **2019**, *17*, 139, doi:10.1186/s12964-019-0437-0.
104. Li, K.; Qiu, J.; Pan, J.; Pan, J.-P. Pyroptosis and Its Role in Cervical Cancer. *Cancers* **2022**, *14*, 5764, doi:10.3390/cancers14235764.
105. Tamura, R.E.; de Vasconcellos, J.F.; Sarkar, D.; Libermann, T.A.; Fisher, P.B.; Zerbini, L.F. GADD45 Proteins: Central Players in Tumorigenesis. *Curr. Mol. Med.* **2012**, *12*, 634–651, doi:10.2174/156652412800619978.
106. Jin, S.; Mazzacurati, L.; Zhu, X.; Tong, T.; Song, Y.; Shujuan, S.; Petrik, K.L.; Rajasekaran, B.; Wu, M.; Zhan, Q. Gadd45a Contributes to P53 Stabilization in Response to DNA Damage. *Oncogene* **2003**, *22*, 8536–8540, doi:10.1038/sj.onc.1206907.
107. Carrier, F.; Smith, M.L.; Bae, I.; Kilpatrick, K.E.; Lansing, T.J.; Chen, C.Y.; Engelstein, M.; Friend, S.H.; Henner, W.D.; Gilmer, T.M. Characterization of Human Gadd45, a P53-Regulated Protein. *J. Biol. Chem.* **1994**, *269*, 32672–32677.
108. Zhan, Q.; Fan, S.; Smith, M.L.; Bae, I.; Yu, K.; Alamo, I.; O'Connor, P.M.; Fornace, A.J. Abrogation of P53 Function Affects Gadd Gene Responses to DNA Base-Damaging Agents and Starvation. *DNA Cell Biol.* **1996**, *15*, 805–815, doi:10.1089/dna.1996.15.805.
109. Zhan, Q.; Antinore, M.J.; Wang, X.W.; Carrier, F.; Smith, M.L.; Harris, C.C.; Fornace, A.J. Association with Cdc2 and Inhibition of Cdc2/Cyclin B1 Kinase Activity by the P53-Regulated Protein Gadd45. *Oncogene* **1999**, *18*, 2892–2900, doi:10.1038/sj.onc.1202667.
110. Vairapandi, M.; Balliet, A.G.; Hoffman, B.; Liebermann, D.A. GADD45b and GADD45g Are Cdc2/CyclinB1 Kinase Inhibitors with a Role in S and G2/M Cell Cycle Checkpoints Induced by Genotoxic Stress. *J. Cell. Physiol.* **2002**, *192*, 327–338, doi:10.1002/jcp.10140.
111. Nakayama, K.; Hara, T.; Hibi, M.; Hirano, T.; Miyajima, A. A Novel Oncostatin M-Inducible Gene OIG37 Forms a Gene Family with MyD118 and GADD45 and Negatively Regulates Cell Growth. *J. Biol. Chem.* **1999**, *274*, 24766–24772, doi:10.1074/jbc.274.35.24766.
112. Jin, S.; Tong, T.; Fan, W.; Fan, F.; Antinore, M.J.; Zhu, X.; Mazzacurati, L.; Li, X.; Petrik, K.L.; Rajasekaran, B.; et al. GADD45-Induced Cell Cycle G2-M Arrest Associates with Altered Subcellular Distribution of Cyclin B1 and Is Independent of P38 Kinase Activity. *Oncogene* **2002**, *21*, 8696–8704, doi:10.1038/sj.onc.1206034.

113. Zhu, Q.-S.; Ren, W.; Korchin, B.; Lahat, G.; Dicker, A.; Lu, Y.; Mills, G.; Pollock, R.E.; Lev, D. Soft Tissue Sarcoma Are Highly Sensitive to AKT Blockade: A Role for P53 Independent Up-Regulation of GADD45α. *Cancer Res.* **2008**, *68*, 2895–2903, doi:10.1158/0008-5472.CAN-07-6268.
114. Geromichalos, G.D. Importance of Molecular Computer Modeling in Anticancer Drug Development. *J. BUON Off. J. Balk. Union Oncol.* **2007**, *12 Suppl 1*, S101-118.
115. Garofalo, M.; Grazioso, G.; Cavalli, A.; Sgrignani, J. How Computational Chemistry and Drug Delivery Techniques Can Support the Development of New Anticancer Drugs. *Mol. Basel Switz.* **2020**, *25*, 1756, doi:10.3390/molecules25071756.
116. Baig, M.H.; Ahmad, K.; Rabbani, G.; Danishuddin, M.; Choi, I. Computer Aided Drug Design and Its Application to the Development of Potential Drugs for Neurodegenerative Disorders. *Curr. Neuropharmacol.* **2018**, *16*, 740–748, doi:10.2174/1570159X15666171016163510.
117. Geromichalos, G.D.; Alifieris, C.E.; Geromichalou, E.G.; Trafalis, D.T. Overview on the Current Status on Virtual High-Throughput Screening and Combinatorial Chemistry Approaches in Multi-Target Anticancer Drug Discovery; Part II. *J. BUON Off. J. Balk. Union Oncol.* **2016**, *21*, 1337–1358.
118. Cui, W.; Aouidate, A.; Wang, S.; Yu, Q.; Li, Y.; Yuan, S. Discovering Anti-Cancer Drugs via Computational Methods. *Front. Pharmacol.* **2020**, *11*, 733, doi:10.3389/fphar.2020.00733.
119. Agoni, C.; Olotu, F.A.; Ramharack, P.; Soliman, M.E. Druggability and Drug-Likeness Concepts in Drug Design: Are Biomodelling and Predictive Tools Having Their Say? *J. Mol. Model.* **2020**, *26*, 120, doi:10.1007/s00894-020-04385-6.
120. Daina, A.; Michielin, O.; Zoete, V. SwissADME: A Free Web Tool to Evaluate Pharmacokinetics, Drug-Likeness and Medicinal Chemistry Friendliness of Small Molecules. *Sci. Rep.* **2017**, *7*, 42717, doi:10.1038/srep42717.
121. Gm, M.; M, L.-W. Molecular Docking. *Methods Mol. Biol. Clifton NJ* **2008**, *443*, doi:10.1007/978-1-59745-177-2_19.
122. Bitencourt-Ferreira, G.; Pintro, V.O.; de Azevedo, W.F. Docking with AutoDock4. *Methods Mol. Biol. Clifton NJ* **2019**, *2053*, 125–148, doi:10.1007/978-1-4939-9752-7_9.
123. Hollingsworth, S.A.; Dror, R.O. Molecular Dynamics Simulation for All. *Neuron* **2018**, *99*, 1129–1143, doi:10.1016/j.neuron.2018.08.011.
124. Lindahl, E.R. Molecular Dynamics Simulations. *Methods Mol. Biol. Clifton NJ* **2008**, *443*, 3–23, doi:10.1007/978-1-59745-177-2_1.
125. Hernández-Rodríguez, M.; Rosales-Hernández, M.C.; Mendieta-Wejebe, J.E.; Martínez-Archundia, M.; Basurto, J.C. Current Tools and Methods in Molecular Dynamics (MD) Simulations for Drug Design. *Curr. Med. Chem.* **2016**, *23*, 3909–3924, doi:10.2174/0929867323666160530144742.
126. Hermanowicz, J.M.; Kalaska, B.; Pawlak, K.; Sieklucka, B.; Miklosz, J.; Mojzych, M.; Pawlak, D. Preclinical Toxicity and Safety of MM-129-First-in-Class BTK/PD-L1 Inhibitor as a Potential Candidate against Colon Cancer. *Pharmaceutics* **2021**, *13*, 1222, doi:10.3390/pharmaceutics13081222.
127. Mojzych, M.; Bernat, Z.; Karczmarzyk, Z.; Matysiak, J.; Fruziński, A. Synthesis, Structural Characterization, and Biological Activity of New Pyrazolo[4,3-e][1,2,4]Triazine Acyclonucleosides. *Molecules* **2020**, *25*, 221, doi:10.3390/molecules25010221.

128. Mojzych, M.; Karczmarzyk, Z.; Wysocki, W.; Ceruso, M.; Supuran, C.T.; Kryštof, V.; Urbańczyk-Lipkowska, Z.; Kalicki, P. New Approaches to the Synthesis of Sildenafil Analogues and Their Enzyme Inhibitory Activity. *Bioorg. Med. Chem.* **2015**, *23*, 1421–1429, doi:10.1016/j.bmc.2015.02.026.
129. Matysiak, J.; Skrzypek, A.; Tarasiuk, P.; Mojzych, M. QSAR Study of Pyrazolo[4,3-e][1,2,4]Triazine Sulfonamides against Tumor-Associated Human Carbonic Anhydrase Isoforms IX and XII. *Comput. Biol. Chem.* **2017**, *71*, 57–62, doi:10.1016/j.compbiolchem.2017.09.006.
130. Angeli, A.; Carta, F.; Nocentini, A.; Winum, J.-Y.; Zalubovskis, R.; Akdemir, A.; Onnis, V.; Eldehna, W.M.; Capasso, C.; Simone, G.D.; et al. Carbonic Anhydrase Inhibitors Targeting Metabolism and Tumor Microenvironment. *Metabolites* **2020**, *10*, 412, doi:10.3390/metabo10100412.
131. Kciuk, M.; Gielecińska, A.; Mujwar, S.; Mojzych, M.; Marciniak, B.; Drozda, R.; Kontek, R. Targeting Carbonic Anhydrase IX and XII Isoforms with Small Molecule Inhibitors and Monoclonal Antibodies. *J. Enzyme Inhib. Med. Chem.* **2022**, *37*, 1278–1298, doi:10.1080/14756366.2022.2052868.
132. Mahon, B.P.; Pinard, M.A.; McKenna, R. Targeting Carbonic Anhydrase IX Activity and Expression. *Molecules* **2015**, *20*, 2323–2348, doi:10.3390/molecules20022323.
133. Martínez, L. Automatic Identification of Mobile and Rigid Substructures in Molecular Dynamics Simulations and Fractional Structural Fluctuation Analysis. *PLoS ONE* **2015**, *10*, e0119264, doi:10.1371/journal.pone.0119264.
134. Sargsyan, K.; Grauffel, C.; Lim, C. How Molecular Size Impacts RMSD Applications in Molecular Dynamics Simulations. *J. Chem. Theory Comput.* **2017**, *13*, 1518–1524, doi:10.1021/acs.jctc.7b00028.
135. Jain, A.N. Scoring Functions for Protein-Ligand Docking. *Curr. Protein Pept. Sci.* **2006**, *7*, 407–420, doi:10.2174/138920306778559395.
136. Li, J.; Fu, A.; Zhang, L. An Overview of Scoring Functions Used for Protein-Ligand Interactions in Molecular Docking. *Interdiscip. Sci. Comput. Life Sci.* **2019**, *11*, 320–328, doi:10.1007/s12539-019-00327-w.
137. Guvench, O.; MacKerell, A.D. Comparison of Protein Force Fields for Molecular Dynamics Simulations. *Methods Mol. Biol. Clifton NJ* **2008**, *443*, 63–88, doi:10.1007/978-1-59745-177-2_4.
138. Monticelli, L.; Tieleman, D.P. Force Fields for Classical Molecular Dynamics. *Methods Mol. Biol. Clifton NJ* **2013**, *924*, 197–213, doi:10.1007/978-1-62703-017-5_8.
139. Freeman-Cook, K.D.; Autry, C.; Borzillo, G.; Gordon, D.; Barbacci-Tobin, E.; Bernardo, V.; Briere, D.; Clark, T.; Corbett, M.; Jakubczak, J.; et al. Design of Selective, ATP-Competitive Inhibitors of Akt. *J. Med. Chem.* **2010**, *53*, 4615–4622, doi:10.1021/jm1003842.
140. Heerding, D.A.; Rhodes, N.; Leber, J.D.; Clark, T.J.; Keenan, R.M.; Lafrance, L.V.; Li, M.; Safonov, I.G.; Takata, D.T.; Venslavsky, J.W.; et al. Identification of 4-(2-(4-Amino-1,2,5-Oxadiazol-3-Yl)-1-Ethyl-7-{[(3S)-3-Piperidinylmethyl]Oxy}-1H-Imidazo[4,5-c]Pyridin-4-Yl)-2-Methyl-3-Butyn-2-Ol (GSK690693), a Novel Inhibitor of AKT Kinase. *J. Med. Chem.* **2008**, *51*, 5663–5679, doi:10.1021/jm8004527.
141. Marcotte, D.J.; Liu, Y.-T.; Arduini, R.M.; Hession, C.A.; Miatkowski, K.; Wildes, C.P.; Cullen, P.F.; Hong, V.; Hopkins, B.T.; Mertsching, E.; et al. Structures of Human Bruton's Tyrosine Kinase in Active and Inactive Conformations Suggest a

Mechanism of Activation for TEC Family Kinases. *Protein Sci. Publ. Protein Soc.* **2010**, *19*, 429–439, doi:10.1002/pro.321.

142. Reader, J.C.; Matthews, T.P.; Klair, S.; Cheung, K.-M.J.; Scanlon, J.; Proisy, N.; Addison, G.; Ellard, J.; Piton, N.; Taylor, S.; et al. Structure-Guided Evolution of Potent and Selective CHK1 Inhibitors through Scaffold Morphing. *J. Med. Chem.* **2011**, *54*, 8328–8342, doi:10.1021/jm2007326.
143. Yang, H.; Jiang, X.; Li, B.; Yang, H.J.; Miller, M.; Yang, A.; Dhar, A.; Pavletich, N.P. Mechanisms of MTORC1 Activation by RHEB and Inhibition by PRAS40. *Nature* **2017**, *552*, 368–373, doi:10.1038/nature25023.
144. Butera, R.; Ważyńska, M.; Magiera-Mularz, K.; Plewka, J.; Musielak, B.; Surmiak, E.; Sala, D.; Kitel, R.; de Bruyn, M.; Nijman, H.W.; et al. Design, Synthesis, and Biological Evaluation of Imidazopyridines as PD-1/PD-L1 Antagonists. *ACS Med. Chem. Lett.* **2021**, *12*, 768–773, doi:10.1021/acsmedchemlett.1c00033.
145. Krammer, A.; Kirchhoff, P.D.; Jiang, X.; Venkatachalam, C.M.; Waldman, M. LigScore: A Novel Scoring Function for Predicting Binding Affinities. *J. Mol. Graph. Model.* **2005**, *23*, 395–407, doi:10.1016/j.jmgm.2004.11.007.
146. Krovat, E.M.; Langer, T. Impact of Scoring Functions on Enrichment in Docking-Based Virtual Screening: An Application Study on Renin Inhibitors. *J. Chem. Inf. Comput. Sci.* **2004**, *44*, 1123–1129, doi:10.1021/ci0342728.
147. Muegge, I.; Martin, Y.C. A General and Fast Scoring Function for Protein-Ligand Interactions: A Simplified Potential Approach. *J. Med. Chem.* **1999**, *42*, 791–804, doi:10.1021/jm980536j.
148. Sirico, M.; D'Angelo, A.; Gianni, C.; Casadei, C.; Merloni, F.; De Giorgi, U. Current State and Future Challenges for PI3K Inhibitors in Cancer Therapy. *Cancers* **2023**, *15*, 703, doi:10.3390/cancers15030703.
149. Genheden, S.; Ryde, U. The MM/PBSA and MM/GBSA Methods to Estimate Ligand-Binding Affinities. *Expert Opin. Drug Discov.* **2015**, *10*, 449–461, doi:10.1517/17460441.2015.1032936.
150. Wang, E.; Sun, H.; Wang, J.; Wang, Z.; Liu, H.; Zhang, J.Z.H.; Hou, T. End-Point Binding Free Energy Calculation with MM/PBSA and MM/GBSA: Strategies and Applications in Drug Design. *Chem. Rev.* **2019**, *119*, 9478–9508, doi:10.1021/acs.chemrev.9b00055.
151. Loschwitz, J.; Jäckering, A.; Keutmann, M.; Olagunju, M.; Olubiyi, O.O.; Strodel, B. Dataset of AMBER Force Field Parameters of Drugs, Natural Products and Steroids for Simulations Using GROMACS. *Data Brief* **2021**, *35*, 106948, doi:10.1016/j.dib.2021.106948.
152. Bitencourt-Ferreira, G.; Veit-Acosta, M.; de Azevedo, W.F. Hydrogen Bonds in Protein-Ligand Complexes. *Methods Mol. Biol. Clifton NJ* **2019**, *2053*, 93–107, doi:10.1007/978-1-4939-9752-7_7.
153. Yanao, T.; Koon, W.S.; Marsden, J.E.; Kevrekidis, I.G. Gyration-Radius Dynamics in Structural Transitions of Atomic Clusters. *J. Chem. Phys.* **2007**, *126*, 124102, doi:10.1063/1.2710272.
154. Ahmed, M.C.; Crehuet, R.; Lindorff-Larsen, K. Computing, Analyzing, and Comparing the Radius of Gyration and Hydrodynamic Radius in Conformational Ensembles of Intrinsically Disordered Proteins. *Methods Mol. Biol. Clifton NJ* **2020**, *2141*, 429–445, doi:10.1007/978-1-0716-0524-0_21.

155. Mazurek, A.H.; Szeleszczuk, Ł.; Pisklak, D.M. Periodic DFT Calculations-Review of Applications in the Pharmaceutical Sciences. *Pharmaceutics* **2020**, *12*, 415, doi:10.3390/pharmaceutics12050415.
156. Ye, N.; Yang, Z.; Liu, Y. Applications of Density Functional Theory in COVID-19 Drug Modeling. *Drug Discov. Today* **2022**, *27*, 1411–1419, doi:10.1016/j.drudis.2021.12.017.
157. Shin, D.; Jung, Y. Molecular Electrostatic Potential as a General and Versatile Indicator for Electronic Substituent Effects: Statistical Analysis and Applications. *Phys. Chem. Chem. Phys. PCCP* **2022**, *24*, 25740–25752, doi:10.1039/d2cp03244a.
158. Supruniuk, K.; Czarnomysy, R.; Muszyńska, A.; Radziejewska, I. Anti-Cancer Effects of Pyrazole-Platinum(II) Complexes Combined with Anti-MUC1 Monoclonal Antibody versus Monotherapy in DLD-1 and HT-29 Colon Cancer Cells. *Transl. Oncol.* **2022**, *18*, 101348, doi:10.1016/j.tranon.2022.101348.
159. Ghasemi, S.; Davaran, S.; Sharifi, S.; asgari, D.; Abdollahi, A.; Shahbazi Mojarrad, J. Comparison of Cytotoxic Activity of L778123 as a Farnesyltranferase Inhibitor and Doxorubicin against A549 and HT-29 Cell Lines. *Adv. Pharm. Bull.* **2013**, *3*, 73–77, doi:10.5681/apb.2013.012.
160. Ly, J.D.; Grubb, D.R.; Lawen, A. The Mitochondrial Membrane Potential (Deltapsi(m)) in Apoptosis; an Update. *Apoptosis Int. J. Program. Cell Death* **2003**, *8*, 115–128, doi:10.1023/a:1022945107762.
161. Chao, H.X.; Poovey, C.E.; Privette, A.A.; Grant, G.D.; Chao, H.Y.; Cook, J.G.; Purvis, J.E. Orchestration of DNA Damage Checkpoint Dynamics across the Human Cell Cycle. *Cell Syst.* **2017**, *5*, 445-459.e5, doi:10.1016/j.cels.2017.09.015.
162. Xu, Y.; Ma, H.-B.; Fang, Y.-L.; Zhang, Z.-R.; Shao, J.; Hong, M.; Huang, C.-J.; Liu, J.; Chen, R.-Q. Cisplatin-Induced Necroptosis in TNFα Dependent and Independent Pathways. *Cell. Signal.* **2017**, *31*, 112–123, doi:10.1016/j.cellsig.2017.01.004.
163. Jing, L.; Song, F.; Liu, Z.; Li, J.; Wu, B.; Fu, Z.; Jiang, J.; Chen, Z. MLKL-PITPα Signaling-Mediated Necroptosis Contributes to Cisplatin-Triggered Cell Death in Lung Cancer A549 Cells. *Cancer Lett.* **2018**, *414*, 136–146, doi:10.1016/j.canlet.2017.10.047.
164. Luo, R.; Onyshchenko, K.; Wang, L.; Gaedicke, S.; Grosu, A.-L.; Firat, E.; Niedermann, G. Necroptosis-Dependent Immunogenicity of Cisplatin: Implications for Enhancing the Radiation-Induced Abscopal Effect. *Clin. Cancer Res. Off. J. Am. Assoc. Cancer Res.* **2023**, *29*, 667–683, doi:10.1158/1078-0432.CCR-22-1591.
165. Gonzalez, V.M.; Fuertes, M.A.; Alonso, C.; Perez, J.M. Is Cisplatin-Induced Cell Death Always Produced by Apoptosis? *Mol. Pharmacol.* **2001**, *59*, 657–663, doi:10.1124/mol.59.4.657.
166. Moriwaki, K.; Bertin, J.; Gough, P.J.; Orlowski, G.M.; Chan, F.K.M. Differential Roles of RIPK1 and RIPK3 in TNF-Induced Necroptosis and Chemotherapeutic Agent-Induced Cell Death. *Cell Death Dis.* **2015**, *6*, e1636, doi:10.1038/cddis.2015.16.
167. Liu, Y.; Chen, P.; Xu, L.; Ouyang, M.; Wang, D.; Tang, D.; Yang, L.; Xie, M.; Cao, L.; Yang, M. Extracellular HMGB1 Prevents Necroptosis in Acute Myeloid Leukemia Cells. *Biomed. Pharmacother. Biomedecine Pharmacother.* **2019**, *112*, 108714, doi:10.1016/j.biopha.2019.108714.
168. Wu, Y.; Dong, G.; Sheng, C. Targeting Necroptosis in Anticancer Therapy: Mechanisms and Modulators. *Acta Pharm. Sin. B* **2020**, *10*, 1601–1618, doi:10.1016/j.apsb.2020.01.007.

169. Oliver Metzig, M.; Fuchs, D.; Tagscherer, K.E.; Gröne, H.-J.; Schirmacher, P.; Roth, W. Inhibition of Caspases Primes Colon Cancer Cells for 5-Fluorouracil-Induced TNF-α-Dependent Necroptosis Driven by RIP1 Kinase and NF-KB. *Oncogene* **2016**, *35*, 3399–3409, doi:10.1038/onc.2015.398.
170. Su, J.; Cheng, H.; Zhang, D.; Wang, M.; Xie, C.; Hu, Y.; Chang, H.C.-W.; Li, Q. Synergistic Effects of 5-Fluorouracil and Gambogenic Acid on A549 Cells: Activation of Cell Death Caused by Apoptotic and Necroptotic Mechanisms via the ROS-Mitochondria Pathway. *Biol. Pharm. Bull.* **2014**, *37*, 1259–1268, doi:10.1248/bpb.b13-00972.
171. Wu, S.; Zhou, Y.; Liu, P.; Zhang, H.; Wang, W.; Fang, Y.; Shen, X. MicroRNA-29b-3p Promotes 5-Fluorouracil Resistance via</Em> Suppressing TRAF5-Mediated Necroptosis in Human Colorectal Cancer. *Eur. J. Histochem. EJH* **2021**, *65*, 3247, doi:10.4081/ejh.2021.3247.
172. Akara-Amornthum, P.; Lomphithak, T.; Choksi, S.; Tohtong, R.; Jitkaew, S. Key Necroptotic Proteins Are Required for Smac Mimetic-Mediated Sensitization of Cholangiocarcinoma Cells to TNF-α and Chemotherapeutic Gemcitabine-Induced Necroptosis. *PloS One* **2020**, *15*, e0227454, doi:10.1371/journal.pone.0227454.
173. Pietkiewicz, S.; Eils, R.; Krammer, P.H.; Giese, N.; Lavrik, I.N. Combinatorial Treatment of CD95L and Gemcitabine in Pancreatic Cancer Cells Induces Apoptotic and RIP1-Mediated Necroptotic Cell Death Network. *Exp. Cell Res.* **2015**, *339*, 1–9, doi:10.1016/j.yexcr.2015.10.005.
174. Huisman, C.; Ferreira, C.G.; Bröker, L.E.; Rodriguez, J.A.; Smit, E.F.; Postmus, P.E.; Kruyt, F.A.E.; Giaccone, G. Paclitaxel Triggers Cell Death Primarily via Caspase-Independent Routes in the Non-Small Cell Lung Cancer Cell Line NCI-H460. *Clin. Cancer Res. Off. J. Am. Assoc. Cancer Res.* **2002**, *8*, 596–606.
175. Niu, X.; Wu, T.; Yin, Q.; Gu, X.; Li, G.; Zhou, C.; Ma, M.; Su, L.; Tang, S.; Tian, Y.; et al. Combination of Paclitaxel and PXR Antagonist SPA70 Reverses Paclitaxel-Resistant Non-Small Cell Lung Cancer. *Cells* **2022**, *11*, 3094, doi:10.3390/cells11193094.
176. Zhou, H.; Liu, L.; Ma, X.; Wang, J.; Yang, J.; Zhou, X.; Yang, Y.; Liu, H. RIP1/RIP3/MLKL-Mediated Necroptosis Contributes to Vinblastine-Induced Myocardial Damage. *Mol. Cell. Biochem.* **2021**, *476*, 1233–1243, doi:10.1007/s11010-020-03985-3.
177. Su, Z.; Yang, Z.; Xie, L.; DeWitt, J.P.; Chen, Y. Cancer Therapy in the Necroptosis Era. *Cell Death Differ.* **2016**, *23*, 748–756, doi:10.1038/cdd.2016.8.
178. Tang, R.; Xu, J.; Zhang, B.; Liu, J.; Liang, C.; Hua, J.; Meng, Q.; Yu, X.; Shi, S. Ferroptosis, Necroptosis, and Pyroptosis in Anticancer Immunity. *J. Hematol. Oncol.J Hematol Oncol* **2020**, *13*, 110, doi:10.1186/s13045-020-00946-7.
179. Wan, P.; Yan, J.; Liu, Z. Methodological Advances in Necroptosis Research: From Challenges to Solutions. *J. Natl. Cancer Cent.* **2022**, *2*, 291–297, doi:10.1016/j.jncc.2022.08.007.
180. Li, S.; Yue, M.; Xu, H.; Zhang, X.; Mao, T.; Quan, M.; Ma, J.; Wang, Y.; Ge, W.; Wang, Y.; et al. Chemotherapeutic Drugs-Induced Pyroptosis Mediated by Gasdermin E Promotes the Progression and Chemoresistance of Pancreatic Cancer. *Cancer Lett.* **2023**, *564*, 216206, doi:10.1016/j.canlet.2023.216206.

181. Wang, Y.; Gao, W.; Shi, X.; Ding, J.; Liu, W.; He, H.; Wang, K.; Shao, F. Chemotherapy Drugs Induce Pyroptosis through Caspase-3 Cleavage of a Gasdermin. *Nature* **2017**, *547*, 99–103, doi:10.1038/nature22393.
182. Wang, Y.; Wu, X.; Ren, Z.; Li, Y.; Zou, W.; Chen, J.; Wang, H. Overcoming Cancer Chemotherapy Resistance by the Induction of Ferroptosis. *Drug Resist. Updat. Rev. Comment. Antimicrob. Anticancer Chemother.* **2023**, *66*, 100916, doi:10.1016/j.drup.2022.100916.

10. Streszczenie w języku polskim

Na całym świecie liczba zachorowań na choroby nowotworowe stale wzrasta, a rozwój oporności komórek w odpowiedzi na stosowane środki chemioterapeutyczne przyczynia się do ograniczonej skuteczności ich leczenia. Pomimo postępów w leczeniu chorób nowotworowych, chemioterapia nadal pozostaje jednym z głównych sposobów walki z nowotworami. Poszukiwanie nowych, skutecznych leków chemioterapeutycznych jest, zatem jednym z głównych obszarów badań naukowych. Wiele obecnie stosowanych leków przeciwnowotworowych zawiera w swojej strukturze pierścienie heterocykliczne.

W niniejszej pracy oceniono aktywność biologiczną nowych, syntetycznych sulfonamidowych pochodnych pirazolo[4,3-*e*]tetrazolo[1,5-*b*][1,2,4]triazyny (związków **MM**). Badania miały na celu ocenę mechanizmów komórkowych odpowiedzialnych za aktywność tych związków. Badano stopień cytotoksyczności, genotoksyczności, zdolność do indukowania apoptozy oraz stresu oksydacyjnego w komórkach nowotworowych i prawidłowych człowieka w układzie *in vitro*. Sulfonamidowe pochodne pirazolo[4,3-*e*]tetrazolo[1,5-*b*][1,2,4]triazyny wykazały wyższą aktywność cytotoksyczną wobec komórek nowotworowych gruczolakoraka trzustki (BxPC-3), raka jelita grubego (HCT-116) i raka prostaty (PC-3), niż wobec komórek prawidłowych. Największą wrażliwość na działanie cytotoksyczne badanych pochodnych wykazały komórki linii PC-3, następnie komórki linii BxPC-3 oraz komórki linii HCT-116, przy czym najwyższą aktywność cytotoksyczną wykazywał związek **MM137.** Stwierdzono wzrost uszkodzeń DNA w komórkach nowotworowych poddanych inkubacji z badanymi związkami, co potwierdziło genotoksyczne działanie sulfonamidowych pochodnych pirazolo[4,3-*e*]tetrazolo[1,5-*b*][1,2,4]triazyny. Badane związki wykazywały również działanie proapoptotyczne oraz prooksydacyjne, szczególnie w komórkach linii BxPC-3. Analiza ekspresji genów wskazuje na udział białka GADD45α (ang. *growth arrest and DNA-damage-inducible, alpha*) w zahamowaniu proliferacji oraz klonogenności

komórek nowotworowych w odpowiedzi na badane pochodne oraz na indukcję nekroptozy i/lub apoptozy komórek nowotworowych. Badania *in silico* sugerują obiecujące właściwości farmakokinetyczne badanych związków oraz wskazują na kinazę AKT2, jako główny cel molekularnego działania sulfonamidowych pochodnych pirazolo[4,3-*e*]tetrazolo[1,5-*b*][1,2,4]triazyny.

Strategiczne włączenie układu heterocyklicznego pirazolo[4,3-*e*]tetrazolo[1,5-*b*][1,2,4]triazyny w chemiczną strukturę cząsteczek nowych potencjalnych leków może mieć istotne znaczenie dla projektowania związków o wysokiej aktywności przeciwnowotworowej oraz selektywności.

11. Streszczenie w języku angielskim

The number of cancer cases is constantly increasing, and the development of cell resistance to chemotherapy drugs contributes to the limited effectiveness of treating this disease. Despite advances in cancer treatment, chemotherapy remains one of the main methods of therapy. Therefore, the search for new and effective chemotherapeutic drugs is one of the main areas of scientific research. Many currently used anticancer drugs contain heterocyclic rings in their structure.

In this study, the biological activity of new synthetic sulfonamide derivatives of pyrazolo[4,3-*e*]tetrazolo[1,5-*b*][1,2,4]triazine (**MM** compounds) was evaluated. The research aimed to assess the cellular mechanisms responsible for the activity of these compounds. The compound's cytotoxicity, genotoxicity, ability to induce apoptosis, and oxidative stress in cancer cells and normal human cells were investigated *in vitro*.

Sulfonamide derivatives of pyrazolo[4,3-e]tetrazolo[1,5-b][1,2,4]triazine exhibited higher cytotoxic activity against pancreatic adenocarcinoma (BxPC-3), colorectal cancer (HCT-116), and prostate cancer (PC-3) cells compared to normal cells. The highest sensitivity to the cytotoxic effects of the tested derivatives was observed in PC-3 cell line, followed by BxPC-3 and HCT-116 cell lines, with compound **MM137** displaying the highest cytotoxic activity. Increased DNA damage was observed in cancer cells incubated with the tested compounds, confirming the genotoxic effects of sulfonamide derivatives of pyrazolo[4,3-e]tetrazolo[1,5-b][1,2,4]triazine. The compounds also demonstrated pro-apoptotic and pro-oxidative effects, particularly in BxPC-3 cell line. Gene expression analysis indicated the involvement of growth arrest and DNA-damage-inducible alpha protein (GADD45α) in the inhibition of the proliferation and clonogenicity of cancer cells in response to the tested derivatives, as well as the induction of necroptosis and/or apoptosis in cancer cells. *In silico* studies suggested promising pharmacokinetic properties of the tested compounds and identified AKT2 kinase as

the main molecular target for the action of sulfonamide derivatives of pyrazolo[4,3-*e*]tetrazolo[1,5-*b*][1,2,4]triazine.

The strategic incorporation of the heterocyclic system of pyrazolo[4,3-e]tetrazolo[1,5-b][1,2,4]triazine into the chemical structure of new potential drugs can be of significant importance for designing compounds with high anticancer activity and selectivity

12. Kopie publikacji wchodzących w zakres rozprawy doktorskiej

molecules

MDPI

Review

Review of the Synthesis and Anticancer Properties of Pyrazolo[4,3-*e*][1,2,4]triazine Derivatives

Zofia Bernat [1], Anna Szymanowska [2], Mateusz Kciuk [3,4], Katarzyna Kotwica-Mojzych [5] and Mariusz Mojzych [1,*]

1 Department of Chemistry, Siedlce University of Natural Sciences and Humanities, 3 Maja 54, 08-110 Siedlce, Poland; zosiabernat@wp.pl
2 Department of Biotechnology, Medical University of Bialystok, Kilinskiego 1, 15-222 Bialystok, Poland; anna.szymanowska@umb.edu.pl
3 Department of Molecular Biotechnology and Genetics, Laboratory of Cytogenetics, University of Lodz, Banacha 12/16, 90-237 Lodz, Poland; mateusz.kciuk@unilodz.eu
4 Doctoral School of Exact and Natural Sciences, University of Lodz, Banacha Street 12/16, 90-237 Lodz, Poland
5 Department of Histology, Embryology and Cytophysiology, Medical University of Lublin, Radziwiłłowska 11, (Collegium Medicum), 20-080 Lublin, Poland; katarzynakotwicamojzych@umlub.pl
* Correspondence: mmojzych@yahoo.com; Tel.: +48-025-643-1113

Academic Editors: Simona Collina and Mariarosaria Miloso
Received: 8 July 2020; Accepted: 24 August 2020; Published: 29 August 2020

Abstract: This review focuses on the cytotoxic effect of new synthetic pyrazolo[4,3-*e*][1,2,4]triazine derivatives against different tumor cell lines. Some annulated pyrazolotriazines i.e., pyrazolo[4,3-*e*][1,2,4]triazolo[4,3-*b*][1,2,4]triazines and pyrazolo[4,3-*e*]tetrazolo[1,5-*b*][1,2,4]triazine demonstrated significant broad cytotoxic activity in micromolar range concentration, which could have excellent potential to be new candidate therapeutic agents in cancer chemotherapy.

Keywords: pyrazolo[4,3-*e*][1,2,4]triazines; anticancer activity; sulfonamides; 1,2,4-triazine; fused tetrazole derivatives; fluviols

1. Introduction

Despite the significant progress that has been made in recent years in the treatment of cancer, tumors still represent a high risk for humanity, and therefore the development of effective cancer therapy is still a challenge for modern medicine. The choice of treatment depends on the type of cancer and its stage at the time of diagnosis. Both chemotherapy, radiotherapy, and immunotherapy have a number of side effects that reduce the effectiveness of drugs and can reduce the quality of life of patients. Therefore, it is extremely important to search for new therapeutic strategies, as well as to develop drugs with a better pharmacological profile that act specifically on cancer cells and do not have a toxic effect on normal cells. The search for new lead structures involves identifying new chemical compounds that affect well-defined molecular targets. Triazine derivatives are an interesting group of compounds with potential anti-tumor activity, and this scaffold has been used in oncological therapy since 1965.

Since that time, a number of studies have been undertaken to modify the structure of 1,2,4-triazine derivatives, which were to provide molecules with stronger cytotoxic properties and at the same time giving fewer side effects. Thanks to this research, a number of benzo- or hetero-fused 1,2,4-triazine derivatives have been found and described in the literature as new antitumor agents. Compounds in which the 1,2,4-triazine nucleus is condensed with five-membered heterocycles have received considerable attention because they are bioisosteric with purine core. Among the 1,2,4-triazine condensed with one heterocycle, compounds bearing a pyrrole ring, such as pyrrolo[2,1-*c*][1,2,4]triazine and pyrrolo[2,1-*f*][1,2,4]triazine, represent the most abundant class of triazine with antitumor activity.

However, another very interesting group of fused 1,2,4-triazines with five-membered heterocycles are derivatives of the little-known pyrazolo[4,3-*e*][1,2,4]triazine ring system. It is a novel scaffold which, despite of the fact that it is an important source for bioactive molecules, has been less studied so far in comparison with the pyrrolotriazines. In the past few decades, the isolation and structural characterization of seven naturally occurring pyrazolo[4,3-*e*][1,2,4]triazines: pseudoiodinine [1], nostocine A [2], and fluviols A–E [3] (Figure 1) have been reported. These natural compounds with wide antibiotic and antitumor activities were found as extracellular metabolites of some microorganism of the class *Pseudomonas fluorescens* var. *pseudoiodinine* and *Nostoc spongiaeforme*. Structures of two natural pigments of this group, namely nostocine A and fluviol A (*normethylpseudoiodinine*), have been clearly defined by X-ray crystallographic analysis [2] and further confirmed by total synthesis [4]. The data cited above indicate the role of this heterocyclic system in the search for new pharmacologically active compounds.

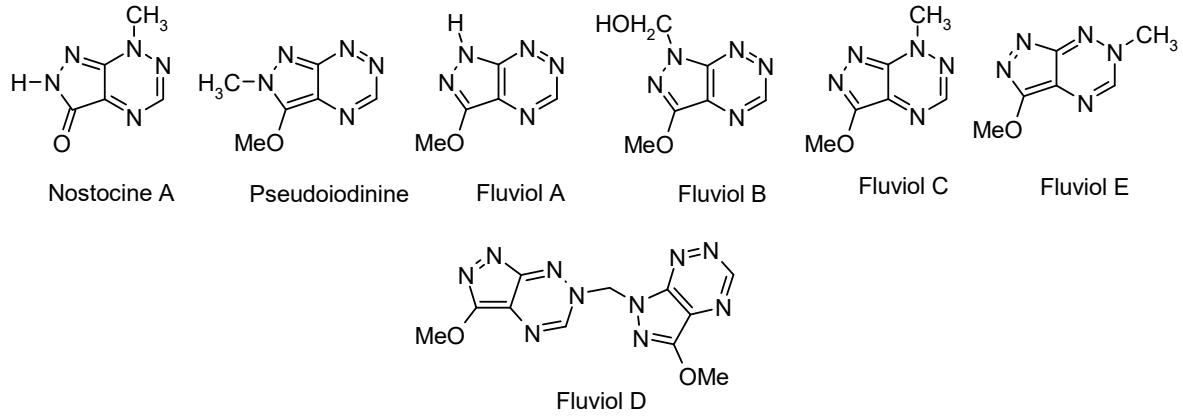

Figure 1. Naturally occurring pyrazolo[4,3-*e*][1,2,4]triazines.

This review presents the methods for the synthesis and functionalization of the pyrazolo[4,3-*e*][1,2,4]triazine ring system, which in the group of fused pyrazolotriazines is little known and also little described in the literature. It is known that proper functionalization of the heterocyclic core is a key element to design new molecules with potential biological properties. Therefore, the collection of the results of the current scientific research on this valuable heterocyclic system is necessary and justified. The results of experimental studies published so far have shown that a series of derivatives of this heterocyclic system possess various biological activity including antitumor property, which is the main and leading topic of this review. The paper also presents the methods used for the preparation of pyrazolo[4,3-*e*][1,2,4]triazine sulfonamide derivatives, their activity against cancer cell lines, and the inhibition of two carbonic anhydrase isozymes (CAIX and CAXII) that are highly overexpressed in hypoxic tumors and show very restricted expression in normal tissues. Among the presented data, the tricyclic pyrazolo[4,3-*e*][1,2,4[triazines fused with triazole or tetrazole ring are of particular interest. They constitute new groups of heterocyclic systems and are characterized by high antitumor activity, and it seems that they may be a source of new chemotherapeutic agents.

2. Approach to the Construction of Pyrazolo[4,3-*e*][1,2,4]triazine Ring System

2.1. Synthesis from 4-Amino-5-acylhydrazinopyrazole

There are few different methods described in the literature for the construction of 1,3,5-trisubstituted pyrazolo[4,3-*e*][1,2,4]triazines [4–12]. These methods can be divided into two groups, one including the building of the 1,2,4-triazine core on a pyrazole derivative (Scheme 1) and the second one incorporating the construction of the pyrazole ring onto the 1,2,4-triazine nucleus [4–6,12] (Scheme 2) [10,11].

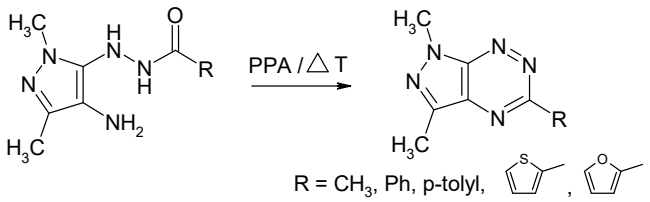

Scheme 1. Synthesis of pyrazolo[4,3-*e*][1,2,4]triazines using pyrazole derivatives.

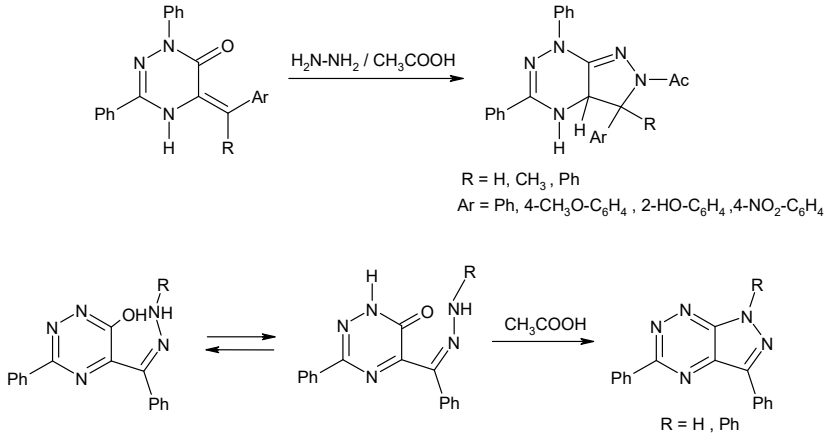

Scheme 2. Synthesis of pyrazolo[4,3-*e*][1,2,4]triazines on 1,2,4-triazine core.

2.2. Synthesis from 3,5-Disubstituted-1,2,4-triazin-6(1H)-one with Cytotoxic Activity

In a similar manner 1,5-diaryl-3-(3,4,5-trimethoxyphenyl)pyrazolo[4,3-*e*][1,2,4]triazines have been synthetized by Gucký et al. (Scheme 3) [12]. These derivatives showed selective inhibitory activity against the A549 cell line, while they are generally less active against leukemia cell lines, including otherwise highly chemosensitive CEM lymphoblasts. The results of cytotoxic activity for some derivatives are summarized in Table 1.

The above-mentioned methods for the synthesis of the pyrazolo[4,3-*e*][1,2,4]triazine derivatives had a little importance to further study on their functionalization and determining structure-activity relationship (SAR) because they did not contain appropriate functional groups.

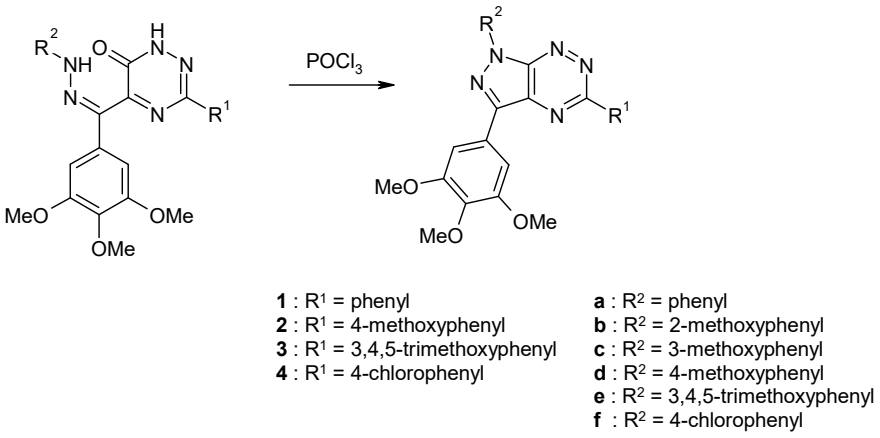

Scheme 3. Synthesis of 1,5-diaryl-3-(3,4,5-trimethoxyphenyl)pyrazolo[4,3-*e*][1,2,4]triazines.

Table 1. Cytotoxic activity of 1,5-diaryl-3-(3,4,5-trimethoxyphenyl)pyrazolo[4,3-*e*][1,2,4]triazines.

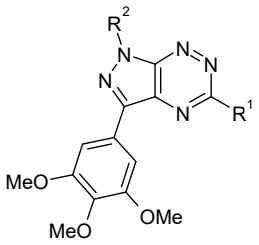

Compd.	R^1	R^2	MTT Assay, IC_{50} (μM) [1]				
			CEM	CEM DNR Bulk	K562	K562 Tax	A549
1b	Ph	2-OCH_3-Ph	109	118	182	94.3	**5.41**
1c	Ph	3-OCH_3-Ph	**8.41**	99.3	117	159	**0.61**
1d	Ph	4-OCH_3-Ph	117	100	84.4	150	39.0
1e	Ph	3,4,5-$(OCH_3)_3$-Ph	65.2	129	52.6	99.9	**2.16**
2b	4-OCH_3-Ph	2-OCH_3-Ph	105	119	178	155	**6.58**
2c	4-OCH_3-Ph	3-OCH_3-Ph	54.5	184	115	174	124
3b	3,4,5-$(OCH_3)_3$-Ph	2-OCH_3-Ph	126	125	182	156	**15.0**
3c	3,4,5-$(OCH_3)_3$-Ph	3-OCH_3-Ph	**48.3**	109	164	141	163
3d	3,4,5-$(OCH_3)_3$-Ph	4-OCH_3-Ph	**36.9**	118	66.2	161	75.6
3f	3,4,5-$(OCH_3)_3$-Ph	4-Cl-Ph	82.2	115	158	196	**8.26**
4a	4-Cl-Ph	Ph	**11.6**	113	220	225	130
4b	4-Cl-Ph	2-OCH_3-Ph	53.8	**35.7**	**48.7**	**20.7**	**3.62**
4c	4-Cl-Ph	3-OCH_3-Ph	54.7	108	192	219	**2.86**
4e	4-Cl-Ph	3,4,5-$(OCH_3)_3$-Ph	99.9	117	192	210	**15.0**
4f	4-Cl-Ph	4-Cl-Ph	68.9	126	190	222	155

[1] All experiments were performed as described in the literature [12]. The underline and bold marked the most active compounds.

2.3. Synthesis from 3-Substituted-1,2,4-triazine with Cytotoxic Activity

This fact encouraged Mojzych's research group to develop a new, simple and useful way for the synthesis of the mentioned bicyclic system from readily available oximes of 5-acyl-1,2,4-triazines [13] or ketones [14] with hydrazine derivatives. The new methods are based on nucleophilic substitution reaction of hydrogen and allows for obtaining different pyrazolo[4,3-*e*][1,2,4]triazines useful to determine their structure-activity relationship [8,9,15,16]. 5-Acyl-1,2,4-triazine derivatives were obtained in good yield in the reaction of 1,2,4-triazines with nitroalkane anions under nucleophilic substitution of hydrogen (Scheme 4) [13]. In this process, nitroalkanes play a role of masked acylating agent yielding in the first step oximes of 5-acyl-1,2,4-triazines, which may be easily converted to the corresponding ketones [14] which were used to receive the corresponding hydrazones as a key intermediate for the construction of 1H-pyrazolo[4,3-*e*][1,2,4]triazines (Scheme 4) [8]. The method seems to be general and tolerates a wide range of substituents and, comparing this method with the previously described in literature, we can easily see that the approach does not need a good leaving group in the position C6 of the triazine ring. It has to be noted that pyrazolo[4,3-*e*][1,2,4]triazine formation strongly depends on the kind of substituent on the phenyl ring of phenylhydrazones. The shorter reaction time and higher yield was observed for electron donating groups (methyl or methoxy group), but, for electron withdrawing groups (Cl, NO_2), the time reaction was much longer and the yield was low, which could be observed for the NO_2 group. Based on these observations, we have proposed the mechanism of the intramolecular ring closure of hydrazones [8,16]. The most probable reaction proceeds via the protonated hydrazone intermediate, followed by ring closure involving intramolecular electron pair attack of a hydrazine nitrogen atom onto the C6 of 1,2,4-triazine ring to give the adduct σ^H, that, via an air oxidation, gives final pyrazolo[4,3-*e*][1,2,4]triazine (Scheme 4).

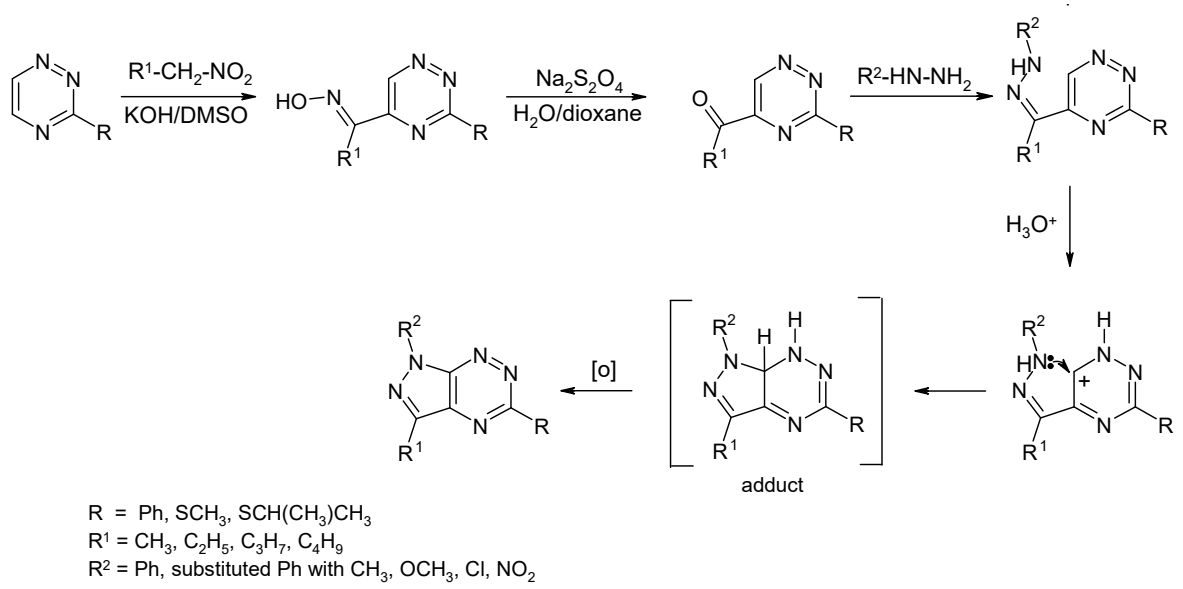

Scheme 4. The new and general synthetic route of pyrazolo[4,3-*e*][1,2,4]triazine derivatives.

We have to underline that the new method for the preparation of pyrazolo[4,3-*e*][1,2,4]triazine derivatives is convenient to introduce a number of substituents at N1 and C3 position of the pyrazole ring. Introduction of new substituents at the C5 position is possible by nucleophilic substitution reaction of a suitable nucleofugal group. However, the methylsulfanyl group in pyrazolo[4,3-*e*][1,2,4]triazine was unreactive in the reaction with nucleophilic agents. In order to increase the activity of the heterocyclic system in the S_NAr reactions, the methylsulfanyl group was replaced with more electron-withdraw methylsulfonyl substituent. This group is considered as one of the better leaving groups in nucleophilic substitution reactions of 1,2,4-triazine [17,18]. Utilizing the methylsulfonyl group, Mojzych et al. developed a method for the functionalization of pyrazolo[4,3-*e*][1,2,4]triazine system via nucleophilic substitution at the C5 position using O-, N-, S- and C-nucleophiles (Scheme 5) [19].

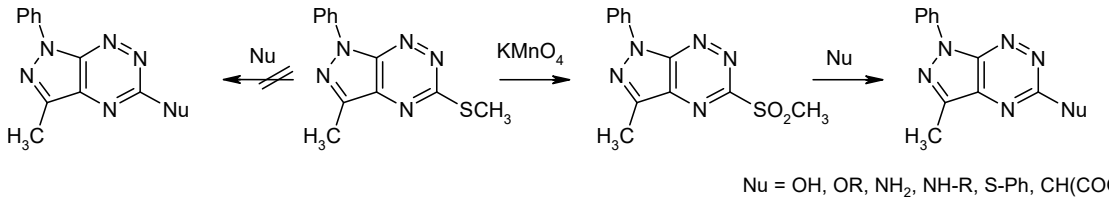

Scheme 5. Functionalization of the pyrazolo[4,3-*e*][1,2,4]triazine system by S_NAr.

Using the nucleophilic substitution reaction of the methylsulfonyl group at the C5 position of 1H-pyrazolo[4,3-*e*][1,2,4]triazine, a series of new derivatives of this system were obtained.

In the group of simple synthesized pyrazolo[4,3-*e*][1,2,4]triazines [8,9,15,16,19–21], only a few derivatives showed moderate activity against variety of human tumor cell lines: prostate cancer (PC-3), breast cancer (MCF-7), non-small-cell lung cancer (H460), colorectal adenocarcinoma (Colo205). Their structures and cytotoxicity are presented in Table 2. It is worth noting that the 3-methyl-1-phenyl-5-phenylaminopyrazolo[4,3-*e*][1,2,4]triazine derivative showed the highest degree of reduced cell viability with IC_{50} value 4 μM in Colo205 cells.

Table 2. Cytotoxicity of simple pyrazolo[4,3-*e*][1,2,4]triazines.

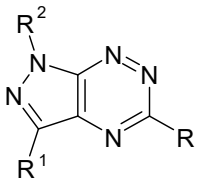

MTT Assay, IC_{50} (μM)						
R	**R^1**	**R^2**	**PC-3**	**MCF-7**	**H460**	**Colo205**
SCH_3	C_2H_5	4-NO_2-Ph	98	78	36	75
Ph	CH_3	Ph	98	NA [1]	NA [1]	NA [1]
SO_2CH_3	CH_3	Ph	25	50	25	25
NH-Ph	CH_3	Ph	81	90	86	4
NH-Bu	CH_3	Ph	66	77	NA [1]	25
NH-CH_2-Ph	CH_3	Ph	NA [1]	NA [1]	NA [1]	50
NH_2	CH_3	Ph	NA[1]	NA [1]	NA [1]	72
OCH_3	CH_3	Ph	NA[1]	NA [1]	NA [1]	91

[1]—not active.

3. Synthesis and Anticancer Activity of Pyrazolo[4,3-*e*][1,2,4]triazine Sulfonamides

3.1. Synthesis from 5-Methylsulfanylpyrazolo[4,3-e][1,2,4]triazine

The lack of significant antitumor activity in the group of simple substituted pyrazolotriazine derivatives encouraged scientists to complete further functionalization of the heterocyclic core. The combination of the naturally occurring pyrazolo[4,3-*e*][1,2,4]triazine ring system with pharmacophore groups enabled the design of new derivatives with higher potential biological activity.

One of the most important pharmacophore groups is a sulfonamide moiety characteristic for many chemical compounds used in medicine [22,23]. Their importance stems from the fact of diverse biological activity which includes antibacterial, antimalarial, hypotensive, diuretic, hypoglycemic, antithyroid, antiparasitic, anti-inflammatory, and antiglaucomatous properties [24]. Furthermore, research studies have shown that sulfonamides may exhibit an antitumor effect by inhibiting the activity of protein kinases including cyclin-dependent kinases (CDKs) [25,26] or carbonic anhydrase (**CA**; EC 4.2.1.1) [27–29].

Protein kinases participate in many signal transduction pathways including those involved in growth, differentiation, and cell division. The overexpression or mutation of some protein kinases can lead to cancer. Several protein kinases represent targets for cancer chemotherapy. These targets include the Bcr-Abl protein kinase, the RAF protein-serine/threonine protein kinase, the epidermal growth factor receptor protein tyrosine kinase, protein kinase C, and anaplastic lymphoma protein-tyrosine kinase [30–32]. In chronic myelogenous leukemia, the reciprocal translocation between chromosomes 9 and 22 lead to the chimeric formation of a portion of the Bcr gene and the Abl gene. The product of this translocation is Bcr-Abl p210 protein isoform with tyrosine kinase activity. The Abl gene was first described in the genome of the Abelson murine leukaemia virus. The Bcr-Abl oncoprotein was a target for drug discovery, and imatinib (STI 571, Gleevec) was one product of this research. Gleevec, an ATP analog, is a specific and competitive inhibitor of the Bcr-Abl protein kinase that is being used to treat chronic myelogenous leukemia.

The cyclin-dependent kinases (CDKs) are a family of Ser/Thr kinases, which, in association with specific cyclins, play critical roles as regulators of the different phases of the cell cycle. These enzymes and their direct regulators are frequently mutated, amplified, or deleted in malignant cells, suggesting that pharmacological CDK inhibition may be an effective strategy for treating cancer [33].

During the last decade, carbonic anhydrase became an attractive and promising scientific target for anticancer therapy since two cancer-associated isozymes CA IX and XII [29,34–40] were found to be overexpressed in many tumors [41,42]. These two transmembrane proteins play a key role in tumor progression and response to treatment [34]. It has been demonstrated that CA IX is overexpressed in hypoxic tumor, participate in acidification of the environment of tumor cells, and contribute to disease progression giving a poor prognosis for treatment. As CA IX is an important oncotarget, much attention has been focused to find new CA IX inhibitors as anticancer drugs.

The first sulfonamide derivatives of the pyrazolo[4,3-*e*][1,2,4]triazine were prepared according to Scheme 6 and their antitumor activity was tested. One group constitutes 5-phenylaminosulfonamide derivatives of pyrazolo[4,3-*e*][1,2,4]triazine **9a–l** [43] being analogs of known inhibitors of protein kinases and the other group includes sildenafil analogs **12a–l** in which HN-C=O moiety has been replaced by two triazine nitrogen atoms [44,45].

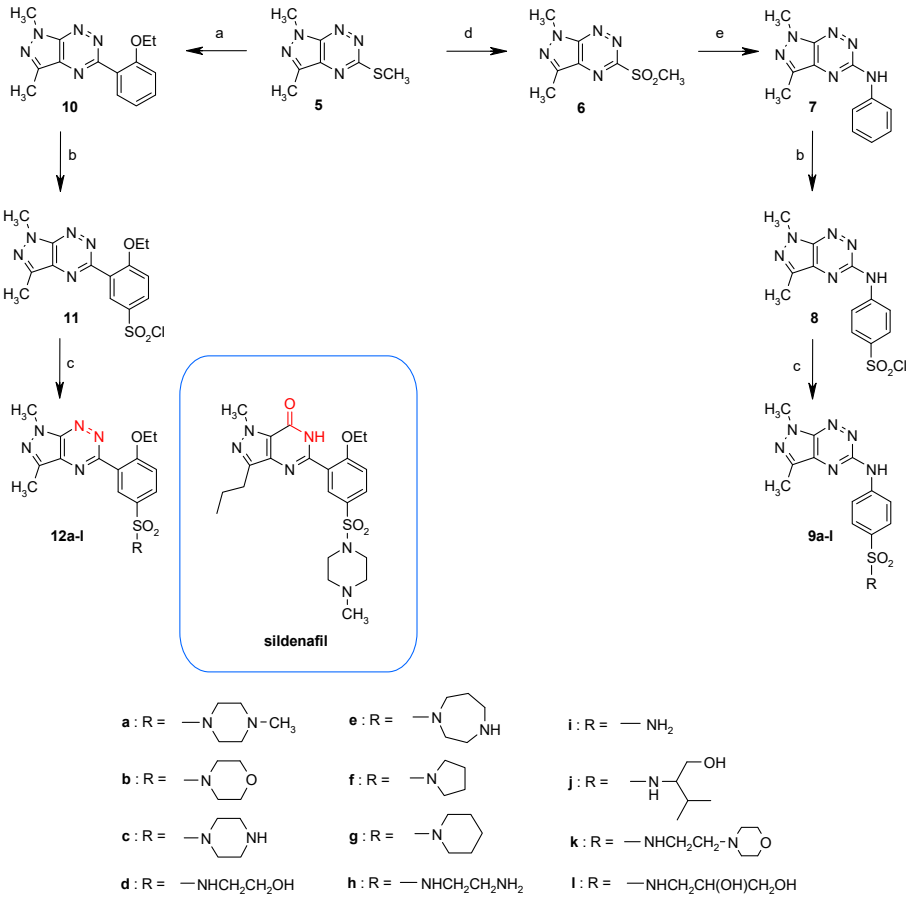

Scheme 6. Synthesis of sulfonamides. The reagents and reaction conditions: (**a**) 2-ethoxyphenylboronic acid, $Pd(PPh_3)_4$, CuMeSal, THF, Ar, reflux, 12 h; (**b**) $ClSO_3H$, 0–20 °C, 2 h; (**c**) NH_3/H_2O or amine, MeCN, 20 °C; (**d**) $KMnO_4$, Bu_4NBr, CH_3COOH, benzene-H_2O, 20 °C, 1 h; (**e**) aniline, 9 days, 150 °C, Carius tube.

Due to the similarity of derivatives **9a–l** to known inhibitors of protein kinases, only this group of sulfonamides has been studied as inhibitors of the Abl protein kinase. In tests, the most active compounds were **9c** and **9e**. Their IC_{50} values are expressed in micromolar concentration range (IC_{50} = 5.8–5.9 μM). To better understand the activity of pyrazolo[4,3-*e*][1,2,4]triazines **9c** and **9e** and the binding of Abl, kinase molecular modeling was performed, the results of which suggested that compounds **9c** and **9e** might bind to Abl in a similar manner as described for the pyrido[2,3-*d*]pyrimidine PD180970, interacting with the protein via non-polar interactions and hydrogen bonds with the NH group of the amino acid M318 in the main chain [46].

On the other hand, this sulfonamide group displayed lack of activity towards CDK2. Molecular docking suggested that the negative results of the biochemical assays are due to the relatively unfavorable mode of binding adopted by the pyrazolo[4,3-*e*][1,2,4]triazines in the CDK2 active site [43].

The sulfonamides **9a–l** were also investigated against leukemia cell lines (K562, BV173, HL60, CCRF-CEM) using the MTT assay (Table 3) [43,44]. The concentration-dependent activity was observed for all tested compounds **9a–l** and **12a–l**. The breast carcinoma cell lines were much less sensitive to the tested compounds in comparison to the leukemia cell lines. It is noteworthy that the IC_{50} values for the most active derivatives **9e** and **9c** against leukemia cells are 5–7 times lower than the IC_{50} values for the breast cancer cells. This fact suggests that the tested compounds exhibit significant selectivity for tumor cells.

Table 3. In vitro antiproliferative activity of new sulfonamide derivatives of pyrazolo[4,3-*e*][1,2,4]triazines.

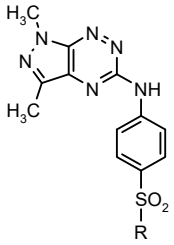

Compd.	R	MTT Assay, IC_{50} (μM)			
		K562	BV173	HL60	CCRF-CEM
9a	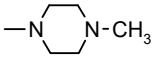	66 ± 5	40 ± 8	49 ± 2	36 ± 2
9b	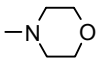	90 ± 8	58 ± 5	39 ± 1	69 ± 8
9c	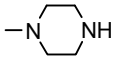	27 ± 4	22 ± 6	55 ± 2	20 ± 2
9d	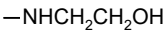	100 ± 4	41 ± 10	42 ± 5	49 ± 8
9e	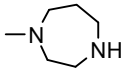	21 ± 5	22 ± 4	38 ± 1	36 ± 12
9f		102 ± 1	47 ± 14	56± 6	30 ± 2
9g		98 ± 2	36 ± 9	24 ± 2	30 ± 2
9h	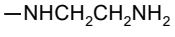	77 ± 7	39 ± 8	42 ± 6	56 ± 2
9i		106 ± 8	45 ± 11	58 ± 3	50 ± 1
9j	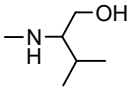	>200	58 ± 9	40 ± 2	54 ± 8
9k	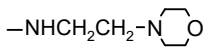	96 ± 3	39 ± 8	41 ± 1	64 ± 6
9l	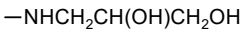	101 ± 2	42 ± 9	44 ± 5	57 ± 3
Chlorambucil		84 ± 6	34 ± 8	38 ± 2	21 ± 8
Imatinib		13 ± 2	20 ± 6	55 ± 7	45 ± 1

Moreover, for both sulfonamide groups, the potential anticancer activity in MCF-7 and MDA-MB-231 cells was determined by [^{3}H]thymidine incorporation assay and MTT test, where proliferation and viability of breast cancer cells were analyzed (Tables 4 and 5) [44]. All tested compounds showed concentration dependent activity but with different potency.

Table 4. Cytotoxic and cytostatic activities of new sulfonamides derivatives of pyrazolo[4,3-*e*][1,2,4]triazines **9a**–**l**.

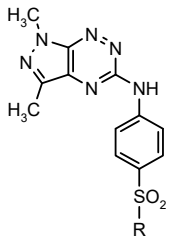

Compd.	R	MTT Assay, IC_{50} (μM)		[^{3}H]Thymidine Incorporation, IC_{50} (μM)	
		MCF-7	MDA-MB-231	MCF-7	MDA-MB-231
9a	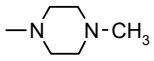	102 ± 2	99 ± 2	87 ± 2	80 ± 2
9b	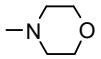	>200	>200	>200	>200
9c	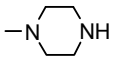	150 ± 2	130 ± 2	170 ± 2	103 ± 2
9d	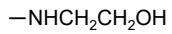	>200	>200	>200	>200
9e	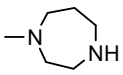	140 ± 3	155 ± 2	123 ± 1	150 ± 2
9f		>200	>200	>200	>200
9g		200 ± 2	140 ± 1	150 ± 2	135 ± 1
9h	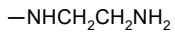	126 ± 1	120 ± 1	85 ± 1	90 ± 1
9i		>200	>200	nt [1]	nt [1]
9j	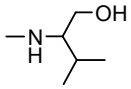	>200	>200	nt [1]	nt [1]
9k	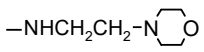	146 ± 1	125 ± 2	99 ± 1	120 ± 2
9l	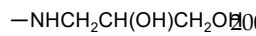	200 ± 2	140 ± 2	nt [1]	nt [1]
Chlorambucil		97 ± 2	93 ± 2	56 ± 2	49 ± 2

[1]—not tested.

Table 5. Cytotoxic and cytostatic activities of new sulfonamides derivatives of pyrazolo[4,3-*e*][1,2,4]triazines **12a–l** after 24 h incubation.

Compd.	MTT Assay, IC_{50} (μM)		[^{3}H]Thymidine Incorporation, IC_{50} (μM)	
	MCF-7	MDA-MB-231	MCF-7	MDA-MB-231
12a	110 ± 2	115 ± 2	140 ± 1	152 ± 2
12b	181 ± 2	189 ± 2	148 ± 1	160 ± 1
12c	172 ± 2	182 ± 2	150 ± 2	164 ± 2
12d	>200	>200	>200	>200
12e	123 ± 2	130 ± 1	129 ± 2	115 ± 1
12f	112 ± 2	120 ± 2	130 ± 2	159 ± 1
12g	105 ± 3	98 ± 2	112 ± 1	126 ± 2
12h	190 ± 1	>200	>200	200 ± 1
12i	nt [1]	nt [1]	nt [1]	nt [1]
12j	nt [1]	nt [1]	nt [1]	nt [1]
12k	132 ± 2	136 ± 2	145 ± 1	156 ± 2
12l	nt [1]	nt [1]	nt [1]	nt [1]
Chlorambucil	97 ± 2	93 ± 2	56 ± 2	49 ± 2

[1]—not tested.

The influence of sulfonamides **9a–k** on collagen biosynthesis in breast cancer cells (MCF-7 and MDA-MB-231) was also examined (Table 6). In both cell lines, compound **9a** was found to be more effective inhibitor of collagen biosynthesis than chlorambucil. IC_{50} for **9a** and chlorambucil (in MDA-MB-231: 47 μM and 52 μM, in MCF-7: 58 μM and 72 μM, respectively) showed specific inhibitory effect of compound **9a** on collagen biosynthesis.

Table 6. Collagen synthesis, measured by 5-[^{3}H]-proline incorporation into proteins susceptible to the action of bacterial collagenase, in MCF-7 and MDA-MB-231 breast cancer cells in the presence of compounds **9a–k** and chlorambucil.

Compd.	IC_{50} (μM)	
	MCF-7	MDA-MB-231
9a	47 ± 1	58 ± 2
9b	>200	>200
9c	175 ± 1	180 ± 2
9d	>200	>200
9e	133 ± 1	135 ± 2
9f	>200	>200
9g	163 ± 2	145 ± 1
9h	112 ± 1	95 ± 1
9i	nt [1]	nt [1]
9j	nt [1]	nt [1]
9k	140 ± 1	137 ± 2
Chlorambucil	52 ± 1	72 ± 2

[1]—not tested.

Biological research revealed that both classes of sulfonamide derivatives (**9a–l** and **12a–l**) had cytotoxic activity against estrogen receptor positive breast cancer cells—MCF-7 and estrogen receptor negative breast cancer—MDA-MB-231. In addition to this, compounds **9a–l** affect collagen synthesis, which may have a role in metabolism and function of human breast cancer cells.

Obtained sulfonamides **9a–l** were also evaluated for their inhibitory potency against carbonic anhydrase, particularly against two isozymes, namely cancer-associated isoforms hCA IX and XII [44]. The best results against hCA IX were observed for sulfonamide **9h** (K_I = 23.7 nM) and **9d** (K_I = 26.5 nM), which were similar to results obtained for the standard—acetazolamide (K_I = 25 nM) (Table 6). The best activity was observed in tests against hCA XII. In this study, all derivatives showed a good inhibition of

the enzyme with K_I in the range of 5.3 nM to 9.0 nM. The lowest value of K_I was observed for derivative **9a** (K_I = 5.3 nM), which is the best chemotherapeutic agent among all investigated sulfonamides. The tumor-associated isoforms hCA IX and XII were inhibited by some of the investigated derivatives. Thus, hCA IX was not at all inhibited by four of the new derivatives (**9a**, **9c**, **9e** and **9g**), was weakly inhibited by two of them (**9f** and **9k**), whereas **5**, **6**, **9d**, **9h** and **9i** were more effective as hCA IX inhibitors, with K_Is in the range of 23.7–89 nM. On the contrary, hCA XII was potently inhibited (K_Is < 10 nM) by all the reported compounds (Table 7).

Table 7. CA IX and XII inhibition data for compounds **5**, **6** and sulfonamides **9a–j**.

Compd.	K_I (nM)	
	hCA IX	hCA XII
5	89	6.6
6	82	9.0
9a	>50,000	5.3
9b	nt [1]	nt [1]
9c	>50,000	5.7
9d	26.5	7.5
9e	>50,000	5.9
9f	652	8.1
9g	>50,000	6.2
9h	23.7	7.1
9i	43.8	7.9
9j	nt [1]	nt [1]
9k	824	6.2
Acetazolamide	25	5.8

[1]—not tested.

3.2. Synthesis from 3-Methylsulfanyl-1,2,4-triazine

Continuing research on sildenafil analogs a new approach to the synthesis of the sulfonamides was reported and their cytotoxicity against two human cancer cell lines: breast cancer (MCF-7) and human myelogenous leukemia (K562) were determined (Scheme 7) [45].

The results of biological study showed that none of the sildenafil analogs exhibited cytotoxicity in the tested concentrations. In addition, the ability of the derivatives to inhibit protein kinase CDK2/cyclin E and Abl was investigated. In the group of tested compounds, only sulfonamide **12e** showed moderate activity against kinase CDK2 (IC_{50} = 44.3 μM). Other compounds are inactive.

However, the group of sulfonamides appeared to be active against tumor associated carbonic anhydrase hCA IX and hCA XII [45]. The most active inhibitors against hCA IX were derivatives **12p** (K_I = 15.4 nM) and **12b** (K_I = 24.4 nM). Compounds **12r** (K_I = 3.8 nM) and **12i** (K_I = 5.5 nM) are the most active structures against hCA XII. The other compounds showed activity against hCA XII with K_I value in the range of 40–610 nM. Moreover, the structure of the sildenafil analogs was confirmed by X-ray analysis performed for the single crystal of derivative **12i** [45].

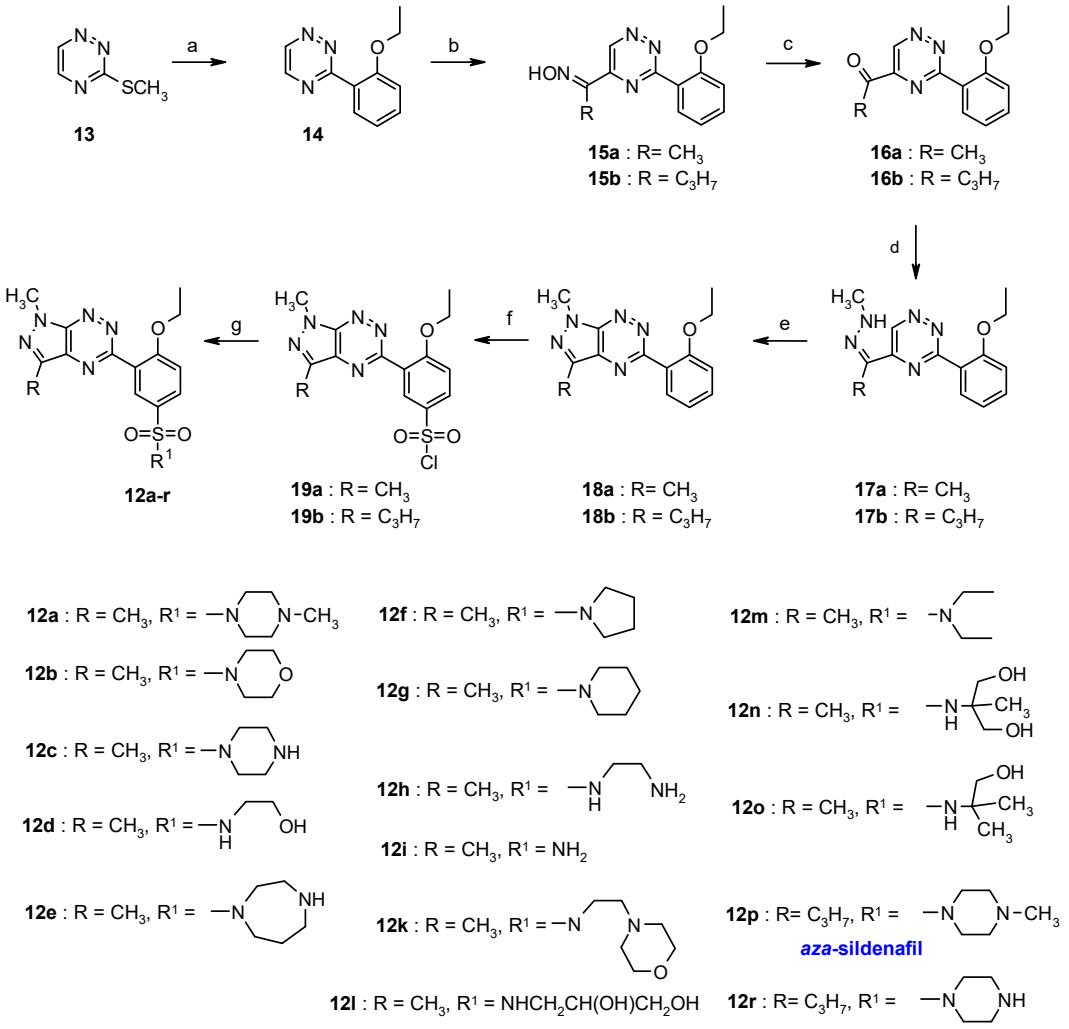

Scheme 7. Synthesis of sildenafil analogues. The reagents and reaction conditions: (**a**) 2-ethoxyphenylboronic acid, $Pd(PPh_3)_4$, CuMeSal, THF, Ar, reflux, 12 h; (**b**) RCH_2NO_2, KOH, DMSO, 2 h; (**c**) $Na_2S_2O_4$, H_2O/1,4-dioxane, 20 °C, 12 h; (**d**) CH_3NH-NH_2, 10% HCl, EtOH, rt, 1h; (**e**) 10% HCl, EtOH, reflux, 1h; (**f**) $ClSO_3H$, 0–20 °C, 2 h; (**g**) $aqNH_3$ or appropriate amine, anhydrous MeCN, 20 °C, 12 h.

Another group of sulfonamides constitutes sildenafil analogs in which the methyl group at the nitrogen atom N1 on the pyrazole was replaced by the aryl ring (Scheme 8) [47]. The aim of this study was to investigate whether the replacement of a methyl group by aryl substituent will have an effect on the antitumor activity and inhibition of human carbonic anhydrase isozymes.

Obtained sulfonamides were subjected to biological tests against breast carcinoma cells MCF-7 and MDA-MB-231 [47]. The most active derivatives are compounds **24b**, **24d** and **24i**, which showed moderate cytostatic activity against MCF-7 and MDA-MB-231 cells with IC_{50} value in the range of 126 ± 2 μM–185 ± 2 μM (Table 8). Other derivatives were inactive. In order to verify the mechanism responsible for the growth inhibitory effect on cancer cells, biosynthesis DNA in the presence of sulfonamides **24a–k** and chlorambucil as a standard was examined. The concentration of **24b**, **24d,** and **24i** necessary to inhibit the biosynthesis DNA in human breast cancer cells MCF-7 and MDA-MB-231 by 50% (IC_{50}) was in the range of 132 ± 2 μM do 173 ± 2 μM. For the other compounds, necessary concentration to inhibit [^{3}H]thymidine incorporation into DNA by 50% was found to be more than 200 μM.

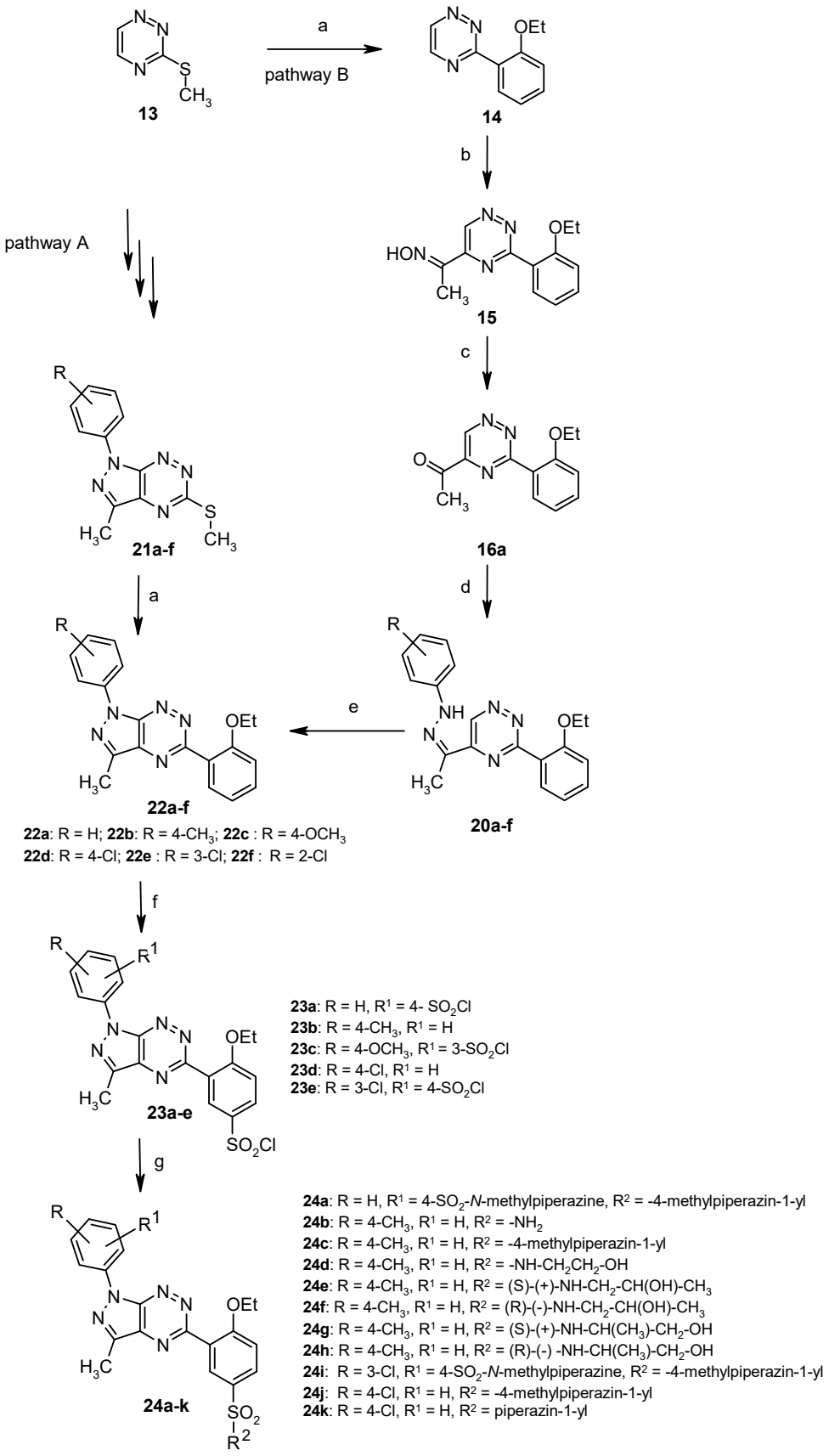

Scheme 8. Synthesis of sulfonamides **24a–k**. The reagents and reaction conditions: (**a**) 2-ethoxyphenylboronic acid, $Pd(PPh_3)_4$, CuMeSal, THF, Ar, reflux, 12 h; (**b**) $CH_3CH_2NO_2$, KOH, DMSO, 2 h; (**c**) $Na_2S_2O_4$, H_2O/dioxane, 20 °C, 12 h; (**d**) Ar-NH-NH_2, 10% HCl, EtOH; (**e**) 10% HCl, EtOH, reflux; (**f**); $ClSO_3H$, from 0 °C to 20 °C, 2 h; (**g**) 20% aqNH_3 or appropriate amine, anhydrous MeCN, 20 °C, 12 h.

Table 8. Cytotoxic and cytostatic activities of new sulfonamides derivatives of pyrazolo[4,3-*e*][1,2,4]triazines **24a–k.**

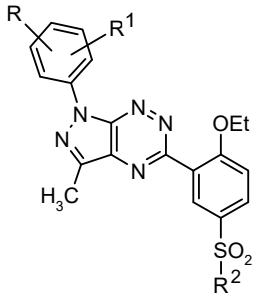

Compd.	R^1	R^2	R^3	MTT Assay, IC_{50} (μM)		[^{3}H]Thymidine Incorporation, IC_{50} (μM)	
				MCF-7	MDA-MB-231	MCF-7	MDA-MB-231
24a	H	4-SO_2	4-methylpiperazin-1-yl	>200	>200	>200	>200
24b	4-CH_3	H	NH_2	154 ± 2	171 ± 2	155 ± 2	148 ± 2
24c	4-CH_3	H	4-methylpiperazin-1-yl	>200	>200	>200	>200
24d	4-CH_3	H	$NHCH_2CH_2OH$	126 ± 2	147 ± 2	132 ± 2	136 ± 2
24e	4-CH_3	H	(S)-(+)-$NHCH_2CH(OH)CH_3$	>200	>200	>200	>200
24f	4-CH_3	H	(R)-(+)-$NHCH_2CH(OH)CH_3$	>200	>200	>200	>200
24g	4-CH_3	H	(S)-(+)-$NHCH(CH_3)CH_2OH$	>200	>200	>200	>200
24h	4-CH_3	H	(R)-(+)-$NHCH(CH_3)CH_2OH$	>200	>200	>200	>200
24i	3-Cl	4-SO_2-*N*-methylpiperazine	4-methylpiperazin-1-yl	160 ± 2	185 ± 2	173 ± 2	169 ± 2
24j	4-Cl	H	4-methylpiperazin-1-yl	>200	>200	>200	>200
24k	4-Cl	H	piperazin-1-yl	>200	>200	>200	>200
Chlorambucil				97 ± 2	93 ± 2	56 ± 2	49 ± 2

Despite moderate cytostatic activity, sulfonamides achieved have shown greater inhibition of human carbonic anhydrase isoenzymes. hCA IX was efficiently inhibited by most of the obtained compounds, with inhibition constants ranging between 13.8 and 417 nM (Table 9) [47]. Poor inhibition of this isoforms (K_Is of 403–417 nM) showed derivatives **24i** and **24j**. Furthermore, these studies demonstrated that both the primary sulfonamides and the tertiary ones showed similar inhibition, although their mechanisms of inhibitory activity are very different. The primary sulfonamide binds to the metal ion, whereas the tertiary ones probably in the coumarin-binding site. hCA XII was also inhibited by the new reported compounds with inhibition constants ranging between 70.3 and 536 nM. Compound **24a** was a poor hCA XII inhibitor (K_I of 536 nM), whereas the remaining ones were medium potency inhibitors with K_Is in the range of 70.3–93.1 nM.

Table 9. CA IX and XII inhibition data for compounds **24a–k**.

Compd.	K_I (nM)	
	hCA IX	**hCA XII**
24a	29.6	536
24b	28.7	77.5
24c	**25.4**	78.1
24d	**24.5**	91.5
24e	**13.8**	82.8
24f	35.6	77.8
24g	**27.7**	77.6
24h	**26.6**	70.3
24i	417	79.4
24j	403	81.5
24k	42.3	93.1
Acetazolamide	25	5.8

4. Synthesis and Anticancer Activity of Annulated Pyrazolo[4,3-*e*][1,2,4]triazines: Pyrazolo[4,3-*e*][1,2,4]triazolo[4,3-*b*][1,2,4]triazines and Pyrazolo[4,3-*e*]tetrazolo[1,5-*b*][1,2,4]triazines

A very interesting group of compounds with anticancer activity constitute the fused pyrazolo[4,3-*e*][1,2,4]triazines with 1,2,4-triazole or tetrazole ring. The general synthesis pathway leading to the tricyclic derivatives is depicted in Scheme 9 [21,48,49].

Preliminary biological studies have shown that the obtained tricyclic derivatives have anti-cancer properties, which were demonstrated in tests on various tumor cell lines. The highest antitumor activity (in the nanomolar concentration range) was shown by tetrazole derivative **30b** (Table 10) [21]. At this point, it should be added that, in heterocyclic systems with a terminal tetrazole ring, a valence tautomerism may occur i.e., the equilibrium between the azide derivative and the tricyclic system [48,50,51]. The shift of the equilibrium depends on the environment of this process, e.g., solvent properties [48,50]. Tautomeric equilibrium is an important and interesting chemical phenomenon because the various tautomers of the same compound have different physico-chemical properties. Therefore, the same compound may have different reactivity, or even biochemical properties, depending on the tautomeric form. For that reason, prediction of the tautomeric mixture composition is important for the design of new biologically active compounds as well as technological processes or understanding processes of life. Thus, the research results on tautomeric equilibrium in pyrazolo[4,3-*e*][1,2,4]triazine derivatives fused with tetrazole ring were described in literature [48,50].

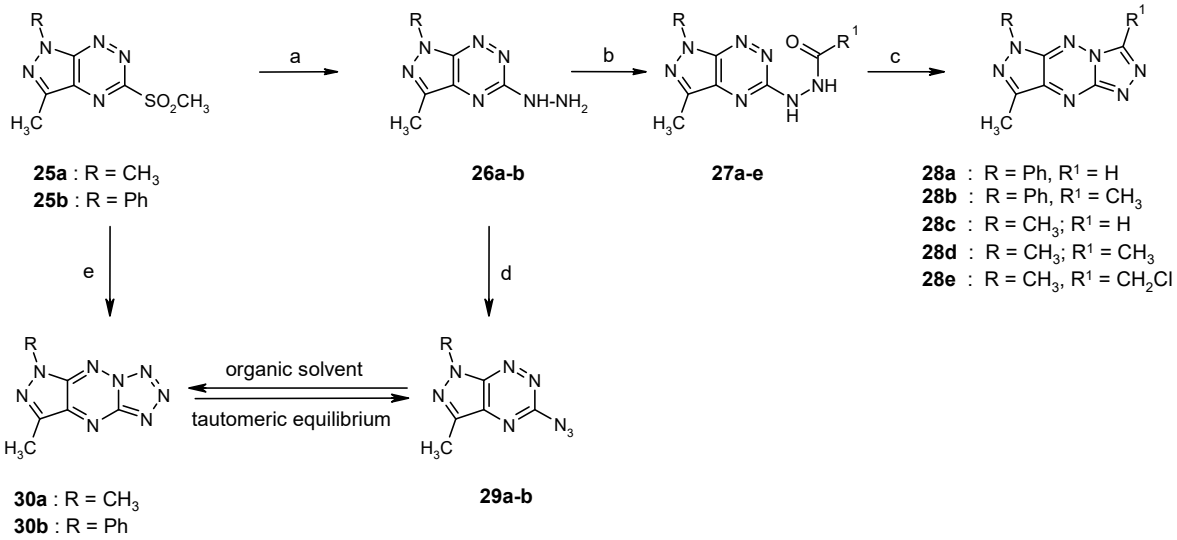

Scheme 9. The synthesis of new triazole and tetrazole derivatives condensed with 1H-pyrazolo[4,3-*e*][1,2,4]triazine system. Reagents and conditions: (**a**) H_2N-NH_2, THF, 20 °C, 12 h; (**b**) R^1-COOH, in CH_2Cl_2, reflux; (**c**) CH_3COOH, reflux.; (**d**) $NaNO_2$, CH_3COOH, 0–5 °C; (**e**) NaN_3, EtOH, reflux, 12 h.

Table 10. Cytotoxic activity of **30b** against tumor cell lines determined by MTT assay.

Compd.	IC_{50} (μM)					
	LS180	**Colo205**	**H460**	**MCF-7**	**PC-3**	**LN229**
30b	0.131	<0.400	<0.400	0.500	<0.400	0.270

Another valuable group of tricyclic compounds with anti-cancer properties are pyrazolo[4,3-*e*][1,2,4]triazolo[4,3-b][1,2,4]triazine derivatives. Their antiproliferative activity was evaluated against human lung cancer A549 and colon cancer LS180 using MTT tests. Obtained results revealed a concentration-dependent decrease in cancer cell proliferation. It was observed that pyrazolo-triazolo-triazines were more active than the intermediates. As shown in Table 11, compound **28c** with chloromethyl substituent was the most active. In contrast, compound **28b** with methyl substituent was the least active. It was observed that lung cancer A549 cells were more sensitive for pyrazolo[4,3-*e*][1,2,4]triazolo[4,3-b][1,2,4]triazine derivatives action than colon cancer LS180 cells. It should be noted that the tested compounds showed higher antiproliferative activity than common cytotoxic drugs, cisplatin (lung carcinoma), and 5-fluorouracil (colon adenocarcinoma).

Table 11. Antiproliferative activity of pyrazolo[4,3-*e*][1,2,4]triazolo[4,3-b][1,2,4]triazine derivatives in lung cancer A549 and colon cancer LS180 cells.

Compd.	IC_{50} (μM)	
	A549	**LS180**
26	17.4	>25
27c	>25	>25
28a	2.1	5.6
28b	9.4	37.6
28c	2.0	2.4
cisplatin	3.4	-
5-fluorouracil	-	19.2

5. Conclusions

In the review, we have summarized the results of research on the synthesis and anticancer activity of the new synthetic derivatives of the little-known pyrazolo[4,3-*e*][1,2,4]triazine ring system. One of the presented derivatives constitute sulfonamides with potential antitumor activity on the cancer cell lines MCF-7, MDA-MB-231, BV173, HL60, CCRF-CEM, and the ability to inhibit protein kinases Bcr-Abl and CDKs, as well as two isozymes of carbonic anhydrase. Positive results were obtained for inhibition of isoforms hCA IX and hCA XII associated with cancer. Derivatives **9d** and **9h** are the most active hCA IX inhibitors, whereas compounds **9a**, **9c** and **9e** show the highest activity against hCA XII and are also the best cytostatics among all investigated sulfonamides. Another very interesting group with good cytostatic activity were derivatives of annulated pyrazolo[4,3-*e*][1,2,4]triazines i.e., pyrazolo[4,3-*e*][1,2,4]triazolo[4,3-*b*][1,2,4]triazines and pyrazolo[4,3-*e*]tetrazolo[1,5-*b*][1,2,4]triazine. Presented compounds showed higher antiproliferative activity than popular cytostatics such as cisplatin (lung carcinoma) and 5-fluorouracil (colon adenocarcinoma). Therefore, they may constitute a new group of candidates for drugs useful in the treatment of various cancers.

Author Contributions: Z.B., A.S. and M.K. conceived the project and wrote the draft. K.K.-M. edited the manuscript. M.M. revised the manuscript. All authors have read and agreed to the published version of the manuscript.

Funding: This research received no external funding. The APC was funded by Siedlce University of Natural Sciences and Humanities.

Conflicts of Interest: The authors declare no conflict of interest.

Abbreviations

PPA	polyphosphoric acid
A549	lung adenocarcinoma cells
CEM	T-lymphoblastic leukemia cells
CEM DNR Bulk	T-lymphoblastic leukemia daunorubicin resistant cells
K562	myeloid leukemia cells
K562 tax	myeloid leukemia, paclitaxel resistant cells
SAR	structure–activity relationship
S_NAr	reaction of nucleophillic aromatic substitution
PC-3	prostate cancer cells
MCF-7	estrogen receptor positive breast cancer cells
H460	non-small-cell lung cancer
Colo205	colorectal adenocarcinoma cells
CDK	cyclin dependent kinase
CA, EC 4.2.1.1	carbonic anhydrase
RAF kinase	rapidly accelerated fibrosarcoma
CA IX	carbonic anhydrase IX
CA XII	carbonic anhydrase XII
CDK2	cyclin-dependent kinase 2
MDA-MB-231	estrogen receptor negative breast cancer cells
BV173	leukemia cells
HL60	leukemia cells
CCRF-CEM	leukemia cells
K_I	inhibitory constant
hCA IX	human carbonic anhydrase IX
hCA XII	human carbonic anhydrase XII
LN229	glioblastoma tumor cells
LS180	colon adenocarcinoma cells

References

1. Lindner, H.J.; Schaden, G. Pyrazolo(4.3-e)as-triazine, a new heterocyclic system from *Pseudomonas fluorescens* var. *Pseudoidinum*. *Chem. Ber.* **1972**, *105*, 1949–1955. [CrossRef]
2. Hirata, K.; Nakagami, H.; Takashina, J.; Mahmud, T.; Kobayashi, M.; In, Y.; Ishida, T.; Miyamoto, K. Novel violet pigment, nostocine A, an extracellular metabolite from Cyanobacterium Nostoc spongiaeforme. *Heterocycles* **1996**, *43*, 1513–1519.
3. Smirnov, V.V.; Kiprianova, E.A.; Garagulya, A.D.; Esipov, S.E.; Dovjenko, S.A. Fluviols, bicyclic nitrogen-rich antibiotics produced by *Pseudomonas fluorescens*. *Fems Microbiol. Lett.* **1997**, *153*, 357–361. [CrossRef]
4. Kelly, T.R.; Elliott, E.L.; Lebedev, R.; Pagalday, J. Synthesis of the pyrazolo[4,3-*e*][1,2,4]triazine family of natural products: nostocine A, fluviol A, and pseudoiodinine. *J. Am. Chem. Soc.* **2006**, *128*, 5646–5647. [CrossRef] [PubMed]
5. Badr, M.Z.A.; Aly, M.M.; Khalil, Z.H.; Attalla, A.A. ChemInform Abstract: Synthesis and Reactions of 1,3-Diphenyl-As-Triazin-6-One. *Indian J. Chem. Sect. B* **1982**, *21B*, 115. [CrossRef]
6. Nálepa, K.; Slouka, J. Cyclisierungsreaktionen von Hydrazonen. XVI: Eine einfache Synthese einiger Pyrazolo[4,3-*e*]-1,2,4-triazinen. *Pharmazie* **1984**, *39*, 504–505.
7. Nálepa, K.; Gucký, T. Synthesis of some new pyrazolo[4,3-*e*]1,2,4-triazines. *Acta Univ. Palacki Olomuc Fac Rer. Nat. Chem.* **2001**, 49.
8. Rykowski, A.; Mojzych, M.; Karczmarzyk, Z. A new synthesis of pyrazolo[4,3-*e*][l,2,4]triazines via acid promoted ring closure of the phenylhydrazones of 5-acyl-l,2,4-triazines. *Heterocycles* **2000**, *53*, 2175–2181. [CrossRef]
9. Mojzych, M.; Rykowski, A. Thermal transformations of phenylhydrazones of 5-acyl-1,2,4-triazines towards pyrazolo[4,3-*e*][1,2,4]triazine and 4-cyanopyrazole derivative under acidic and no acidic conditions. *J. Heterocycl. Chem.* **2007**, *44*, 1003–1007. [CrossRef]
10. Youssef, M.S.K.; Hassan, K.M.; Atta, F.M.; Abbady, M.S. Synthesis of 1*H*-pyrazolo[3,4-*e*]-s-triazolo[3,4-*c*]-*as*-triazines, 8*H*-pyrazolo[3,4-*e*]tetrazolo[5,1-*c*]-as-triazine and 1,7-dihydro-8*H*-pyrazolo[3,4-*e*]-as-triazine derivatives. *J Heterocycl. Chem.* **1984**, *21*, 1565–1568. [CrossRef]
11. Abu Safieh, A.K.; Abu Mahthieh, A.M.; El-Abadelah, M.M.; Ayoub, M.T.; Voelter, W. Synthesis of 5-substituted 1,3-dimethylpyrazolo[4,3-*e*][1,2,4]triazines. *Monatsh. Chem.* **2007**, *138*, 157–160. [CrossRef]
12. Gucký, T.; Frysová, I.; Slouka, J.; Hajdúch, M.; Dzubák, P. Cyclocondensation reaction of heterocyclic carbonyl compounds. Part XIII: Synthesis and cytotoxic activity of some 3,7-diaryl-5-(3,4,5-trimethoxyphenyl)pyrazolo[4,3-*e*][1,2,4]triazines. *Eur. J. Med. Chem.* **2009**, *44*, 891–900.
13. Rykowski, A.; Mąkosza, M. Reaction of 1,2,4-triazines with nitronate anions, direct nucleophilic acylation of 1,2,4-triazines. *Tetrahedron Lett.* **1984**, *25*, 4795–4796. [CrossRef]
14. Rykowski, A.; Lipińska, T. A concise route to a key intermediate in the total synthesis of sempervirine. *Synth. Commun.* **1996**, *26*, 4409–4414. [CrossRef]
15. Mojzych, M.; Rykowski, A. Direct synthesis of pyrazolo[4,3-*e*][1,2,4]triazine derivatives from oximes of 5-acyl- and 5-formyl-1,2,4-triazines. *Heterocycl. Commun.* **2006**, *12*, 191–194. [CrossRef]
16. Mojzych, M.; Rykowski, A. One-step synthesis and regioselective alkylation of substituted 1*H*-pyrazolo[4,3-*e*][l,2,4]triazine. *Pol. J. Chem.* **2003**, *77*, 1797–1803.
17. Shepherd, R.G.; Federic, J.L. Reactivity of azine, benzoazine, and azinoazine derivatives with simple nucleophiles. In *Advances in Heterocyclic Chemistry*, 1st ed.; Katritzky, A.R., Boulton, A.J., Lagowski, J.M., Eds.; Academic Press Inc.: London, UK, 1965; Volume 4, pp. 145–423.
18. Oae, S.; Furukawa, N. Heteroaromatic sulfoxides and sulfones: Ligand exchange and coupling in sulfuranes and ipso-substitutions. In *Advances in Heterocyclic Chemistry*; Katritzky, A.R., Ed.; Academic Press Limited: London, UK, 1990; Volume 48, pp. 1–63.
19. Mojzych, M.; Rykowski, A. Synthesis of functionalized 1*H*-pyrazolo[4,3-*e*][l,2,4]-triazines and their fused derivatives via ipso-substitution of methylsulfonyl group with *O*-, *N*-, *S*- and *C*-nucleophiles. *Heterocycles* **2004**, *63*, 1829–1838.
20. Mojzych, M.; Rykowski, A. Synthesis of aza-analog of N-methylated acycloformycine A. *Heterocycles* **2007**, *71*, 2449–2456. [CrossRef]
21. Mojzych, M. Cytotoxic activity of some pyrazolo[4,3-*e*][1,2,4]triazines against human cancer cell lines. *J. Chem. Soc. Pak.* **2011**, *33*, 123–128.

22. Supuran, C.T.; Casini, A.; Scozzafava, A. Protease inhibitors of the sulfonamide type: Anticancer, antiinflammatory, and antiviral agents. *Med. Res. Rev.* **2003**, *5*, 535–558. [CrossRef]
23. Scozzafava, A.; Owa, T.; Mastrolorenzo, A.; Supuran, C.T. Anticancer and antiviral sulfonamides. *Curr. Med. Chem.* **2003**, *10*, 925–953. [CrossRef] [PubMed]
24. Kleemann, A.; Engel, J. *Pharmaceutical Substances, Syntheses, Patents, Applications*, 3rd ed.; Thieme: Stuttgart, Germany, 1999.
25. Byth, K.F.; Culshaw, J.D.; Green, S.; Oakes, S.E.; Thomas, A.P. Imidazo[1,2-*b*]pyridazines: A potent and selective class of cyclin-dependent kinase inhibitors. *Bioorg. Med. Chem. Lett.* **2004**, *14*, 2249–2252. [CrossRef]
26. Shah, S.S.A.; Rivera, G.; Ashfaq, M. Recent advances in medicinal chemistry of sulfonamides. Rational design as anti-tumoral, anti-bacterial and anti-inflammatory agents. *Mini Rev. Med. Chem.* **2013**, *13*, 70–86. [CrossRef] [PubMed]
27. Supuran, C.T.; Scozzafava, A.; Casini, A. Carbonic anhydrase inhibitors. *Med. Res. Rev.* **2003**, *23*, 146–189. [CrossRef] [PubMed]
28. Supuran, C.T. Carbonic anhydrases: Catalytic and inhibition mechanisms, distribution and physiological roles. In *Carbonic Anhydrase: Its Inhibitors and Activators*; Supuran, C.T., Scozzafava, A., Conway, J., Eds.; CRC Press: Boca Raton, FL, USA, 2004; pp. 1–23.
29. Supuran, C.T.; Scozzafava, A. Carbonic anhydrases as targets for medicinal chemistry. *Bioorg. Med. Chem.* **2007**, *15*, 4336–4350. [CrossRef] [PubMed]
30. Roskoski, R. Enzyme Structure and Function. In *xPharm: The Comprehensive Pharmacology Reference*; Byland, D.B., Enna, S.J., Eds.; Elsevier Science Inc.: New York, NY, USA, 2007.
31. Roskoski, R., Jr. An anticancer protein-tyrosine kinase inhibitor. *Biochem. Biophys. Res. Commun.* **2003**, *303*, 709–717. [CrossRef]
32. Roskoski, R., Jr. The ErbB/HER protein-tyrosine kinases and cancer. *Pharmacol. Res.* **2014**, *79*, 34–74. [CrossRef]
33. Kryštof, V.; Uldrijan, S. Cyclin-dependent kinase inhibitors as anticancer drugs. *Curr. Drug Targets* **2010**, *11*, 291–302. [CrossRef]
34. Pastorek, J.; Pastoreková, S. Cancer-related carbonic anhydrase Isozymes and their Inhibition. In *Carbonic Anhydrase: Its Inhibitors and Activators*; Supuran, C.T., Scozzafava, A., Conway, J., Eds.; CRC Press: Boca Raton, FL, USA, 2004; pp. 255–281.
35. Supuran, C.T. Carbonic anhydrases as drug targets-an overview. *Curr Top Med Chem.* **2007**, *7*, 825–833. [CrossRef]
36. Scozzafava, A.; Mastrolorenzo, A.; Supuran, C.T. Carbonic anhydrase inhibitors and activators and their use in therapy. *Expert Opin. Pat.* **2006**, *16*, 1627–1664. [CrossRef]
37. Pastoreková, S.; Kopacek, J.; Pastorek, J. Carbonic anhydrase inhibitors and the management of cancer. *Curr. Top. Med. Chem.* **2007**, *7*, 865–878. [CrossRef] [PubMed]
38. Pastorek, J.; Pastoreková, S.; Callebaut, I.; Mornon, J.-P.; Zelník, V.; Opavský, R.; Zat'Ovicová, M.; Liao, S.; Portetelle, D.; Stanbridge, E.J. Cloning and characterization of MN, a human tumor-associated protein with a domain homologous to carbonic anhydrase and a putative helix-loop-helix DNA binding segment. *Oncogene* **1994**, *9*, 2788–2888.
39. Opavský, R.; Pastoreková, S.; Zelník, V.; Gibadulinová, A.; Stanbridge, E.J.; Závada, J.; Kettmann, R.; Pastorek, J. Human MN/CA9 Gene, a Novel Member of the Carbonic Anhydrase Family: Structure and Exon to Protein Domain Relationships. *Genomics* **1996**, *33*, 480–487. [CrossRef]
40. Türeci, Ö.; Şahin, U.; Vollmar, E.; Siemer, S.; Göttert, E.; Seitz, G.; Parkkila, A.-K.; Shah, G.N.; Grubb, J.H.; Pfreundschuh, M.; et al. Human carbonic anhydrase XII: cDNA cloning, expression, and chromosomal localization of a carbonic anhydrase gene that is overexpressed in some renal cell cancers. *Proc. Natl. Acad. Sci. USA* **1998**, *95*, 7608–7613. [CrossRef]
41. Winum, J.-Y.; Scozzafava, A.; Montero, J.-L.; Supuran, C.T. Inhibition of carbonic anhydrase IX: A new strategy against cancer. *Anti-Cancer Agents Med. Chem.* **2009**, *9*, 693–702. [CrossRef]
42. Winum, J.-Y.; Rami, M.; Scozzafava, A.; Montero, J.-L.; Supuran, C.T. Carbonic anhydrase IX: A new druggable target for the design of antitumor agents. *Med. Res. Rev.* **2008**, *28*, 445–463. [CrossRef]
43. Mojzych, M.; Šubertová, V.; Bielawska, A.; Bielawski, K.; Bazgier, V.; Berka, K.; Gucký, T.; Fornal, E.; Kryštof, V. Synthesis and kinase inhibitory activity of new sulfonamide derivatives of pyrazolo[4,3-*e*][1,2,4]triazines. *Eur. J. Med. Chem.* **2014**, *78*, 217–224. [CrossRef]

44. Mojzych, M.; Bielawska, A.; Bielawski, K.; Ceruso, M.; Supuran, C.T. Pyrazolo[4,3-*e*][1,2,4]triazine sulfonamides as carbonic anhydrase inhibitors with antitumor activity. *Bioorganic Med. Chem.* **2014**, *22*, 2643–2647. [CrossRef]
45. Mojzych, M.; Karczmarzyk, Z.; Wysocki, W.; Ceruso, M.; Supuran, C.T.; Kryštof, V.; Urbańczyk-Lipkowska, Z.; Kalicki, P. New approaches to the synthesis of sildenafil analogues and their enzyme inhibitory activity. *Bioorganic Med. Chem.* **2015**, *23*, 1421–1429. [CrossRef]
46. Cowan-Jacob, S.W.; Fendrich, G.; Floersheimer, A.; Furet, P.; Liebetanz, J.; Rummel, G.; Rheinberger, P.; Centeleghe, M.; Fabbro, D.; Manley, P.W. Structural biology contributions to the discovery of drugs to treat chronic myelogenous leukaemia. *Acta. Cryst. Sect. D Boil. Cryst.* **2006**, *63*, 80–93. [CrossRef]
47. Mojzych, M.; Ceruso, M.; Bielawska, A.; Bielawski, K.; Fornal, E.; Supuran, C.T. New pyrazolo[4,3-*e*][1,2,4]triazine sulfonamides as carbonic anhydrase inhibitors. *Bioorg. Med. Chem.* **2015**, *23*, 3674–3680. [CrossRef] [PubMed]
48. Mojzych, M.; Karczmarzyk, Z.; Wysocki, W.; Urbańczyk-Lipkowska, Z.; Żaczek, N. Valence tautomerism of new pyrazolo[4,3-*e*]tetrazole[4,5-b][1,2,4]triazines. *J. Mol. Struct.* **2014**, *1067*, 147–153. [CrossRef]
49. Mojzych, M.; Tarasiuk, P.; Karczmarzyk, Z.; Juszczak, M.; Rzeski, W.; Fruziński, A.; Woźny, A. Synthesis, Structure and Antiproliferative Activity of New pyrazolo[4,3-*e*]triazolo[4,5-b][1,2,4]triazine Derivatives. *Med. Chem.* **2018**, *14*, 53–59. [CrossRef] [PubMed]
50. Cmoch, P. Multinuclear magnetic resonance study of the structure and tautomerism of azide and iminophosphorane derivatives of chloropyridazines. *Magn. Reson. Chem.* **2002**, *40*, 507–516. [CrossRef]
51. Karczmarzyk, Z.; Mojzych, M.; Rykowski, A. Synthesis and structure of a novel mesomeric betaine 6,7-dimethyl-2*H*-pyrazolo[4,3-*e*]tetrazolo[4,5-*b*][1,2,4]triazine. *J. Mol. Struct.* **2007**, *829*, 22–28. [CrossRef]

International Journal of
Molecular Sciences

MDPI

Article

Preparation of Novel Pyrazolo[4,3-*e*]tetrazolo[1,5-*b*][1,2,4]triazine Sulfonamides and Their Experimental and Computational Biological Studies

Mateusz Kciuk [1,2,*], Somdutt Mujwar [3], Anna Szymanowska [4], Beata Marciniak [1], Karol Bukowski [1], Mariusz Mojzych [4] and Renata Kontek [1]

1 Department of Molecular Biotechnology and Genetics, University of Lodz, 90-237 Lodz, Poland; beata.marciniak@biol.uni.lodz.pl (B.M.); karol.bukowski@edu.uni.lodz.pl (K.B.); renata.kontek@biol.uni.lodz.pl (R.K.)
2 Doctoral School of Exact and Natural Sciences, University of Lodz, 90-237 Lodz, Poland
3 M.M. College of Pharmacy, Maharishi Markandeshwar (Deemed to be University) Mullana, Ambala 133207, India; somduttmujwar@gmail.com
4 Department of Chemistry, Siedlce University of Natural Sciences and Humanities, 08-110 Siedlce, Poland; anna.szymanowska@umb.edu.pl (A.S.); mariusz.mojzych@uph.edu.pl (M.M.)
* Correspondence: mateusz.kciuk@edu.uni.lodz.pl

Abstract: Pyrazolo[4,3-*e*]tetrazolo[1,5-*b*][1,2,4]triazine sulfonamides constitute a novel class of heterocyclic compounds with broad biological activity, including anticancer properties. Investigated in this study, MM-compounds (**MM134**, **MM136**, **MM137**, and **MM139**) exhibited cytotoxic and proapoptotic activity against cancer cell lines (BxPC-3, PC-3, and HCT-116) in nanomolar concentrations without causing cytotoxicity in normal cells (L929 and WI38). In silico predictions indicate that tested compounds exhibit favorable pharmacokinetic profiles and may exert anticancer activity through the inhibition of BTK kinase, the AKT-mTOR pathway and PD1-PD-L1 interaction. Our findings point out that these sulfonamide derivatives may constitute a source of new anticancer drugs after optimization.

Keywords: cancer cells; cytotoxicity; apoptosis; pyrazolo[4,3-*e*]tetrazolo[1,5-*b*][1,2,4]triazine; sulfonamides

check for updates

Citation: Kciuk, M.; Mujwar, S.; Szymanowska, A.; Marciniak, B.; Bukowski, K.; Mojzych, M.; Kontek, R. Preparation of Novel Pyrazolo[4,3-*e*]tetrazolo[1,5-*b*][1,2,4]triazine Sulfonamides and Their Experimental and Computational Biological Studies. *Int. J. Mol. Sci.* **2022**, *23*, 5892. https://doi.org/10.3390/ijms23115892

Academic Editor: Claudiu T. Supuran

Received: 5 May 2022
Accepted: 17 May 2022
Published: 24 May 2022

1. Introduction

The chemistry of heterocyclic compounds is still a developing field that offers many opportunities for novel drug discovery, which is confirmed by the fact that many modern drugs used in medicine contain a heterocyclic core. Moreover, new methods of synthesis and modern organic chemistry techniques have led to the rapid expansion of this branch of science. Anticancer drug development is one of the main objectives of heterocyclic chemistry [1].

One of the common strategies used in anticancer drug development is the synthesis of antimetabolites that structurally resemble naturally occurring key substrates of metabolic processes. Blocking of these crucial processes slows down the proliferation of cells and triggers their apoptotic cell death [2–4]. Apoptosis is considered to be a crucial component of the vital processes of living organisms. It is responsible for the proper development and functioning of the immune system. Apoptosis deregulation results in the development of a multitude of human conditions, including neurodegenerative diseases, autoimmune disorders, and many types of cancer. Apoptosis is a genetically designed process of active cell destruction. Cells undergoing apoptosis remain intact without lysis, inflammation, and causing damage to neighboring cells. The activation of apoptosis pathways is a key mechanism of action for many cytotoxic drugs. Moreover, defects in apoptosis signaling contribute to drug resistance in many tumors. Cytotoxic drugs activate either the mitochondrial (intrinsic) or death receptor (extrinsic) apoptosis pathway [5,6]. Nowadays,

most anticancer drugs exhibit proapoptotic properties. Moreover, the majority of them are designed to take advantage of cell division in order to achieve selective action. The selectivity is based on the more rapid division of cancer cells compared to their normal counterparts. However, these molecules are not sufficiently selective for cancer cells and result in toxicity to normal cells, which provokes serious consequences for patients [6]. Therefore, there is an urgent need to explore both the cytotoxic and proapoptotic properties of new potential anticancer drugs. One of the characteristic changes occurring during apoptosis is the translocation of phosphatidylserine from the inner side of a cell membrane to the surface of a cell. This allows rapid and accurate estimation of proapoptotic properties of anticancer compounds with the use of annexin V, which forms conjugates with a fluorescent dye (FITC) and allows the detection of phosphatidylserine exposition on the cell surface with the use of flow cytometry [7,8].

Pyrazolotriazines were identified as biologically active compounds with inhibitory activity towards histone deacetylases [9], metalloproteinases [10], tubulin [11], urease and tyrosinase [12,13]. Moreover, some of them inhibit protein kinases engaged in pivotal signaling pathways driving cancer cell proliferation, including ABL kinase [14,15], cyclin-dependent kinases (CDKs) [16,17], casein kinase 2 (CK2) [18,19], and glycogen synthase kinase 3 (GSK3) [20]. The addition of the sulfonamide moiety to the pyrazolotriazine scaffold allowed for the broadening of the array of possible molecular targets of these compounds [21]. For example, pyrazolo[4,3-*e*][1,2,4]triazine derivatives have been shown to have ABL protein kinase inhibitory activity in the micromolar concentration range (IC_{50} = 5.8–5.9 μM). Furthermore, sulfonamide-bearing compounds are the most abundant class of carbonic anhydrase (CA) inhibitors. The inhibition of tumor isoforms of CA (CA-IX and XII) has been shown to significantly reduce the survival of hypoxic tumors. Nowadays, sulfonamide compounds have been tested in clinical trials, with SLC-0011 being one of the most prominent examples of this type of agents [22]. The best results against hCA-IX were observed with pyrazolo[4,3-*e*][1,2,4]triazines with dissociation constants (KI values) of 23.7 and 26.5 nM, which were similar to reference sulfonamide compound acetazolamide (KI = 25 nM). In contrast, all derivatives tested in these studies showed a good inhibition of CA-XII with KIs in the range of 5.3 nM to 9.0 nM [23,24].

The findings of experimental research published to date have demonstrated that a variety of derivatives of the pyrazolo-triazine heterocyclic system exhibit a wide range of biological activity, including anticancer activity. Tricyclic pyrazolo[4,3-*e*][1,2,4] triazines fused with a triazole or tetrazole ring are of special interest. They represent novel heterocyclic systems with strong anticancer activity and suggest that they may be a source of new chemotherapeutic drugs in the future. The biological activity of a number of the pyrazolo[4,3-*e*][1,2,4]triazines described in the literature was recently reviewed by the Mojzych group [16].

More recently, a novel **MM129** (pyrazolo[4,3-*e*]tetrazolo[1,5-*b*][1,2,4]triazine sulfonamide) has been shown to efficiently suppress cell viability through the inhibition of Bruton's tyrosine kinase (BTK). Activation of antiapoptotic pathways has been shown to play a significant role in the growth of tumors, and BTK has been implicated in this process. In turn, BTK inhibition can trigger apoptosis activation in a variety of cell types. Compared to the routinely used chemotherapeutic agent (5-fluorouracil, 5-FU), **MM129** exhibited a substantially higher anticancer efficacy at a relatively low dose. Apoptosis was found to be the primary response of colorectal cancer cells (DLD-1 and HT-29 cell lines) to **MM129** treatment. **MM129** also inhibited tumor development in a zebrafish embryo xenograft model, where it had a notably synergistic anticancer impact when given in conjunction with 5-FU [25].

It was found that **MM129** possesses antitumor activity in xenograft mouse models of colon cancer. The mechanistic analysis found that **MM129** not only has the potential to inhibit intracellular pathways that promote carcinogenesis but also has the potential to decrease the protein levels of PD-L1 [26]. Immune checkpoint pathways, such as the programmed death receptor-1 and programmed death ligand-1 (PD-1/PD-L1) signaling

pathway, are critical in regulating self-tolerance and controlling self-damage, and can be manipulated by cancer cells to avoid immune surveillance [27,28]. Recent clinical trials have demonstrated the efficacy of PD-1/PD-L1-targeted therapy in a variety of malignancies, heralding the beginning of a new era in cancer immunotherapy [29]. Furthermore, the treatment of cells with this novel derivative in combination with 5-FU appears to sensitize tumor cells to this extensively used chemotherapeutic agent. In both DLD-1 and HT-29 cells, exposure to **MM129** resulted in a decrease in the expression of AKT and mTOR serine/threonine-protein kinases [26]. The AKT/mTOR pathway plays a crucial role in the regulation of a variety of processes associated with cell growth, metabolism, survival, and proliferation. Increased expression of the mTOR kinase is observed in many types of cancer. The activation of the mTOR pathway is responsible for the stimulation of tumor growth and metastasis. A total of 60–70% of human colon malignancies have been found to have over-activated AKT-mTOR signaling [30–32]. Many mTOR inhibitors have been approved by the FDA for the treatment of cancer, but a large number of them are still being investigated in numerous clinical trials [33,34]. Both **MM-129** and 5-FU treatment resulted in a significant upregulation of cellular tumor antigen p53 (TP53), as well as a corresponding downregulation of CDK2, in both cell lines after 24 h exposure to the compounds. This alteration was most likely the cause of the cell cycle arrest [26].

MM129 possesses good pharmacokinetic properties, with rapid absorption and bioavailability of 68.6% after intraperitoneal administration. There have been no reports of significant adverse events associated with the use of **MM129**, confirming that this chemical has a positive safety profile in mice. At an anticancer-effective dose of 10 μM/kg, it was not lethal or harmful to mice, and it exhibited no toxicity [35].

Another new pyrazolo[4,3-*e*]tetrazolo[1,5-*b*][1,2,4]triazine sulfonamide (**MM131**) demonstrated promising anticancer potential. It exhibited an inhibitory effect on the viability and proliferation of the DLD-1 and HT-29 cells. The stimulation of both extrinsic and intrinsic apoptotic pathways is thought to be the molecular mechanism of action for this compound. This is associated with increased activity of caspase-8 and caspase-9 enzymes. Inhibition of key proteins involved in the progression and metastasis of colorectal cancer, such as sICAM-1, cathepsin B, and mTOR kinase, following incubation of cells with **MM131,** was observed. After 24 h of incubation, **MM131** was able to significantly lower mTOR concentrations in both colon cancer cell lines as compared to untreated cells, and the inhibitory impact was significantly larger than that of the reference drug. In addition, sICAM-1, which is elevated in the sera of patients with various malignancies and is thought to be a prognostic marker in patients with colorectal cancer, is an important molecule that is reduced following exposure to **MM131**. Moreover, it reduced cathepsin B implicated in enhanced invasion and angiogenesis of cancer cells, while at the same time increasing levels of beclin with tumor-suppressing properties [36].

In this paper, we present preparation of new pyrazolo[4,3-*e*]tetrazolo[1,5-*b*][1,2,4]triazine sulfonamide derivatives (Figure 1) and their anticancer activity including cytotoxic and proapoptotic potential. To estimate the cytotoxic effect of tested compounds, the MTT assay was used [37].

Moreover, in our research, we focused on the detection of apoptosis by membrane alterations (externalization of phosphatidylserine on the outer plasma membrane of apoptotic cells). Double staining with acridine orange and ethidium bromide was additionally applied to visualize the morphological features of apoptosis and/or necrosis in cancer cells incubated with tested compounds. The changes in the mitochondria membrane potential (MMP; $\Delta\Psi m$) following incubation with tested compounds were assessed with MitoTracker Red [38] as an indicator of mitochondrial function and apoptosis activation [39,40].

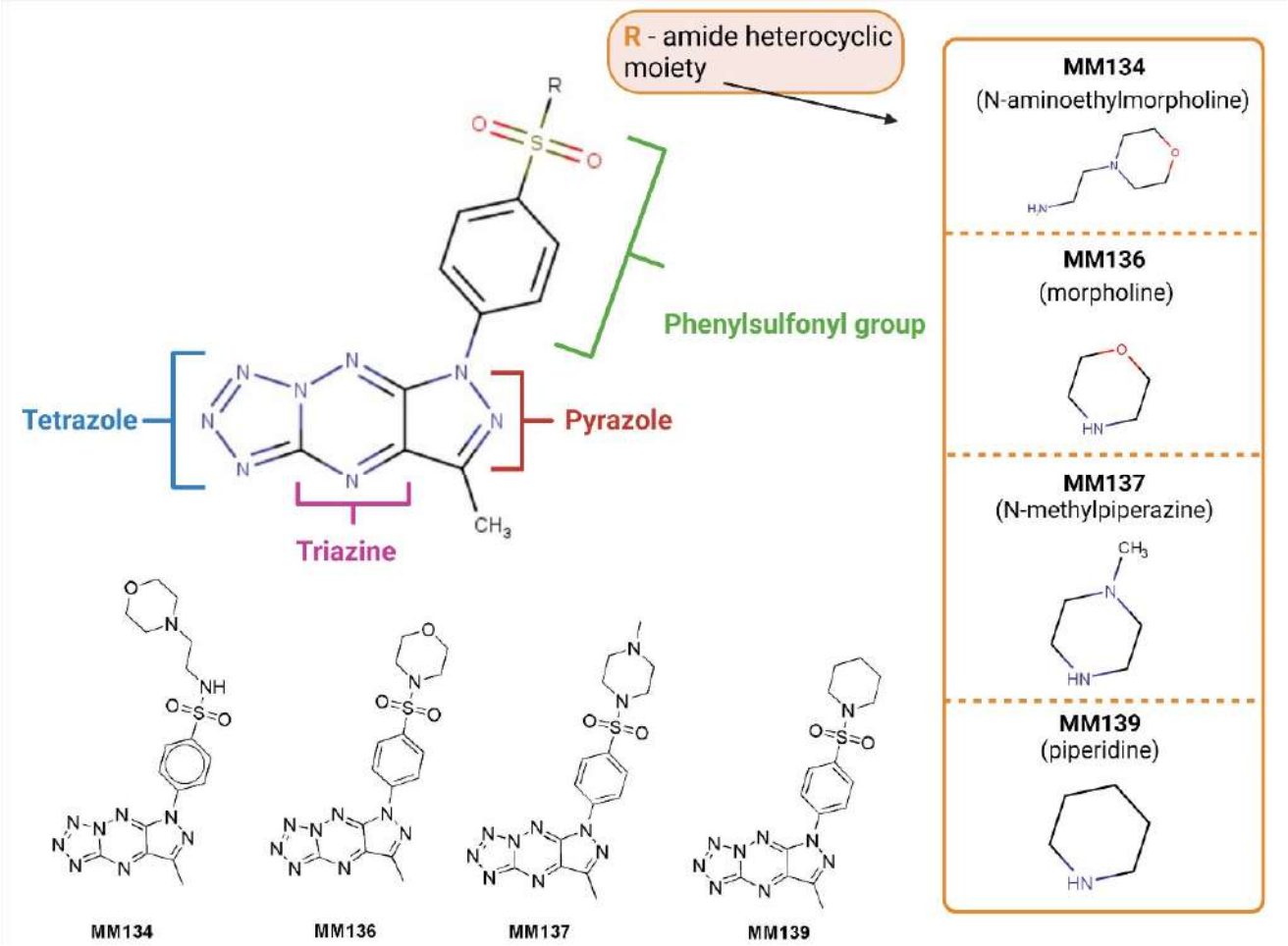

Figure 1. Chemical structure of investigated sulfonamides **MM134**, **MM136**, **MM137**, and **MM139**. Created with Biorender.com.

Additionally, using molecular docking and molecular dynamics techniques, selectivity for molecular targets with an established role in cancer pathogenesis was evaluated. Molecular docking results and predicted physicochemical parameters of the tested compounds were compared with the results obtained for the **MM129** and **MM131** derivatives that have been previously described in the literature [26,35,36].

2. Results

2.1. Chemistry

The multi-step preparation of compound **1**, which is a crucial intermediate for the synthesis of the pyrazolo[4,3-*e*]tetrazolo[1,5-*b*][1,2,4]triazine sulfonamides (**MMs**), has been described in detail in our earlier work [41]. Chlorosulfone **1** readily reacts with cyclic amines to give the corresponding sulfone **2a-d** which undergo nucleophilic substitution reaction with sodium azide to provide the final tricyclic derivatives of the pyrazolo[4,3-*e*]tetrazolo[1,5-*b*][1,2,4]triazine ring system (**MM-sulfonamides**). Sulfonamide **3d** with a piperidine substituent in the C5 position was formed as a by-product of the synthesis of the corresponding sulfonamide **2d** (Figure 2). The NMR spectrum for **3d** lacks at $\delta = 3.63$ ppm the characteristic singlet for the SO_2CH_3 group which is present on the NMR spectrum for the derivative **2d**. Instead of the singlet, there is a multiplet for the hydrogens of the piperidine ring in the range 1.6–1.8 ppm, which corresponds to 10 protons. The structure of all obtained compounds was confirmed by spectroscopic methods.

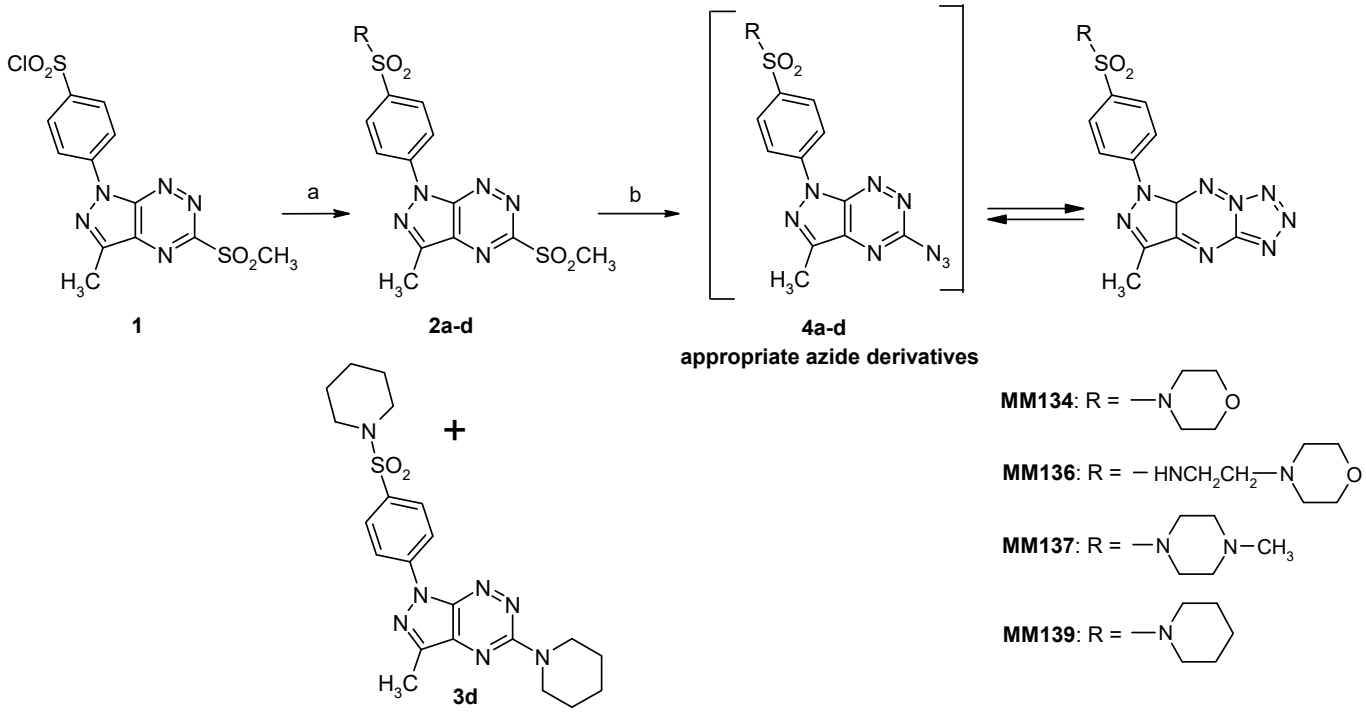

Figure 2. Reagents and conditions: (a) appropriate amine, MeCN, rt, overnight; (b) NaN_3, EtOH, reflux.

Many previous studies show that fused derivatives of the pyrazolo[4,3-*e*]tetrazolo[1,5-*b*][1,2,4]triazine in solution exist in tautomeric equilibrium with the corresponding 5-azido derivative of the pyrazolo[4,3-*e*][1,2,4]triazine ring system [25,36,41–45]. The ^{1}H NMR spectrum recorded immediately after dissolution of the compound **MM134** in deuterated chloroform exhibited one singlet at δ = 2.92 ppm for CH_3 group and two triplets at δ = 3.06 ppm and δ = 3.77 pp which can only relate to the morpholine ring and two doublets in aromatic region at 7.98 ppm and 8.50 ppm corresponding to protons in the phenyl ring of the tetrazole form **MM134** (Figure 3A). Moreover, there is one small singlet at 2.75 ppm and two very small doublets at 7.94 and 8.65 ppm that correspond to the methyl group and aromatic protons present in the appropriate azide form **4a**. The ^{1}H NMR measurement for the same sample repeated after 24 h showed the shift of the tautomeric equilibrium toward the slight dominance of the azide form relative to tetrazole form (Figure 3B). Much more effective increase in the azide form was observed after 48 h and the ratio of the populations was 1:0.7 in favor of azide structure (Figure 3C). However, despite the partial decomposition of the investigated sample, the ^{1}H NMR spectrum recorded after 2 weeks shows that in the solution again tetrazole derivative exists as the main form and the azide tautomer accounts for about 34%. A similar effect was observed for other presented tetrazole derivatives. It should be noted that these experiments showed that the tetrazole form was predominant after tautomeric equilibrium was established, which is consistent with earlier research results and literature data [42–45]. The ^{1}H NMR spectra were also presented in Figure S1 of the SM1.PDF file in the Supplementary Material section.

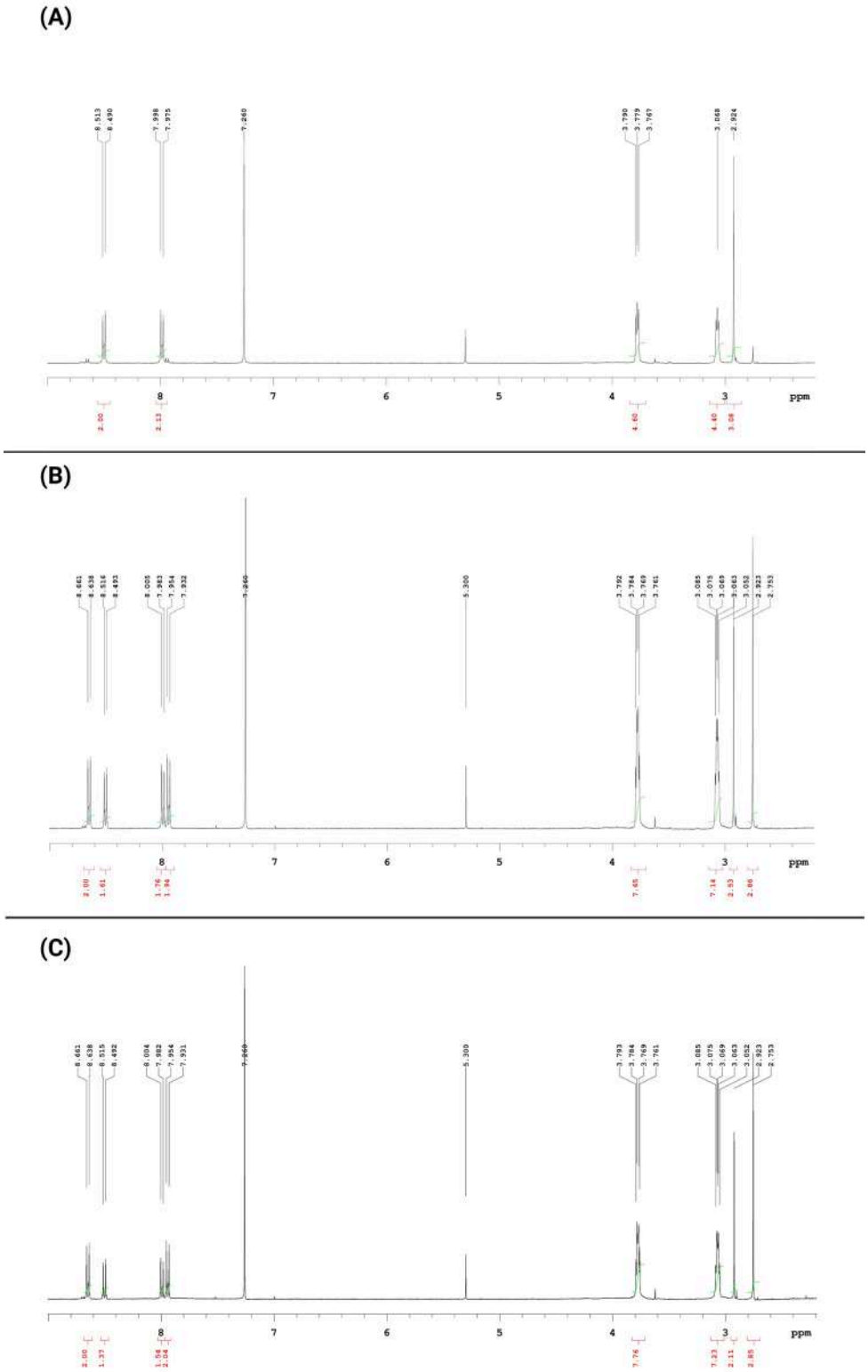

Figure 3. The ^{1}H NMR spectrum (**A**) recorded immediately after solution of the compound **MM134** in deuterated chloroform and repeated (**B**) after 24 h and (**C**) after 48 h.

2.2. Biological Studies

2.2.1. MTT Assay

The MTT assay used to determine cell viability showed that all tested novel pyrazolo[4,3-*e*][1,2,4]triazine-containing compounds possess cytotoxic activity towards cancer cell lines (BxPC-3, HCT-116, and PC-3) and, to a lesser extent, towards normal mouse (L929 cell line)

and human (WI-38 cell line) fibroblasts. A reduction in cell viability after 72 h incubation with tested compounds was observed in all experimental series. The IC_{50} values obtained in the MTT assay are shown in Table 1. The cytotoxic effect was specific to cancer cells. Dose–response curves obtained from two independent experiments after 72 h exposure of cancer cells (BxPC-3, HCT-116, PC-3) and normal mouse (L929 cell line) and human (WI-39 cell line) fibroblasts to MM-compounds in shown in Figures 4 and 5. The decrease in cell viability correlates with the increasing concentration of the compounds. The PC-3 cell line was more sensitive to the tested compounds than BxPC-3 and HCT-116 cells, which may indicate some degree of selectivity of the tested compounds for this cell line. MM-compounds exhibited more cytotoxic activity in the cancer cells than in normal mouse and human fibroblasts.

Table 1. Mean IC_{50} obtained after a 72 h incubation of tested cells with MM-compounds in MTT assay ± SD.

MM-Compounds	Cell Lines				
	Mean IC_{50} [μM]				
	BxPC-3	**HCT-116**	**PC-3**	**L929**	**WI-38**
MM134	0.32 ± 0.1	0.38 ± 0.03	0.16 ± 0.02	0.58 ± 0.005	0.65 ± 0.07
MM136	0.25 ± 0.08	0.25 ± 0.07	0.13 ± 0.01	0.22 ± 0.08	0.48 ± 0.09
MM137	0.16 ± 0.04	0.14 ± 0.02	0.11 ± 0.007	0.18 ± 0.0008	0.27 ± 0.04
MM139	0.33 ± 0.14	0.35 ± 0.05	0.17 ± 0.003	0.26 ± 0.02	0.54 ± 0.06

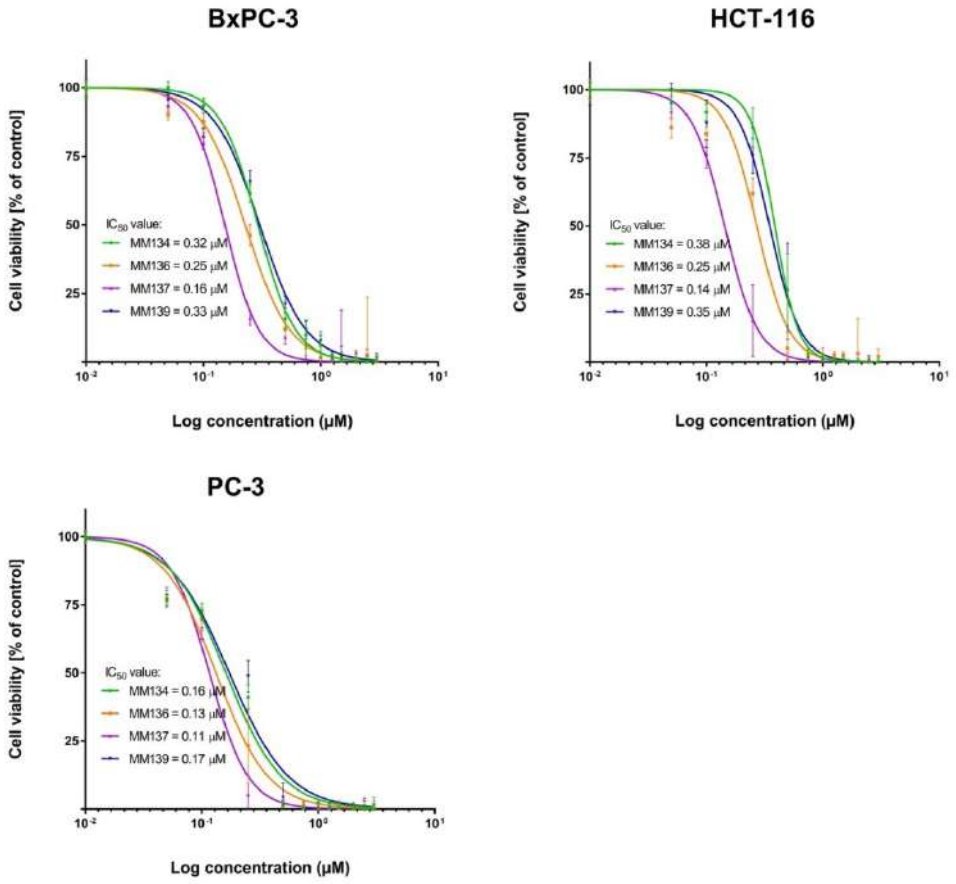

Figure 4. Determination of relative cancer cell viability of pancreas adenocarcinoma cell line (BxPC-3), colorectal carcinoma cell line (HCT-116) and prostate adenocarcinoma cell line (PC-3) treated with MM-compounds; ±SEM.

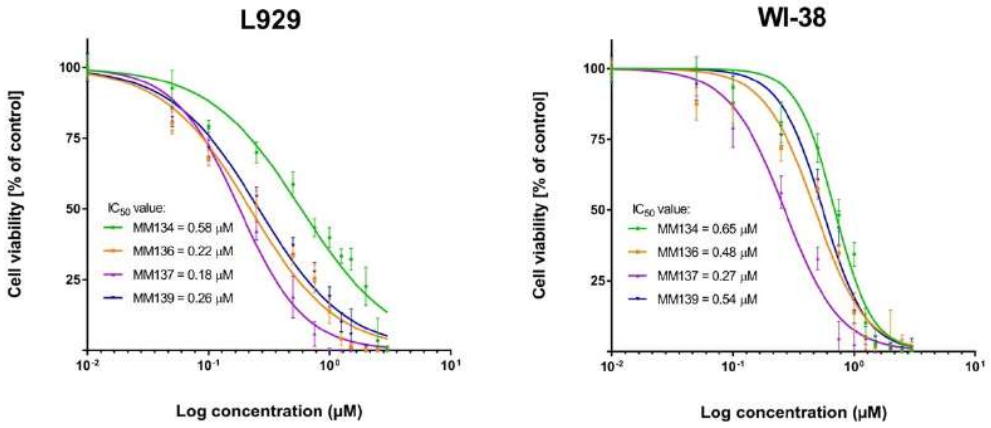

Figure 5. Determination of relative cell viability of mouse fibroblast cell line (L929) and human normal fibroblast cell line (WI-38) treated with MM-compounds; ±SEM.

2.2.2. Annexin V and Propidium Iodide Flow Cytometry Analysis

Tested cell lines that exhibited the most sensitivity to the cytotoxic effects of MM-compounds were selected for the study of their proapoptotic properties. The values obtained in the MTT test for the HCT-116 and BxPC-3 lines were very similar. It was decided that the pancreatic cancer line, which belongs to the neoplasms with a high mortality rate and a very aggressive course, will be used for further research. The apoptotic status of BxPC-3 and PC-3 cells after 24 and 48 h of incubation with triazine derivatives used in IC_{50} and $2xIC_{50}$ concentrations obtained in the MTT assay was determined utilizing flow cytometry using dual annexin V and propidium iodide staining (Figures 6 and 7). Flow cytometry Supplementary Materials can be found in Figure S2 (BxPC-3 cell line) and Figure S3 (PC-3 cell line) of SM1.PDF file.

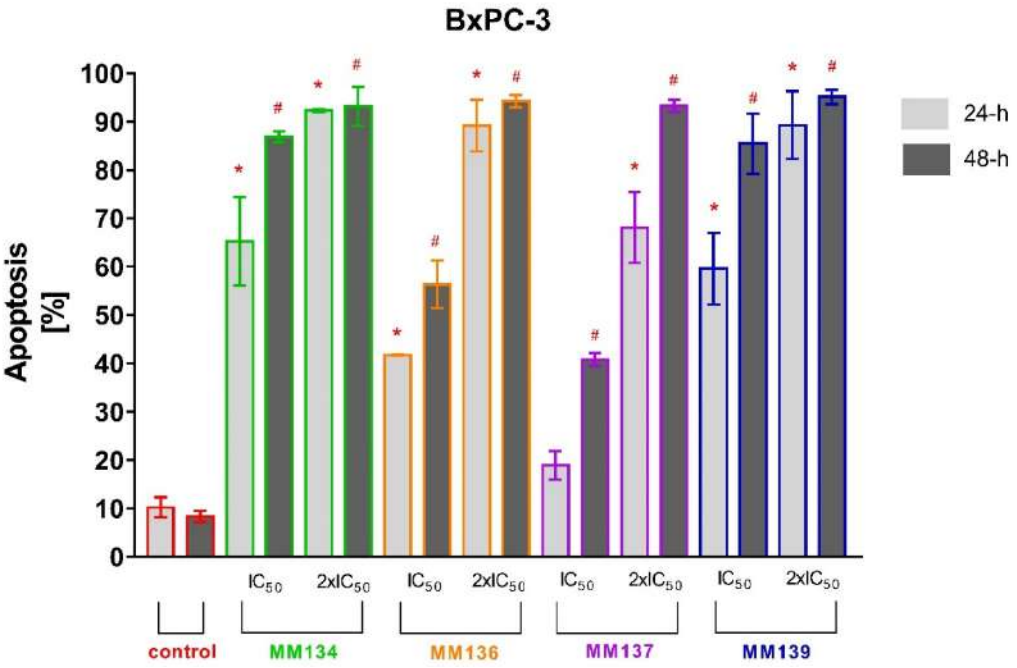

Figure 6. Determination of apoptosis induction in BxPC-3 cell line treated with IC_{50} and $2xIC_{50}$ concentrations of MM-compounds measured with Annexin V FITC. Data are presented as mean percentage of apoptotic cells (early and late apoptotic) ± SD values. The differences between the experimental samples and vehicle control were evaluated by the ANOVA test followed by Tukey's test ($p < 0.05$). * significant difference compared to the negative control (24 h incubation time); # significant difference compared to the negative control (48 h incubation time); $p < 0.05$; $N = 1 \times 10^4$.

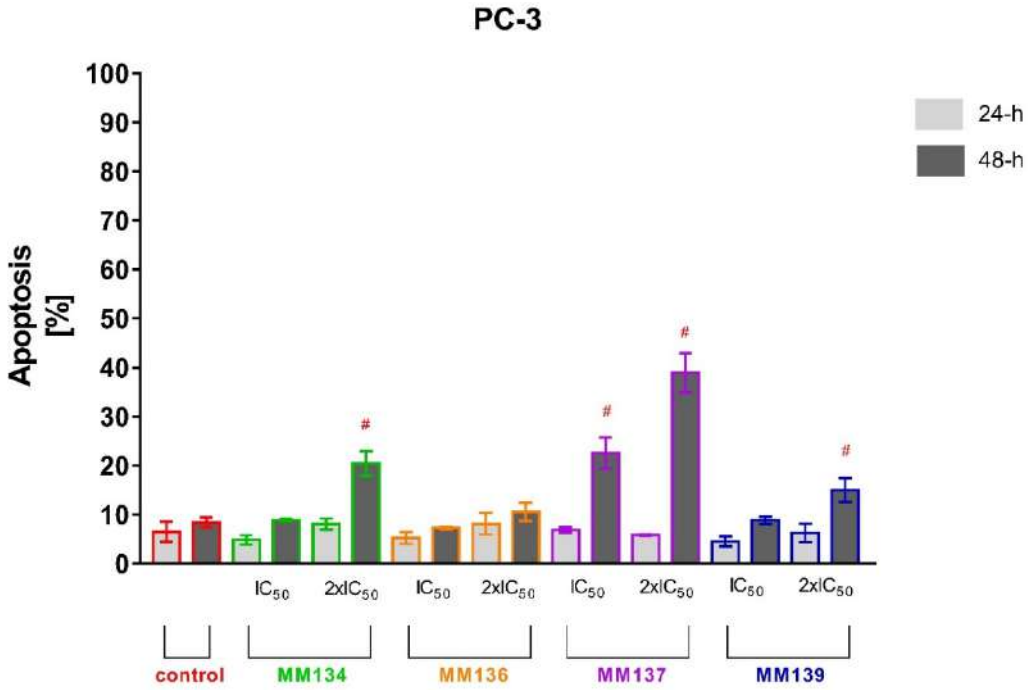

Figure 7. Determination of apoptosis induction in PC-3 cell line treated with IC_{50} and $2xIC_{50}$ concentrations of MM-compounds measured with Annexin V FITC following 24 and 48 h incubation time. Data are presented as mean percentage of apoptotic cells (early and late apoptotic) ± SD values. The differences between the experimental samples and vehicle control were evaluated by the ANOVA test followed by Tukey's test ($p < 0.05$). # significant difference compared to the negative control (48 h incubation time); $p < 0.05$; $N = 1 \times 10^4$.

A very high increase in the apoptotic cell fraction was observed after 24 and 48 h incubation of BxPC-3 cells with $2xIC_{50}$ concentrations of all MM-compounds (from 68.1 ± 7.33% to 95.1 ± 1.48%), compared to the control group: 10.3 ± 2.09% (24 h incubation) and 8.3 ± 1.13% (48 h incubation).

The apoptotic response increased in order of **MM137** (18.9 ± 2.95%), **MM136** (41.7 ± 0.17%), **MM139** (59.6 ± 7.42%), and **MM134** (65.3 ± 9.1%) after 24 h incubation with IC_{50} concentrations of tested compounds and in analogous order of **MM137** (40.8 ± 1.36%), **MM136** (56.33 ± 4.96%), **MM139** (85.4 ± 6.25%), and **MM134** (86.9 ± 1.16%) after 48 h incubation. The number of necrotic cells following 24 and 48 h incubation of BxPC-3 cells with MM-compounds did not exceed 10% in all experimental series.

For 24 h incubation of PC-3 cells, no statistically significant increase in % of apoptotic cells was observed compared to negative control (6.5 ± 2.05%). In contrast, **MM134** (20.37 ± 2.5%), **MM137** (38.93 ± 4%), and **MM139** (15 ± 2.42%) used in $2xIC_{50}$ concentrations induced a statistically significant increase in mean percentage of apoptotic cells compared with negative control (8.37 ± 1.06%) after 48 h incubation of PC-3 cells. Moreover, a statistically significant increase in apoptosis was observed after 48 h incubation of cells with **MM137** (22.57 ± 3.18%) used in IC_{50} concentration. No statistically significant differences were observed in other experimental series after 48h incubation. The number of necrotic cells following 24 and 48 h incubation of PC-3 cells and BxPC-3 with MM-compounds did not exceed 10% in all experimental series. The obtained results indicate that the BxPC-3 cancer cells were more sensitive to the proapoptotic activity of the tested compounds used in both concentrations than the PC-3 cell line. Additionally, the **MM134** and **MM139** compounds had the most profound pro-apoptotic effects on BxPC-3 cancer cells.

2.2.3. Dual Acridine Orange/Ethidium Bromide (AO/EB) Fluorescent Staining

Apoptosis induction estimated by flow cytometry analysis was confirmed with acridine orange/ethidium bromide staining (Figures 8 and 9). This method combines the differential uptake of fluorescent DNA-binding dyes AO and EB with the morphologic aspect of chromatin condensation in the stained nucleus, allowing one to distinguish viable, apoptotic, and necrotic cells (Figure 10) [46].

Similarly to the flow cytometry results, a high increase in the apoptotic cell fraction was observed after 24 and 48 h incubation of BxPC-3 cells with 2xIC_{50} concentrations of all MM-compounds (from 28.8 ± 3.46% to 70.35 ± 7.57%), compared to the control group: 5 ± 4.24% (24 h incubation) and 2.5 ± 0.7% (48 h incubation). **MM134** and **MM139** used in both tested concentrations induced a statistically significant increase in the apoptotic cell fraction following 24 and 48 h incubation of BxPC-3 cells. Only **MM136** and **MM137** used in IC_{50} concentrations did not induce a significant increase in apoptotic fraction following 24 h incubation of BxPC-3 cells with the compounds.

No statistically significant increase in apoptosis % was detected following 24 h incubation of PC-3 cells with tested compounds. **MM134**, **MM137**, and **MM139** induced a statistically significant increase in % of apoptotic cells in the PC-3 line following 48 h incubation compared to control group (1.5 ± 0.7%) in both tested concentrations. The mean % of apoptotic cells did not exceed 30% following 48 h incubation with tested compounds and were: **MM134** IC_{50} (8.5 ± 0.7%), **MM134** 2xIC_{50} (11 ± 1.41%), **MM136** 2xIC_{50} (14.5 ± 0.7%), **MM137** IC_{50} (15 ± 2.82%), **MM137** 2xIC_{50} (24 ± 1.41%), **MM139** IC_{50} (13.5 ± 3.53%), and **MM139** 2xIC_{50} (12.5 ± 0.7%). Again, a stronger apoptotic response was observed in BxPC-3 cells following 24 and 48 h incubation with the tested compounds.

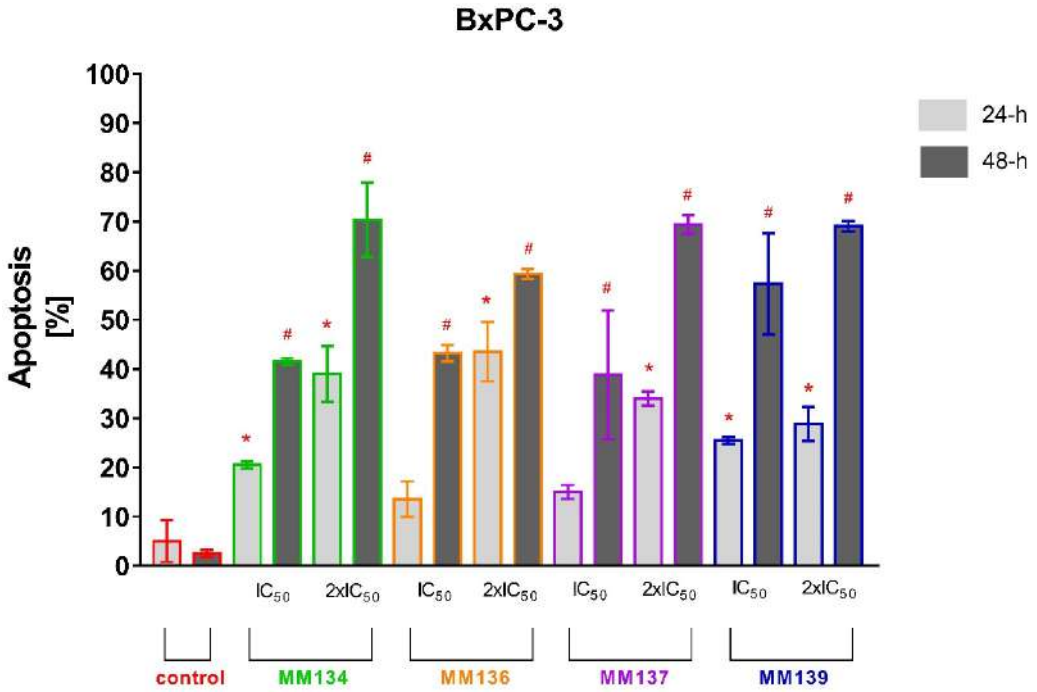

Figure 8. Determination of apoptosis induction in PC-3 cell line treated with IC_{50} and 2xIC_{50} concentrations of MM-compounds measured with AO/EB double staining following 24 and 48 h incubation time. Data are presented as mean percentage of apoptotic cells (early and late apoptotic) ± SD values. The differences between the experimental samples and vehicle control were evaluated by the ANOVA test followed by Tukey's test ($p < 0.05$). * significant difference compared to the negative control (24 h incubation time); # significant difference compared to the negative control (48 h incubation time); $p < 0.05$; $N = 200$.

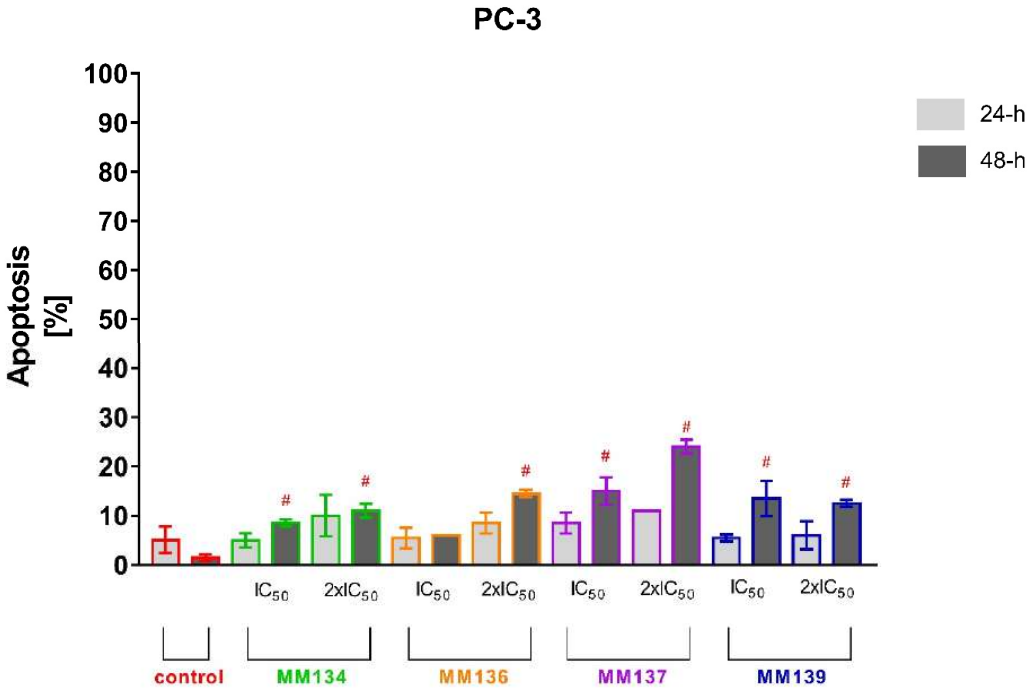

Figure 9. Determination of apoptosis induction in PC-3 cell line treated with IC_{50} and $2xIC_{50}$ concentrations of MM-compounds measured with AO/EB double staining following 24 and 48 h incubation time. Data are presented as mean percentage of apoptotic cells (early and late apoptotic) ± SD values. The differences between the experimental samples and vehicle control were evaluated by the ANOVA test followed by Tukey's test ($p < 0.05$). # significant difference compared to the negative control (48 h incubation time); $p < 0.05$; $N = 200$.

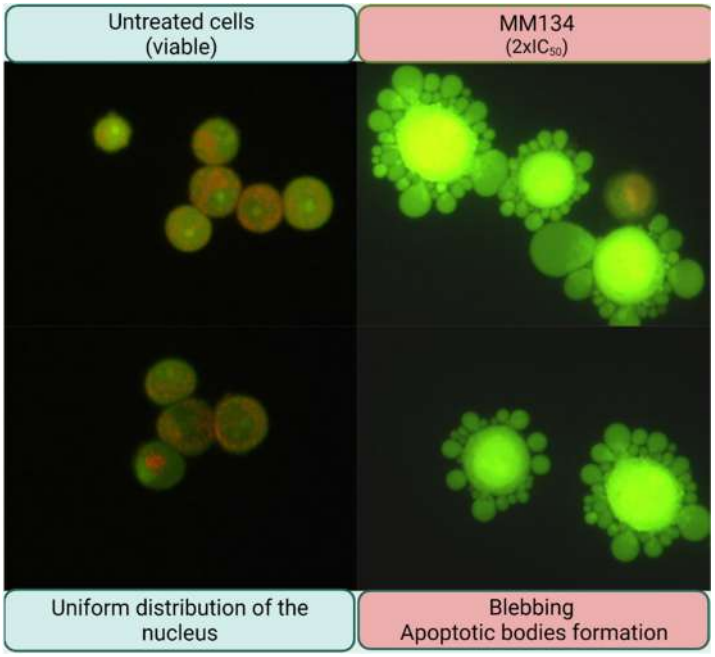

Figure 10. Typical morphological features of apoptosis in BxPC-3 following treatment with **MM136** compound. Characteristic membrane blebbing can be observed in cancer cells after the treatment with the tested compound in $2xIC_{50}$ concentration compared with cells from control group in which cells are rounded and exhibit uniformly distributed nucleus. Cells were visualized under a fluorescence microscope OLYMPUS BX60, magnification 40×.

2.2.4. Changes in Transmembrane Mitochondrial Potential-MitoTracker Red

The fitness of the mitochondria and changes in MMP were assessed using MitoTracker Red. Data for experimental groups were presented as mean percentage of control group fluorescence intensity ± SD value (Figure 11, Table 2).

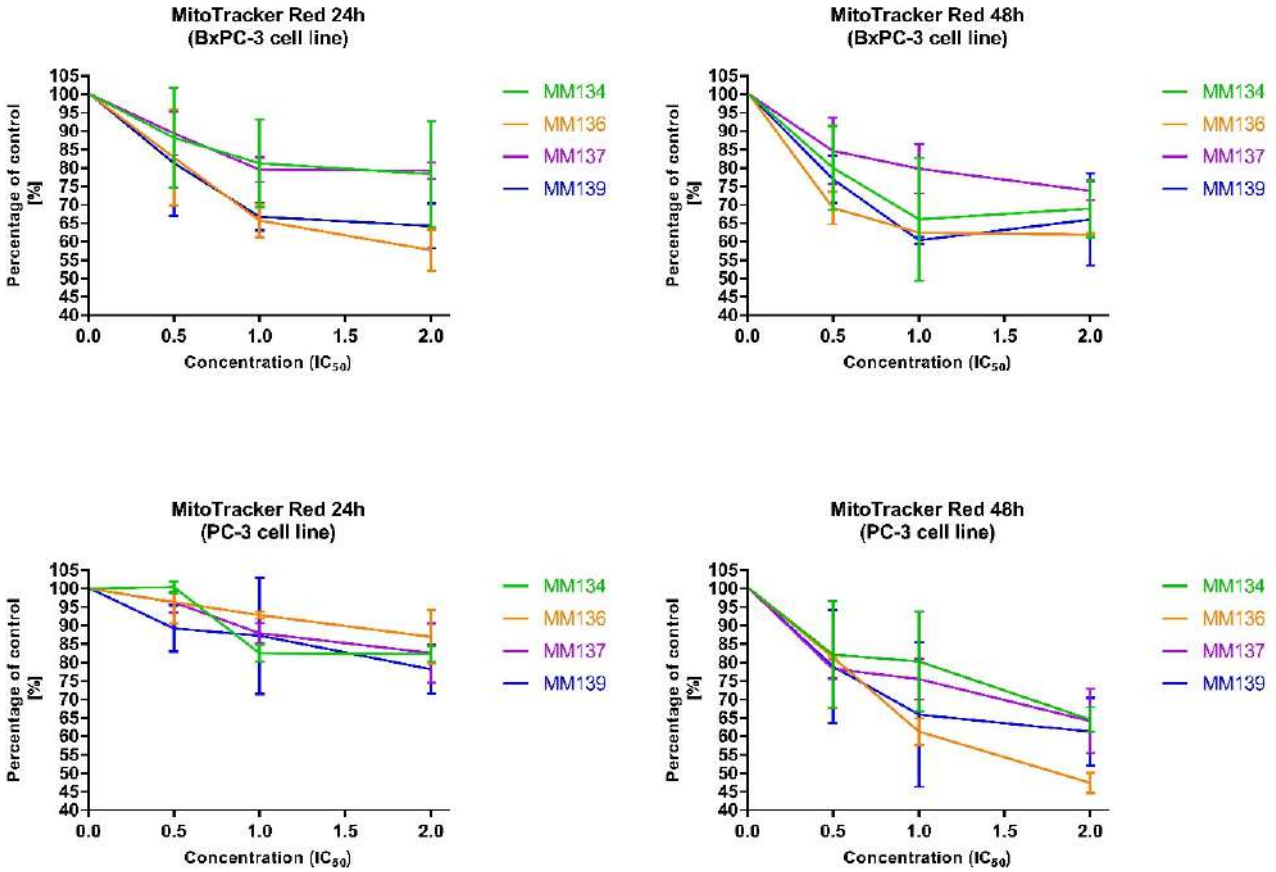

Figure 11. Changes in the mitochondria membrane potential (MMP) after 24 h and 48 h incubation with MM-compounds in all tested cancer cell lines; ±SD value.

After 24 and 48 h incubation of BxPC-3 and PC-3 cells with tested compounds used in concentrations followed by IC_{50} values ($0.5xIC_{50}$, IC_{50}, and $2xIC_{50}$), a decrease in fluorescence intensity reflecting a reduction in MMP was observed. Following 24 and 48 h incubation of BxPC-3 cells with tested compounds used in $2IC_{50}$ concentrations, MMP decreased with an increase in compound concentration in the order of **MM137, MM134, MM139** and **MM136**. For the 48 h incubation of BxPC-3 cell lines, a decrease in MMP was observed after use of **MM134** and **MM139** compounds in $0.5xIC_{50}$ and IC_{50} concentrations with an increase in MMP following incubation with $2xIC_{50}$ concentrations. After both 24 and 48 h incubation times, the **MM136** used in $2xIC_{50}$ concentrations induced the highest reduction in MMP (% of control were: 57.67 ± 5.56% and 61.83 ± 0,46% for 24 h and 48 h incubation, respectively).

The 24 and 48 h incubation of PC-3 cells also led to a decrease in MMP. **MM139** (78.14 ± 6.56%) and **MM136** (47.38 ± 2.74%) used in the concentration of $2xIC_{50}$ induced the highest reduction in MMP among the MM-compounds in PC-3 cells after 24 and 48 h incubation, respectively.

Table 2. Results of MitoTracker Red analysis in tested cancer cell lines. Data for individual compounds are presented as mean percentage of control group fluorescence intensity ± SD value.

BxPC-3			
24 h incubation			
Compound/Concentration	$0.5IC_{50}$	IC_{50}	$2xIC_{50}$
MM134	88.19 ± 13.62	81.23 ± 11.94	78.31 ± 14.34
MM136	82.83 ± 13.02	65.68 ± 4.58	57.67 ± 5.56
MM137	89.34 ± 5.91	79.5 ± 3.34	79.22 ± 2.22
MM139	81.28 ± 14.44	66.73 ± 3.72	64.23 ± 6.08
48 h incubation			
MM134	79.98 ± 11.47	66.04 ± 16.7	68.95 ± 7.78
MM136	69.08 ± 4.40	62.37 ± 0.05	61.83 ± 0.46
MM137	84.62 ± 9.01	79.8 ± 6.76	73.8 ± 2.58
MM139	76.9 ± 6.40	60.35 ± 0.91	65.95 ± 12.53
PC-3			
24 h incubation			
MM134	100.35 ± 1.57	82.5 ± 2.21	82.34 ± 2.13
MM136	96.3 ± 5.74	92.78 ± 0.9	86.9 ± 7.22
MM137	96.26 ± 2.83	87.9 ± 2.71	82.5 ± 7.99
MM139	89.2 ± 6.28	87.28 ± 15.8	78.14 ± 6.55
48 h incubation			
MM134	82.1 ± 14.45	80.26 ± 13.44	64.56 ± 3.33
MM136	81.34 ± 0.4	61.24 ± 3.62	47.38 ± 2.74
MM137	78.26 ± 2.62	75.49 ± 5.55	64.19 ± 8.72
MM139	78.91 ± 15.21	65.93 ± 19.56	61.28 ± 9.16

2.3. Data Analysis

2.3.1. MTT Assay

A statistical program (*Graphpad Prism 7*) was used to analyze obtained data (MTT test). The dose–response analysis was performed to estimate the inhibitory concentration (IC_{50}) of the tested compounds. The IC_{50} value is defined as a concentration of the tested compound that leads to a reduction in cell pool viability by 50% compared to the negative control (accepted as 100%).

$$\%\ cell\ viability = \frac{(Absorbance\ value\ of\ treated\ cells - Absorbance\ value\ of\ blank)}{(Absorbance\ value\ of\ untreated\ cells - Absorbance\ value\ of\ blank)} \times 100\%$$

2.3.2. Apoptosis Detection

Data are presented as mean percentage of apoptotic cells (early and late apoptotic) ± SD values. The differences between the experimental samples and vehicle control were evaluated by the ANOVA test followed by Tukey's test ($p < 0.05$). Experiments were performed in triplicate. For flow cytometry analysis with Annexin V-FITC staining, the approximate number of analyzed cells was ($N = 1 \times 10^4$), contrasting with the dual acridine orange/ethidium bromide (AO/EB) fluorescent staining ($N = 200$).

2.4. Computational Studies

2.4.1. Molecular Docking Simulation

The PDB codes for the downloaded proteins were 4wa9 [47], 2xyn [48], 3mvh [49], 3d0e [50], 2x18 [51], 5n7e [52], 3gen [53], 6qn5 [54], 6qnl [54], 3bhu [55], 2w9z [56], 5l2s [57], 1ua2 [58], 5mza [59], 6bcx [60], 6zwo [61], 7bea [62] for ABL1, ABL2, AKT1, AKT2, AKT3, BCR, BTK, CA-IX, CA-XII, CDK2, CDK4, CDK6, CDK7, ICAM-1, mTOR1, mTOR2 and PD-L1, respectively. Downloaded macromolecular targets were prepared for molecular docking simulation by addition of hydrogens, removal of redundant water molecules, computing Gasteiger charge, and assigning Autodock-4 (AD4) [63,64] atom type followed by saving them in the default autodock format PDBQT [65,66].

All the rotatable, non-rotatable, and un-rotatable bonds were assigned in all the six triazine sulfonamide derivatives, followed by saving their structures in the protein databank (PDB) format.

A suitable grid box covering all the extending conformations of the complexed reference ligands as well as the majority of the interacting macromolecular residues were formed for the examined molecular targets. The grid parameters for each of the targets were saved in a respective grid parameter file (GPF) for each anticancer target to be utilized by the Autogrid utility of the Autodock suite for the generation of map files required for performing molecular docking simulations. The grid parameters for each of the anticancer targets used in this study are tabulated in Table 3.

Table 3. The coordinates of the grid box for all the anticancer targets used in the current study.

Drug Target	PDB Code	x-D	y-D	z-D	Spacing (Å)	x Center	y Center	z Center
ABL1	4wa9	40	40	40	0.431	23.95	127.557	14.335
ABL2	2xyn	40	40	40	0.536	−54.025	48.668	−7.666
AKT1	3mvh	40	40	40	0.453	17.948	−1.885	27.56
AKT2	3d0e	40	40	40	0.475	22.521	−19.611	7.41
AKT3	2x18	40	40	40	0.458	25.066	66.608	−19.071
BCR	5n7e	40	40	40	0.636	22.531	−2.925	111.276
BTK	3gen	40	40	40	0.492	−16.796	6.794	−14.126
CA-IX	6qn5	40	40	40	0.375	−29.939	−3.656	0.027
CA-XII	6qnl	40	40	40	0.375	−41.046	6.288	31.866
CDK2	3bhu	40	40	40	0.375	−7.638	20.962	−21.4
CDK4	2w9z	50	50	50	0.453	20.281	25.506	8.713
CDK6	5l2s	50	50	50	0.403	22.452	38.566	−8.687
CDK7	1ua2	40	40	40	0.375	41.304	−4.892	23.033
ICAM-1	5mza	40	40	40	0.531	6.393	−16.531	9.728
mTOR1	6bcx	40	40	40	0.625	247.93	204.864	264.981
mTOR2	6zwo	40	40	40	0.625	249.818	191.487	206.7
PD-L1	7bea	40	40	40	0.492	−5.537	−10.417	19.104

The map files for various atom types of the macromolecular target as well as ligands generated by the Autogrid utility were utilized by the Autodock software to perform the molecular docking simulation. The molecular docking simulation process for each macromolecular target was validated by considering the chemical resemblance as well as the overlay of the docked conformation of the ligand regarding its bioactive conformation [67,68].

Once the molecular docking simulation process was validated by considering the above-stated parameters, similar parameters were utilized to perform the simulation studies of the newly designed triazine sulfonamide analogs.

Molecular docking simulation-based screening of the designed triazine analogs against the anticancer drug targets, which are actively involved in the pathophysiology of human cancers, revealed that the molecules **MM136** and **MM139** were the most potent inhibitors of all the anticancer targets considered in the current experimental study [66,69–71]. The binding scores of four new triazine sulfonamide analogs and previously studied compounds (**MM129** and **MM131**) as well as all the reference ligands for all the macromolecular targets are shown in Table 4.

Table 4. Molecular docking results of six triazine sulfonamide analogs as well as all the reference ligands.

S. No.	Ligand	Binding Energy ABL1 (4wa9)	Binding Energy ABL2 (2xyn)	Binding Energy AKT1 (3mvh)	Binding Energy AKT2 (3d0e)	Binding Energy AKT3 (2x18)	Binding Energy BCR (5n7e)	Binding Energy BTK (3gen)	Binding Energy CA-IX (6qn5)	Binding Energy CA-XII (6qnl)	Binding Energy CDK2 (3bhu)	Binding Energy CDK4 (2w9z)	Binding Energy CDK6 (5ls2)	Binding Energy CDK7 (1ua2)	Binding Energy ICAM-1 (5mza)	Binding Energy mTOR1 (6bcx)	Binding Energy mTOR2 (6zwo)	Binding Energy PD-L1 (7bea)
1	Reference Ligand	−9.35 (AXI)	−9.28 (VX6)	−10.51 (WFE)	−9.54 (G93)	−4.4 (EPE)	-	−9.31 (B43)	−8.18 (J8N)	−7.63 (J92)	−7.67 (MHR)	−5.7 (NAG)	−9.4 (6ZV)	−7.64 (ATP)	-	−3.26 (ATP)	−4.71 (AGS)	−10.09 (TK2)
3	**MM129**	−9.71	−9.17	−10.70	−9.52	−6.68	−8.63	−8.52	−8.44	−8.21	−9.61	−8.97	−10.83	−10.04	−6.86	−8.31	−8.12	−9.86
4	**MM131**	−9.48	−9.23	−9.92	−9.62	−6.74	−8.62	−8.76	−7.90	−7.87	−8.80	−8.52	−9.01	−8.74	−6.51	−7.19	−7.44	−9.88
5	**MM134**	−9.88	−10.08	−11.35	−11.81	−6.94	−9.51	−10.11	−8.01	−8.04	−9.63	−8.08	−9.69	−9.14	−7.20	−8.45	−7.64	−10.30
6	**MM136**	−9.53	−9.81	−12.42	−9.93	−6.63	−9.04	−9.55	−8.39	−8.54	−8.60	−8.97	−9.26	−9.40	−7.68	−9.08	−8.79	−12.33
7	**MM137**	−10.11	−10.46	−11.51	−10.79	−6.84	−8.49	−10.06	−7.86	−8.52	−8.31	−8.78	−8.31	−9.78	−7.19	−8.57	−7.95	−11.54
8	**MM139**	−10.42	−9.84	−12.16	−10.55	−7.24	−8.52	−10.51	−9.34	−9.06	−10.02	−9.62	−9.68	−9.88	−7.68	−8.46	−8.29	−11.43

MM134 was found to inhibit AKT2 (binding energy of −11.81) the strongest of the tested compounds. Based upon the binding score obtained after performing molecular docking simulation-based virtual screening of **MM136** against all macromolecular anticancer targets, it was observed that the **MM136** molecule strongly interacts with AKT1, mTOR1, mTOR2, and PD-L1 (respective binding scores: −12.42, −9.08, −8.79, and −12.33), and is supposed to give anticancer activity through the inhibition of the given enzymes. **MM137** is the most potent inhibitor of ABL2 (binding score: −10.46) of all tested compounds. In contrast, **MM139** was found to be a potent inhibitor of nine of all seventeen macromolecular anticancer drug targets, i.e., ABL1, AKT3, BTK, CA-IX, CA-XII, CDK2, CDK4, CDK7, or ICAM-1, considered in the current study [72,73]. **MM134**, **MM136**, **MM137**, and **MM139** derivatives exhibited better molecular docking results than the previously described **MM129** and **MM131** derivatives in terms of binding to ABL2, AKT1, AKT2, BTK, ICAM-1, mTOR1, and PD-L1, while **MM129** exhibited the highest binding activity towards CDK6 (binding energy of −10.83) and CDK7 (binding energy of −10.04).

The two-dimensional binding interactions of **MM136** against human AKT1 and PD-L1 are shown in Figure 12A,B, respectively, while the two-dimensional binding interactions of **MM139** against human AKT1 and PD-L1 are shown in Figure 13A,B, respectively.

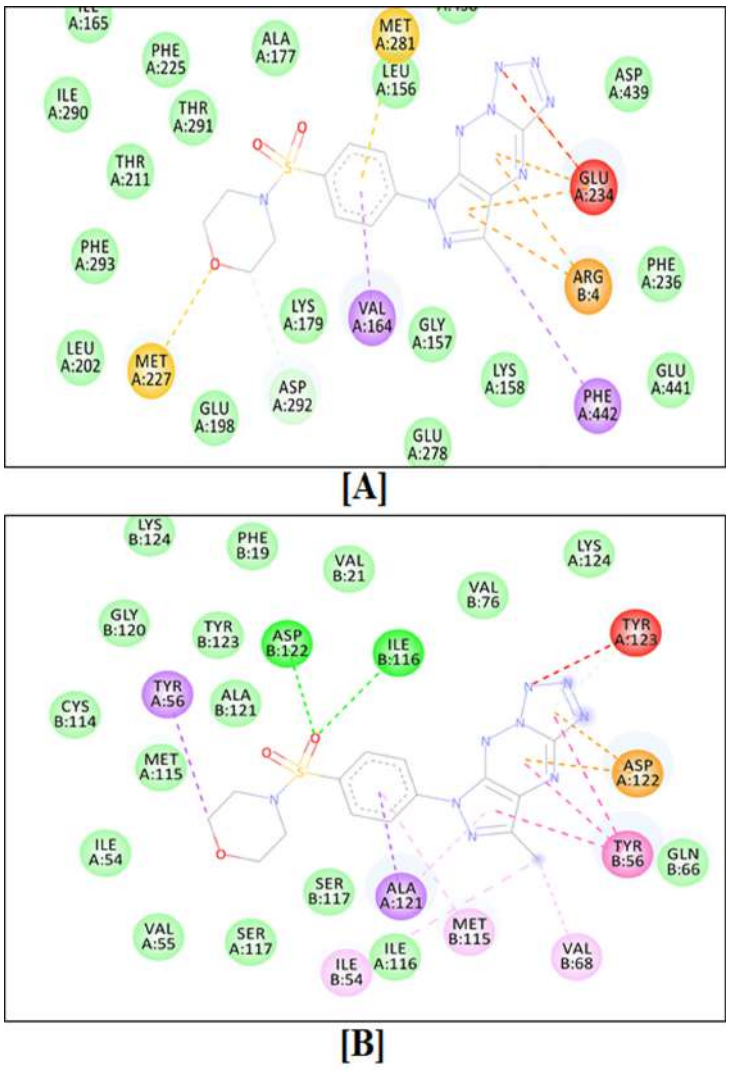

Figure 12. Two-dimensional binding interactions of the triazine sulfonamide analog **MM136** against human AKT1 (**A**) and PD-L1 (**B**).

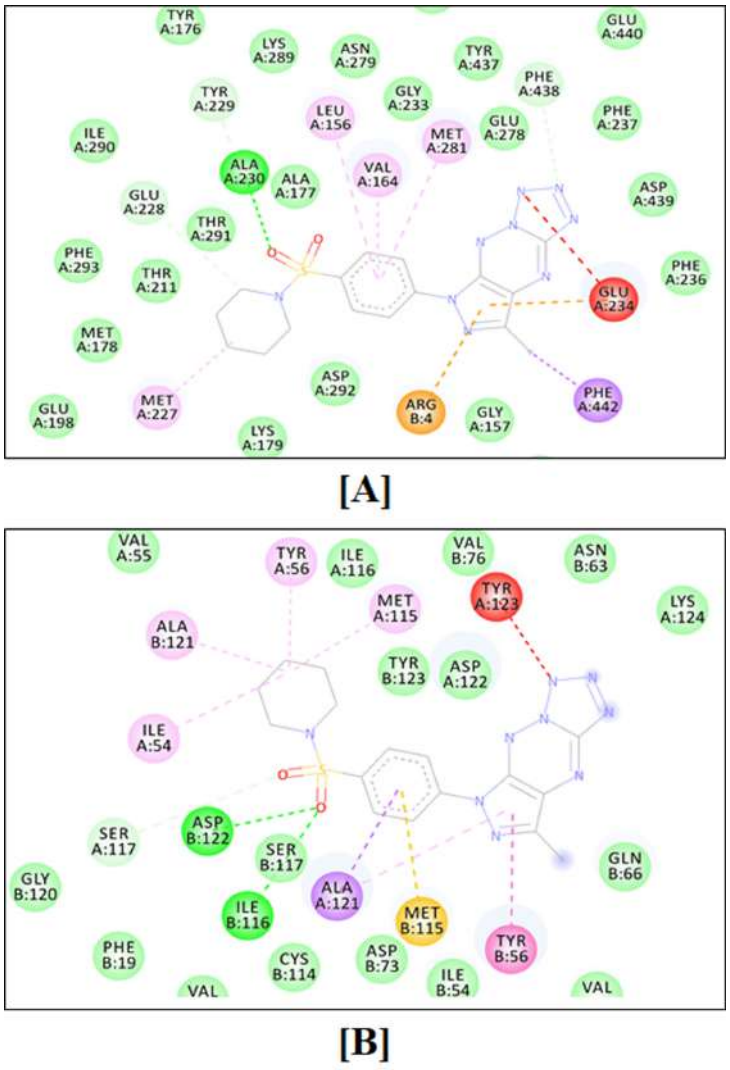

Figure 13. Two-dimensional binding conformation of the triazine sulfonamide analog **MM139** against human AKT1 (**A**) and PD-L1 (**B**).

2.4.2. Molecular Dynamics Simulations

Molecular dynamics simulations revealed that the macromolecular complexes of ligands **MM136** and **MM139** against AKT1 as well as PD-L1 enzymes were found to be most stable throughout the simulation time concluding that both of these ligands are supposed to be potent anticancer agents and their therapeutic effect is executed via synergistic targeting of both the AKT1 and PD-L1 enzyme.

The target enzyme AKT1 has 300 residues distributed in a macromolecular chain consisting of 2450 heavy atoms out of a total of 4885 atoms. The macromolecular target has 40% of secondary structures in the form of 26% of alpha helices and 17% of beta-strands, which were found to be conserved during the simulation process. **MM136** possesses 28 heavy atoms out of a total of 43 atoms. Dynamic simulation of the macromolecular complex of **MM136** against the AKT1 target clearly showed that the root mean square deviation (RMSD) for the fluctuation of the protein backbone was in-between 1.2 and 1.8 Å which is well within the acceptable range. Similarly, the ligand **MM136** showed some initial fluctuations up to 20 ns while making certain moves within the active site to achieve the stable conformation followed by its stabilized vibrations within the range of 1.8–2.4 Å. Afterward, the complexed ligand had attained the most stable conformation and remained stable throughout the simulation process with very little fluctuation. The root mean square fluctuation (RMSF) of the macromolecular backbone was found to be well within the range

of 0.9–1.2 Å throughout the simulation process. Macromolecular residues such as Val164, Ala177, Ala230, Met281, Asp292, Asp439, and Phe442 of AKT1 were found to be interacting with the ligand **MM136** throughout the simulation process.

MM139 has 28 heavy atoms out of a total of 47 atoms. Dynamic simulation of the macromolecular complex of **MM139** against AKT1 clearly showed RMSD in-between 1.5 and 2.8 Å which is well within the acceptable range of 3 Å. Similarly, the ligand **MM139** showed minimal fluctuations throughout the simulation process and remained stable within the 0.8–1.8 Å range throughout the simulation process. The RMSF value observed for the AKT1 macromolecule was found to be in-between 0.8 and 2.0 while the RMSF for **MM139** was found to be within 1.0–2.1 Å throughout the simulation process. Residues such as Leu156, Phe161, Ala177, Ala230, Glu234, Met281, Tyr437, Phe438, Asp439, and Phe442 of AKT1 were found to be interacting with the ligand **MM139**.

The target enzyme PD-L1 has 249 residues distributed in two macromolecular chains consisting of 1906 heavy atoms out of a total of 3791 atoms. The macromolecular target has 40% of secondary structures in the form of 2% alpha helices and 39% of beta-strands, which were found to be conserved during the simulation process. **MM136** possesses 28 heavy atoms out of a total of 43 atoms. Dynamic simulation of the macromolecular complex of **MM136** has clearly shown that the RMSD for the fluctuation of the protein backbone was in-between 1.8 and 4.8 Å which is well within the acceptable range of 3 Å. Similarly, the ligand **MM136** showed some little fluctuations in-between the range of 1.8 Å in the initial 10 ns timeframe, while making certain moves within the active site to achieve the stable conformation. Afterward, the complexed ligand had attained the most stable conformation and remained it throughout the simulation process with very little fluctuation. Except for a few residues, the RMSF of the macromolecular backbone was found to be well within the range of 0.8–2.4 Å. The two macromolecular residues showing the RMSF value up to 5.6 Å were found, which is common in all the simulation processes. The RMSF value observed for **MM136** was found to be within 0.5–1.5 Å throughout the simulation process. Macromolecular residues such as Ile54, Tyr56, Met115, Ser117, Ala121, Asp122, and Tyr123 of chain-A as well as Tyr56, Val68, and Tyr123 of chain-B of PD-L1 were found to be interacting with the ligand **MM136** throughout the simulation process.

MM139 has 28 heavy atoms out of a total of 47 atoms. Dynamic simulation of the macromolecular complex of **MM139** has clearly shown RMSD in-between 2.4 and 4.8 Å which is well within the acceptable range of 3 Å. Similarly, the ligand **MM139** showed minimal fluctuations throughout the simulation process and remained stable within the 1.0–3.2 Å range. The RMSF value observed for **MM139** was found to be within 1.5–2.2 Å throughout the simulation process. Residues such as Ile54, Tyr56, Ala121, Asp122, Tyr123, and Lys124 of chain-A as well as Ile54, Tyr56, Ser117, and Tyr123 of chain-B of PD-L1 were found to be interacting with the ligand **MM139**.

Dynamics simulations of the macromolecular complexes of **MM136** as well as **MM137** against both AKT1 and PD-L1 target enzymes revealed that both of the ligands were interacting strongly within the active site of the target enzyme and that both the target enzymes as well as complex ligands remained stable throughout the simulation process. The dynamic simulation of MM136 and MM139 complexed with AKT1 enzyme has shown strong binding interactions of the complexed ligand with adequate stability observed during the simulation process when compared with the macromolecular complex of ligands **MM136** and **MM139** against PD-L1 enzyme.

The computational results have revealed that these compounds are found to be potent anticancer agents and they are supposed to execute their therapeutic effect by interacting with the human AKT1 and PD-L1 enzymes.

The detailed reports of molecular dynamics simulation of MM-compounds can be found in Supplementary Materials for **MM136** with AKT1 (SM2.PDF) and PD-L1 (SM3.PDF), **MM139** with AKT1 (SM4.PDF) and PD-L1 (SM5.PDF) and **MM137** with PD-L1 (SM6.PDF).

2.4.3. Drug Likeness and ADMET

Swiss-ADME (http://www.swissadme.ch, accessed on 1 May 2022) [74] was used to estimate drug likeness and ADMET properties of MM-compounds. The bioavailability of compounds is estimated based on five critical parameters indicating drug lipophilicity, size, polarity, insolubility, flexibility, and insaturation. The optimal range for each property is as follows: flexibility (no more than nine rotatable bonds), lipophilicity (XLOGP3 between −0.7 and +5.0), size: molecular weight (MW between 150 and 500 g/mol), polarity (topological polar surface area (TPSA) between 20 and 130 Å2), solubility (LogS not higher than 6), and saturation (fraction of carbons in the sp3 hybridization (Csp3) not less than 0.25). The tested compounds may not be orally bioavailable due to high polarity and TPSA, considering sulfur and phosphorus as polar atoms (Table 5). Tested MM-compounds may not be orally bioavailable due to high polarity (too high TPSA values; TPSA > 130 Å2).

Table 5. Chosen physicochemical properties of tested compounds.

Property	Parameter	MM129	MM131	MM134	MM136	MM137	MM139
Flexibility	Num. rotatable bonds	5	5	6	3	3	3
Lipophilicity	XLOGP3	−0.31	−0.21	−0.30	−0.15	0.04	1.07
Molecular weight	MW	459.44 g/mol	389.39 g/mol	444.47 g/mol	401.40 g/mol	414.44 g/mol	399.43 g/mol
Polarity	TPSA	178.97 $Å^2$	161.46 $Å^2$	153.70 $Å^2$	141.67 $Å^2$	135.68 $Å^2$	132.44 $Å^2$
Saturation	Fraction Csp3	0.35	0.29	0.41	0.33	0.38	0.38

The tested compounds showed no BBB permeability. Moreover, derivatives may constitute the substrate for glycoprotein P (PGP) that belongs to ABC-transporters that restrict the compounds from entering the central nervous system and are involved in tumor multidrug resistance. MM137 and MM139 showed good overall HIA.

50 to 90% of therapeutic molecules are the substrates of isoforms of cytochrome P450, including CYP2D6 and CYP3A4. The MM137 molecule possesses the best pharmacokinetic parameters, including high GI absorption and no inhibitory activity against CYP enzymes. The ADMET properties predicted by using Swiss-ADME (http://www.swissadme.ch, accessed on 1 May 2022) [74] are tabulated in Table 6.

Table 6. Predicted ADMET properties of tested compounds.

Compound	MM129	MM131	MM134	MM136	MM137	MM139
GI absorption	Low	Low	Low	Low	High	High
BBB permeant	No	No	No	No	No	No
P-gp substrate	Yes	Yes	Yes	Yes	Yes	Yes
CYP2D6 Inhibitor	No	No	No	No	No	No
CYP3A4 Inhibitor	No	No	Yes	No	No	No

Again, MM137 showed the best drug-likeness properties with one violation according to the Lipiński rule (number of nitrogen or oxygen atoms (NorO) > 10) (Table 7).

Table 7. Predicted molecular properties related to Lipinski's rule of five.

Compound	MM129	MM131	MM134	MM136	MM137	MM139
Molecular weight	459.44 g/mol	389.39 g/mol	444.47 g/mol	401.40 g/mol	414.44 g/mol	399.43 g/mol
Num. H-bond acceptors	12	10	11	10	10	9
Num. H-bond donors	1	2	1	0	0	0
Consensus Log $P_{o/w}$	0.07	0.28	0.35	0.51	0.41	1.31
Lipinski violation	1	1	1	1	1	1

3. Discussion

The MTT assay used to determine cell viability showed that all tested MM-compounds possess cytotoxic activity towards cancer cell lines (BxPC-3, HCT-116, PC-3) and to a lesser extent towards the normal mouse fibroblast (L929) cell line and human fibroblasts (WI-38 cell line). The cytotoxic effect was specific for cancer cells. The MM137 compound exhibited the highest cytotoxic activity with IC_{50} values in cancer cells ranging from 0.11 to 0.16 μM. The highest difference between the cytotoxic activity of compounds between cancer and normal cells was observed for the MM134 compound, where the compound exhibited 4 times higher cytotoxic activity in the PC-3 cell line compared to normal human fibroblasts (WI-38 cell line).

In our study, the activation of apoptosis was detected after 24 and 48 h exposure of BxPC-3 and PC-3 cells to tested compounds in IC_{50} and $2xIC_{50}$ concentrations. Tested compounds were used in concentrations followed by IC_{50} values to establish whether the cytotoxic effects were due to apoptosis induction. **MM134**, **MM136**, **MM137**, and **MM139** induced increase in number of apoptotic cells both in BxPC3 and PC-3 cell lines; however, the effect was more profound in the BxPC-3 cell line where tested compounds induced apoptosis of 18.9–65.3% cells for 24 h incubation with tested compounds in IC_{50} values, and 40.8–86.9% following 48 h incubation with the derivatives as indicated by flow cytometry analysis using annexin V-FITC staining. The percentage of apoptotic cells following incubation of BxPC-3 cells with tested compounds increased in order of **MM137, MM136, MM139** and **MM134.**

No statistically significant increase in the number of apoptotic cells was observed following 24 h incubation of PC-3 cells with IC_{50} or $2xIC_{50}$ concentrations of MM-compounds. In contrast, **MM134** (20.37 ± 2.5%), **MM137** (38.93 ± 4%), and **MM139** (15 ± 2.42%) used in $2xIC_{50}$ concentrations induced as statistically significant increase in mean percentage of apoptotic cells compared with negative control after 48 h incubation of PC-3 cells.

Similar results were obtained with acridine orange/ethidium bromide double staining; however, the mean percentage of apoptotic cells was lower than this indicated by annexin V-FITC staining. This may be due to the large sample size in annexin V-FITC analysis (10,000 cells) compared with 200 cells analyzed in the acridine orange/ethidium bromide double staining. Moreover, annexin V-FITC cytometry analysis uses automate cell sorting, and therefore remains a more reliable method of apoptosis detection than manual counting and identification of apoptotic cells using fluorescence microscopy. Despite that, the apoptosis induction was seen using acridine orange/ethidium bromide double staining.

It is one of the initial alterations linked with programmed cell death to observe a decrease in MMP. It is known that the mitochondrial membrane permeability increases during apoptosis. As a result, mitochondrial proteins such as cytochrome c and apoptosis-inducing factor (AIF) are released into the cytosol, leading to the activation of the intrinsic apoptosis pathway. After both 24 and 48 h incubation times, **MM136** used in the $2xIC_{50}$ concentration induced the highest reduction in MMP in the BxPC-3 cell line. **MM139** and **MM136** used in the concentration of $2xIC_{50}$ induced the highest reduction in MMP among MM compounds in PC-3 cells after 24 and 48 h incubation, respectively. However, the induction of intrinsic and extrinsic apoptosis pathways needs to be elucidated.

Based on previously identified potential targets of pyrazolo-triazine derivatives (**MM129**, **MM131**), we performed molecular docking to identify the most potent compound among the newly designed pyrazolo[4,3-*e*]tetrazolo[1,5-*b*][1,2,4]triazine sulfonamides (**MM134, MM136, MM137** and **MM139**) and to establish the most probable molecular mechanism of these molecules. For this purpose, we estimated the binding capacity of the tested MM-compounds to a multitude of molecular targets with established roles in cancer: ABL1, ABL2, AKT1, AKT2, AKT3, BCR, BTK, CA-IX, CA-XII, CDK2, CDK4, CDK6, CDK7, ICAM-1, mTOR, mTOR2, and PD-L1. **MM134** was found to be the most potent inhibitor of AKT2, while **MM136** strongly bound to AKT1, mTOR1, mTOR2, and PD-L1. In contrast, **MM139** was found to be the most potent inhibitor (of all MM-compounds included in the docking screening) of nine of seventeen targets evaluated in this study, including: ABL1, AKT3, BTK, CA-IX, CA-XII, CDK2, CDK4, CDK7 and ICAM-1. **MM134, MM136, MM137,** and **MM139** exhibited better binding scores in dockings towards ABL2, AKT2, BTK, ICAM-1, mTOR1 and PD-L1, than **MM129** and **MM131** compounds. **MM129** exhibited the highest binding activity towards CDK6 and CDK7 enzymes. This may suggest that **MM134, MM136, MM137** and **MM139** compounds may exert biological activity through the inhibition of the AKT-mTOR pathway, while **MM129** and **MM131** may exhibit antiproliferative potential through their binding with CDK enzymes. Moreover, **MM134**, **MM136**, **MM137**, and **MM139** compounds were shown to strongly bind to AKT1 and PD-L1. The stability of complexes formed between macromolecule targets and ligands preselected in a docking procedure was assessed during molecular dynamics simulation. The macromolecular complex of AKT1 with **MM136** and **MM139** was found to be highly stable throughout the simulation timeframe of 100 ns. This clearly indicates the inhibitory potential of **MM136** and **MM139** against the AKT1. The molecular dynamics simulation also revealed that **MM136** and **MM139** compounds bind to the PD-L1 active site and form the most stable complexes. The comparative analysis of the molecular dynamic simulation of AKT1 and PD-L1 against **MM136** and **MM139** indicates that these ligands are found to be more stable while interacting with the AKT1 target as compared with PD-L1. These results indicate that **MM134, -6, -7,** and **-9** may work as potential dual AKT-mTOR and PD-L1 inhibitors, with **MM136** exhibiting the best in silico results.

Furthermore, in in vivo studies, **MM129** exhibited a good pharmacokinetics profile with rapid absorption and bioavailability of 68.6% following intraperitoneal administration. Therefore, we decided to compare the computationally estimated pharmacokinetic properties of **MM129** and **MM131** with **MM134, MM136, MM137,** and **MM139** compound profiles using the Swiss-ADME web tool (http://www.swissadme.ch, accessed on 1 May 2022) [74]. We have shown that tested compounds may exhibit better bioavailability than **MM129** and **MM131**. Moreover, **MM137** and **MM139** showed good gastrointestinal absorption in silico. Furthermore, **MM137** showed no inhibitory activity against CYP enzymes and the best drug likeliness properties of all compounds. This may limit potential drug–drug interactions in the living organisms [75–77]. However, all tested derivatives included in the study were shown not to be BBB-permeable and may work as substrates for the PGP enzyme, limiting their use in the central nervous system, and this may restrict their antitumor effects [78,79]. These estimates need confirmation in the following in vivo studies.

Many questions regarding the MM derivatives remain unanswered. First, the reduction in MMP levels may indicate the activation of an intrinsic pathway of apoptosis. However, further investigations, e.g., exploration of caspase levels associated with activation of intrinsic and extrinsic apoptosis pathways, need to be performed. Studies of **MM137** derivative in DLD-1 and HT-29 cell lines suggest the activation of both apoptosis pathways [41]. The inhibitory activity of compounds associated with the AKT-mTOR pathway and the PD1-PD-L1 association needs to be confirmed in screening assays and biological systems in in vivo conditions. The exploration of biological activity of other analogs of MM derivatives may lead to optimization and discovery of novel, safe and

potent inhibitors of AKT-mTOR or PD1-PD-L1 interaction. The probable mechanism of action of **MM134**, **MM136**, **MM137**, and **MM139** compounds is shown in Figure 14.

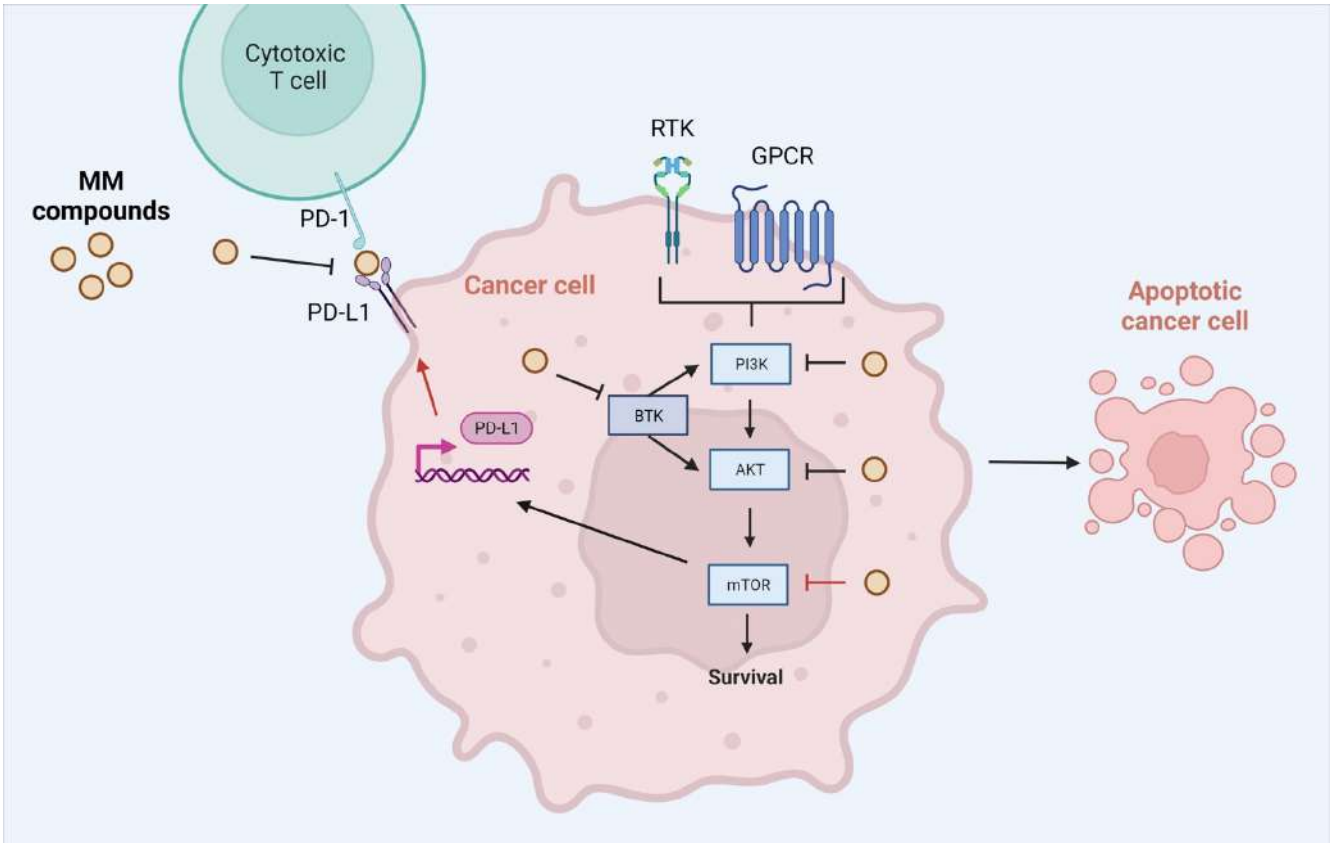

Figure 14. Probable mechanism of action of pyrazolo[4,3-*e*]tetrazolo[4,5-*b*][1,2,4]triazine sulphonamides (MM-compounds). Abbreviations: AKT—protein kinase B BTK—Bruton's tyrosine kinase; JAK—tyrosine-protein kinase JAK; mTOR—mammalian target of rapamycin; PI3K—phosphoinositide 3-kinases; PD-1—Programmed cell death protein 1; PD-L1—Programmed death-ligand 1. Created with Biorender.com.

Moreover, it has been found that the addition of 5-FU to **MM129** exhibited a synergistic effect on cancer cells with reduced PD-L1 mRNA and protein levels in DLD-1 and HT-29 cell lines [26]. Previously, Kim et al., reported that AKT activation may lead to the development of resistance to 5-FU [80]. In accordance with these findings, the use of **MM129** with 5-FU led to a decrease in phosphorylation of AKT compared with 5-FU alone [26]. According to a study conducted by Lastwika et al., the PI3K/AKT/mTOR pathway is involved in the formation of tumor cell immune resistance. mTOR kinase activation is substantially related to the surface expression of the tumor suppressor protein PD-L1 in human lung cancer cells, and the stimulation of the AKT/mTOR axis facilitates immune evasion through increased PD-L1 expression. PI3K/Akt/mTOR inhibition restricts cell proliferation, migration, and survival, at the same time facilitating immune surveillance and immune-cell-dependent tumor cell killing [81].

Increased expression of PD-L1 is a critical mechanism by which tumor cells are able to evade T-cell immunity. According to emerging evidence, chemotherapeutic drugs can affect the expression of PD-L1 on cancer cells, which may have an influence on immune evasion. Human colon cancer cell lines usually do not express the PD-L1 protein on their cell surfaces, but treatment with 5-FU induces its expression significantly. Therefore, the combination of drugs may enhance the effectiveness of colon cancer treatment [82]. AKT/PI3K activation can boost PD-L1 expression by increasing extrinsic signaling or decreasing the expression of negative regulators such as phosphatase and tensin homolog (PTEN). It is possible

that downregulation of PTEN may result in the activation of PI3K/AKT, which will then facilitate the production of PD-L1. Furthermore, blocking the PD-1/PD-L1 pathway in gastrointestinal stromal tumors can reduce the apoptosis of CD8+ T cells by governing the PI3K/AKT/mTOR pathway. In addition, it has been found that the overexpression of PD-L1 in colorectal cancer cells may result in the activation of the PI3K/AKT pathway [83]. Moreover, inhibition of mTOR kinase may enhance the expression of PD-L1 on cancer cell surfaces, contributing to the reduced efficacy of mTOR inhibitors. Therefore, the increased expression of PD-L1 in cancer cells may increase the availability of epitopes to which anti-PD-L1 antibodies may bind. Similarly, CDK4/6 inhibition may increase PD-L1 levels in cancer cells, making them substantially more sensitive to PD-1 blocking therapy [84]. Taken together, these findings of dual inhibition of AKT-mTOR or CDK4/6 and PD-L1 may constitute an important way of targeting cancer [85].

4. Materials and Methods

4.1. Chemical Synthesis

Melting points were determined on a Mel-Temp apparatus and were uncorrected. ^{1}H and ^{13}C NMR spectra were recorded on a Varian spectrometer (400 MHz for ^{1}H and 100 MHz for ^{13}C). The chemical shift values were expressed in ppm (part per million) with tetramethylsilane (TMS) as an internal reference. Molecular weight of final compounds was assessed by electrospray ionization mass spectrometry (ESI/MS) on an Agilent Technologies 6538 UHD Accurate Mass Q-TOF LC/MS (Agilent Technologies, Inc., Santa Clara, CA, USA). Elemental compositions were within ±0.4% of the calculated values. For preparation and spectroscopic data of compound **1,** see the literature [86].

4.1.1. Synthesis of Sulfonamides (**2a**–**d**)

Derivative **1** (194 mg, 0.5 mmol) was dissolved in anhydrous acetonitrile (5 mL) and appropriate amine (1.75 mmol) was added. The reaction was stirred overnight at room temperature; then, the reaction mixture was concentrated in vacuo to afford the crude sulfonamide, as a yellow solid. The residue was purified on silica gel using a mixture of CH_2Cl_2:EtOH (25:1) as eluent to give the titled compounds as a yellow solid.

N-(2-morpholinoeth-1-yl)-4-(3-methyl-5-methylsulfonyl-1*H*-pyrazolo[4,3-*e*][1,2,4]triazyn-1-yl)benzenesulfonamide (**2a**).

Yield 77%. Melting point: 209–212 °C; ^{1}H NMR (DMSO) δ: 2.80 (s, 3H), 2.93–2.96 (m, 4H), 3.63 (s, 3H), 3.64–3.67 (m, 4H), 8.06 (d, 2H, J = 8.8 Hz), 8.63 (d, 2H, J = 8.8 Hz); ^{13}C NMR (DMSO) δ: 11.11, 40.77, 45.94, 65.30, 120.13, 129.72, 132.33, 138.45, 141.18, 146.33, 148.45, 161.06; HRMS (ESI, *m*/*z*) Calcd for $C_{16}H_{19}N_6O_5S_2$ [M^+ + H] 439.08529. Found [M^+ + H] 439.08567. Anal. Calcd for $C_{16}H_{18}N_6O_5S_2$: C, 43.82; H, 4.13; N, 19.16. Found: C, 43.55; H, 4.18; N, 19.04.

N-(morpholin-1-yl)-4-(3-methyl-5-methylsulfonyl-1*H*-pyrazolo[4,3-*e*][1,2,4]triazyn-1-yl) benzenesulfonamide (**2b**).

Yield 80%. Melting point: 266–269 °C; ^{1}H NMR (DMSO) δ: 2.79 (s, 3H), 3.10–3.20 (m, 8H), 3.63 (s, 3H), 3.70–4.00 (m, 4H), 8.15 (d, 2H, J = 8.8 Hz), 8.28 (bs, 1H, exchanged with D_2O), 8.58 (d, 2H, J = 8.8 Hz); ^{13}C NMR (DMSO) δ: 11.12, 36.85, 40.78, 51.24, 55.22, 63.08, 120.19, 128.71, 137.61, 138.29, 140.62, 146.17, 148.34, 161.01; HRMS (ESI, *m*/*z*) Calcd for $C_{18}H_{24}N_7O_5S_2$ [M^+ + H] 482.12748. Found [M^+ + H] 482.12792. Anal. Calcd for $C_{18}H_{23}N_7O_5S_2$: C, 46.43; H, 4.97; N, 21.06. Found: C, 46.08; H, 5.02; N, 20.89.

N-(4-methylpiperazin-1-yl)-4-(3-methyl-5-methylsulfonyl-1*H*-pyrazolo[4,3-*e*][1,2,4]triazyn-1-yl)benzenesulfonamide (**2c**).

Yield 60%. Melting point:231–235 °C; ^{1}H NMR (DMSO) δ: 1.66–1.69 (m, 4H), 2.79 (s, 3H), 3.19–3.23 (m, 4H), 3.33 (s, 3H), 3.63 (s, 3H), 8.13 (d, 2H, J = 8.8 Hz), 8.59 (d, 2H, J = 8.8 Hz); ^{13}C NMR (DMSO) δ: 11.11, 40.74, 41.86, 43.10, 51.49, 120.21, 129.69, 132.21, 138.47, 141.38, 146.41, 148.47, 161.08; HRMS (ESI, *m*/*z*) Calcd for $C_{17}H_{22}N_7O_4S_2$ [M^+ + H] 452.11692. Found [M^+ + H] 452.11728. Anal. Calcd for $C_{17}H_{21}N_7O_4S_2$: C, 45.22; H, 4.68; N, 21.71. Found: C, 44.86; H, 4.74; N, 21.54.

N-(1-piperidinyl)-4-(3-methyl-5-methylsulfonyl-1*H*-pyrazolo[4,3-*e*][1,2,4]triazyn-1-yl) benzenesulfonamide (**2d**).

Yield 70%. Melting point: 215–220 °C; ^{1}H NMR (DMSO) δ: 1.35–1.41 (m, 2H), 1.53–1.60 (m, 4H), 2.79 (s, 3H), 2.96 (t, 4H, J = 5.2 Hz), 3.63 (s, 3H), 8.05 (d, 2H, J = 8.4 Hz), 8.60 (d, 2H, J = 8.4 Hz); ^{13}C NMR (DMSO) δ: 11.11, 22.83, 24.70, 40.77, 46.65, 120.11, 129.45, 133.51, 138.37, 140.87, 146.24, 148.39, 161.03; HRMS (ESI, *m*/*z*) Calcd for $C_{17}H_{21}N_6O_4S_2$ [M^+ + H] 437.10602. Found [M^+ + H] 437.10638. Anal. Calcd for $C_{17}H_{20}N_6O_4S_2$: C, 46.77; H, 4.61; N, 19.25. Found: C, 46.39; 4.67; N, 19.09.

N-(1-piperidinyl)-4-(3-methyl-5-piperidine-1*H*-pyrazolo[4,3-*e*][1,2,4]triazyn-1-yl)benzenesulfonamide (**3d**).

Yield 7%. Melting point: 192–196 °C; ^{1}H NMR ($CDCl_3$) δ: 1.40–1.44 (m, 2H), 1.60–1.80 (m, 10H), 2.61 (s, 3H), 3.02 (t, 4H, J = 5.6 Hz), 3.98 (t, 4H, J = 5.6 Hz), 7.87 (d, 2H, J =8.8 Hz), 8.55 (d, 2H, J = 8.8 Hz).

4.1.2. Synthesis of Tricyclic Suflonamides (MMs)

Sulfonamide derivative with a methylsulfonyl group (0.33 mmole) was dissolved in anhydrous ethanol (15 mL), and sodium azide (21 mg, 0.33 mmole) was added. The reaction mixture was refluxed until the substrate disappeared (control TLC). Then, the solvent was evaporated and the crude product was purified using column chromatography and CH_2Cl_2. MeOH (50:1) mixture as eluent to give the final compounds as a yellow solid.

N-(2-morpholinoeth-1-yl)-4-[7-methyl-5*H*-pyrazolo[4,3-*e*]tetrazolo[1,5-*b*][1,2,4]triazin-5-yl)]benzenesulfonamide (**MM-134**):

Yield 80%. Melting point: 200–202 °C; ^{1}H NMR ($CDCl_3$) δ: 2.92 (s, 3H), 3.06 (t, 4H, J = 4.8 Hz), 3.77 (t, 4H, J = 4.8 Hz), 7.98 (d, 2H, J = 9.2 Hz), 8.50 (d, 2H, J = 9.2 Hz); HRMS (ESI, *m*/*z*) Calcd for $C_{15}H_{16}N_9O_3S$ [M^+ + H] 402.10186. Found [M^+ + H] 402.10189. Anal. Calcd for $C_{14}H_{15}N_9O_3S$: C, 43.18; H, 3.88; N, 32.37. Found: C, 42.98; H, 3.91; N, 32.22.

N-(morpholin-1-yl)-4-[7-methyl-5*H*-pyrazolo[4,3-*e*]tetrazolo[1,5-*b*][1,2,4]triazin-5-yl)] benzenesulfonamide (**MM-136**):

Yield 84%. Melting point: 150–155 °C; ^{1}H NMR ($CDCl_3$) δ: 2.32 (t, 4H, J = 4.4 Hz), 2.46 (t, 2H, J = 5.6 Hz), 2.91 (s, 3H), 3.09 (t, 2H, J = 5.6 Hz), 3.64 (t, 4H, J = 4.4 Hz), 8.12 (d, 2H, J = 8.8 Hz), 8.46 (d, 2H, J = 8.8 Hz); ^{13}C NMR ($CDCl_3$) δ: 11.45, 38.92, 52.95, 56.23, 66.73, 119.26, 128.91, 137.83, 140.33, 140.71, 144.37, 145.14, 147.52; HRMS (ESI, *m*/*z*) Calcd for $C_{17}H_{21}N_{10}O_3S$ [M^+ + H] 445.15131. Found [M^+ + H] 445.15107. Anal. Calcd for $C_{17}H_{20}N_{10}O_3S$: C, 45.93; H, 4.53; N, 31.51. Found: C, 45.75; H, 4.56; N, 31.38.

N-(morpholin-1-yl)-4-[7-methyl-5*H*-pyrazolo[4,3-*e*]tetrazolo[1,5-*b*][1,2,4]triazin-5-yl)] benzenesulfonamide (**MM-137**):

Yield 90%. Melting point: 210–212 °C; ^{1}H NMR ($CDCl_3$) δ: 2.27 (s, 3H), 2.49 (t, 4H, J = 4.8 Hz), 2.91 (s, 3H), 3.08 (t, 4H, J = 4.8 Hz), 7.94 (d, 2H, J = 8.8 Hz); ^{13}C NMR ($CDCl_3$) δ: 11.45, 29.68, 45.95, 53.99, 118.92, 129.59, 132.80, 133.43, 140.50, 144.38, 145.20, 147.56; HRMS (ESI, *m*/*z*) Calcd for $C_{16}H_{19}N_{10}O_2S$ [M^+ + H] 415.14080. Found [M^+ + H] 415.14029. Anal. Calcd for $C_{16}H_{18}N_{10}O_2S$: C, 46.36; H, 4.37; N, 33.79. Found: C, 46.16; H, 4.40; N, 33.65.

N-(morpholin-1-yl)-4-[7-methyl-5*H*-pyrazolo[4,3-*e*]tetrazolo[1,5-*b*][1,2,4]triazin-5-yl)] benzenesulfonamide (**MM-139**):

Yield 86%. Melting point:212–214 °C; ^{1}H NMR ($CDCl_3$) δ: 1.43 (t, 2H, J = 5.6 Hz), 1.65 (q, 4H, J = 5.6 Hz), 2.91 (s, 3H), 3.02 (t, 4H, J = 5.6 Hz); HRMS (ESI, *m*/*z*) Calcd for $C_{16}H_{18}N_9O_2S$ [M^+ + H] 400.12991. Found [M^+ + H] 400.12969. Anal. Calcd for $C_{16}H_{17}N_9O_2S$: C, 48.11; H, 4.28; N, 31.56. Found: C, 47.89; H, 4.33; N, 31.34.

4.2. Biological Studies

4.2.1. Chemicals

Trypsin-EDTA and all culture media (RPMI-1640, DMEM-F12, MEM) were purchased from Biowest (CytoGen, Zgierz, Poland). Acridine orange/ethidium bromide (AO/BE), amino acids solution (MEM), buffered saline (PBS), β-mercaptoethanol, penicillin-streptomycin solution stabilized, fetal bovine serum (FBS), dimethyl sulfoxide (DMSO),

and MTT 3-(4,5-dimethylthiazol-2-yl)-2,3-diphenyltetrazolium bromide were supplied by Merck/Sigma Aldrich Chemical Co (Burlington, MA, USA). FITC Annexin V Apoptosis Detection Kit I was purchased from B.D. Biosciences (Franklin Lakes, NJ, USA). MitoTracker Red was purchased from Invitrogen (Waltham, MA, USA).

4.2.2. Cell Culture

Cancer cell lines: BxPC-3 (pancreas adenocarcinoma, ATCC® CRL-1687™), HCT-116 (colorectal carcinoma, ATCC® CCL-247™), PC-3 (prostate cancer, ATCC® CRL-1435™), and normal cell lines: L929 (mouse fibroblast, ATCC® CCL-1™) and WI-38 (human lung fibroblasts, ATCC® CCL-75™) were obtained from American Type Culture Collection (ATCC, Rockville, MD, USA). Compositions of culture media used to cultivate cells are presented in Table 8.

Table 8. Compositions of culture media used to cultivate cells.

Type of Cells	Medium	Supplements
BxPC-3 HCT-116	RPMI-1640	10% (*v*/*v*) FBS, L-Glutamine, 25 mM Hepes, 1% penicillin-streptomycin
PC-3	DMEM-F12	10% (*v*/*v*) FBS, L-Glutamine, 15 mM Hepes 1% penicillin-streptomycin
L929	RPMI-1640	10% (*v*/*v*) FBS, L-Glutamine, 25 mM Hepes, 1% penicillin-streptomycin 1% β-mercaptoethanol
WI-38	MEM	10% (*v*/*v*) FBS, L-Glutamine, 25 mM Hepes 1% penicillin-streptomycin

Cells were grown at 37 °C in a humidified atmosphere of 5% CO_2 in the air. The culture medium was changed every 24–48 h. Subculture was performed using 0.25% trypsin/EDTA after cells reached confluence.

4.2.3. MTT Assay

To estimate cell viability following 72 h incubation with the tested MM-compounds (**MM134**, **MM136**, **MM137**, and **MM139**), the MTT test was used according to the PN-EN ISO 10993-5. It is a quantitative method based on the tetrazolium yellow dye MTT [3(4,5-dimethyl-2-thiazolyl)-2,5-diphenyl-2*H*-tetrazolium bromide], which is converted by living cells to a purple product, formazan, the concentration of which was measured colorimetrically. The MTT assay was performed according to the procedure described by Mosmann [87] with modifications. At a density of approximately 8×10^3 cells per 100 µL/well, 96-well plates were seeded. Following the given incubation period in controlled conditions (37 °C; 5% CO_2), cells were exposed to different concentrations of tested compounds in DMSO (range 0.05–3 µM) in a volume of 100 µL medium per well. Final solvent concentration of DMSO was < 0.5% *v*/*v* [88]. The experimental design included vehicle controls and blanks (wells without cells).

After 72 h of incubation of cells with tested MM-compounds, 20 µL of MTT tetrazolium salt (5 mg/mL in PBS) was added to each well, and plates were incubated once again in a humidified atmosphere for 3 h (37 °C; 5% CO_2). Following the incubation time, the solutions were removed and 100 µL of DMSO was added to dissolve the formazan complexes. Subsequently, a spectrophotometer (microplate reader Power Wave XS BioTek Instruments, Inc., Winooski, VT, USA) reading was performed at 570 nm. The experiments were performed in duplicates.

4.3. Apoptosis Detection

4.3.1. Flow Cytometry Analysis with Annexin V-FITC Staining

The Annexin V-FITC Apoptosis Detection Kit was used to estimate the apoptosis induction following 24 and 48 h incubation with the tested MM-compounds. During apoptosis, phosphatidylserine is transformed from the inner cell membrane to the cell surface, which can be detected by the annexin-FITC complex. The addition of propidium iodide to the reaction mixture allows the assessment of cell membrane integrity. Using flow cytometry analysis, four subpopulations of cells can be distinguished: alive (non-stained), necrotic (propidium iodide stained), early apoptotic (annexin V stained cells), or late-apoptotic cells (propidium iodide and annexin V stained) [89]. BxPC-3 and PC-3 cells were seeded at appropriate density on a 6-well plate (Table 9).

Table 9. Density of BxPC-3 and PC-3 cells used in the experimental series in Annexin V-FITC staining (the white panel), MitoTracker Red (the yellow panel) and dual acridine orange/ethidium bromide fluorescent staining (the grey panel).

Cancer Cell Lines	Cell Density/2 mL Culture Medium Annexin V-FITC	
	24 h Incubation	**48 h Incubation**
BxPC-3	6×10^5	5×10^5
PC-3	7×10^5	5×10^5
	Cell density/200 µL culture medium MitoTracker Red	
	24 h incubation	48 h incubation
BxPC-3	2×10^4	1.5×10^4
PC-3	1.2×10^4	1.5×10^4
	Cell density/mL culture medium AO/EB	
	24 h incubation	48 h incubation
BxPC-3	1.5×10^5	1×10^5
PC-3	1.5×10^5	1×10^5

After 24 h, cells were exposed to two concentrations of tested MM-compounds obtained in the 72 h MTT assay: IC_{50}, and $2xIC_{50}$. The experimental design included vehicle control (final solvent concentration was < 0.5% v/v DMSO), and cells treated with 2 µM SN-38 (active metabolite of irinotecan) used as a positive compensation control. Cells were left for incubation for another 24 or 48 h (37 °C; 5% CO_2). After exposure, cells were trypsinized and transferred to cytometric tubes, left for 40 min, and centrifuged at 1400 rpm for 10 min at 4 °C. Afterward, the supernatant was removed, and the precipitate was diluted in 1 mL of PBS. The rest of the procedure was performed according to the manufacturer's instructions. The results were obtained from three independent experiments.

4.3.2. Dual Acridine Orange/Ethidium Bromide (AO/EB) Fluorescent Staining

Acridine orange/ethidium bromide (AO/EB) staining is used to detect nuclear alterations and the development of apoptotic bodies, which are both indicative of apoptosis. Acridine orange penetrates into living cells, emitting green fluorescence after intercalation into DNA. The second dye, ethidium bromide, emits red fluorescence in cells with an altered cell membrane. The cells are divided into three categories as follows: living cells (green nucleus with red orange cytoplasm); apoptotic (green irregularly nuclei with chromatin condensation or fragmentation); and necrotic cells (uniformly orange-stained cell nuclei) [90]. Programmed cell death is measured by counting the number of cells that undergo apoptosis under a fluorescent microscope [46].

BxPC-3 and PC-3 cells were seeded at an appropriate density on 12-well plates (Table 9). After 24 h, cells were exposed to **MM134**, **MM136**, **MM137** and **MM139** in concentrations followed by IC_{50} values obtained in the MTT assay (IC_{50} and $2xIC_{50}$ concentration) for 24 or 48 h. Following the incubation period, cells were incubated with fluorochromes (AO/EB: 100 µM; 1:1, *v*/*v*) for 5 min at 37 °C in the dark.

Viable, apoptotic, or necrotic cells were distinguished using this method based on differential uptake of fluorescent DNA-binding dyes (AO/EB) with the structural aspect of chromatin condensation in the stained nucleus. Cells were analyzed using a fluorescence microscope (Olympus BX60 F5 Olympus Optical Co., Ltd., Nagano, Japan) at 360 nm. The results were obtained from three independent experiments.

4.3.3. Changes in Transmembrane Mitochondrial Potential-MitoTracker Red (ΔΨm)

Mitotracker Red is deposited in the mitochondrial matrix in response to changes in the inner transmembrane potential of the mitochondria. The intensity of fluorescence reflects the fitness of the mitochondria and alters with changes in MMP [91]. BxPC-3 and PC-3 cells were seeded at appropriate density on a 96-well plates (Table 9).

Cells were incubated with the following concentrations of **MM134**, **MM136**, **MM137**, and **MM139**: $0.5xIC_{50}$, IC_{50} and $2xIC_{50}$. After appropriate incubation time, cells were incubated with MitoTracker Red (0.1 µM/200 µL PBS/well) for 40 min. Afterward, MitoTracker Red solution was removed from the wells and PBS (200 µL/well) was added. Fluorescence was read at an absorbance/emission of 581/644 nm using the SpectraMax® i3x Multi-Mode Detection Platform.

4.4. Computational Studies

4.4.1. Molecular Docking Simulations

Triazine sulfonamide derivatives were designed and evaluated for their binding interactions with various drug targets involved in cancer pathophysiology with the intent of identifying their probable mechanism of action for their anticancer potential. Three-dimensional structures of all triazine sulfonamide derivatives, i.e., **MM129**, **MM131**, **MM134**, **MM136**, **MM137**, and **MM139**, were prepared by using the ChemDraw Ultra 9.0 tool. These designed ligands were computationally screened against ABL tyrosine-protein kinases (ABL1, ABL2), serine/threonine-protein kinases (AKT1, AKT2, AKT3), breakpoint cluster region protein (BCR), tyrosine-protein kinase (BTK), carbonic anhydrases (CA-IX and CA-XII), cyclin-dependent kinases (CDK2, CDK4, CDK6, and CDK7), intercellular adhesion molecule 1 (ICAM-1), mechanistic target of the rapamycin (mTOR1 and mTOR2) and programmed cell death 1 ligand 1 (PD-L1) by using molecular docking simulation [69].

Three-dimensional structure models of all macromolecular targets having an active involvement in cancer pathophysiology in humans were procured from the protein data bank (PDB) [51].

For the process validation of molecular docking simulation, the structure models of all the prepared macromolecular targets were initially docked against their reference ligands, which were already complex in their structural models. All the reference ligands, i.e., J8N, J92, MHR, and ATP were docked against their respective macromolecular targets, i.e., ABL1, ABL2, AKT1, AKT2, AKT3, BCR, BTK, CA-IX, CA-XII, CDK2, CDK4, CDK6, CDK7, ICAM-1, mTOR, mTOR2 and PD-L1 for the process validation [67].

After successful validation of all the macromolecular targets used in the current study, the designed triazine sulfonamide analogs were screened against them to identify their affinities against each of the macromolecular targets.

4.4.2. Molecular Dynamics Simulations

The obtained docking results were further validated for the stability of the macromolecular drug–receptor complex concerning time by performing molecular dynamics simulation. Based upon the best docking score, the macromolecular complexes of the ligands **MM136**,

MM137, and **MM139** against AKT1 and PD-L1 enzyme were shortlisted given the best docking results for performing a dynamics simulation at the molecular level for a time frame of 100 nanoseconds (ns) at constant temperature and pressure conditions [69,92].

4.4.3. Drug Likeness and ADMET Prediction

The potential drug-like molecule needs to possess distinct properties that facilitate long-lasting therapeutic effects inside the human body. In the drug development process, it is crucial to estimate the ADME parameters (absorption, distribution, metabolism, and excretion) of a given molecule. Computer models are reliable for the prediction of the pharmacokinetic profile of a newer ligand and may constitute an alternative to biological experiments, leading to a reduction in animal use in drug research, but they cannot fully replace them. Swiss-ADME web tool (http://www.swissadme.ch, accessed on 1 May 2022) [74] was used to estimate critical physicochemical, pharmacological, and drug-like properties of tested compounds based on the Lipiski rule, which states that orally active agents are prohibited from having more than one violation of the following rules: (1) the log P of the octanol/water partition coefficient (log P) should not be higher than five; (2) the molecular weight of the compound should be less than 500 Da; (3) the number of hydrogen bond donors should not be greater than five; and (4) the number of hydrogen donors should not be greater than ten [93,94]. SwissADME allows easy estimation of major pharmacokinetic parameters including, passive human gastrointestinal absorption (HIA) and blood–brain barrier (BBB) permeation [95]. SwissADME allows screening compounds for their cytochrome P450 (CYP) inhibitory activity. This is an important issue given that CYP isoforms are involved in drug elimination through metabolic biotransformation and thus impact the efficiency of therapy and affect the drug toxicity and adverse effects [93].

5. Conclusions

The conducted research provides the necessary information on the biological response of cancer and normal human cells to MM-compounds with an innovative, modified chemical structure, showing oncotherapeutic potential. Pyrazolo[4,3-*e*]tetrazolo[1,5-*b*][1,2,4]triazine sulfonamides are emerging as an important scaffold for drug discovery. Here we have shown the utility of four pyrazolo-triazine derivatives (**MM134**, **MM136**, **MM137,** and **MM139**) as potential anticancer compounds with selective cytotoxic and proapoptotic properties in various cancer cell line models. Our data indicate that antitumor potential may result from the dual inhibition of AKT-mTOR and PD-1-PD-L1 pathways in cancer cells. The exploration of biological activity of other analogs of MM derivatives may lead to optimization and discovery of novel, safe and potent inhibitors of these pathways with more selective action against neoplastic cells and minimized cytotoxicity against normal human cells.

Supplementary Materials: The following supporting information can be downloaded at: https://www.mdpi.com/article/10.3390/ijms23115892/s1.

Author Contributions: Conceptualization, B.M., M.K., M.M. and R.K.; collected literature, B.M., M.K. and R.K.; wrote the manuscript, A.S., K.B., M.K. and S.M.; supervised project and proofread the paper, M.K., M.M. and R.K. All authors have read and agreed to the published version of the manuscript.

Funding: This research received no external funding.

Institutional Review Board Statement: Not applicable.

Informed Consent Statement: Not applicable.

Data Availability Statement: The data presented in this study are available in the main text of this article/supplementary materials of this article or on request from the corresponding author.

Conflicts of Interest: The authors declare no conflict of interest.

Abbreviations

ABL	ABL tyrosine-protein kinase
AIF	apoptosis-inducing factor
AKT	serine/threonine-protein kinase
AO/EB	Acridine orange/ethidium bromide
BBB	blood–brain barrier
BTK	Bruton's tyrosine kinase
CA	carbonic anhydrase
CDK	cyclin-dependent kinases
Csp3	carbons in the sp3 hybridization
CYP	cytochrome P450
DMSO	dimethyl sulfoxide
FBS	fetal bovine serum
HIA	human gastrointestinal absorption
ICAM-1	intercellular adhesion molecule 1
MEM	amino acids solution
MMP	mitochondria membrane potential
mTOR	mechanistic target of the rapamycin
MTT	3-(4,5-dimethylthiazol-2-yl)-2,3-diphenyltetrazolium bromide
MW	molecular weight
PBS	buffered saline
PD-1	programmed death receptor-1
PDB	protein data bank
PD-L1	programmed death ligand-1
PGP	glycoprotein P
PI3K	phosphoinositide-3-kinase
PTEN	phosphatase and tensin homolog
RMSD	root mean square deviation
RMSF	root mean square fluctuation
TP53	cellular tumor antigen p53
TPSA	topological polar surface area

References

1. Lee, C.-I.; Lee, C.-L.; Hwang, J.-F.; Lee, Y.-H.; Wang, J.-J. Monascus-fermented red mold rice exhibits cytotoxic effect and induces apoptosis on human breast cancer cells. *Appl. Microbiol. Biotechnol.* **2012**, *97*, 1269–1278. [CrossRef] [PubMed]
2. Hatse, S.; De Clercq, E.; Balzarini, J. Role of antimetabolites of purine and pyrimidine nucleotide metabolism in tumor cell differentiation. *Biochem. Pharmacol.* **1999**, *58*, 539–555. [CrossRef]
3. Parker, W.B. Enzymology of Purine and Pyrimidine Antimetabolites Used in the Treatment of Cancer. *Chem. Rev.* **2009**, *109*, 2880–2893. [CrossRef] [PubMed]
4. Pizzorno, G.; Diasio, R.B.; Cheng, Y.-C. Pyrimidine and Purine Antimetabolites. In *Holland-Frei Cancer Medicine*, 6th ed.; BC Decker: Hamilton, ON, Canada, 2003; Chapter 50. Available online: https://www.ncbi.nlm.nih.gov/books/NBK13028/ (accessed on 1 May 2022).
5. Brunelle, J.K.; Zhang, B. Apoptosis assays for quantifying the bioactivity of anticancer drug products. *Drug Resist. Updates* **2010**, *13*, 172–179. [CrossRef] [PubMed]
6. D'Arcy, M.S. Cell death: A review of the major forms of apoptosis, necrosis and autophagy. *Cell Biol. Int.* **2019**, *43*, 582–592. [CrossRef]
7. Vermes, I.; Haanen, C.; Steffens-Nakken, H.; Reutellingsperger, C. A novel assay for apoptosis Flow cytometric detection of phosphatidylserine expression on early apoptotic cells using fluorescein labelled Annexin V. *J. Immunol. Methods* **1995**, *184*, 39–51. [CrossRef]
8. Crowley, L.; Marfell, B.J.; Scott, A.P.; Waterhouse, N.J. Quantitation of Apoptosis and Necrosis by Annexin V Binding, Propidium Iodide Uptake, and Flow Cytometry. *Cold Spring Harb. Protoc.* **2016**, *2016*, pdb-rot087288. [CrossRef]
9. Bouchain, G.; Delorme, D. Novel hydroxamate and anilide derivatives as potent histone deacetylase inhibitors: Synthesis and antiproliferative evaluation. *Curr. Med. Chem.* **2003**, *10*, 2359–2372. [CrossRef]
10. Cheng, X.-C.; Wang, Q.; Fang, H.; Xu, W.-F. Role of sulfonamide group in matrix metalloproteinase inhibitors. *Curr. Med. Chem.* **2008**, *15*, 368–373. [CrossRef]
11. Lu, Y.; Chen, J.; Xiao, M.; Li, W.; Miller, D.D. An Overview of Tubulin Inhibitors That Interact with the Colchicine Binding Site. *Pharm. Res.* **2012**, *29*, 2943–2971. [CrossRef]

12. Mojzych, M.; Dolashki, A.; Voelter, W. Synthesis of pyrazolo[4,3-*e*][1,2,4]triazine sulfonamides, novel Sildenafil analogs with tyrosinase inhibitory activity. *Bioorg. Med. Chem.* **2014**, *22*, 6616–6624. [CrossRef] [PubMed]
13. Mojzych, M.; Tarasiuk, P.; Kotwica-Mojzych, K.; Rafiq, M.; Seo, S.-Y.; Nicewicz, M.; Fornal, E. Synthesis of chiral pyrazolo[4,3-*e*][1,2,4]triazine sulfonamides with tyrosinase and urease inhibitory activity. *J. Enzym. Inhib. Med. Chem.* **2016**, *32*, 99–105. [CrossRef] [PubMed]
14. Mojzych, M.; Šubertová, V.; Bielawska, A.; Bielawski, K.; Bazgier, V.; Berka, K.; Gucký, T.; Fornal, E.; Kryštof, V. Synthesis and kinase inhibitory activity of new sulfonamide derivatives of pyrazolo[4,3-*e*][1,2,4]triazines. *Eur. J. Med. Chem.* **2014**, *78*, 217–224. [CrossRef] [PubMed]
15. Cowan-Jacob, S.W.; Fendrich, G.; Floersheimer, A.; Furet, P.; Liebetanz, J.; Rummel, G.; Rheinberger, P.; Centeleghe, M.; Fabbro, D.; Manley, P.W. Structural biology contributions to the discovery of drugs to treat chronic myelogenous leukaemia. *Acta Crystallogr. Sect. D Biol. Crystallogr.* **2006**, *63*, 80–93. [CrossRef]
16. Bernat, Z.; Szymanowska, A.; Kciuk, M.; Kotwica-Mojzych, K.; Mojzych, M. Review of the Synthesis and Anticancer Properties of Pyrazolo[4,3-*e*][1,2,4]triazine Derivatives. *Molecules* **2020**, *25*, 3948. [CrossRef]
17. Byth, K.F.; Cooper, N.; Culshaw, J.D.; Heaton, D.W.; Oakes, S.E.; Minshull, C.A.; Norman, R.A.; Pauptit, R.A.; Tucker, J.A.; Breed, J.; et al. Imidazo[1,2-*b*]pyridazines: A potent and selective class of cyclin-dependent kinase inhibitors. *Bioorg. Med. Chem. Lett.* **2004**, *14*, 2249–2252. [CrossRef]
18. Nie, Z.; Perretta, C.; Erickson, P.; Margosiak, S.; Almassy, R.; Lu, J.; Averill, A.; Yager, K.M.; Chu, S. Structure-based design, synthesis, and study of pyrazolo[1,5-*a*][1,3,5]triazine derivatives as potent inhibitors of protein kinase CK2. *Bioorg. Med. Chem. Lett.* **2007**, *17*, 4191–4195. [CrossRef]
19. Filhol, O.; Cochet, C. Protein Kinase CK2 in Health and Disease. *Exp.* **2009**, *66*, 1830–1839. [CrossRef]
20. Sciú, M.L.; Sebastián-Pérez, V.; Martinez-Gonzalez, L.; Benitez, R.; Perez, D.I.; Pérez, C.; Campillo, N.E.; Martinez, A.; Moyano, E.L. Computer-aided molecular design of pyrazolotriazines targeting glycogen synthase kinase 3. *J. Enzym. Inhib. Med. Chem.* **2018**, *34*, 87–96. [CrossRef]
21. Scozzafava, A.; Owa, T.; Mastrolorenzo, A.; Supuran, C.T. Anticancer and Antiviral Sulfonamides. *Curr. Med. Chem.* **2003**, *10*, 925–953. [CrossRef]
22. Kciuk, M.; Gielecińska, A.; Mujwar, S.; Mojzych, M.; Marciniak, B.; Drozda, R.; Kontek, R. Targeting carbonic anhydrase IX and XII isoforms with small molecule inhibitors and monoclonal antibodies. *J. Enzym. Inhib. Med. Chem.* **2022**, *37*, 1278–1298. [CrossRef] [PubMed]
23. Mojzych, M.; Bielawska, A.; Bielawski, K.; Ceruso, M.; Supuran, C.T. Pyrazolo[4,3-*e*][1,2,4]triazine sulfonamides as carbonic anhydrase inhibitors with antitumor activity. *Bioorg. Med. Chem.* **2014**, *22*, 2643–2647. [CrossRef] [PubMed]
24. Mojzych, M.; Karczmarzyk, Z.; Wysocki, W.; Ceruso, M.; Supuran, C.T.; Kryštof, V.; Urbańczyk-Lipkowska, Z.; Kalicki, P. New approaches to the synthesis of sildenafil analogues and their enzyme inhibitory activity. *Bioorg. Med. Chem.* **2015**, *23*, 1421–1429. [CrossRef] [PubMed]
25. Hermanowicz, J.M.; Szymanowska, A.; Sieklucka, B.; Czarnomysy, R.; Pawlak, K.; Bielawska, A.; Bielawski, K.; Kalafut, J.; Przybyszewska, A.; Surazynski, A.; et al. Exploration of novel heterofused 1,2,4-triazine derivative in colorectal cancer. *J. Enzym. Inhib. Med. Chem.* **2021**, *36*, 535–548. [CrossRef]
26. Hermanowicz, J.; Pawlak, K.; Sieklucka, B.; Czarnomysy, R.; Kwiatkowska, I.; Kazberuk, A.; Surazynski, A.; Mojzych, M.; Pawlak, D. MM-129 as a Novel Inhibitor Targeting PI3K/AKT/mTOR and PD-L1 in Colorectal Cancer. *Cancers* **2021**, *13*, 3203. [CrossRef] [PubMed]
27. Jiang, Y.; Chen, M.; Nie, H.; Yuan, Y. PD-1 and PD-L1 in cancer immunotherapy: Clinical implications and future considerations. *Hum. Vaccines Immunother.* **2019**, *15*, 1111–1122. [CrossRef] [PubMed]
28. Salmaninejad, A.; Valilou, S.F.; Shabgah, A.G.; Aslani, S.; Alimardani, M.; Pasdar, A.; Sahebkar, A. PD-1/PD-L1 pathway: Basic biology and role in cancer immunotherapy. *J. Cell. Physiol.* **2019**, *234*, 16824–16837. [CrossRef]
29. Guan, J.; Lim, K.S.; Mekhail, T.; Chang, C.-C. Programmed Death Ligand-1 (PD-L1) Expression in the Programmed Death Receptor-1 (PD-1)/PD-L1 Blockade: A Key Player Against Various Cancers. *Arch. Pathol. Lab. Med.* **2017**, *141*, 851–861. [CrossRef]
30. Hassan, B.; Akcakanat, A.; Holder, A.M.; Meric-Bernstam, F. Targeting the PI3-Kinase/Akt/mTOR Signaling Pathway. *Surg. Oncol. Clin. N. Am.* **2013**, *22*, 641–664. [CrossRef]
31. Yu, J.S.L.; Cui, W. Proliferation, survival and metabolism: The role of PI3K/AKT/mTOR signalling in pluripotency and cell fate determination. *Development* **2016**, *143*, 3050–3060. [CrossRef]
32. Liu, R.; Chen, Y.; Liu, G.; Li, C.; Song, Y.; Cao, Z.; Li, W.; Hu, J.; Lu, C.; Liu, Y. PI3K/AKT pathway as a key link modulates the multidrug resistance of cancers. *Cell Death Dis.* **2020**, *11*, 1–12. [CrossRef] [PubMed]
33. Ersahin, T.; Tuncbag, N.; Cetin-Atalay, R. The PI3K/AKT/mTOR interactive pathway. *Mol. BioSyst.* **2015**, *11*, 1946–1954. [CrossRef] [PubMed]
34. Porta, C.; Paglino, C.; Mosca, A. Targeting PI3K/Akt/mTOR Signaling in Cancer. *Front. Oncol.* **2014**, *4*, 64. [CrossRef]
35. Hermanowicz, J.M.; Kalaska, B.; Pawlak, K.; Sieklucka, B.; Miklosz, J.; Mojzych, M.; Pawlak, D. Preclinical Toxicity and Safety of MM-129—First-in-Class BTK/PD-L1 Inhibitor as a Potential Candidate against Colon Cancer. *Pharmaceutics* **2021**, *13*, 1222. [CrossRef] [PubMed]
36. Gornowicz, A.; Szymanowska, A.; Mojzych, M.; Czarnomysy, R.; Bielawski, K.; Bielawska, A. The Anticancer Action of a Novel 1,2,4-Triazine Sulfonamide Derivative in Colon Cancer Cells. *Molecules* **2021**, *26*, 2045. [CrossRef] [PubMed]

37. Stockert, J.C.; Horobin, R.W.; Colombo, L.L.; Blázquez-Castro, A. Tetrazolium salts and formazan products in Cell Biology: Viability assessment, fluorescence imaging, and labeling perspectives. *Acta Histochem.* **2018**, *120*, 159–167. [CrossRef] [PubMed]
38. Chazotte, B. Labeling Mitochondria with MitoTracker Dyes. *Cold Spring Harb. Protoc.* **2011**, *2011*, 990–992. [CrossRef]
39. Ricci, J.E.; Muñoz-Pinedo, C.; Fitzgerald, P.; Bailly-Maitre, B.; Perkins, G.A.; Yadava, N.; Scheffler, I.E.; Ellisman, M.H.; Green, D.R. Disruption of Mitochondrial Function during Apoptosis Is Mediated by Caspase Cleavage of the p75 Subunit of Complex I of the Electron Transport Chain. *Cell* **2004**, *117*, 773–786. [CrossRef]
40. Krysko, D.V.; Roels, F.; Leybaert, L.; D'Herde, K. Mitochondrial Transmembrane Potential Changes Support the Concept of Mitochondrial Heterogeneity During Apoptosis. *J. Histochem. Cytochem.* **2001**, *49*, 1277–1284. [CrossRef]
41. Gornowicz, A.; Szymanowska, A.; Mojzych, M.; Bielawski, K.; Bielawska, A. The Effect of Novel 7-methyl-5-phenyl-pyrazolo[4,3-*e*]tetrazolo[4,5-*b*][1,2,4]triazine Sulfonamide Derivatives on Apoptosis and Autophagy in DLD-1 and HT-29 Colon Cancer Cells. *Int. J. Mol. Sci.* **2020**, *21*, 5221. [CrossRef]
42. Mojzych, M.; Karczmarzyk, Z.; Rykowski, A. Synthesis and structure of 7-methyl-5-phenyl-1H-pyrazolo[4,3-*e*]tetrazolo[4,5-*b*][1,2,4]triazine(1). *J. Chem. Crystallogr.* **2005**, *35*, 151–155. [CrossRef]
43. Karczmarzyk, Z.; Mojzych, M.; Rykowski, A. Synthesis and structure of a novel mesomeric betaine 6,7-dimethyl-2H-pyrazolo[4,3-*e*]tetrazolo[4,5-*b*][1,2,4]triazine. *J. Mol. Struct.* **2007**, *829*, 22–28. [CrossRef]
44. Mojzych, M.; Karczmarzyk, Z.; Wysocki, W.; Urbańczyk-Lipkowska, Z.; Żaczek, N. Valence tautomerism of new pyrazolo[4,3-*e*]tetrazole[4,5-*b*][1,2,4]triazines. *J. Mol. Struct.* **2014**, *1067*, 147–153. [CrossRef]
45. Deev, S.L.; Shestakova, T.S.; Charushin, V.N.; Chupakhin, O.N. Synthesis and azido-tetrazole tautomerism of 3-azido-1,2,4-triazines. *Chem. Heterocycl. Compd.* **2017**, *53*, 963–975. [CrossRef]
46. Kasibhatla, S.; Amarante-Mendes, G.P.; Finucane, D.; Brunner, T.; Bossy-Wetzel, E.; Green, D.R. Acridine Orange/Ethidium Bromide (AO/EB) Staining to Detect Apoptosis. *Cold Spring Harb. Protoc.* 2006. [CrossRef]
47. Pemovska, T.; Johnson, E.; Kontro, M.; Repasky, G.A.; Chen, J.; Wells, P.; Cronin, C.N.; McTigue, M.; Kallioniemi, O.; Porkka, K.; et al. Axitinib effectively inhibits BCR-ABL1(T315I) with a distinct binding conformation. *Nat. Cell Biol.* **2015**, *519*, 102–105. [CrossRef]
48. Salah, E.; Ugochukwu, E.; Barr, A.J.; von Delft, F.; Knapp, S.; Elkins, J.M. Crystal Structures of ABL-Related Gene (ABL2) in Complex with Imatinib, Tozasertib (VX-680), and a Type I Inhibitor of the Triazole Carbothioamide Class. *J. Med. Chem.* **2011**, *54*, 2359–2367. [CrossRef]
49. Freeman-Cook, K.D.; Autry, C.; Borzillo, G.; Gordon, D.; Barbacci-Tobin, E.; Bernardo, V.; Briere, D.; Clark, T.; Corbett, M.; Jakubczak, J.; et al. Design of Selective, ATP-Competitive Inhibitors of Akt. *J. Med. Chem.* **2010**, *53*, 4615–4622. [CrossRef]
50. Heerding, D.A.; Rhodes, N.; Leber, J.D.; Clark, T.J.; Keenan, R.M.; Lafrance, L.V.; Li, M.; Safonov, I.G.; Takata, D.T.; Venslavsky, J.W.; et al. Identification of 4-(2-(4-Amino-1,2,5-oxadiazol-3-yl)-1-ethyl-7-{[(3*S*)-3-piperidinylmethyl]oxy}-1*H*-imidazo [4,5-*c*]pyridin-4-yl)-2-methyl-3-butyn-2-ol (GSK690693), a Novel Inhibitor of AKT Kinase. *J. Med. Chem.* **2008**, *51*, 5663–5679. [CrossRef]
51. Berman, H.M.; Westbrook, J.; Feng, Z.; Gilliland, G.; Bhat, T.N.; Weissig, H.; Shindyalov, I.N.; Bourne, P.E. The Protein Data Bank. *Nucleic Acids Res.* **2000**, *28*, 235–242. [CrossRef]
52. Reckel, S.; Gehin, C.; Tardivon, D.; Georgeon, S.; Kükenshöner, T.; Löhr, F.; Koide, A.; Buchner, L.; Panjkovich, A.; Reynaud, A.; et al. Structural and functional dissection of the DH and PH domains of oncogenic Bcr-Abl tyrosine kinase. *Nat. Commun.* **2017**, *8*, 1–14. [CrossRef] [PubMed]
53. Marcotte, D.J.; Liu, Y.-T.; Arduini, R.M.; Hession, C.A.; Miatkowski, K.; Wildes, C.P.; Cullen, P.F.; Hong, V.; Hopkins, B.T.; Mertsching, E.; et al. Structures of human Bruton's tyrosine kinase in active and inactive conformations suggest a mechanism of activation for TEC family kinases. *Protein Sci.* **2010**, *19*, 429–439. [CrossRef] [PubMed]
54. Zakšauskas, A.; Čapkauskaitė, E.; Jezepčikas, L.; Linkuvienė, V.; Paketurytė, V.; Smirnov, A.; Leitans, J.; Kazaks, A.; Dvinskis, E.; Manakova, E.; et al. Halogenated and di-substituted benzenesulfonamides as selective inhibitors of carbonic anhydrase isoforms. *Eur. J. Med. Chem.* **2020**, *185*, 111825. [CrossRef] [PubMed]
55. Bettayeb, K.; Tirado, O.M.; Lambot, S.M.; Ferandin, Y.; Lozach, O.; Morris, J.; Mateo-Lozano, S.; Drueckes, P.; Schächtele, C.; Kubbutat, M.H.; et al. Meriolins, a New Class of Cell Death–Inducing Kinase Inhibitors with Enhanced Selectivity for Cyclin-Dependent Kinases. *Cancer Res.* **2007**, *67*, 8325–8334. [CrossRef] [PubMed]
56. Day, P.J.; Cleasby, A.; Tickle, I.J.; O'Reilly, M.; Coyle, J.E.; Holding, F.P.; McMenamin, R.L.; Yon, J.; Chopra, R.; Lengauer, C.; et al. Crystal structure of human CDK4 in complex with a D-type cyclin. *Proc. Natl. Acad. Sci. USA* **2009**, *106*, 4166–4170. [CrossRef] [PubMed]
57. Chen, P.; Lee, N.V.; Hu, W.; Xu, M.; Ferre, R.A.; Lam, H.; Bergqvist, S.; Solowiej, J.; Diehl, W.; He, Y.-A.; et al. Spectrum and Degree of CDK Drug Interactions Predicts Clinical Performance. *Mol. Cancer Ther.* **2016**, *15*, 2273–2281. [CrossRef] [PubMed]
58. Lolli, G.; Lowe, E.D.; Brown, N.R.; Johnson, L.N. The Crystal Structure of Human CDK7 and Its Protein Recognition Properties. *Structure* **2004**, *12*, 2067–2079. [CrossRef]
59. Lennartz, F.; Adams, Y.; Bengtsson, A.; Olsen, R.W.; Turner, L.; Ndam, N.T.; Ecklu-Mensah, G.; Moussiliou, A.; Ofori, M.F.; Gamain, B.; et al. Structure-Guided Identification of a Family of Dual Receptor-Binding PfEMP1 that Is Associated with Cerebral Malaria. *Cell Host Microbe* **2017**, *21*, 403–414. [CrossRef]
60. Yang, H.; Jiang, X.; Li, B.; Yang, H.J.; Miller, M.; Yang, A.; Dhar, A.; Pavletich, N.P. Mechanisms of mTORC1 activation by RHEB and inhibition by PRAS40. *Nature* **2017**, *552*, 368–373. [CrossRef]

61. Scaiola, A.; Mangia, F.; Imseng, S.; Boehringer, D.; Berneiser, K.; Shimobayashi, M.; Stuttfeld, E.; Hall, M.N.; Ban, N.; Maier, T. The 3.2-Å resolution structure of human mTORC2. *Sci. Adv.* **2020**, *6*, eabc1251. [CrossRef]
62. Butera, R.; Ważyńska, M.; Magiera-Mularz, K.; Plewka, J.; Musielak, B.; Surmiak, E.; Sala, D.; Kitel, R.; de Bruyn, M.; Nijman, H.W.; et al. Design, Synthesis, and Biological Evaluation of Imidazopyridines as PD-1/PD-L1 Antagonists. *ACS Med. Chem. Lett.* **2021**, *12*, 768–773. [CrossRef] [PubMed]
63. Morris, G.M.; Huey, R.; Lindstrom, W.; Sanner, M.F.; Belew, R.K.; Goodsell, D.S.; Olson, A.J. AutoDock4 and AutoDockTools4: Automated docking with selective receptor flexibility. *J. Comput. Chem.* **2009**, *30*, 2785–2791. [CrossRef] [PubMed]
64. Bitencourt-Ferreira, G.; Pintro, V.O.; de Azevedo, W.F. Docking with AutoDock4. *Methods Mol. Biol.* **2019**, *2053*, 125–148. [CrossRef] [PubMed]
65. Jain, R.; Mujwar, S. Repurposing metocurine as main protease inhibitor to develop novel antiviral therapy for COVID-19. *Struct. Chem.* **2020**, *31*, 2487–2499. [CrossRef] [PubMed]
66. Mujwar, S.; Kumar, V. Computational Drug Repurposing Approach to Identify Potential Fatty Acid-Binding Protein-4 Inhibitors to Develop Novel Antiobesity Therapy. *ASSAY Drug Dev. Technol.* **2020**, *18*, 318–327. [CrossRef] [PubMed]
67. Shah, K.; Mujwar, S.; Krishna, G.; Gupta, J.K. Computational Design and Biological Depiction of Novel Naproxen Derivative. *ASSAY Drug Dev. Technol.* **2020**, *18*, 308–317. [CrossRef]
68. Shah, K.; Mujwar, S.; Gupta, J.K.; Shrivastava, S.K.; Mishra, P. Molecular Docking and In Silico Cogitation Validate Mefenamic Acid Prodrugs as Human Cyclooxygenase-2 Inhibitor. *ASSAY Drug Dev. Technol.* **2019**, *17*, 285–291. [CrossRef]
69. Mujwar, S.; Deshmukh, R.; Harwansh, R.K.; Gupta, J.K.; Gour, A. Drug Repurposing Approach for Developing Novel Therapy Against Mupirocin-Resistant *Staphylococcus aureus*. *ASSAY Drug Dev. Technol.* **2019**, *17*, 298–309. [CrossRef]
70. Mishra, I.; Mishra, R.; Mujwar, S.; Chandra, P.; Sachan, N. A retrospect on antimicrobial potential of thiazole scaffold. *J. Heterocycl. Chem.* **2020**, *57*, 2304–2329. [CrossRef]
71. Mujwar, S.; Shah, K.; Gupta, J.K.; Gour, A. Docking based screening of curcumin derivatives: A novel approach in the inhibition of tubercular DHFR. *Int. J. Comput. Biol. Drug Des.* **2021**, *14*, 297. [CrossRef]
72. Sharma, K.K.; Singh, B.; Mujwar, S.; Bisen, P.; Kaushal, S.K.; Brijendra, S.; Prakash, B.S. Molecular Docking Based Analysis to Elucidate the DNA Topoisomerase IIβ as the Potential Target for the Ganoderic Acid; A Natural Therapeutic Agent in Cancer Therapy. *Curr. Comput. Aided-Drug Des.* **2020**, *16*, 176–189. [CrossRef] [PubMed]
73. Minaz, N.; Razdan, R.; Hammock, B.D.; Mujwar, S.; Goswami, S.K. Impact of diabetes on male sexual function in streptozotocin-induced diabetic rats: Protective role of soluble epoxide hydrolase inhibitor. *Biomed. Pharmacother.* **2019**, *115*, 108897. [CrossRef] [PubMed]
74. SwissADME. Available online: http://www.swissadme.ch (accessed on 4 May 2022).
75. Dresser, G.K.; Spence, J.D.; Bailey, D. Pharmacokinetic-Pharmacodynamic Consequences and Clinical Relevance of Cytochrome P450 3A4 Inhibition. *Clin. Pharmacokinet.* **2000**, *38*, 41–57. [CrossRef] [PubMed]
76. Fontana, E.; Dansette, P.M.; Poli, S.M. Cytochrome P450 Enzymes Mechanism Based Inhibitors: Common Sub-Structures and Reactivity. *Curr. Drug Metab.* **2005**, *6*, 413–451. [CrossRef] [PubMed]
77. Zhou, S.-F. Drugs Behave as Substrates, Inhibitors and Inducers of Human Cytochrome P450 3A4. *Curr. Drug Metab.* **2008**, *9*, 310–322. [CrossRef]
78. Miller, D.S.; Bauer, B.; Hartz, A.M.S. Modulation of P-Glycoprotein at the Blood-Brain Barrier: Opportunities to Improve Central Nervous System Pharmacotherapy. *Pharmacol. Rev.* **2008**, *60*, 196–209. [CrossRef]
79. Robinson, K.; Tiriveedhi, V. Perplexing Role of P-Glycoprotein in Tumor Microenvironment. *Front. Oncol.* **2020**, *10*, 265. [CrossRef]
80. Kim, E.-J.; Kang, G.-J.; Kang, J.-I.; Boo, H.-J.; Hyun, J.W.; Koh, Y.S.; Chang, W.-Y.; Kim, Y.R.; Kwon, J.-M.; Maeng, Y.H.; et al. Over-activation of AKT signaling leading to 5-Fluorouracil resistance in SNU-C5/5-FU cells. *Oncotarget* **2018**, *9*, 19911–19928. [CrossRef]
81. Lastwika, K.J.; Wilson, W., III; Li, Q.K.; Norris, J.; Xu, H.; Ghazarian, S.R.; Kitagawa, H.; Kawabata, S.; Taube, J.M.; Yao, S.; et al. Control of PD-L1 Expression by Oncogenic Activation of the AKT–mTOR Pathway in Non–Small Cell Lung Cancer. *Cancer Res.* **2016**, *76*, 227–238. [CrossRef]
82. Van Der Kraak, L.; Goel, G.; Ramanan, K.; Kaltenmeier, C.; Zhang, L.; Normolle, D.P.; Freeman, G.J.; Tang, D.; Nason, K.S.; Davison, J.M.; et al. 5-Fluorouracil upregulates cell surface B7-H1 (PD-L1) expression in gastrointestinal cancers. *J. Immunother. Cancer* **2016**, *4*, 65. [CrossRef]
83. Han, Y.; Liu, D.; Li, L. PD-1/PD-L1 Pathway: Current Researches in Cancer. *Am. J. Cancer Res.* **2020**, *10*, 727–742. [PubMed]
84. Sun, S.-Y. Searching for the real function of mTOR signaling in the regulation of PD-L1 expression. *Transl. Oncol.* **2020**, *13*, 100847. [CrossRef] [PubMed]
85. Langdon, S.; Hughes, A.; Taylor, M.A.; Kuczynski, E.A.; Mele, D.A.; Delpuech, O.; Jarvis, L.; Staniszewska, A.; Cosulich, S.; Carnevalli, L.S.; et al. Combination of dual mTORC1/2 inhibition and immune-checkpoint blockade potentiates anti-tumour immunity. *OncoImmunology* **2018**, *7*, e1458810. [CrossRef]
86. Mojzych, M.; Rykowski, A. Synthesis of Functionalized 1H-Pyrazolo[4,3-*e*][1,2,4]triazines and Their Fused Derivatives via Ipso-Substitution of Methylsulfonyl Group with O-, N-, S- and C-Nucleophiles. *Heterocycles* **2004**, *63*, 1829–1838.
87. Mosmann, T. Rapid colorimetric assay for cellular growth and survival: Application to proliferation and cytotoxicity assays. *J. Immunol. Methods* **1983**, *65*, 55–63. [CrossRef]

88. Da Violante, G.; Zerrouk, N.; Richard, I.; Provot, G.; Chaumeil, J.C.; Arnaud, P. Evaluation of the Cytotoxicity Effect of Dimethyl Sulfoxide (DMSO) on Caco2/TC7 Colon Tumor Cell Cultures. *Biol. Pharm. Bull.* **2002**, *25*, 1600–1603. [CrossRef] [PubMed]
89. Wlodkowic, D.; Skommer, J.; Darzynkiewicz, Z. Flow Cytometry-Based Apoptosis Detection. In *Apoptosis*; Humana Press: Totowa, NJ, USA, 2009; Volume 559, pp. 19–32. [CrossRef]
90. Kontek, R.; Jakubczak, M.; Matlawska-Wasowska, K. The antioxidants, vitamin A and E but not vitamin C and melatonin enhance the proapoptotic effects of irinotecan in cancer cells in vitro. *Toxicol. Vitr.* **2014**, *28*, 282–291. [CrossRef]
91. Xiao, B.; Deng, X.; Zhou, W.; Tan, E.-K. Flow Cytometry-Based Assessment of Mitophagy Using MitoTracker. *Front. Cell. Neurosci.* **2016**, *10*, 76. [CrossRef]
92. Mujwar, S. Computational repurposing of tamibarotene against triple mutant variant of SARS-CoV-2. *Comput. Biol. Med.* **2021**, *136*, 104748. [CrossRef]
93. Daina, A.; Michielin, O.; Zoete, V. SwissADME: A free web tool to evaluate pharmacokinetics, drug-likeness and medicinal chemistry friendliness of small molecules. *Sci. Rep.* **2017**, *7*, 42717. [CrossRef]
94. Daina, A.; Zoete, V. Application of the SwissDrugDesign Online Resources in Virtual Screening. *Int. J. Mol. Sci.* **2019**, *20*, 4612. [CrossRef] [PubMed]
95. Daina, A.; Zoete, V. A BOILED-Egg To Predict Gastrointestinal Absorption and Brain Penetration of Small Molecules. *ChemMedChem* **2016**, *11*, 1117–1121. [CrossRef] [PubMed]

A)

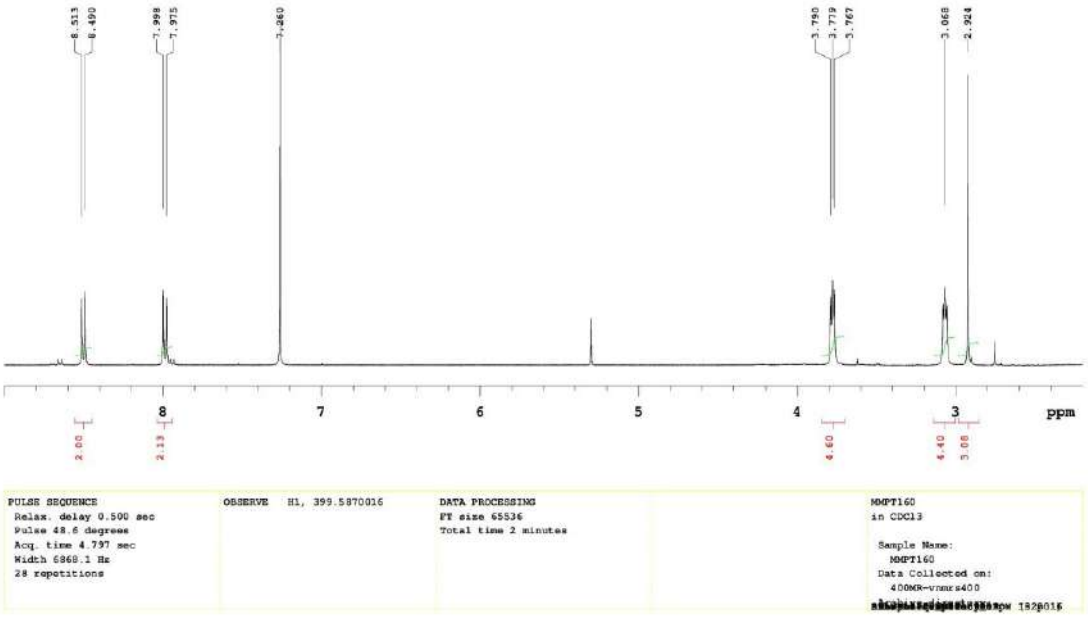

PULSE SEQUENCE
Relax. delay 0.500 sec
Pulse 48.6 degrees
Acq. time 4.797 sec
Width 6868.1 Hz
28 repetitions

OBSERVE H1, 399.5870016

DATA PROCESSING
FT size 65536
Total time 2 minutes

MMPT160
in CDCl3

Sample Name:
MMPT160
Data Collected on:
400MR-vnmrs400

B)

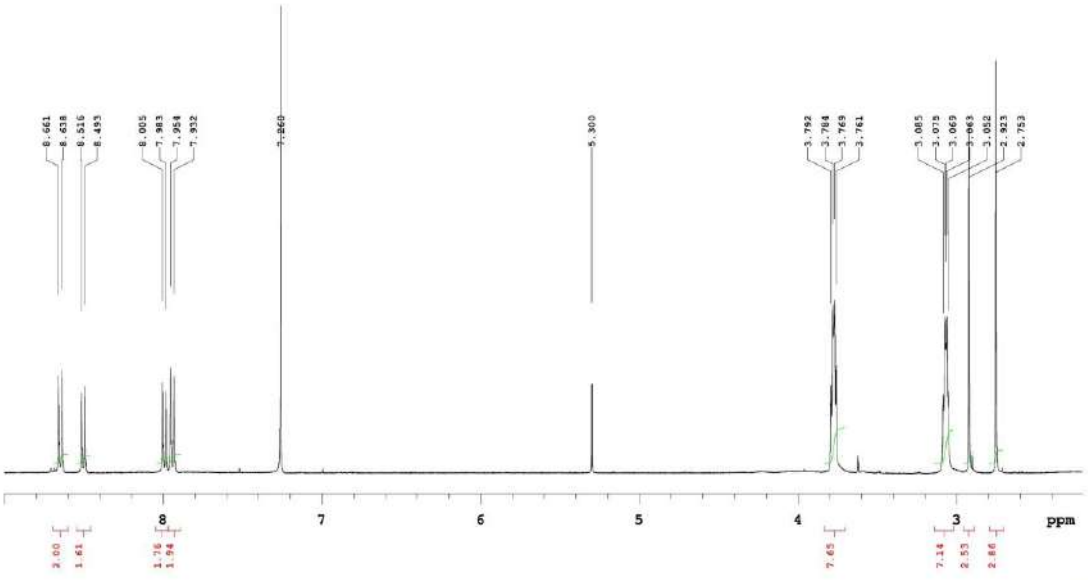

PULSE SEQUENCE
Relax. delay 0.500 sec
Pulse 48.6 degrees
Acq. time 4.797 sec
Width 6868.1 Hz
56 repetitions

OBSERVE H1, 399.5870016

DATA PROCESSING
FT size 65536
Total time 4 minutes

MMPT160_24hrs
in CDCl3

Sample Name:
MMPT160_24hrs
Data Collected on:
400MR-vnmrs400

C)

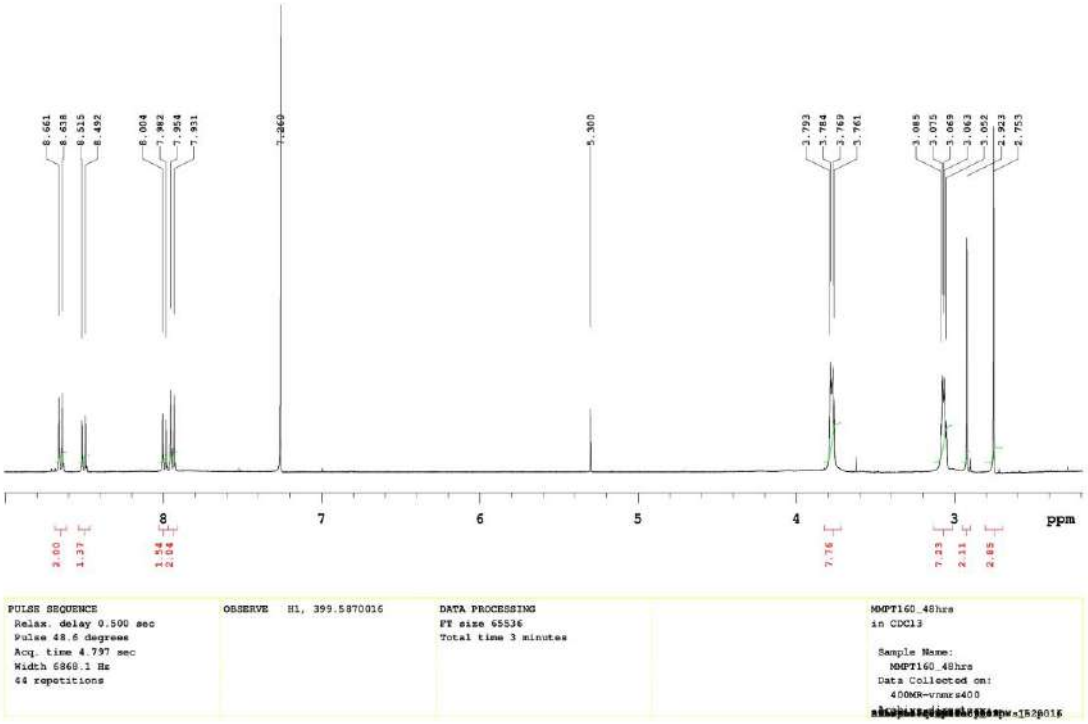

Supplementary material Figure S1: The ^{1}H NMR spectrum (**A**) recorded immediately after solution of the compound **MM134** in deuterated chloroform and repeated (**B**) after 24 h and (**C**) after 48 h.

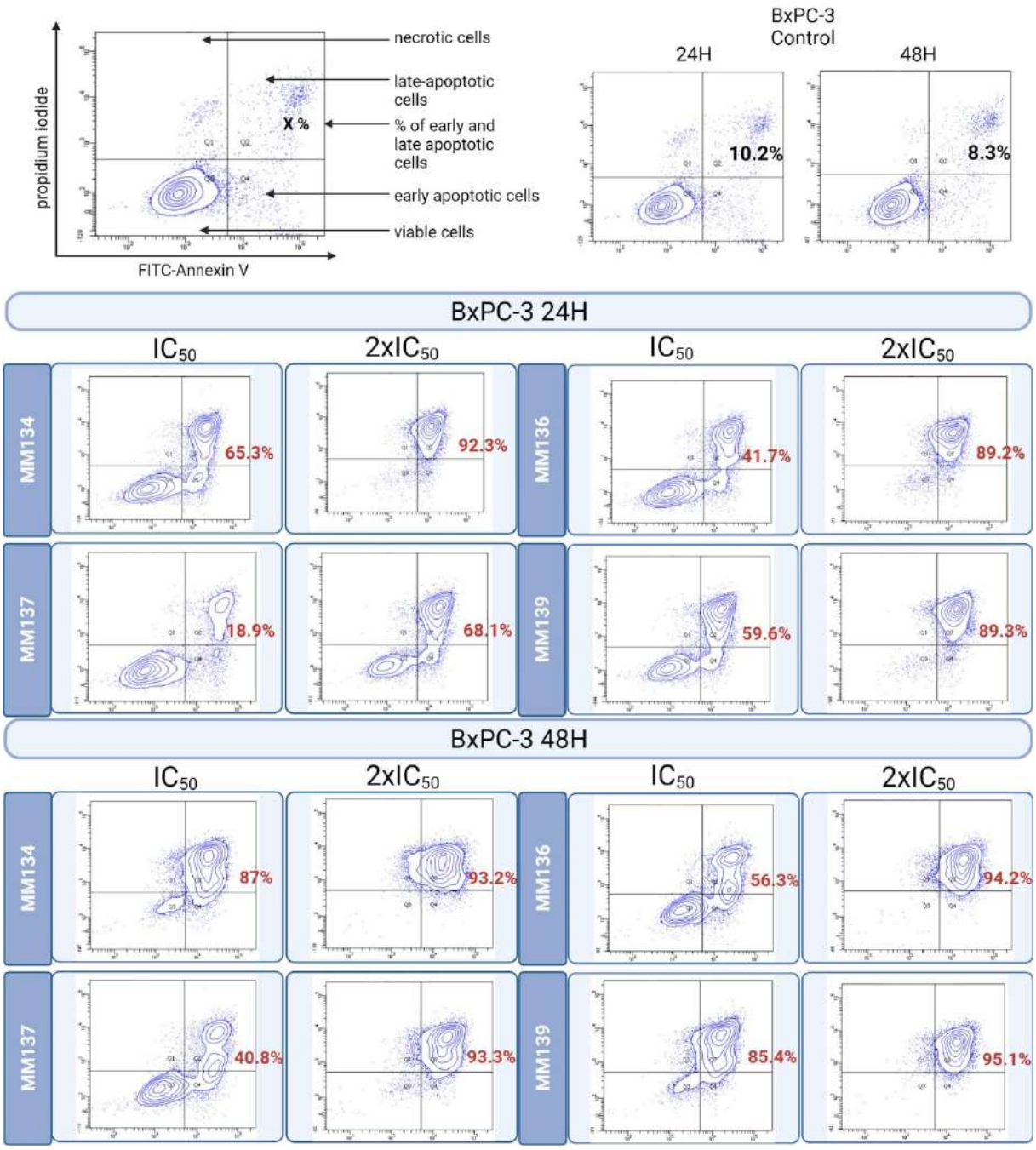

Supplementary material Figure S2: Apoptosis detection by flow cytometry with Annexin V-FITC staining in BxPC-3 cells exposed to IC_{50} and $2xIC_{50}$ concentrations of **MM134**, **-6**, **-7**, and **-9** for 24 and 48-h Left bottom square represents live cells, right bottom early apoptotic cells, the top left square necrotic cells, and top right late apoptotic cells.

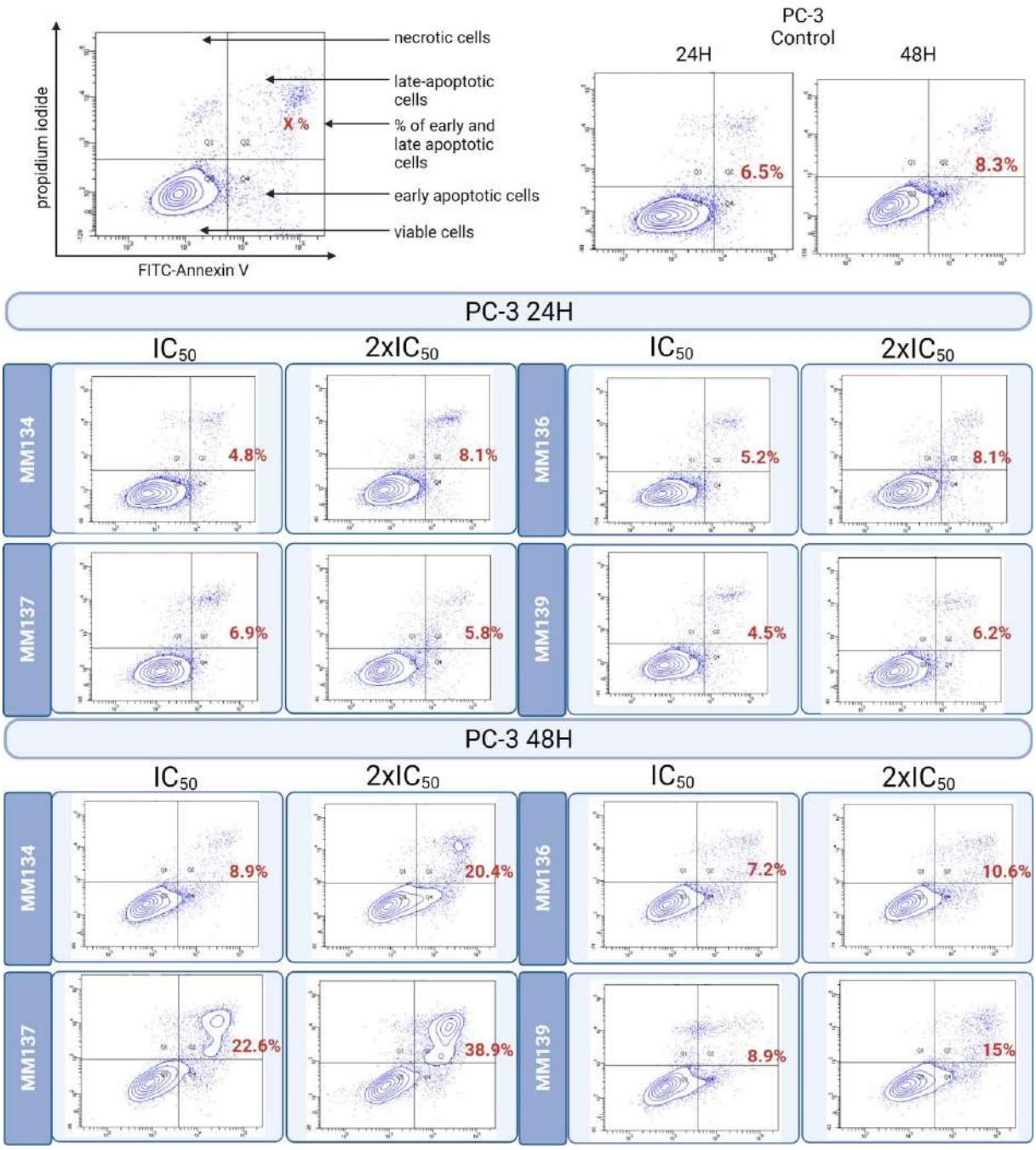

Supplementary material Figure S3: Apoptosis detection by flow cytometry with Annexin V-FITC staining in PC-3 cells exposed to IC_{50} and $2xIC_{50}$ concentrations of **MM134**, **-6**, **-7**, and **-9** for 24 and 48-h Left bottom square represents live cells, right bottom early apoptotic cells, the top left square necrotic cells, and top right late apoptotic cells.

Simulation Interactions Diagram Report

Simulation Details

Jobname: desmond_md_job_2
Entry title: Full System

CPU #	Job Type	Ensemble	Temp. [K]	Sim. Time [ns]	# Atoms	# Waters	Charge
16	mdsim	NPT	300.0	100.102	32430	9150	0

Protein Information

Tot. Residues	Prot. Chain(s)	Res. in Chain(s)	# Atoms	# Heavy Atoms	Charge
300	'A'	300	4885	2450	-2

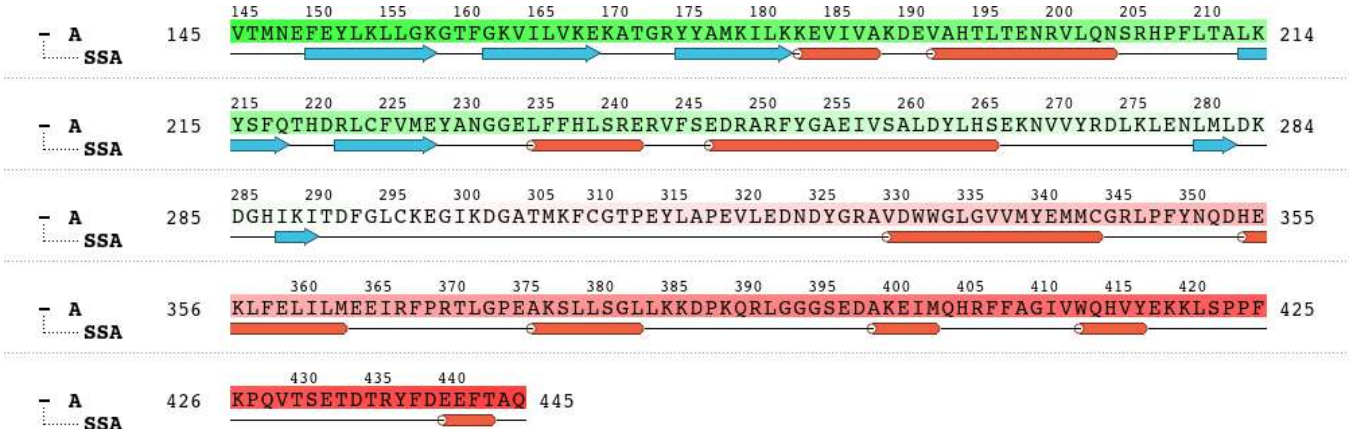

Ligand Information

SMILES	n1nnc(n2)n1nc(c23)n(nc3C)-c4ccc(cc4)S(=O)(=O)N5CCOCC5
PDB Name	'UNK'
Num. of Atoms	43 (total) 28 (heavy)
Atomic Mass	401.409 au
Charge	0
Mol. Formula	C15H15N9O3S
Num. of Fragments	2
Num. of Rot. Bonds	3

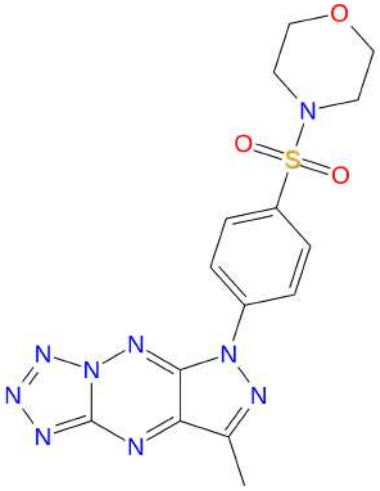

Counter Ion/Salt Information

Type	Num.	Concentration [mM]	Total Charge
Na	27	53.651	+27
Cl	25	49.677	-25

Protein-Ligand RMSD

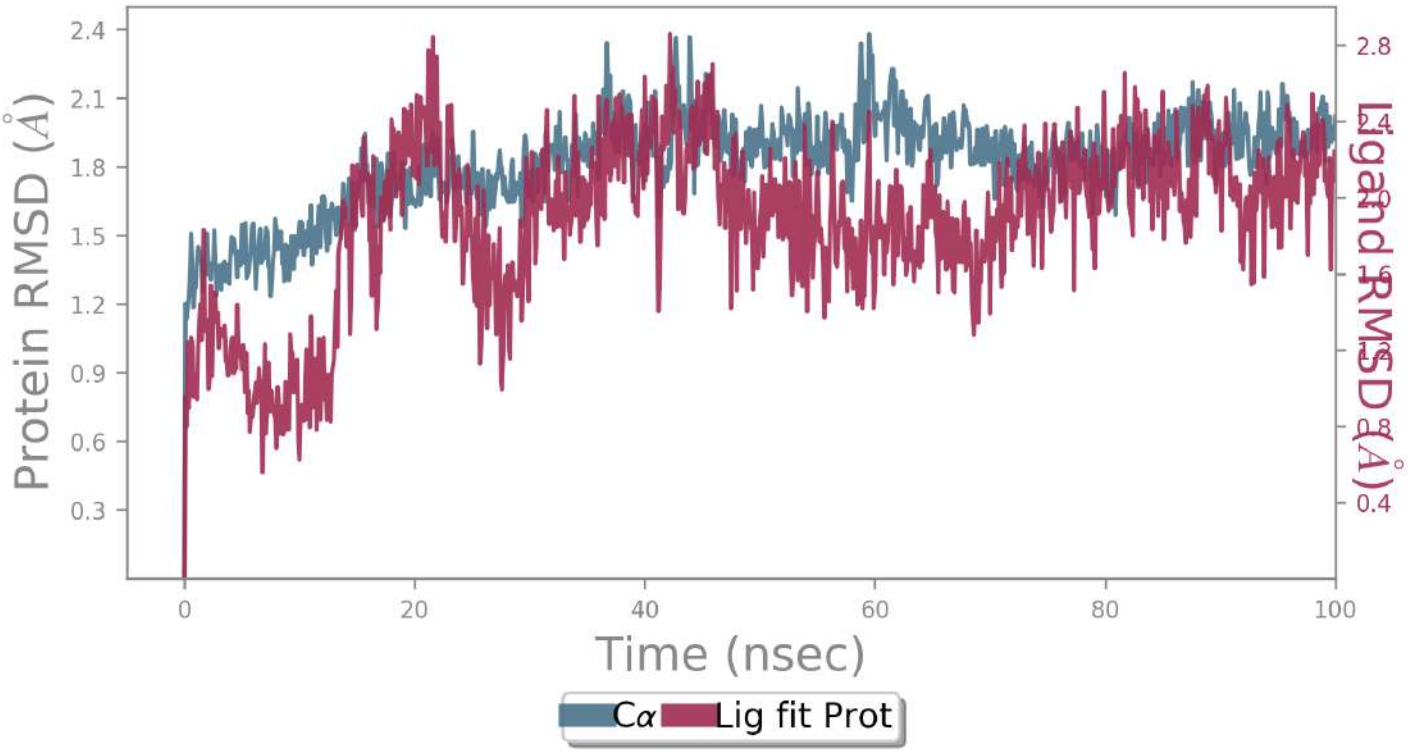

The Root Mean Square Deviation (RMSD) is used to measure the average change in displacement of a selection of atoms for a particular frame with respect to a reference frame. It is calculated for all frames in the trajectory. The RMSD for frame *x* is:

$$RMSD_x = \sqrt{\frac{1}{N}\sum_{i=1}^{N}(r_i'(t_x)) - r_i(t_{ref}))^2}$$

where *N* is the number of atoms in the atom selection; t_{ref} is the reference time, (typically the first frame is used as the reference and it is regarded as time *t*=0); and *r'* is the position of the selected atoms in frame *x* after superimposing on the reference frame, where frame *x* is recorded at time t_x. The procedure is repeated for every frame in the simulation trajectory.

Protein RMSD: The above plot shows the RMSD evolution of a protein (left *Y*-axis). All protein frames are first aligned on the reference frame backbone, and then the RMSD is calculated based on the atom selection. Monitoring the RMSD of the protein can give insights into its structural conformation throughout the simulation. RMSD analysis can indicate if the simulation has equilibrated — its fluctuations towards the end of the simulation are around some thermal average structure. Changes of the order of 1-3 Å are perfectly acceptable for small, globular proteins. Changes much larger than that, however, indicate that the protein is undergoing a large conformational change during the simulation. It is also important that your simulation converges — the RMSD values stabilize around a fixed value. If the RMSD of the protein is still increasing or decreasing on average at the end of the simulation, then your system has not equilibrated, and your simulation may not be long enough for rigorous analysis.

Ligand RMSD: Ligand RMSD (right *Y*-axis) indicates how stable the ligand is with respect to the protein and its binding pocket. In the above plot, 'Lig fit Prot' shows the RMSD of a ligand when the protein-ligand complex is first aligned on the protein backbone of the reference and then the RMSD of the ligand heavy atoms is measured. If the values observed are significantly larger than the RMSD of the protein, then it is likely that the ligand has diffused away from its initial binding site.

Protein RMSF

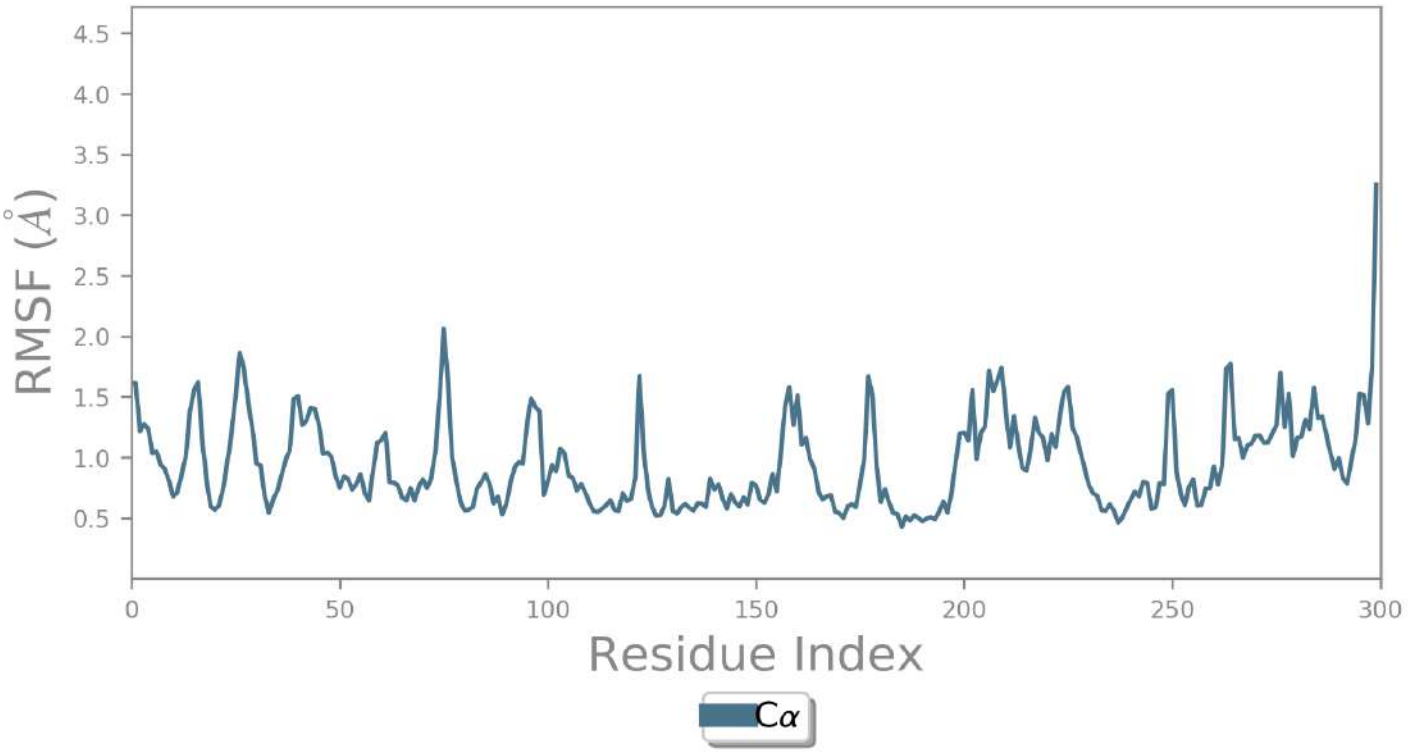

The Root Mean Square Fluctuation (RMSF) is useful for characterizing local changes along the protein chain. The RMSF for residue *i* is:

$$RMSF_i = \sqrt{\frac{1}{T}\sum_{t=1}^{T} < (r_i'(t)) - r_i(t_{ref}))^2 >}$$

where T is the trajectory time over which the RMSF is calculated, t_{ref} is the reference time, r_i is the position of residue i; r' is the position of atoms in residue i after superposition on the reference, and the angle brackets indicate that the average of the square distance is taken over the selection of atoms in the residue.

On this plot, peaks indicate areas of the protein that fluctuate the most during the simulation. Typically you will observe that the tails (*N*- and *C*-terminal) fluctuate more than any other part of the protein. Secondary structure elements like alpha helices and beta strands are usually more rigid than the unstructured part of the protein, and thus fluctuate less than the loop regions.

Protein Secondary Structure

% Helix	% Strand	% Total SSE
26.49	16.65	43.14

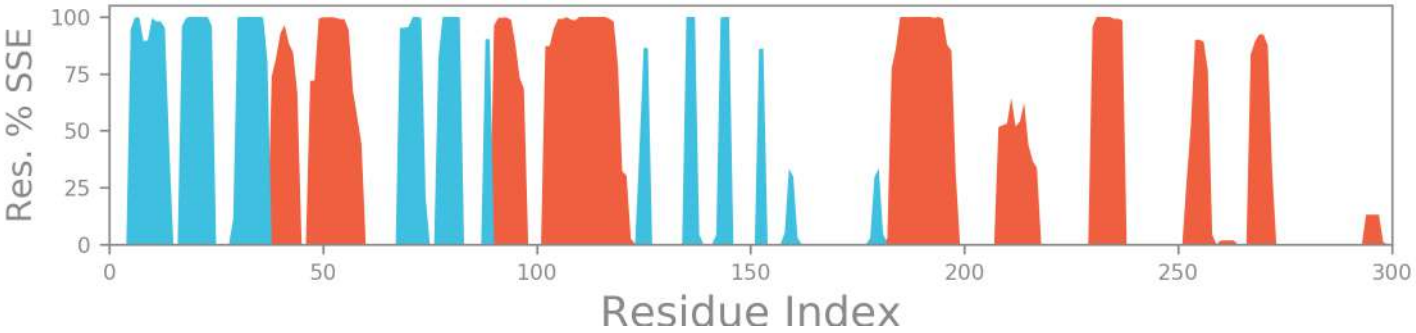

Protein secondary structure elements (SSE) like alpha-helices and beta-strands are monitored throughout the simulation. The plot above reports SSE distribution by residue index throughout the protein structure. The plot below summarizes the SSE composition for each trajectory frame over the course of the simulation, and the plot at the bottom monitors each residue and its SSE assignment over time.

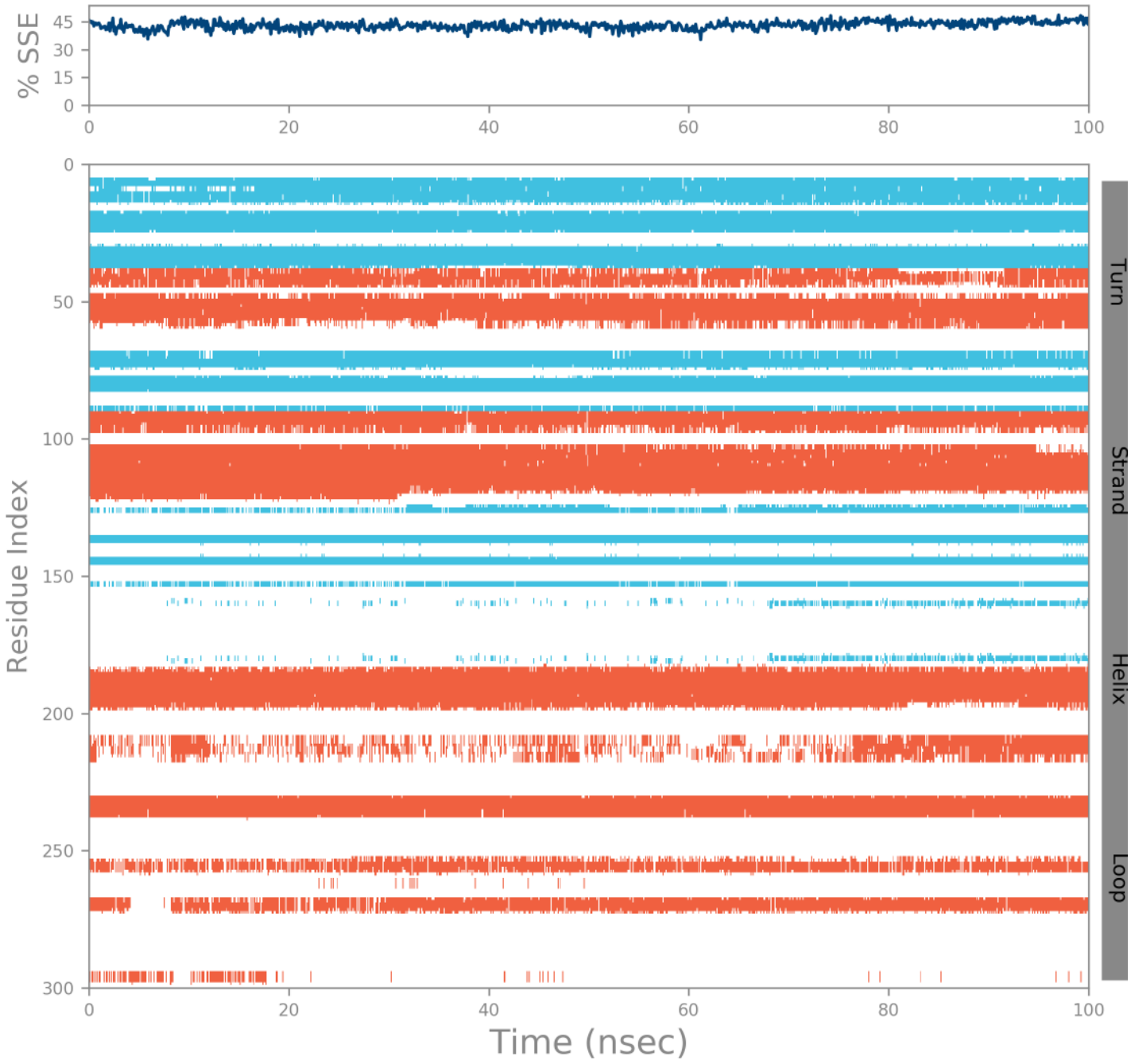
% SSE
45
30
15
0
0
20
40
60
80
100
Residue Index
0
50
100
150
200
250
300
Time (nsec)
Turn
Strand
Helix
Loop

Ligand RMSF

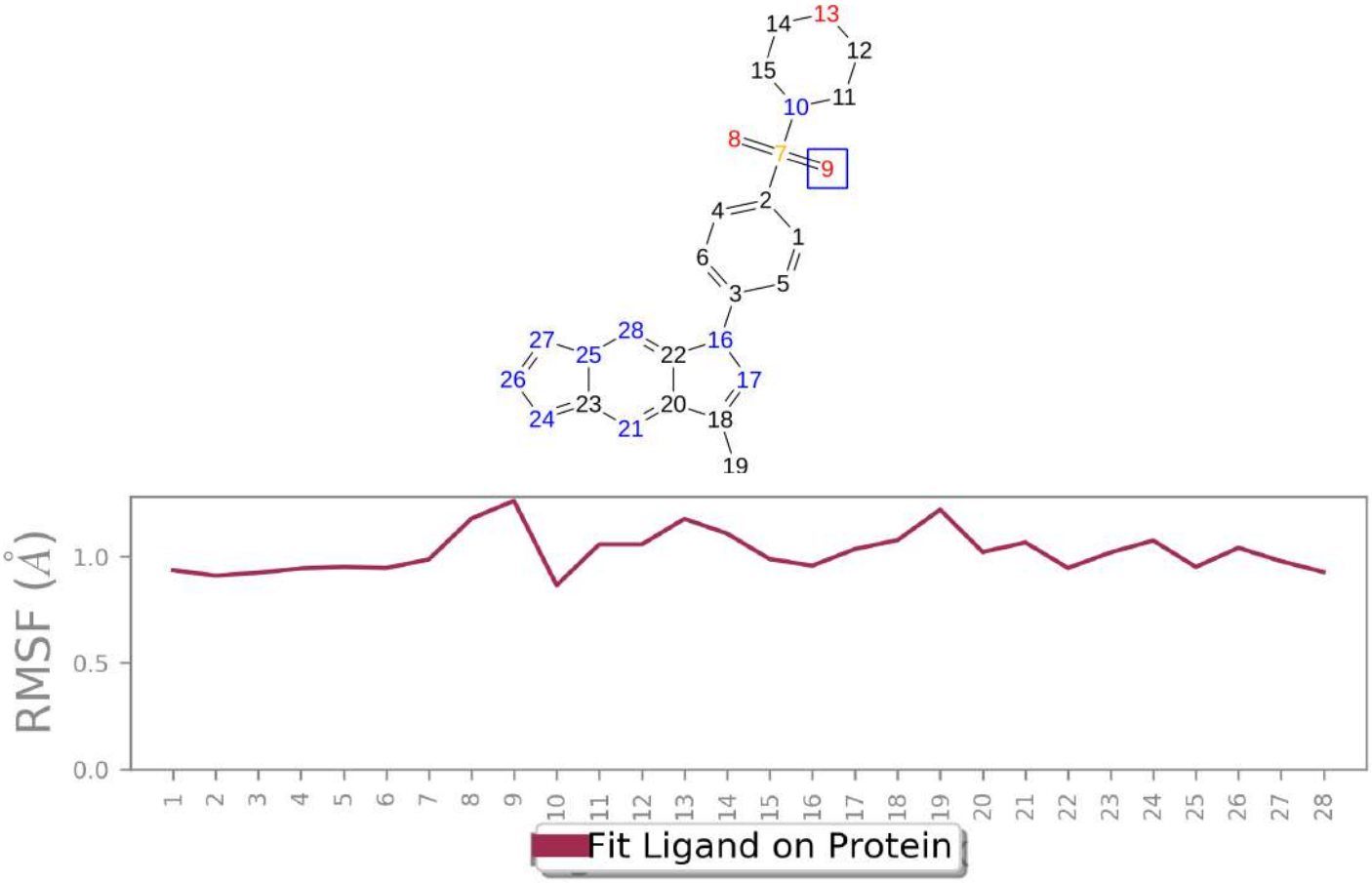

The Ligand Root Mean Square Fluctuation (L-RMSF) is useful for characterizing changes in the ligand atom positions. The RMSF for atom *i* is:

$$RMSF_i = \sqrt{\frac{1}{T}\sum_{t=1}^{T}(r_i'(t)) - r_i(t_{ref}))^2}$$

where *T* is the trajectory time over which the RMSF is calculated, t_{ref} is the reference time (usually for the first frame, and is regarded as the *zero* of time); *r* is the position of atom *i* in the reference at time t_{ref}, and *r'* is the position of atom *i* at time *t* after superposition on the reference frame.

Ligand RMSF shows the ligand's fluctuations broken down by atom, corresponding to the 2D structure in the top panel. The ligand RMSF may give you insights on how ligand fragments interact with the protein and their entropic role in the binding event. In the bottom panel, the 'Fit Ligand on Protein' line shows the ligand fluctuations, with respect to the protein. The protein-ligand complex is first aligned on the protein backbone and then the ligand RMSF is measured on the ligand heavy atoms.

Protein-Ligand Contacts

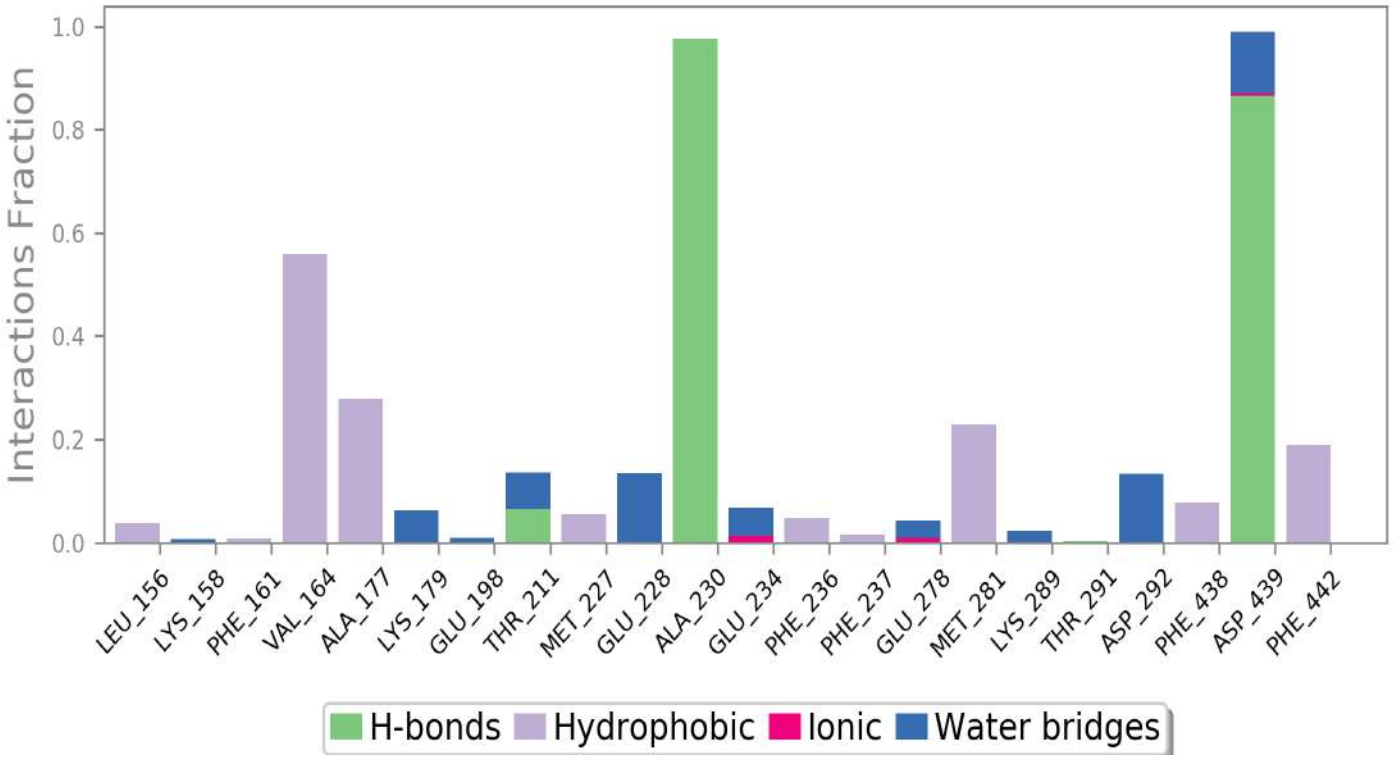

Protein interactions with the ligand can be monitored throughout the simulation. These interactions can be categorized by type and summarized, as shown in the plot above. Protein-ligand interactions (or 'contacts') are categorized into four types: Hydrogen Bonds, Hydrophobic, Ionic and Water Bridges. Each interaction type contains more specific subtypes, which can be explored through the 'Simulation Interactions Diagram' panel. The stacked bar charts are normalized over the course of the trajectory: for example, a value of 0.7 suggests that 70% of the simulation time the specific interaction is maintained. Values over 1.0 are possible as some protein residue may make multiple contacts of same subtype with the ligand.

Hydrogen Bonds: (H-bonds) play a significant role in ligand binding. Consideration of hydrogen-bonding properties in drug design is important because of their strong influence on drug specificity, metabolization and adsorption. Hydrogen bonds between a protein and a ligand can be further broken down into four subtypes: backbone acceptor; backbone donor; side-chain acceptor; side-chain donor.
The current geometric criteria for protein-ligand H-bond is: distance of 2.5 Å between the donor and acceptor atoms (D—H···A); a donor angle of ≥120° between the donor-hydrogen-acceptor atoms (D—H···A); and an acceptor angle of ≥90° between the hydrogen-acceptor-bonded_atom atoms (H···A—X).

Hydrophobic contacts: fall into three subtypes: π-Cation; π-π; and Other, non-specific interactions. Generally these type of interactions involve a hydrophobic amino acid and an aromatic or aliphatic group on the ligand, but we have extended this category to also include π-Cation interactions.
The current geometric criteria for hydrophobic interactions is as follows: π-Cation — Aromatic and charged groups within 4.5 Å; π-π — Two aromatic groups stacked face-to-face or face-to-edge; Other — A non-specific hydrophobic sidechain within 3.6 Å of a ligand's aromatic or aliphatic carbons.

Ionic interactions: or polar interactions, are between two oppositely charged atoms that are within 3.7 Å of each other and do not involve a hydrogen bond. We also monitor Protein-Metal-Ligand interactions, which are defined by a metal ion coordinated within 3.4 Å of protein's and ligand's heavy atoms (except carbon). All ionic interactions are broken down into two subtypes: those mediated by a protein backbone or side chains.

Water Bridges: are hydrogen-bonded protein-ligand interactions mediated by a water molecule. The hydrogen-bond geometry is slightly relaxed from the standard H-bond definition.
The current geometric criteria for a protein-water or water-ligand H-bond are: a distance of 2.8 Å between the donor and acceptor atoms (D—H···A); a donor angle of ≥110° between the donor-hydrogen-acceptor atoms (D—H···A); and an acceptor angle of ≥90° between the hydrogen-acceptor-bonded_atom atoms (H···A—X).

Protein-Ligand Contacts (cont.)

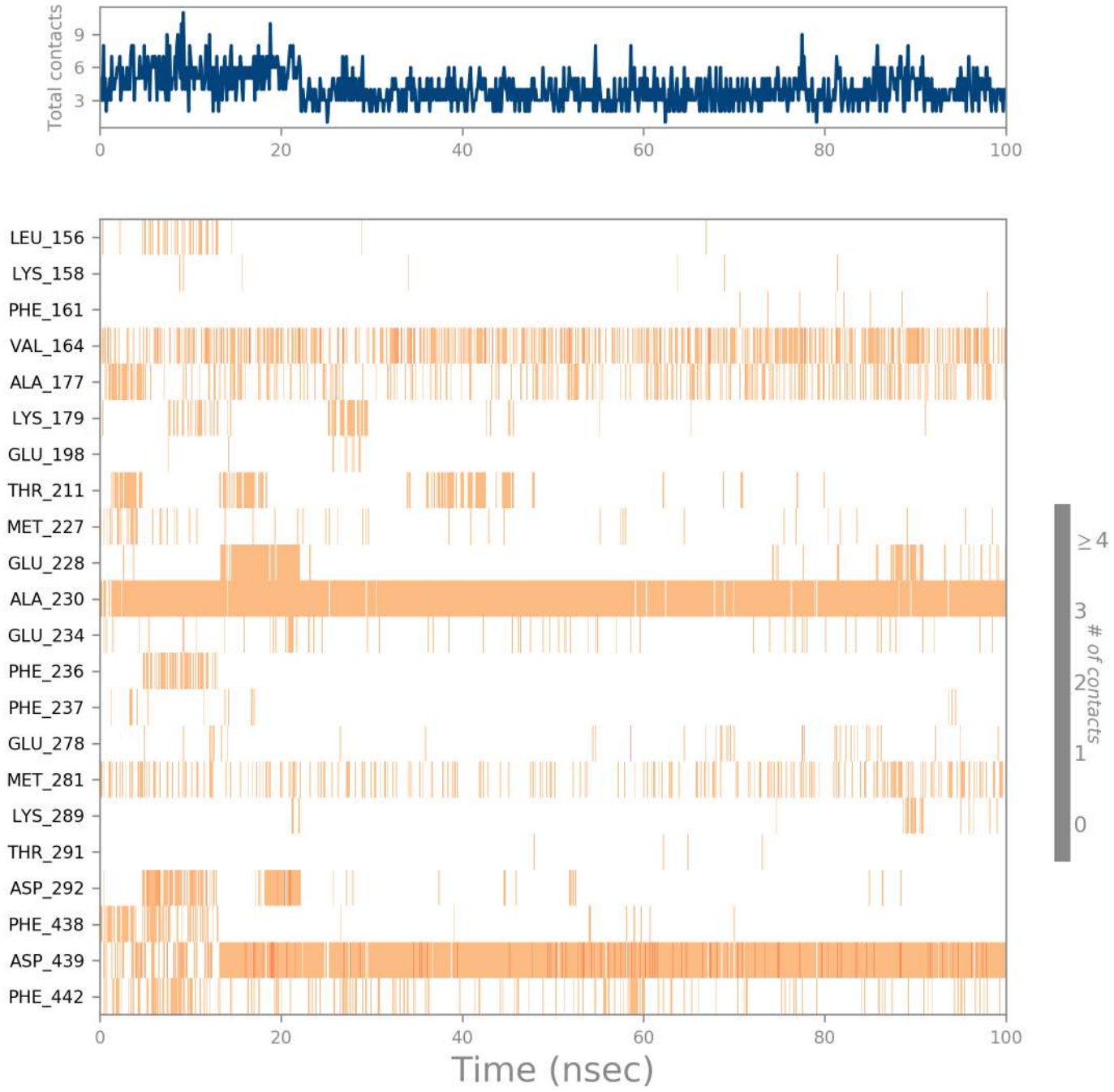

A timeline representation of the interactions and contacts (**H-bonds**, **Hydrophobic**, **Ionic**, **Water bridges**) summarized in the previous page. The top panel shows the total number of specific contacts the protein makes with the ligand over the course of the trajectory. The bottom panel shows which residues interact with the ligand in each trajectory frame. Some residues make more than one specific contact with the ligand, which is represented by a darker shade of orange, according to the scale to the right of the plot.

Ligand-Protein Contacts

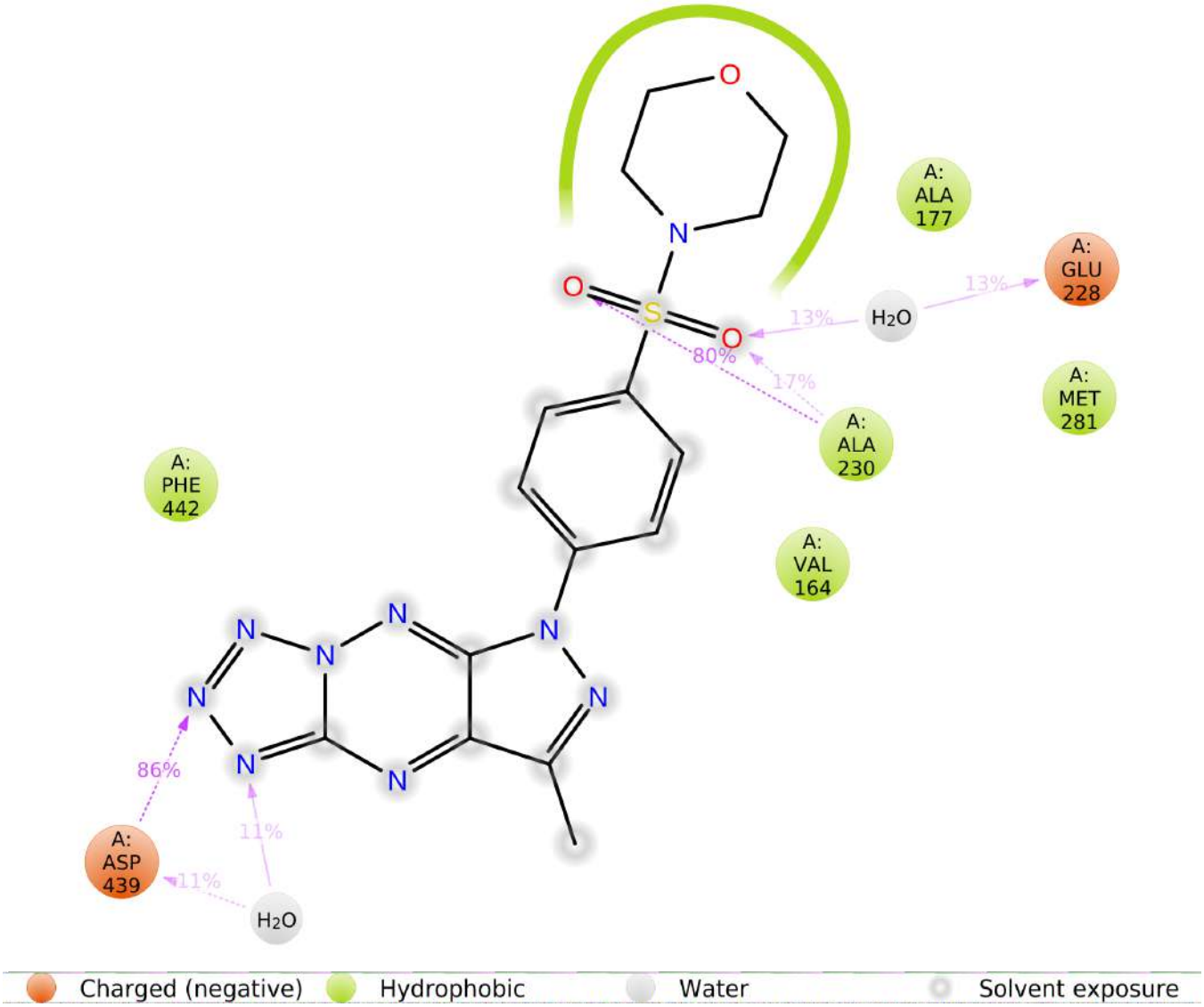

A schematic of detailed ligand atom interactions with the protein residues. Interactions that occur more than **11.0%** of the simulation time in the selected trajectory (0.00 through 100.00 nsec), are shown.
Note: it is possible to have interactions with >100% as some residues may have multiple interactions of a single type with the same ligand atom. For example, the ARG side chain has four H-bond donors that can all hydrogen-bond to a single H-bond acceptor.

Ligand Torsion Profile

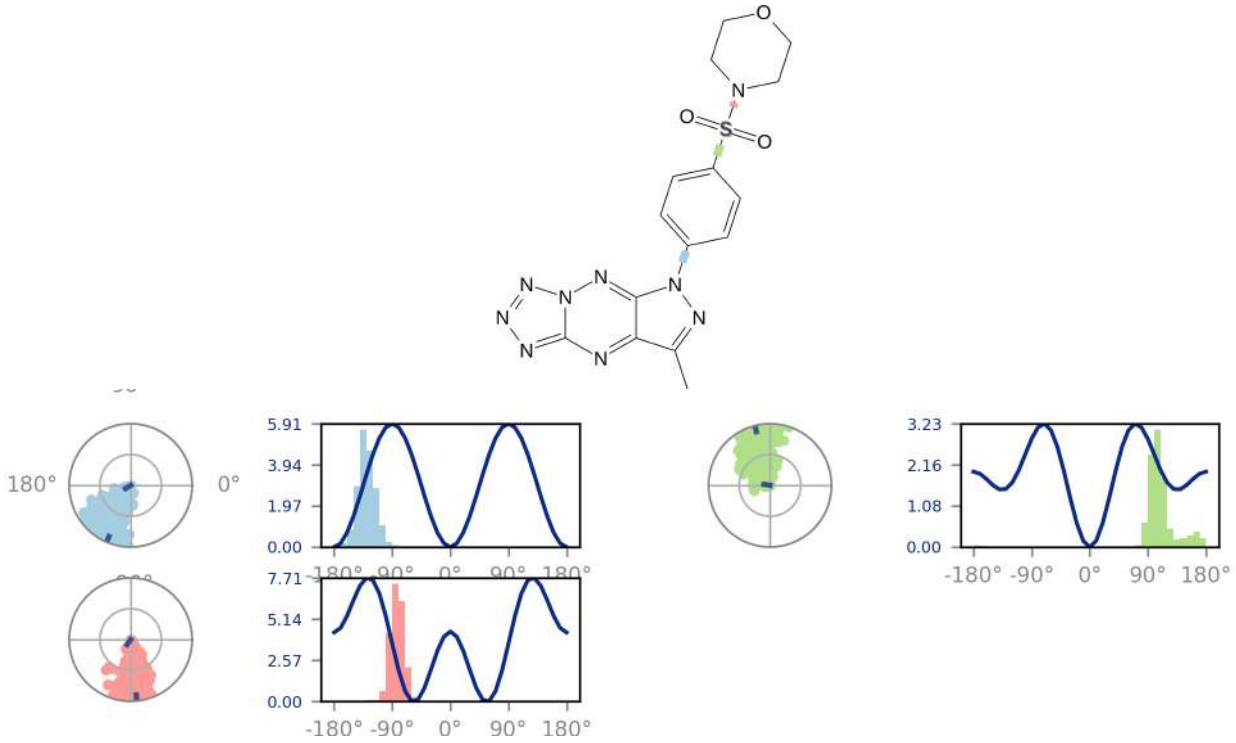

The ligand torsions plot summarizes the conformational evolution of every rotatable bond (RB) in the ligand throughout the simulation trajectory (0.00 through 100.00 nsec). The top panel shows the 2d schematic of a ligand with color-coded rotatable bonds. Each rotatable bond torsion is accompanied by a dial plot and bar plots of the same color.

Dial (or radial) plots describe the conformation of the torsion throughout the course of the simulation. The beginning of the simulation is in the center of the radial plot and the time evolution is plotted radially outwards.

The bar plots summarize the data on the dial plots, by showing the probability density of the torsion. If torsional potential information is available, the plot also shows the potential of the rotatable bond (by summing the potential of the related torsions). The values of the potential are on the left *Y*-axis of the chart, and are expressed in *kcal/mol*. Looking at the histogram and torsion potential relationships may give insights into the conformational strain the ligand undergoes to maintain a protein-bound conformation.

Ligand Properties

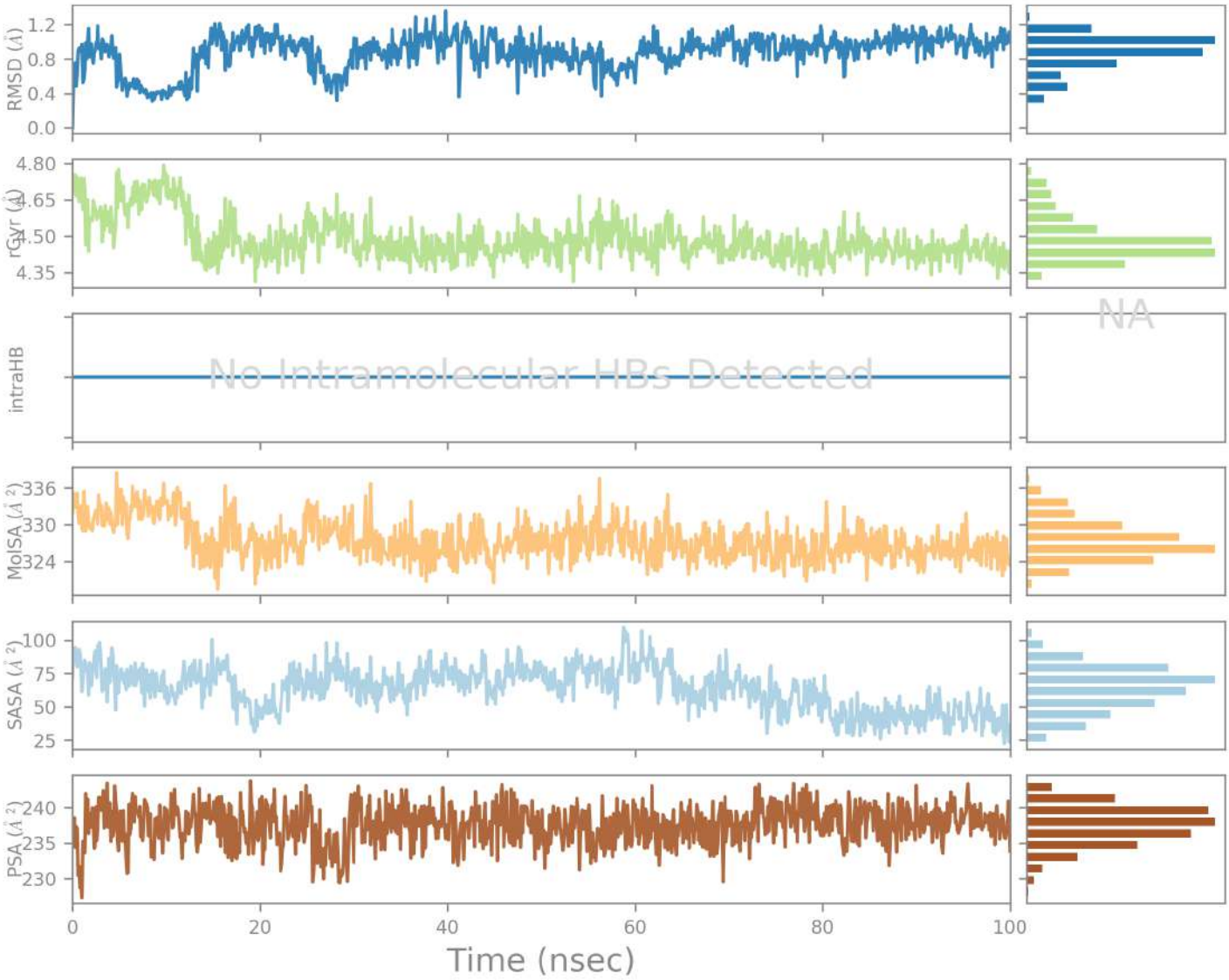

Ligand RMSD: Root mean square deviation of a ligand with respect to the reference conformation (typically the first frame is used as the reference and it is regarded as time *t*=0).

Radius of Gyration (rGyr): Measures the 'extendedness' of a ligand, and is equivalent to its principal moment of inertia.

Intramolecular Hydrogen Bonds (intraHB): Number of internal hydrogen bonds (HB) within a ligand molecule.

Molecular Surface Area (MolSA): Molecular surface calculation with 1.4 Å probe radius. This value is equivalent to a van der Waals surface area.

Solvent Accessible Surface Area (SASA): Surface area of a molecule accessible by a water molecule.

Polar Surface Area (PSA): Solvent accessible surface area in a molecule contributed only by oxygen and nitrogen atoms.

Simulation Interactions Diagram Report

Simulation Details

Jobname: desmond_md_job_2
Entry title: XXXX - hbond-opt

CPU #	Job Type	Ensemble	Temp. [K]	Sim. Time [ns]	# Atoms	# Waters	Charge
1	mdsim	NPT	300.0	100.102	34595	10232	0

Protein Information

Tot. Residues	Prot. Chain(s)	Res. in Chain(s)	# Atoms	# Heavy Atoms	Charge
249	'A', 'B'	ict_values([126, 123]	3791	1906	-7

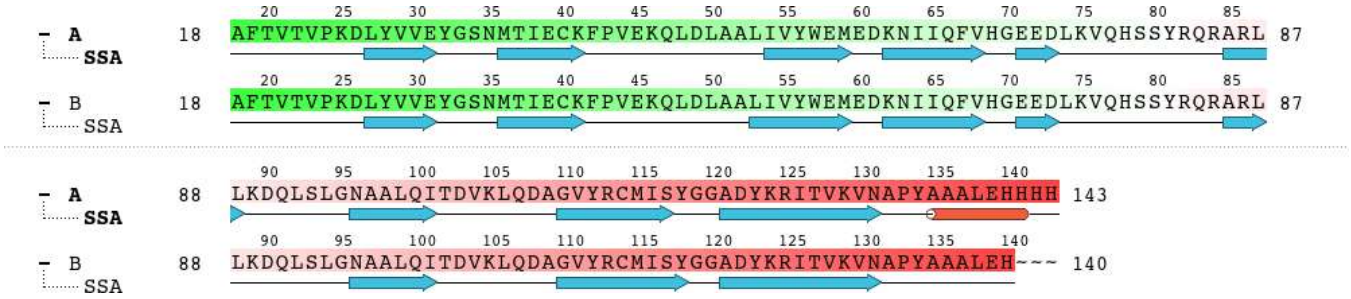

Ligand Information

SMILES	n1nnc(n2)n1nc(c23)n(nc3C)-c4ccc(cc4)S(=O)(=O)N5CCOCC5
PDB Name	'UNK'
Num. of Atoms	43 (total) 28 (heavy)
Atomic Mass	401.409 au
Charge	0
Mol. Formula	C15H15N9O3S
Num. of Fragments	2
Num. of Rot. Bonds	3

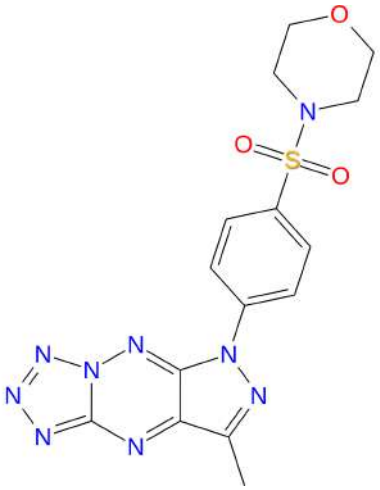

Counter Ion/Salt Information

Type	Num.	Concentration [mM]	Total Charge
Na	36	63.970	+36
Cl	29	51.532	-29

Protein-Ligand RMSD

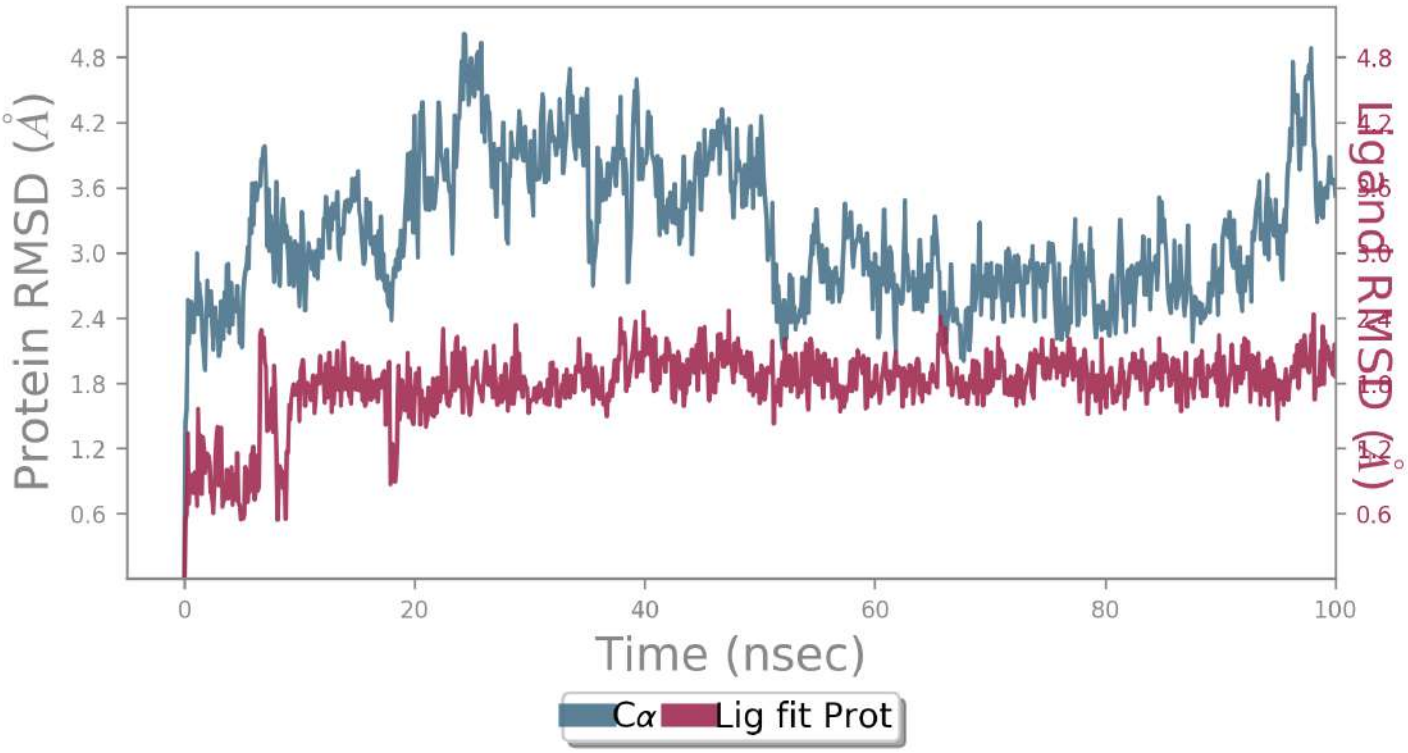

The Root Mean Square Deviation (RMSD) is used to measure the average change in displacement of a selection of atoms for a particular frame with respect to a reference frame. It is calculated for all frames in the trajectory. The RMSD for frame *x* is:

$$RMSD_x = \sqrt{\frac{1}{N}\sum_{i=1}^{N}(r_i'(t_x)) - r_i(t_{ref}))^2}$$

where *N* is the number of atoms in the atom selection; t_{ref} is the reference time, (typically the first frame is used as the reference and it is regarded as time *t*=0); and *r'* is the position of the selected atoms in frame *x* after superimposing on the reference frame, where frame *x* is recorded at time t_x. The procedure is repeated for every frame in the simulation trajectory.

Protein RMSD: The above plot shows the RMSD evolution of a protein (left *Y*-axis). All protein frames are first aligned on the reference frame backbone, and then the RMSD is calculated based on the atom selection. Monitoring the RMSD of the protein can give insights into its structural conformation throughout the simulation. RMSD analysis can indicate if the simulation has equilibrated — its fluctuations towards the end of the simulation are around some thermal average structure. Changes of the order of 1-3 Å are perfectly acceptable for small, globular proteins. Changes much larger than that, however, indicate that the protein is undergoing a large conformational change during the simulation. It is also important that your simulation converges — the RMSD values stabilize around a fixed value. If the RMSD of the protein is still increasing or decreasing on average at the end of the simulation, then your system has not equilibrated, and your simulation may not be long enough for rigorous analysis.

Ligand RMSD: Ligand RMSD (right *Y*-axis) indicates how stable the ligand is with respect to the protein and its binding pocket. In the above plot, 'Lig fit Prot' shows the RMSD of a ligand when the protein-ligand complex is first aligned on the protein backbone of the reference and then the RMSD of the ligand heavy atoms is measured. If the values observed are significantly larger than the RMSD of the protein, then it is likely that the ligand has diffused away from its initial binding site.

Protein RMSF

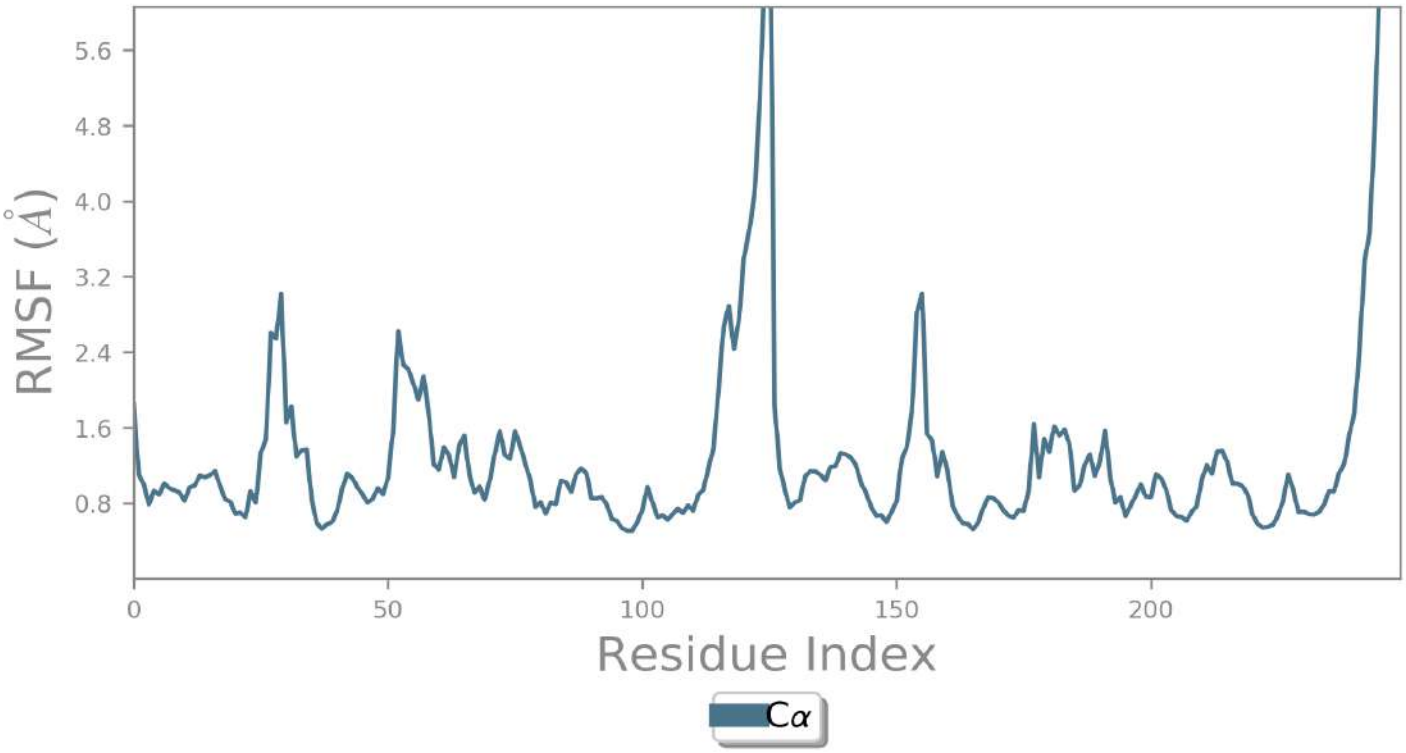

The Root Mean Square Fluctuation (RMSF) is useful for characterizing local changes along the protein chain. The RMSF for residue *i* is:

$$RMSF_i = \sqrt{\frac{1}{T}\sum_{t=1}^{T} < (r_i'(t)) - r_i(t_{ref}))^2 >}$$

where *T* is the trajectory time over which the RMSF is calculated, t_{ref} is the reference time, r_i is the position of residue *i*; *r'* is the position of atoms in residue *i* after superposition on the reference, and the angle brackets indicate that the average of the square distance is taken over the selection of atoms in the residue.

On this plot, peaks indicate areas of the protein that fluctuate the most during the simulation. Typically you will observe that the tails (*N*- and *C*-terminal) fluctuate more than any other part of the protein. Secondary structure elements like alpha helices and beta strands are usually more rigid than the unstructured part of the protein, and thus fluctuate less than the loop regions.

Protein Secondary Structure

% Helix	% Strand	% Total SSE
1.91	38.85	40.76

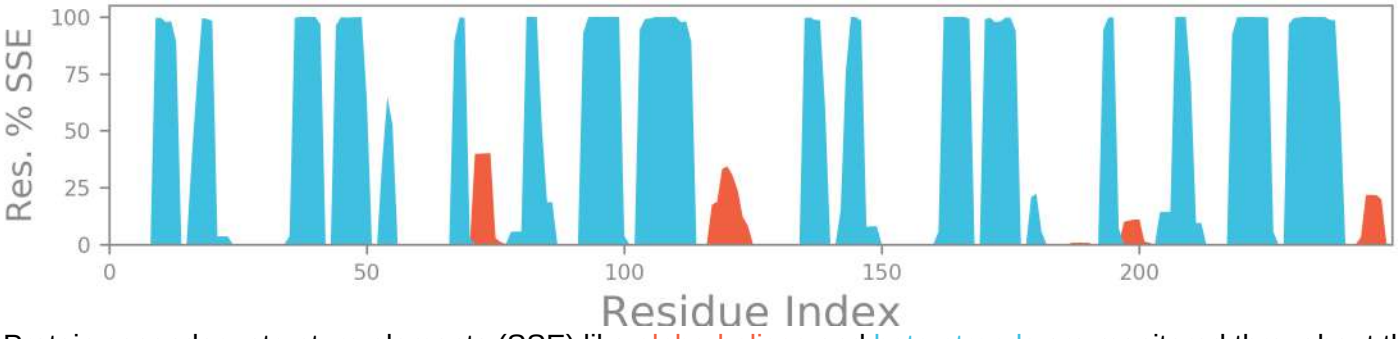

Protein secondary structure elements (SSE) like alpha-helices and beta-strands are monitored throughout the simulation. The plot above reports SSE distribution by residue index throughout the protein structure. The plot below summarizes the SSE composition for each trajectory frame over the course of the simulation, and the plot at the bottom monitors each residue and its SSE assignment over time.

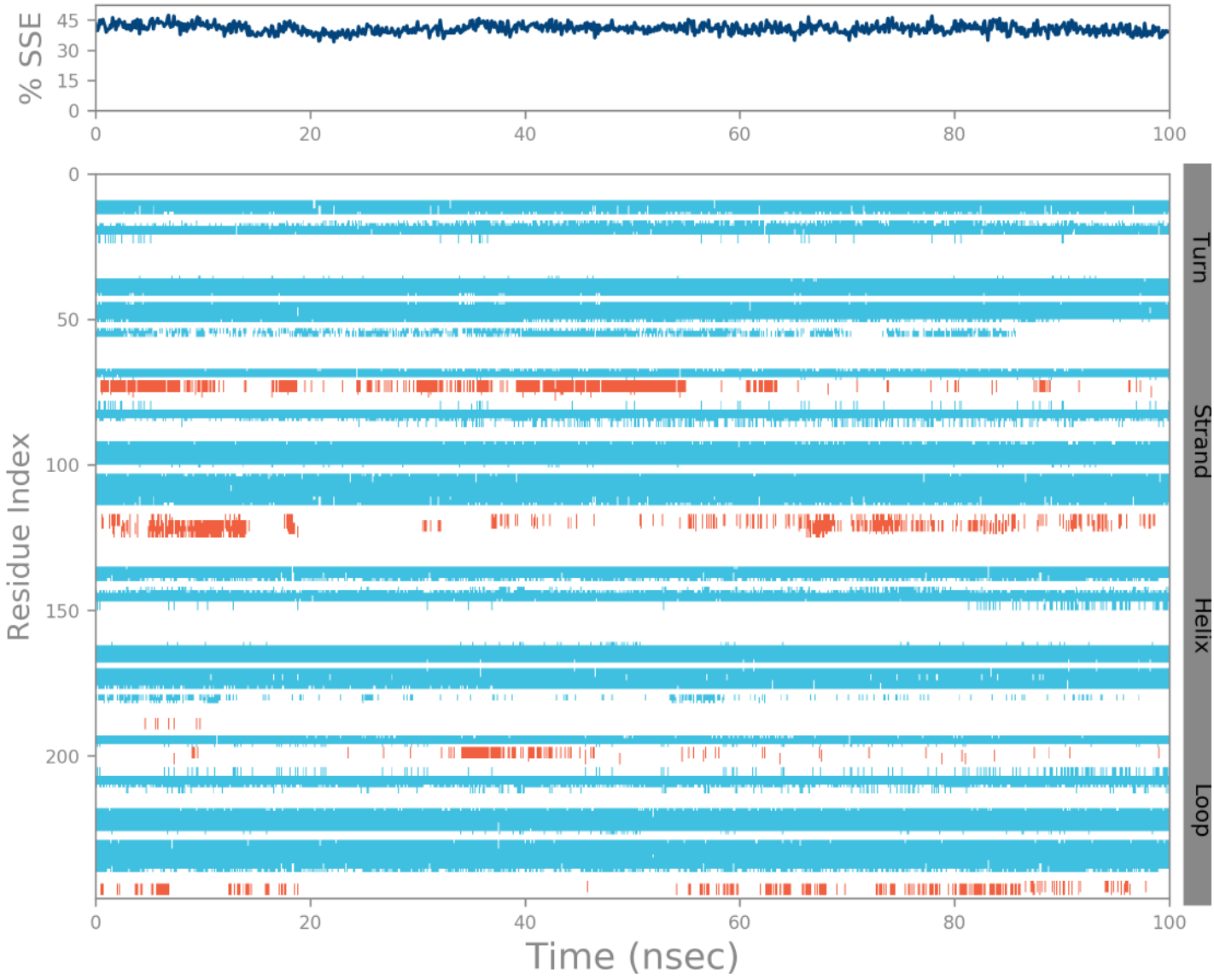

Ligand RMSF

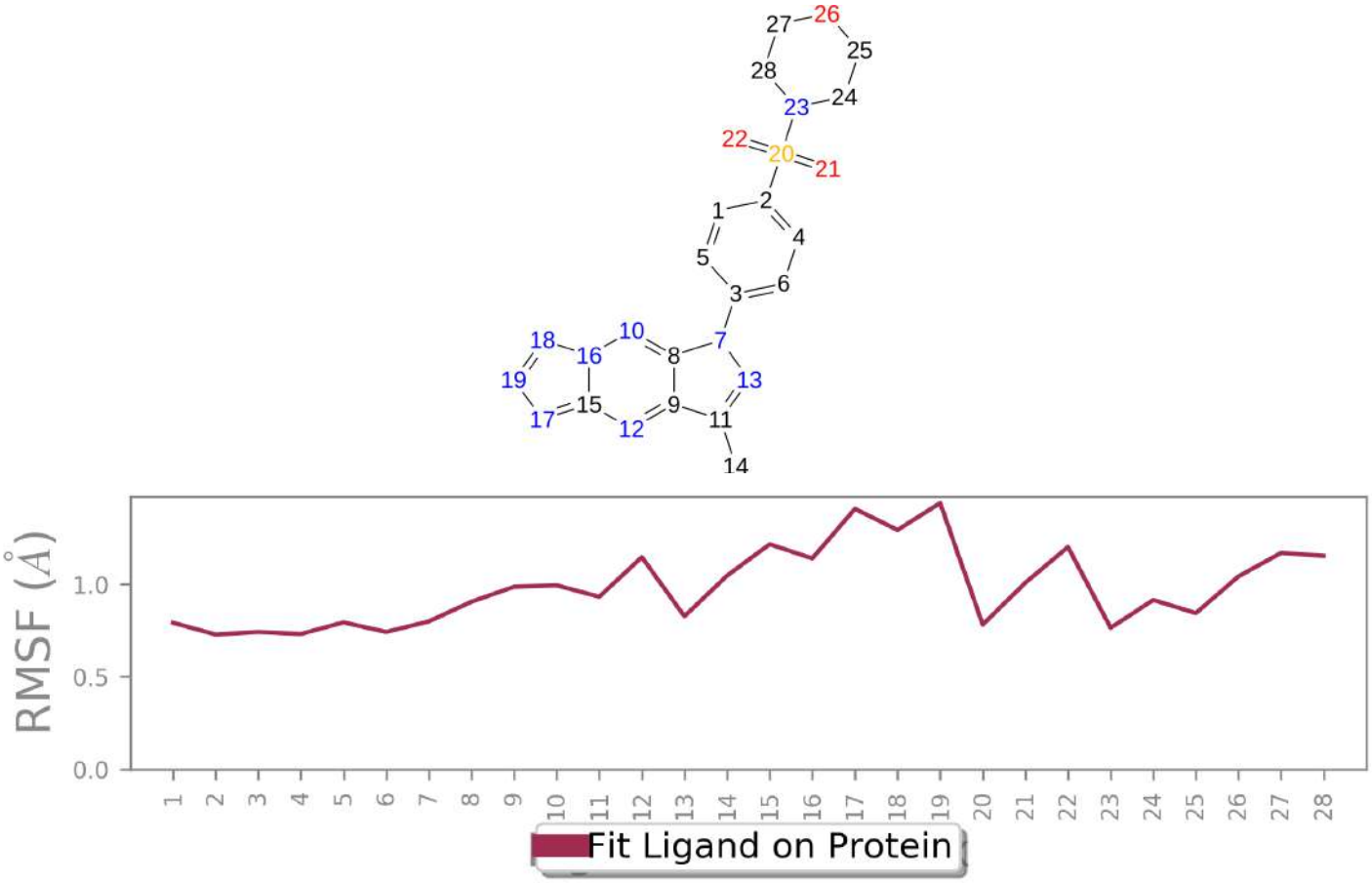

The Ligand Root Mean Square Fluctuation (L-RMSF) is useful for characterizing changes in the ligand atom positions. The RMSF for atom *i* is:

$$RMSF_i = \sqrt{\frac{1}{T}\sum_{t=1}^{T}(r_i'(t)) - r_i(t_{ref}))^2}$$

where *T* is the trajectory time over which the RMSF is calculated, t_{ref} is the reference time (usually for the first frame, and is regarded as the *zero* of time); *r* is the position of atom *i* in the reference at time t_{ref}, and *r'* is the position of atom *i* at time *t* after superposition on the reference frame.

Ligand RMSF shows the ligand's fluctuations broken down by atom, corresponding to the 2D structure in the top panel. The ligand RMSF may give you insights on how ligand fragments interact with the protein and their entropic role in the binding event. In the bottom panel, the 'Fit Ligand on Protein' line shows the ligand fluctuations, with respect to the protein. The protein-ligand complex is first aligned on the protein backbone and then the ligand RMSF is measured on the ligand heavy atoms.

Protein-Ligand Contacts

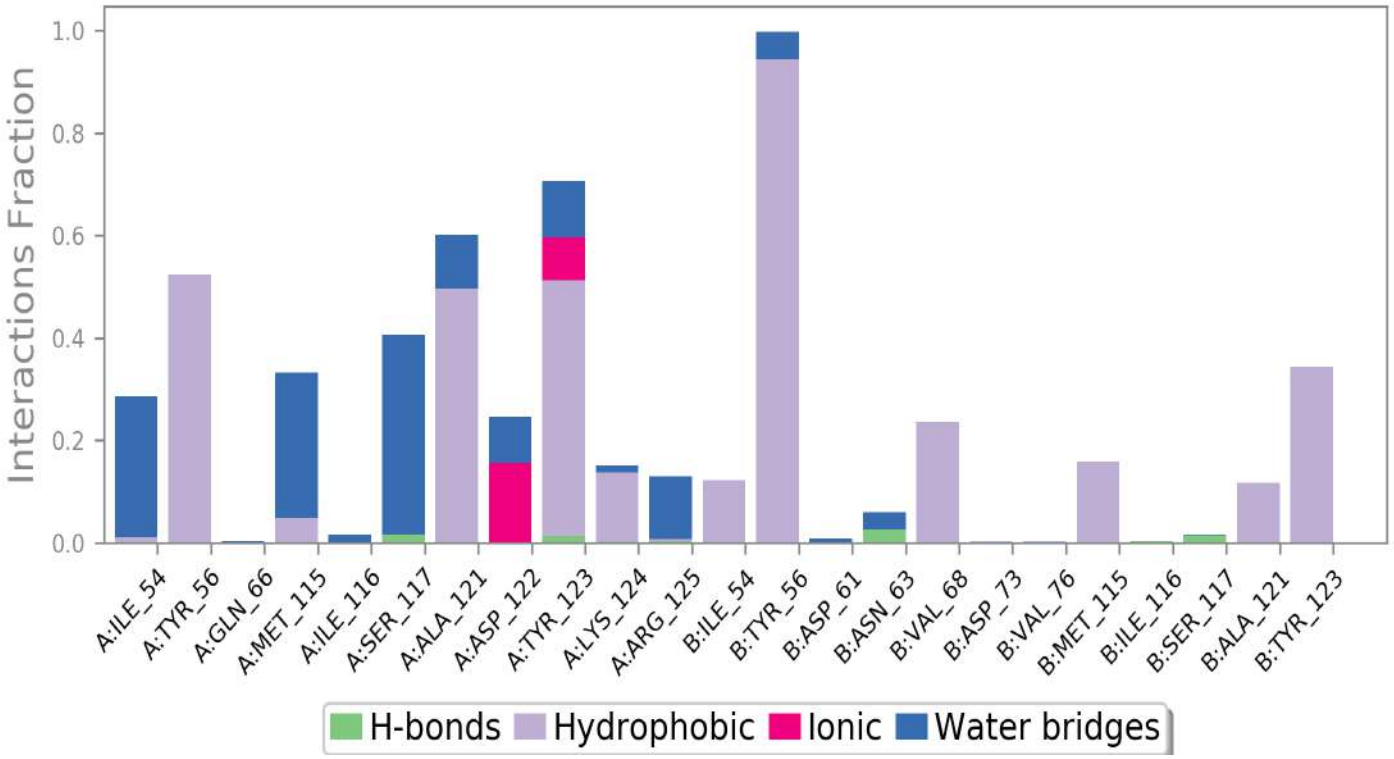

Protein interactions with the ligand can be monitored throughout the simulation. These interactions can be categorized by type and summarized, as shown in the plot above. Protein-ligand interactions (or 'contacts') are categorized into four types: Hydrogen Bonds, Hydrophobic, Ionic and Water Bridges. Each interaction type contains more specific subtypes, which can be explored through the 'Simulation Interactions Diagram' panel. The stacked bar charts are normalized over the course of the trajectory: for example, a value of 0.7 suggests that 70% of the simulation time the specific interaction is maintained. Values over 1.0 are possible as some protein residue may make multiple contacts of same subtype with the ligand.

Hydrogen Bonds: (H-bonds) play a significant role in ligand binding. Consideration of hydrogen-bonding properties in drug design is important because of their strong influence on drug specificity, metabolization and adsorption. Hydrogen bonds between a protein and a ligand can be further broken down into four subtypes: backbone acceptor; backbone donor; side-chain acceptor; side-chain donor.
The current geometric criteria for protein-ligand H-bond is: distance of 2.5 Å between the donor and acceptor atoms (D—H···A); a donor angle of ≥120° between the donor-hydrogen-acceptor atoms (D—H···A); and an acceptor angle of ≥90° between the hydrogen-acceptor-bonded_atom atoms (H···A—X).

Hydrophobic contacts: fall into three subtypes: π-Cation; π-π; and Other, non-specific interactions. Generally these type of interactions involve a hydrophobic amino acid and an aromatic or aliphatic group on the ligand, but we have extended this category to also include π-Cation interactions.
The current geometric criteria for hydrophobic interactions is as follows: π-Cation — Aromatic and charged groups within 4.5 Å; π-π — Two aromatic groups stacked face-to-face or face-to-edge; Other — A non-specific hydrophobic sidechain within 3.6 Å of a ligand's aromatic or aliphatic carbons.

Ionic interactions: or polar interactions, are between two oppositely charged atoms that are within 3.7 Å of each other and do not involve a hydrogen bond. We also monitor Protein-Metal-Ligand interactions, which are defined by a metal ion coordinated within 3.4 Å of protein's and ligand's heavy atoms (except carbon). All ionic interactions are broken down into two subtypes: those mediated by a protein backbone or side chains.

Water Bridges: are hydrogen-bonded protein-ligand interactions mediated by a water molecule. The hydrogen-bond geometry is slightly relaxed from the standard H-bond definition.
The current geometric criteria for a protein-water or water-ligand H-bond are: a distance of 2.8 Å between the donor and acceptor atoms (D—H···A); a donor angle of ≥110° between the donor-hydrogen-acceptor atoms (D—H···A); and an acceptor angle of ≥90° between the hydrogen-acceptor-bonded_atom atoms (H···A—X).

Protein-Ligand Contacts (cont.)

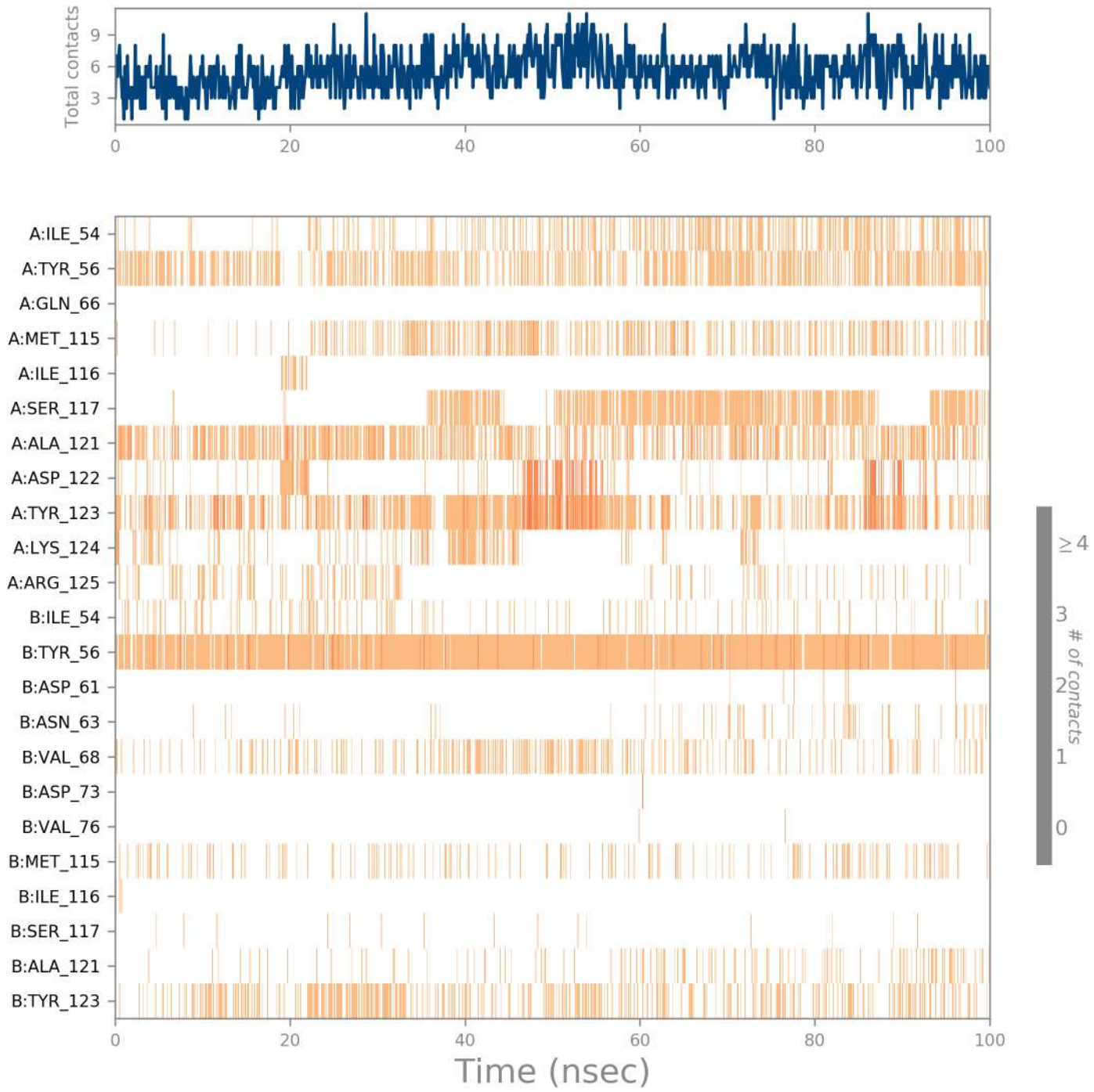

A timeline representation of the interactions and contacts (**H-bonds**, **Hydrophobic**, **Ionic**, **Water bridges**) summarized in the previous page. The top panel shows the total number of specific contacts the protein makes with the ligand over the course of the trajectory. The bottom panel shows which residues interact with the ligand in each trajectory frame. Some residues make more than one specific contact with the ligand, which is represented by a darker shade of orange, according to the scale to the right of the plot.

Ligand-Protein Contacts

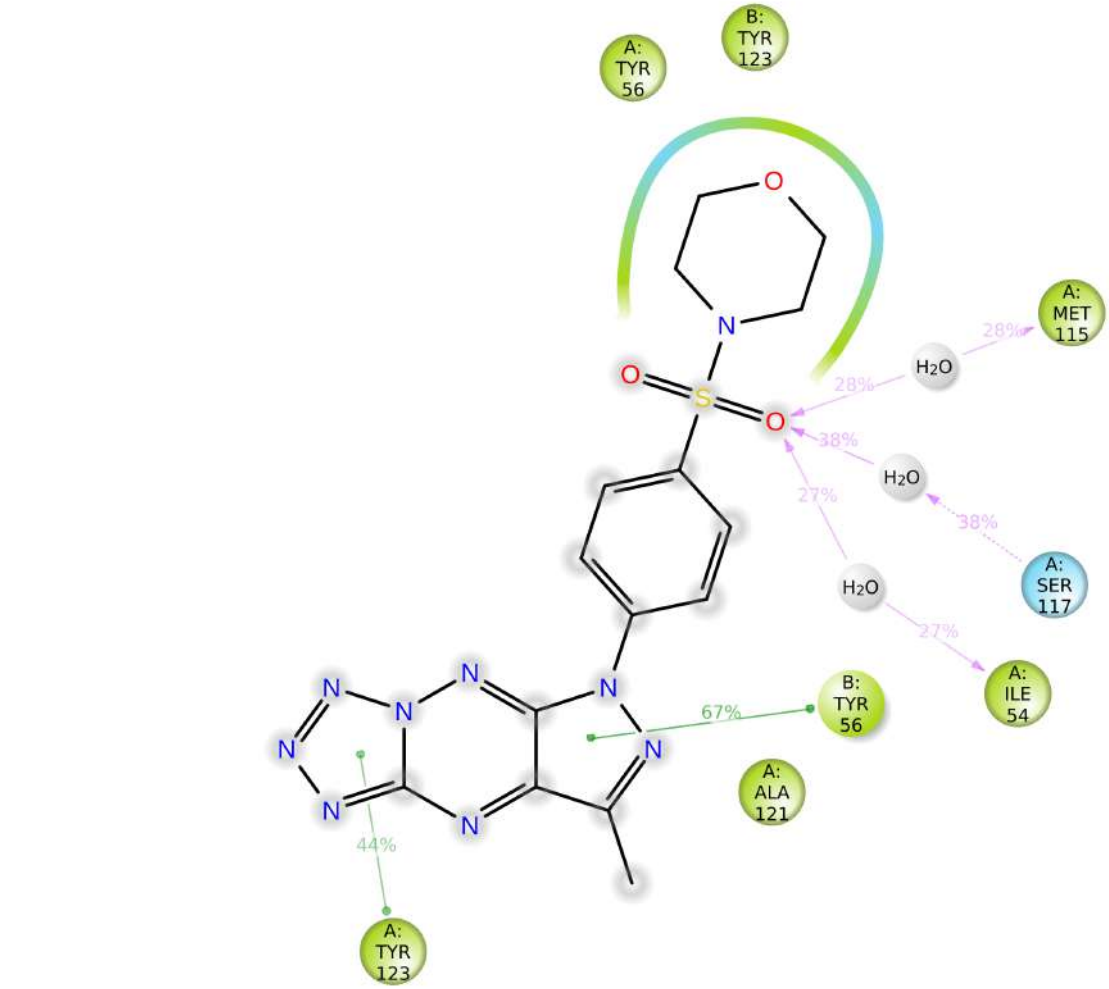

Hydrophobic
Polar
Water
Pi-Pi stacking
Solvent exposure

A schematic of detailed ligand atom interactions with the protein residues. Interactions that occur more than **25.0%** of the simulation time in the selected trajectory (0.00 through 100.00 nsec), are shown.
Note: it is possible to have interactions with >100% as some residues may have multiple interactions of a single type with the same ligand atom. For example, the ARG side chain has four H-bond donors that can all hydrogen-bond to a single H-bond acceptor.

Ligand Torsion Profile

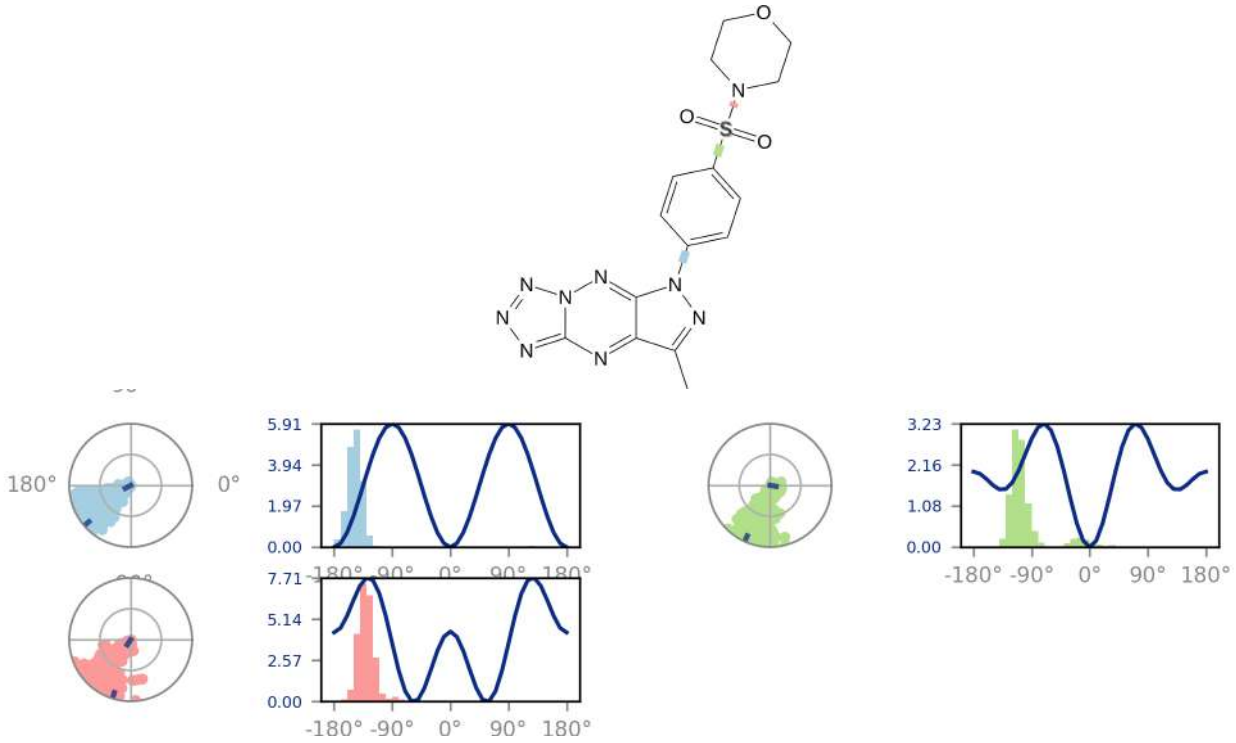

The ligand torsions plot summarizes the conformational evolution of every rotatable bond (RB) in the ligand throughout the simulation trajectory (0.00 through 100.00 nsec). The top panel shows the 2d schematic of a ligand with color-coded rotatable bonds. Each rotatable bond torsion is accompanied by a dial plot and bar plots of the same color.

Dial (or radial) plots describe the conformation of the torsion throughout the course of the simulation. The beginning of the simulation is in the center of the radial plot and the time evolution is plotted radially outwards.

The bar plots summarize the data on the dial plots, by showing the probability density of the torsion. If torsional potential information is available, the plot also shows the potential of the rotatable bond (by summing the potential of the related torsions). The values of the potential are on the left *Y*-axis of the chart, and are expressed in *kcal/mol*. Looking at the histogram and torsion potential relationships may give insights into the conformational strain the ligand undergoes to maintain a protein-bound conformation.

Ligand Properties

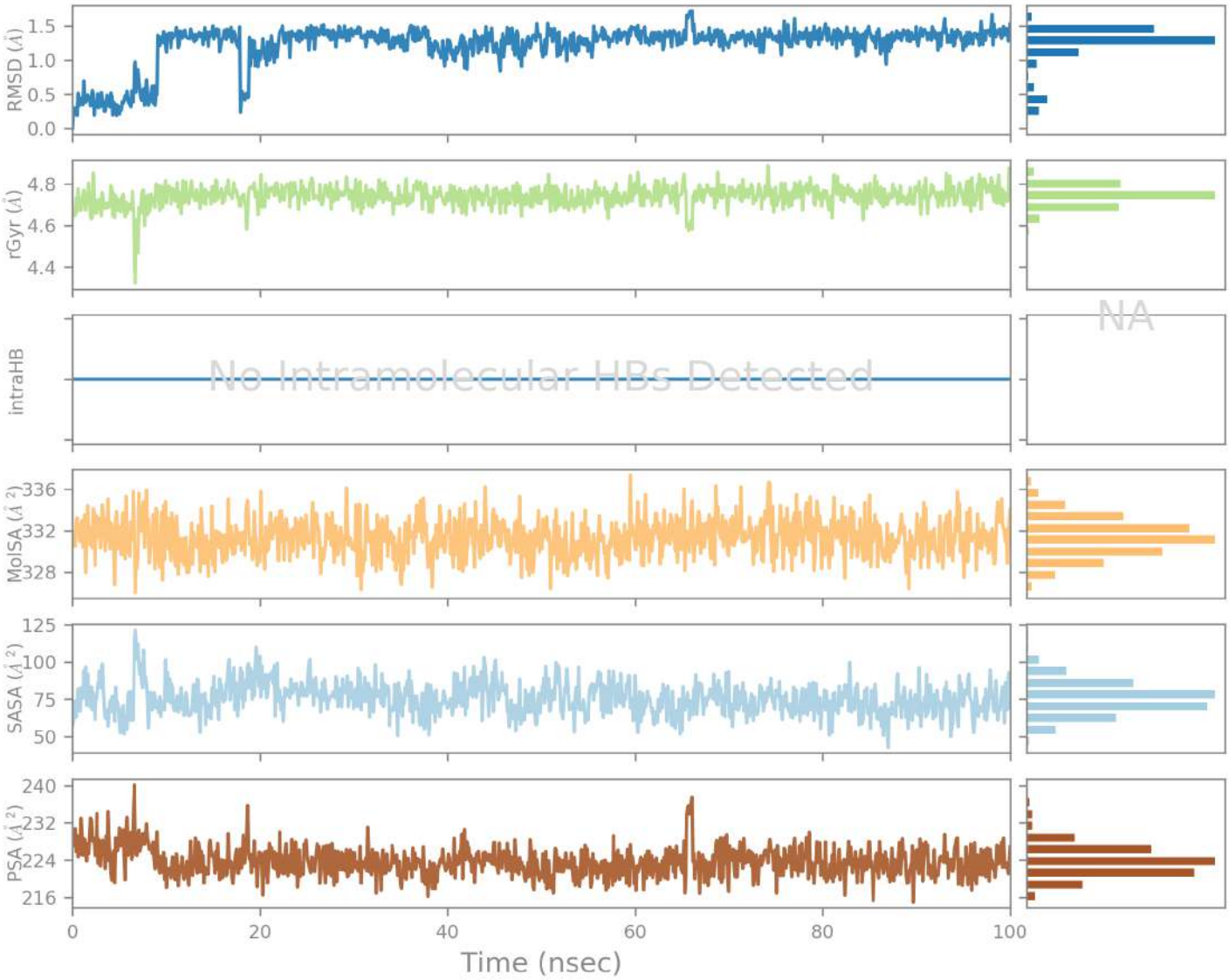

Ligand RMSD: Root mean square deviation of a ligand with respect to the reference conformation (typically the first frame is used as the reference and it is regarded as time *t*=0).

Radius of Gyration (rGyr): Measures the 'extendedness' of a ligand, and is equivalent to its principal moment of inertia.

Intramolecular Hydrogen Bonds (intraHB): Number of internal hydrogen bonds (HB) within a ligand molecule.

Molecular Surface Area (MolSA): Molecular surface calculation with 1.4 Å probe radius. This value is equivalent to a van der Waals surface area.

Solvent Accessible Surface Area (SASA): Surface area of a molecule accessible by a water molecule.

Polar Surface Area (PSA): Solvent accessible surface area in a molecule contributed only by oxygen and nitrogen atoms.

Simulation Interactions Diagram Report

Simulation Details

Jobname: desmond_md_job_2
Entry title: Full System

CPU #	Job Type	Ensemble	Temp. [K]	Sim. Time [ns]	# Atoms	# Waters	Charge
16	mdsim	NPT	300.0	100.102	32434	9150	0

Protein Information

Tot. Residues	Prot. Chain(s)	Res. in Chain(s)	# Atoms	# Heavy Atoms	Charge
300	'A'	300	4885	2450	-2

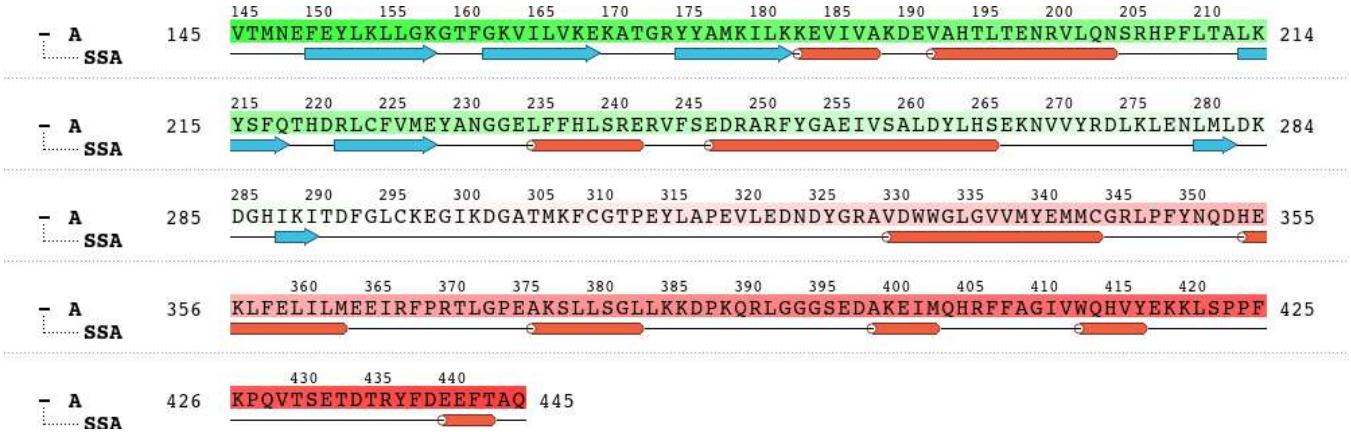

Ligand Information

SMILES	n1nnc(N2)n1Nc(c23)n(nc3C)-c4ccc(cc4)S(=O)(=O)N5CCCCC5
PDB Name	'UNK'
Num. of Atoms	47 (total) 28 (heavy)
Atomic Mass	401.453 au
Charge	0
Mol. Formula	C16H19N9O2S
Num. of Fragments	2
Num. of Rot. Bonds	3

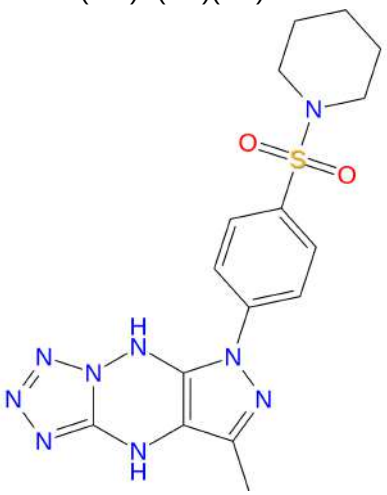

Counter Ion/Salt Information

Type	Num.	Concentration [mM]	Total Charge
Na	27	53.651	+27
Cl	25	49.677	-25

Protein-Ligand RMSD

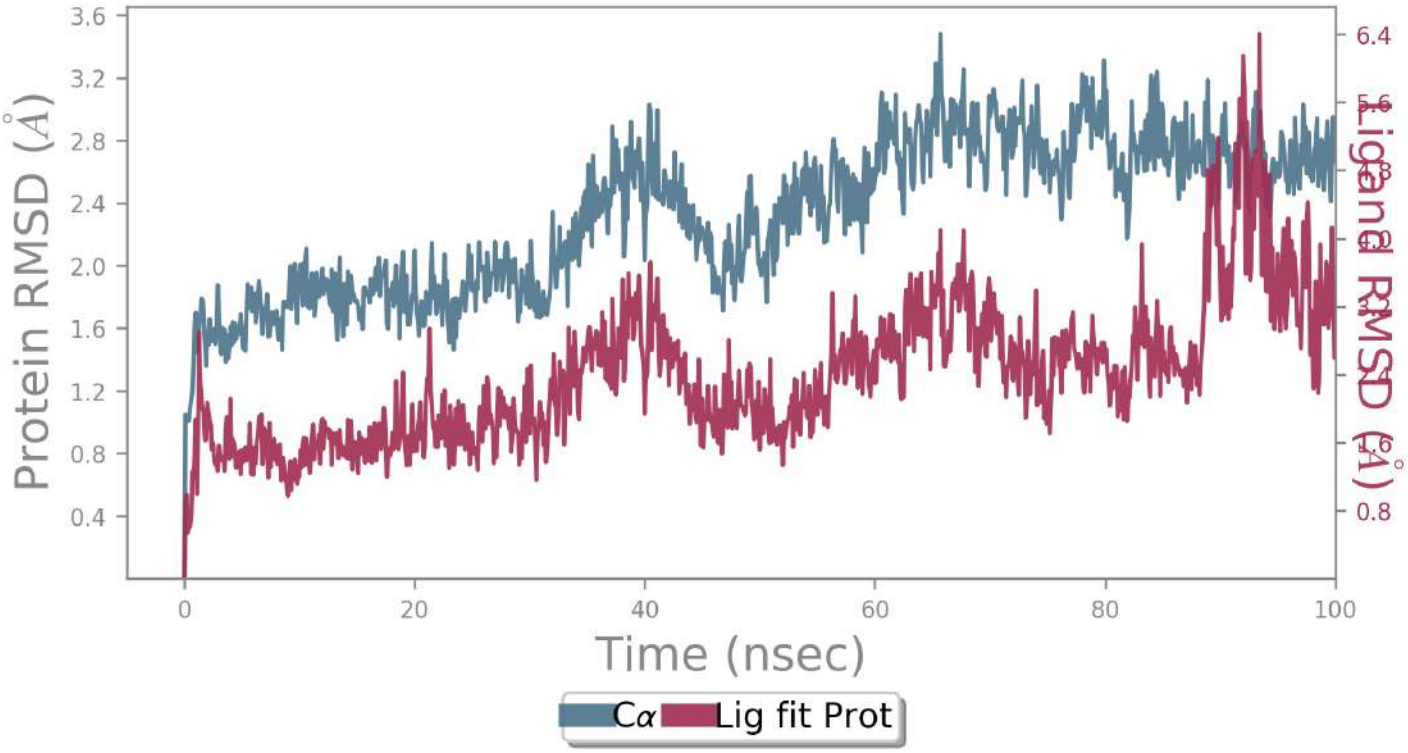

The Root Mean Square Deviation (RMSD) is used to measure the average change in displacement of a selection of atoms for a particular frame with respect to a reference frame. It is calculated for all frames in the trajectory. The RMSD for frame *x* is:

$$RMSD_x = \sqrt{\frac{1}{N}\sum_{i=1}^{N}(r_i'(t_x)) - r_i(t_{ref}))^2}$$

where *N* is the number of atoms in the atom selection; t_{ref} is the reference time, (typically the first frame is used as the reference and it is regarded as time *t*=0); and *r'* is the position of the selected atoms in frame *x* after superimposing on the reference frame, where frame *x* is recorded at time t_x. The procedure is repeated for every frame in the simulation trajectory.

Protein RMSD: The above plot shows the RMSD evolution of a protein (left *Y*-axis). All protein frames are first aligned on the reference frame backbone, and then the RMSD is calculated based on the atom selection. Monitoring the RMSD of the protein can give insights into its structural conformation throughout the simulation. RMSD analysis can indicate if the simulation has equilibrated — its fluctuations towards the end of the simulation are around some thermal average structure. Changes of the order of 1-3 Å are perfectly acceptable for small, globular proteins. Changes much larger than that, however, indicate that the protein is undergoing a large conformational change during the simulation. It is also important that your simulation converges — the RMSD values stabilize around a fixed value. If the RMSD of the protein is still increasing or decreasing on average at the end of the simulation, then your system has not equilibrated, and your simulation may not be long enough for rigorous analysis.

Ligand RMSD: Ligand RMSD (right *Y*-axis) indicates how stable the ligand is with respect to the protein and its binding pocket. In the above plot, 'Lig fit Prot' shows the RMSD of a ligand when the protein-ligand complex is first aligned on the protein backbone of the reference and then the RMSD of the ligand heavy atoms is measured. If the values observed are significantly larger than the RMSD of the protein, then it is likely that the ligand has diffused away from its initial binding site.

Protein RMSF

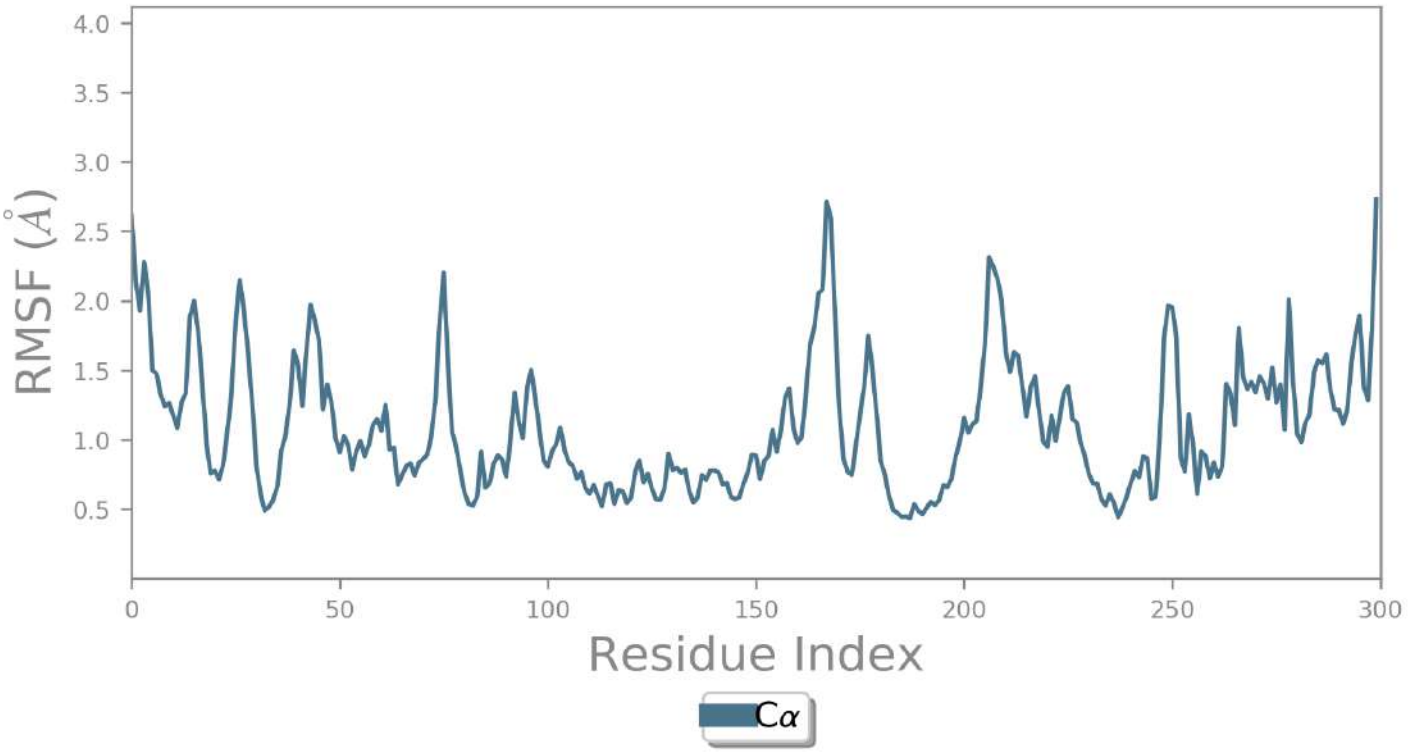

The Root Mean Square Fluctuation (RMSF) is useful for characterizing local changes along the protein chain. The RMSF for residue *i* is:

$$RMSF_i = \sqrt{\frac{1}{T}\sum_{t=1}^{T} < (r_i'(t)) - r_i(t_{ref}))^2 >}$$

where T is the trajectory time over which the RMSF is calculated, t_{ref} is the reference time, r_i is the position of residue i; r' is the position of atoms in residue i after superposition on the reference, and the angle brackets indicate that the average of the square distance is taken over the selection of atoms in the residue.

On this plot, peaks indicate areas of the protein that fluctuate the most during the simulation. Typically you will observe that the tails (*N*- and *C*-terminal) fluctuate more than any other part of the protein. Secondary structure elements like alpha helices and beta strands are usually more rigid than the unstructured part of the protein, and thus fluctuate less than the loop regions.

Protein Secondary Structure

% Helix	% Strand	% Total SSE
27.32	15.42	42.74

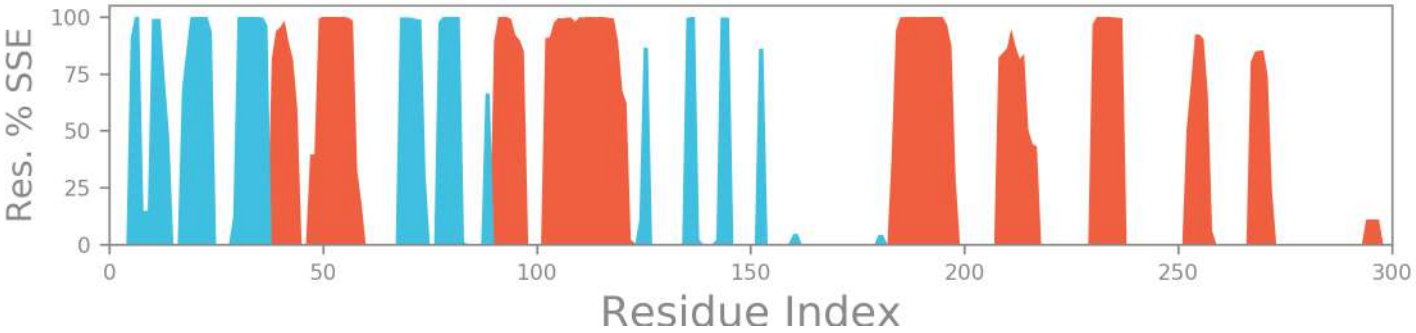

Protein secondary structure elements (SSE) like alpha-helices and beta-strands are monitored throughout the simulation. The plot above reports SSE distribution by residue index throughout the protein structure. The plot below summarizes the SSE composition for each trajectory frame over the course of the simulation, and the plot at the bottom monitors each residue and its SSE assignment over time.

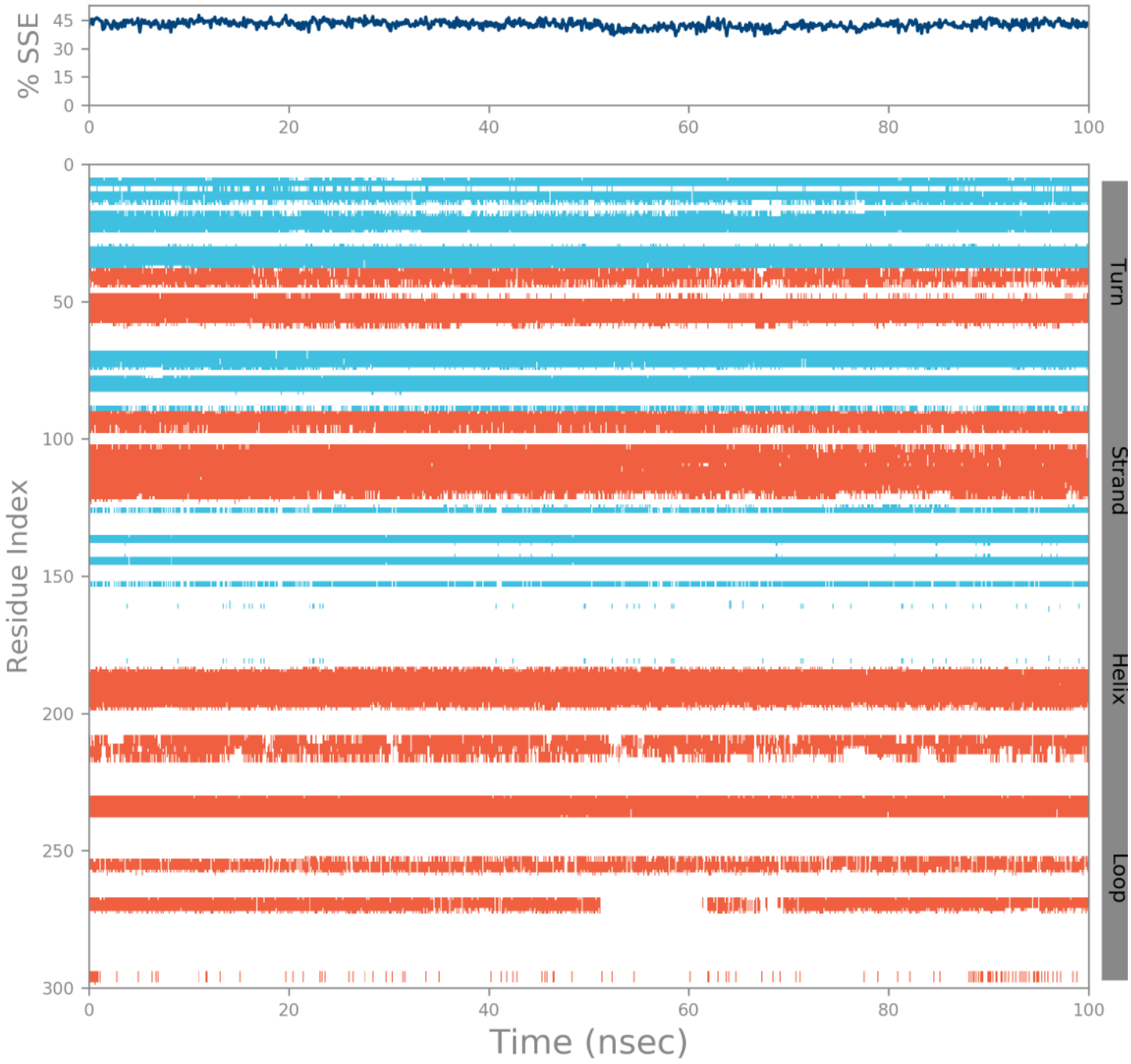
% SSE
45
30
15
0
0
20
40
60
80
100
Residue Index
0
50
100
150
200
250
300
Time (nsec)
Turn
Strand
Helix
Loop

Ligand RMSF

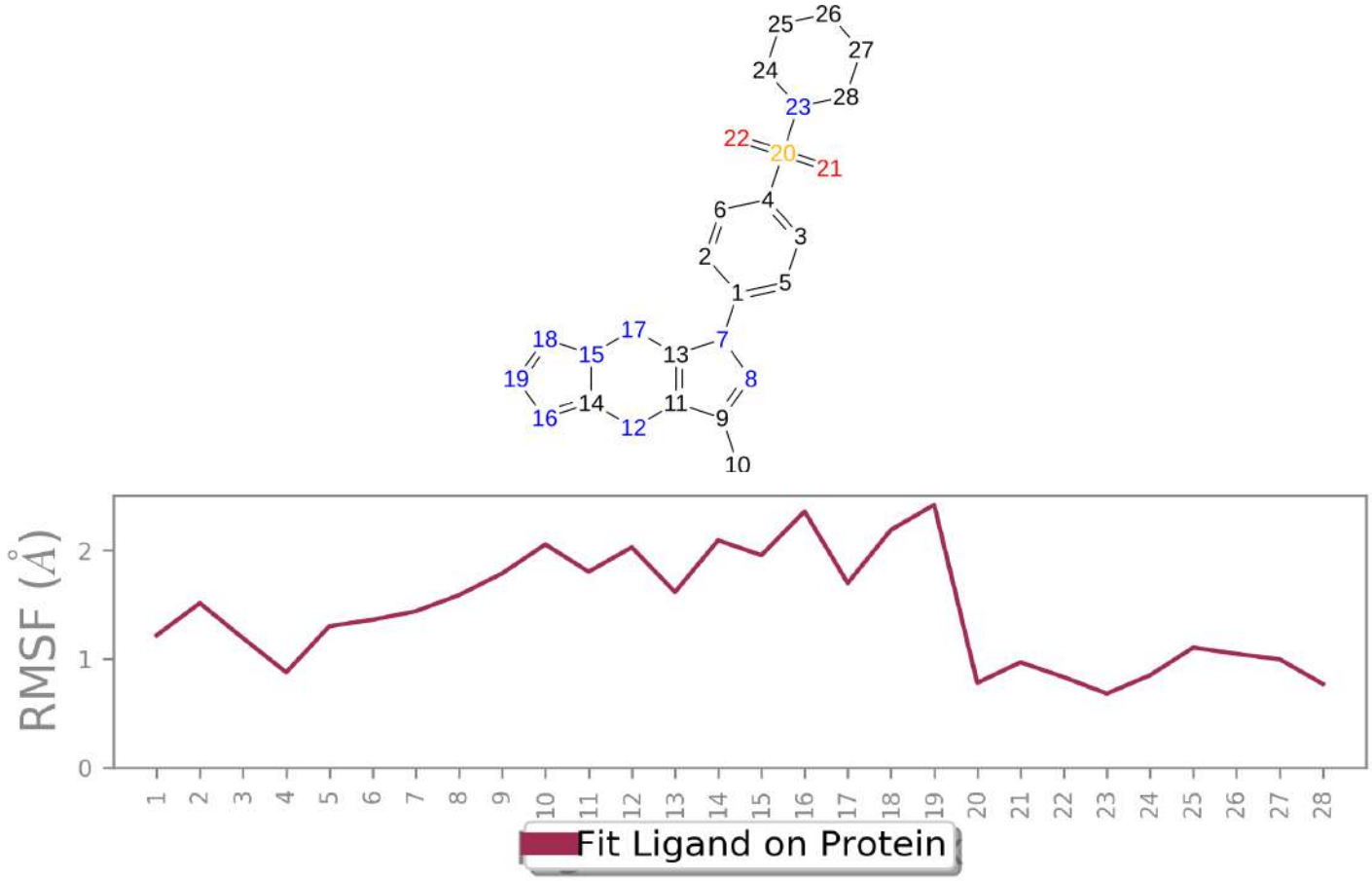

The Ligand Root Mean Square Fluctuation (L-RMSF) is useful for characterizing changes in the ligand atom positions. The RMSF for atom *i* is:

$$RMSF_i = \sqrt{\frac{1}{T}\sum_{t=1}^{T}(r_i'(t)) - r_i(t_{ref}))^2}$$

where *T* is the trajectory time over which the RMSF is calculated, t_{ref} is the reference time (usually for the first frame, and is regarded as the *zero* of time); *r* is the position of atom *i* in the reference at time t_{ref}, and *r'* is the position of atom *i* at time *t* after superposition on the reference frame.

Ligand RMSF shows the ligand's fluctuations broken down by atom, corresponding to the 2D structure in the top panel. The ligand RMSF may give you insights on how ligand fragments interact with the protein and their entropic role in the binding event. In the bottom panel, the 'Fit Ligand on Protein' line shows the ligand fluctuations, with respect to the protein. The protein-ligand complex is first aligned on the protein backbone and then the ligand RMSF is measured on the ligand heavy atoms.

Protein-Ligand Contacts

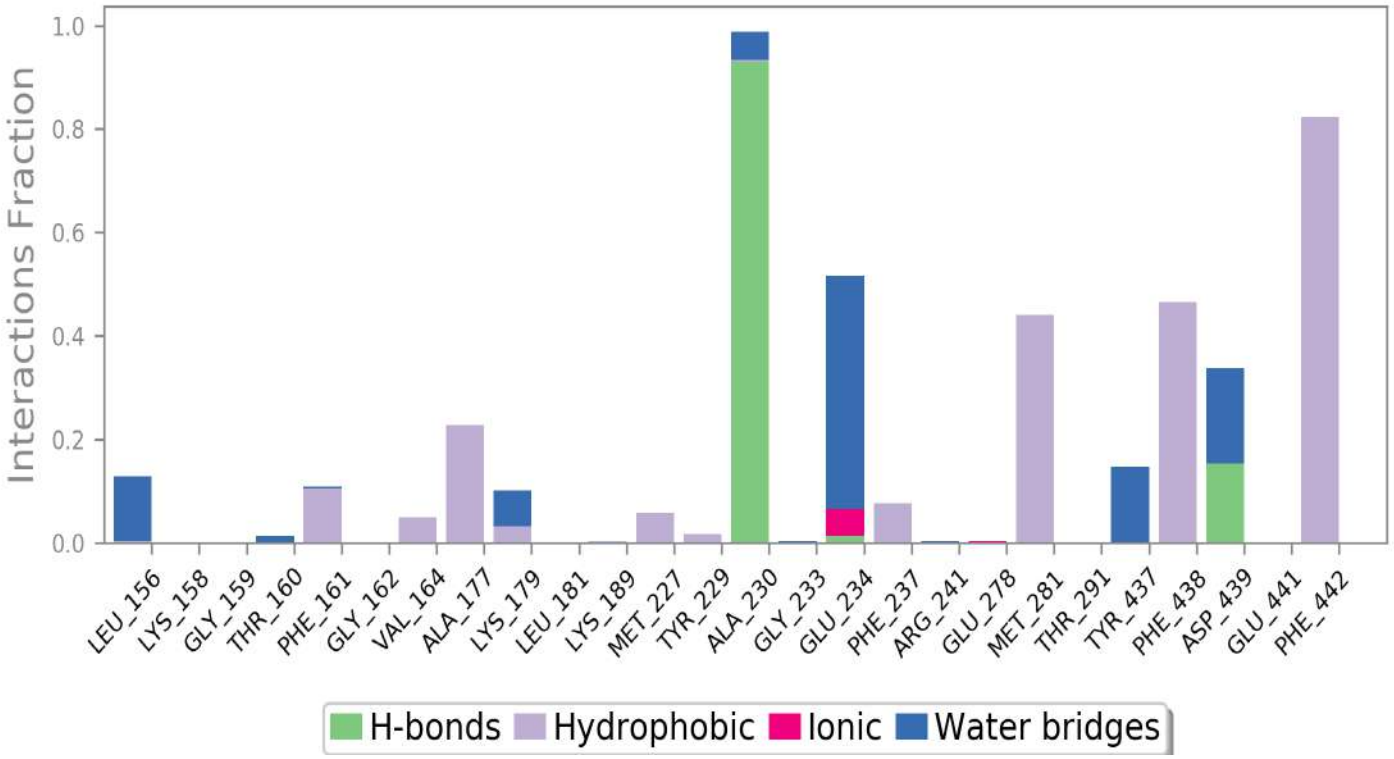

Protein interactions with the ligand can be monitored throughout the simulation. These interactions can be categorized by type and summarized, as shown in the plot above. Protein-ligand interactions (or 'contacts') are categorized into four types: Hydrogen Bonds, Hydrophobic, Ionic and Water Bridges. Each interaction type contains more specific subtypes, which can be explored through the 'Simulation Interactions Diagram' panel. The stacked bar charts are normalized over the course of the trajectory: for example, a value of 0.7 suggests that 70% of the simulation time the specific interaction is maintained. Values over 1.0 are possible as some protein residue may make multiple contacts of same subtype with the ligand.

Hydrogen Bonds: (H-bonds) play a significant role in ligand binding. Consideration of hydrogen-bonding properties in drug design is important because of their strong influence on drug specificity, metabolization and adsorption. Hydrogen bonds between a protein and a ligand can be further broken down into four subtypes: backbone acceptor; backbone donor; side-chain acceptor; side-chain donor.
The current geometric criteria for protein-ligand H-bond is: distance of 2.5 Å between the donor and acceptor atoms (D—H···A); a donor angle of ≥120° between the donor-hydrogen-acceptor atoms (D—H···A); and an acceptor angle of ≥90° between the hydrogen-acceptor-bonded_atom atoms (H···A—X).

Hydrophobic contacts: fall into three subtypes: π-Cation; π-π; and Other, non-specific interactions. Generally these type of interactions involve a hydrophobic amino acid and an aromatic or aliphatic group on the ligand, but we have extended this category to also include π-Cation interactions.
The current geometric criteria for hydrophobic interactions is as follows: π-Cation — Aromatic and charged groups within 4.5 Å; π-π — Two aromatic groups stacked face-to-face or face-to-edge; Other — A non-specific hydrophobic sidechain within 3.6 Å of a ligand's aromatic or aliphatic carbons.

Ionic interactions: or polar interactions, are between two oppositely charged atoms that are within 3.7 Å of each other and do not involve a hydrogen bond. We also monitor Protein-Metal-Ligand interactions, which are defined by a metal ion coordinated within 3.4 Å of protein's and ligand's heavy atoms (except carbon). All ionic interactions are broken down into two subtypes: those mediated by a protein backbone or side chains.

Water Bridges: are hydrogen-bonded protein-ligand interactions mediated by a water molecule. The hydrogen-bond geometry is slightly relaxed from the standard H-bond definition.
The current geometric criteria for a protein-water or water-ligand H-bond are: a distance of 2.8 Å between the donor and acceptor atoms (D—H···A); a donor angle of ≥110° between the donor-hydrogen-acceptor atoms (D—H···A); and an acceptor angle of ≥90° between the hydrogen-acceptor-bonded_atom atoms (H···A—X).

Protein-Ligand Contacts (cont.)

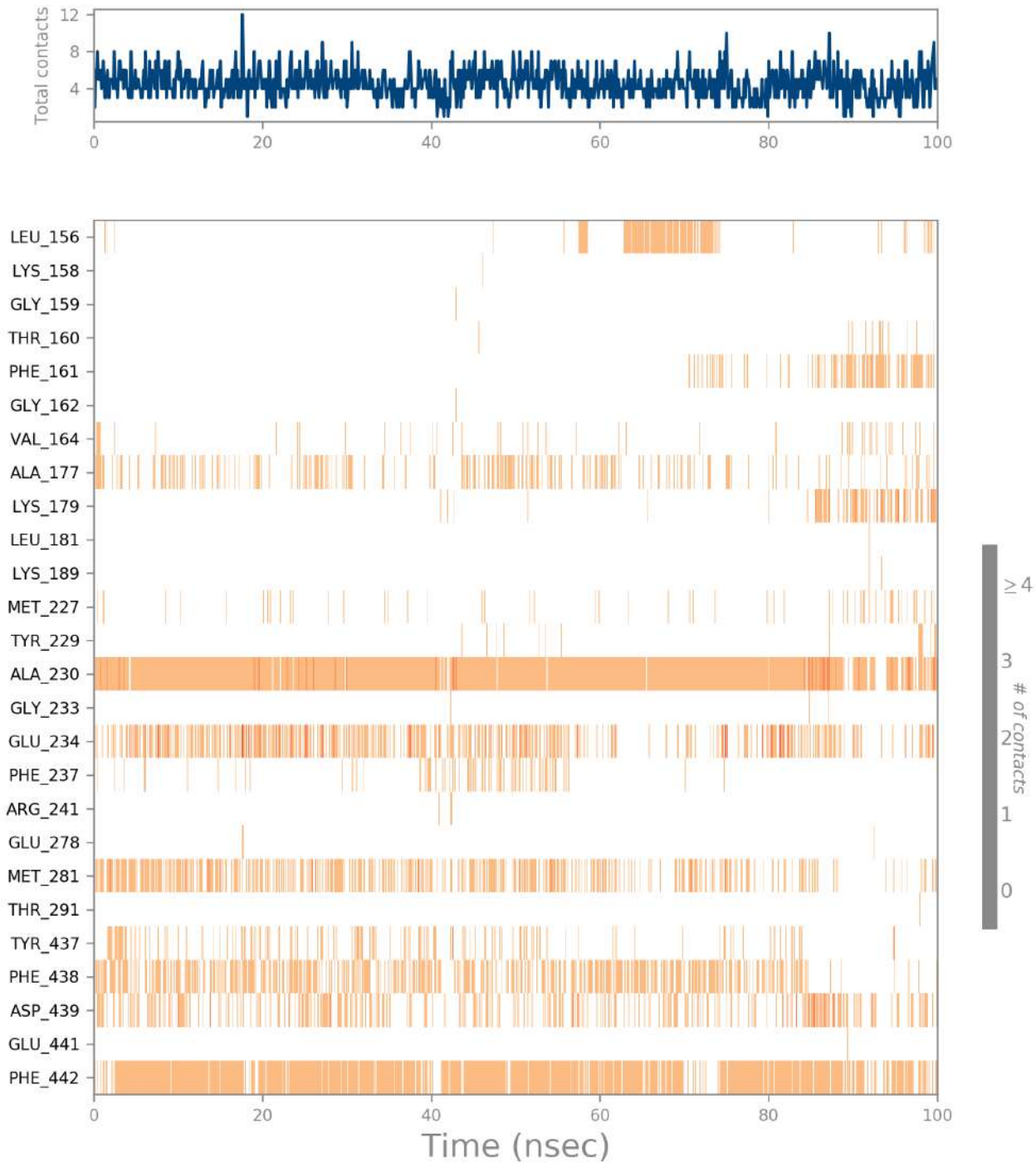

A timeline representation of the interactions and contacts (**H-bonds**, **Hydrophobic**, **Ionic**, **Water bridges**) summarized in the previous page. The top panel shows the total number of specific contacts the protein makes with the ligand over the course of the trajectory. The bottom panel shows which residues interact with the ligand in each trajectory frame. Some residues make more than one specific contact with the ligand, which is represented by a darker shade of orange, according to the scale to the right of the plot.

Ligand-Protein Contacts

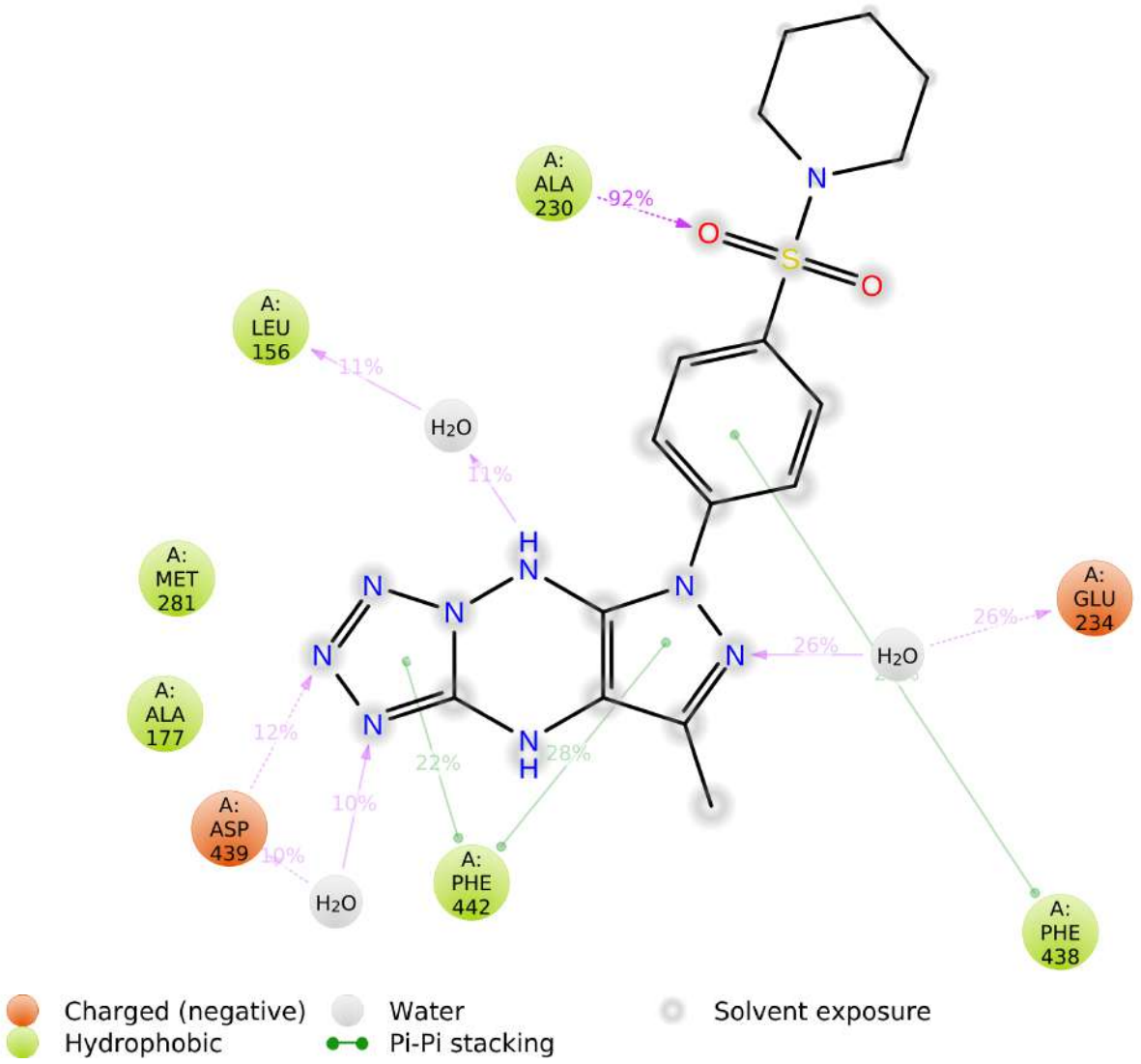

A schematic of detailed ligand atom interactions with the protein residues. Interactions that occur more than **10.0%** of the simulation time in the selected trajectory (0.00 through 100.00 nsec), are shown.
Note: it is possible to have interactions with >100% as some residues may have multiple interactions of a single type with the same ligand atom. For example, the ARG side chain has four H-bond donors that can all hydrogen-bond to a single H-bond acceptor.

Ligand Torsion Profile

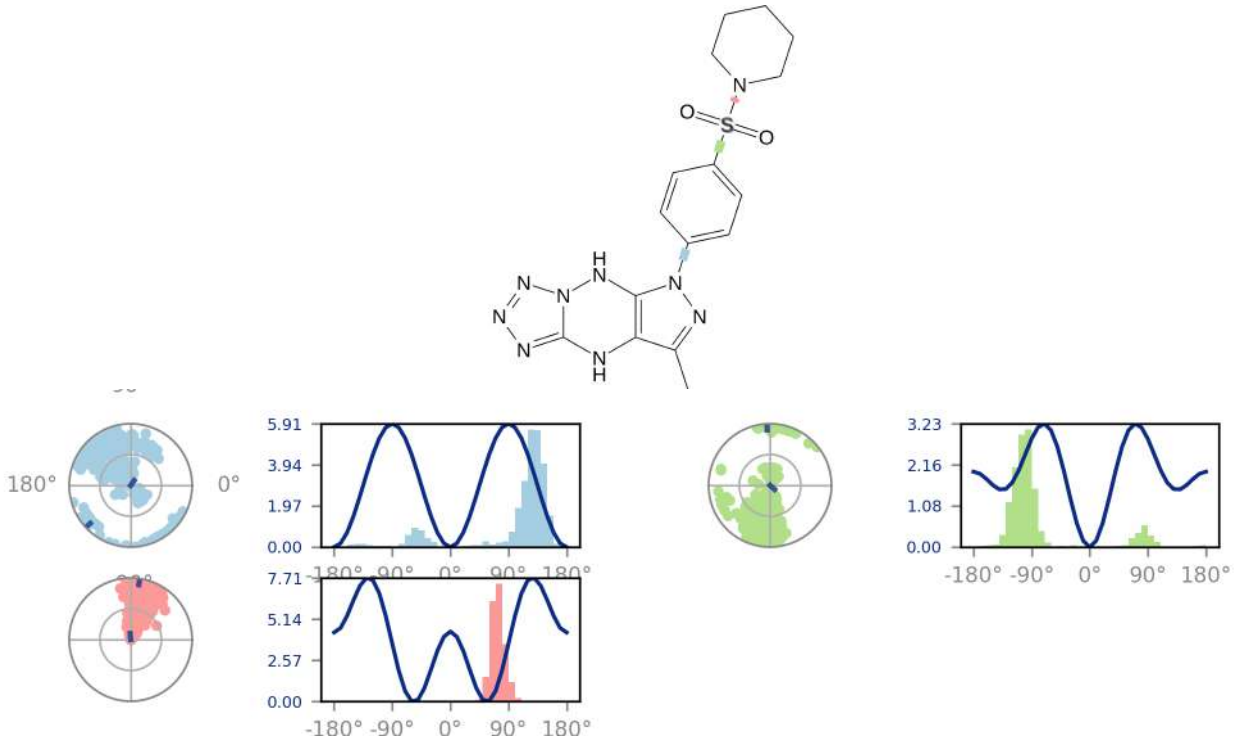

The ligand torsions plot summarizes the conformational evolution of every rotatable bond (RB) in the ligand throughout the simulation trajectory (0.00 through 100.00 nsec). The top panel shows the 2d schematic of a ligand with color-coded rotatable bonds. Each rotatable bond torsion is accompanied by a dial plot and bar plots of the same color.

Dial (or radial) plots describe the conformation of the torsion throughout the course of the simulation. The beginning of the simulation is in the center of the radial plot and the time evolution is plotted radially outwards.

The bar plots summarize the data on the dial plots, by showing the probability density of the torsion. If torsional potential information is available, the plot also shows the potential of the rotatable bond (by summing the potential of the related torsions). The values of the potential are on the left *Y*-axis of the chart, and are expressed in *kcal/mol*. Looking at the histogram and torsion potential relationships may give insights into the conformational strain the ligand undergoes to maintain a protein-bound conformation.

Ligand Properties

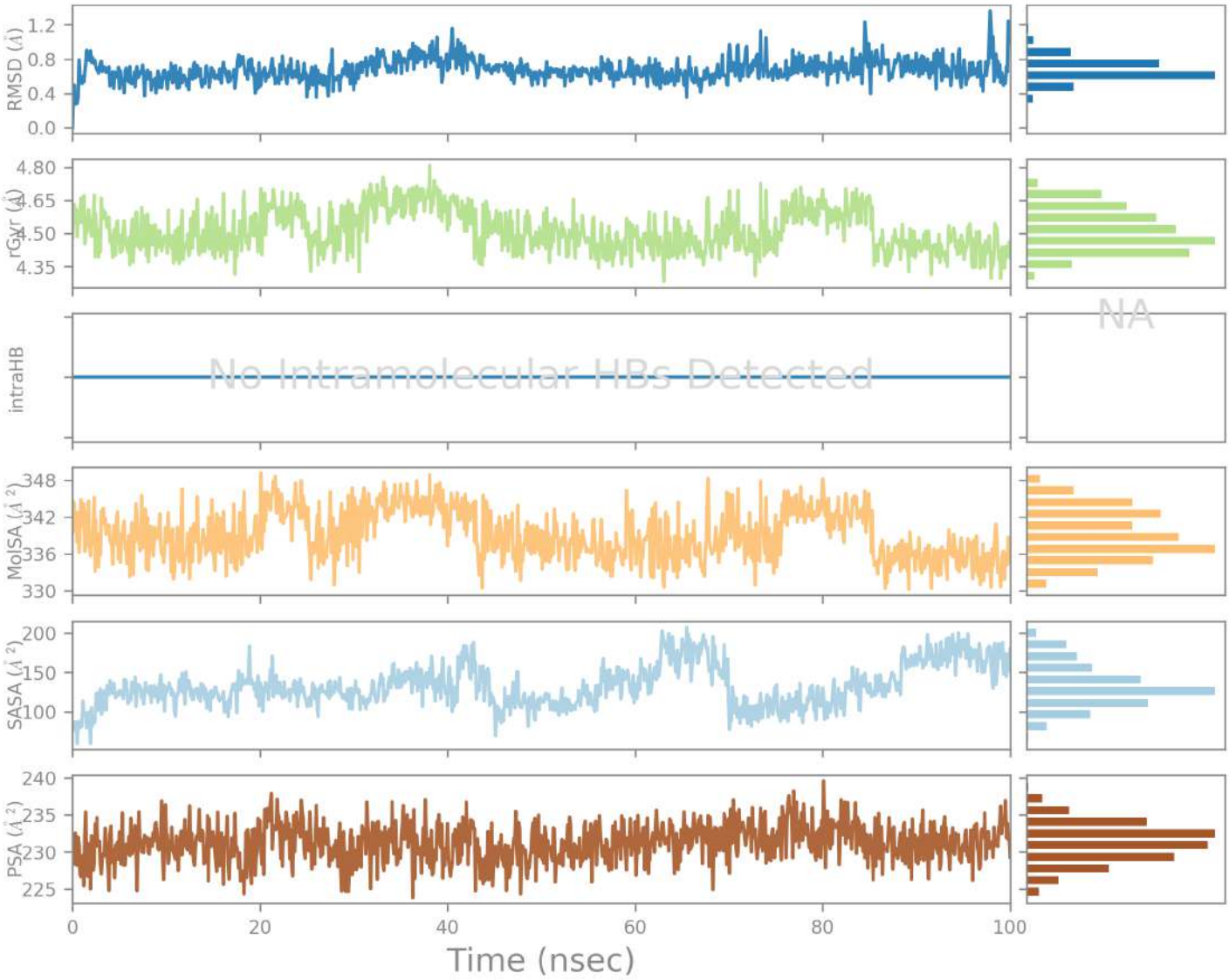

Ligand RMSD: Root mean square deviation of a ligand with respect to the reference conformation (typically the first frame is used as the reference and it is regarded as time *t*=0).

Radius of Gyration (rGyr): Measures the 'extendedness' of a ligand, and is equivalent to its principal moment of inertia.

Intramolecular Hydrogen Bonds (intraHB): Number of internal hydrogen bonds (HB) within a ligand molecule.

Molecular Surface Area (MolSA): Molecular surface calculation with 1.4 Å probe radius. This value is equivalent to a van der Waals surface area.

Solvent Accessible Surface Area (SASA): Surface area of a molecule accessible by a water molecule.

Polar Surface Area (PSA): Solvent accessible surface area in a molecule contributed only by oxygen and nitrogen atoms.

Simulation Interactions Diagram Report

Simulation Details

Jobname: desmond_md_job_1
Entry title: XXXX - hbond-opt

CPU #	Job Type	Ensemble	Temp. [K]	Sim. Time [ns]	# Atoms	# Waters	Charge
1	mdsim	NPT	300.0	100.102	34602	10233	0

Protein Information

Tot. Residues	Prot. Chain(s)	Res. in Chain(s)	# Atoms	# Heavy Atoms	Charge
249	'A', 'B'	ict_values([126, 123]	3791	1906	-7

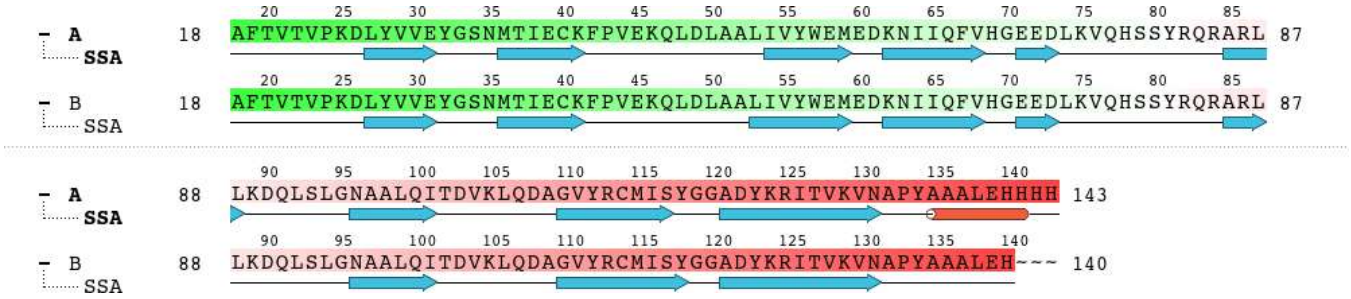

Ligand Information

SMILES	n1nnc(N2)n1Nc(c23)n(nc3C)-c4ccc(cc4)S(=O)(=O)N5CCCCC5
PDB Name	'UNK'
Num. of Atoms	47 (total) 28 (heavy)
Atomic Mass	401.453 au
Charge	0
Mol. Formula	C16H19N9O2S
Num. of Fragments	2
Num. of Rot. Bonds	3

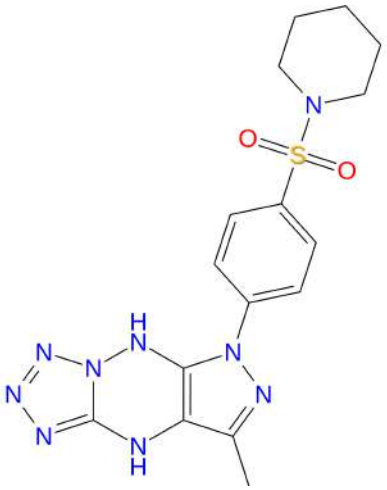

Counter Ion/Salt Information

Type	Num.	Concentration [mM]	Total Charge
Na	36	63.964	+36
Cl	29	51.527	-29

Protein-Ligand RMSD

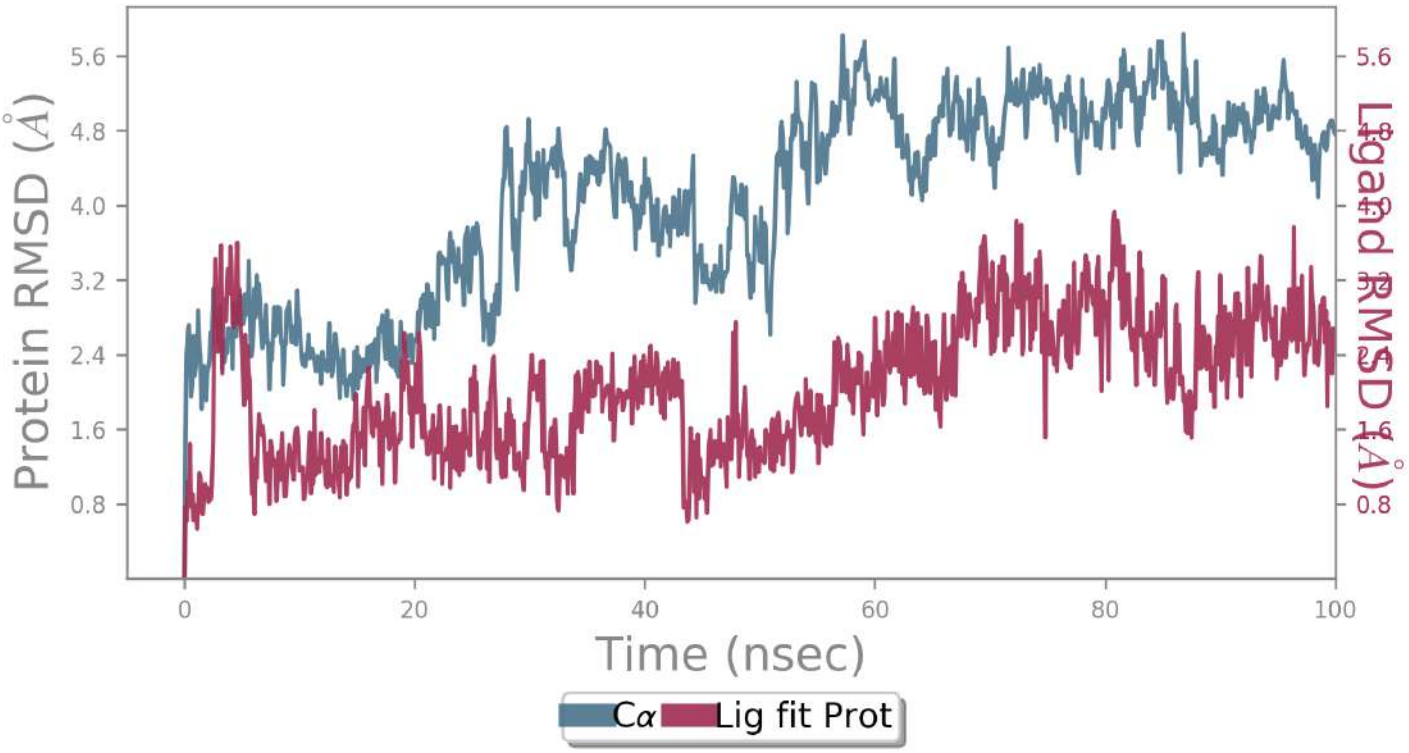

The Root Mean Square Deviation (RMSD) is used to measure the average change in displacement of a selection of atoms for a particular frame with respect to a reference frame. It is calculated for all frames in the trajectory. The RMSD for frame *x* is:

$$RMSD_x = \sqrt{\frac{1}{N}\sum_{i=1}^{N}(r_i'(t_x)) - r_i(t_{ref}))^2}$$

where *N* is the number of atoms in the atom selection; t_{ref} is the reference time, (typically the first frame is used as the reference and it is regarded as time *t*=0); and *r'* is the position of the selected atoms in frame *x* after superimposing on the reference frame, where frame *x* is recorded at time t_x. The procedure is repeated for every frame in the simulation trajectory.

Protein RMSD: The above plot shows the RMSD evolution of a protein (left *Y*-axis). All protein frames are first aligned on the reference frame backbone, and then the RMSD is calculated based on the atom selection. Monitoring the RMSD of the protein can give insights into its structural conformation throughout the simulation. RMSD analysis can indicate if the simulation has equilibrated — its fluctuations towards the end of the simulation are around some thermal average structure. Changes of the order of 1-3 Å are perfectly acceptable for small, globular proteins. Changes much larger than that, however, indicate that the protein is undergoing a large conformational change during the simulation. It is also important that your simulation converges — the RMSD values stabilize around a fixed value. If the RMSD of the protein is still increasing or decreasing on average at the end of the simulation, then your system has not equilibrated, and your simulation may not be long enough for rigorous analysis.

Ligand RMSD: Ligand RMSD (right *Y*-axis) indicates how stable the ligand is with respect to the protein and its binding pocket. In the above plot, 'Lig fit Prot' shows the RMSD of a ligand when the protein-ligand complex is first aligned on the protein backbone of the reference and then the RMSD of the ligand heavy atoms is measured. If the values observed are significantly larger than the RMSD of the protein, then it is likely that the ligand has diffused away from its initial binding site.

Protein RMSF

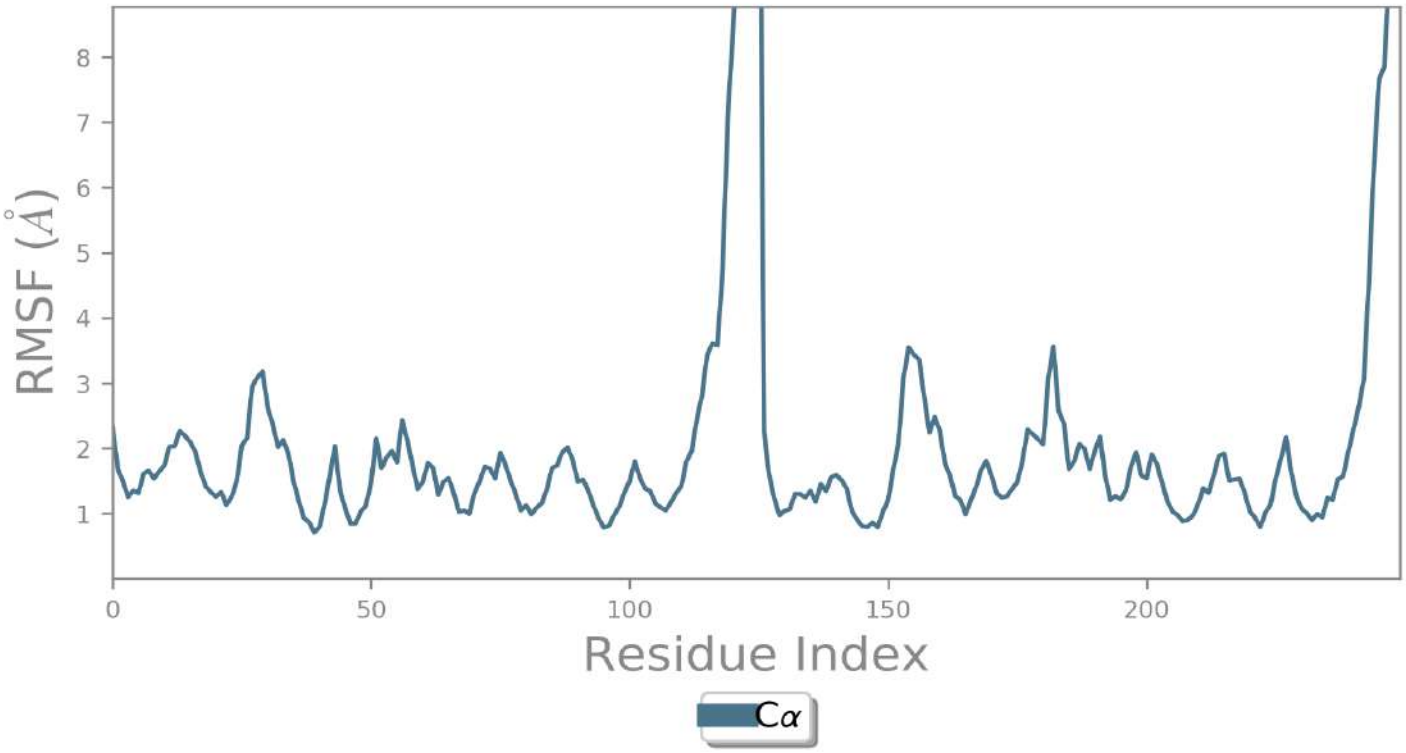

The Root Mean Square Fluctuation (RMSF) is useful for characterizing local changes along the protein chain. The RMSF for residue *i* is:

$$RMSF_i = \sqrt{\frac{1}{T}\sum_{t=1}^{T} < (r_i'(t)) - r_i(t_{ref}))^2 >}$$

where *T* is the trajectory time over which the RMSF is calculated, t_{ref} is the reference time, r_i is the position of residue *i*; *r'* is the position of atoms in residue *i* after superposition on the reference, and the angle brackets indicate that the average of the square distance is taken over the selection of atoms in the residue.

On this plot, peaks indicate areas of the protein that fluctuate the most during the simulation. Typically you will observe that the tails (*N*- and *C*-terminal) fluctuate more than any other part of the protein. Secondary structure elements like alpha helices and beta strands are usually more rigid than the unstructured part of the protein, and thus fluctuate less than the loop regions.

Protein Secondary Structure

% Helix	% Strand	% Total SSE
0.85	37.85	38.70

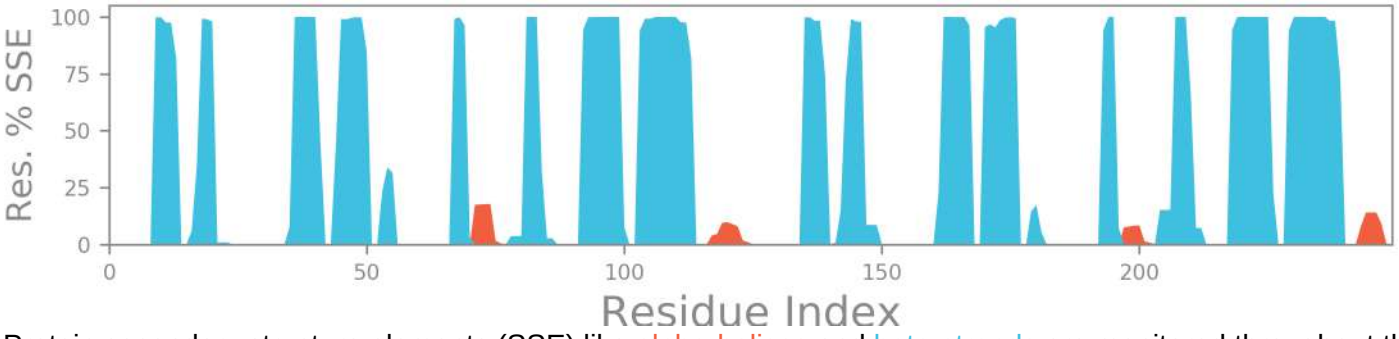

Protein secondary structure elements (SSE) like alpha-helices and beta-strands are monitored throughout the simulation. The plot above reports SSE distribution by residue index throughout the protein structure. The plot below summarizes the SSE composition for each trajectory frame over the course of the simulation, and the plot at the bottom monitors each residue and its SSE assignment over time.

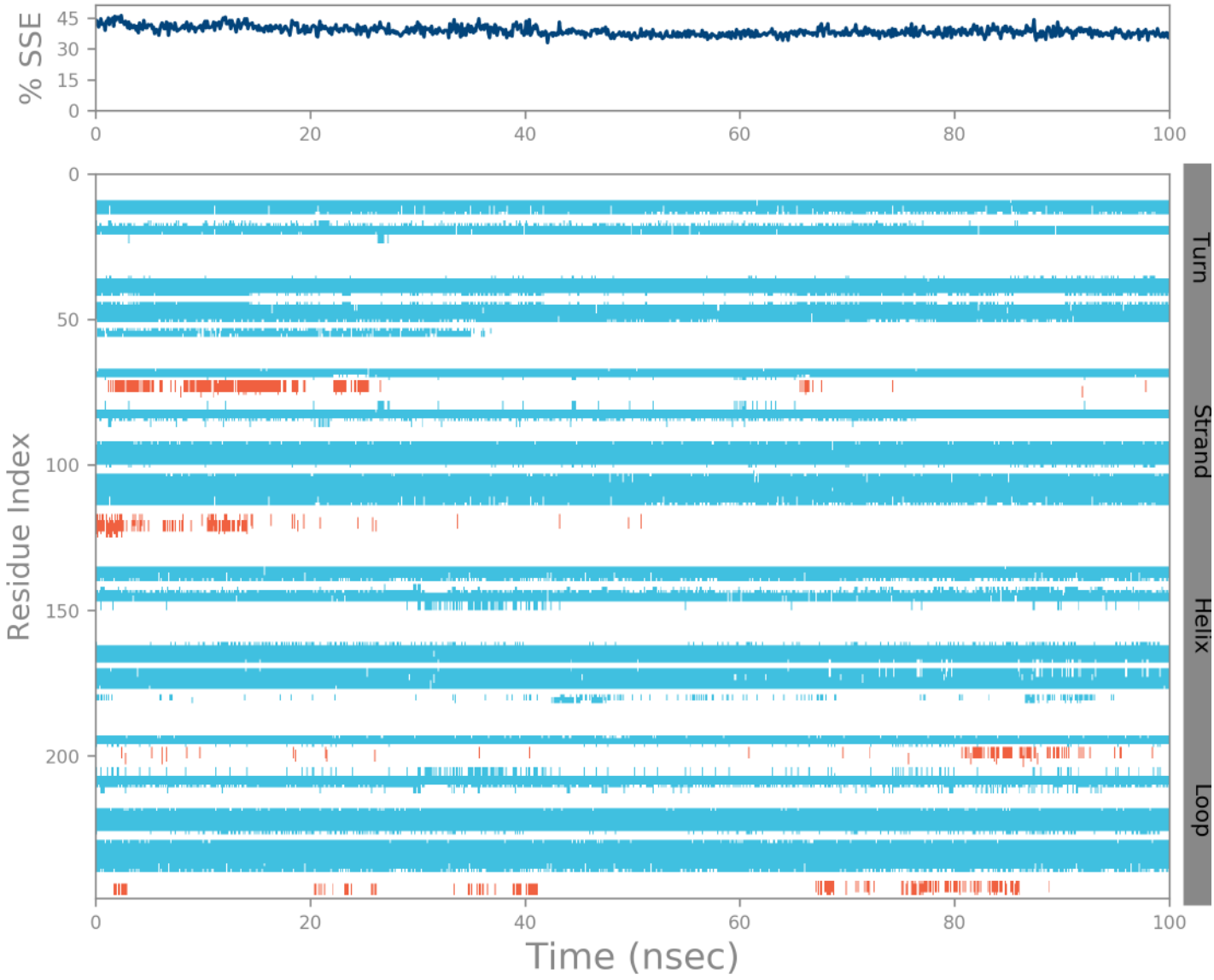

Ligand RMSF

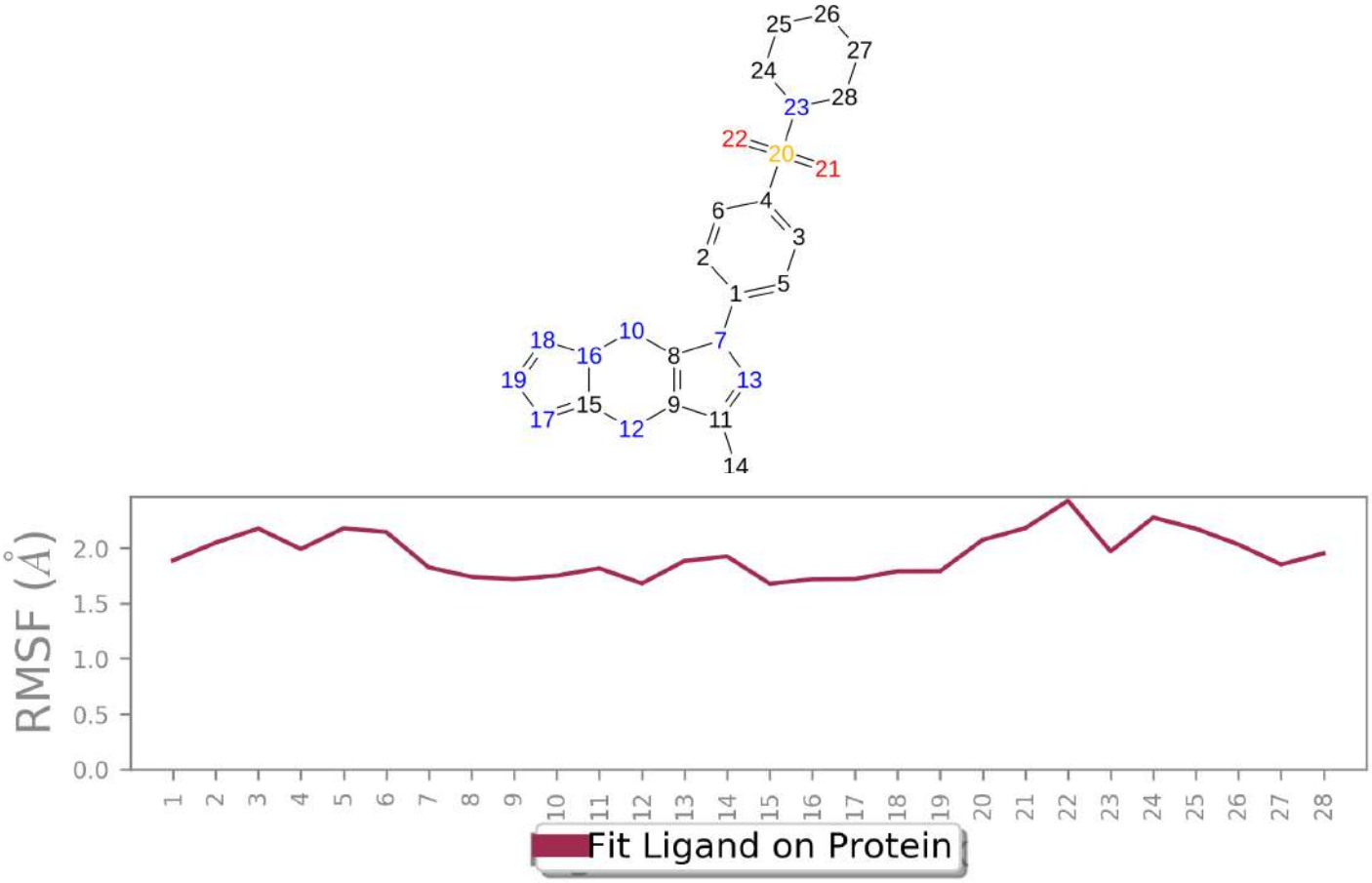

The Ligand Root Mean Square Fluctuation (L-RMSF) is useful for characterizing changes in the ligand atom positions. The RMSF for atom *i* is:

$$RMSF_i = \sqrt{\frac{1}{T}\sum_{t=1}^{T}(r_i'(t)) - r_i(t_{ref}))^2}$$

where *T* is the trajectory time over which the RMSF is calculated, t_{ref} is the reference time (usually for the first frame, and is regarded as the *zero* of time); *r* is the position of atom *i* in the reference at time t_{ref}, and *r'* is the position of atom *i* at time *t* after superposition on the reference frame.

Ligand RMSF shows the ligand's fluctuations broken down by atom, corresponding to the 2D structure in the top panel. The ligand RMSF may give you insights on how ligand fragments interact with the protein and their entropic role in the binding event. In the bottom panel, the 'Fit Ligand on Protein' line shows the ligand fluctuations, with respect to the protein. The protein-ligand complex is first aligned on the protein backbone and then the ligand RMSF is measured on the ligand heavy atoms.

Protein-Ligand Contacts

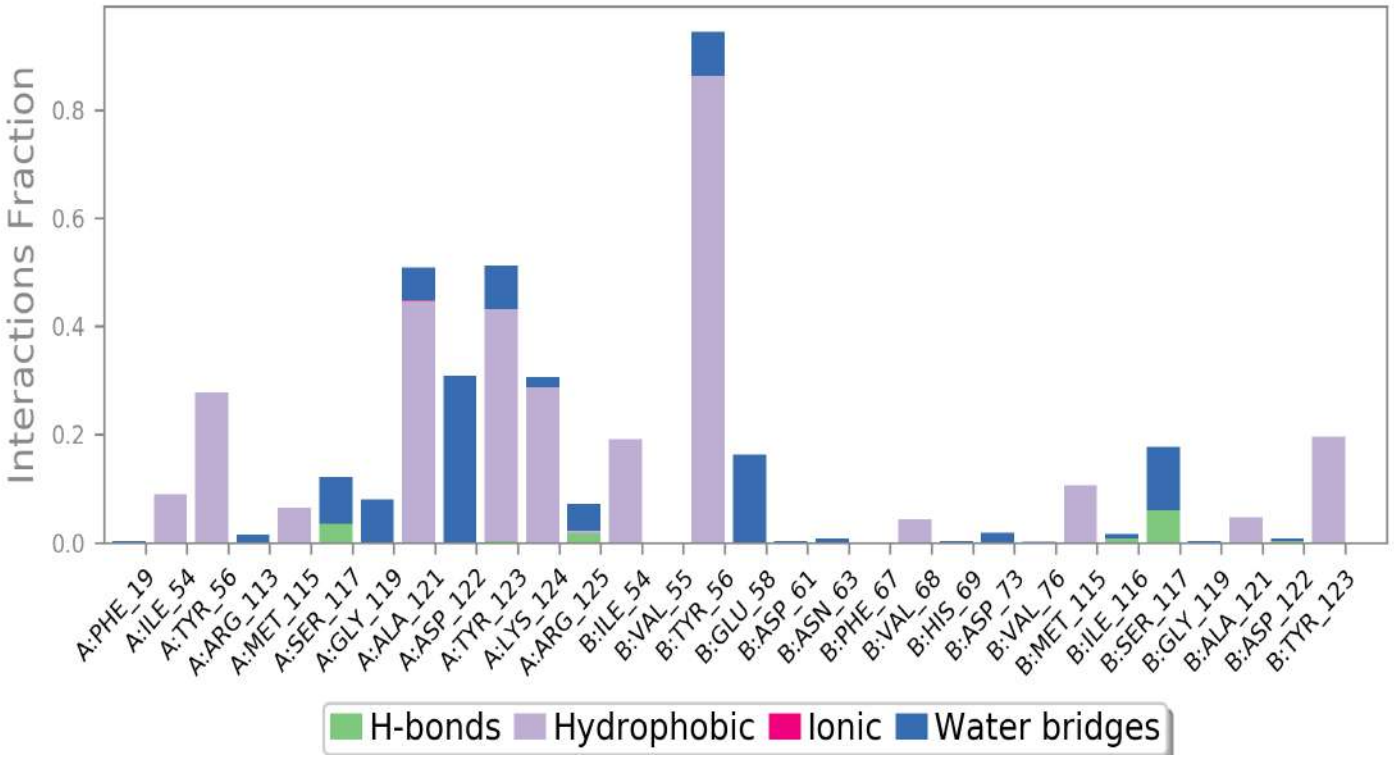

Protein interactions with the ligand can be monitored throughout the simulation. These interactions can be categorized by type and summarized, as shown in the plot above. Protein-ligand interactions (or 'contacts') are categorized into four types: Hydrogen Bonds, Hydrophobic, Ionic and Water Bridges. Each interaction type contains more specific subtypes, which can be explored through the 'Simulation Interactions Diagram' panel. The stacked bar charts are normalized over the course of the trajectory: for example, a value of 0.7 suggests that 70% of the simulation time the specific interaction is maintained. Values over 1.0 are possible as some protein residue may make multiple contacts of same subtype with the ligand.

Hydrogen Bonds: (H-bonds) play a significant role in ligand binding. Consideration of hydrogen-bonding properties in drug design is important because of their strong influence on drug specificity, metabolization and adsorption. Hydrogen bonds between a protein and a ligand can be further broken down into four subtypes: backbone acceptor; backbone donor; side-chain acceptor; side-chain donor.
The current geometric criteria for protein-ligand H-bond is: distance of 2.5 Å between the donor and acceptor atoms (D—H···A); a donor angle of ≥120° between the donor-hydrogen-acceptor atoms (D—H···A); and an acceptor angle of ≥90° between the hydrogen-acceptor-bonded_atom atoms (H···A—X).

Hydrophobic contacts: fall into three subtypes: π-Cation; π-π; and Other, non-specific interactions. Generally these type of interactions involve a hydrophobic amino acid and an aromatic or aliphatic group on the ligand, but we have extended this category to also include π-Cation interactions.
The current geometric criteria for hydrophobic interactions is as follows: π-Cation — Aromatic and charged groups within 4.5 Å; π-π — Two aromatic groups stacked face-to-face or face-to-edge; Other — A non-specific hydrophobic sidechain within 3.6 Å of a ligand's aromatic or aliphatic carbons.

Ionic interactions: or polar interactions, are between two oppositely charged atoms that are within 3.7 Å of each other and do not involve a hydrogen bond. We also monitor Protein-Metal-Ligand interactions, which are defined by a metal ion coordinated within 3.4 Å of protein's and ligand's heavy atoms (except carbon). All ionic interactions are broken down into two subtypes: those mediated by a protein backbone or side chains.

Water Bridges: are hydrogen-bonded protein-ligand interactions mediated by a water molecule. The hydrogen-bond geometry is slightly relaxed from the standard H-bond definition.
The current geometric criteria for a protein-water or water-ligand H-bond are: a distance of 2.8 Å between the donor and acceptor atoms (D—H···A); a donor angle of ≥110° between the donor-hydrogen-acceptor atoms (D—H···A); and an acceptor angle of ≥90° between the hydrogen-acceptor-bonded_atom atoms (H···A—X).

Protein-Ligand Contacts (cont.)

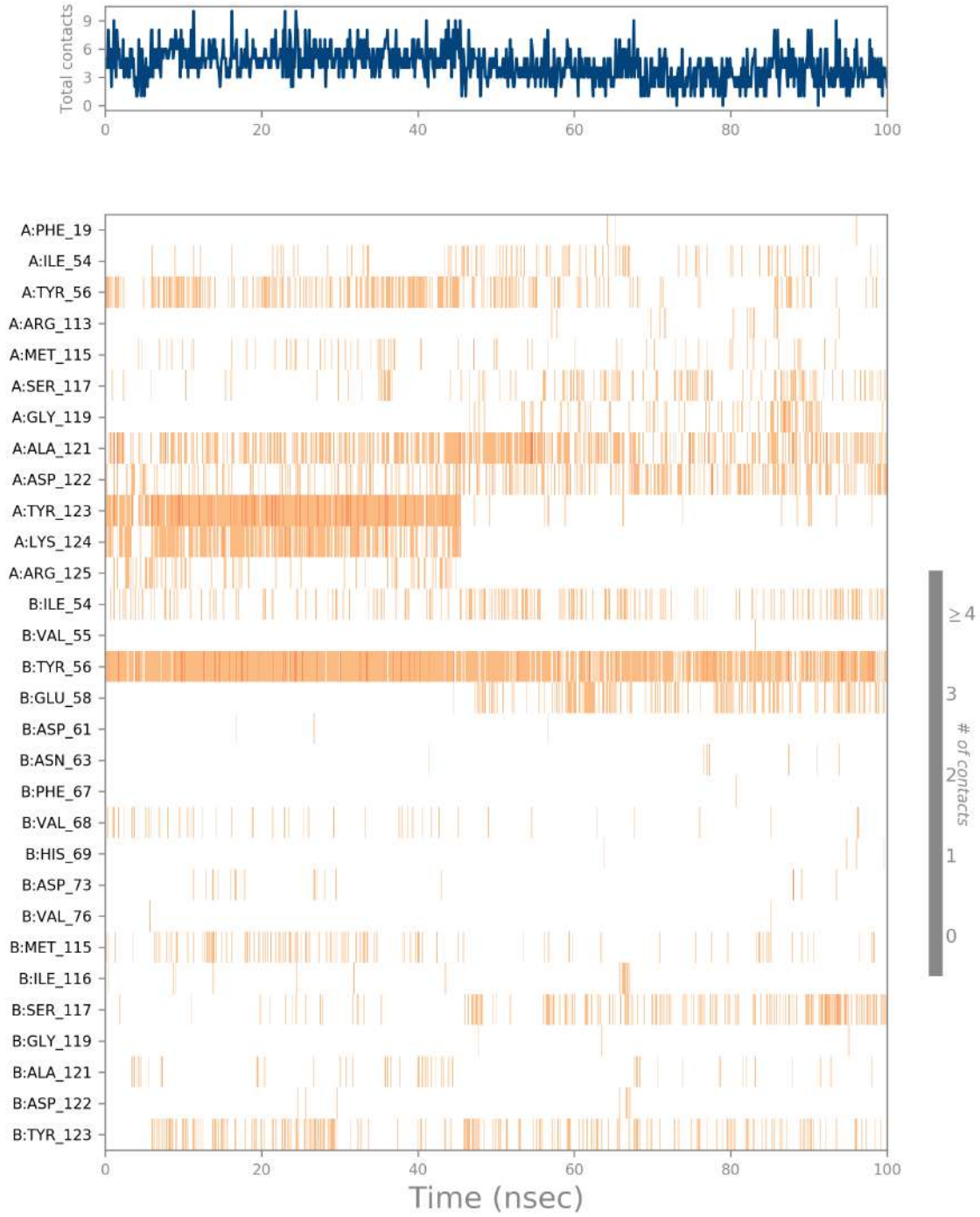

A timeline representation of the interactions and contacts (**H-bonds**, **Hydrophobic**, **Ionic**, **Water bridges**) summarized in the previous page. The top panel shows the total number of specific contacts the protein makes with the ligand over the course of the trajectory. The bottom panel shows which residues interact with the ligand in each trajectory frame. Some residues make more than one specific contact with the ligand, which is represented by a darker shade of orange, according to the scale to the right of the plot.

Ligand-Protein Contacts

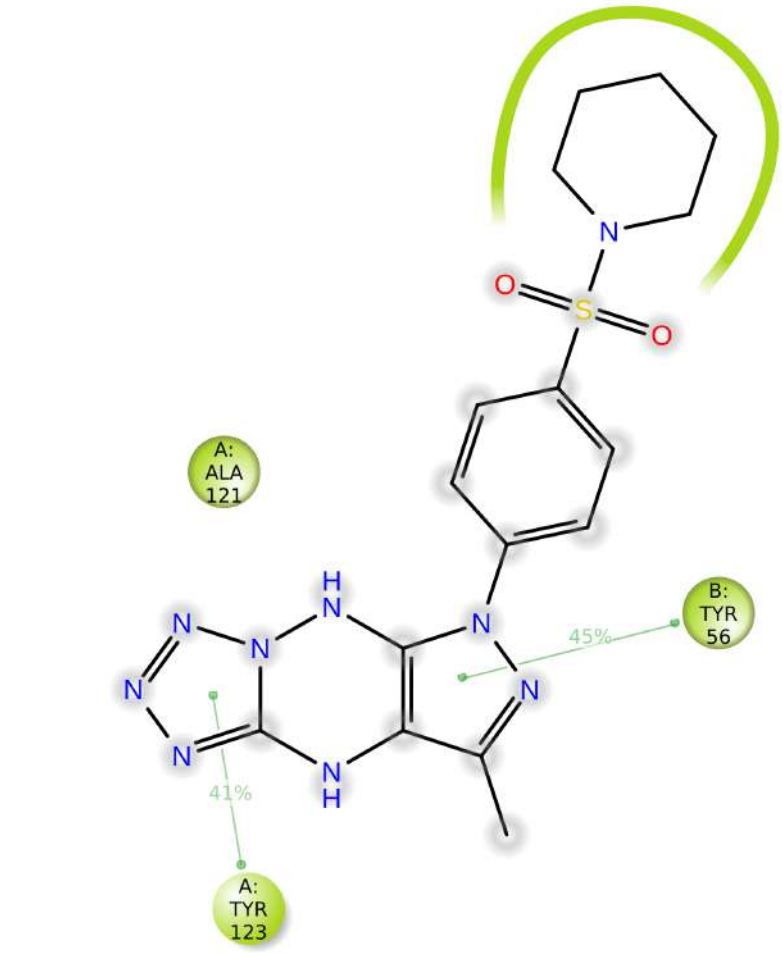

Hydrophobic Pi-Pi stacking Solvent exposure

A schematic of detailed ligand atom interactions with the protein residues. Interactions that occur more than **30.0%** of the simulation time in the selected trajectory (0.00 through 100.00 nsec), are shown.
Note: it is possible to have interactions with >100% as some residues may have multiple interactions of a single type with the same ligand atom. For example, the ARG side chain has four H-bond donors that can all hydrogen-bond to a single H-bond acceptor.

Ligand Torsion Profile

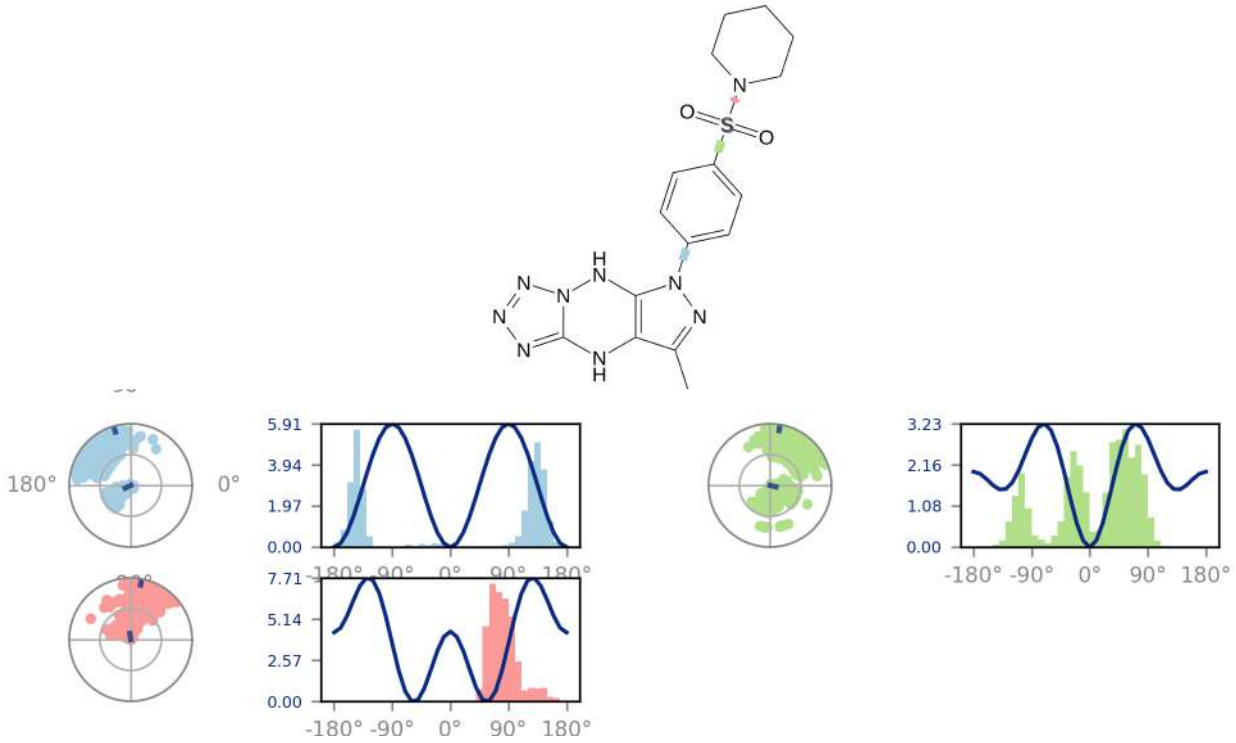

The ligand torsions plot summarizes the conformational evolution of every rotatable bond (RB) in the ligand throughout the simulation trajectory (0.00 through 100.00 nsec). The top panel shows the 2d schematic of a ligand with color-coded rotatable bonds. Each rotatable bond torsion is accompanied by a dial plot and bar plots of the same color.

Dial (or radial) plots describe the conformation of the torsion throughout the course of the simulation. The beginning of the simulation is in the center of the radial plot and the time evolution is plotted radially outwards.

The bar plots summarize the data on the dial plots, by showing the probability density of the torsion. If torsional potential information is available, the plot also shows the potential of the rotatable bond (by summing the potential of the related torsions). The values of the potential are on the left *Y*-axis of the chart, and are expressed in *kcal/mol*. Looking at the histogram and torsion potential relationships may give insights into the conformational strain the ligand undergoes to maintain a protein-bound conformation.

Ligand Properties

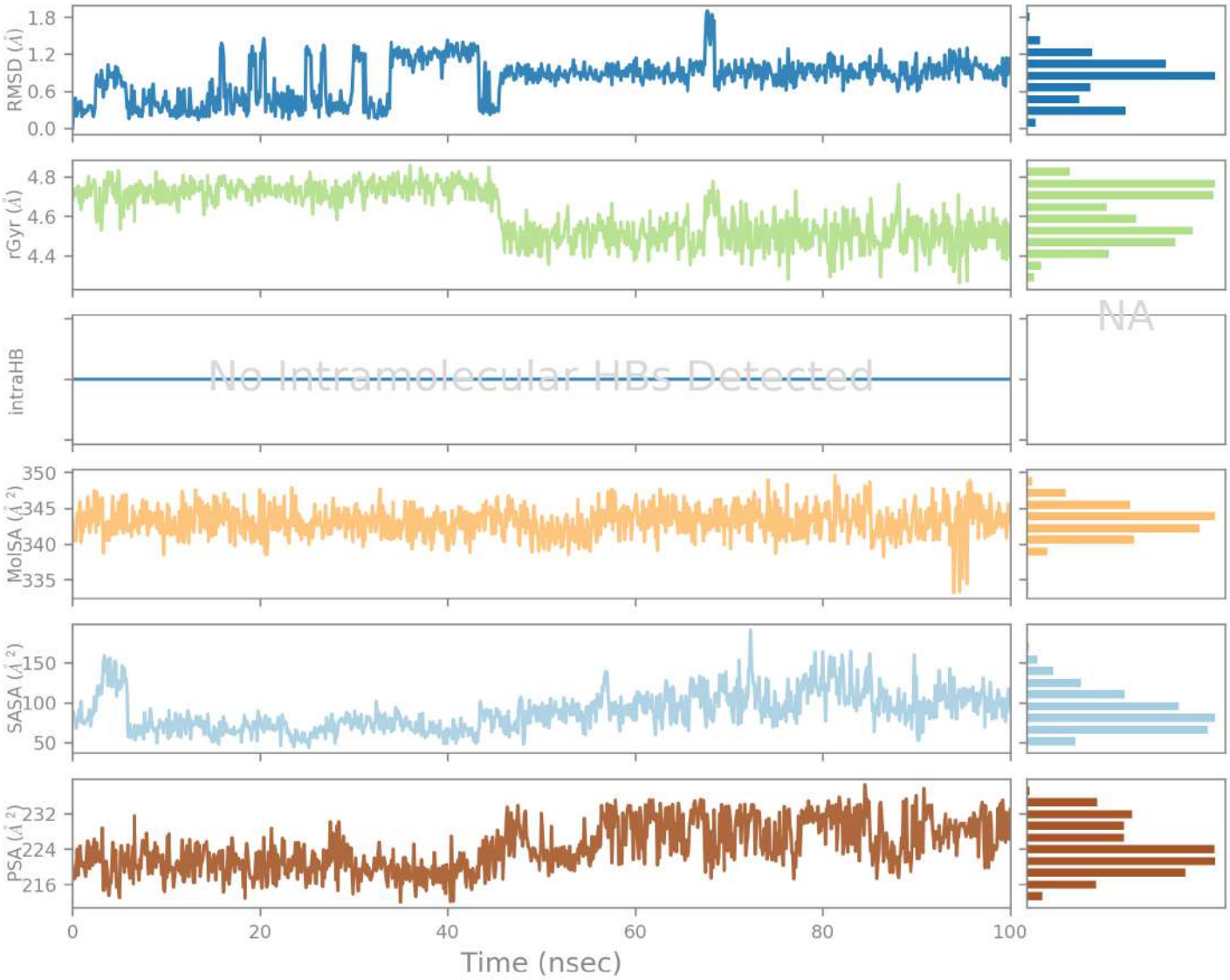

Ligand RMSD: Root mean square deviation of a ligand with respect to the reference conformation (typically the first frame is used as the reference and it is regarded as time *t*=0).

Radius of Gyration (rGyr): Measures the 'extendedness' of a ligand, and is equivalent to its principal moment of inertia.

Intramolecular Hydrogen Bonds (intraHB): Number of internal hydrogen bonds (HB) within a ligand molecule.

Molecular Surface Area (MolSA): Molecular surface calculation with 1.4 Å probe radius. This value is equivalent to a van der Waals surface area.

Solvent Accessible Surface Area (SASA): Surface area of a molecule accessible by a water molecule.

Polar Surface Area (PSA): Solvent accessible surface area in a molecule contributed only by oxygen and nitrogen atoms.

Simulation Interactions Diagram Report

Simulation Details

Jobname: desmond_md_job_1
Entry title: XXXX - hbond-opt

CPU #	Job Type	Ensemble	Temp. [K]	Sim. Time [ns]	# Atoms	# Waters	Charge
1	mdsim	NPT	300.0	100.102	34674	10257	0

Protein Information

Tot. Residues	Prot. Chain(s)	Res. in Chain(s)	# Atoms	# Heavy Atoms	Charge
249	'A', 'B'	ict_values([126, 123]	3791	1906	-7

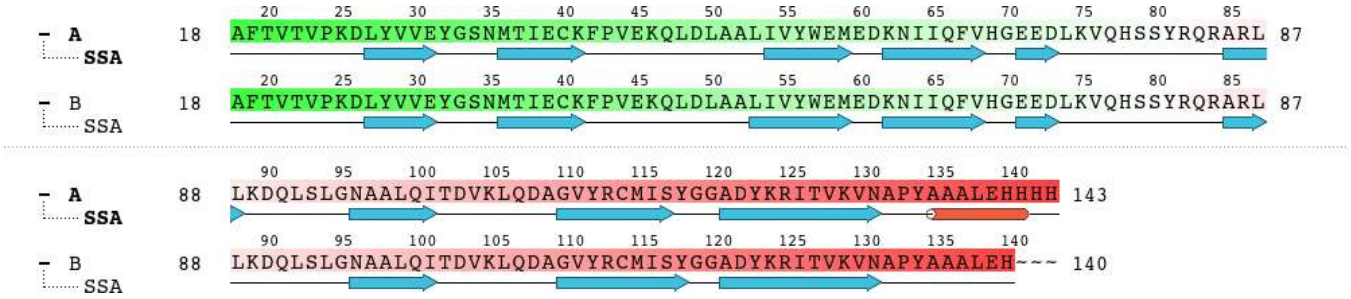

Ligand Information

SMILES	n1nnc(n2)n1nc(c23)n(nc3C)-c4ccc(cc4)S(=O)(=O)N(CC5)CCN5C
PDB Name	'UNK'
Num. of Atoms	47 (total) 29 (heavy)
Atomic Mass	414.452 au
Charge	0
Mol. Formula	C16H18N10O2S
Num. of Fragments	2
Num. of Rot. Bonds	3

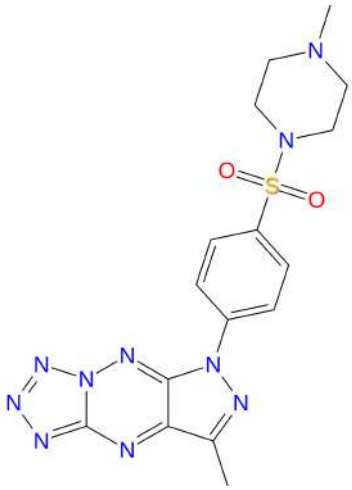

Counter Ion/Salt Information

Type	Num.	Concentration [mM]	Total Charge
Na	36	63.815	+36
Cl	29	51.406	-29

Protein-Ligand RMSD

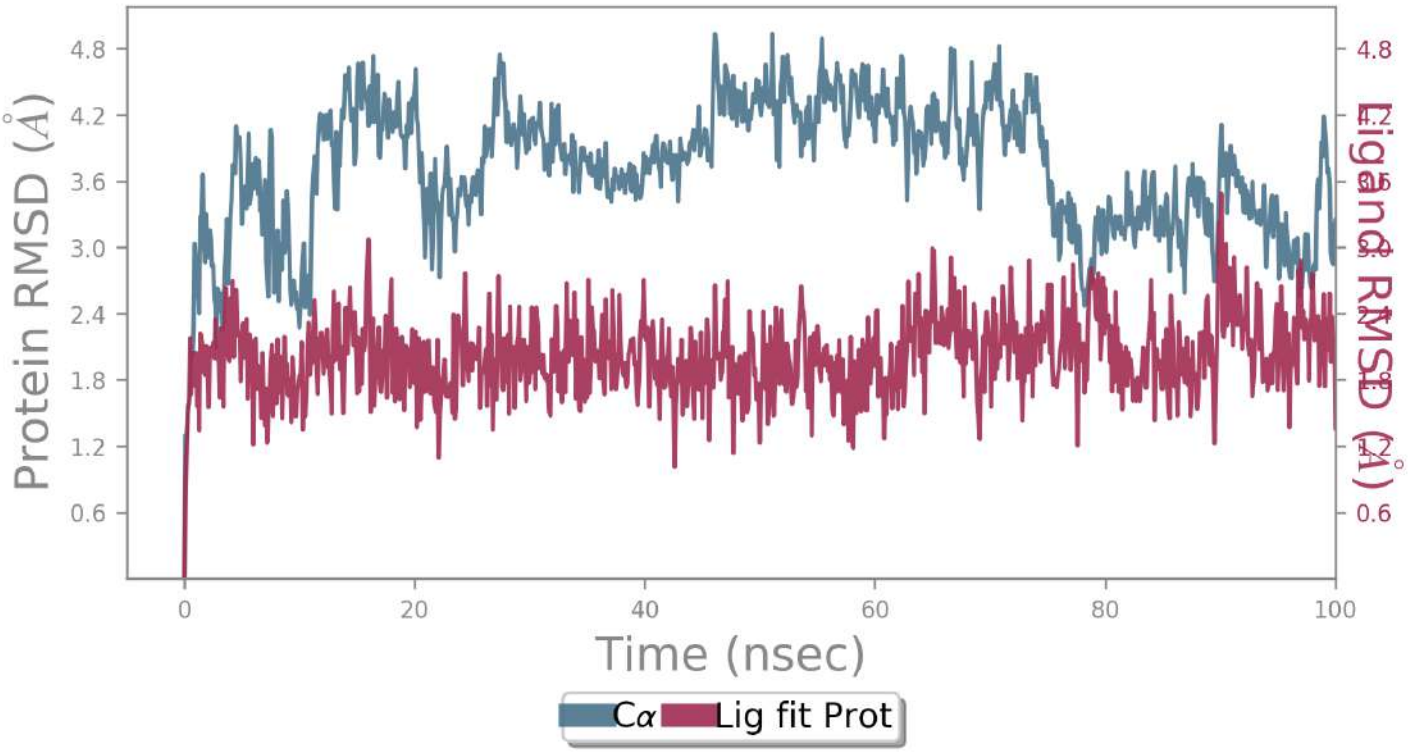

The Root Mean Square Deviation (RMSD) is used to measure the average change in displacement of a selection of atoms for a particular frame with respect to a reference frame. It is calculated for all frames in the trajectory. The RMSD for frame *x* is:

$$RMSD_x = \sqrt{\frac{1}{N}\sum_{i=1}^{N}(r_i'(t_x)) - r_i(t_{ref}))^2}$$

where *N* is the number of atoms in the atom selection; t_{ref} is the reference time, (typically the first frame is used as the reference and it is regarded as time *t*=0); and *r'* is the position of the selected atoms in frame *x* after superimposing on the reference frame, where frame *x* is recorded at time t_x. The procedure is repeated for every frame in the simulation trajectory.

Protein RMSD: The above plot shows the RMSD evolution of a protein (left *Y*-axis). All protein frames are first aligned on the reference frame backbone, and then the RMSD is calculated based on the atom selection. Monitoring the RMSD of the protein can give insights into its structural conformation throughout the simulation. RMSD analysis can indicate if the simulation has equilibrated — its fluctuations towards the end of the simulation are around some thermal average structure. Changes of the order of 1-3 Å are perfectly acceptable for small, globular proteins. Changes much larger than that, however, indicate that the protein is undergoing a large conformational change during the simulation. It is also important that your simulation converges — the RMSD values stabilize around a fixed value. If the RMSD of the protein is still increasing or decreasing on average at the end of the simulation, then your system has not equilibrated, and your simulation may not be long enough for rigorous analysis.

Ligand RMSD: Ligand RMSD (right *Y*-axis) indicates how stable the ligand is with respect to the protein and its binding pocket. In the above plot, 'Lig fit Prot' shows the RMSD of a ligand when the protein-ligand complex is first aligned on the protein backbone of the reference and then the RMSD of the ligand heavy atoms is measured. If the values observed are significantly larger than the RMSD of the protein, then it is likely that the ligand has diffused away from its initial binding site.

Protein RMSF

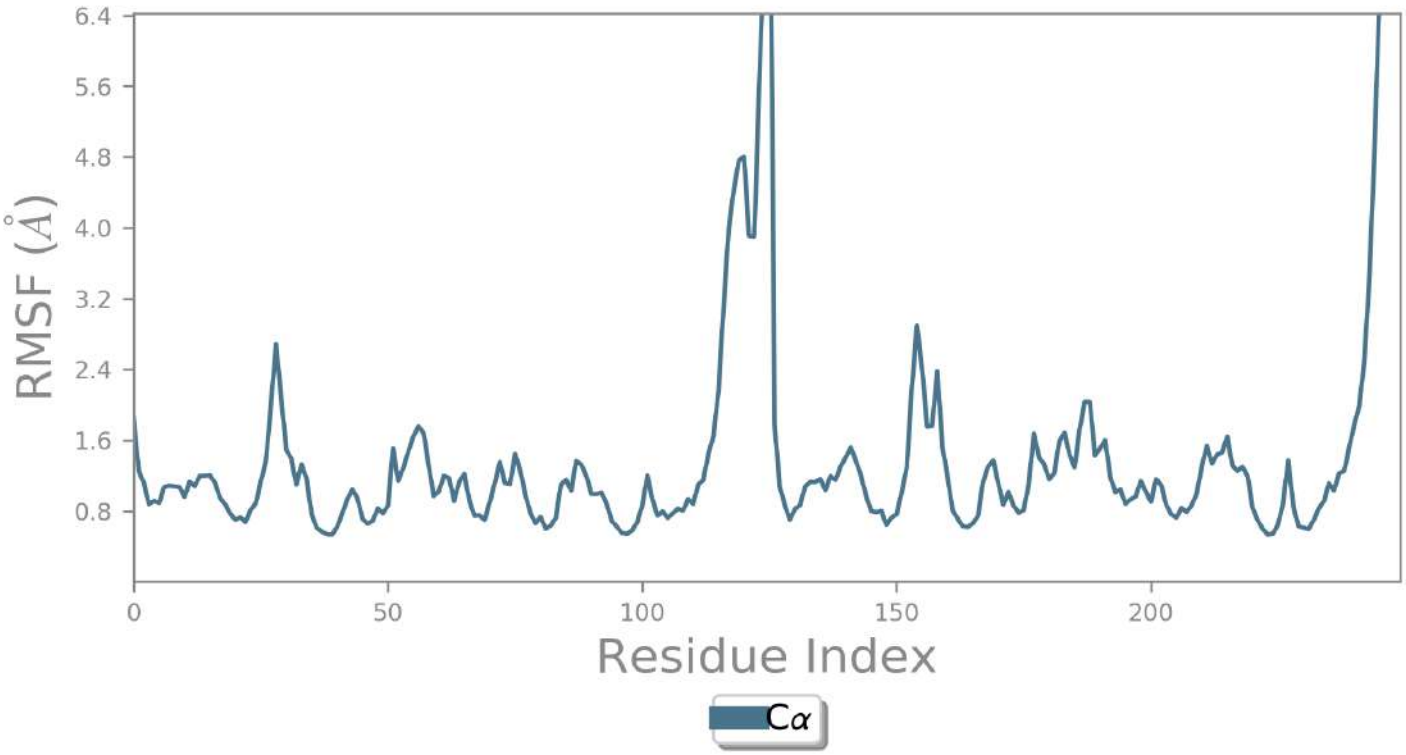

The Root Mean Square Fluctuation (RMSF) is useful for characterizing local changes along the protein chain. The RMSF for residue *i* is:

$$RMSF_i = \sqrt{\frac{1}{T}\sum_{t=1}^{T} < (r_i'(t)) - r_i(t_{ref}))^2 >}$$

where *T* is the trajectory time over which the RMSF is calculated, t_{ref} is the reference time, r_i is the position of residue *i*; *r'* is the position of atoms in residue *i* after superposition on the reference, and the angle brackets indicate that the average of the square distance is taken over the selection of atoms in the residue.

On this plot, peaks indicate areas of the protein that fluctuate the most during the simulation. Typically you will observe that the tails (*N*- and *C*-terminal) fluctuate more than any other part of the protein. Secondary structure elements like alpha helices and beta strands are usually more rigid than the unstructured part of the protein, and thus fluctuate less than the loop regions.

Protein Secondary Structure

% Helix	% Strand	% Total SSE
0.89	39.43	40.32

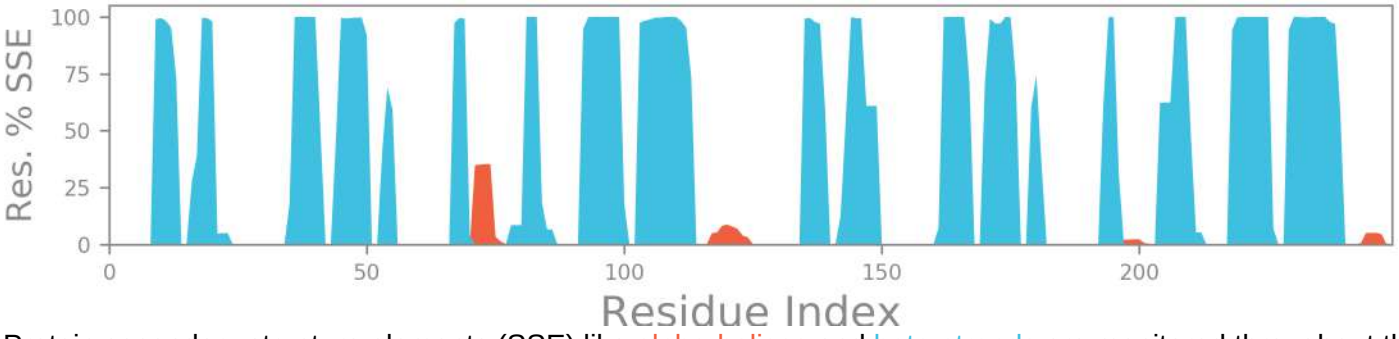

Protein secondary structure elements (SSE) like alpha-helices and beta-strands are monitored throughout the simulation. The plot above reports SSE distribution by residue index throughout the protein structure. The plot below summarizes the SSE composition for each trajectory frame over the course of the simulation, and the plot at the bottom monitors each residue and its SSE assignment over time.

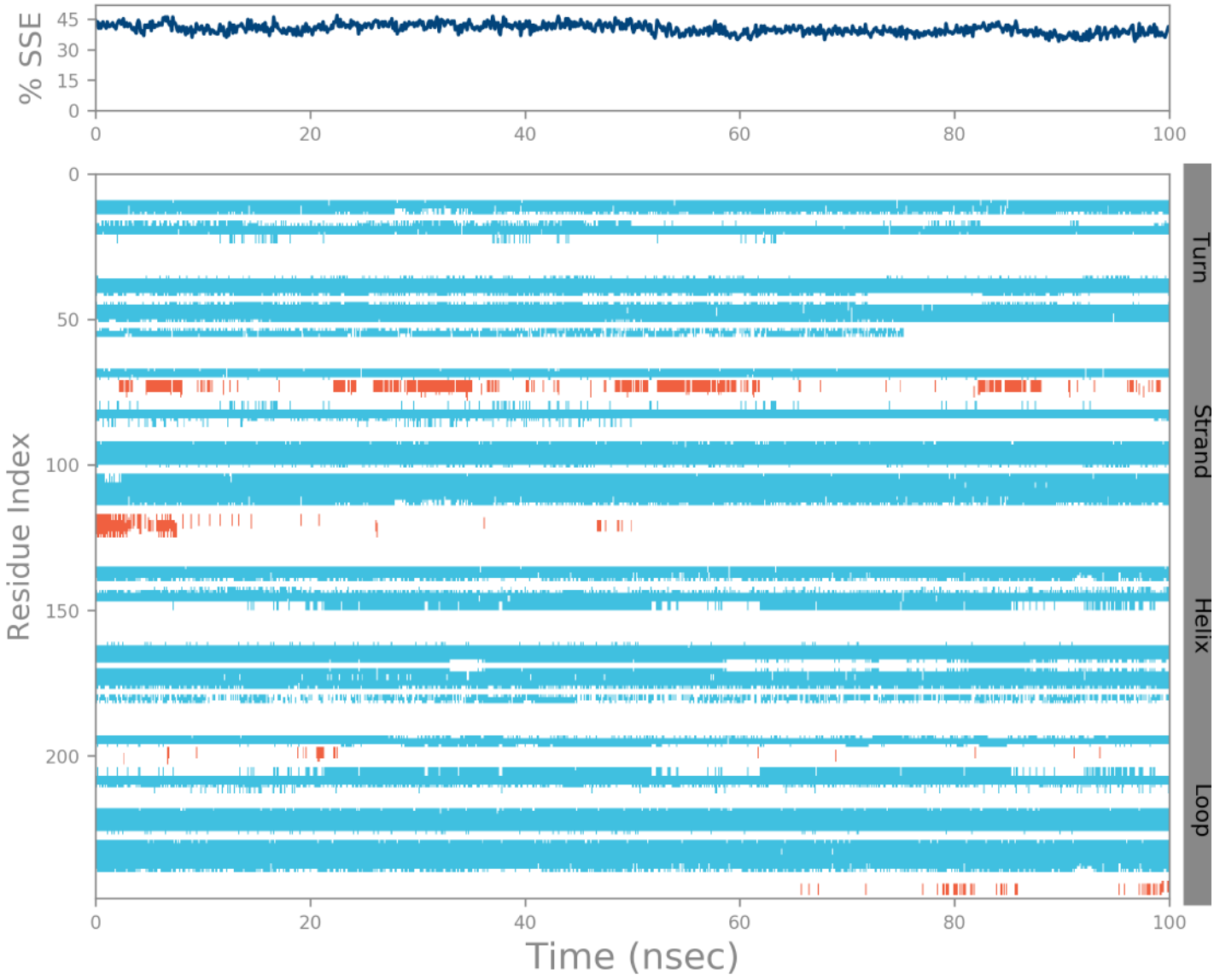

Ligand RMSF

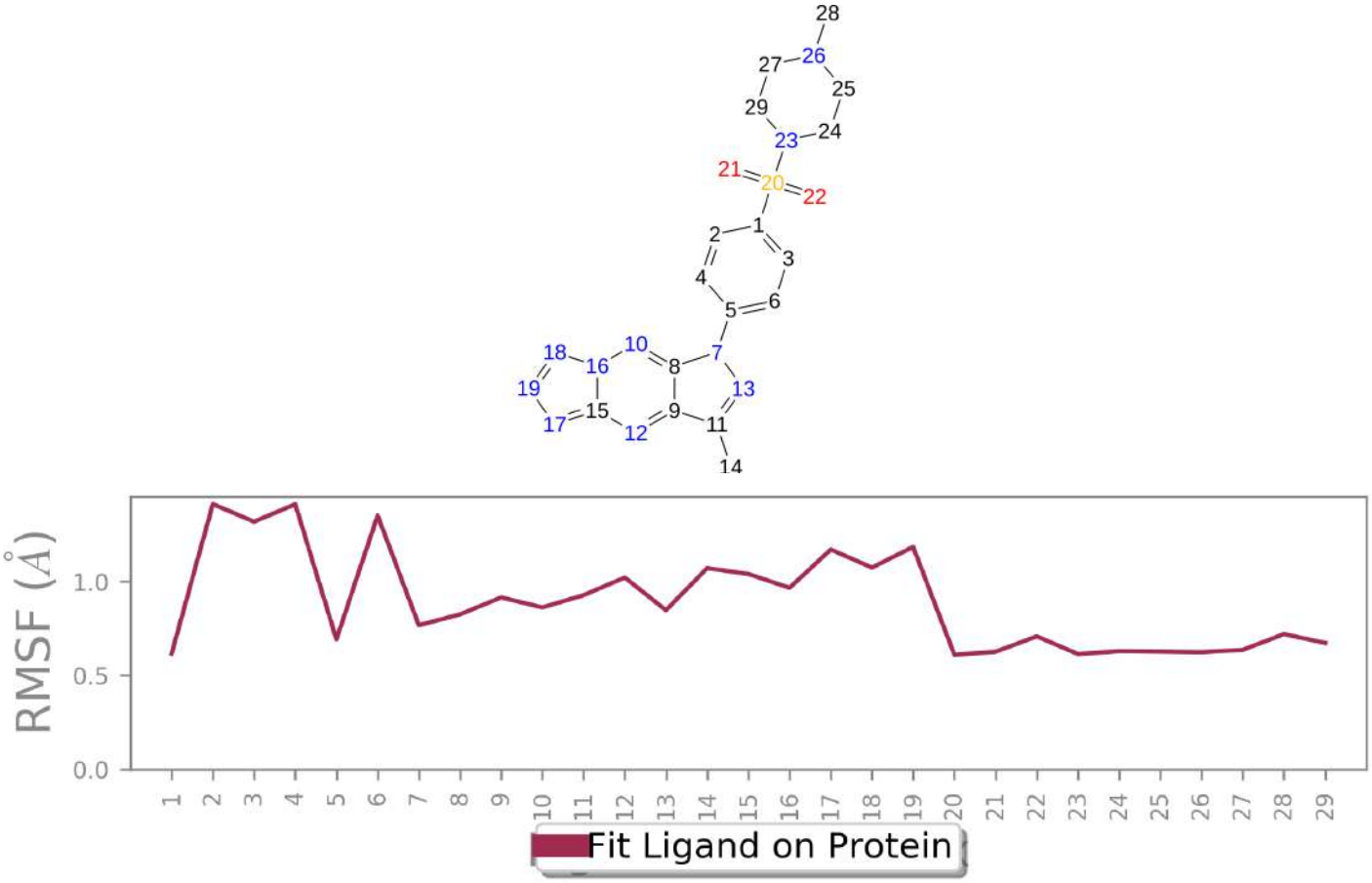

The Ligand Root Mean Square Fluctuation (L-RMSF) is useful for characterizing changes in the ligand atom positions. The RMSF for atom *i* is:

$$RMSF_i = \sqrt{\frac{1}{T}\sum_{t=1}^{T}(r_i'(t)) - r_i(t_{ref}))^2}$$

where *T* is the trajectory time over which the RMSF is calculated, t_{ref} is the reference time (usually for the first frame, and is regarded as the *zero* of time); *r* is the position of atom *i* in the reference at time t_{ref}, and *r'* is the position of atom *i* at time *t* after superposition on the reference frame.

Ligand RMSF shows the ligand's fluctuations broken down by atom, corresponding to the 2D structure in the top panel. The ligand RMSF may give you insights on how ligand fragments interact with the protein and their entropic role in the binding event. In the bottom panel, the 'Fit Ligand on Protein' line shows the ligand fluctuations, with respect to the protein. The protein-ligand complex is first aligned on the protein backbone and then the ligand RMSF is measured on the ligand heavy atoms.

Protein-Ligand Contacts

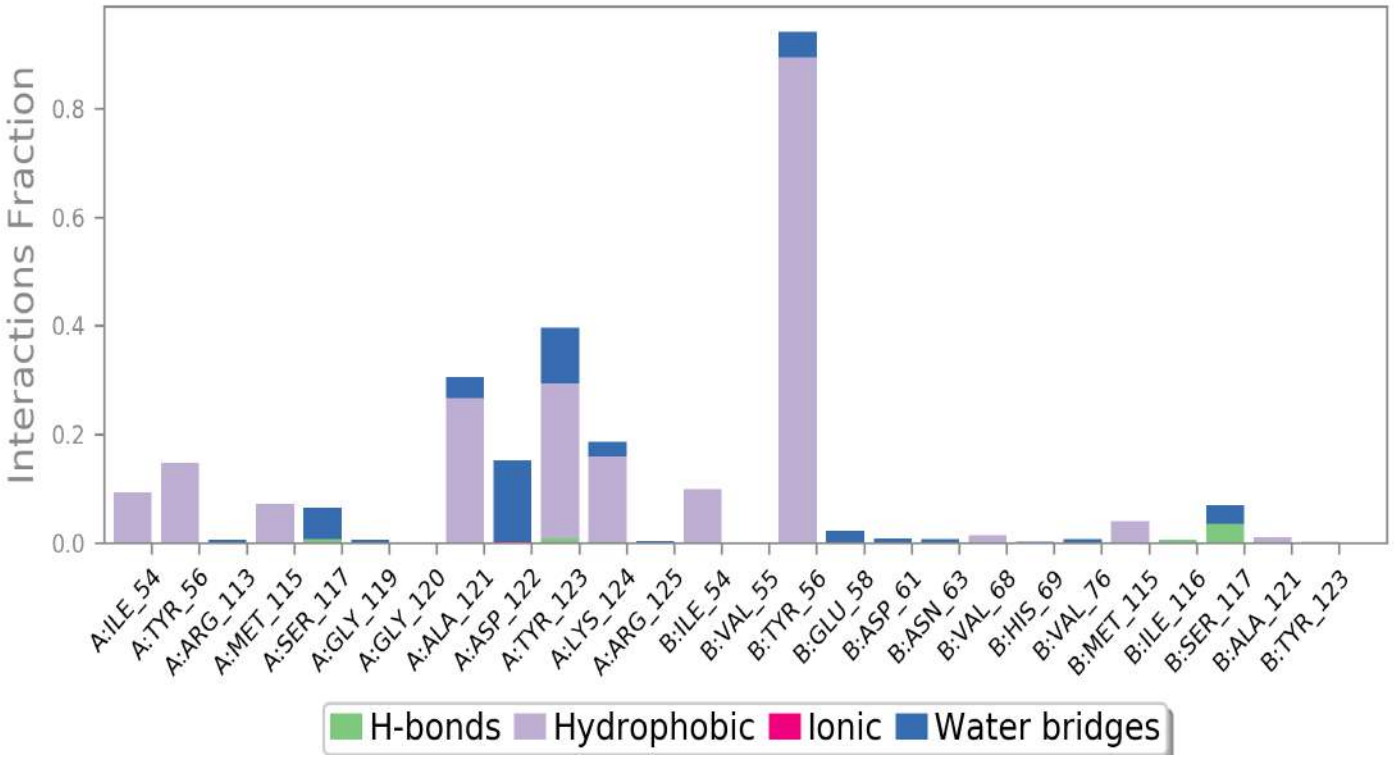

Protein interactions with the ligand can be monitored throughout the simulation. These interactions can be categorized by type and summarized, as shown in the plot above. Protein-ligand interactions (or 'contacts') are categorized into four types: Hydrogen Bonds, Hydrophobic, Ionic and Water Bridges. Each interaction type contains more specific subtypes, which can be explored through the 'Simulation Interactions Diagram' panel. The stacked bar charts are normalized over the course of the trajectory: for example, a value of 0.7 suggests that 70% of the simulation time the specific interaction is maintained. Values over 1.0 are possible as some protein residue may make multiple contacts of same subtype with the ligand.

Hydrogen Bonds: (H-bonds) play a significant role in ligand binding. Consideration of hydrogen-bonding properties in drug design is important because of their strong influence on drug specificity, metabolization and adsorption. Hydrogen bonds between a protein and a ligand can be further broken down into four subtypes: backbone acceptor; backbone donor; side-chain acceptor; side-chain donor.
The current geometric criteria for protein-ligand H-bond is: distance of 2.5 Å between the donor and acceptor atoms (D—H···A); a donor angle of ≥120° between the donor-hydrogen-acceptor atoms (D—H···A); and an acceptor angle of ≥90° between the hydrogen-acceptor-bonded_atom atoms (H···A—X).

Hydrophobic contacts: fall into three subtypes: π-Cation; π-π; and Other, non-specific interactions. Generally these type of interactions involve a hydrophobic amino acid and an aromatic or aliphatic group on the ligand, but we have extended this category to also include π-Cation interactions.
The current geometric criteria for hydrophobic interactions is as follows: π-Cation — Aromatic and charged groups within 4.5 Å; π-π — Two aromatic groups stacked face-to-face or face-to-edge; Other — A non-specific hydrophobic sidechain within 3.6 Å of a ligand's aromatic or aliphatic carbons.

Ionic interactions: or polar interactions, are between two oppositely charged atoms that are within 3.7 Å of each other and do not involve a hydrogen bond. We also monitor Protein-Metal-Ligand interactions, which are defined by a metal ion coordinated within 3.4 Å of protein's and ligand's heavy atoms (except carbon). All ionic interactions are broken down into two subtypes: those mediated by a protein backbone or side chains.

Water Bridges: are hydrogen-bonded protein-ligand interactions mediated by a water molecule. The hydrogen-bond geometry is slightly relaxed from the standard H-bond definition.
The current geometric criteria for a protein-water or water-ligand H-bond are: a distance of 2.8 Å between the donor and acceptor atoms (D—H···A); a donor angle of ≥110° between the donor-hydrogen-acceptor atoms (D—H···A); and an acceptor angle of ≥90° between the hydrogen-acceptor-bonded_atom atoms (H···A—X).

Protein-Ligand Contacts (cont.)

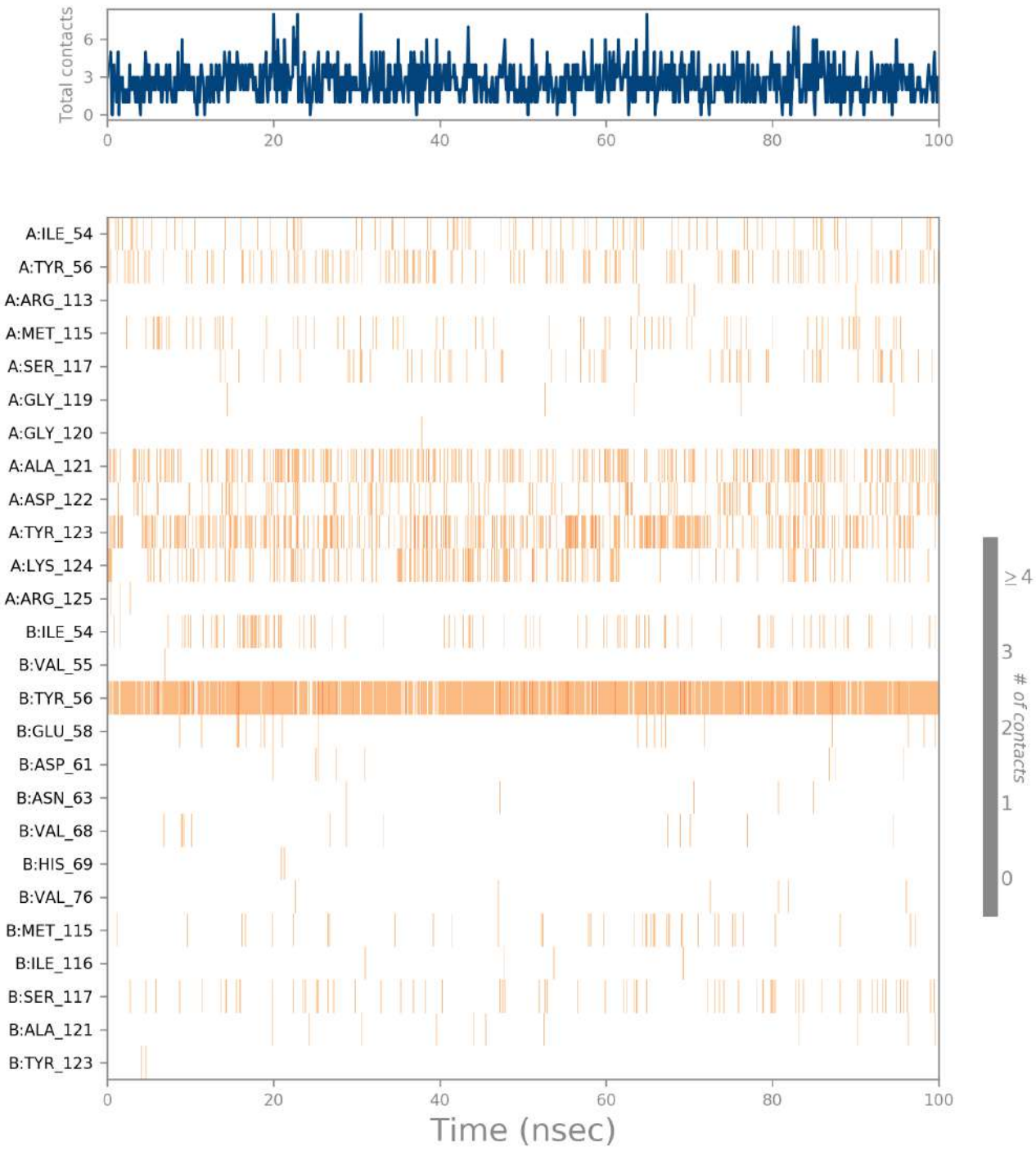

A timeline representation of the interactions and contacts (**H-bonds**, **Hydrophobic**, **Ionic**, **Water bridges**) summarized in the previous page. The top panel shows the total number of specific contacts the protein makes with the ligand over the course of the trajectory. The bottom panel shows which residues interact with the ligand in each trajectory frame. Some residues make more than one specific contact with the ligand, which is represented by a darker shade of orange, according to the scale to the right of the plot.

Ligand-Protein Contacts

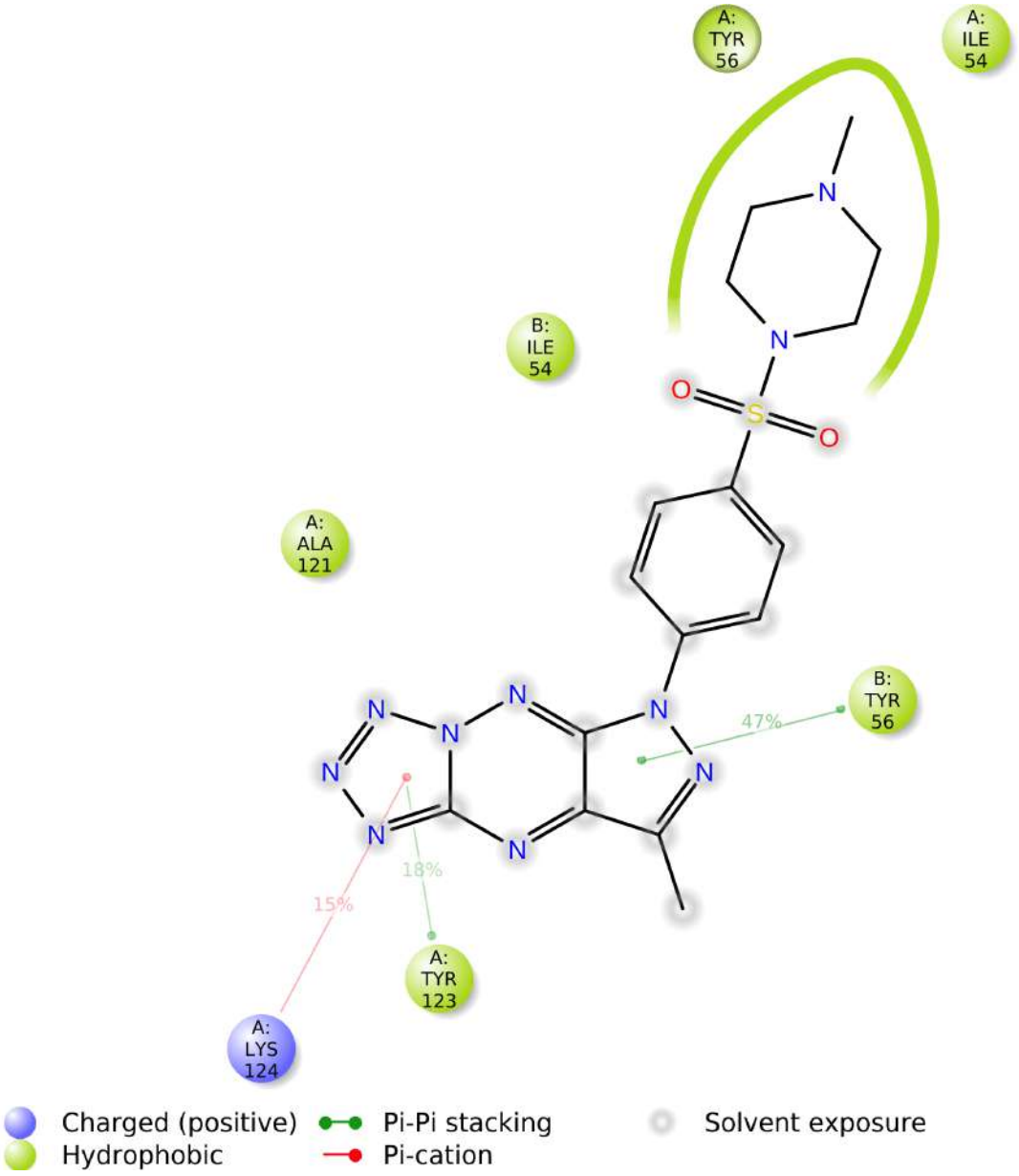

A schematic of detailed ligand atom interactions with the protein residues. Interactions that occur more than **8.0%** of the simulation time in the selected trajectory (0.00 through 100.00 nsec), are shown.
Note: it is possible to have interactions with >100% as some residues may have multiple interactions of a single type with the same ligand atom. For example, the ARG side chain has four H-bond donors that can all hydrogen-bond to a single H-bond acceptor.

Ligand Torsion Profile

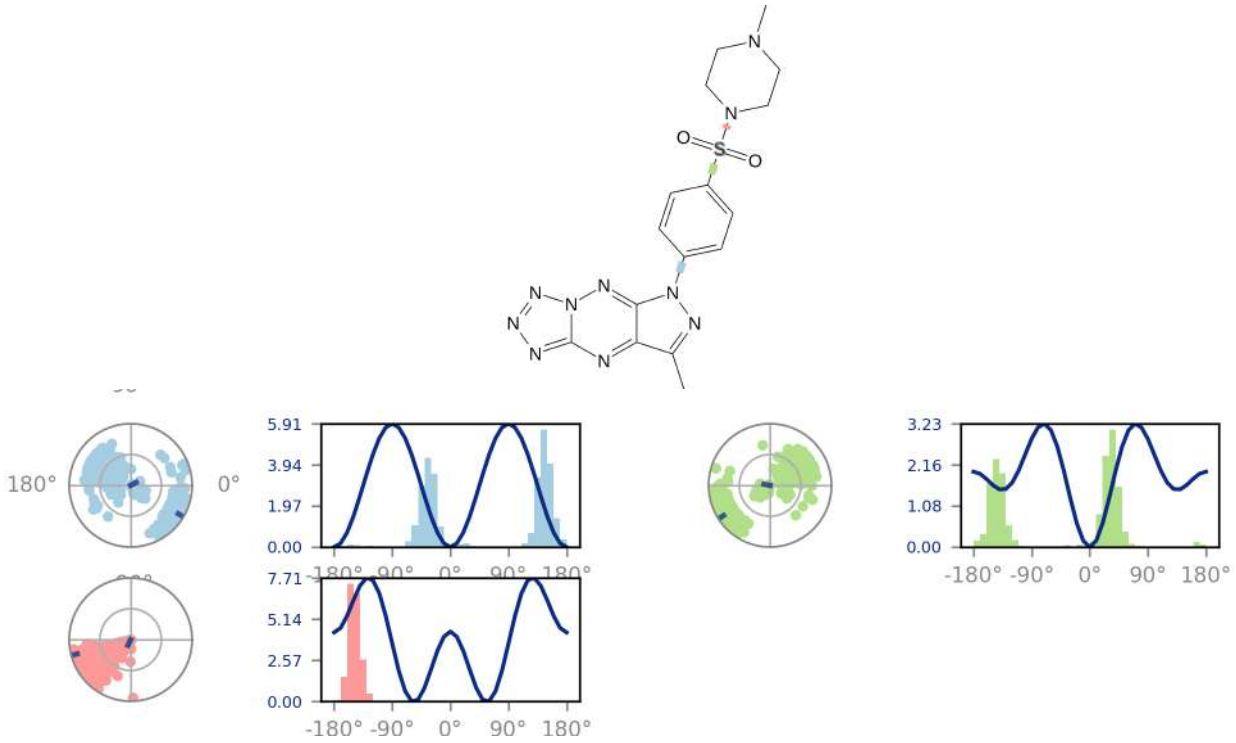

The ligand torsions plot summarizes the conformational evolution of every rotatable bond (RB) in the ligand throughout the simulation trajectory (0.00 through 100.00 nsec). The top panel shows the 2d schematic of a ligand with color-coded rotatable bonds. Each rotatable bond torsion is accompanied by a dial plot and bar plots of the same color.

Dial (or radial) plots describe the conformation of the torsion throughout the course of the simulation. The beginning of the simulation is in the center of the radial plot and the time evolution is plotted radially outwards.

The bar plots summarize the data on the dial plots, by showing the probability density of the torsion. If torsional potential information is available, the plot also shows the potential of the rotatable bond (by summing the potential of the related torsions). The values of the potential are on the left *Y*-axis of the chart, and are expressed in *kcal/mol*. Looking at the histogram and torsion potential relationships may give insights into the conformational strain the ligand undergoes to maintain a protein-bound conformation.

Ligand Properties

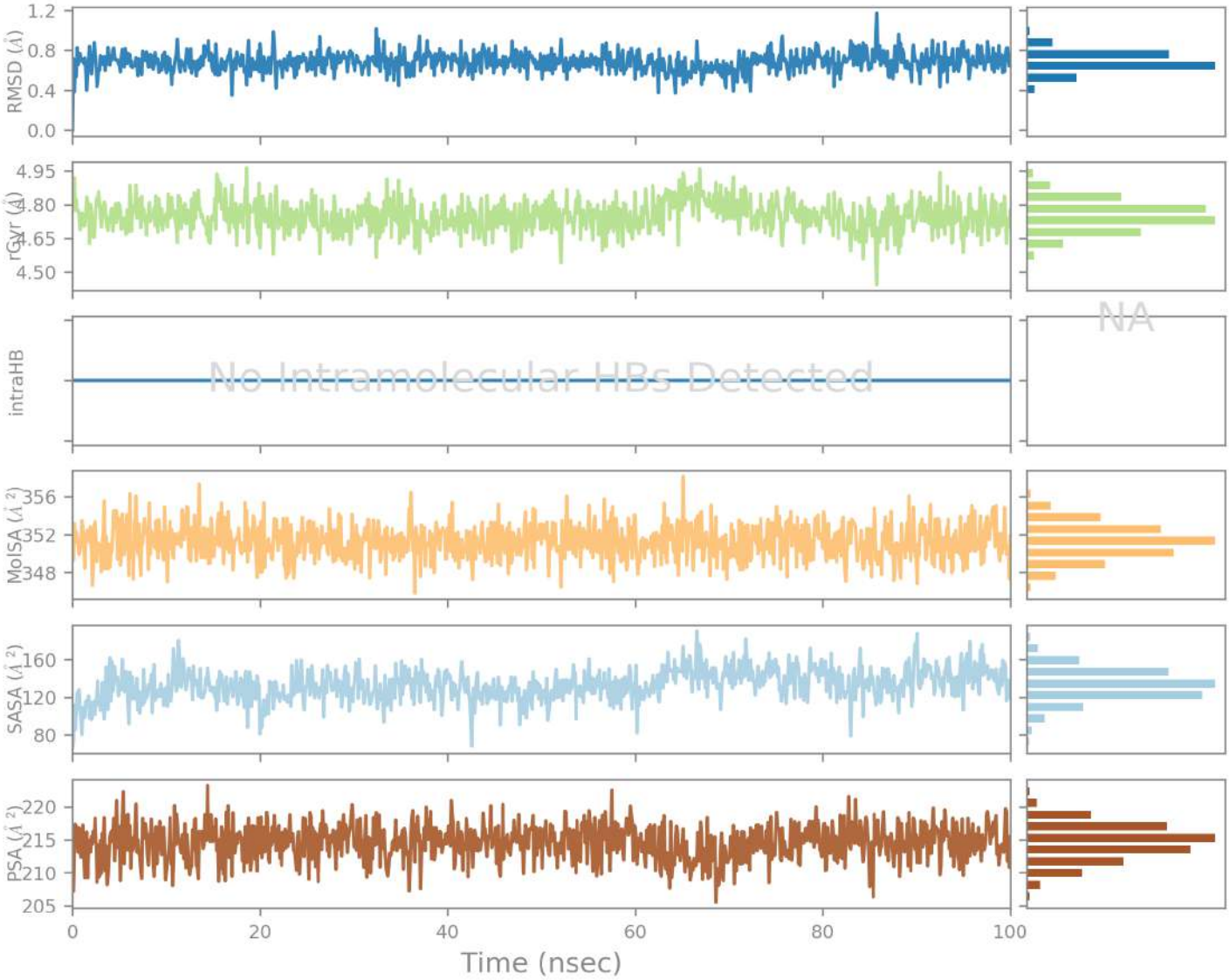

Ligand RMSD: Root mean square deviation of a ligand with respect to the reference conformation (typically the first frame is used as the reference and it is regarded as time *t*=0).

Radius of Gyration (rGyr): Measures the 'extendedness' of a ligand, and is equivalent to its principal moment of inertia.

Intramolecular Hydrogen Bonds (intraHB): Number of internal hydrogen bonds (HB) within a ligand molecule.

Molecular Surface Area (MolSA): Molecular surface calculation with 1.4 Å probe radius. This value is equivalent to a van der Waals surface area.

Solvent Accessible Surface Area (SASA): Surface area of a molecule accessible by a water molecule.

Polar Surface Area (PSA): Solvent accessible surface area in a molecule contributed only by oxygen and nitrogen atoms.

International Journal of
Molecular Sciences

MDPI

Article

Genotoxicity of Novel Pyrazolo[4,3-*e*]tetrazolo[1,5-*b*][1,2,4]triazine Sulfonamides in Normal and Cancer Cells In Vitro

Mateusz Kciuk [1,2,*], Somdutt Mujwar [3], Beata Marciniak [1], Adrianna Gielecińska [1,2], Karol Bukowski [1], Mariusz Mojzych [4] and Renata Kontek [1]

[1] Department of Molecular Biotechnology and Genetics, University of Lodz, Banacha 12/16, 90-237 Lodz, Poland
[2] Doctoral School of Exact and Natural Sciences, University of Lodz, Banacha Street 12/16, 90-237 Lodz, Poland
[3] Chitkara College of Pharmacy, Chitkara University, Rajpura 140401, Punjab, India
[4] Department of Chemistry, Siedlce University of Natural Sciences and Humanities, 3 Maja 54, 08-110 Siedlce, Poland
* Correspondence: mateusz.kciuk@edu.uni.lodz.pl

Abstract: Pyrazolo[4,3-*e*]tetrazolo[1,5-*b*][1,2,4]triazine sulfonamides constitute a novel group of heterocyclic compounds with broad biological activities including anticancer properties. The compounds investigated in this study (**MM134**, **-6**, **-7**, and **9**) were found to have antiproliferative activity against BxPC-3 and PC-3 cancer cell lines in micromolar concentrations (IC_{50} 0.11–0.33 μM). Here, we studied the genotoxic potential of the tested compounds with alkaline and neutral comet assays, accompanied by immunocytochemical detection of phosphorylated γH2AX. We found that pyrazolo tetrazolo[1,5-*b*][1,2,4]triazine sulfonamides induce significant levels of DNA damage in BxPC-3 and PC-3 cells without causing genotoxic effects in normal human lung fibroblasts (WI-38) when used in their respective IC_{50} concentrations (except for **MM134**) and showed a dose-dependent increase in DNA damage following 24 h incubation of tested cancer cells with these agents. Furthermore, the influence of **MM** compounds on DNA damage response (DDR) factors was assessed using molecular docking and molecular dynamics simulation.

Keywords: comet assay; genotoxicity; pyrazolo[4,3-*e*]tetrazolo[4,5-*b*][1,2,4]triazine; sulfonamides

Citation: Kciuk, M.; Mujwar, S.; Marciniak, B.; Gielecińska, A.; Bukowski, K.; Mojzych, M.; Kontek, R. Genotoxicity of Novel Pyrazolo[4,3-*e*]tetrazolo [1,2,4]triazine Sulfonamides in Normal and Cancer Cells In Vitro. *Int. J. Mol. Sci.* **2023**, *24*, 4053. https://doi.org/10.3390/ijms24044053

Academic Editor: Antonella Zannetti

Received: 19 January 2023
Revised: 14 February 2023
Accepted: 15 February 2023
Published: 17 February 2023

1. Introduction

DNA-damaging agents are frequently used in oncology to treat both hematological and solid malignancies. Platinum compounds (cisplatin, oxaliplatin, and carboplatin), cyclophosphamide, chlorambucil, and temozolomide are some of the most frequently utilized agents in cancer treatment. The above-mentioned drugs trigger apoptosis in cancer cells by altering the chemical structure of DNA. Unfortunately, the efficacy of these drugs can be greatly diminished by a variety of factors that contribute to drug resistance development. When drug efflux and/or metabolism rise, the intracellular concentration of an anticancer agent can be reduced, which impairs its capacity to inflict sufficient DNA damage and cell death [1,2].

Many of the cytotoxic drugs that are routinely used to treat cancer induce significant levels of DNA damage, which causes cell cycle checkpoint activation and results in cell cycle arrest and/or cell death [3]. However, the activity of anticancer drugs is not sufficiently selective, and damage to normal cells and tissues can occur. This may result in a variety of undesirable side effects [4]. Significant research effort has been devoted to the development of protein kinase inhibitors as therapeutic targets for the treatment of many human disorders, including diabetes, cancer, and hypertension. To date, Gleevec is one of the most prominent examples of an agent that targets an ABL protein kinase involved in several types of malignancies. The purinome consists of approximately 2000 distinct proteins expressed by the genome that utilize purines as substrates or as co-factors in

the form of NAD, NADP, and co-enzyme A. The structures of representative gene family members within the purinome have revealed that these proteins bind purines in the same orientations as those reported in all protein kinases. The purinome is a rich pool of therapeutic targets. However, it also contains a wide collection of different proteins whose suppression may have unintended side effects [5].

A growing research area of heterocyclic compounds is still in the early stages of development, but it holds great promise for the discovery of new drugs. The development of new synthesis methods and the use of modern organic chemistry techniques have resulted in the rapid expansion of this area [6,7]. One of the primary goals of heterocyclic compound chemistry is the discovery of anticancer drugs, and one of the primers in organic anticancer chemistry is the synthesis of anticancer agents that structurally resemble the substrates of naturally occurring metabolic processes. Cell proliferation is slowed and apoptotic cell death is triggered when these critical mechanisms are interfered with [8–10]. Undoubtedly, the 1,2,4-triazines fused with five-membered heterocycles, which have exhibited bioisosteric resemblance to the purine core, are one of the most promising classes of agents with significant biological activity [11,12].

The pyrazolo[4,3-*e*][1,2,4]triazine class of compounds encompasses many unique chemical structures with broad biological activity, including inhibitory activity against carbonic anhydrase (CAs) [13,14], tyrosinase [15,16], urease [16], and anticancer activity as a result of their capacity to inhibit protein kinases such as cyclin-dependent kinases (CDKs) [17,18].

Previously we have shown that the pyrazolo[4,3-*e*]tetrazolo[1,5-*b*][1,2,4]triazine sulfonamides (**MM134**, **MM136**, **MM137**, and **MM139**) (Figure 1) investigated in this study exhibited selective cytotoxic potential in pancreas adenocarcinoma (BxPC-3) and prostate cancer (PC-3) cell lines without causing a cytotoxic effect on human lung fibroblasts (WI-38). Moreover, **MM134**, **-6**, **-7**, and **-9** exhibited pro-apoptotic activity in BxPC-3 and PC-3 cells and are predicted to act through inhibition of AKT-mTOR and PD-1/PD-L1 pathways in cancer cells, as indicated by in silico results [19]. The proposed mechanism of action of pyrazolo[4,3-*e*]tetrazolo[1,5-*b*][1,2,4]triazine sulfonamides (**MM compounds**) is shown in Figure 2.

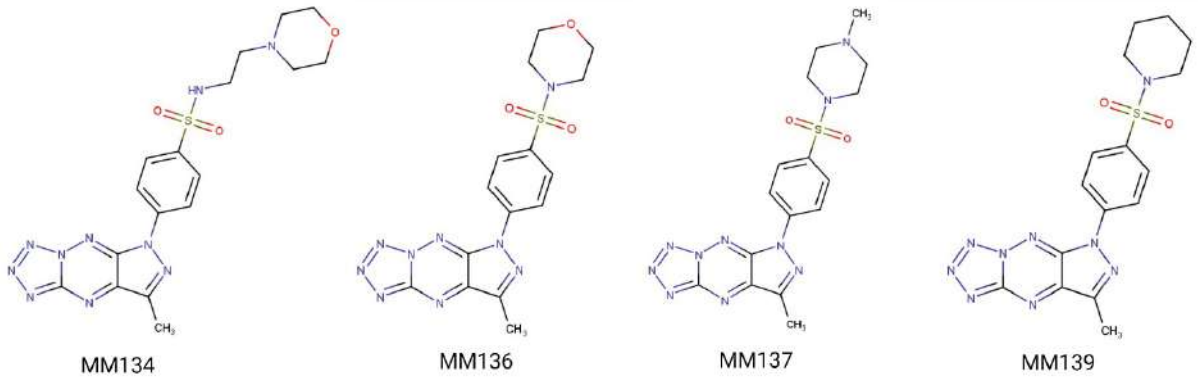

Figure 1. Investigated **MM** compounds: chemical structure of the four investigated sulfonamides **MM134**, **MM136**, **MM137**, and **MM139**.

In this paper, we present the genotoxic activity of pyrazolo[4,3-*e*]tetrazolo[1,5-*b*][1,2,4]triazine derivatives (**MM134**, **-6**, **-7** and **-9**) examined with alkaline and neutral comet assays, accompanied by immunocytochemical detection of phosphorylated histone protein (γH2AX).

In addition, a trypan blue test was performed to assess the viability of tested cells, and the Alamar blue test to explore the metabolic activity of the cells after treatment with the tested compounds.

Molecular docking and molecular dynamic simulation studies were employed to assess the binding potential of tested compounds with target enzymes belonging to the DNA damage response (DDR) pathway.

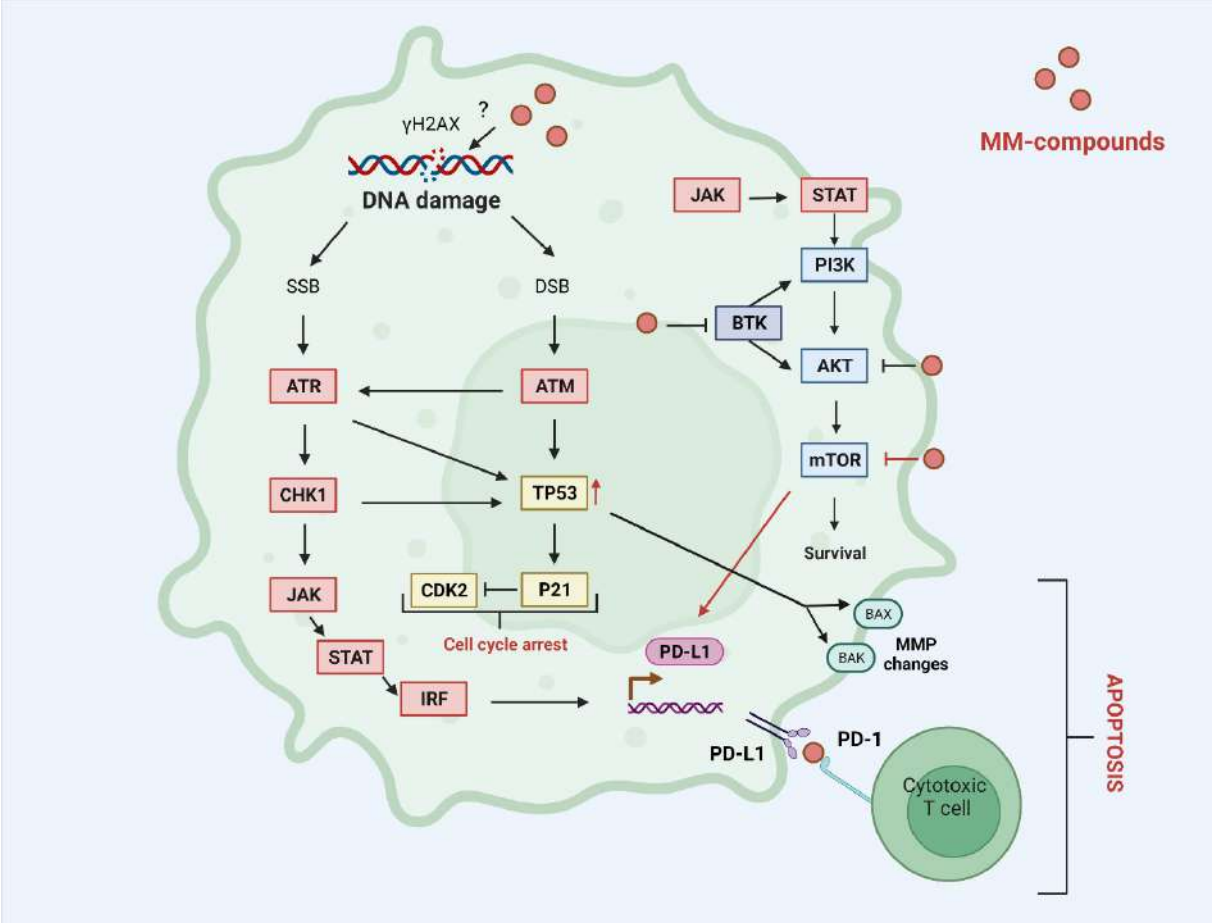

Figure 2. Predicted mechanism of action of **MM** compounds: **MM** compounds may act as BTK, PI3K-AKT-mTOR, and PD-L1 inhibitors that reduce cell survival and trigger apoptosis in a cytotoxic T-cell-dependent mechanism. Inhibition of mTOR kinase leads to up-regulation of PD-L1 expression. Increased expression of PD-L1 may result from the accumulation of DNA damage and activation of ATM/ATR/CHK1 and JAK/STAT/IRF signaling pathways. DNA damage leads to the up-regulation of TP53 tumor suppressor and induction of pro-apoptotic proteins including BAK and BAX involved in the intrinsic apoptosis pathway associated with MMP changes and increased production of P21 that works as an inhibitor of CDK2. AKT—RAC-alpha serine/threonine-protein kinase; ATM/ATR—serine-protein kinase ATM/ATR; BAX/BAK—pro-apoptotic protein BAX/BAK; BTK—tyrosine-protein kinase BTK; CDK2—cyclin-dependent kinase 2; CHK1—serine/threonine-protein kinase CHK1; DSB—double-strand break; IRF1—interferon regulatory factor 1; JAK—tyrosine-protein kinase JAK; MMP—mitochondrial membrane potential; mTOR—serine/threonine-protein kinase mTOR; PI3K—phosphatidylinositol-4,5-bisphosphate 3-kinase; PD-L1—programmed cell death 1 ligand 1; RTK—receptor tyrosine kinase; STAT—signal transducer and activator of transcription; TP53—cellular tumor antigen p53; γH2AX—phosphorylated histone protein H2AX.

2. Results

2.1. Trypan Blue Staining

Trypan blue staining used to determine cell viability in cancer cell lines (BxPC-3 (A), PC-3 (B)) and normal human fibroblasts (WI-38) (C) showed that all concentrations of the tested compounds **MM134**, **-6**, **-7**, and **-9** resulted in a minor decrease in cell viability following 24 h incubation at 37 °C; 5% CO_2. The decrease in viability did not exceed the extreme value of 70% in any experimental series. However, **MM134** induced the highest reduction in cell viability in all tested cell lines (Figure 3).

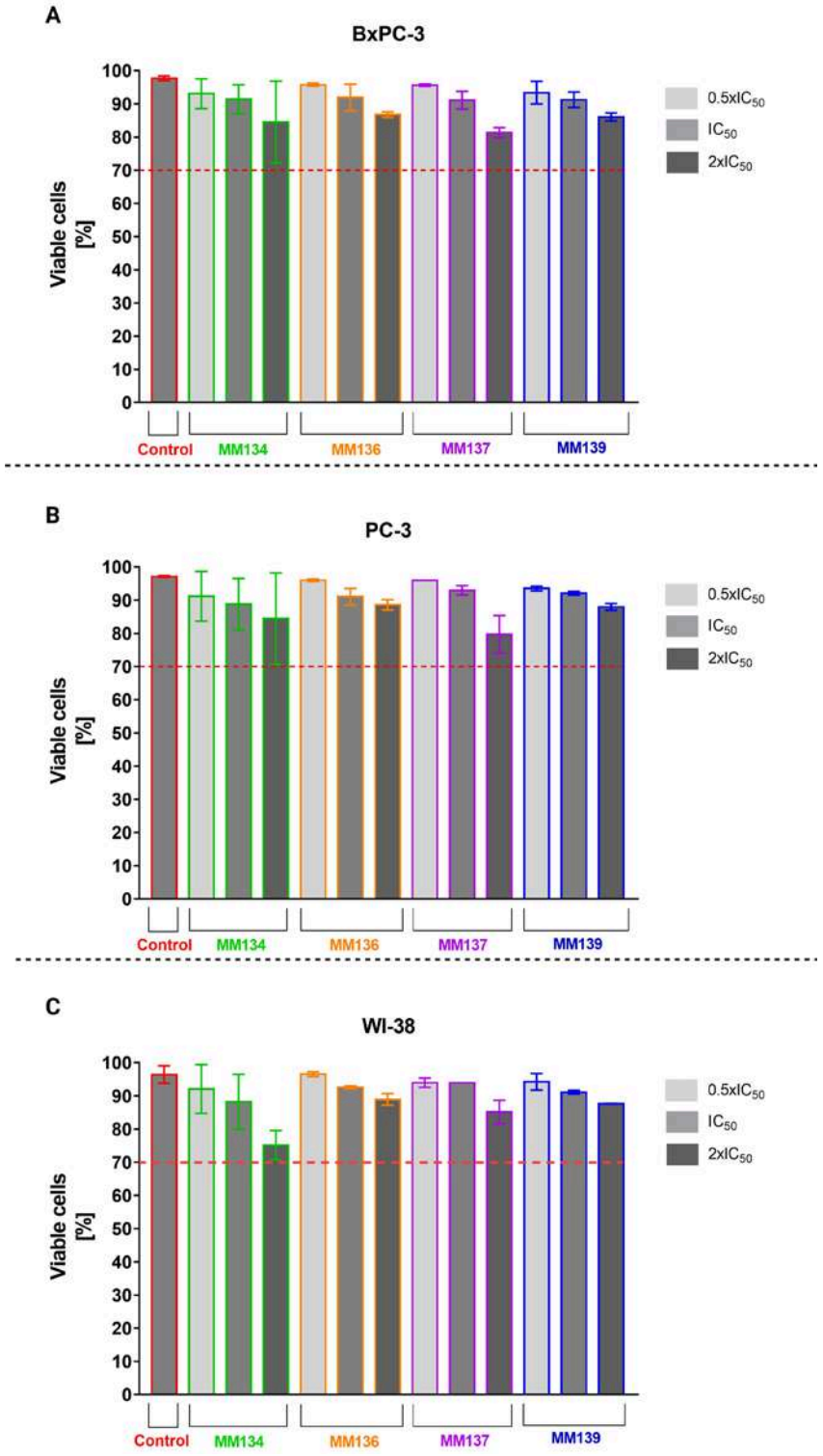

Figure 3. Trypan blue staining: effect of **MM134**, **-6**, **-7**, and **-9** used in concentrations of 0.5 (light gray), 1 (gray), and 2 (dark gray) times IC_{50} values on cancer cell (BxPC-3 (**A**) and PC-3 (**B**)) and normal human fibroblast (WI-38) (**C**) cell viability measured with trypan blue staining assay. Cells were exposed to tested compounds for 24 h at 37 °C. The mean values were obtained from three independent experiments. ±SD values.

2.2. Alamar Blue

The alamar blue assay was used to confirm the results obtained with the trypan blue assay and was performed before the assessment of the compounds' genotoxicity with the

neutral comet assay. The results obtained from two independent experiments are presented in Figure 4.

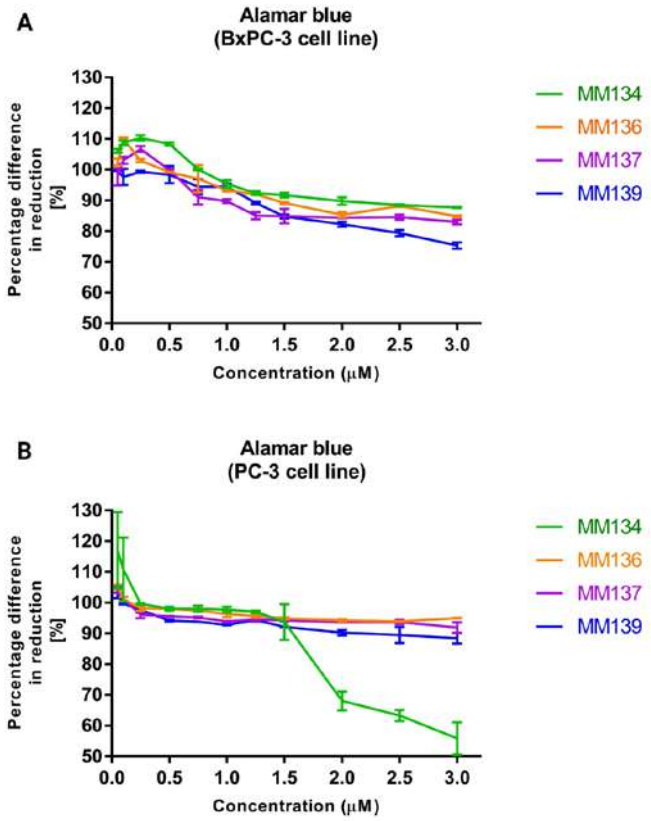

Figure 4. Alamar blue assay: the effect of **MM134**, **-6**, **-7**, and **-9** used in concentrations ranging from 0.05–3 μM on BxPC-3 (**A**) and PC-3 (**B**) cancer cells was measured with alamar blue assay. Cells were exposed to tested compounds for 24 h at 37 °C. The mean values were obtained from three independent experiments. ±SD values.

Twenty-four hour incubation of BxPC-3 and PC-3 cells with tested compounds reduced the viability of cells up to the level of 75.3 ± 0.99% (**MM139**) in the BxPC-3 cell line, and 88.4 ± 1.72% (**MM139**) in the PC-3 cell line with the highest (3 μM) concentration used in the assay. Similarly to the trypan blue assay, tested compounds did not reduce cell viability to a point below 75% when used in concentrations ranging from 0.08–0.66 μM for the BxPC-3 cell line and 0.055–0.34 μM in the PC-3 cell line, where the concentration range represents the concentration values between the lowest 0.5 × IC_{50} value and highest 2 × IC_{50} value obtained for all tested compounds in a given cell line. Moreover, a higher reduction of cell viability was observed in the BxPC-3 cell line compared with the PC-3 cell line (except for the **MM134** compound). **MM139** derivative caused the highest decrease in cell viability in BxPC-3 cells (75.3 ± 0.99% for 3 μM concentration). In contrast, in the PC-3 cell line, the **MM134** compound induced a rapid decrease in cell viability in concentrations above 1.5 μM, reaching 55.8 ± 5.27% at the concentration of 3 μM.

2.3. Alkaline Comet Assay

2.3.1. Cancer Cells

DNA damage was assessed using an alkaline comet assay with the support of *CASP* software [20]. Data were presented as median tail DNA percent (%) with interquartile range and minimal and maximal values. Median tail DNA (%) following incubation of cells with three concentrations (0.5 × IC_{50}, IC_{50}, and 2 × IC_{50}) of **MM134**, **-6**, **-7**, and **-9** were compared to negative (estimated DNA damage for BxPC-3 cells: median = 0.18%; mean = 2.04%; and PC-3 cells: median = 0.9%; mean = 3.33%) and positive control (20 μM

of bleomycin) (estimated DNA damage for BxPC-3 cells: median = 50.8%; mean = 48.3%; and PC-3 cells: median = 19.31%; mean = 22.07%) as shown in Figure 5 (for the BxPC-3 cell line (A) and PC-3 cell line (B)) and in Figure 6 for the WI-38 cell line. An increase in DNA damage was observed following 24 h incubation with the tested compounds that was not due to their cytotoxicity as determined by the trypan blue viability test. Examples of comet images obtained in an alkaline comet assay for the PC-3 cell line are shown in Figure 7.

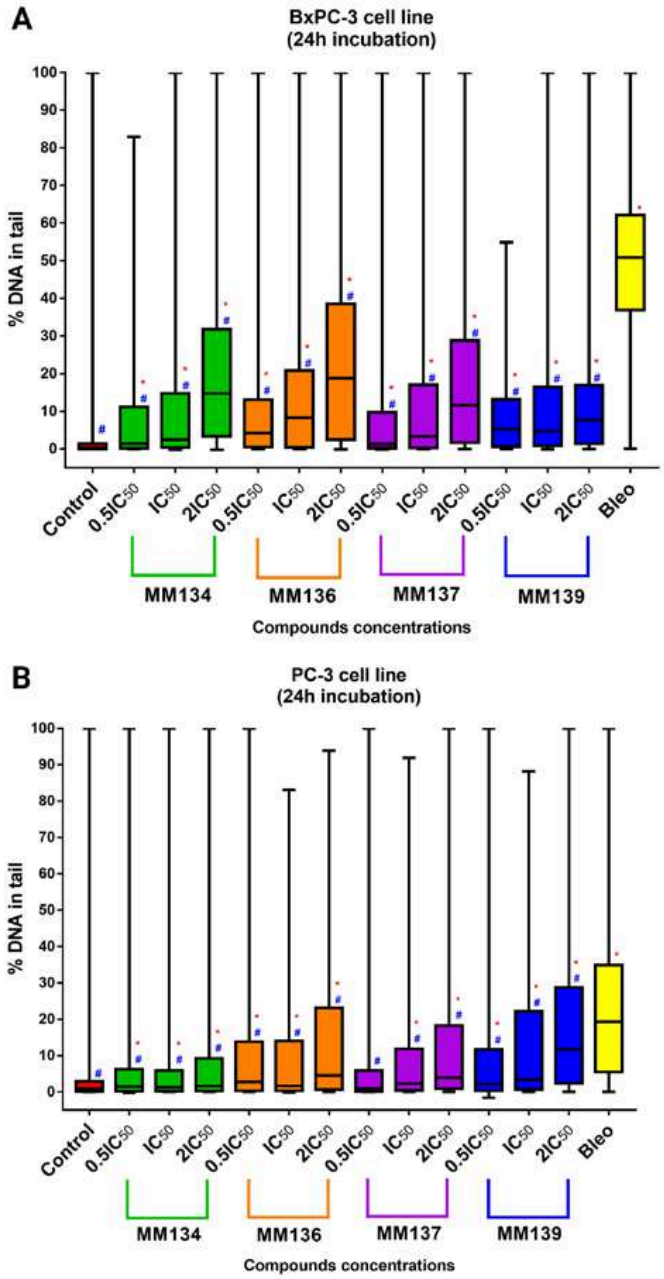

Figure 5. DNA damage in cancer cells estimated with 24 h alkaline comet assay: determination of DNA damage induced by 0.5 × IC_{50}, IC_{50}, and 2 × IC_{50} concentrations of **MM134**, **-6**, **-7**, and **-9** in cancer cell lines (BxPC-3 (**A**), PC-3 (**B**)). Data are represented as median tail DNA % with interquartile range and minimal and maximal values. The Kruskal–Wallis test was used to show a statistically significant difference between groups. Multiple comparisons using mean ranks for all groups module of Statistica software were used. In all groups, $N > 200$. * significant difference compared to the negative control; $p < 0.05$. # significant difference compared to the positive control (20 μM bleomycin); $p < 0.05$.

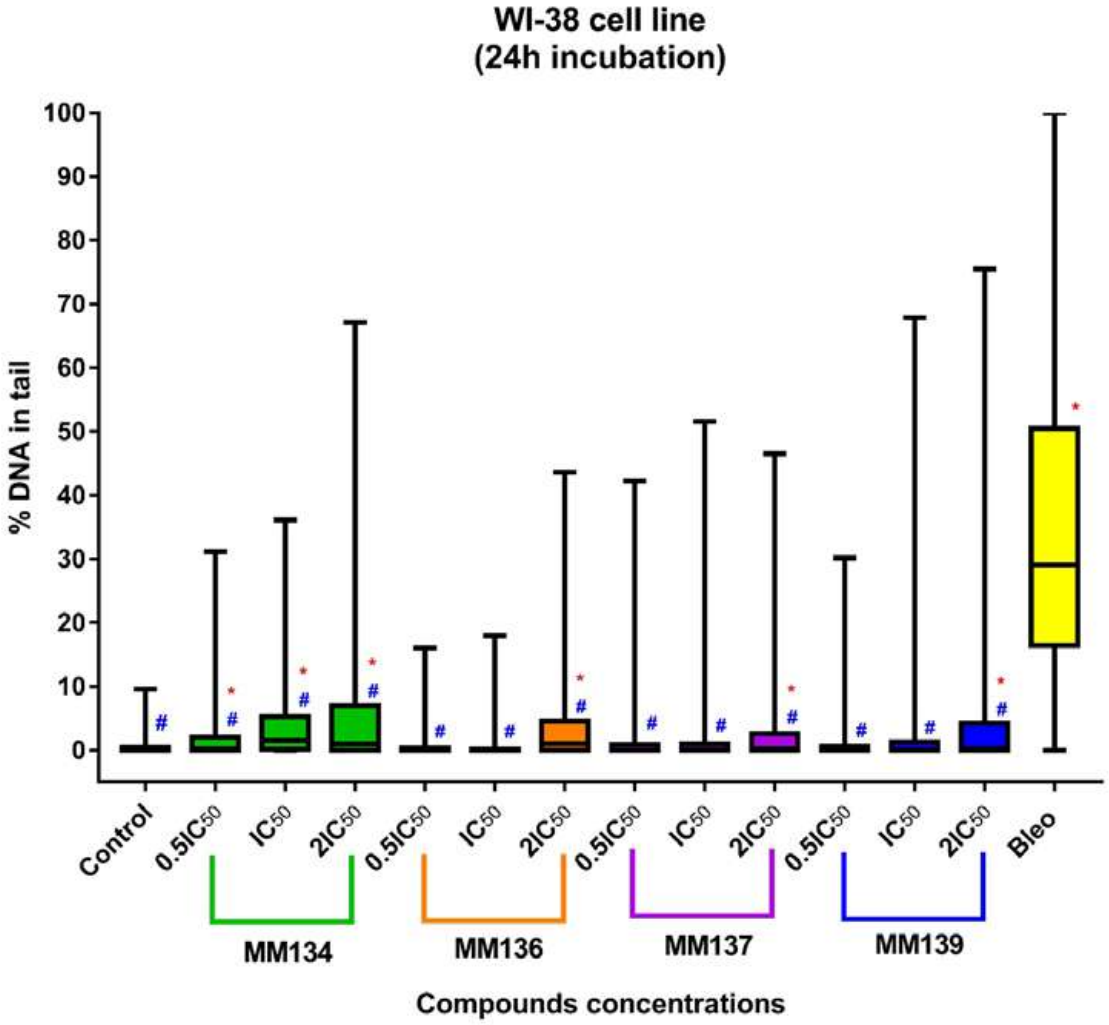

Figure 6. DNA damage in normal cells estimated with 24 h alkaline comet assay: determination of DNA damage induced by 0.5 × IC_{50}, IC_{50}, and 2 × IC_{50} concentrations of **MM134**, **-6**, **-7**, and **-9** in the WI-38 cell line. Data are represented as median tail DNA % with interquartile range and minimal and maximal values. The Kruskal–Wallis test was used to show a statistically significant difference between groups. Multiple comparisons using mean ranks for all groups module of Statistica software were used. In all groups, $N > 200$. * significant difference compared to the negative control; $p < 0.05$. # significant difference compared to the positive control (20 μM bleomycin); $p < 0.05$.

Tested compounds used in concentrations followed by IC_{50} values (0.5 × CI_{50}, IC_{50}, and 2 × IC_{50}) induced a dose-dependent and statistically significant increase in DNA damage compared with the negative and positive control ($p < 0.05$) in both BxPC-3 and PC-3 cell line (except **MM137** used in 0.5 × IC_{50} compared to negative control in PC-3 cell line) following 24 h incubation time. DNA damage expressed as a median of "tail DNA %" parameter obtained in CASP software for cells incubated with IC_{50} concentrations of tested pyrazolo[4,3-*e*]tetrazolo[1,5-*b*][1,2,4]triazine derivatives descendent in the order of: **MM136** (IC_{50} = 0.25 μM; median = 8.28%; mean = 14.36%), **MM139** (IC_{50} = 0.33 μM; median = 4.74%; mean = 10.85%), **MM137** (IC_{50} = 0.16 μM; median = 3.28%; mean = 12.07%) and **MM134** (IC_{50} = 0.32 μM; median = 2.5%; mean = 10.9%) for BxPC-3 cell line and **MM139** (IC_{50} = 0.17 μM; median = 3.35%; mean = 14.22%), **MM137** (IC_{50} = 0.11 μM; median = 2.32%; mean = 11.05%), **MM136** (IC_{50} = 0.13 μM; median = 1.63%; mean = 12.08%) and **MM134** (IC_{50} = 0.16 μM; median = 1.03%; mean = 7.37%) for PC-3 cell line (Figure 5).

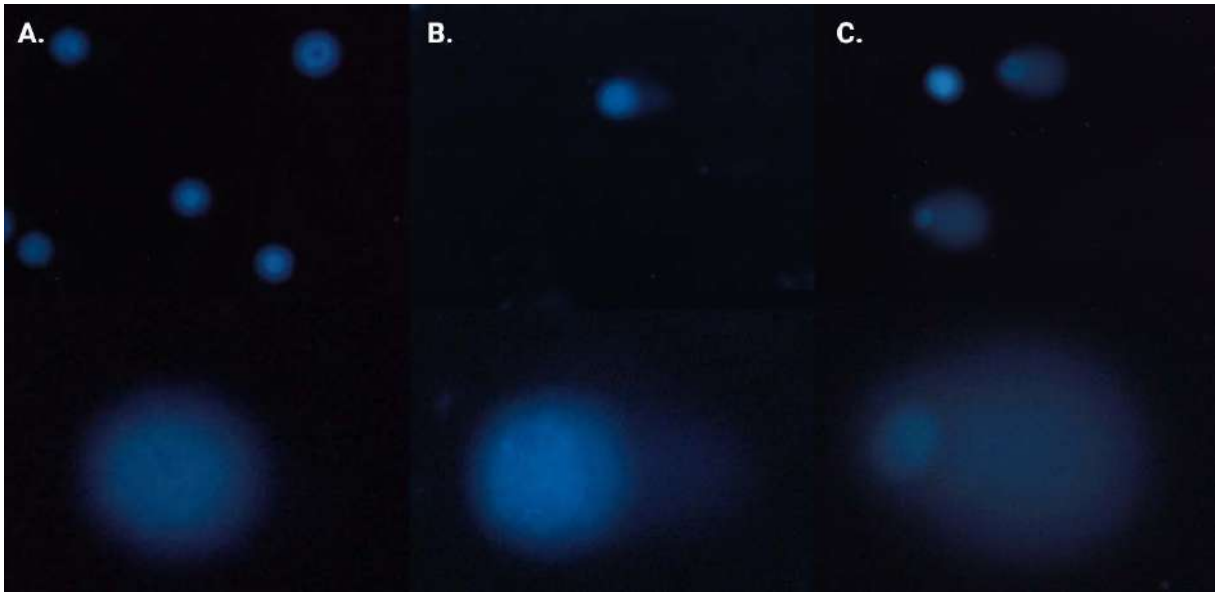

Figure 7. Alkaline comet assay results: images of comets were obtained in an alkaline comet assay for the PC-3 cell line: (**A**) control samples, (**B**) cells treated with 2 × IC_{50} (0.34 μM) of **MM139**, and (**C**) 20 μM bleomycin. Upper images are shown in magnification of 20×. Lower images are shown in arbitrary magnification.

2.3.2. Normal Human Fibroblasts (WI-38 Cell Line)

In contrast, in the WI-38 cell line (Figure 6), **MM136**, **-7**, and **-9** induced statistically significant ($p < 0.05$) increases in DNA damage compared with negative (median = 0.05%; mean = 0.58%) and positive control (median = 29.13%; mean = 32.6%) only in 2 × IC_{50} concentrations. **MM134** induced a statistically significant increase in DNA damage compared with either negative or positive control. DNA damage was expressed as a median of the tail DNA % parameter following incubation of cells with tested pyrazolo[4,3-*e*]tetrazolo[1,5-*b*][1,2,4]triazine derivatives in IC_{50} concentrations descendent in the order of: **MM134** (IC_{50} = 0.65 μM; median = 1.5%; mean = 4.19%), **MM137** (IC_{50} = 0.27; μM; median = 0.09%; mean = 1.26%), **MM139** (IC_{50} = 0.54 μM; median = 0.085%; mean = 2.97%) and **MM136** (IC_{50} = 0.48 μM; median = 0.01%; mean = 0.72%). Once again, an increase in DNA damage levels was observed with an increase in the compound concentration used (dose–response relationship), which is characteristic of genotoxic compounds. However, in most cases, the increase was not statistically significant (except for **MM134** in all tested concentrations and **MM136**, **-7**, **-9** in 2 × IC_{50} concentrations). Of particular importance, the tested compounds induced lower levels of DNA damage in the normal cell line compared with cancer cell lines.

The difference between the genotoxic activity of the tested compounds and positive control was more profound in the BxPC-3 cell line compared with the PC-3 cell line, where derivatives induced levels of DNA damage more closely similar to that induced by bleomycin.

In summary, **MM134**, **-6**, **-7**, and **-9** exhibited genotoxic activity in BxPC-3 and PC-3 cancer cell lines. The tested compounds exhibited varied DNA-damaging capacities across the cell lines used in the study. DNA damage observed after 24 h incubation with the compounds in IC_{50} concentrations was highest in the BxPC-3 cell line when cells were exposed to **MM136** and **MM139** derivatives, while exposure to **MM139** and **MM137** resulted in the most profound induction of DNA damage in the PC-3 cell line. Furthermore, the BxPC-3 cell line exhibited higher sensitivity to both compounds and bleomycin used in the experiment as a positive control. In contrast, incubation of normal human fibroblasts (WI-38 cell line) with the tested compounds resulted in the induction of lower levels of DNA damage compared with the cancer cell lines. Moreover, a dose-dependent increase in DNA damage was observed after a 24 h incubation of cancer cells with increasing concentrations

of the tested compounds (dose–response relationship), which is considered a hallmark of genotoxic compounds.

The treatment of cells with **MM** compounds resulted in a substantial heterogeneity of DNA damage, with values ranging from 0 to 100% tail DNA in the samples, which is consistent with the results obtained by other authors. This matter of producing 100% of tail DNA % can be attributed to some sort of bias using the software or the quality of the obtained images [21,22]. The occurrence of comets with >90% of DNA in the tail in the negative control samples could be attributed to the apoptosis of single cells and is a natural phenomenon, resulting, for example, from the preparation of samples. These comets are commonly referred to as "hedgehogs". Hedgehogs are produced, for example, when cells are subjected to moderate exposure to hydrogen peroxide; however, they are no longer visible after the cells have been incubated for a short amount of time. This is not because the DNA has become even more damaged and disappeared from the gel; rather, it is because the DNA is being repaired. The comet assay has the potential to identify the first stages of apoptosis; however, as the process continues, the comets vanish, leaving behind a smear of unattached DNA. It is evident that hedgehogs can correspond to one level on a continuum of genotoxic damage, that they are not diagnostic of apoptosis, and that they should not be viewed as a sign of cytotoxicity [23].

2.4. Neutral Comet Assay

In contrast to the alkaline comet assay, which detects various types of DNA damage, including DNA double-strand breaks (DSBs), single-strand breaks (SSBs), and alkali-labile sites, the neutral comet assay is specific for the assessment of DSB induction [24].

The neutral comet assay was performed analogously to the alkaline version of the method. Again, *CASP* software [20] was used to obtain median tail DNA percent (%) values with interquartile range and minimal and maximal values. Median tail DNA (%) following incubation of cancer cells (BxPC-3 (A) and PC-3 (B)) with three concentrations (0.5 × IC_{50}, IC_{50}, and 2 × IC_{50}) of **MM134**, **-6**, **-7**, and **-9** was compared to a negative and positive control (20 μM of bleomycin) (Figure 8).

The tested compounds used in concentrations followed by IC_{50} values (0.5 × IC_{50}, $IC_{50,}$ and 2 × IC_{50}) induced a dose-dependent and statistically significant increase in DNA damage compared with the negative and positive control ($p < 0.05$) in 2 × IC_{50} concentrations for both BxPC-3 and PC-3 cells following 24 h incubation time. A statistically significant increase in DNA damage compared to negative and positive control was also observed for cells incubated with IC_{50} concentrations of **MM134**, **-6**, and **-9** in the BxPC-3 cell line and for all compounds in the PC-3 cell line. DNA damage was expressed as a median of the tail DNA % parameter obtained in CASP software for cells incubated with IC_{50} concentrations of tested compounds descendent in the order of: **MM134** (IC_{50} = 0.32 μM; median = 4.21%; mean = 5.11%), **MM136** (IC_{50} = 0.25 μM; median = 4.10%; mean = 5.08%), and **MM139** (IC_{50} = 0.33 μM; median = 3.72%; mean = 4.86%) for the BxPC-3 cell line and **MM139** (IC_{50} = 0.17 μM; median = 5%; mean = 6.07%), **MM136** (IC_{50} = 0.13 μM; median = 4.6%; mean = 8%), **MM134** (IC_{50} = 0.16 μM; median = 4.09%; mean = 5.72%), and **MM137** (IC_{50} = 0.11 μM; median = 2.82%; mean = 4.45%) in the PC-3 cell line. DNA migration increased with the escalation of compound dose, which is characteristic of genotoxic compounds (dose–response relationship). All compounds induced statistically significant lower levels of DNA damage compared with 20 μM bleomycin used as the positive control (estimated DNA damage for BxPC-3 cells: median = 9.7%; mean = 11.15%; and PC-3 cells: median = 10.4%; mean = 12.9%).

In summary, the tested compounds induced a statistically significant increase in DSB frequency in the BxPC-3 and PC-3 cell lines. **MM134** and **MM136** induced the highest levels of DSBs in the BxPC-3 cell line, while **MM139** and **MM136** induced more DSBs in PC-3 cells. For most of the compounds, an increase in DSB frequency was observed following incubation of cells with increasing concentrations of the compound. A dose–response relationship characteristic of genotoxic compounds was observed. Images of

comets obtained in the neutral comet assay for the BxPC-3 and PC-3 cells after incubation with **MM134** and **MM139** are presented in Figure 9.

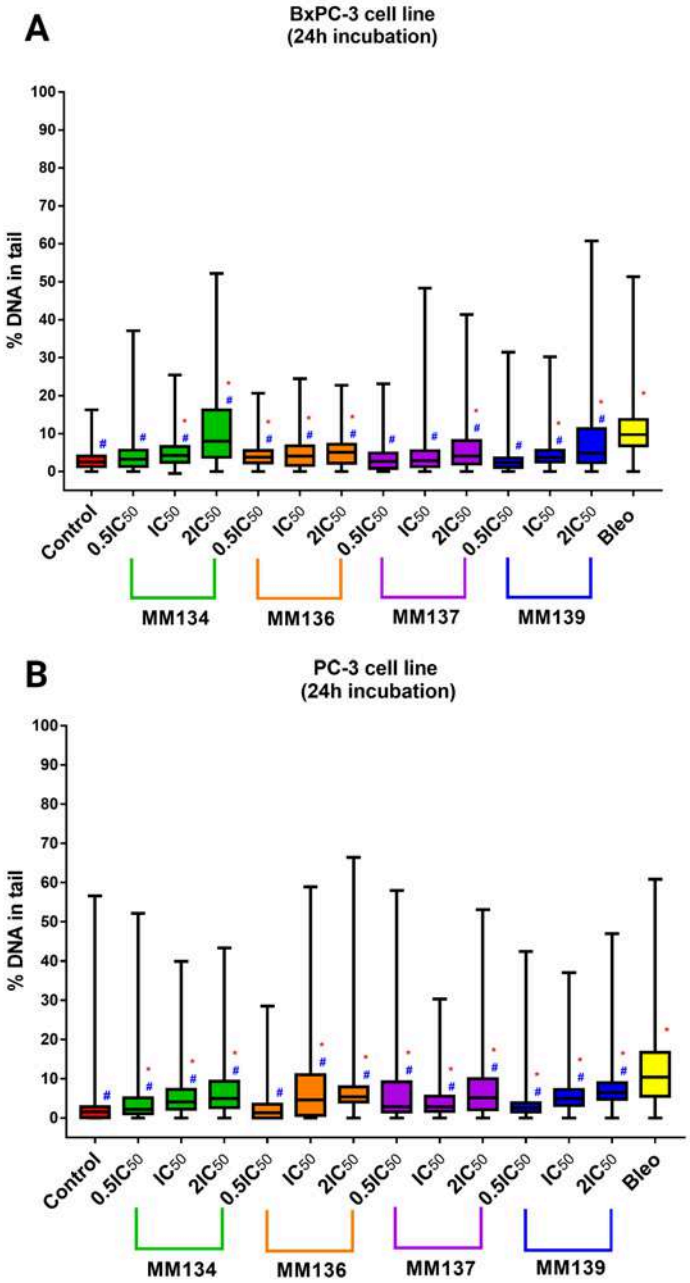

Figure 8. DNA damage in cancer cells estimated with 24 h neutral comet assay: determination of DNA damage (double-strand breaks) induced by 0.5 × IC_{50}, IC_{50}, and 2 × IC_{50} concentrations of **MM134**, **-6**, **-7**, and **-9** in cancer cell lines (BxPC-3 (**A**), PC-3 (**B**)) after 24 h incubation of cells with tested compounds. Data are represented as median tail DNA % with interquartile range and minimal and maximal values. The Kruskal–Wallis test was used to show a statistically significant difference between groups. Multiple comparisons using mean ranks for all groups module of Statistica software were used. In all groups, $N > 200$. * significant difference compared to the negative control; $p < 0.05$. # significant difference compared to the positive control (20 µM bleomycin); $p < 0.05$.

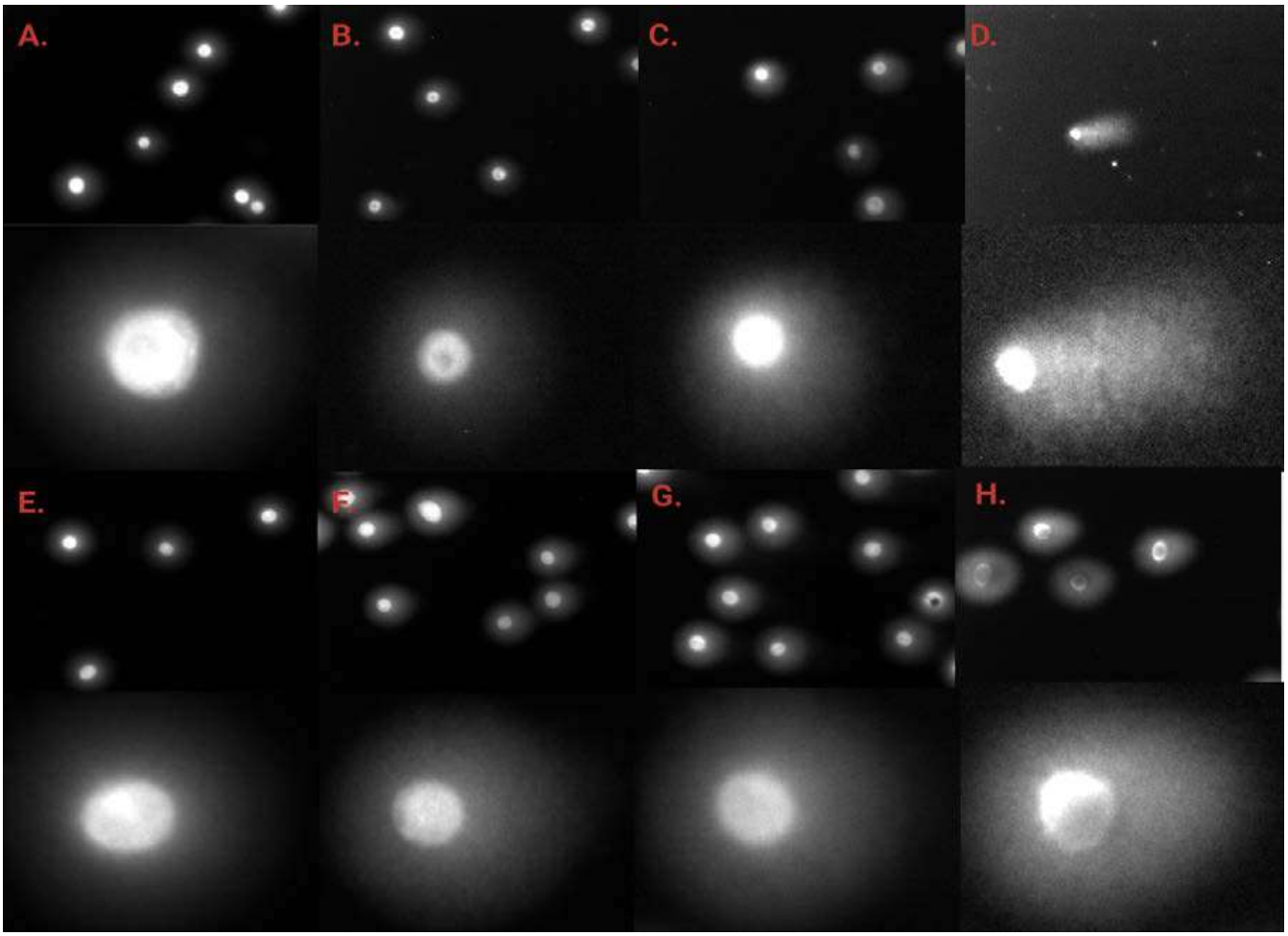

Figure 9. Neutral comet assay results: images of comets obtained in neutral comet assay for the BxPC-3 (**A**–**D**) and PC-3 (**E**–**H**) cells after incubation with **MM134** (**A**) control samples, (**B**) cells treated with 0.5 × IC_{50}, (**C**) IC_{50} and (**D**) 2 × IC_{50} concentrations of the tested compound, and **MM139** (**E**) control samples, (**F**) cells treated with 0.5 × IC_{50}, (**G**) IC_{50} and (**H**) 2 × IC_{50} concentrations of the tested compound. Upper images are shown in magnification of 20×. Lower images are shown in arbitrary magnification.

2.5. γH2AX Staining

To further examine DSB occurrence following 24 h incubation of cells with the tested compounds, a γH2AX staining assay was performed. γH2AX phosphorylation on serine 139 occurs following the occurrence of DNA damage and activation of a complex signaling network known as DDR. Therefore, γH2AX works as a sophisticated marker of DSBs [25]. The median numbers of γH2AX foci for PC-3 cells incubated with IC_{50} and 2 × IC_{50} concentrations of tested compounds were obtained using ImageJ software. PC-3 cells were used due to their large size, allowing an accurate measurement of foci quantity with good resolution. For BxPC-3 cells, we could not obtain the resolution necessary to quantify individual foci. Therefore, we decided to use only one cell line in the assay (Figure 10).

A statistically significant increase ($p < 0.05$) in γH2AX foci formation was observed after 24 h incubation with the tested compounds compared to a negative control (median = 4; mean = 5.68 γH2AX foci). For cells incubated with IC_{50} concentrations of the tested compounds, the median numbers of γH2AX foci were descendent in the order of: **MM134** (IC_{50} = 0.16 μM; median = 21; mean = 25.8), **MM137** (IC_{50} = 0.11 μM; median = 15; mean = 17.52), **MM139** (IC_{50} = 0.17 μM; median = 12; mean = 15.37) and **MM136** (IC_{50} = 0.13 μM; median = 11; mean = 14.71). Examples of anti-γH2AX stained cells are shown in Figure 11.

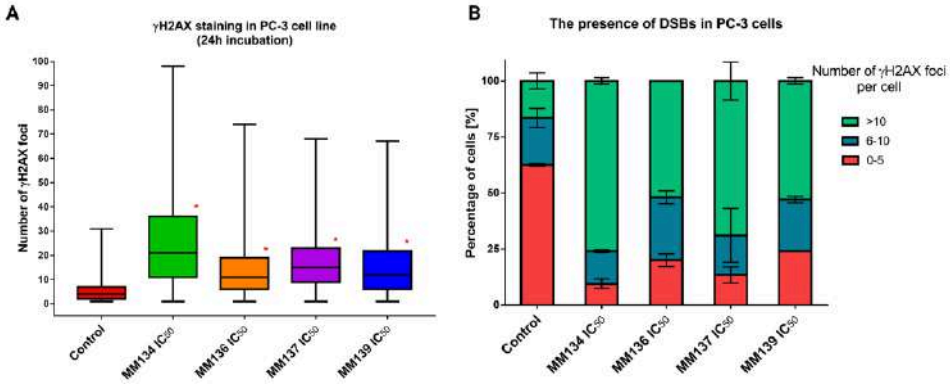

Figure 10. γH2AX staining results in PC-3 cells: determination of DNA damage (double-strand breaks—DSBs) induced by IC_{50} concentrations of **MM134**, **-6**, **-7**, and **-9** in PC-3 cancer cell line. (**A**) Data are represented as median γH2AX foci number per cell in each group with interquartile range and minimal and maximal values. The Kruskal–Wallis test was used to show a statistically significant difference between groups. Multiple comparisons using mean ranks for all groups module of Statistica software were used. In all groups, $N > 200$. * significant difference compared to the negative control ($p < 0.05$). (**B**) The graph presents the mean (±SD) percentage of cells that have a defined number of γH2AX foci in the sample.

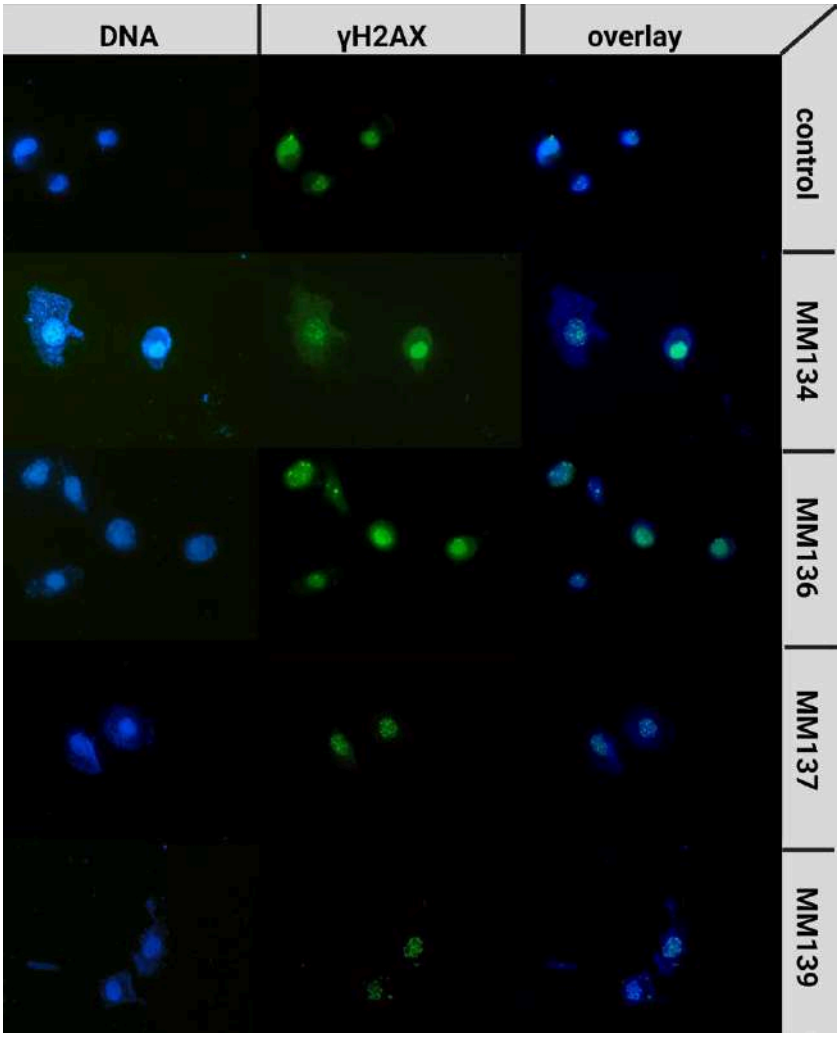

Figure 11. Examples of γ-H2AX stained cells: PC-3 cells were treated with **MM134**, **-6**, **-7**, and **-9** in concentrations concerning their IC_{50} values. Images are shown in magnification of 40×.

2.6. Computational Studies

2.6.1. Molecular Docking

Molecular docking studies were performed to examine the binding modes and binding affinities of **MM** compounds with macromolecular targets from DDR. Moreover, the obtained results were compared with the binding properties evaluated for reference ligands that were co-crystalized with the macromolecular structures. The results are shown in Table 1. Conformations of MM compounds as well as native ligands with DDR targets were produced using Autodock and were clustered using the cluster module according to the root mean square deviation (RMSD) criterion of the same software. The clusters that were ranked to have the lowest binding energies (kcal/mol) were chosen for further investigations.

Table 1. Molecular docking results: the results of molecular docking studies of **MM** compounds and reference ligands against macromolecular structures of proteins involved in the DDR pathway. The common binding residues for MM compounds and reference ligands are bolded.

MM Compound	Binding Energy (Kcal/mol)	Binding Residues	Reference Ligand	Binding Energy (Kcal/mol)	Binding Residues
APE-1 DNA-(apurinic or apyrimidinic site) endonuclease 6MKO					
MM134	−9.18	**Asp308**, **His309**, Gly176, Gly178, Arg177, Ala230, Trp280, Asn174	Methoxyamine (No native ligand was complexed)	−5.74	Asn212, Asp210, His309, Asn68, Asp308, Glu96
MM136	−8.07	Gly178, Arg177, Gly176, **Asp308**, Trp280, **His309**, Leu282, Phe266			
MM137	−9.64	**Asp308**, **His309**, Gly176, Ala230, Trp280, Phe266, Asn212, Tyr171			
MM139	−7.63	Tyr269, Phe266, Met270, Thr268, Ala230, Asn174, Gly231			
ATR Serine/threonine-protein kinase ATR 4WAF					
MM134	−10.06	Asp933, Ile848, Tyr836, **Ile932**, **Val850**, **Met922**, Trp780, Thr856, His855	N,N-dimethyl-4-[(6R)-6-methyl-5-(1H-pyrrolo[2,3-b]pyridin-4-yl)-4,5,6,7-tetrahydropyrazolo[1,5-a]pyrazin-3-yl]benzenesulfonamide	−10.62	Ile848, **Ile932**, **Val850**, Val851, **Met922**, Glu849, Thr856, His855, Gln859, Lys802, Met800
MM136	−10.32	Tyr836, **Ile932**, **Val850**, Arg852, Val851, **Met922**, Asn853, Ser854, Trp780			
MM137	−10.95	Tyr836, Val851, **Met922**, **Val850**, **Ile932**, Trp780, Ser854, Arg852			
MM139	−10.34	Ile848, **Ile932**, **Val850**, Trp780, Thr856, His855			
ATM Serine/threonine-protein kinase ATR 7NI5					
MM134	−9.02	Pro2775, Gln2874, Trp2769, **Leu2767**, Leu2715, Ile2888, **Tyr2755**	KU-55933	−10.58	**Tyr2755**, **Cys2770**, Glu2768, **Leu2767**, Lys2717, Trp2769, Leu2715, Pro2699, Ala2693, Pro2775, Leu2877
MM136	−9.17	Asp2720, Lys2717, Leu2877, Trp2769, Thr2773, **Cys2770**, **Tyr2755**, **Leu2767**, Ile2888, Asn2697			
MM137	−9.16	Ala2693, Glu2778, Ile2888, Lys2717, **Tyr2755**, **Leu2767**, Cys2770, Trp2769, Leu2877, Pro2775, Val2774			
MM139	−10.05	Trp2769, Leu2877, **Tyr2755**, Ile2888, Gly2694, Pro2699, Leu2715, **Cys2770**			
CHK1 Serine/threonine-protein kinase Chk1 2YM8					
MM134	−9.75	**Cys87**, **Ala36**, **Leu137**, Leu15, **Val23**, **Leu84**, **Lys38**, Phe149	(R)-5-(8-chloroisoquinolin-3-ylamino)-3-(1-(dimethylamino)propan-2-yloxy)pyrazine-2-carbonitrile	−9.14	**Ala36**, **Leu84**, Glu85, Val68, **Lys38**, Glu134, Asn135, **Leu137**, **Val23**, **Cys87**, Tyr86, Leu15
MM136	−10.44	**Cys87**, Tyr86, **Leu137**, **Leu84**, **Ala36**, Val68, Phe149, Lys38, **Val23**, Gly90			
MM137	−10–82	**Cys87**, **Ala36**, **Leu137**, **Val23**, Val68, **Lys38**, **Leu84**, Phe149, Asn59, Tyr86			
MM139	−10.61	Cys87, Phe149, **Lys38**, **Val23**, **Ala36**, **Leu137**, Leu15			

Table 1. *Cont.*

MM Compound	Binding Energy (Kcal/mol)	Binding Residues	Reference Ligand	Binding Energy (Kcal/mol)	Binding Residues
CHK2 Serine/threonine-protein kinase Chk2 2W0J					
MM134	−9.72	Leu301, **Lys249**, Asn352, Ile299, Glu308, **Val234**, Leu354, **Leu226**	4,4′-diacetyldiphenylurea-bis(guanyl-hydrazone)	−9.76	Glu273, Thr367, Ile299, **Lys249**, Leu301, **Val234**, Leu303, **Leu226**, Glu305
MM136	−9.64	**Leu226**, Met304, Ala247, Leu301, Ile299, **Lys249**, Thr367, Leu354, **Val234**			
MM137	−9.72	**Leu226**, Met304, Ala247, **Val234**, Leu354, **Lys249**, Leu301, Ile299			
MM139	−10.23	Phe369, **Lys249**, Ala247, Leu354, **Leu226**, Met304, Leu303, **Val234**, Thr367			
PARP-1 Poly [ADP-ribose] polymerase 1 7ONS					
MM134	−10.51	Glu763, Tyr889, Asp766, Ala880, Leu877, Arg878, Leu769, Pro881, Tyr896	7-[[4-(1,5-dimethylimidazol-2-yl)piperazin-1-yl]methyl]-3-ethyl-1~{H}-quinolin-2-one	−10.36	Gly863, **Arg878**, Leu769, Pro881, Asp770, Asn767, Tyr896, **Tyr907**, Lys903, **His862**, Ala898
MM136	−9.88	**Tyr907**, **His862**, Asp766, Asp770, Leu877, Ile872, Arg878, Ala880			
MM137	−10.29	Arg878, Ala898, **Tyr907**, Tyr896, **His862**, Ile879			
MM139	−10.36	Ala880, Leu769, Pro881, Arg878, Asn767, Arg865, His909, **Tyr907**, **His862**, Asp770			
RPA70 Replication protein A 70 kDa DNA-binding subunit 4IJL					
MM134	−5.81	Arg41, **Ile95**, Ile83	{[5-(3-chloro-1-benzothiophen-2-yl)-4-phenyl-4H-1,2,4-triazol-3-yl]sulfanyl}acetic acid	−5.97	Leu87, Met57, Arg41, Ala59, Thr60, **Ile95**, Val93, Asn85
MM136	−6.16	Met97, Ala59, Gln61, Ile83, **Ile95**			
MM137	−5.71	Arg41, Met92, Ala59, **Ile95**, Met57, Ile83			
MM139	−7.08	Met57, **Ile95**, Ile83			
TOP1 Topoisomerase I 1TL8					
MM134	−9.81	Met428, Asn352, Lys436, **Arg364**, Lys425, Thrr426, **DA13**, DA14	2,3-dimethoxy-12H-[1,3]dioxolo[5,6]indeno[1,2]isoquinolin-6-ium	−9.53	Asn722, Thr718, **Arg364**, DT10, DG12, **DA13**
MM136	−10.44	Lys425, **Arg364**, Glu356, Asn722, DT10, DG12, **DA13**			
MM137	−10.69	Lys425, Lys374, **Arg364**, DT10, DG12, **DA13**			
MM139	−10.34	Lys532, DT10			
TOP2B Topoisomerase II 3QX3					
MM134	−8.54	Glu477, Gly478, DC8, **DA12**, **DG13**	Etoposide	−9.98	Asp479, Arg503, Gly478, Met782, DC8, **DA12**, **DG13**
MM136	−8.24	Arg503, Ala779, Met782, **DA12**, **DG13**			
MM137	−8.32	Ser480, Leu502, Asp559, Asp557			
MM139	−7.76	Gly478, Arg503, DC8, **DA12**, **DG13**			
WEE1 Wee1-like protein kinase 2IN6					
MM134	−9.14	Asp386, **Ile305**, **Cys379**, **Phe433**, **Val313**, **Ala326**, Ser307	PD311839	−9.45	Gly382, **Cys379**, **Phe433**, **Ala326**, Glu377, **Val313**, Val360, Asn376, **Lys328**, **Ile305**, Gly306, Ser307
MM136	−9.99	**Cys379**, Asn376, Ile374, His350, Gly382, **Val313**, **Ala326**, **Phe433**, Val360, **Lys328**, Asp463			
MM137	−10.07	**Ile305**, **Val313**, **Lys328**, Asp463, Ile374, Asn376, **Phe433**, Val360, **Ala326**, **Cys379**			
MM139	−9.92	**Lys328**, **Val313**, **Ala326**, **Phe433**, **Ile305**, Tyr378, Gly382, Ser383			

Molecular docking studies revealed that **MM** compounds exhibited better binding affinities for APE1, CHK1, and TOPI macromolecular targets than the respective reference ligands because of the increased number of chemical interactions observed. Figure 12 depicts the two-dimensional binding interactions of **MM137** with APE1 (a), CHK1 (b), and TOPI (c), respectively.

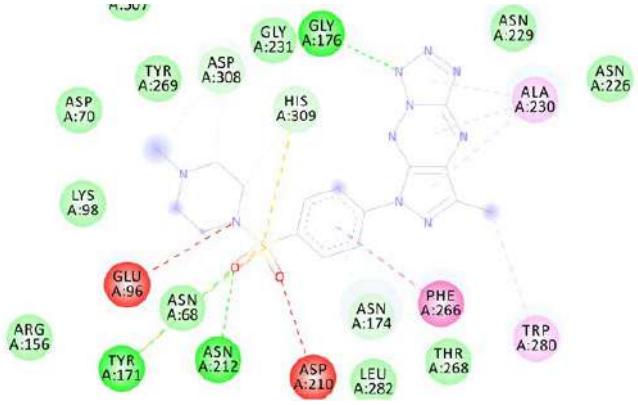

(**a**)

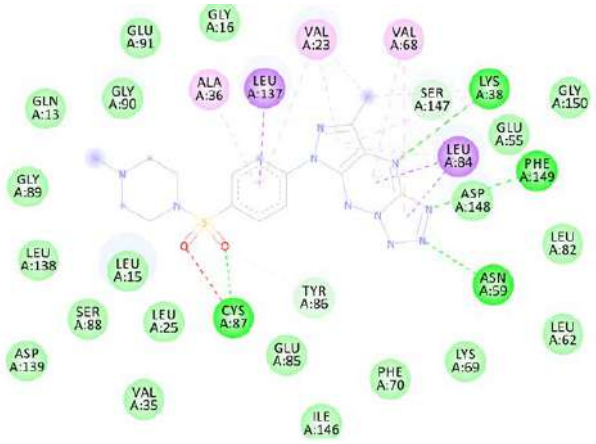

(**b**)

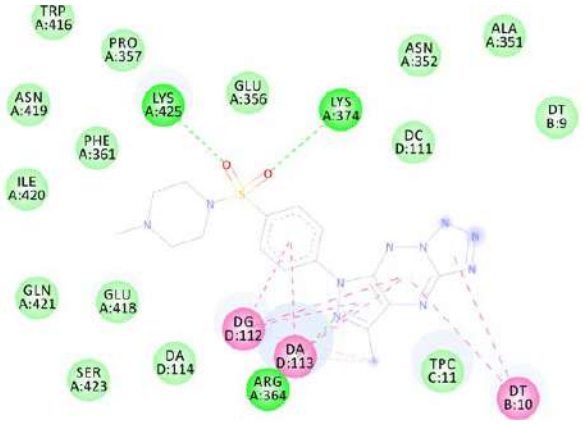

(**c**)

Figure 12. Graphical representation of molecular docking results: two-dimensional binding interactions of **MM137** with human APE1 (**a**), CHK1 (**b**), and TOPO1 (**c**).

2.6.2. Molecular Dynamics

The macromolecular complexes of **MM137** against five target proteins—ATR, APE1, CHK1, TOPO1, and WEE1—exhibited the highest binding; however, the energy differences required for the competitive inhibition of target enzymes ATR and WEE1 were relatively small when compared with their reference ligands. Thus, the macromolecular complexes of **MM137** with APE1, CHK1, and TOPO1 were considered for executing simulation analysis. Molecular dynamics was used to assess the thermodynamic stability of **MM137** with APE1, CHK1, and TOPO1 by performing a molecular dynamic (MD) simulation of 100 ns using Schrodinger's Desmond software. The molecular dynamics simulation of the three shortlisted macromolecular complexes of **MM137** with APE1, CHK1, and TOPO1 revealed that the macromolecular complex **MM137** with the CHK1 kinase was highly stabilized for the whole 100 ns of the simulation timeframe. RMSD analysis was performed. It was observed that the macromolecular backbone as well as the complex ligand maintained a stable conformation throughout the simulation period of 100 ns, with an RMSD value ranging within 1.6–2.8 Å for the macromolecular backbone and 2.4–4.8 Å for the ligand molecule (Figure 13). The protein–ligand interactions and contacts indicated the important amino acid residues that were crucial in providing stability to the complex. These important amino acid residues included Ala36, Leu84, Glu85, Val68, Lys38, Glu134, Asn135, Leu137, Val23, Cys87, Tyr86, and Leu15. During the simulation, the residues Cys87, Asn59, and Asp148 were directly involved in H-bonding. Therefore, it was concluded from the MD simulation studies that the H-bonding and water-linking interactions that were previously identified via Cys87, Asn59, and Asp148 residues are essential for stabilization of the protein–ligand complex.

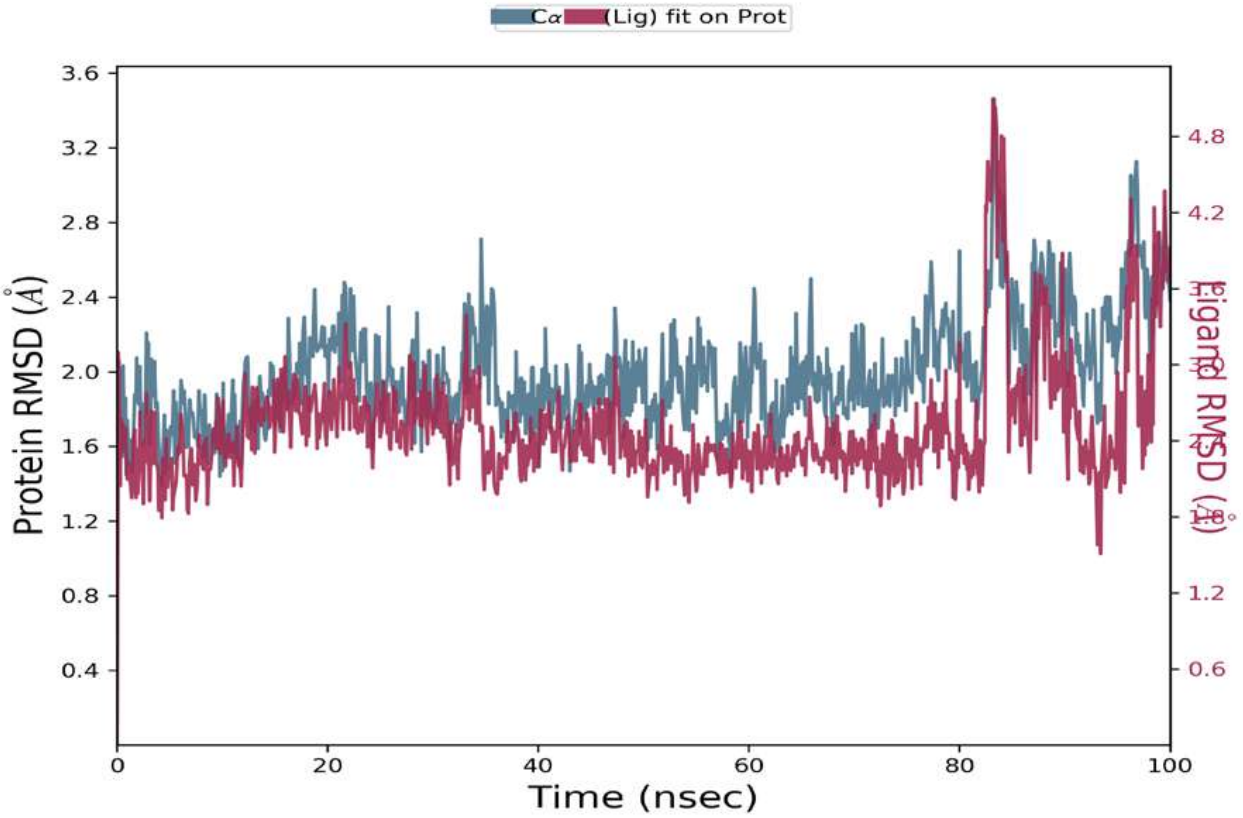

Figure 13. The RMSD plot for molecular dynamics simulation of **MM137** and CHK1: RMSD values of the ligand **MM137** complexed with CHK1 recorded during the MD simulation for 100 ns.

It was discovered that the root-mean-square fluctuation (RMSF) (Figure 14), except for a few residues, remained within the range of 2.0 Å for the macromolecular backbone and 1.5 Å for the complexed ligand, indicating fluctuation within the acceptable range.

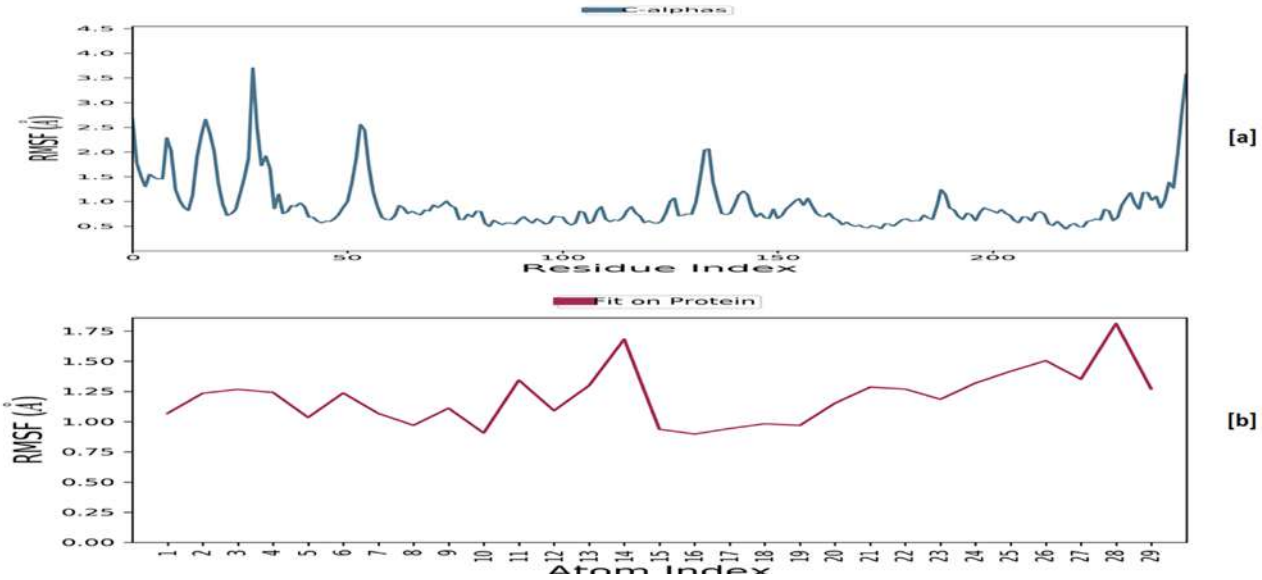

Figure 14. The RMSF plot for **MM137** and CHK1: RMSF for the **MM137** (**a**) and the macromolecular backbone of CHK1 (**b**) obtained after MD simulation.

3. Discussion

Genotoxicity describes the property of a chemical that has a harmful effect on the genetic material of a cell (DNA and/or RNA), hence impairing the integrity of the cell genome. Genetic toxicology is an area of research that is concerned with the investigation of agents or substances that have the potential to cause damage to DNA and chromosomes. It should be noted that genotoxicity is frequently confused with mutagenicity. All mutagens are also genotoxic, but not all genotoxic compounds are mutagenic. The interaction of the genotoxic chemical with the DNA structure and sequence results in the destruction of genetic material [26,27]. Many well-established in vitro assays exist and have been successfully used to predict the genotoxicity of compounds. However, at this time, they cannot be considered a complete replacement for the animal experiments that are currently used to evaluate the safety of drugs [28]. Mitosis is a critical phase in the cellular response to genotoxic agents in human cells. Cells with damaged DNA recruit phosphorylated γH2AX, ATM, and ATR serine-protein kinases that phosphorylate checkpoint kinase 1 (CHK1), which in consecutive events triggers G2-phase cell cycle arrest or apoptosis [29].

More recently, a new compound known as **MM129** (pyrazolo[4,3-*e*]tetrazolo[1,5-*b*][1,2,4]triazine sulfonamide) has been demonstrated to effectively limit cell viability by inhibiting Bruton's tyrosine kinase (BTK), which is involved in cell proliferation [30]. Furthermore, **MM129** exhibits anticancer efficacy in colon cancer xenograft mouse models. Not only does **MM129** have the potential to inhibit intracellular pathways that promote carcinogenesis, but it also has the potential to lower the protein levels of programmed death ligand 1 (PD-L1). It is known that PD-L1 is the primary ligand of programmed death 1 (PD-1), a coinhibitory receptor that can be expressed either constitutively or be induced in myeloid cells, lymphoid cells, normal epithelial cells, and cancer cells. PD-1/PD-L1 interaction is critical in the establishment of immunological tolerance under physiological conditions because it prevents excessive immune cell activity that can lead to tissue destruction and autoimmunity. The expression of PD-L1 is an immune evasion strategy used by a variety of cancers, and it is often associated with a much worse treatment prognosis [31,32]. Exposure of DLD-1 and HT-29 cells to **MM129** resulted in a decrease in the expression of RAC-alpha serine/threonine-protein kinase (AKT), serine/threonine-protein kinase (mTOR), and CDK2 [31]. Furthermore, incubation of colon cancer cells with **MM131**—another pyrazolo[4,3-*e*]tetrazolo[1,5-*b*][1,2,4]triazine sulfonamide—induced apoptosis of DLD-1 and HT-29 cells with observed down-regulation of mTOR kinase, soluble intercellular adhesion molecule-1 (sICAM-1), and cathepsin, together with up-regulation of beclin-1

B [33]. We have also shown, with the use of an alkaline/neutral version of the comet assay and γ-H2AX staining, that **MM129**, **MM130**, and **MM131** sulfonamides exhibited genotoxic activity in four investigated cancer cell lines (HeLa, HCT-116, PC-3, and BxPC-3) [34]. The occurrence of DNA damage following exposure to genotoxic agents would normally trigger the DDR responsible for the activation of DNA repair mechanisms or elimination of the severely damaged cell. It was also shown that via activation of cell cycle checkpoints, generation of neoantigen epitopes, and other mechanisms, DDR can regulate the expression of PD-L1 on tumor cells. Several investigations supported the evidence that the main DDR branch—the ATM/ATR/CHK1 pathway—may upregulate the expression of PD-L1 through the JAK-STAT1/3-IRF1 pathway (for full names of the proteins, see abbreviations section) [35,36]. Furthermore, inhibition of the mTOR kinase may increase the expression of PD-L1 on cancer cell surfaces. Higher levels of PD-L1 expressed by cancer cells may increase the availability of epitopes to which anti-PD-L1 agents can bind [37].

In our previous studies [19], **MM134**, **-6**, **-7**, and **-9** exhibited cytotoxicity against cancer cell lines including a pancreas adenocarcinoma cell line (BxPC-3), where they showed activity in the range of 0.16–0.33 μM, and prostate adenocarcinoma cell line (PC-3), where the activity ranged from 0.11–0.17 μM as estimated in the 72 h MTT assay. At the same time, tested derivatives showed lower cytotoxicity in human normal lung fibroblasts (WI-38), where IC_{50} values varied between 0.27–0.65 μM. **MM139** was the least cytotoxic to cancer cell lines, with a cytotoxicity range of 0.17–0.33 μM, while **MM137** exhibited the highest cytotoxic potential in all tested cell lines (IC_{50} values: 0.16 μM for BxPC-3, 0.11 μM for PC-3, and 0.27 μM for WI-38 cells). Apoptosis induction was the direct cause of the cytotoxic activity of the compounds, as indicated by the flow cytometry analysis with annexin V-FITC staining and acridine orange/ethidium bromide double staining. Moreover, a decrease in mitochondria membrane potential (MMP) was observed following the incubation of BxPC-3 and PC-3 cells with the tested compound, which indicated activation of the intrinsic apoptosis pathway. In silico studies suggest [19] that **MM134**, **-6**, **-7**, and **-9** compounds may act as potent and selective inhibitors of the AKT-mTOR pathway, BTK, and PD-1/PD-L1 interaction. The molecular dynamics simulation suggested that the tested compounds bind strongly and durably with molecular targets and may exert an anti-cancer effect through their inhibition [19]. Furthermore, structurally similar compounds **MM129**, **MM130**, and **MM131** exhibited cytotoxic activity with IC_{50} concentrations of 0.17–1.15 μM in four cancer cell lines (HeLa, HCT 116, PC-3, and BxPC-3) and genotoxic activity, as indicated by alkaline/neutral comet assays and γH2AX staining [34].

These facts encouraged us to explore the genotoxic activity of new **MM** derivatives (**MM134**, **-6**, **-7**, and **-9**). The tested sulfonamides exhibited genotoxic potential in BxPC-3 and PC-3 cell lines, as shown in the alkaline and neutral comet assays. Moreover, the induction of DSBs was confirmed with anti-γH2AX immunocytochemical staining. We used these assays because of the inability of alkaline and neutral comet assays to identify some kinds of DNA damage including inter- and intra-strand crosslinks induced by some agents, e.g., mitomycin. SSBs and DSBs are generated as repair intermediates during crosslink repair; however, the amount of damage formed was clearly below the detection level in both the alkaline and neutral comet assays. These lesions, on the other hand, have the potential to trigger the DNA damage response, resulting in the formation of large numbers of γH2AX foci [38].

After, 24 h incubation of cells with the tested compounds, an increase in DNA damage was observed with the concentration of compound used in the experiment, which is characteristic of genotoxic compounds. Moreover, the increase in DNA damage in the above-mentioned cells was not due to the cytotoxic activity of the compounds, as determined by the alamar blue and trypan blue viability tests. The examined compounds exhibited similar genotoxic potential in a given cell line; however, the BxPC-3 cell line was generally more prone to the DNA damaging activity of the **MM** derivatives, and 20 μM bleomycin was used in the study as a positive control. The DNA damage observed following incubation with **MM** compounds did not exceed that caused by bleomycin.

However, **MM** derivatives were used in 60 to 180 times lower concentrations (for the IC_{50} values in cancer cell lines) compared to the positive control. **MM136** was the most genotoxic compound in the BxPC-3 cell line, while **MM139** exhibited the highest DNA damaging capacity in the PC-3 cell line, as estimated by the alkaline comet assay. However, neutral comet assay results indicated that in the BxPC-3 cell line, **MM134** induced the highest levels of DSBs, while PC-3 cells were more susceptible to the activity of the **MM139** compound. It is, however, difficult to compare the outcomes of the incubation with the compounds, because **MM** derivatives were used in respect of their IC_{50} values, not an arbitrarily established concentration allowing such comparison. The main objective of this study, however, was to explore whether the compounds exhibit a genotoxic effect in cancer cells. Of importance, we included the normal cell line WI-38 in the study design to examine whether the genotoxicity induced by the compounds is selective for cancer cells. Similarly to cancer cells, the WI-38 cells were treated with compounds in concentrations corresponding to the obtained IC_{50} values, which were higher (IC_{50} range: 0.27–0.65 μM) than the concentrations used to treat cancer cells (IC_{50} range: 0.11–0.33 μM). Despite that fact, the derivatives induced lower levels of DNA damage in normal cells, as indicated by the alkaline comet assay. These results only indicate potential selectivity for cancer cells and should be further examined with other cancer and normal cell lines, especially in 3D models or in vivo studies.

The induction of DSBs was confirmed with γ-H2AX staining, where the compounds induced a statistically significant increase in γ-H2AX foci formation compared to the control group. This indicated the formation of DSBs in the PC-3 cell line after 24 h incubation time with **MM** compounds. Treatment of cells with **MM134** and **MM137** induced the highest increase in γ-H2AX foci, which was somehow different from the results obtained with the neutral comet assay, where **MM139** and **MM136** exhibited the highest DSB-inducing potential. This may have resulted from discrepancies in the methodologies of both assays, the type of DNA damage they detect, and the very similar genotoxic potential of all compounds.

Our molecular docking and molecular dynamics studies indicated that the genotoxic potential of the tested compounds may result from inhibition of the CHK1 kinase involved in DDR signaling. CHK1 is a serine/threonine kinase that plays an important role in the regulation of various checkpoints within the cell cycle. These checkpoints are responsible for a variety of processes, such as the repair and stabilization of replication forks upon DNA damage. Many different CHK1 inhibitors have been developed [39]. New evidence suggests that CHK1 inhibitors may demonstrate considerable single-agent efficacy in cancers, especially those with specific DNA repair deficiencies, a constitutively active DDR, or with oncogene-induced replicative stress. This is accompanied by the increase in γ-H2AX foci formation and accumulation of DNA damage [40,41] that were observed in our study.

Prediction of the molecular targets of these compounds is crucial to understand how they affect cellular physiology. This is pivotal for the initial estimation of side effects exhibited by the compounds. Our previous studies indicated other possible targets of **MM** compounds through molecular docking and molecular dynamics approaches. These studies indicated that the apoptotic potential of the compounds may result from inhibition of the AKT-mTOR pathway, BTK kinase, and PD-1/PD-L1 interaction. This, however, needs further confirmation in in vitro and in vivo experiments. Furthermore, previous studies indicated that the compounds exhibit favorable physicochemical parameters, including drug-likeness properties, that represent an advantage for drug design purposes [19].

4. Materials and Methods

4.1. Chemicals

Trypsin-EDTA and all culture media (RPMI-1640, DMEM-F12, MEM) were purchased from Biowest (CytoGen, Poland). Agarose NMP (normal melting point), buffered saline (PBS), bleomycin sulfate, fetal bovine serum (FBS), low-melting point agarose (LMP), penicillin-

streptomycin solution stabilized, sodium acetate, (NaOAc), tris(hydroxymethyl)aminomethane (TRIS), Triton X-100, Tween 20 and trypan blue were supplied by Sigma Aldrich Chemical Co. (USA). Alamar blue reagent was purchased from BioRad (USA). For γH2AX immuno-staining, bovine serum albumin (BSA) (Sigma Aldrich Chemical Co., (USA)), paraformaldehyde (PHA) (Polysciences, Inc., Warrington), fluoromount G (Invitrogen, UK), normal goat serum (Abcam), and the antibodies anti-p-H2AX Ser139 (Abcam, Cambridge, UK) and Alexa Fluor 594 goat anti-mouse (LifeTechnology, Warsaw, Poland) were used.

4.2. Cell Culture

BxPC-3 (pancreas adenocarcinoma, ATCC® CRL-1687™), PC3 (prostate cancer, ATCC® CRL-1435™), and WI-38 (human lung fibroblasts, ATCC® CCL-75™) cell lines were obtained from American Type Culture Collection (ATCC, Rockville, USA). BxPC-3 cells were grown in RPMI-1640 medium supplemented with 10% (*v*/*v*) fetal bovine serum (FBS) and 1% (*v*/*v*) of both antibiotics (streptomycin and penicillin). PC-3 cells were cultured with DMEM-F12 supplemented with 10% (*v*/*v*) FBS and 1% (*v*/*v*) of antibiotics (streptomycin and penicillin). WI-38 cells were grown in MEM supplemented with 10% (*v*/*v*) fetal bovine serum (FBS) and 1% (*v*/*v*) of both antibiotics (streptomycin and penicillin).

Cells were grown at 37 °C in a humidified atmosphere of 5% CO_2 in the air. The culture medium was changed every 24–48 h. Subculture was performed using 0.25% trypsin/EDTA after cells reached confluence.

MycoBlue™ Mycoplasma Detector kit (Vazyme biotech Co., Ltd.) was used at least every month for the control of mycoplasma contamination in the cell cultures.

The cytotoxic activity of the pyrazolo[4,3-*e*][1,2,4]triazines investigated in this study was recently published by our group [19].

4.3. Cell Treatment

The concentrations of the pyrazolo[4,3-*e*][1,2,4]triazine derivatives (**MM134**, **-6**, **-7**, and **-9**) used in the subsequent assays were based on previously published MTT assay results and are shown in Table 2 [19]. We decided to use these concentrations in subsequent analyses to make the workflow consistent and correlate with the previous published results.

Table 2. MTT results after 72 h: mean IC_{50} values ± SD obtained after 72 h incubation of cells with the tested **MM** compounds (**MM134**, **-6**, **-7** and **-9**) using MTT assay.

Compound	Cell Line		
	IC_{50} Value ± SD		
	BxPC-3	**PC-3**	**WI-28**
MM134	0.32 ± 0.1	0.16 ± 0.02	0.65 ± 0.07
MM136	0.25 ± 0.08	0.13 ± 0.01	0.48 ± 0.09
MM137	0.16 ± 0.04	0.11 ± 0.007	0.27 ± 0.04
MM139	0.33 ± 0.14	0.17 ± 0.003	0.64 ± 0.06

4.4. Trypan Blue Staining

Trypan blue is a diazo dye that has been used for viability assessment for years. Viable cells with undamaged cellular membranes are resistant to staining and thus allow the discrimination from blue-stained dead cells with disrupted membranes [42]. Cells were seeded at a density of 1.5 × 10^5/mL onto 12-well plates. After 24 h, cells were exposed to three concentrations of tested **MM** compounds (0.5 × IC_{50}, IC_{50}, and 2 × IC_{50}). Cells were left for incubation for another 24 h (37 °C; 5% CO_2). After exposure, they were transferred to Eppendorf tubes and centrifuged at 1400 rpm for 10 min at 4 °C. Afterward, the supernatant was removed, and the precipitate was diluted in PBS. Cell suspensions were mixed with 0.4% trypan blue solution in a 1:1 ratio. Approximately 300 cells were

counted under a light microscope. The experiment was repeated three times. The results were represented as mean viability (%) with SD values.

4.5. Alamar Blue

Alamar blue works as a non-toxic and membrane-permeable redox indicator that is often used to assess the metabolic activity of cells. Over the past 50 years, the alamar blue reagent has been used to measure cell viability and cytotoxicity in a variety of cell types [43]. In this study, alamar blue (BioRAD) was used to assess cell viability before the performance of the neutral comet assay. Nunc microtiter, flat-bottomed 96-well plates were seeded at a density of approximately 1×10^4 cells per 100 µL medium per well. Following the given incubation period in controlled conditions (37 °C; 5% CO_2), cells were exposed to 11 different concentrations of tested compounds in DMSO (range 0.05–3 µM) in a volume of 100 µL medium per well. The final solvent concentration was <0.5% v/v. The experimental design included negative controls and blanks (wells without cells).

Following a 24 h incubation period, 20 µL of alamar blue was added to each well of the experimental plate. Cells were incubated in a humidified atmosphere for 4 h (37 °C; 5% CO_2). The absorbance reading was performed at 570 and 600 nm using a spectrophotometer (microplate reader Power Wave XS BioTek Instruments, Inc., USA). The experiments were performed in triplicate.

The percentage difference between treated and control cells was calculated using the formula provided by the producer (BioRad).

$$Percentage\ difference\ between\ treated\ and\ control\ cells = \frac{(O2 \times A1) - (O1 \times A2)}{(O2 \times P1) - (O1 \times P2)} \times 100 \quad (1)$$

$O1$ = molar extinction coefficient (E) of oxidized alamar blue (blue) at 570 nm ($O1$ = 80,586).

$O2$ = E of oxidized alamar blue at 600 nm ($O2$ = 117,216).

$A1$ = absorbance of test wells at 570 nm; $A2$ = absorbance of test wells at 600 nm.

$P1$ = absorbance of positive growth control well (cells plus alamar blue but no test agent) at 570 nm.

$P2$ = absorbance of positive growth control well (cells plus alamar blue but no test agent) at 600 nm.

4.6. Comet Assays

4.6.1. Alkaline Comet Assay

The comet assay is one of the most commonly used strategies utilized in the assessment of genetic toxicity caused by DNA-damaging agents. High sensitivity, simplicity, and versatility make the comet assay extremely valuable in the elucidation of possible mechanisms of genotoxicity and DNA repair at a single-cell level. The alkaline comet assay allows rapid detection of alkali-labile sites that can be easily converted into SSBs under alkali conditions (pH > 13) and the highly cytotoxic DSBs [44–46].

The microscopic image obtained after single-cell electrophoresis resembles a comet, where the head of the comet represents intact DNA, while the tail consists of DNA fragmented after exposure to a genotoxic agent [47].

In the alkaline comet assay, pretreated cells are usually mixed with LMP agarose and embedded on slides covered in NMP agarose [48]. Following treatment with lysis buffer allows DNA to be released from the head of the comet during electrophoresis. Commercially available software such as Open Comet or CaspLab enables easy estimation of DNA damage induced by genotoxic agents [48–50].

The alkaline version of the comet assay was performed according to Singh et al. (1988) [51], with modifications. BxPC-3 and PC-3 cancer cells and normal human fibroblasts (WI-38) were seeded at a density of 1.2×10^5/mL onto 12-well plates. After 24 h, cells were exposed to three concentrations of tested compounds followed by IC_{50} values ($0.5 \times IC_{50}$, IC_{50}, and $2 \times IC_{50}$) or bleomycin (20 µM) used in the experiment as a positive control. The experimental design included negative controls (cells treated with DMSO at 0.4% for 24 h at 37 °C). Cells were left for incubation for another 24 h (37 °C; 5% CO_2). After exposure,

they were transferred to Eppendorf tubes and centrifuged at 1400 rpm for 10 min at 4 °C. Afterward, the supernatant was removed, and the precipitate was diluted in PBS. The next steps were performed as previously described by Kontek and Nowicka [52].

After electrophoresis (conditions: 12 V, 300 mA, 25 min), slides were stained with 1 μg/mL of the intercalating agent 4′,6-diamidino-2-phenylindole (DAPI) and coverslipped. DNA damage was assessed with a fluorescence microscope at 360 nm using CellSens (Olympus) software. A total number of approximately 50 cells per slide was chosen for further analysis.

4.6.2. Neutral Comet Assay

In addition to the alkaline comet assay, we also performed the comet assay in pH conditions close to neutral pH (pH = 9) to estimate the levels of DSBs induced following 24 h incubation with the tested compounds in concentrations followed by IC_{50} values (0.5 × IC_{50}, IC_{50}, and 2 × IC_{50}) or bleomycin (20 μM) used as a positive control in cancer cell lines (BxPC-3 and PC-3). The majority of the neutral comet assay steps were performed analogously to the alkaline version except for the electrophoresis step. In contrast to the alkaline comet assay, electrophoresis was performed in a buffer comprising 100 mM TRIS and 300 mM sodium acetate with the pH of the solution adjusted to 9.0 by glacial acetic acid, as described previously by Bukowski et al. [34]. Electrophoresis was run at 12 V, 50 mA for 60 min. Cells were washed with distilled water twice, stained with DAPI, and analyzed as described for the alkaline comet assay.

4.7. γH2AX Staining

PC-3 cells were seeded at a density of 3 × 10^4/mL onto round coverslips placed on the bottom of 12-well plates. After 24 h, cells were exposed to two concentrations of the tested compounds followed by IC_{50} values (IC_{50} and 2 × IC_{50}). After 24 h, cells were washed once with cold PBS and placed in 4% paraformaldehyde (PHA) in PBS for 10 min. at room temperature. After that, PHA was removed, and cells were permeabilized using 0.1% Triton X-100 for 10 min at 20 °C, followed by incubation in a blocking solution (1 mL/well) containing 2.5% BSA, 1.5% goat serum, and 0.1% Triton X-100 in PBS for 10 min at room temperature. The blocking solution was removed, and coverslips containing cells were incubated with anti-γ-H2AX primary antibodies in blocking solution (anti-gamma-H2AX (phosphor-Ser139) (Abcam, Cambridge, UK; 1:100)) for 1 h at room temperature. Cells were transferred into 12-well plates, washed twice in PBS (5 min each), transferred to plates, and incubated with Goat anti-Mouse IgG Cross-adsorbed antibody, Alexa Fluor 488 (Invitrogen; 1:500 in PBS) for 1 h at room temperature. Cells were washed twice in PBS, followed by incubation with DAPI solution (1 μg/mL) for 10 min at room temperature and two washes in PBS and distilled water. Coverslips were removed using tweezers and placed on microscope slides with a drop of Fluoromount-G mounting medium. The slides were placed flat at room temperature for 24 h and then stored at 4 °C. The slides were analyzed with a fluorescence microscope using CellSens (Olympus) software. A total number of approximately 100 cells per slide was chosen for further analysis. The experiment was performed in duplicate. In BxPC-3 cells, inefficient or non-specific staining was observed despite attempts to optimize the assay. Therefore, we discontinued further work on these cells with the assay.

4.8. Data Analysis

4.8.1. Alkaline and Neutral Comet Assays

CASP: Comet Assay Software Project Lab (http://casplab.com (accessed on 1 January 2023)) was used to establish the median value of DNA (%) in comet tails. This parameter provides a very clear picture of what the actual appearance of the comets was like. In contrast, the tail moment is merely the product of the tail length and the tail intensity, is not linear in relation to dose, and does not provide any information regarding the comet's physical appearance [53]. The data were presented with an interquartile range and minimal and

maximal values using Graphpad Prism 7. Statistical analysis of comet assay results was performed using Statistica software. The Kruskal–Wallis test was used to show a statistically significant difference between groups. Multiple comparisons using mean ranks for all groups module of Statistica software were used. A p-value less than 0.05 was considered statistically significant. In all groups, $N > 200$.

4.8.2. γH2AX Staining

Images for green γ-H2AX (Alexa Fluor 488) and blue nuclear signals (DAPI) were taken using an Olympus camera. ImageJ software "find maxima" and "count" functions were used to determine the number of γ-H2AX foci in each cell. The "preview point selection" option and "prominence" were chosen based on the accuracy of coverage of γ-H2AX foci. Data were analyzed using GraphPad Prism 7.0 software system (GraphPad Prism Software Inc., USA) and Statistica software. The Kruskal–Wallis test was used to show a statistically significant difference between groups. Multiple comparisons using mean ranks for all groups module of Statistica software were used. A p-value less than 0.05 was considered statistically significant ($p < 0.05$). In all groups, $N > 200$.

4.9. Computational Studies

4.9.1. Molecular Docking

The atomic coordinates of the investigated factors belonging to the DDR pathway were obtained from the PDB databank (http://www.rcsb.org/ (accessed on 1 January 2023)). Macromolecules were prepared for docking through the assignment of autodock atom type (AD4), the addition of Gasteiger charge, and its equal distribution among the macromolecular residues followed by saving them in the default autodock format PDBQT using AutoDock Tools (The Scripps Research Institute, La Jolla, CA, USA).

The structures of **MM** ligands (**MM134**, **-6**, **-7**, and **-9**) were drawn using ChemDraw 8.0 software and converted into three-dimensional structures with subsequent energy minimization using the MM2 force field. The ligands were prepared for molecular docking simulation through the detection of aromatic carbons and rotatable bonds, setting of automatic torsion number, margin non-polar hydrogens, and addition of Gasteiger charges using AutoDock Tools.

For each of the investigated DDR proteins, a grid box was constructed that was adequate for covering all of the extended conformations of the complexed reference ligands and the majority of the macromolecular residues that were involved in the interactions (Table 3). The grid parameters for each of the targets were saved in a respective grid parameter file (GPF) for each DDR factor. This was performed using the Autogrid utility of the Autodock suite to further generate the map files that are necessary for carrying out molecular docking simulations. The dockings of reference ligands (that were already co-crystalized with PDB macromolecule targets) with the macromolecules were performed alongside the docking of **MM** compounds.

4.9.2. Molecular Dynamics

The molecular dynamics simulations of **MM137** with APE1, CHK1, and TOPO1 (complexes exhibiting highest binding affinities) were performed using the Desmond software with an OPLS force field at the time frame of 100 nanoseconds (ns) at constant temperature and pressure conditions, as previously described in NVT condition. Analyses of trajectories were performed using Desmond utilities to evaluate root-mean-square deviation (RMSD), root-mean-square fluctuation (RMSF), the radius of gyration, and interacting bonds.

Table 3. Grid box coordinates used in molecular docking studies: the coordinates of the grid box for all of the macromolecular targets belonging to the DDR pathway used in the current study.

Target	Full Name	PDB Code	x-D	y-D	z-D	Spacing (Å)	X-Center	Y-Center	Z-Center
APE-1	DNA-(apurinic or apyrimidinic site) endonuclease	6MKO	50	50	50	0.381	20.283	22.147	20.508
ATR	Serine/threonine-protein kinase ATR	4WAF	40	40	46	0.397	−1.215	8.294	−17.439
ATM	Serine/threonine-protein kinase ATR	7NI5	40	40	40	0.397	111.559	150.337	210.394
CHK1	Serine/threonine-protein kinase Chk1	2YM8	40	40	40	0.414	15.394	−1.219	11.745
CHK2	Serine/threonine-protein kinase Chk2	2W0J	40	40	46	0.408	37.373	−31.962	9.087
PARP-1	Poly [ADP-ribose] polymerase 1	7ONS	40	40	46	0.397	10.962	42.743	7.819
RPA70	Replication protein A 70 kDa DNA-binding subunit	4IJL	40	40	46	0.369	−5.944	−9.334	1.963
TOP1	Topoisomerase I	1TL8	40	40	40	0.392	22.245	−4.32	27.329
TOP2B	Topoisomerase II	3QX3	40	40	40	0.553	32.884	95.413	50.785
WEE1	Wee1-like protein kinase	2IN6	40	40	40	0.408	3.987	52.579	26.054

5. Conclusions

The present findings showed diverse cellular responses to the tested pyrazolo[4,3-*e*]tetrazolo[1,5-*b*][1,2,4]triazine sulfonamides, which were specific for the cell line and dependent on the compound used in the experiment. Genotoxicity testing confirmed the high antineoplastic properties of **MM134**, **-6**, **-7**, and **9**. Moreover, these effects were restricted mainly to cancer cells, indicating selectivity in targeting malignant cells. The DNA damaging potential of the compounds may be associated with CHK1 kinase inhibition, as suggested by in silico investigations. However, this needs confirmation in further studies.

Author Contributions: Conceptualization, M.K., B.M., A.G. and R.K.; Methodology, M.K., S.M., B.M., M.M. and R.K.; Supervision, M.K., B.M., A.G., K.B., M.M. and R.K.; Visualization, M.K.; Writing—original draft, M.K., S.M., A.G. and K.B.; Writing—review and editing, M.K., S.M., B.M., A.G., K.B., M.M. and R.K. All authors have read and agreed to the published version of the manuscript.

Funding: This research received no external funding.

Institutional Review Board Statement: Not applicable.

Informed Consent Statement: Not applicable.

Data Availability Statement: The data presented in this study are available in the main text of this article or on request from the corresponding author.

Conflicts of Interest: The authors declare no conflict of interest.

Abbreviations

ABL	ABL protein kinase
AKT	RAC-alpha serine/threonine-protein kinase
ATM	serine/threonine protein kinase ATM
ATR	serine/threonine protein kinase ATR
BAX/BAK	pro-apoptotic protein BAX/BAK
BSA	bovine serum albumin
BTK	Bruton's tyrosine kinase
CA	carbonic anhydrase
CDK	cyclin-dependent kinase

CHK1	serine/threonine protein kinase CHK1
DAPI	4′,6-diamidino-2-phenylindole
DDR	DNA damage response
DSB	double-strand breaks
FBS	fetal bovine serum
IRF1	Interferon regulatory factor 1
JAK	tyrosine-protein kinase JAK
MMP	mitochondria membrane potential
mTOR	mammalian target of rapamycin
NMP	normal melting point agarose
PARP1	poly[ADP-ribose] polymerase 1
PBS	buffered saline
PD-1	programmed death 1
PD-L1	programmed death ligand 1
PHA	paraformaldehyde
PI3K	phosphatidylinositol-4,5-bisphosphate 3-kinase
s-ICAM-1	soluble intercellular adhesion molecule-1
SSBs	single-strand breaks
STAT1/3	signal transducer and activator of transcription 1/3
TP53	cellular tumor antigen p53
TRIS	tris(hydroxymethyl)aminomethane

References

1. Choi, J.-S.; Berdis, A. Combating resistance to DNA damaging agents. *Oncoscience* **2018**, *5*, 134–136. [CrossRef]
2. Mukhtar, M.; Bilal, M.; Rahdar, A.; Barani, M.; Arshad, R.; Behl, T.; Brisc, C.; Banica, F.; Bungau, S. Nanomaterials for Diagnosis and Treatment of Brain Cancer: Recent Updates. *Chemosensors* **2020**, *8*, 117. [CrossRef]
3. Swift, L.H.; Golsteyn, R.M. Genotoxic Anti-Cancer Agents and Their Relationship to DNA Damage, Mitosis, and Checkpoint Adaptation in Proliferating Cancer Cells. *Int. J. Mol. Sci.* **2014**, *15*, 3403–3431. [CrossRef]
4. Novak, M.; Žegura, B.; Modic, B.; Heath, E.; Filipič, M. Cytotoxicity and genotoxicity of anticancer drug residues and their mixtures in experimental model with zebrafish liver cells. *Sci. Total. Environ.* **2017**, *601*, 293–300. [CrossRef]
5. Haystead, T.A.J. The Purinome, a Complex Mix of Drug and Toxicity Targets. *Curr. Top. Med. Chem.* **2006**, *6*, 1117–1127. [CrossRef]
6. Lee, C.-I.; Lee, C.-L.; Hwang, J.-F.; Lee, Y.-H.; Wang, J.-J. Monascus-fermented red mold rice exhibits cytotoxic effect and induces apoptosis on human breast cancer cells. *Appl. Microbiol. Biotechnol.* **2012**, *97*, 1269–1278. [CrossRef]
7. Lang, D.K.; Kaur, D.; Arora, R.; Saini, B.; Arora, S. Nitrogen-Containing Heterocycles as Anticancer Agents: An Overview. *Anti-Cancer Agents Med. Chem.* **2020**, *20*, 2150–2168. [CrossRef]
8. Hatse, S.; De Clercq, E.; Balzarini, J. Role of antimetabolites of purine and pyrimidine nucleotide metabolism in tumor cell differentiation. *Biochem. Pharmacol.* **1999**, *58*, 539–555. [CrossRef]
9. Parker, W.B. Enzymology of Purine and Pyrimidine Antimetabolites Used in the Treatment of Cancer. *Chem. Rev.* **2009**, *109*, 2880–2893. [CrossRef]
10. Pizzorno, G.; Diasio, R.B.; Cheng, Y.-C. Pyrimidine and Purine Antimetabolites. In *Holland-Frei Cancer Medicine*, 6th ed.; Kufe, D.W., Pollock, R.E., Weichselbaum, R.R., Bast, R.C., Gansler, T.S., Holland, J.F., Frei, E., III, Eds.; BC Decker: Hamilton, ON, Canada, 2003; Chapter 50. Available online: https://www.ncbi.nlm.nih.gov/books/NBK13028/ (accessed on 1 January 2023).
11. Saad, H.A.; Moustafa, A.H. Synthesis and Anticancer Activity of Some New S-Glycosyl and S-Alkyl 1,2,4-Triazinone Derivatives. *Molecules* **2011**, *16*, 5682–5700. [CrossRef]
12. Kabbaj, Y.; Lazrek, H.B.; Barascut, J.L.; Imbach, J.L. Synthesis and Biological Activity of Some Unsaturated 6-Azauracil Acyclonucleosides. *Nucleosides Nucleotides Nucleic Acids* **2005**, *24*, 161–172. [CrossRef] [PubMed]
13. Mojzych, M.; Ceruso, M.; Bielawska, A.; Bielawski, K.; Fornal, E.; Supuran, C.T. New pyrazolo[4,3-*e*][1,2,4]triazine sulfonamides as carbonic anhydrase inhibitors. *Bioorganic Med. Chem.* **2015**, *23*, 3674–3680. [CrossRef] [PubMed]
14. Mojzych, M.; Bielawska, A.; Bielawski, K.; Ceruso, M.; Supuran, C.T. Pyrazolo[4,3-*e*][1,2,4]triazine sulfonamides as carbonic anhydrase inhibitors with antitumor activity. *Bioorganic Med. Chem.* **2014**, *22*, 2643–2647. [CrossRef] [PubMed]
15. Mojzych, M.; Dolashki, A.; Voelter, W. Synthesis of pyrazolo[4,3-*e*][1,2,4]triazine sulfonamides, novel Sildenafil analogs with tyrosinase inhibitory activity. *Bioorganic Med. Chem.* **2014**, *22*, 6616–6624. [CrossRef] [PubMed]
16. Mojzych, M.; Tarasiuk, P.; Kotwica-Mojzych, K.; Rafiq, M.; Seo, S.-Y.; Nicewicz, M.; Fornal, E. Synthesis of chiral pyrazolo[4,3-*e*][1,2,4]triazine sulfonamides with tyrosinase and urease inhibitory activity. *J. Enzym. Inhib. Med. Chem.* **2016**, *32*, 99–105. [CrossRef] [PubMed]
17. Bernat, Z.; Szymanowska, A.; Kciuk, M.; Kotwica-Mojzych, K.; Mojzych, M. Review of the Synthesis and Anticancer Properties of Pyrazolo[4,3-*e*][1,2,4]triazine Derivatives. *Molecules* **2020**, *25*, 3948. [CrossRef]

18. Byth, K.F.; Cooper, N.; Culshaw, J.D.; Heaton, D.W.; Oakes, S.E.; Minshull, C.A.; Norman, R.A.; Pauptit, R.A.; Tucker, J.A.; Breed, J.; et al. Imidazo[1,2-*b*]pyridazines: A potent and selective class of cyclin-dependent kinase inhibitors. *Bioorganic Med. Chem. Lett.* **2004**, *14*, 2249–2252. [CrossRef]
19. Kciuk, M.; Mujwar, S.; Szymanowska, A.; Marciniak, B.; Bukowski, K.; Mojzych, M.; Kontek, R. Preparation of Novel Pyrazolo[4,3-*e*]tetrazolo[1,5-*b*][1,2,4]triazine Sulfonamides and Their Experimental and Computational Biological Studies. *Int. J. Mol. Sci.* **2022**, *23*, 5892. [CrossRef]
20. Końca, K.; Lankoff, A.; Banasik, A.; Lisowska, H.; Kuszewski, T.; Góźdź, S.; Koza, Z.; Wojcik, A. A cross-platform public domain PC image-analysis program for the comet assay. *Mutat. Res. Toxicol. Environ. Mutagen.* **2002**, *534*, 15–20. [CrossRef]
21. Luo, M.; Bao, Z.; Xu, F.; Wang, X.; Li, F.; Li, W.; Chen, Z.; Ying, S.; Shen, H. Unrepaired DNA damage in macrophages causes elevation of particulate matter-induced airway inflammatory response. *Aging* **2018**, *10*, 549–560. [CrossRef]
22. Duez, P.; Dehon, G.; Kumps, A.; Dubois, J. Statistics of the Comet assay: A key to discriminate between genotoxic effects. *Mutagenesis* **2003**, *18*, 159–166. [CrossRef]
23. Lorenzo, Y.; Costa, S.; Collins, A.; Azqueta, A. The comet assay, DNA damage, DNA repair and cytotoxicity: Hedgehogs are not always dead. *Mutagenesis* **2013**, *28*, 427–432. [CrossRef] [PubMed]
24. Fairbairn, D.W.; Olive, P.L.; O'Neill, K.L. The comet assay: A comprehensive review. *Mutat. Res. Genet. Toxicol.* **1995**, *339*, 37–59. [CrossRef]
25. Nagelkerke, A.; Span, P.N. Staining Against Phospho-H2AX (γ-H2AX) as a Marker for DNA Damage and Genomic Instability in Cancer Tissues and Cells. *Adv. Exp. Med. Biol.* **2016**, *899*, 1–10. [CrossRef]
26. Phillips, D.H.; Arlt, V.M. Genotoxicity: Damage to DNA and Its Consequences. *EXS* **2009**, *99*, 87–110. [CrossRef]
27. Barabadi, H.; Najafi, M.; Samadian, H.; Azarnezhad, A.; Vahidi, H.; Mahjoub, M.A.; Koohiyan, M.; Ahmadi, A. A Systematic Review of the Genotoxicity and Antigenotoxicity of Biologically Synthesized Metallic Nanomaterials: Are Green Nanoparticles Safe Enough for Clinical Marketing? *Medicina* **2019**, *55*, 439. [CrossRef] [PubMed]
28. Corvi, R.; Madia, F. In vitro genotoxicity testing–Can the performance be enhanced? *Food Chem. Toxicol.* **2017**, *106*, 600–608. [CrossRef] [PubMed]
29. Kubara, P.M.; Kernéis-Golsteyn, S.; Studény, A.; Lanser, B.B.; Meijer, L.; Golsteyn, R.M. Human cells enter mitosis with damaged DNA after treatment with pharmacological concentrations of genotoxic agents. *Biochem. J.* **2012**, *446*, 373–381. [CrossRef] [PubMed]
30. Hermanowicz, J.M.; Szymanowska, A.; Sieklucka, B.; Czarnomysy, R.; Pawlak, K.; Bielawska, A.; Bielawski, K.; Kalafut, J.; Przybyszewska, A.; Surazynski, A.; et al. Exploration of novel heterofused 1,2,4-triazine derivative in colorectal cancer. *J. Enzym. Inhib. Med. Chem.* **2021**, *36*, 535–548. [CrossRef]
31. Hermanowicz, J.M.; Pawlak, K.; Sieklucka, B.; Czarnomysy, R.; Kwiatkowska, I.; Kazberuk, A.; Surazynski, A.; Mojzych, M.; Pawlak, D. MM-129 as a Novel Inhibitor Targeting PI3K/AKT/mTOR and PD-L1 in Colorectal Cancer. *Cancers* **2021**, *13*, 3203. [CrossRef]
32. Jiang, Y.; Chen, M.; Nie, H.; Yuan, Y. PD-1 and PD-L1 in cancer immunotherapy: Clinical implications and future considerations. *Hum. Vaccines Immunother.* **2019**, *15*, 1111–1122. [CrossRef] [PubMed]
33. Gornowicz, A.; Szymanowska, A.; Mojzych, M.; Czarnomysy, R.; Bielawski, K.; Bielawska, A. The Anticancer Action of a Novel 1,2,4-Triazine Sulfonamide Derivative in Colon Cancer Cells. *Molecules* **2021**, *26*, 2045. [CrossRef] [PubMed]
34. Bukowski, K.; Marciniak, B.; Kciuk, M.; Mojzych, M.; Kontek, R. Pyrazolo[4,3-*e*]tetrazolo[1,5-*b*][1,2,4]triazine Sulfonamides as Novel Potential Anticancer Agents: Cytotoxic and Genotoxic Activities In Vitro. *Molecules* **2022**, *27*, 3761. [CrossRef]
35. Zhang, T.; Zheng, S.; Liu, Y.; Li, X.; Wu, J.; Sun, Y.; Liu, G. DNA damage response and PD-1/PD-L1 pathway in ovarian cancer. *DNA Repair* **2021**, *102*, 103112. [CrossRef]
36. Sato, H.; Jeggo, P.A.; Shibata, A. Regulation of programmed death-ligand 1 expression in response to DNA damage in cancer cells: Implications for precision medicine. *Cancer Sci.* **2019**, *110*, 3415–3423. [CrossRef]
37. Sun, S.-Y. Searching for the real function of mTOR signaling in the regulation of PD-L1 expression. *Transl. Oncol.* **2020**, *13*, 100847. [CrossRef]
38. Nikolova, T.; Marini, F.; Kaina, B. Genotoxicity testing: Comparison of the γH2AX focus assay with the alkaline and neutral comet assays. *Mutat. Res. Toxicol. Environ. Mutagen.* **2017**, *822*, 10–18. [CrossRef] [PubMed]
39. Rogers, R.F.; Walton, M.I.; Cherry, D.L.; Collins, I.; Clarke, P.A.; Garrett, M.D.; Workman, P. CHK1 Inhibition is Synthetically Lethal with Loss of B-Family DNA Polymerase Function in Human Lung and Colorectal Cancer Cells. *Cancer Res.* **2020**, *80*, 1735–1747. [CrossRef] [PubMed]
40. Bryant, C.; Scriven, K.; Massey, A.J. Inhibition of the checkpoint kinase Chk1 induces DNA damage and cell death in human Leukemia and Lymphoma cells. *Mol. Cancer* **2014**, *13*, 147. [CrossRef] [PubMed]
41. Syljuåsen, R.G.; Sørensen, C.S.; Hansen, L.T.; Fugger, K.; Lundin, C.; Johansson, F.; Helleday, T.; Sehested, M.; Lukas, J.; Bartek, J. Inhibition of Human Chk1 Causes Increased Initiation of DNA Replication, Phosphorylation of ATR Targets, and DNA Breakage. *Mol. Cell Biol.* **2005**, *25*, 3553–3562. [CrossRef]
42. Tran, S.-L.; Puhar, A.; Ngo-Camus, M.; Ramarao, N. Trypan Blue Dye Enters Viable Cells Incubated with the Pore-Forming Toxin HlyII of Bacillus cereus. *PLoS ONE* **2011**, *6*, e22876. [CrossRef] [PubMed]
43. Rampersad, S.N. Multiple Applications of Alamar Blue as an Indicator of Metabolic Function and Cellular Health in Cell Viability Bioassays. *Sensors* **2012**, *12*, 12347–12360. [CrossRef] [PubMed]

44. Czubaszek, M.; Szostek, M.; Wójcik, E.; Andraszek, K. The comet assay as a method of identifying chromosomes instability. *Postep. Hig. Med. Dosw.* **2014**, *68*, 695–700. [CrossRef] [PubMed]
45. Faust, F.; Kassie, F.; Knasmüller, S.; Boedecker, R.H.; Mann, M.; Mersch-Sundermann, V. The use of the alkaline comet assay with lymphocytes in human biomonitoring studies. *Mutat. Res. Mol. Mech. Mutagen.* **2004**, *566*, 209–229. [CrossRef] [PubMed]
46. Horváthová, E.; Slamenová, D.; Gabelova, A. Use of single cell gel electrophoresis (comet assay) modifications for analysis of DNA damage. *Gen. Physiol. Biophys.* **1999**, *18*, 70–74.
47. Moller, P. Assessment of reference values for DNA damage detected by the comet assay in human blood cell DNA. *Mutat. Res. Mol. Mech. Mutagen.* **2006**, *612*, 84–104. [CrossRef]
48. Hartmann, A.; Agurell, E.; Beevers, C.; Brendler-Schwaab, S.; Burlinson, B.; Clay, P.; Collins, A.; Smith, A.; Speit, G.; Thybaud, V.; et al. Recommendations for Conducting the in Vivo Alkaline Comet Assay. 4th International Comet Assay Workshop. *Mutagenesis* **2003**, *18*, 45–51. [CrossRef]
49. Liao, W.; McNutt, M.A.; Zhu, W.-G. The comet assay: A sensitive method for detecting DNA damage in individual cells. *Methods* **2009**, *48*, 46–53. [CrossRef]
50. De Lapuente, J.; Lourenço, J.; Mendo, S.A.; Borràs, M.; Martins, M.G.; Costa, P.M.; Pacheco, M. The Comet Assay and its applications in the field of ecotoxicology: A mature tool that continues to expand its perspectives. *Front. Genet.* **2015**, *6*, 180. [CrossRef]
51. Singh, N.P.; McCoy, M.T.; Tice, R.R.; Schneider, E.L. A simple technique for quantitation of low levels of DNA damage in individual cells. *Exp. Cell Res.* **1988**, *175*, 184–191. [CrossRef]
52. Kontek, R.; Nowicka, H. The modulatory effect of melatonin on genotoxicity of irinotecan in healthy human lymphocytes and cancer cells. *Drug Chem. Toxicol.* **2012**, *36*, 335–342. [CrossRef] [PubMed]
53. Collins, A.R. The Comet Assay: Principles, Applications, and Limitations. *Methods Mol. Biol.* **2002**, *203*, 163–177. [CrossRef] [PubMed]

International Journal of
Molecular Sciences

MDPI

Article

Pyrazolo[4,3-*e*]tetrazolo[1,5-*b*][1,2,4]triazine Sulfonamides as an Important Scaffold for Anticancer Drug Discovery—In Vitro and In Silico Evaluation

Mateusz Kciuk [1,2], Beata Marciniak [1], Ismail Celik [3], Enfale Zerroug [4], Amit Dubey [5,6], Rajamanikandan Sundaraj [7], Somdutt Mujwar [8], Karol Bukowski [1], Mariusz Mojzych [9] and Renata Kontek [1,*]

1 Department of Molecular Biotechnology and Genetics, University of Lodz, Banacha 12/16, 90-237 Lodz, Poland; mateusz.kciuk@edu.uni.lodz.pl (M.K.)
2 Doctoral School of Exact and Natural Sciences, University of Lodz, Banacha Street 12/16, 90-237 Lodz, Poland
3 Department of Pharmaceutical Chemistry, Faculty of Pharmacy, Erciyes University, Kayseri 38280, Turkey
4 Group of Computational and Pharmaceutical Chemistry, LMCE Laboratory, University of Biskra, BP 145, Biskra 07000, Algeria
5 Computational Chemistry and Drug Discovery Division, Quanta Calculus, Greater Noida 274203, Uttar Prades, India
6 Department of Pharmacology, Saveetha Dental College and Hospital, Saveetha Institute of Medical and Technical Sciences, Chennai 602105, Tamil Nadu, India
7 Centre for Drug Discovery, Department of Biochemistry, Karpagam Academy of Higher Education, Coimbatore 641021, Tamil Nadu, India
8 Chitkara College of Pharmacy, Chitkara University, Rajpura 140401, Punjab, India
9 Department of Chemistry, Siedlce University of Natural Sciences and Humanities, 3 Maja 54, 08-110 Siedlce, Poland
* Correspondence: renata.kontek@biol.uni.lodz.pl

Citation: Kciuk, M.; Marciniak, B.; Celik, I.; Zerroug, E.; Dubey, A.; Sundaraj, R.; Mujwar, S.; Bukowski, K.; Mojzych, M.; Kontek, R. Pyrazolo[4,3-*e*]tetrazolo[1,5-*b*][1,2,4]triazine Sulfonamides as an Important Scaffold for Anticancer Drug Discovery—In Vitro and In Silico Evaluation. *Int. J. Mol. Sci.* **2023**, *24*, 10959. https://doi.org/10.3390/ijms241310959

Academic Editors: Andrea Spallarossa and Chiara Brullo

Received: 17 June 2023
Revised: 26 June 2023
Accepted: 28 June 2023
Published: 30 June 2023

Abstract: Pyrazolo[4,3-*e*]tetrazolo[1,5-*b*][1,2,4]triazine sulfonamides (**MM**-compounds) are a relatively new class of heterocyclic compounds that exhibit a wide variety of biological actions, including anticancer properties. Here, we used caspase enzyme activity assays, flow cytometry analysis of propidium iodide (PI)-stained cells, and a DNA laddering assay to investigate the mechanisms of cell death triggered by the **MM**-compounds (**MM134**, **-6**, **-7**, and **-9**). Due to inconsistent results in caspase activity assays, we have performed a bromodeoxyuridine (BrdU) incorporation assay, colony formation assay, and gene expression profiling. The compounds' cytotoxic and pro-oxidative properties were also assessed. Additionally, computational studies were performed to demonstrate the potential of the scaffold for future drug discovery endeavors. MM-compounds exhibited strong micromolar (0.06–0.35 μM) anti-proliferative and pro-oxidative activity in two cancer cell lines (BxPC-3 and PC-3). Activation of caspase 3/7 was observed following a 24-h treatment of BxPC-3 cells with IC_{50} concentrations of **MM134**, **-6,** and **-9** compounds. However, no DNA fragmentation characteristics for apoptosis were observed in the flow cytometry and DNA laddering analysis. Gene expression data indicated up-regulation of BCL10, GADD45A, RIPK2, TNF, TNFRSF10B, and TNFRSF1A (TNF-R1) following treatment of cells with the **MM134** compound. Moreover, in silico studies indicated AKT2 kinase as the primary target of compounds. **MM**-compounds exhibit strong cytotoxic activity with pro-oxidative, pro-apoptotic, and possibly pro-necroptotic properties that could be employed for further drug discovery approaches.

Keywords: apoptosis; cytotoxicity; heterocycles; pyrazolo[4,3-*e*]tetrazolo[4,5-*b*][1,2,4]triazine; sulfonamides

1. Introduction

More than seventy years ago, the cytostatic activity of N-mustard and its derivatives was discovered, marking the beginning of cancer chemotherapy. This finding paved

the way for the synthesis of numerous antitumor molecules, including alkylating agents, antimetabolites, and antimitotics, which are effective against a wide range of human cancers [1]. The clinical efficacy of the many different anticancer treatments currently in use is diminished by drug resistance and the severe adverse effects of chemotherapeutic medications. As a result, there is perpetual demand for the discovery of novel or synergistic anticancer medications that produce fewer adverse effects [2]. Because of their prevalence in currently available pharmaceuticals, inherent diversity, and distinctive physicochemical features, heterocycle molecules have established themselves as true cornerstones of medicinal chemistry. Numerous agents are being studied that show promise against several cancers, in addition to those already on the market. Strategic inclusion of heterocyclic elements with certain physicochemical features is crucial for the design of compounds with high potency and selectivity [3,4].

There are many naturally occurring and synthetically produced physiologically active chemicals that contain the 1,2,4-triazine ring [5]. The pyrazolo[4,3-*e*][1,2,4]triazine ring system is a fascinating and understudied member of the group of 1,2,4-triazines, fused with a five-membered heterocycle that constitutes one of the most promising scaffolds for drug discovery. Many pyrazolo[4,3-*e*][1,2,4]triazines have exhibited anticancer activity in vitro. Specifically, tricyclic pyrazolo[4,3-*e*][1,2,4]triazines fused with a triazole or tetrazole ring have been found to possess cytotoxic and [6] and genotoxic activity [7,8] that result in the induction of apoptotic cell death [9–11].

Previous research has demonstrated that **MM129** (pyrazolo[4,3-*e*]tetrazolo1,5-*b*][1,2,4]-triazine sulfonamide) efficiently limits cell viability by inhibiting Bruton's tyrosine kinase (BTK) [10]. Furthermore, **MM129** exhibits antitumor activity in colon cancer xenograft mice. These results could be related to a decrease in serine/threonine-protein kinase AKT (AKT), cyclin-dependent kinase 2 (CDK2), mammalian target of rapamycin kinase (mTOR), and programmed death-ligand 1 (PD-L1) expression [12]. Here we have focused on the assessment of anticancer activity of four **MM129** analogues—**MM134**, **-6**, **-7,** and **-9** pyrazolo[4,3-*e*]tetrazolo[1,5-*b*][1,2,4]triazine sulfonamides. These **MM**-compounds exhibit cytotoxic and genotoxic activity in cancer cells in micromolar concentrations and show pro-apoptotic properties, as indicated by the externalization of phosphatidylserine (PS) on the outer plasma membrane of apoptotic cells, morphological changes explored with dual staining with acridine orange/ethidium bromide, and changes in the mitochondrial membrane potential (MMP; $\Delta\Psi m$). These effects are selective for cancer cells compared with normal cells [8,11].

In the present study, we further explored the mechanisms of apoptotic cell death triggered in response to the incubation of the pancreas adenocarcinoma cell line (BxPC-3) and prostate adenocarcinoma cell line (PC-3) cells with the **MM**-compounds (**MM134**, **-6**, **-7** and **-9**) using caspase enzyme activity assays and flow cytometry analysis of cells stained with propidium iodide (PI). Due to the conflicting results obtained in the assays that estimate caspase activity, we performed a bromodeoxyuridine (BrdU) incorporation assay, colony formation assay, and gene expression profiling. The induction of reactive oxygen species (ROS) and their contribution to the cytotoxicity of the compounds were also evaluated. Additionally, computational studies were carried out to establish the primary target of the compounds based on the findings of **MM129** investigations, and to demonstrate the usefulness of this scaffold in further drug discovery approaches. The workflow of this study based on previous studies is presented in Figure S1 of the Supplementary Materials.

2. Results

2.1. Biological Studies

2.1.1. Neutral Red Uptake Assay

A neutral red uptake assay was used to re-evaluate the cytotoxicity of **MM134**, **-6**, **-7**, and **-9** compounds following 24-h incubation with BxPC-3 and PC-3 cancer cells. The respective IC_{50} values obtained from two independent experiments with corresponding

coefficients of determination (R^2) are shown in Table S1 of the Supplementary Materials, together with the calculated mean IC_{50} values ± SD (standard deviation).

MM-compounds exhibited cytotoxic activity in BxPC-3 (IC_{50} range: 0.18–0.35 μM) and PC-3 (IC_{50} range: 0.06–0.17 μM) cancer cell lines following a 24-h incubation time. The PC-3 cell line was more prone to the cytotoxic activity of the compounds. **MM137** sulfonamide exhibited the highest cytotoxic potential in both cell lines, with IC_{50} values of 0.18 and 0.06 μM for the BxPC-3 and PC-3 cell lines, respectively.

2.1.2. Reactive Oxygen Species (ROS) Formation

Cellular ROS levels were estimated using a 2,7-dichlorodihydrofluorescein diacetate (DCFH-DA) fluorescent probe. After diffusion across the plasma membrane, 2′,7′-dichlorodihydrofluorescein (DCFH2) is generated by esterase cleavage of the acetate groups and is sequestered in the cytoplasm. Oxidation of DCFH2 leads to the generation of fluorescent 2′,7′-dichlorofluorescein (DCF, λ_{ex} = 503 nm, λ_{em} = 523 nm), which can be measured spectrofluorometrically. DCFH2 undergoes reactions with several different oxidants, although the reaction constants for each are different. Therefore, the probe is a great sensor for redox changes and general oxidative stress, as it reacts with multiple ROS including hydrogen peroxide, hydroxyl radicals, and peroxynitrite [13]. Induction of ROS in BxPC-3 and PC-3 cells following 1-h incubation with the **MM134**, **-6**, **-7**, and **-9** was estimated using DCFH-DA, as shown in Figure 1.

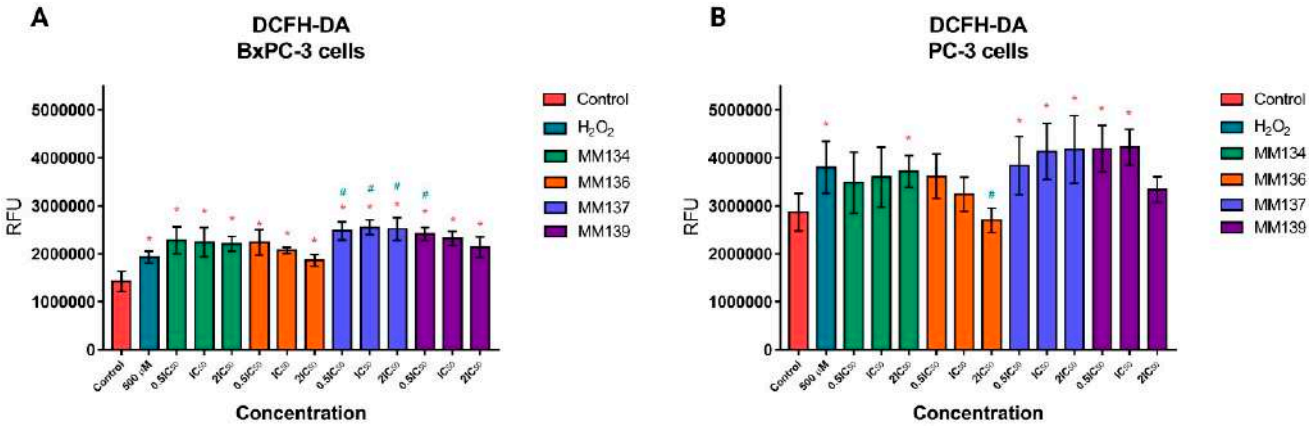

Figure 1. Induction of ROS in BxPC-3 (**A**) and PC-3 (**B**) cells following 1-h incubation with the **MM134**, **-6**, **-7**, and **-9** compounds in 0.5xIC_{50}, IC_{50}, and 2xIC_{50} concentrations, with hydrogen peroxide (H_2O_2) used as a positive control. The data are presented as relative fluorescence units (RFU) ± SD. The differences between the experimental samples and control samples were estimated using an ANOVA followed by Tukey's post-hoc test ($p < 0.05$). * Significant difference compared with negative control; # Significant difference compared with positive control (500 μM H_2O_2).

Following 1-h incubation of BxPC-3 cells (Figure 1A) with **MM134**, **-6**, **-7**, and **-9** compounds used in all tested concentrations (0.5xIC_{50}, IC_{50}, and 2xIC_{50}), a statistically significant ($p < 0.05$) increase in ROS production compared with negative control was observed. A decrease in ROS production was observed with the increase in compound concentration for the **MM134**, **MM136**, and **MM139** compounds. **MM137** used in an IC_{50} concentration induced the highest increase in ROS production compared with other compounds, while the **MM136** compound used in a 2xIC_{50} concentration had the lowest pro-oxidative activity. A statistically significant increase in ROS production was shown for cells incubated with 500 μM H_20_2 compared with the negative control. The increase in ROS production exceeded the pro-oxidative activity of 500 μM H_2O_2 used as a positive control for **MM137** in 0.5xIC_{50}, IC_{50}, and 2xIC_{50} concentrations, and **MM139** used in a 0.5xIC_{50} concentration ($p < 0.05$).

In the PC-3 cell line (Figure 1B), a statistically significant ($p < 0.05$) increase in ROS production (indicated as an increase in mean RFU) was observed following 1-h incubation of cells with **MM134** used in 2xIC$_{50}$ concentration, **MM137** used in all tested concentrations (0.5xIC$_{50}$, IC$_{50}$ and 2xIC$_{50}$), and **MM139** used in 0.5xIC$_{50}$ and IC$_{50}$ concentrations compared with the negative control. The **MM139** used in the above-mentioned concentrations induced the highest levels of ROS compared with the negative control. ROS production increased with the increase in compound concentration for the **MM134** and **MM137** compounds. No statistical significance was detected in comparisons to ROS levels of **MM**-treated cells with cells treated with 500 µM H_2O_2. Only the **MM136** derivative used in the 2xIC$_{50}$ concentration induced statistically significant ($p < 0.05$) decreased levels of ROS compared with the positive control.

2.1.3. Caspase 3/7/8/9 Detection

We have also previously shown that **MM134**, **-6**, **-7**, and **-9** compounds exhibit moderate DNA damage [8] and strong pro-apoptotic activity in both BxPC-3 and PC-3 cells, as indicated by mitochondrial membrane permeabilization (MMP), PS exposure on the cell surface, and differential uptake of fluorescent dyes—acridine orange/ethidium bromide (AO/EB) [11]. Here, we explored the influence of compounds on caspases enzymatic activity. The effect of 24-h incubation of BxPC-3 (Figure 2A) and PC-3 (Figure 2B) cells with **MM**-compounds (used in 0.5xIC$_{50}$, IC$_{50,}$ and 2xIC$_{50}$ concentration) and 2 µM SN-38 (the active metabolite of camptothecin) on caspase 3/7 activity and caspase 8/9 activity for BxPC-3 cells (Figure 2C,D), respectively.

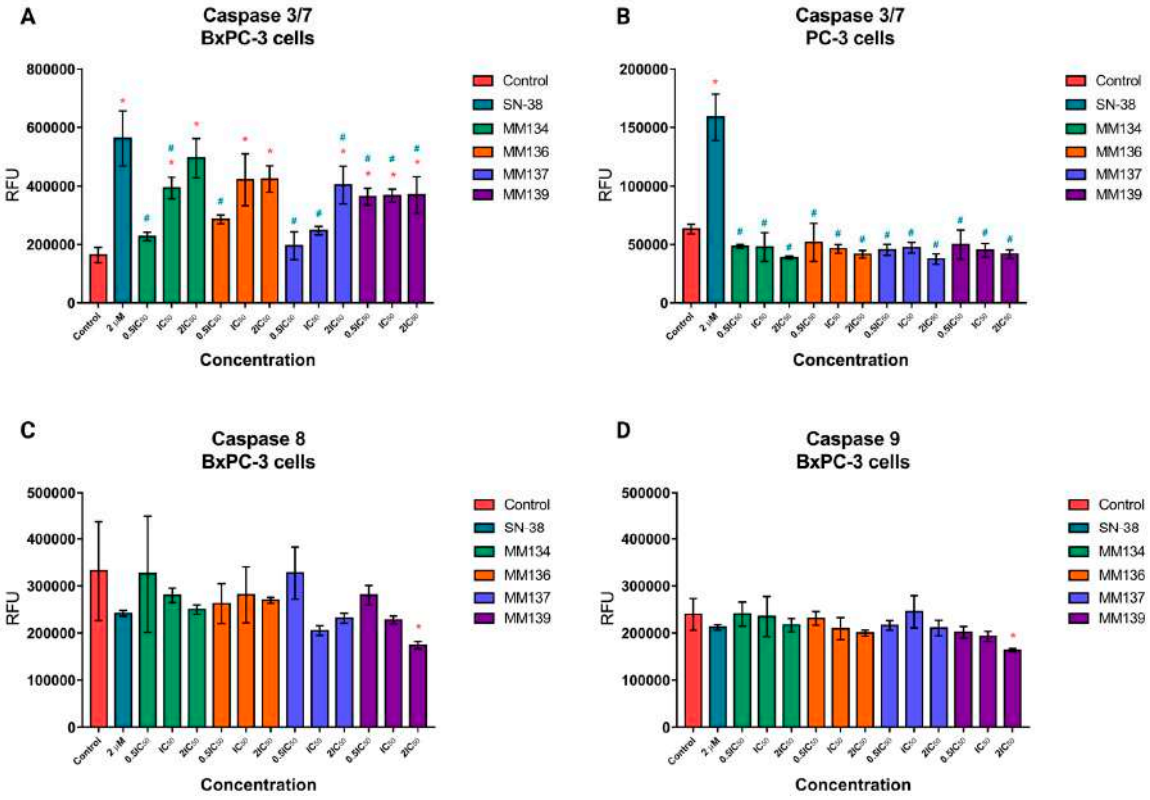

Figure 2. Caspase 3/7 activity in BxPC-3 (**A**) and PC-3 (**B**) cells following 24-h incubation with **MM**-compounds used at 0.5xIC$_{50}$, IC$_{50}$, and 2xIC$_{50}$ concentrations and 2 µM SN-38 (used as positive control). Caspase 8 (**C**) and caspase 9 (**D**) activity in BxPC-3 cells treated with the same concentrations of the compounds and for the same incubation time. The data are presented as relative fluorescence units (RFU) ± SD. The differences between the experimental samples and control samples were estimated using an ANOVA followed by Tukey's post-hoc test ($p < 0.05$). * Significant difference compared with negative control; # Significant difference compared with positive control (2 µM SN-38).

In BxPC-3 cells (Figure 2A), the **MM134** and **MM136** compounds used with the IC_{50} and $2xIC_{50}$ concentration induced statistically significant ($p < 0.05$) increases in caspase 3/7 activity (indicated as the increase in mean RFU) compared with the negative control. The **MM139** compound induced a statistically significant increase in caspase 3/7 activity in all tested concentrations ($0.5xIC_{50}$, IC_{50}, and $2xIC_{50}$) compared to the negative control. In contrast, the **MM137** compound induced a statistically significant increase in caspase 3/7 activity only in the $2xIC_{50}$ concentration compared to the negative control. The caspase 3/7 activation did not exceed the activity of 2 µM SN-38 in any of the experiments. To our surprise, **MM**-compounds in PC-3 cells (Figure 2B) did not induce a statistically significant ($p < 0.05$) increase in caspase 3/7 activity compared with the negative control. Only 2 µM of SN-38 induced a statistically significant increase in caspase 3/7 activity compared with the negative control.

Therefore, we decided to focus on the estimation of caspase 8/9 activity in BxPC-3 cells. In BxPC-3 cells (Figure 2C,D), only **MM139** used in the $2xIC_{50}$ concentration induced a statistically significant ($p < 0.05$) decrease in caspase 8/9 activity. In other experimental series and following incubation of cells with 2 µM SN-38, no statistically significant changes in caspase 8/9 activity were detected. The observed decrease in caspase activity in PC-3 cells, and in some cases in BxPC-3 cells (note that no statistically significant changes in caspase 8/9 activity were detected in BxPC-3 cells except at the $2xIC_{50}$ concentration of **MM139**), could be attributed to the decrease in cell proliferation. Therefore, we explored the effect of **MM**-compounds on PC-3 cell proliferation using a BrdU incorporation assay and a clonogenic assay.

2.1.4. Bromodeoxyuridine (BrdU) Incorporation Assay

The effects of **MM**-compounds used in $0.5xIC_{50}$, IC_{50}, and $2xIC_{50}$ concentrations on PC-3 cell proliferation following 24-h incubation using a BrdU incorporation assay are shown in Figure 3. Additionally, 10 µM cisplatin was used in the experimental design as a positive control. The experiment was performed as a duplicate, and a total of at least 500 cells per experiment were counted using a fluorescence microscope. The data are presented as % of proliferating cells. The differences between the experimental samples and untreated control were evaluated using an ANOVA followed by Tukey's test. A *p*-value less than 0.05 was considered statistically significant ($p < 0.05$).

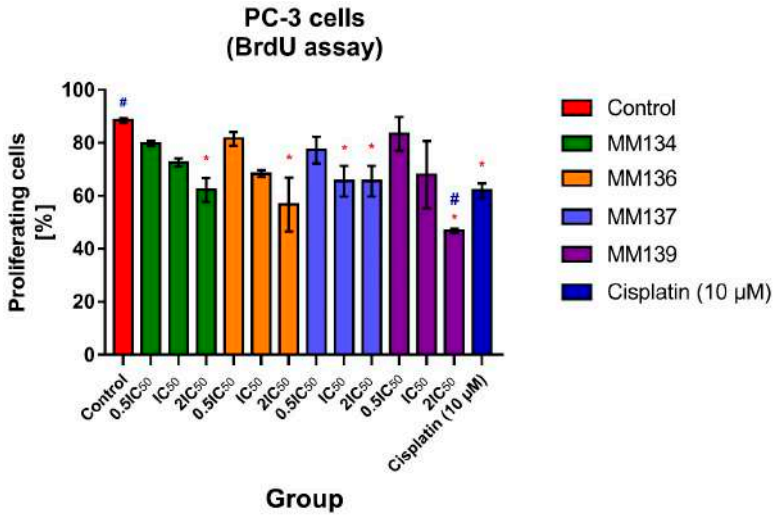

Figure 3. Effect of **MM**-compounds used in ($0.5xIC_{50}$, IC_{50}, and $2xIC_{50}$) concentrations and 10 µM cisplatin (used as positive control) on PC-3 cell proliferation following 24-h incubation. Data are presented as a mean percentage [%] of proliferating cells ± SD. An ANOVA followed by Tukey's test was used to show statistically significant changes ($p < 0.05$) in the mean % of proliferating cells in samples compared with a negative control (indicated with *) and positive control (indicated with #).

MM-compounds used in the 2xIC_{50} concentration induced a statistically significant ($p < 0.05$) decrease in the mean % of proliferating cells in the tested samples compared with the negative control (% of proliferating cells = 88.5 ± 0.98). Incubation of PC3 cells with **MM137** compound used in the IC_{50} concentration also induced a statistically significant decrease in the mean % of proliferating cells (% of proliferating cells = 65.6 ± 5.79; $p = 0.04$). The **MM139** compound used in the highest (2xIC_{50}) concentration induced the most profound reduction in cell proliferation (% of proliferating cells = 46.8 ± 0.77; $p = 0.0002$), and showed a superior effect compared to the 10 μM of cisplatin used in the experiment as a positive control (% of proliferating cells = 62 ± 2.8). The % of proliferating cells observed following the use of **MM**-compounds in the IC_{50} and 2xIC_{50} concentrations are shown in Table S2 of Supplementary Materials.

2.1.5. Clonogenic Assay

The clonogenic assay, also known as the colony formation assay, is a type of in vitro cell survival assay that evaluates a single cell's potential to form a colony. Cells are seeded out in appropriate dilutions either before or after treatment to establish colonies within one to three weeks. Colonies are counted after being fixed with glutaraldehyde (6.0% v/v), then stained with crystal violet (0.5% w/v) [14].

In the first step, the plating efficiencies were established by seeding different dilutions of cells. The examples of images obtained after seeding 100, 200, 500, 1000, and 2000 BxPC-3 or PC-3 cells per well of six-well plates are shown in Figure S2 of Supplementary Materials.

To establish the optimal seeding numbers for BxPC-3 and PC-3 cells for the colony assay, we plated 100–2000 cells in six-well plates. The plating efficiencies were 25% per 100 cells, 26.25% per 200 cells, 27.4% per 500 cells, 25.85% per 1000 cells, and 17.8% per 2000 for BxPC-3 cells, and 37% per 100 cells, 25.3% per 200 cells, 37.3% per 500 cells, 31.6% per 1000 cells, and 24.45% per 2000. Therefore, we seeded 500 cells in six-well plates to test the effects of different concentrations of **MM** compounds on cell clonogenic ability. Figure 4 presents the effects of **MM**-compounds on the clonogenic potential of BxPC-3 (Figure 4A) and PC-3 (Figure 4B) cells, while Figure 4C shows the effect of the IC_{50} concentration of the **MM137** compound on clonogenicity of PC-3 cells compared with the control sample.

A statistically significant ($p < 0.05$) decrease in colony formation was observed following the incubation of cells with **MM**-compounds, both in BxPC-3 (Figure 4A) and PC-3 (Figure 4) cells.

In BxPC-3 cells, the **MM136** and **MM139** compounds exhibited the highest inhibitory effects on colony formation (mean numbers of colonies = 15.5 and 0 for cells incubated with thr 0.5xIC_{50} and IC_{50} concentrations of **MM136**, and 4 and 0 for cells incubated with **MM139** in the same concentrations, respectively).

In PC-3 cells, **MM137** and **MM139** exhibited the highest inhibitory potential, with mean numbers of colonies of 11 and 0.5 for **MM137** used in the 0.5xIC_{50} and IC_{50} concentrations, and 5.7 and 2.5 for **MM139** used in the same concentrations, respectively.

2.1.6. Cell Cycle Analysis with Propidium Iodide (PI) Staining

During the cell cycle, the amount of DNA found in the parent cell rises because new DNA is synthesized in the S phase of the cell cycle. During the G2/M phase of the cell cycle, when there are two complete copies of the DNA, the cell divides into two new cells. Consequently, cells that are at various phases of the cell cycle contain varying amounts of DNA. A cell that is damaged or unable to complete the cell cycle is intended to die through apoptosis, protecting the integrity of the cell genome. As a direct consequence of this, apoptotic cells contain a lower proportion of DNA compared to live cells. Staining cells with propidium iodide (PI), a fluorescent reagent that intercalates with DNA, enables the measurement of the pro-apoptotic activity of compounds. The amount of DNA found in a cell has a direct and proportional relationship to the amount of PI fluorescence found in that cell [15,16].

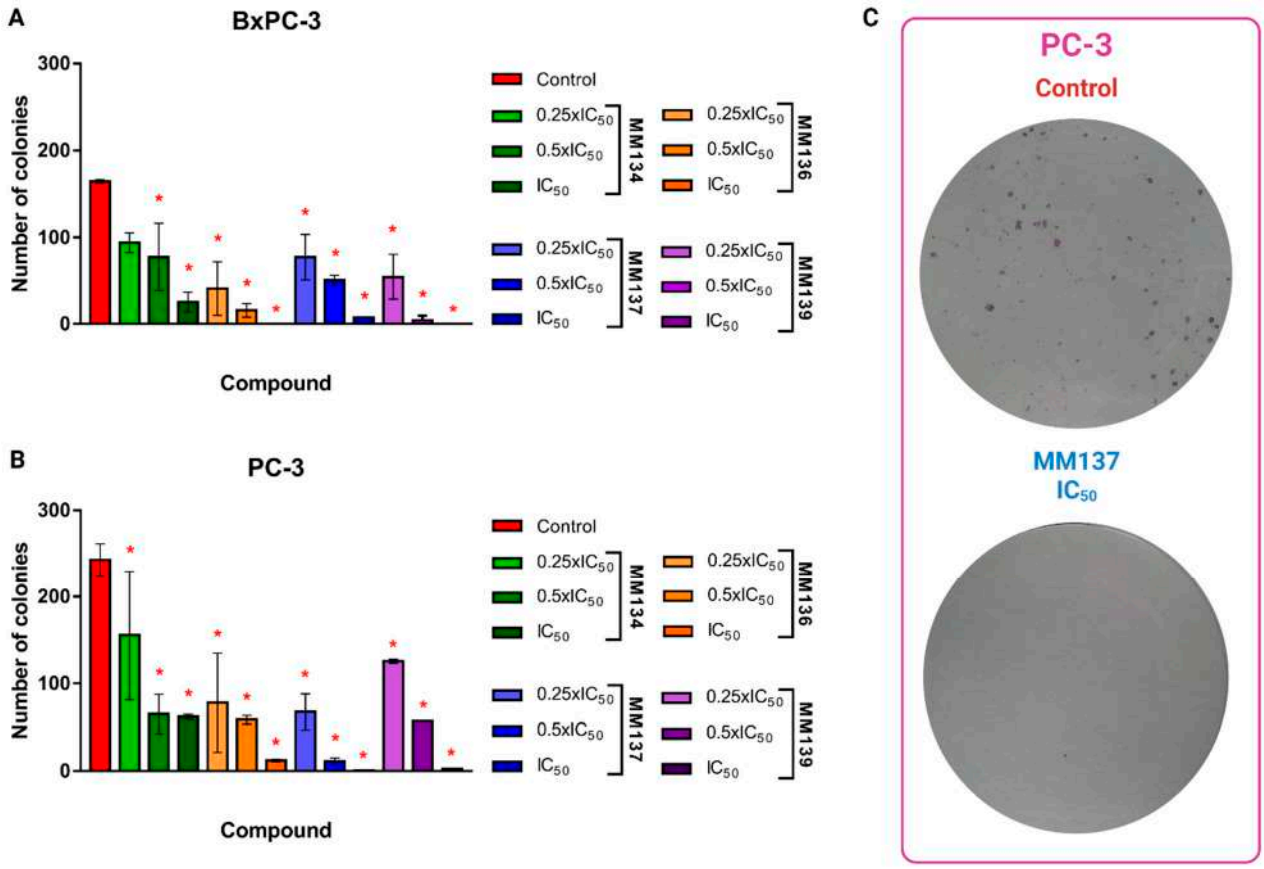

Figure 4. Effect of **MM**-compounds used in 0.25xIC_{50}, 0.5xIC_{50}, and IC_{50} concentrations on the clonogenic potential of BxPC-3 (**A**) and PC-3 (**B**) cells. (**C**) shows the effect of the IC_{50} concentration of the **MM137** compound on the clonogenicity of PC-3 cells compared with the control sample. Data are presented as the mean number of colonies ± SD. An ANOVA followed by Tukey's test was used to show statistically significant changes ($p < 0.05$) between mean number of colonies in the samples (indicated with *). Created using BioRender.com, accessed on 24 April 2023.

The effect of **MM**-compounds on the cell cycle of BxPC-3 and PC-3 cells is shown in Figure 5A,B, respectively.

A slight increase in the subG1 cell fraction (reflecting apoptosis induction) was observed following 24-h incubation of BxPC-3 cells with the IC_{50} concentration of **MM134** (2.8%), 0.5xIC_{50} and IC_{50} of **MM136** (3.3% and 2.9%), and IC_{50} of **MM137** (2.49%) compared with control cells (2.43%). However, no statistical significance ($p < 0.05$) was detected.

In contrast, the number of cells in the G0/G1 phase of the cell cycle seemed to decrease with the increase in **MM**-compounds concentration relative to the control, with an increase in cells in the S-phase of the cell cycle and a decrease in cells in the G2/M fraction, but no statistical significance was detected in these comparisons.

In the PC-3 cell line, an increase in the subG1 fraction was observed only for the IC_{50} concentration of **MM139** (1.31%) compared with the negative control (1.2%). However, this was not statistically significant ($p < 0.05$). Similar to BxPC-3 cells, a decrease in the G0/G1 and G2/M fractions and an increase in the S fraction was observed; however, no statistical significance ($p < 0.05$) was observed.

2.1.7. DNA Laddering

Classical apoptotic cell death can be differentiated from other types of cell death by distinct morphological and biochemical characteristics. DNA fragmentation is a defining component of apoptosis. Endonucleases cleave DNA during apoptosis, culminating in the fragmentation of chromatin into nucleosomal components, which are multiples of

approximately 180-bp oligomers. When the fragmented DNA is separated on an agarose gel, this distinctive DNA fragmentation may be seen as a ladder-like pattern [17,18]. BxPC-3 cells were used in this assay, as they are more responsive to the pro-apoptotic properties of the compounds [11]. However, similar to the cell cycle analysis (where no subG1 cell fraction was observed), no DNA fragmentation was detected. In contrast, DNA fragmentation was seen after the treatment of cells with an apoptosis-inducing agent: 7-ethyl-10-hydroxycamptothecin (SN-38) (Figure 6).

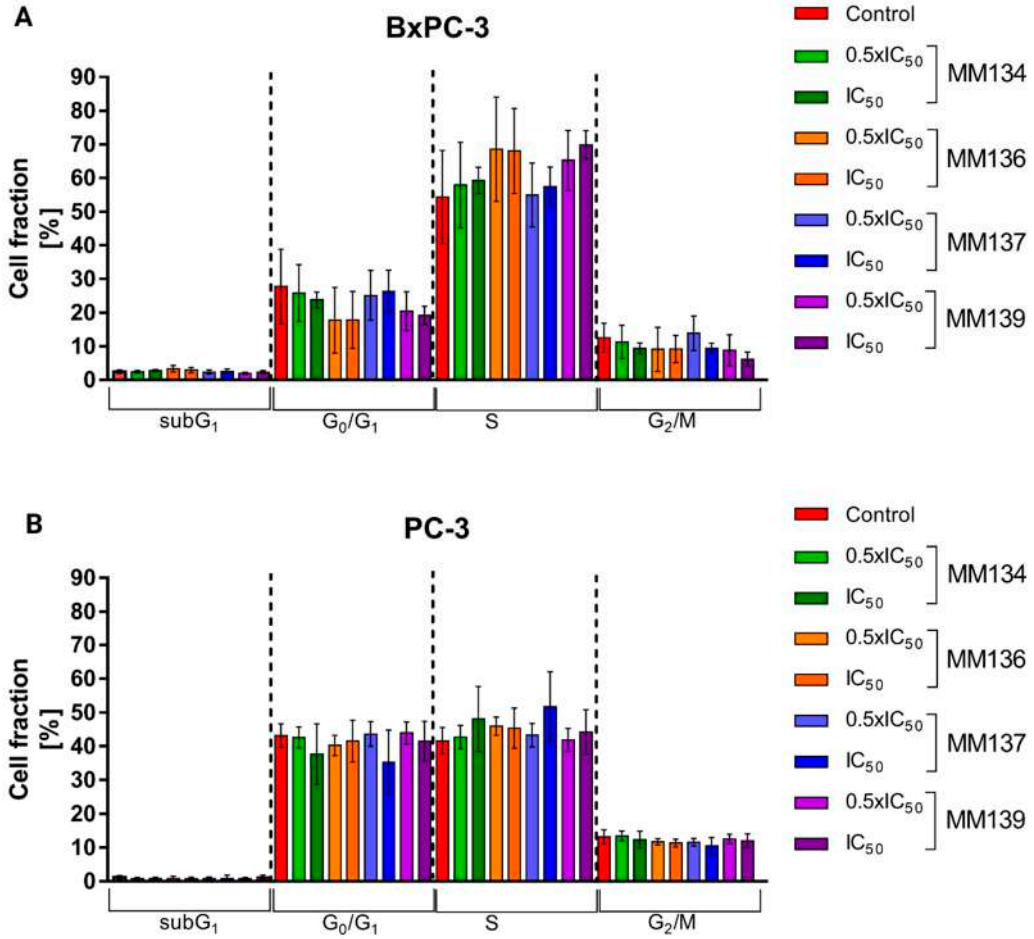

Figure 5. Effect of **MM**-compounds (**MM134**, **-6**, **-7** and **-9**) on the cell cycle of BxPC-3 (**A**) and PC-3 cells (**B**) following 24-h incubation of test with tested pyrazolo[4,3-*e*]tetrazolo[1,5,-*b*][1,2,4] triazine sulfonamides.

2.1.8. Gene Expression Analysis

To further explore the cell death pathway activated in response to **MM**-compounds, gene expression profiling using RT^2 Profiler™ PCR array human apoptosis was performed. **MM134** compound was selected as the most pro-apoptotic of investigated compounds, as evidenced by PS exposure on the cell surface in our earlier investigations and the observation of morphological changes [11]. The impact of the IC_{50} concentration of **MM134** on BxPC-3 gene expression is shown in Figure 7. Gene expression differences between the control and treatment groups were considered significant with $p < 0.05$ and an absolute fold regulation > 2 as a cut-off. Upregulated genes are marked in red, and the downregulated genes are indicated in green. Fold-regulation is a biologically applicable representation of fold-change results. Fold-change values above one indicate upregulation of a gene, and the fold-regulation equals the fold-change. Fold-change values below one indicate downregulation of gene expression, and the fold-regulation represents the negative inverse of the fold-change.

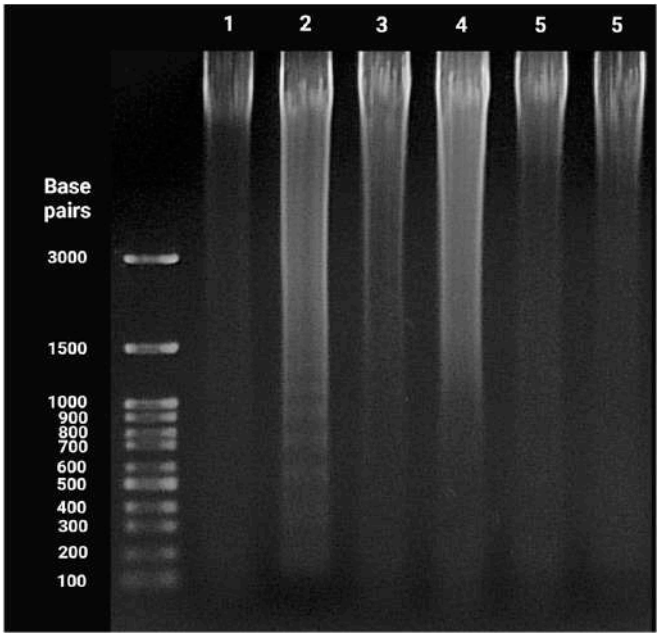

Figure 6. DNA fragmentation in BxPC-3 cells treated with the **MM134** (3), **MM136** (4), **MM137** (5), and **MM139** (6) compounds in their respective IC_{50} concentrations obtained using the neutral red uptake test. (1) Negative control: DMSO treated cells; (2) positive control: cells treated with 7-ethyl-10-hydroxycamptothecin (SN-38) in a 2 μM concentration.

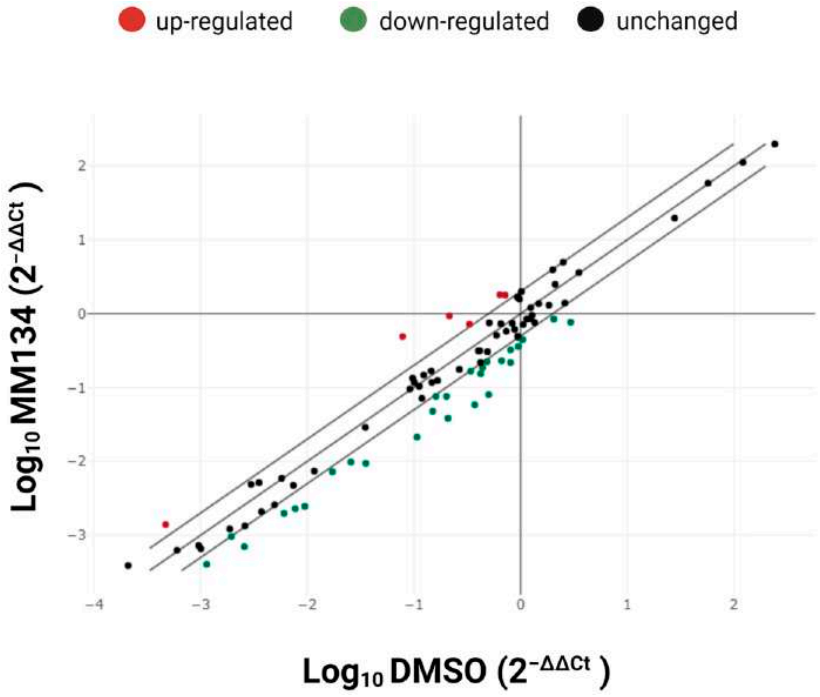

Figure 7. Differential gene expression in BxPC-3 cells following treatment with the **MM134** compound, expressed as a scatterplot of the 96 genes included in the current study.

A total set of 33 target genes were found to be differentially expressed ($p < 0.05$) (Table 1).

Table 1. Differentially expressed genes ($p < 0.05$) between **MM134**-treated cells and control (DMSO-treated cells). Upregulated genes str marked in red, while down-regulated str indicated in green.

Gene Symbol	Description	Fold Regulation	*p*-Value
BCL10	B-cell CLL/lymphoma 10	2.50	0.019800
GADD45A	Growth arrest and DNA-damage-inducible, alpha	6.24	0.000393
RIPK2	Receptor-interacting serine-threonine kinase 2	2.83	0.002422
TNF	Tumor necrosis factor	2.96	0.042660
TNFRSF10B	Tumor necrosis factor receptor superfamily, member 10b	4.36	0.001260
TNFRSF1A	Tumor necrosis factor receptor superfamily, member 1A	2.18	0.018576
ABL1	C-abl oncogene 1, non-receptor tyrosine kinase	−2.65	0.006966
AIFM1	Apoptosis-inducing factor, mitochondrion-associated, 1	−2.48	0.001081
APAF1	Apoptotic peptidase activating factor 1	−2.74	0.002161
BAD	BCL2-associated agonist of cell death	−2.36	0.006358
BAG1	BCL2-associated athanogene	−2.11	0.006014
BCL2L10	BCL2-like 10 (apoptosis facilitator)	−2.38	0.019800
BIRC5	Baculoviral IAP repeat containing 5	−5.01	0.003025
BNIP3	BCL2/adenovirus E1B 19kDa interacting protein 3	−2.04	0.009433
BNIP3L	BCL2/adenovirus E1B 19kDa interacting protein 3-like	−2.01	0.005716
CASP1	Caspase 1, apoptosis-related cysteine peptidase (interleukin 1, beta, convertase)	−3.76	0.033341
CASP14	Caspase 14, apoptosis-related cysteine peptidase	−2.83	0.000610
CASP2	Caspase 2, apoptosis-related cysteine peptidase	−2.63	0.009949
CASP6	Caspase 6, apoptosis-related cysteine peptidase	−2.87	0.016235
CD27	CD27 molecule	−3.05	0.001928
CD70	CD70 molecule	−3.67	0.000879
CIDEA	Cell death-inducing DFFA-like effector a	−2.03	0.001025
CIDEB	Cell death-inducing DFFA-like effector b	−2.15	0.002795
CRADD	CASP2 and RIPK1 domain containing adaptor with death domain	−3.37	0.001127
DFFA	DNA fragmentation factor, 45kDa, alpha polypeptide	−2.34	0.020318
FADD	Fas (TNFRSF6)-associated via death domain	−3.68	0.000243
FAS	Fas (TNF receptor superfamily, member 6)	−5.41	0.000181
NAIP	NLR family, apoptosis inhibitory protein	−6.35	0.025237
NOD1	Nucleotide-binding oligomerization domain containing 1	−3.13	0.000604
PYCARD	PYD and CARD domain containing	−2.41	0.010219
TNFRSF11B	Tumor necrosis factor receptor superfamily, member 11b	−3.85	0.000160
TNFSF10	Tumor necrosis factor (ligand) superfamily, member 10	−6.25	0.000372
TP53	Tumor protein p53	−3.84	0.023076

2.2. Computational Analysis

2.2.1. Density Functional Theory (DFT) Calculations

Frontier orbital energies, such as the highest occupied molecular orbital (HOMO) and lowest occupied molecular orbital (LUMO), were estimated to obtain the electronic properties of the chemical molecules. LUMO directly corresponds to electron affinity and has the tendency to accept electrons, while HOMO depicts the ionization energy of a molecule [19]. The energy difference between HOMO and LUMO determines the chemical stability. A molecule with a low HOMO–LUMO energy gap (HLG) implies high polarizability, high reactivity, and low stability [20]. Based on the results, it was observed that the molecules (**MM134**, **MM136**, **MM137**, and **MM139**) displayed low HLG values. The HOMO and LUMO energy values ranged between −0.25 eV to −0.23 eV and −0.22 eV to −0.20 eV, indicating the fragile nature of the bound electrons. The energy gap values of the compounds varied between 0.04 eV and 0.01 eV. The calculated frontier orbital energy values for the compounds were tabulated (Table 2).

The electron distribution profile of the compounds is shown in Figure S3 of Supplementary Materials.

Table 2. Density functional theory calculation of the **MM134**, **MM136**, **MM137**, and **MM139** compounds.

Compound ID	HOMO (eV)	LUMO (eV)	HLG (eV)
MM134	−0.238	−0.224	−0.014
MM136	−0.239	−0.208	−0.030
MM137	−0.243	−0.220	−0.022
MM139	−0.250	−0.201	−0.049

Figure S3 shows that both HOMO and LUMO orbitals are localized in two distinct parts of the molecules. HOMO map analysis of **MM134** showed that the electrons are located on the phenylsulfonyl group and the LUMO maps are localized on the pyrazole and triazine groups. In the case of **MM136**, the HOMO orbitals are widely dispersed around the morpholine region, whereas the LUMO is localized on the pyrazole group. The HOMO distributions for **MM137** and **MM139** were observed on the phenylsulfonyl and piperazine groups, while the LUMO was observed on the pyrazole, triazine (**MM137**), and phenylsulfonyl and piperazine groups (**MM139**). However, compared to other compounds, **MM139** showed increased HOMO and decreased LUMO energy values. In addition, **MM139** showed higher energy gap values (0.049 eV) compared to the other compounds. The energy distribution profile of HOMO and LUMO on the surface of the compounds provides information on the possible reactive sites. The low energy gap values obtained imply the high reactive nature of the compounds. In addition, molecular electrostatic potential (MESP) analysis was carried out to explore the reactivity and molecular bonding patterns in the compounds. The electrophilic and nucleophilic reactive sites are represented as negative (red) and positive (blue) regions, respectively (Figure 8).

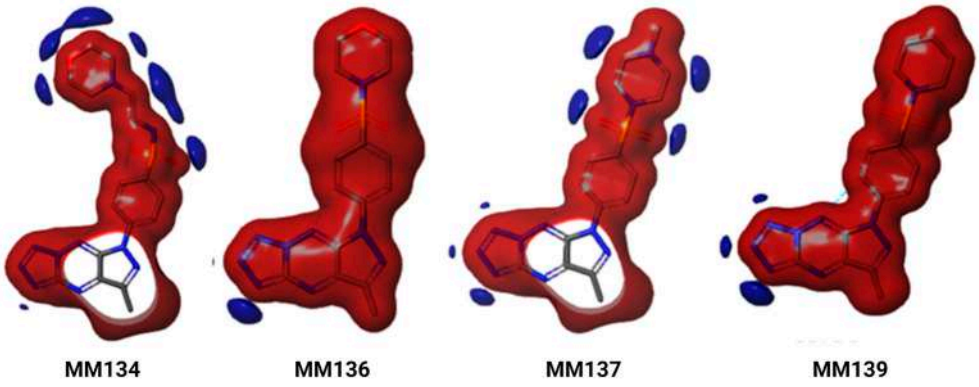

Figure 8. Molecular electrostatic potential (MESP) analysis. The electrophilic and nucleophilic reactive sites are represented as negative (red) and positive (blue) regions.

In the case of **MM134** and **MM137**, the negative electrostatic potential (ESP) is localized on the entire molecule, except pyrazole and triazine regions, whereas the positive ESP is localized on the sulfur, nitrogen, and oxygen atoms of phenylsulfonyl, aminoethylmorpholine, and methylpiperazine groups. The MESP analysis of **MM136** and **MM139** indicates that both the molecules showed the deepest negative ESP for the entire molecules, with the positive ESP localized in the tetrazole region. The obtained results indicate the crucial sites that are responsible for the intermolecular and intramolecular interactions.

2.2.2. Molecular Docking Studies of MM-Compounds

In the previous investigations, Hermanowicz et al. [12,21] explored the molecular basis of **MM129** compound anticancer activity. The authors declared that pyrazolo tetrazolo[1,5-*b*][1,2,4]triazine sulfonamides can work as AKT, BTK, CDK2, mTOR, and PD-L1 inhibitors. However, this was based on the gene expression changes in colorectal cancer cells and did not evaluate the exact inhibitory effects of the compound on the

proteins. In the initial in silico research, we performed molecular docking and molecular dynamics studies of the previously studied **MM129** compound and the compounds investigated in the present work (**MM134**, **-6**, **-7**, and **-9**). We found that compounds may inhibit the molecular targets to a similar or greater extent than previously investigated **MM**-compounds (including **MM129**) [8,11]. However, these results were established with the use of single molecular docking and dynamics software. Nevertheless, they allowed us to prioritize molecular targets for further in silico investigations. Therefore, in the present work, we included docking (with various scoring functions and conditions) and dynamics with previously unutilized dynamics software (Gromacs 2020.4). Performing in silico docking and dynamics studies using different software can be valuable for validation of the results, consensus prediction, and overcoming the limitations of a single software.

In the first step, molecular docking simulations were carried out to predict the molecular anticancer targets of the triazine sulfonamide analogs, and to evaluate the binding affinities and binding modes of these compounds with the predicted binding pockets of the target proteins. The Protein Data Bank (PDB) was mined for the 3D coordinates of AKT1 (PDBid = 3MVH) [22], AKT2 (PDB id = 3D0E) [23], BTK (PDBid = 3GEN) [24], serine/threonine-protein kinase CHK1 (CHK1) (PDBid = 2YM8) [25], mTOR1 (PDBid = 6BCX) [26], and PD-L1 (PDBid = 7BEA) [27] crystal structures, which originate from *Homo sapiens* organisms and exhibit high resolution. Hydrogen atoms were introduced to the protein using Discovery Studio 4.5 templates for protein residues. Hydration water molecules were kept or removed as required [28–30], and the protein structure was used in docking experiments without energy minimization. We performed the docking study using the Libdock docking engine [31], which treats the receptor as rigid and ligand molecules as flexible structures. Subsequently, high-ranking docking solutions were scored by seven different scoring functions (Jain [32], LigScore1, LigScore2 [33], PLP1, PLP2 [34], PMF, and PMF04 [35]). To determine the binding affinity between the ligand and receptor, we specifically considered the binding energy. The molecular docking simulation process for each anticancer target was validated by considering both chemical similarity and the superposition of the docked ligand conformation with its co-crystallized conformation [36,37]. Following this, we utilized similar parameters to perform simulation studies on the triazine sulfonamide analogs.

Table 3 displays the four anticancer targets (AKT2, BTK, CHK1, and PD-L1) for which the docked pose of triazine sulfonamide derivatives (**MM134**, **MM136**, **MM137**, and **MM139**) exhibited a high binding affinity. These four targets were selected from the previously identified six targets. The results presented in Table 3 were obtained using precise docking conditions. The optimal outcomes were obtained using the Ligscore 2 scoring function for BTK, CHK1, and PD-L1, while the Ligscore 1 scoring function was utilized for the AKT2 target. Moreover, the **MM134**, **-6**, **-7**, and **-9** compounds were docked into the hydrous binding site of the CHK1 and BTK targets and the anhydrous binding pocket of the AKT2 and PD-L1 targets.

Table 3. Libdock-based docking conditions for **MM134**, **-6**, **-7**, and **-9** compounds with cancer targets and their corresponding binding energies.

Drug Target (PDB Code)	Docking Conditions		Binding Energy (BE) [b] of Inhibitors			
	Explicit Water [a]	Scoring Function	MM134	MM136	MM137	MM139
AKT2 (3D0E)	Absent	Ligscore1	−70.158	−96.359	−52.722	−15.722
BTK (3GEN)	Present	Ligscore2	−7.85	−15.726	−32.198	−48.185
CHK1 (2YM8)	Present	Ligscore2	−31.609	−10.281	−22.055	−9.749
PD-L1 (7BEA)	Absent	Ligscore2	−60.955	−8.811	−24.089	−4.587

[a]: Crystallographic explicit water of hydration. [b]: Unit of binding energy kcal/mol.

The **MM134**, **MM136**, **MM137**, and **MM139** compounds exhibited better binding energy (BE) scores with AKT2 and BTK targets. The sulfonamide derivatives **MM134**, **MM136**, and **MM137** exhibited higher binding energy scores when docked into the anhydrous binding pocket of AKT2, with binding energy scores of −70.158, −96.359, and −52.722, respectively. In contrast, **MM139** showed high-affinity to the hydrous binding site of BTK, with a BE score of −48.185. These results are consistent with our previous studies on these triazine sulfonamide analogs [8,11], which suggested that the compounds' apoptotic potential may arise from their ability to inhibit the activity of AKT2, BTK [11], CHK1 [8], and PD-L1 [11] (Table 4). Figure 9 displays the 2D/3D interaction plots of AKT2's active binding pockets (PDB:3D0E) with the **MM134**, **-6**, and **-7** compounds.

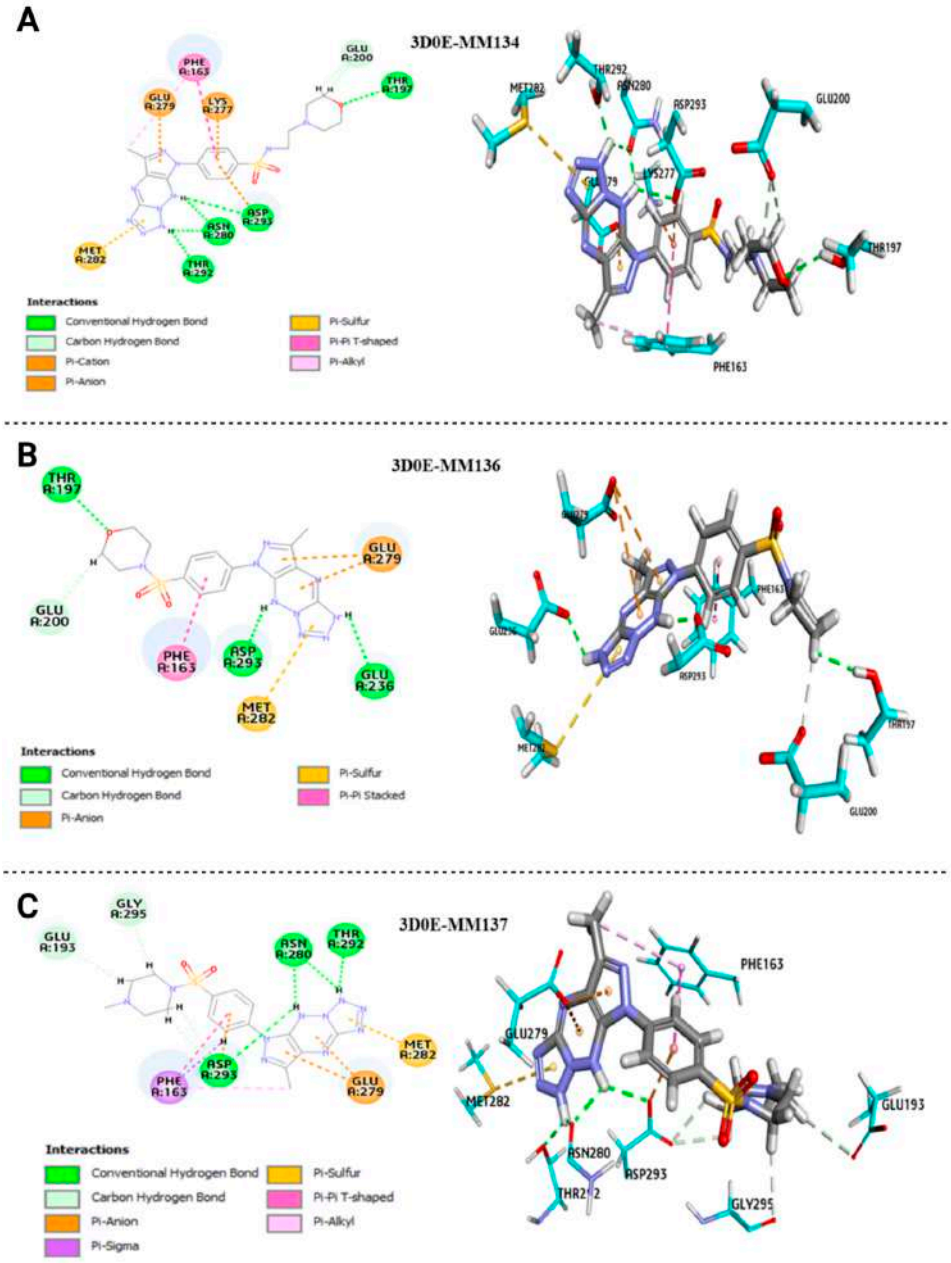

Figure 9. Binding interactions of **MM134** (**A**), **MM136** (**B**), and **MM137** (**C**) compounds with the crystal structure of AKT2 (3D0E). The 2D/3D interaction plots are represented on the left and right, respectively. The legends for the type of interactions are provided in respective 2D plots.

These plots revealed a shared agreement among the **MM134**, **MM136**, and **MM137** compounds, which were docked accurately, in placing the NH atoms of triazine and tetrazole groups close to the carbonyl groups of Asn280, Asp293, and Thr292 amino acids of AKT2 through the formation of hydrogen bond interactions in these positions. The **MM136** compound exhibited a similar interaction pattern, but only with the carbonyl groups of the Asp293 and Glu236 amino acids.

The oxygen atom of the morphine fragment of the **MM134** and **MM136** ligands forms conventional hydrogen bond interactions with the carbonyl groups of the Thr197 amino acid in the protein structure. **MM134** and **MM136** showed a similar binding pattern, where H atoms of the morpholine formed hydrogen bond interaction with Glu200:O amino acids of the protein. Similarly, the **MM137** compound exhibited the same interaction, but with the Gly295:O and Glu193:O amino acids.

When docked, the **MM134**, **MM136**, and **MM137** compounds shared the same binding feature, where tetrazole rings interacted with the Met282:S amino acid. This dictated a π–sulfur interaction at this position. The benzene of the phenylsulfonyl group in the **MM134**, **MM136**, and **MM137** compounds established a π–π interaction with the hydrophobic side chain of Phe163. Furthermore, the latter formed a π–alkyl interaction with the alkyl functional group of pyrazole in the **MM134** and **MM137** compounds. The residue Glu279:O formed a π–anion interaction with the tetrazole and triazine groups of the **MM136** and **MM137** compounds, as well as with the pyrazole fragment of the **MM134** compound.

The binding mode of triazine sulfonamide derivatives (**MM134**, **MM136**, and **MM137** compounds) involved the same residues in AKT2, namely Asn280, Asp293, Thr292, Thr197, Met282, Phe163, Glu279, Glu36, Glu200, Gly295:O, and Glu193. There is evidence in the literature to suggest that the activity of AKT2 may indeed depend on the presence of these residues [38,39]. The binding mode of the **MM134** and **MM137** compounds in AKT2 offers valuable insights into the binding and inhibition of AKT2 by these compounds. Nevertheless, the **MM139** compound exhibited a different binding mode with AKT2 compared with the other **MM**-compounds, with different amino acids interacting than those for the **MM134**, **MM136**, and **MM137** compounds. This disparity in binding mode could potentially explain why the **MM139** ligand has a lower binding energy with the AKT2 but has a higher binding affinity with the BTK.

The 2D/3D interaction plots of the **MM139** compounds with a hydrous binding pocket of BTK (3GEN) are displayed in Figure 10.

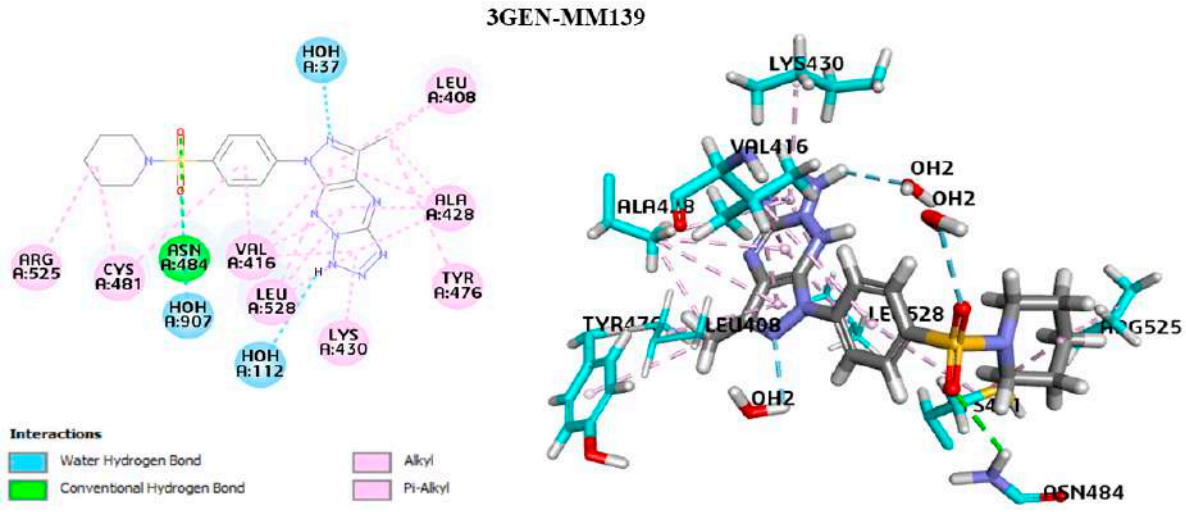

Figure 10. Binding interactions of the **MM139** compound with a hydrous binding pocket of BTK (3GEN). The 2D/3D interaction plots are represented on the left and right, respectively. The legends for the type of interactions are provided in respective 2D plots.

It was found that the entire structure of **MM139** was favorably located in the BTK pocket. The carbonyl of the **MM139** compound's sulfone fragment formed a conventional hydrogen bond with the Asn484:HD22 amino acid. Furthermore, the π–alkyl interaction is established with Leu408, Tyr476, Ala428, Leu528, Cys481, Lys430, and Val416 of BTK and triazine, tetrazole, and pyrazole fragments. These amino acids constitute a well-established active binding pocket for BTK kinase [40]. SKS151, a known BTK inhibitor, was previously found to engage in hydrophobic interactions with Leu408, Val416, and Leu528 [23]. Furthermore, the alkyl's pyrazole and pyridine fragments generated alkyl interactions with Ala428, Cys481, Arg525, and Leu408. The **MM139** compound formed hydrogen bonds with water molecules, HOH37:H1, HOH907:H2, and HOH112:OH2. The presence of water molecules is crucial in accurately predicting ligand-protein docking. This is because water molecules can act as a bridge, linking the protein and the ligand to stabilize the complex. It is essential to explicitly include water molecules in the binding process, as demonstrated by the 3GEN–**MM139** complex, which required the presence of binding site hydration molecules to make reasonably accurate predictions. The higher BTK inhibition of compound 14G in the study of Zhao et al. resulted from the formed hydrogen bond interaction with the water molecule, which was similar to the co-crystallized molecule B43 of the BTK (PDB code 3GEN) target [41]. Thus, it is important to consider the role of water molecules in ensuring the accuracy of ligand–protein docking predictions [28,29]. We have focused on the AKT2 enzyme in further research, given its involvement in the pathophysiology of solid tumors, in contrast to the BTK enzyme, which is involved mainly in the development of B-cell malignancies [42].

2.2.3. Prime MM-GBSA Calculations

The binding efficacies of ligands docked into the binding site of AKT2 protein were rescored using prime MM-GBSA. The calculated free energy of binding and free energy components for the protein–ligand complexes are shown in Table 4. The results show that the four complexes showed a binding energy value within the range of −46.50 kcal/mol to −25.15 kcal/mol. The non-polar solvation (ΔG_{solv}), polar solvation ($\Delta G_{solvlipo}$), van der Waals, and coulomb energy were the driving forces for the ligand binding into the protein active site. The compound **MM139** disfavored the covalent binding, as evident from its low covalent binding value compared with the other complexes.

Table 4. Binding free energy calculation for the protein–ligand complexes.

Compound	$\Delta G_{coulomb}$ [a]	ΔG_{vdw} [b]	$\Delta G_{covalent}$ [c]	ΔG_{solv} [d]	$\Delta G_{solvlipo}$ [e]	ΔG_{bind} [f]
MM134	91.46	−46.61	4.15	−76.13	−19.14	−46.50
MM136	159.19	−40.97	6.37	−150.91	−16.10	−45.90
MM137	119.93	−44.90	7.51	−91.23	−16.14	−25.15
MM139	153.58	−42.90	1.23	−134.11	−18.26	−41.19

[a] Contribution to the MM-GBSA free energy of binding from the coulomb energy. [b] Contribution to the MM-GBSA free energy of binding from the van der Waals energy. [c] Contribution to the MM-GBSA free energy of binding from the covalent binding. [d] Contribution to the MM-GBSA free energy of binding from the nonpolar contribution to the solvation energy due to the surface area. [e] Contribution to the MM-GBSA free energy of binding lipophilic binding. [f] Free energy of binding.

2.2.4. Molecular Dynamics of MM-Compounds–AKT2 Complexes

Molecular dynamics simulations are very useful in the drug research process to predict the stability of protein–ligand complexes in the in silico physiological environment [43]. In this study, the stability of **MM134**, **MM136**, **MM137**, and **MM139** with AKT2 (PDB ID: 3D0E) and its native co-crystalized ligand G39 were investigated using an MD simulation [44]. An MD simulation of 200 ns duration was performed. Trajectory root mean square deviation (RMSD) and root mean square fluctuation (RMSF) analyses were performed. RMSD is the basic parameter that numerically expresses the shifts of protein and ligand atoms [45]. As presented in Figure 11A, complexes of **MM134** and **MM136** with AKT2 remained stable after the first 5 ns at 0.6 nm and 1 nm, respectively. The complex of **MM137**

with AKT2 started at 0.2 nm and increased to 0.5 nm in the first 10 ns, then it remained stable for a certain period. It increased to 1 nm after 40 ns and stabilized at 1 nm. The complex of **MM139** with AKT2 remained stable close to 0.5 nm for the first 15 ns, then increased to 1 nm and stabilized.

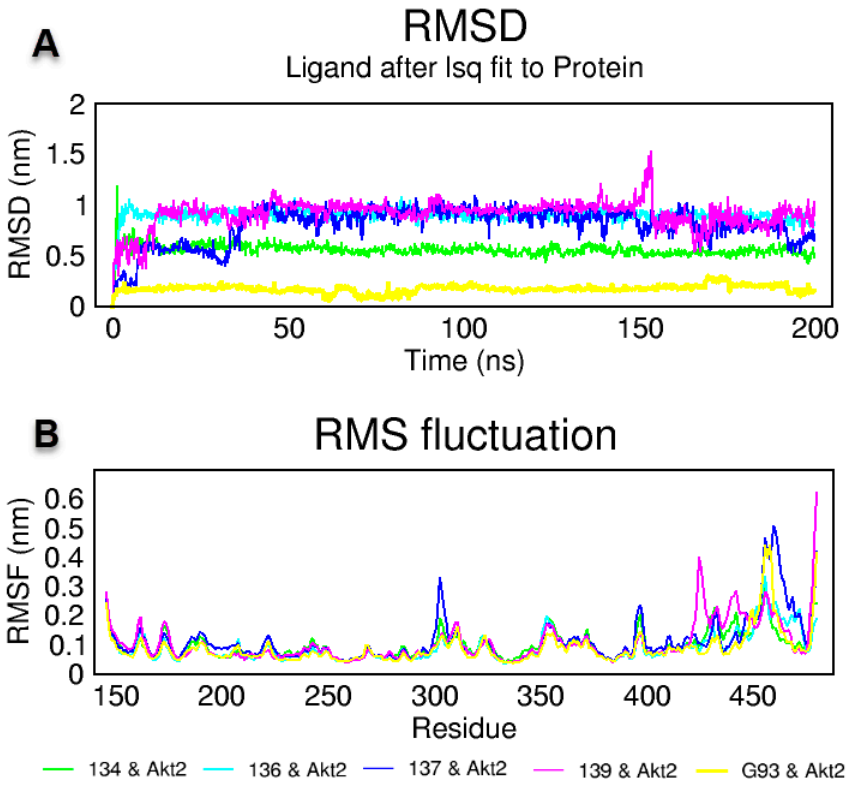

Figure 11. Trajectory analysis of complexes of the compounds **MM134**, **MM136**, **MM137**, **MM139**, and cocrystal ligand G39 with AKT2. Root mean square deviation (RMSD) (**A**) and root mean square fluctuation (RMSF) (**B**) of **MM134**–AKT2, **MM136**–AKT2, **MM137**–AKT2, **MM139**–AKT2, and G39–AKT2 protein–ligand complexes for 200 ns.

RMSF measurements were performed to show the fluctuation and mobility per residue in the protein structure [46]. As provided in Figure 11B, complexes of **MM139** and co-crystalized G39 with AKT2 produced high fluctuations. All AKT2 complexes showed a similar fluctuation trend around active site amino acids 150–300, starting at 0.3 nm and decreasing to 0.1 nm. Finally, animation videos from 285 frames recorded during 200 ns at the AKT2 active site of the compounds were created, as given in the Supplementary Materials for visual inspection. An MD simulation animation of 285 snapshots between 0 and 200 ns was generated.

In addition, AKT2–**MM134**, **-6**, **-7**, **-9**, and G39 protein–ligand interactions at 0 and 200 ns are provided in Figures S4–S6 of Supplementary Materials.

As shown in Figure S4A,B, the van der Waals interaction of the AKT2–**MM134** complex with Gly295, Leu183, Glu193, Gly159, Thr162, and Leu296 was preserved, but the interaction with Lys181 had transformed to a hydrophobic interaction from van der Waals interactions in the 0 and 200 ns MD simulation. Despite this, the complex remained stable. As shown in Figure 11A, in the AKT2–**MM134** complex, the RMSD value was measured below 1 nm and did not increase during the 200 ns MD simulation of this compound. Second, as given in Figure S4C,D, the π–sulfur interaction with Met282 transformed to a π–alkyl interaction at the end of 200 ns in the AKT2–**MM136** complex, while the ligand remained stable. As shown in Figure 11A, in contrast, in the AKT2–**MM136** complex, the RMSD value of **MM136** was calculated to be below 1 nm. As given in Figure S5A,B, interactions with Met282 continued in the AKT–**MM137** complex, but it had transformed to a π–alkyl

interaction from the π–sulfur interactions. The AKT–**MM139** complex had preserved interaction between Lys160, Lys181, and Phe163, but all these interactions transformed at the end of the 200 ns simulation. Lys160 had shown hydrophobic interactions in 0 ns, and at the end of 200 ns, this interaction had transformed into van der Waals interactions. The interaction with Lys181 had transformed into a hydrophobic interaction from van der Waals interactions (Figure S5C,D). The RMSD value of AKT–**MM139** complexes produced high fluctuations between 0.5 nm to 1.5 nm (Figure 11A). Finally, protein–ligand interactions in the AKT–G39 complex were analyzed. As shown in Figure S6A,B, G39's donor–donor interaction with Ala232 and hydrophobic interaction with Glu230 and Ala232 remained stable. For G39, hydrophobic interactions with Val166, Phe294, Phe439, Ala179, and Lue158 were preserved (Figure S6A,B). As shown in Figure 11A, the RMSD value of G39 in the AKT2–G39 complex was calculated to be below 0.5 nm.

Another way to measure protein–ligand stability and potency is to measure the number of H bonds formed between the protein and ligand [47]. In this context, the number of H bonds formed by compounds **MM134**, **MM136**, **MM137**, **MM139,** or a co-crystallized ligand with AKT2 for 200 ns was calculated, as provided in Figure S7A–E of Supplementary Materials. Compound **MM134** usually formed two, sometimes three H bonds with the AKT2 enzyme, while **MM136** established two H bonds. In contrast, **MM137** formed three to four H bonds up to 150 ns, and one H bond after 150 ns. The G93 native (co-crystalized) ligand formed five to seven H bonds with the protein.

One of the most important methods of measuring protein compactness is to measure the Rg value [48]. The Rg value of protein–ligand complexes was calculated, as shown in Figure S7F–J. AKT2–**MM134**, **MM136**, **MM137**, and **MM139** complexes established an Rg value of approximately 2.15 nm, while the AKT2–G93 complex produced an Rg value of approxiamtely 2.1 nm.

The determination of binding energies is crucial for understanding the strength of molecular interactions in protein–ligand complexes [49]. In this study, we examined the binding energies of AKT2 complexes with **MM134**, **MM136**, **MM137**, and **MM139**, and compared them to the AKT2–G39 complex. The binding free energies were calculated using molecular mechanics models, and van der Waals, electrostatic, polar solvation, and SASA contributions were considered, as given in Table 5. Our analysis aimed to assess the relative strengths of binding within the AKT2 complexes and discern their disparities concerning the AKT2–G39 interaction.

Table 5. MM-PBSA calculations of binding free energy of **MM134**, **MM136**, **MM137**, **MM139** and cocrystal ligand G39 with AKT2.

Parameters (Energy)	AKT2–MM134 (kJ/mol)	AKT2–MM136 (kJ/mol)	AKT2–MM137 (kJ/mol)	AKT2–MM139 (kJ/mol)	AKT2–G39 (kJ/mol)
Van der Waals	226.8 ± 16.3	−198.8 ± 11.3	−145.9 ± 16.4	−105.2 ± 19.4	−221.7 ± 15.5
Electrostatic	−58.3 ± 15.5	−11.6 ± 10.8	−43.6 ± 19.1	−29.3 ± 17.1	−86.1 ± 16.2
Polar solvation	221.5 ± 38.2	96.9 ± 22.8	155.9 ± 33.2	70.7 ± 27.7	181.5 ± 32.0
SASA	−21.1 ± 1.1	−16.6 ± 0.9	−15.6 ± 1.6	−10.9 ± 2.3	−20.5 ± 1.1
Binding free	−84.7 ± 23.5	−130.1 ± 20.6	−49.2 ± 25.9	−74.7 ± 16.6	−146.9 ± 38.9

The comparison of binding energies among the AKT2 complexes revealed notable differences. Among the complexes studied, AKT2–**MM136** exhibited the most negative binding free energy, indicating a stronger binding affinity than the other complexes. Following this, AKT2–**MM137** and AKT2–**MM139** displayed the second and third-most negative binding energies, respectively. In contrast, AKT2–**MM134** had the least negative binding free energy, suggesting a weaker binding propensity compared to the other complexes.

Further comparison of the binding energies with the AKT2–G39 complex elucidated additional insights. AKT2–**MM136** exhibited a less negative binding free energy than the AKT2–G39 complex, signifying a relatively weaker binding interaction in comparison. Sim-

ilarly, AKT2–**MM134,** AKT2–**MM137**, and AKT2–**MM139** also demonstrated less negative binding energies than the AKT2–G39 complex.

The investigation of binding energies in AKT2 complexes with **MM134**, **MM136**, **MM137**, **MM139**, and the G39 complex provided valuable insights into their relative binding strengths. The analysis indicated that AKT2–**MM136** exhibited the strongest binding affinity among the complexes studied, while AKT2–**MM134** displayed the weakest binding propensity. Furthermore, a comparative assessment with the AKT2–G39 complex demonstrated that all the other complexes (**MM136**, **MM137**, and **MM139**) exhibited weaker binding energies. These findings contributed to a better understanding of the differential binding characteristics within the AKT2 complexes and their deviations from the reference interaction.

3. Discussion

Purines are the most common and versatile N-heterocyclic chemicals that can be found in nature. Purine is the ideal scaffold for the discovery of innovative therapeutic medicines that target selectively purine-dependent enzymes and receptors. Many drug development efforts have focused on structural alterations of natural purines, especially those involving isosteric ring structures. Seven bicyclic heterocyclic systems isosteric to purine have been produced by fusing the 1,3,5-triazine ring with pyrrole, pyrazole, imidazole, 1,2,3-triazole, or 1,2,4-triazole [50]. The scaffold 1,2,4-triazine is less-known. The 1,2,4-triazine molecule is one of the three potential isomers of the six-membered ring that contains three nitrogen atoms. The 1,2,4-triazine ring is thought to be essential for a variety of different pharmacological actions, including anticancer activity. Therefore, numerous heterocyclic components were fused with this scaffold to enhance the antitumor activity. Pyrrolo[2,1-*c*][1,2,4]triazine and pyrrolo[2,1-*f*][1,2,4]triazine constitute the best examples of triazine compounds with antitumor activities [5,51]. In contrast to pyrrolotriazines, the pyrazolo[4,3-*e*][1,2,4]triazine ring system has been less studied. Because early studies on the group of simple substituted pyrazolotriazine derivatives did not show their considerable anticancer activities, it was decided to combine it with different pharmacophore groups, including sulfonamide moieties. Representatives of this class of compounds exhibited antitumor activity through inhibition of ABL kinase [52], carbonic anhydrases (CAs) [53,54], and CDKs, as previously reviewed [6]. Pyrazolo[4,3-*e*][1,2,4]triazines condensed with 1,2,4-triazole or a tetrazole ring constitute a particularly interesting group of compounds with anticancer activities in the nano and micromolar range [6].

More recently, a novel compound known as **MM129** (pyrazolo[4,3-*e*]tetrazolo[1,5-*b*][1,2,4]triazine sulfonamide) was shown to effectively limit cell viability by inhibiting the BTK protein [10]. BTK is a nonreceptor tyrosine kinase involved in B-lymphocyte development, differentiation, and signaling. The activation of B-cell antigen receptor signaling in secondary lymphatic organs triggers the excessive proliferation of malignant B cells. Over the past decade, BTK inhibitors have become an increasingly popular alternative to chemotherapy-based regimens, particularly in patients who suffer from chronic lymphocytic leukemia (CLL) and mantle cell lymphoma (MCL) [55,56]. **MM129** also exhibited anticancer potential in vivo in colon cancer xenograft mice. This effect might be attributed to the decrease in the expression of AKT, CDK2, mTOR, and PD-L1 [12]. The experimental results obtained for **MM129** are in line with the results of molecular docking and molecular dynamics simulation, where **MM129** and pyrazolo[4,3-*e*]tetrazolo[1,5-*b*][1,2,4]triazine sulfonamide derivatives (**MM131**, **-4**, **-6**, **-7** and **-9**) exhibited inhibitory effect on multiple CDKs, AKT, BTK, mTOR, and PD-L1 [11].

It was shown that **MM131** triggered apoptosis of DLD-1 and HT-29 cells with observed down-regulation of mTOR kinase, soluble intercellular adhesion molecule-1 (sICAM-1), or cathepsin [57]. **MM129** and **MM131**, together with the third sulfonamide derivative of pyrazolo[4,3-*e*]tetrazolo[1,5-*b*][1,2,4]triazine (**MM130**), exhibited cytotoxic and genotoxic activity, as established using an alkaline/neutral comet assay and γ-H2AX staining in four cancer cell lines: HeLa, HCT-116, PC-3, and BxPC-3. **MM129**, **MM130,** and **MM131**

showed cytotoxic activity with IC_{50} concentrations of IC_{50} = 0.17–1.15 μM, as indicated by an MTT assay following 72-h incubation of the four above-mentioned cancer cell lines with the compounds [7].

The compounds investigated in this study (**MM134**, **-6**, **-7**, and **-9**) exhibited micromolar (IC_{50} range: 0.11–0.33 μM) cytotoxic activity in BxPC-3 and PC-3 cancer cells in the same assay, while showing minor cytotoxic activity in human normal lung fibroblasts (WI-38) (where IC_{50} values varied between 0.27–0.65 μM). The genotoxic activity of the compounds in the comet assay and γH2AX staining was also described. Furthermore, it was indicated that the DNA-damaging capability of the compounds may be attributed to the inhibition of CHK1 kinase, as indicated by in silico results [8,11]. Furthermore, these compounds exhibited profound pro-apoptotic activity in the BxPC-3 cell line following 24 and 48 h incubation of cells in vitro, where 2xIC_{50} concentrations of all **MM**-compounds induced apoptosis of 68.1 ± 7.33% to 95.1 ± 1.48% of the cells [11]. In contrast, Gornowicz et al. investigated the effect of 24-h incubation of **MM137** in DLD-1 and HT-29 cells. **MM137** exhibited cytotoxic activity, with IC_{50} values of 0.43 μM in DLD-1 cells and 0.16 μM in HT-29 cells [9]. Similar to the results obtained by our group [11], the authors indicated cancer-cell-specific cytotoxic activity of the compound. The cell viability of fibroblasts was reduced by 13.72% following 24-h incubation with **MM137** at a concentration of 0.5 μM [9]. **MM137** used in the same concentration induced apoptosis of colorectal cancer cells. The number of apoptotic cells was indicated as 68.6% for DLD-1 and 38.1% for HT-29 cells using the FITC-Annexin-V binding assay. The authors also detected a decrease in mitochondrial membrane potential (MMP) following treatment with the **MM137** compound, indicating apoptosis induction [57]. We also found changes in MMP following 24 and 48-h treatment of BxPC-3 and PC-3 cells with the **MM134**, **-6**, **-7**, and **-9** compounds [11]. The cytotoxicity of the pyrazolo[4,3-*e*]tetrazolo[1,5-*b*][1,2,4]triazine sulfonamide compounds (Table S3) is supported by literature data, and the possible molecular mechanism of **MM**-compounds activity, as indicated by the literature, is presented in Figure S8 of the Supplementary Materials.

In this study, we confirmed the cytotoxic activity of **MM**-compounds using a neutral red uptake assay. The investigated compounds exhibited cytotoxic activity in BxPC-3 (IC_{50} range: 0.18–0.35 μM) and PC-3 (IC_{50} range: 0.06–0.17 μM) cancer cell lines following a 24-h incubation time. The PC-3 cell line was more prone to the cytotoxic activity of the compounds. Consistent with previous results [11], **MM137** sulfonamide exhibited the highest cytotoxic potential in both cell lines, with IC_{50} values of 0.18 and 0.06 μM for the BxPC-3 and PC-3 cell lines, respectively. Furthermore, to confirm apoptosis induction following treatment with the **MM**-compounds, we evaluated the caspase activity in BxPC-3 and PC-3 cells. In the BxPC-3 cells (Figure 2), the **MM134** and **MM136** compounds in IC_{50} and 2xIC_{50} concentrations induced an increase in caspase 3/7 activity compared with the negative control. The **MM139** compound induced a statistically significant increase in caspase 3/7 activity across all tested concentrations (0.5xIC_{50}, IC_{50}, and 2xIC_{50}) compared to the negative control. In contrast, the **MM137** compound induced a statistically significant increase in caspase 3/7 activity only in the 2xIC_{50} concentration compared to the negative control. Induction of caspases activity was also previously observed following 24-h treatment of DLD-1 and HT-29 cells to **MM131** [57] and **MM137** [**9**].

No increase in caspase 3/7 activity was observed for PC-3 cells (Figure 2B). This was consistent with the lower pro-apoptotic activity of the compounds in PC-3 cells following 24-h treatment with the tested compounds that were obtained in our previous studies [11]. Surprisingly, we did not observe caspase-8/9 induction in BxPC-3 cells treated with the **MM134**, **-6**, **-7**, and **-9** compounds (Figure 2C,D). This could be attributed to the decrease in the proliferation of cells in the caspase activity assay, which could affect the levels of caspases in each well. Based on the decrease in caspase 3/7 activity in PC-3 cells, we chose this cell line for further investigation. Using a BrdU incorporation assay, we evaluated the effect of **MM**-compounds on cell proliferation. We found cytostatic activity of the investigated compounds, which was especially profound for the **MM139** compound used at the

2xIC_{50} concentration (% of proliferating cells = 46.8 ± 0.78%). These results are consistent with the lowest activity of caspase enzymes observed following the treatment of BxPC-3 and PC-3 cells with this compound. **MM**-compounds also dramatically decreased the clonogenic potential of both BxPC-3 and PC-3 cells, further explaining the obtained results and suggesting that the compounds exhibited more cytostatic than cytotoxic activities.

Following 1 h incubation of BxPC-3 cells and PC-3 cells, an increase in the overall ROS production was observed (Figure 1). The dose-dependent decrease of the fluorescence found in cells incubated with tested compounds could be attributed to the same reason that was indicated for the caspase assays. However, an increase in ROS production in the DCFH-DA assay confirmed the oxidative stress generated by compounds in the studied cell lines. In contrast, no changes in the cell cycle distribution were found after the treatment of BxPC-3 and PC-3 cells with compounds used in 0.5xIC_{50} and IC_{50} concentrations (Figure 5).

Despite the negative results obtained during the 24-h cell cycle analysis, apoptosis induction in cells following treatment with **MM**-compounds was not excluded. The presence of a hypodiploid DNA peak is not proof of apoptotic cell death. The exposed cell can be negative for the sub-G1 peak, as DNA fragments are still retained in the nucleus [15]. Moreover, the presence of DNA strand breaks following incubation with **MM**-compounds was confirmed through the alkaline/neutral comet assay and γ-H2AX staining [7,8]. To further explore apoptosis induction, we performed a DNA fragmentation assay. No DNA laddering was observed following the treatment of cells with IC_{50} concentrations of the **MM134**, **-6**, **-7**, and **-9** compounds. These findings, together with the absence of observed caspase activation (besides caspase-3/7 induction) and the exposure of PS on the cell surface, imply the induction of necroptosis in cells, and not apoptosis. However, observation of apoptotic bodies, especially following prolonged (48-h) incubation of cells with compounds, could also indicate the activation of late stages of apoptosis [9,11,57]. The activation of caspases 3/7 following cancer cell treatment was observed not only in BxPC-3 cells treated with **MM134**, **-6**, **-7**, and **-9** compounds, but also other derivatives investigated by other authors, confirming the pro-apoptotic potential of the pyrazolo[4,3-*e*]tetrazolo[1,5-*b*][1,2,4]triazine sulfonamides. A summary of cellular response to MM-compounds is presented in Figure S9 of Supplementary Materials.

The upregulation of five genes was shown in the gene expression analysis of BxPC-3 cells treated with the **MM134** compound. These included B-cell CLL/lymphoma 10 (BCL10), growth arrest and DNA-damage-inducible, alpha (GADD45A), receptor-interacting serine-threonine kinase 2 (RIPK2), tumor necrosis factor (TNF), tumor necrosis factor receptor superfamily, member 10b (TNFRSF10B) and tumor necrosis factor receptor superfamily, and member 1A (TNFRSF1A; TNF-R1) (Table 1).

BCL10 is a protein from the caspase recruitment domain (CARD) family that regulates apoptosis and the nuclear factor NF-kappa-B (NF-κB) signaling pathway [58]. Overexpression of BCL10 in cell cultures has been shown to promote apoptosis [59]. The CARD domain present at BCL10 amino-terminal domain is thought to mediate the binding of adapter molecules and caspases. These CARD-containing proteins interact with one another in response to a range of stressors, including DNA-damaging agents and cell-death ligands like FAS and TNF. The resulting binding activates downstream signaling, triggering apoptosis [59]. However, BCL10 also participates in the formation of complexes that inhibit apoptosis and is important for cell survival following DNA damage. Cytoplasmic BCL10 translocates to the nucleus to facilitate DNA damage repair, including histone ubiquitination and the accumulation of homologous recombination (HR) repair components [60].

TNFRSF10B (also known as death receptor 5 (DR5)) belongs to the TNF-receptor superfamily and has an intracellular death domain. When stimulated by tumor necrosis factor-related apoptosis-inducing ligand (TNFSF10/TRAIL/APO-2L), this receptor transmits an apoptotic signal through the formation of DISC with FADD and pro-caspase-8 and the activation of a caspase cascade [61]. TRAIL binding with DR5 can also trigger multiple other signaling pathways, including stress kinase activation, conventional NF-κB signaling, and necroptosis [62,63].

TNF-receptor I (TNF-R1)-induced apoptosis is also assumed to occur via recruitment of the adaptor FADD and caspase-8 to the receptor complex. While the apoptotic function of TNF-R1 signaling is well-known, it can also increase survival by activating NF-κB. The process by which this choice between cell death and survival is made is ambiguous. TNFR1-induced apoptosis might be caused by two distinct signaling complexes. The first plasma membrane-bound complex (complex I) is made up of TNF-R1, the adaptor protein tumor necrosis factor receptor type 1-associated DEATH domain (TRADD), receptor-interacting serine/threonine kinase 1 (RIPK1), and TNF receptor-associated factor (TRAF2), and activates NF-κB with a pro-survival function. TRADD and RIPK1 then link with caspase-8 to form a cytoplasmic complex (complex II) which contributes to apoptosis. Activation of caspase-8 directs the pathway toward apoptosis, while its suppression leads to necroptosis [64]. Receptor-interacting serine/threonine kinase 1 and 3 (RIPK1 and RIPK3) interact with each other during necroptosis, leading to the development of a functional heterodimer complex that promotes mixed lineage kinase domain-like pseudokinase (MLKL) oligomerization by phosphorylating it. The oligomeric variant of MLKL migrates from the cytosol to the plasma membrane, resulting in the emergence of the pore and inflammatory response [65,66]. During necroptosis, no DNA laddering, caspase activity increases, or pro-apoptotic gene expression occurs. In contrast, similar to apoptotic cells, necroptotic cells may exhibit PS on the outer membrane. Furthermore, as discussed earlier, TNF is the most well-known cytokine triggering the necroptosis pathway [67–69]. The above-mentioned findings suggest that the cell death observed following treatment with **MM**-compounds may be a combination of both apoptosis and necroptosis, depending on the cell type, incubation time, and compound concentration (Figure 12).

However, the strongest up-regulation of gene expression was observed for GADD45α. GADD45 protein family members undergo rapid activation after DNA damage, leading to cell cycle arrest, DNA repair, and/or cell death. The elevation of GADD45 expression is required for numerous chemotherapeutic agents to mediate their anti-cancer activities, and the absence of GADD45 may negate their effects in cancer cells [70]. GADD45 functions as an upstream effector in the stabilization of cellular tumor antigen p53 (TP53) after DNA damage occurs in cells [71]. The specific DNA-damaging agent appears to be required for GADD45α induction via TP53. In myeloid leukemia cell lines harboring TP53 heterozygous allele, IR can no longer stimulate GADD45α expression, whereas MMS, UV radiation, and serum depletion can still promote GADD45α transcription in breast and colon cancer cell lines with a negative TP53 status [72,73]. Overexpression of GADD45α decreases cell proliferation in a variety of cell types without inducing apoptosis, as evidenced in our investigations [74,75]. This appears to be attributed to the ability of GADD45α to disrupt the interaction between the CDK1/cyclin B1 complex and inhibit its kinase activity, leading to G2/M cell cycle arrest [76,77]. However, through interactions with P21, it can also halt the cell cycle in the G1/S and G2/M phases [70] (Figure 13).

The cell cycle arrest observed by Hermanowicz et al. [12] was shown to be attributed to the upregulation of TP53 expression and downregulation of CDK2. However, we have observed its downregulation in BxPC-3 cells treated with the **MM134** compound. This may indicate a more complex response of cancer cells to **MM**-compounds that might be dependent on GADD45α. In the present work, we also performed extensive in silico studies. In the first stage, we determined the electronic properties of the chemical molecules using HOMO, LUMO, and MESP calculations and re-evaluated the **MM**-compound targets. We found that **MM134**, **-6**, and **-7** compounds form stable complexes with AKT2 kinase, as estimated by the molecular docking, molecular dynamics, and prime MM-GBSA calculations. These complexes and are thought to act through the inhibition of the aforementioned target, while the **MM139** compound could additionally work as a BTK inhibitor. Interestingly, AKT inhibition was found to upregulate the expression of GADD45α independently on TP53 in soft tissue sarcoma cells, indicating the potential mode of activity of the compounds [78] (Figure 13). Nevertheless, enzymatic studies on AKT inhibition should be performed to determine its contribution to the anticancer activity of pyrazole–triazine compounds.

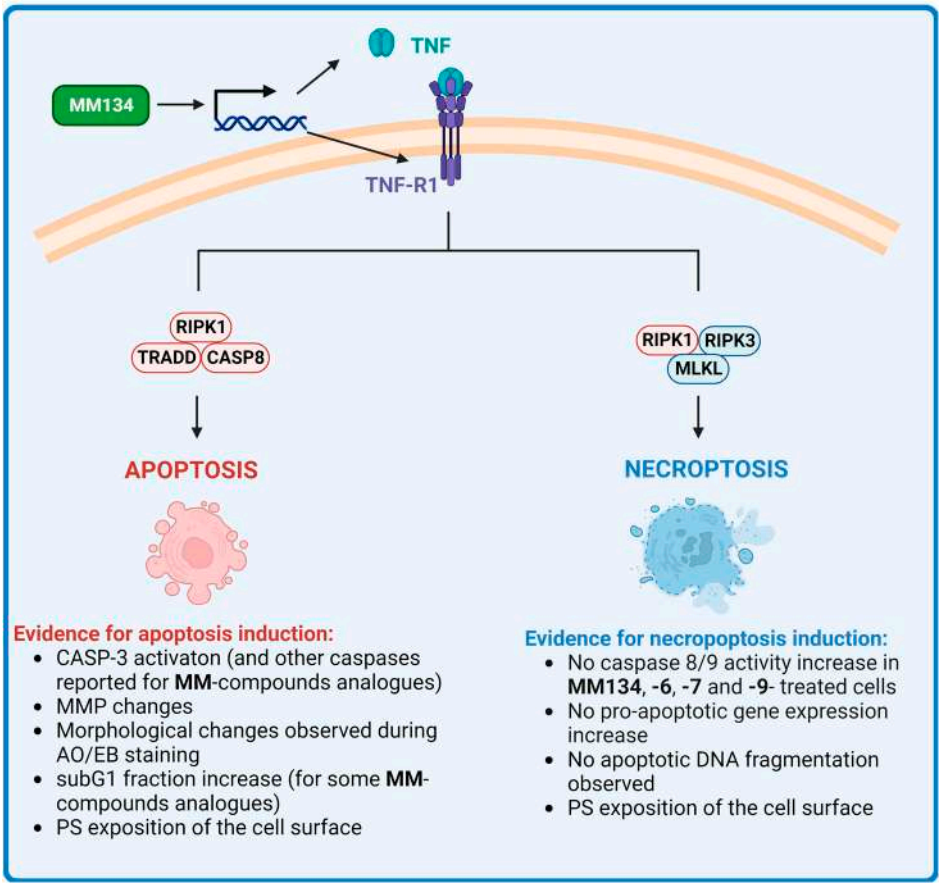

Figure 12. Cell death activated in response to **MM134** (and presumably other pyrazolo[4,3-*e*]tetrazolo[1,5-*b*][1,2,4]triazine sulfonamides (**MM**-compounds)). The treatment of cells with **MM134** induces up-regulation of tumor necrosis factor (TNF) and the tumor necrosis factor receptor superfamily, member 1A (TNFRSF1A; TNF-R1). This event contributes to apoptosis or necroptosis induction with distinct features. Abbreviations: RIPK1/2/3—receptor-interacting serine/threonine kinase 1/2/3; TRADD—tumor necrosis factor receptor type 1-associated DEATH domain; CASP8—caspase-8; MLKL—mixed lineage kinase domain-like pseudokinase.

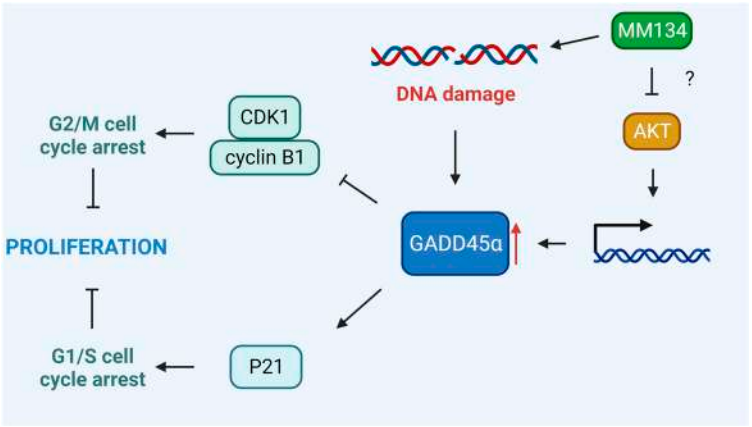

Figure 13. Upregulation of growth arrest and DNA-damage-inducible, alpha (GADD45A) in response to DNA damage induced by **MM**-compounds and inhibition of serine/threonine-protein kinase AKT (as indicated by in silico studies) leads to the activation of cyclin-dependent kinase inhibitor 1 (P21) and disruption of cyclin-dependent kinase 1-cyclin B1 (CDK1-cyclin B1) proteins, contributing to cell cycle proliferation inhibition through G1/S and G2/M phase cell-cycle arrest.

Furthermore, as indicated by the previous investigations, these agents may possess good pharmacokinetic properties and safety profiles, as indicated by the studies of the **MM129** compound. After intraperitoneal treatment, **MM129** exhibited excellent pharmacokinetic features, including fast absorption and a bioavailability of 68.6%. **MM129** also showed a good safety profile in mice, which is supported by the fact that no serious side effects have been reported after in vivo examination [21]. Initially, in silico ADME predictions of **MM134**, **-6**, **-7**, and **-9** suggested that these compounds may exhibit similar or superior properties and should be further investigated for these outcomes.

Altogether, findings of previous studies and the current investigation indicate pyrazolo[4,3-*e*]tetrazolo[1,5-*b*][1,2,4]triazine sulfonamides as an important scaffold for anticancer drug discovery. However, many toxicologic and pharmacodynamic endpoints need to be evaluated in the in vivo setting to confirm the results of these in silico and in vitro studies.

4. Materials and Methods

4.1. Chemicals

Trypsin-EDTA and all culture media (RPMI-1640, DMEM-F12) were purchased from Biowest (CytoGen, Zgierz, Poland). Phosphate-buffered saline (PBS), 5-Bromo-2′-Deoxyuridine (BrdU), crystal violet, 96% ethanol, fetal bovine serum (FBS), glacial acetic acid, hydrochloric acid (HCl), neutral red (3-amino-7-dimethylamino-2-methyl-phenazine hydrochloride), stabilized penicillin–streptomycin solution, Triton X-100, and Tween 20 were supplied by Merck/Sigma Aldrich Chemical Co. (Burlington, MA, USA). The following chemicals were used for the BrdU incorporation assay: bovine serum albumin (BSA) (Sigma Aldrich Chemical Co. (Burlington, MA, USA)), fluoromount G (Invitrogen, Oxford, UK), normal goat serum (Abcam, Cambridge, UK), paraformaldehyde (PHA) (Polysciences, Inc., Warrington, UK). The Alexa Fluor® 647 mouse anti-BrdU (BD Pharmingen™, San Diego, CA, USA) primary antibody and the Alexa Fluor 594/488 goat anti-mouse (LifeTechnology, Warsaw, Poland) secondary antibody were used. For the caspase activity assays, the Caspase-Glo® 3/7 Assay System (Promega Corporation™, Madison, WI, USA) and Cell Meter™ Caspase 8/9 Activity Apoptosis Assay Kits (BIOKOM, Janki, Poland) were used.

4.2. Cell Culture

The BxPC-3 (pancreas adenocarcinoma, ATCC® CRL-1687™) and PC-3 (prostate cancer, ATCC® CRL-1435™) cancer cell lines were obtained from the American Type Culture Collection (ATCC, Rockville, MD, USA). The BxPC-3 cells were grown in RPMI-1640 medium supplemented with 10% (*v*/*v*) fetal bovine serum (FBS) and 1% (*v*/*v*) of both antibiotics (streptomycin and penicillin). The PC-3 cells were grown in DMEM-F12 medium supplemented with 10% (*v*/*v*) fetal bovine serum (FBS) and 1% (*v*/*v*) of both antibiotics (streptomycin and penicillin). The MycoBlue™ Mycoplasma Detector kit (Vazyme Biotech Co., Ltd., Nanjing, China) was used at least every month for the control of mycoplasma contamination in the cell cultures.

The cells were grown at 37 °C in a humidified atmosphere of 5% CO_2 in the air. The culture medium was changed every 24–48 h. Subculture was performed using 0.25% trypsin/EDTA after the cells reached confluence.

4.3. Neutral Red Uptake Assay

The BxPC-3 and PC-3 cells were seeded on 96-well plates at a density of approximately 8–10 × 10^3 cells per 100 µL medium/well. The cells were allowed to grow for 24 h in controlled conditions (37 °C; 5% CO_2). Afterward, the cells were subjected to **MM134**, **-6**, **-7**, and **-9** compounds within the range 0.1–3 µM (final concentration of DMSO was <0.5% *v*/*v*) [79] in the culture medium for another 24 h. The experimental design included non-treated controls and blanks (wells without cells). Following 24-h of incubation, the medium containing the compounds was removed, and 100 µL of neutral red (40 µg/mL) in

fresh cell culture medium was added to each well of the plate. The cells were incubated in controlled conditions (37 °C, 5% CO_2) for two hours. The neutral red medium was removed, and the cells were washed with 150 µL of PBS. Afterward, 150 mL of the neutral red destain solution (50% ethanol 96%, 49% deionized water, 1% glacial acetic acid) was added to each well. The plates were shaken on a microtiter plate shaker for 15 min, and the dissolution of neutral red was monitored under a phase-contrast inverted microscope. An absorbance reading was performed at 540 nm using a microplate reader (Power Wave XS BioTek Instruments, Inc., Winooski, VT, USA). The detailed protocol of the neutral red assay was published by other authors [80]. GraphPad Prism 7 software was used to calculate the concentration of **MM**-compound reflecting a 50% inhibition of the uptake (IC_{50}). The IC_{50} value was defined as the concentration of the tested compound that led to a reduction of cell pool viability by 50% compared to the negative control (accepted as 100%):

$$\% \text{ cell viability} = \frac{(\text{Absorbance value of treated cells} - \text{Absorbance value of blank})}{(\text{Absorbance value of untreated cells} - \text{Absorbance value of blank})} \times 100\%$$

4.4. Oxidative Stress

BxPC-3 and PC-3 cells were seeded on 96-well black clear bottom microplates at density 12 × 10^5/mL and cultured in optimal culture conditions (37 °C; 5% CO_2) for approximately 48 h until they reached the exponential growth phase. Afterward, the culture medium was removed, and the cells were washed three times with 100 µL of PBS. A total of 20 µM of DCFH-DA solution (in PBS) was then added to the cells for 20 min. Afterward, the fluorescent probe was removed, and the cells were washed with PBS and incubated with **MM**-compounds (**MM134**, **-6**, **-7**, and **-9**) in 0.5xIC_{50}, IC_{50}, and 2xIC_{50} concentrations or H_2O_2 at a concentration of 500 µM (positive control). Negative control samples were prepared by incubating the cells in PBS. After the cells were incubated for 1 h at 37 °C in the dark, the ROS induction was assessed. The fluorescence was measured on a SpectraMax i3 Molecular Devices microplate reader using excitation/emission wavelengths of 485 nm and 535 nm.

4.5. Caspase 3/7 Detection

A Promega Caspase-Glo® 3/7 Assay System was used for the detection of caspase activity. BxPC-3 and PC-3 cells were seeded at densities of 2 × 10^4 and 1.5 × 10^4 per 100 µL well of 96-well white-walled multiwall plates, respectively. After 24 h, the medium was removed, and 100 µL of fresh medium containing **MM**-compounds was added at concentrations of 0.5xIC_{50}, IC_{50}, and 2xIC_{50} (that were previously estimated in the neutral red uptake assay). Additionally, a positive control (2 µM SN-38) was included in the assay. After 24 h, 100 µL of Caspase-Glo® 3/7 Reagent was added to each well containing 100 µL of blank, negative control cells or cells treated with **MM**-compounds in the culture medium. The plates were placed on a plate shaker and the well contents were mixed (300–500 rpm for 30 s). The plates were incubated at RT for 2 h. Luminescence was recorded using the SpectraMax® i3x Multi-Mode detection platform.

4.6. Caspase 8/9 Detection

Cell Meter™ Caspase 8/9 Activity Apoptosis Assay Kits were used for the detection of caspase 8/9 activity in BxPC-3 cells. The cells were seeded at a density of 2 × 10^4 per 100 µL well of 96-well clear bottom black welled plates. After 24 h, the medium was removed, and 50 µL of fresh medium containing **MM**-compounds at concentrations of 0.5xIC_{50}, IC_{50}, and 2xIC_{50} (previously obtained in the neural red uptake assay) was added. Additionally, a positive control (2 µM SN-38) was included in the assay. Following 24 h, 50 µL of caspase 8 or 9 substrate working solution was added to each well containing 50 µL of blank, negative control cells or cells treated with **MM**-compounds in the culture medium. The plates were placed on a plate shaker and the well contents were mixed (300–500 rpm for 30 s). The plates were incubated at RT for 1 h. The fluorescence was recorded at

Ex/Em = 490/525 nm (Cutoff = 515 nm) using the SpectraMax® i3x Multi-Mode detection platform.

4.7. Bromodeoxyuridine (BrdU) Incorporation Assay

PC-3 cells were seeded on coverslips placed on the bottom of 12-well plates at a density of 3×10^4 per 1 mL/well. After 24 h, the medium was removed, and fresh medium (1 mL) containing **MM134**, **-6**, **-7**, and **-9** at concentrations of 0.5xIC_{50}, IC_{50}, and 2xIC_{50} or 10 μM of cisplatin (used as positive control), was added to each well. After 24 h, the medium with compounds was removed and BrdU was added (final concentration 10 μM/mL). After 24 more hours, the medium was removed, and the cells were washed with 1 mL of PBS. The cells were fixed in 70% cold ethanol and kept at RT for 20 min. Subsequently, the cells were washed twice with PBS (5 min, RT) and once with PBS + 0.5% triton × 100. The cells were incubated with 0.5 mL of PBS and 0.5 mL of 4HCl (30 min, RT). The cells were washed twice with PBS and incubated in 1 mL sodium borate 0.1 M (1 min, RT). The cells were again washed with PBS and incubated with primary anti-BrdU antibody 10 μL/mL in PBS + 1%BSA + 0.5% tween (1 h, RT, dark). The cells were washed with PBS + 0.5% tween twice (2 × 5 min). Thereafter, the cells were incubated with secondary antibody in PBS + 1% BSA + 0.5% tween (1 h). The cells were washed twice with PBS + 0.5% tween (2 × 5 min) and incubated with 4′,6-diamidino-2-phenylindole (DAPI) 1 μg/mL for 15 min, then washed once with PBS (RT, 5 min). The coverslips were mounted using fluoromount G.

The experiment was performed in duplicate, and a total of at least 500 cells per experiment were counted using a fluorescence microscope at 360 nm using CellSens V2.3 (Olympus, Tokyo, Japan) software. The data were presented as % of proliferating cells. The differences between the experimental samples and untreated control or positive control were evaluated using an ANOVA followed by Tukey's test. A p-value less than 0.05 was considered statistically significant ($p < 0.05$).

4.8. Clonogenic Assay

BxPC-3 and PC-3 cells were seeded at densities of 100, 200, 500, 1000, and 2000 cells per 3 mL in 6-well plates. The cell culture medium was changed every three days. The colonies were counted ten days after plating the cells to establish plating efficiencies (%).

$$\mathrm{PE} = \frac{(\text{Number of counted colonies})}{(\text{Number of plated cells})} \times 100\%$$

The cells were seeded at appropriate densities according to the highest plating efficiencies (500 cells/well for BxPC-3 and cells/well for PC-3 cells). The cells were allowed to attach for 2–3 h and were exposed to 0.25xIC_{50}, 0.5x IC_{50}, and IC_{50} concentrations of **MM**-compounds for 10 days. The medium containing compounds was changed every 2–3 days. After 10 days, the medium containing compounds was removed, and the cells were gently washed with 2 mL of PBS and fixed with 4% formaldehyde for 20 min at RT. The cells were rinsed with PBS, and 0.5% crystal violet in PBS was added for 30 min. The plates were washed by submerging the plates in tap water and air-dried at RT. The colonies were counted using ImageJ V1.53q software. Each treatment was performed in duplicate. The data were analyzed using GraphPad Prism 7.0 software (GraphPad Prism Software Inc., San Diego, CA, USA).

4.9. Cell Cycle Analysis

BxPC-3 and PC-3 cells were seeded at a density of 7×10^5 with a 24 h incubation on a 6-well plate in 2 mL of medium. After 24 h incubation in controlled conditions (37 °C; 5% CO_2), the cells were subjected to **MM134**, **-6**, **-7**, and **-9** compounds in IC_{50} or 0.5 μM concentrations. The experimental design included a vehicle control (final solvent concentration was <0.5% *v/v* DMSO). The cells were incubated for another 24 h (37 °C; 5% CO_2). Upon exposure, the cells were trypsinized and transferred to cytometric tubes, left for 40 min, and centrifuged at 1400 rpm for 10 min at 4 °C. The supernatant was removed,

and the cell pellets were washed with PBS (1 mL). The cells were centrifuged one more time, the supernatant was removed, and cells were re-suspended in 200 µL of ice-cold PBS. The prepared suspensions were transferred to new cytometric tubes containing 1 mL of ice-cold 70% ethanol and mixed. The cells in ethanol were centrifuged (4500 rpm, 10 min, 4 °C), and the supernatant was removed. The cells were incubated with a staining solution (250 µL/tube) containing 5 µL of RNAase A (500 U/mL), 10 µL of PI (500 µg/mL), and 870 µL of PBS for 1 h in the dark at 37 °C and analyzed using flow cytometry.

4.10. Apoptotic DNA Fragmentation

BxPC-3 cells were seeded on 12-well plates at a density of 2×10^5. After 24 h, the cells were subjected to **MM134**, **MM136**, **MM137,** and **MM139** compounds in the IC_{50} concentration or 7-Ethyl-10-hydroxycamptothecin (2 µM) (Sigma Aldrich Chemical Co. (Burlington, MA, USA)) for another 24 h. An apoptotic DNA ladder kit (Alexis Biochemical, Lausen, Switzerland) was used to detect nucleosomal DNA fragmentation according to the manufacturer's instructions. The DNA fragments were visualized on a 1.2% agarose gel.

4.11. Gene Expression Analysis

4.11.1. RNA Extraction and cDNA Preparation

BxPC-3 cells were seeded on 25 cm^3 cell culture flasks Nunc™. After 24 h, the cells were subjected to **MM134** compound used in the IC_{50} concentration or treated with the same volume of DMSO (<0.5% v/v) for another 24 h. Afterward, an RNA extraction kit (Qiagen, Hilden, Germany) was used to obtain the total RNA. The amount of RNA was measured using a NanoDrop spectrophotometer 2000 (Thermo Scientific, Waltham, MA, USA), and the integrity of the RNA was confirmed using agarose gel electrophoresis. An RT2 HT first strand kit (Qiagen, Hilden, Germany) was used to reverse transcribe up to 1 µg of total RNA to cDNA according to the manufacturer's instructions. The cDNA was stored at −20 °C for further quantitative PCR (qPCR) analysis.

4.11.2. RT2 Profiler PCR Array Assay

An RT2 Profler PCR Array analysis of human apoptotic gene expression (PAHS-012Z, Qiagen, Hilden, Germany) was performed using a CFX96™ Touch Real-Time PCR Detection System, Bio-Rad, Hercules, CA, USA. PCR Array system using software version 3.5 (Qiagen, Hilden, Germany). The results were used to assess the mRNA expression levels of target genes using the $2^{-\Delta\Delta Ct}$ method.

4.12. Computational Analysis

4.12.1. Density Functional Theory (DFT) Calculations

DFT calculations were performed using the Jaguar v11.5 module in Schrödinger to predict the chemical reactivity of the molecules. A hybrid DFT with Berke's three-parameter exchange potential and Lee–Yang–Parr correlation functional (B3LYP) using basis set 6-31 G++** level was used to optimize the structures. All the DFT calculations were performed in an aqueous environment using PBF. Calculations such as highest occupied molecular orbitals (HOMO), lowest unoccupied molecular orbitals (LUMO), and molecular electrostatic potential (MESP) were performed.

4.12.2. Molecular Docking Studies of MM-Compounds

Triazine sulfonamide analogs were docked into the binding pocket of AKT2 using the LibDock docking engine [31]. The site-feature docking algorithm (LibDock) docks ligands, after removing their hydrogen atoms, into a putative active site guided by binding hotspots. The ligands' conformations are aligned to polar and apolar receptor interaction sites (i.e., hotspots). LibDock docking follows the following steps: (I) remove hydrogen atoms, (II) rank ligand conformations and prune by solvent accessible surface area (SASA), (III) find hotspots using a grid that is placed into the binding site using polar and apolar probes. The numbers of hotspots are pruned by clustering to a user-defined value.

(IV) Dock ligand poses by aligning to binding site hotspots. This is performed by using triplets (i.e., three ligand atoms are aligned to three receptor hotspots). (V) Poses that result in protein clashes are removed, and (VI) a final BFGS pose optimization stage is performed using a simple pair-wise score (similar to piecewise linear potential). The top-scoring ligand poses are retained. Hydrogen atoms are added back to the docked ligands. Optionally, CHARMm minimization can be carried out to reduce steric clashes caused by added hydrogen atoms.

The following LibDock parameters were implemented in the current study: before docking, the Discovery Studio 2.5.5 module CAT-CONFIRM was used to generate a maximum of 255 conformers (not exceeding an energy threshold of 20 kcal/mol from the most stable conformer) for each ligand employing the "best" conformation generation option. A binding site sphere of 8.81 Å radius surrounding the center of the co-crystallized ligand (PDB code: 3O0G or 3GEN) was used to define the binding site. The number of binding site hotspots (polar and a polar) was set to 100. The ligand-to-hotspots matching RMSD tolerance value was set to 0.25 Å. The maximum number of poses saved for each ligand during hotspots matching before final pose minimization was 100. The maximum number of poses to be saved for each ligand in the binding pocket was 100. The minimum LibDock score (poses below this score are not reported) was 100. The maximum number of rigid body minimization steps during the final pose optimization (using the BFGS method) was 50. The maximum number of steric clashes allowed before the pose-hotspot alignment was terminated (specified as a fraction of the heavy atom count) was 0.1. The maximum value for nonpolar solvent accessible surface area for a particular pose to be reported as successful was 15.0 $Å^2$. The maximum value for the polar solvent-accessible solvent area for a particular pose to be reported as successful was 5.0 $Å^2$. No final ligand minimization was implemented (i.e., in the binding pocket).

4.12.3. Prime MM-GBSA Calculations

The Prime MM-GBSA module of Schrödinger was used to evaluate the binding free energies for the protein–ligand complexes. The protein–ligand complexes were minimized using an optimized potential liquid solvation–all atom (OPLS-AA) force field and generalized Born/Surface (GB/SA) continuum solvent model. The free energy of binding for the protein-ligand complexes was estimated using the following formula:

$$\Delta G_{bind} = G_{complex} - (G_{protein} + G_{ligand})$$

$$G = EMM + GSGB + GNP$$

The energies of the complex, protein, and unbound ligand were represented as $G_{complex}$, $G_{protein}$, and G_{ligand}, respectively. The molecular mechanic's energies (EMM), in addition to the SGB polar solvation model (GSGB) and non-polar solvation (GNP), were together represented as G.

4.12.4. Molecular Dynamic Simulation of MM-Compounds and AKT2

Molecular dynamics (MD) simulations were performed using Gromacs 2020.4 version [81] to examine the stability of protein–ligand complexes obtained from molecular docking studies. The necessary input files were prepared via the CHARMM-GUI server [82]. Topology files of proteins and compounds were prepared using AMBER99SB force fields [83]. Protein–ligand complex structures were solvated using the TIP3 water model, using the rectangular box type, 10 Å away from the protein–ligand complexes, and neutralized by adding 0.15 KCl salt. The created system was minimized to 5000 nsteps with the steep integrator. The system was equilibrated using the Nose–Hoover [84–86] and Parrinello–Rahman algorithms [87] with 0.3 ns duration NVT/NPT ensemble steps at 300 K and 1 atm pressure. A 200-ns MD simulation was run at 2 fs, and 2000 frames were recorded. The root mean square deviation (RMSD), the root mean square fluctuation (RMSF), hydrogen bonds between protein and ligand, and radius of gyration (Rg)

were measured using gmx scripts. The binding free energy molecular mechanics Poisson–Boltzmann surface area (MM-PBSA) was calculated using 100 frames between 150 ns and 200 ns with the g_mmpbsa tool (V1.6) [88]. RMSD, RMSF, H bonds, and Rg plots were created using QtGrace v2.0.6. MD trajectory videos were created using PyMol Molecular Graphics System version 2.5.2 software, and protein–ligand binding pose visualizations were created using BIOVIA Discovery Studio Visualizer v21.

Supplementary Materials: The supporting information can be downloaded at: https://www.mdpi.com/article/10.3390/ijms241310959/s1.

Author Contributions: Conceptualization, M.K. and B.M.; investigation, M.K., I.C., E.Z., A.D., R.S., S.M. and K.B.; methodology, M.K. and I.C.; supervision, B.M., M.M. and R.K.; writing—original draft, M.K., B.M., I.C., E.Z., A.D., R.S., S.M. and K.B.; writing—review and editing, M.K., B.M. and R.K. All authors have read and agreed to the published version of the manuscript.

Funding: This research received no external funding.

Data Availability Statement: The data presented in this study are available in the main text of this article/Supplementary Materials of this article or on request from the corresponding author.

Conflicts of Interest: The authors declare no conflict of interest.

Abbreviations

ABL	tyrosine-protein kinase ABL
ADMET	absorption, distribution, metabolism, excretion, and toxicity
AIFM1	apoptosis-inducing factor, mitochondrion-associated, 1
AKT	serine/threonine-protein kinase AKT
AO/EB	acridine orange/ethidium bromide
APAF-1	apoptotic protease-activating factor 1
BAD	BCL2-associated agonist of cell death
BAG1	BCL2-associated athanogene
BCL10	B-cell CLL/lymphoma 10
BCL2L10	BCL2-like 10 (apoptosis facilitator)
BE	binding energy
BIRC5	baculoviral IAP repeat containing 5
BNIP3	BCL2/adenovirus E1B 19 kDa interacting protein 3
BNIP3L	BCL2/adenovirus E1B 19 kDa interacting protein 3-like
BrdU	Bromodeoxyuridine
BSA	bovine serum albumin
BTK	Bruton's tyrosine kinase
CAs	carbonic anhydrases
CASP1	caspase 1, apoptosis-related cysteine peptidase (interleukin 1, beta, convertase)
CASP14	caspase 14, apoptosis-related cysteine peptidase
CASP2	caspase 2, apoptosis-related cysteine peptidase
CASP6	caspase 6, apoptosis-related cysteine peptidase
CARD	caspase recruitment domain
CDKs	cyclin-dependent kinases
CD27	CD27 molecule
CD70	CD70 molecule
CHK1	serine/threonine-protein kinase CHK1
CIDEA/B	Cell death-inducing DFFA-like effector A/B
CLL	chronic lymphocytic leukemia
CRADD	CASP2 and RIPK1 domain containing adaptor with death domain
CYP	cytochrome
DCF	2′,7′-dichlorofluorescein
DCFH2	2′,7′-dichlorodihydrofluorescein
DCFH-DA	2,7-dichlorodihydrofluorescein diacetate
DFFA	DNA fragmentation factor, 45 kDa, alpha polypeptide

DISC	death-inducing signaling complex
DPT	developmental toxicity potential
EMM	molecular mechanic's energies
ESP	electrostatic potential
FADD	FAS-associated death domain protein
FAS	Fas (TNF receptor superfamily, member 6)
FBS	fetal bovine serum
GADD45α	growth arrest and DNA-damage-inducible, alpha
GB/SA	generalized Born/Surface continuum solvent model
GNP	non-polar solvation
HCl	hydrochloric acid
HLG	HOMO-LUMO energy gap
HOMO	highest occupied molecular orbital
LD50	50% lethal dose
LOAEL	lowest observable adverse effects level
LUMO	lowest occupied molecular orbital
MCL	mantle cell lymphoma
MD	molecular dynamics
MESP	molecular electrostatic potential
MLKL	mixed lineage kinase domain like pseudokinase
MMP	mitochondrial membrane potential
mTOR	mammalian target of rapamycin kinase
NAIP	NLR family, apoptosis inhibitory protein
NF-κB	nuclear factor kappa-B
NOD1	nucleotide-binding oligomerization domain containing 1
OPLS-AA	optimized potential liquid solvation-all atom
OPS	optimal prediction space
PBS	phosphate-buffered saline
P21	Cyclin-dependent kinase inhibitor 1 (also known as Waf1/Cip1)
PD-1	programmed cell death protein 1
PD-L1	programmed death-ligand 1
PHA	Paraformaldehyde
PI	propidium iodide
PPB	plasma protein binding
PS	phosphatidylserine
PYCARD	PYD and CARD domain containing
QSAR	quantitative structure-activity relationship
RFU	relative fluorescence units
RIPK2	receptor-interacting serine-threonine kinase 2
RMSD	trajectory root mean square deviation
RMSF	root mean square fluctuation
ROS	reactive oxygen species
SASA	solvent accessible surface area
sICAM-1	soluble intercellular adhesion molecule-1
SMILES	simplified molecular input line entry system
TOPKAT	toxicity prediction by computer-aided technology
TNF	tumor necrosis factor
TNFRSF10B	tumor necrosis factor receptor superfamily, member 10b
TNFRSF11B	tumor necrosis factor receptor superfamily, member 11b
TNFRSF1A	tumor necrosis factor receptor superfamily, member 1A
TNFSF10	tumor necrosis factor (ligand) superfamily, member 10
TP53	cellular tumor antigen p53
TRADD	tumor necrosis factor receptor type 1-associated DEATH domain
TRAF2	TNF receptor-associated factor 2
TRAIL	tumor necrosis factor-related apoptosis inducing ligand
λem	emission wavelength
λex	excitation wavelength

References

1. Eckhardt, S. Recent Progress in the Development of Anticancer Agents. *Curr. Med. Chem. Anticancer Agents* **2002**, *2*, 419–439. [CrossRef]
2. Ali, R.; Mirza, Z.; Ashraf, G.M.D.; Kamal, M.A.; Ansari, S.A.; Damanhouri, G.A.; Abuzenadah, A.M.; Chaudhary, A.G.; Sheikh, I.A. New Anticancer Agents: Recent Developments in Tumor Therapy. *Anticancer Res.* **2012**, *32*, 2999–3005.
3. Martins, P.; Jesus, J.; Santos, S.; Raposo, L.R.; Roma-Rodrigues, C.; Baptista, P.V.; Fernandes, A.R. Heterocyclic Anticancer Compounds: Recent Advances and the Paradigm Shift towards the Use of Nanomedicine's Tool Box. *Molecules* **2015**, *20*, 16852–16891. [CrossRef]
4. Lang, D.K.; Kaur, R.; Arora, R.; Saini, B.; Arora, S. Nitrogen-Containing Heterocycles as Anticancer Agents: An Overview. *Anticancer Agents Med. Chem.* **2020**, *20*, 2150–2168. [CrossRef]
5. Cascioferro, S.; Parrino, B.; Spanò, V.; Carbone, A.; Montalbano, A.; Barraja, P.; Diana, P.; Cirrincione, G. An Overview on the Recent Developments of 1,2,4-Triazine Derivatives as Anticancer Compounds. *Eur. J. Med. Chem.* **2017**, *142*, 328–375. [CrossRef]
6. Bernat, Z.; Szymanowska, A.; Kciuk, M.; Kotwica-Mojzych, K.; Mojzych, M. Review of the Synthesis and Anticancer Properties of Pyrazolo[4,3-*e*][1,2,4]triazine Derivatives. *Molecules* **2020**, *25*, 3948. [CrossRef]
7. Bukowski, K.; Marciniak, B.; Kciuk, M.; Mojzych, M.; Kontek, R. Pyrazolo[4,3-*e*]tetrazolo[1,5-*b*][1,2,4]triazine Sulfonamides as Novel Potential Anticancer Agents: Cytotoxic and Genotoxic Activities In Vitro. *Molecules* **2022**, *27*, 3761. [CrossRef] [PubMed]
8. Kciuk, M.; Mujwar, S.; Marciniak, B.; Gielecińska, A.; Bukowski, K.; Mojzych, M.; Kontek, R. Genotoxicity of Novel Pyrazolo[4,3-*e*]tetrazolo[1,5-*b*][1,2,4]triazine Sulfonamides in Normal and Cancer Cells In Vitro. *Int. J. Mol. Sci.* **2023**, *24*, 4053. [CrossRef] [PubMed]
9. Gornowicz, A.; Szymanowska, A.; Mojzych, M.; Bielawski, K.; Bielawska, A. The Effect of Novel 7-Methyl-5-phenyl-pyrazolo[4,3-*e*]tetrazolo[4,5-*b*][1,2,4]triazine Sulfonamide Derivatives on Apoptosis and Autophagy in DLD-1 and HT-29 Colon Cancer Cells. *Int. J. Mol. Sci.* **2020**, *21*, 5221. [CrossRef] [PubMed]
10. Hermanowicz, J.M.; Szymanowska, A.; Sieklucka, B.; Czarnomysy, R.; Pawlak, K.; Bielawska, A.; Bielawski, K.; Kalafut, J.; Przybyszewska, A.; Surazynski, A.; et al. Exploration of Novel Heterofused 1,2,4-Triazine Derivative in Colorectal Cancer. *J. Enzym. Inhib. Med. Chem.* **2021**, *36*, 535–548. [CrossRef] [PubMed]
11. Kciuk, M.; Mujwar, S.; Szymanowska, A.; Marciniak, B.; Bukowski, K.; Mojzych, M.; Kontek, R. Preparation of Novel Pyrazolo[4,3-*e*]tetrazolo[1,5-*b*][1,2,4]triazine Sulfonamides and Their Experimental and Computational Biological Studies. *Int. J. Mol. Sci.* **2022**, *23*, 5892. [CrossRef]
12. Hermanowicz, J.M.; Pawlak, K.; Sieklucka, B.; Czarnomysy, R.; Kwiatkowska, I.; Kazberuk, A.; Surazynski, A.; Mojzych, M.; Pawlak, D. MM-129 as a Novel Inhibitor Targeting PI3K/AKT/MTOR and PD-L1 in Colorectal Cancer. *Cancers* **2021**, *13*, 3203. [CrossRef] [PubMed]
13. Reiniers, M.J.; van Golen, R.F.; Bonnet, S.; Broekgaarden, M.; van Gulik, T.M.; Egmond, M.R.; Heger, M. Preparation and Practical Applications of 2′,7′-Dichlorodihydrofluorescein in Redox Assays. *Anal. Chem.* **2017**, *89*, 3853–3857. [CrossRef] [PubMed]
14. Franken, N.A.P.; Rodermond, H.M.; Stap, J.; Haveman, J.; van Bree, C. Clonogenic Assay of Cells in Vitro. *Nat. Protoc.* **2006**, *1*, 2315–2319. [CrossRef] [PubMed]
15. Riccardi, C.; Nicoletti, I. Analysis of Apoptosis by Propidium Iodide Staining and Flow Cytometry. *Nat. Protoc.* **2006**, *1*, 1458–1461. [CrossRef] [PubMed]
16. Crowley, L.C.; Chojnowski, G.; Waterhouse, N.J. Measuring the DNA Content of Cells in Apoptosis and at Different Cell-Cycle Stages by Propidium Iodide Staining and Flow Cytometry. *Cold Spring Harb. Protoc.* **2016**, *2016*, pdb-prot08724. [CrossRef]
17. Matassov, D.; Kagan, T.; Leblanc, J.; Sikorska, M.; Zakeri, Z. Measurement of Apoptosis by DNA Fragmentation. *Methods Mol. Biol.* **2004**, *282*, 1–17. [CrossRef]
18. Majtnerová, P.; Roušar, T. An Overview of Apoptosis Assays Detecting DNA Fragmentation. *Mol. Biol. Rep.* **2018**, *45*, 1469–1478. [CrossRef]
19. Amati, M.; Stoia, S.; Baerends, E.J. The Electron Affinity as the Highest Occupied Anion Orbital Energy with a Sufficiently Accurate Approximation of the Exact Kohn-Sham Potential. *J. Chem. Theory Comput.* **2020**, *16*, 443–452. [CrossRef]
20. Curpăn, R.; Avram, S.; Vianello, R.; Bologa, C. Exploring the Biological Promiscuity of High-Throughput Screening Hits through DFT Calculations. *Bioorg. Med. Chem.* **2014**, *22*, 2461–2468. [CrossRef]
21. Hermanowicz, J.M.; Kalaska, B.; Pawlak, K.; Sieklucka, B.; Miklosz, J.; Mojzych, M.; Pawlak, D. Preclinical Toxicity and Safety of MM-129-First-in-Class BTK/PD-L1 Inhibitor as a Potential Candidate against Colon Cancer. *Pharmaceutics* **2021**, *13*, 1222. [CrossRef] [PubMed]
22. Freeman-Cook, K.D.; Autry, C.; Borzillo, G.; Gordon, D.; Barbacci-Tobin, E.; Bernardo, V.; Briere, D.; Clark, T.; Corbett, M.; Jakubczak, J.; et al. Design of Selective, ATP-Competitive Inhibitors of Akt. *J. Med. Chem.* **2010**, *53*, 4615–4622. [CrossRef] [PubMed]
23. Heerding, D.A.; Rhodes, N.; Leber, J.D.; Clark, T.J.; Keenan, R.M.; Lafrance, L.V.; Li, M.; Safonov, I.G.; Takata, D.T.; Venslavsky, J.W.; et al. Identification of 4-(2-(4-Amino-1,2,5-oxadiazol-3-yl)-1-ethyl-7-{[(3*S*)-3-piperidinylmethyl]oxy}-1*H*-imidazo[4,5-*c*]pyridin-4-yl)-2-methyl-3-butyn-2-ol (GSK690693), a Novel Inhibitor of AKT Kinase. *J. Med. Chem.* **2008**, *51*, 5663–5679. [CrossRef] [PubMed]

24. Marcotte, D.J.; Liu, Y.-T.; Arduini, R.M.; Hession, C.A.; Miatkowski, K.; Wildes, C.P.; Cullen, P.F.; Hong, V.; Hopkins, B.T.; Mertsching, E.; et al. Structures of Human Bruton's Tyrosine Kinase in Active and Inactive Conformations Suggest a Mechanism of Activation for TEC Family Kinases. *Protein Sci.* **2010**, *19*, 429–439. [CrossRef]
25. Reader, J.C.; Matthews, T.P.; Klair, S.; Cheung, K.-M.J.; Scanlon, J.; Proisy, N.; Addison, G.; Ellard, J.; Piton, N.; Taylor, S.; et al. Structure-Guided Evolution of Potent and Selective CHK1 Inhibitors through Scaffold Morphing. *J. Med. Chem.* **2011**, *54*, 8328–8342. [CrossRef] [PubMed]
26. Yang, H.; Jiang, X.; Li, B.; Yang, H.J.; Miller, M.; Yang, A.; Dhar, A.; Pavletich, N.P. Mechanisms of MTORC1 Activation by RHEB and Inhibition by PRAS40. *Nature* **2017**, *552*, 368–373. [CrossRef]
27. Butera, R.; Ważyńska, M.; Magiera-Mularz, K.; Plewka, J.; Musielak, B.; Surmiak, E.; Sala, D.; Kitel, R.; de Bruyn, M.; Nijman, H.W.; et al. Design, Synthesis, and Biological Evaluation of Imidazopyridines as PD-1/PD-L1 Antagonists. *ACS Med. Chem. Lett.* **2021**, *12*, 768–773. [CrossRef]
28. Qu, X.; Dong, L.; Zhang, J.; Si, Y.; Wang, B. Systematic Improvement of the Performance of Machine Learning Scoring Functions by Incorporating Features of Protein-Bound Water Molecules. *J. Chem. Inf. Model* **2022**, *62*, 4369–4379. [CrossRef]
29. de Beer, S.B.A.; Vermeulen, N.P.E.; Oostenbrink, C. The Role of Water Molecules in Computational Drug Design. *Curr. Top Med. Chem.* **2010**, *10*, 55–66. [CrossRef]
30. Mitusińska, K.; Raczyńska, A.; Bzówka, M.; Bagrowska, W.; Góra, A. Applications of Water Molecules for Analysis of Macromolecule Properties. *Comput. Struct. Biotechnol. J.* **2020**, *18*, 355–365. [CrossRef]
31. Rao, S.N.; Head, M.S.; Kulkarni, A.; LaLonde, J.M. Validation Studies of the Site-Directed Docking Program LibDock. *J. Chem. Inf. Model* **2007**, *47*, 2159–2171. [CrossRef] [PubMed]
32. Jain, A.N. Scoring Functions for Protein-Ligand Docking. *Curr. Protein Pept. Sci.* **2006**, *7*, 407–420. [CrossRef] [PubMed]
33. Krammer, A.; Kirchhoff, P.D.; Jiang, X.; Venkatachalam, C.M.; Waldman, M. LigScore: A Novel Scoring Function for Predicting Binding Affinities. *J. Mol. Graph. Model* **2005**, *23*, 395–407. [CrossRef]
34. Krovat, E.M.; Langer, T. Impact of Scoring Functions on Enrichment in Docking-Based Virtual Screening: An Application Study on Renin Inhibitors. *J. Chem. Inf. Comput. Sci.* **2004**, *44*, 1123–1129. [CrossRef] [PubMed]
35. Muegge, I.; Martin, Y.C. A General and Fast Scoring Function for Protein-Ligand Interactions: A Simplified Potential Approach. *J. Med. Chem.* **1999**, *42*, 791–804. [CrossRef]
36. Zerroug, E.; Belaidi, S.; Chtita, S. Artificial Neural Network-Based Quantitative Structure–Activity Relationships Model and Molecular Docking for Virtual Screening of Novel Potent Acetylcholinesterase Inhibitors. *J. Chin. Chem. Soc.* **2021**, *68*, 1379–1399. [CrossRef]
37. Shah, K.; Mujwar, S.; Gupta, J.K.; Shrivastava, S.K.; Mishra, P. Molecular Docking and In Silico Cogitation Validate Mefenamic Acid Prodrugs as Human Cyclooxygenase-2 Inhibitor. *Assay Drug Dev. Technol.* **2019**, *17*, 285–291. [CrossRef]
38. Shin, S.Y.; Kim, C.G.; Jung, Y.J.; Lim, Y.; Lee, Y.H. The UPR Inducer DPP23 Inhibits the Metastatic Potential of MDA-MB-231 Human Breast Cancer Cells by Targeting the Akt-IKK-NF-KB-MMP-9 Axis. *Sci. Rep.* **2016**, *6*, 34134. [CrossRef]
39. Vala, R.M.; Tandon, V.; Nicely, L.G.; Guo, L.; Gu, Y.; Banerjee, S.; Patel, H.M. Synthesis of *N*-(4-chlorophenyl) substituted pyrano[2,3-*c*]pyrazoles enabling PKBβ/AKT2 inhibitory and in vitro anti-glioma activity. *Ann. Med.* **2022**, *54*, 2549–2561. [CrossRef]
40. Balasubramanian, P.K.; Balupuri, A.; Cho, S.J. Molecular Modeling Studies on Series of Btk Inhibitors Using Docking, Structure-Based 3D-QSAR and Molecular Dynamics Simulation: A Combined Approach. *Arch. Pharm. Res.* **2016**, *39*, 328–339. [CrossRef]
41. Zhao, X.; Xin, M.; Wang, Y.; Huang, W.; Jin, Q.; Tang, F.; Wu, G.; Zhao, Y.; Xiang, H. Discovery of Thieno[3,2-*c*]pyridin-4-amines as Novel Bruton's Tyrosine Kinase (BTK) Inhibitors. *Bioorg. Med. Chem.* **2015**, *23*, 6059–6068. [CrossRef] [PubMed]
42. Wen, T.; Wang, J.; Shi, Y.; Qian, H.; Liu, P. Inhibitors Targeting Bruton's Tyrosine Kinase in Cancers: Drug Development Advances. *Leukemia* **2021**, *35*, 312–332. [CrossRef]
43. Mortier, J.; Rakers, C.; Bermudez, M.; Murgueitio, M.S.; Riniker, S.; Wolber, G. The Impact of Molecular Dynamics on Drug Design: Applications for the Characterization of Ligand-Macromolecule Complexes. *Drug Discov. Today* **2015**, *20*, 686–702. [CrossRef]
44. Bender, O.; Shoman, M.E.; Ali, T.F.S.; Dogan, R.; Celik, I.; Mollica, A.; Hamed, M.I.A.; Aly, O.M.; Alamri, A.; Alanazi, J.; et al. Discovery of Oxindole-Based FLT3 Inhibitors as a Promising Therapeutic Lead for Acute Myeloid Leukemia Carrying the Oncogenic ITD Mutation. *Arch. Pharm.* **2023**, *356*, e2200407. [CrossRef] [PubMed]
45. Celik, I.; Çevik, U.A.; Karayel, A.; Işık, A.; Kayış, U.; Gül, Ü.D.; Bostancı, H.E.; Konca, S.F.; Özkay, Y.; Kaplancıklı, Z.A. Synthesis, Molecular Docking, Dynamics, Quantum-Chemical Computation, and Antimicrobial Activity Studies of Some New Benzimidazole-Thiadiazole Hybrids. *ACS Omega* **2022**, *7*, 47015–47030. [CrossRef] [PubMed]
46. Vanillin-Based Indolin-2-One Derivative Bearing a Pyridyl Moiety as a Promising Anti-Breast Cancer Agent via Anti-Estrogenic Activity | ACS Omega. Available online: https://pubs.acs.org/doi/10.1021/acsomega.2c07793 (accessed on 5 May 2023).
47. Celik, I.; Tallei, T.E. A Computational Comparative Analysis of the Binding Mechanism of Molnupiravir's Active Metabolite to RNA-Dependent RNA Polymerase of Wild-Type and Delta Subvariant AY.4 of SARS-CoV-2. *J. Cell Biochem.* **2022**, *123*, 807–818. [CrossRef] [PubMed]
48. Celik, I.; Khan, A.; Dwivany, F.M.; Fatimawali; Wei, D.-Q.; Tallei, T.E. Computational Prediction of the Effect of Mutations in the Receptor-Binding Domain on the Interaction between SARS-CoV-2 and Human ACE2. *Mol. Divers* **2022**, *26*, 3309–3324. [CrossRef]

49. Doganc, F.; Celik, I.; Eren, G.; Kaiser, M.; Brun, R.; Goker, H. Synthesis, in Vitro Antiprotozoal Activity, Molecular Docking and Molecular Dynamics Studies of Some New Monocationic Guanidinobenzimidazoles. *Eur. J. Med. Chem.* **2021**, *221*, 113545. [CrossRef]
50. Lim, F.P.L.; Dolzhenko, A.V. 1,3,5-Triazine-Based Analogues of Purine: From Isosteres to Privileged Scaffolds in Medicinal Chemistry. *Eur. J. Med. Chem.* **2014**, *85*, 371–390. [CrossRef]
51. Kumar, R.; Sirohi, T.S.; Singh, H.; Yadav, R.; Roy, R.K.; Chaudhary, A.; Pandeya, S.N. 1,2,4-Triazine Analogs as Novel Class of Therapeutic Agents. *Mini Rev. Med. Chem.* **2014**, *14*, 168–207. [CrossRef]
52. Mojzych, M.; Šubertová, V.; Bielawska, A.; Bielawski, K.; Bazgier, V.; Berka, K.; Gucký, T.; Fornal, E.; Kryštof, V. Synthesis and Kinase Inhibitory Activity of New Sulfonamide Derivatives of Pyrazolo[4,3-*e*][1,2,4]triazines. *Eur. J. Med. Chem.* **2014**, *78*, 217–224. [CrossRef] [PubMed]
53. Mojzych, M.; Ceruso, M.; Bielawska, A.; Bielawski, K.; Fornal, E.; Supuran, C.T. New Pyrazolo[4,3-*e*][1,2,4]triazine Sulfonamides as Carbonic Anhydrase Inhibitors. *Bioorg. Med. Chem.* **2015**, *23*, 3674–3680. [CrossRef] [PubMed]
54. Mojzych, M.; Bielawska, A.; Bielawski, K.; Ceruso, M.; Supuran, C.T. Pyrazolo[4,3-*e*][1,2,4]triazine Sulfonamides as Carbonic Anhydrase Inhibitors with Antitumor Activity. *Bioorg. Med. Chem.* **2014**, *22*, 2643–2647. [CrossRef] [PubMed]
55. Mohamed, A.J.; Yu, L.; Bäckesjö, C.-M.; Vargas, L.; Faryal, R.; Aints, A.; Christensson, B.; Berglöf, A.; Vihinen, M.; Nore, B.F.; et al. Bruton's Tyrosine Kinase (Btk): Function, Regulation, and Transformation with Special Emphasis on the PH Domain. *Immunol. Rev.* **2009**, *228*, 58–73. [CrossRef] [PubMed]
56. Burger, J.A. Bruton Tyrosine Kinase Inhibitors: Present and Future. *Cancer J.* **2019**, *25*, 386–393. [CrossRef]
57. Gornowicz, A.; Szymanowska, A.; Mojzych, M.; Czarnomysy, R.; Bielawski, K.; Bielawska, A. The Anticancer Action of a Novel 1,2,4-Triazine Sulfonamide Derivative in Colon Cancer Cells. *Molecules* **2021**, *26*, 2045. [CrossRef]
58. Wang, L.; Guo, Y.; Huang, W.J.; Ke, X.; Poyet, J.L.; Manji, G.A.; Merriam, S.; Glucksmann, M.A.; DiStefano, P.S.; Alnemri, E.S.; et al. Card10 Is a Novel Caspase Recruitment Domain/Membrane-Associated Guanylate Kinase Family Member That Interacts with BCL10 and Activates NF-κB. *J. Biol. Chem.* **2001**, *276*, 21405–21409. [CrossRef]
59. Yui, D.; Yoneda, T.; Oono, K.; Katayama, T.; Imaizumi, K.; Tohyama, M. Interchangeable Binding of Bcl10 to TRAF2 and CIAPs Regulates Apoptosis Signaling. *Oncogene* **2001**, *20*, 4317–4323. [CrossRef]
60. Luo, Y.; Wu, J.; Zou, J.; Cao, Y.; He, Y.; Ling, H.; Zeng, T. BCL10 in Cell Survival after DNA Damage. *Clin. Chim. Acta* **2019**, *495*, 301–308. [CrossRef]
61. Micheau, O. Regulation of TNF-Related Apoptosis-Inducing Ligand Signaling by Glycosylation. *Int. J. Mol. Sci.* **2018**, *19*, 715. [CrossRef]
62. Nahacka, Z.; Svadlenka, J.; Peterka, M.; Ksandrova, M.; Benesova, S.; Neuzil, J.; Andera, L. TRAIL Induces Apoptosis but Not Necroptosis in Colorectal and Pancreatic Cancer Cells Preferentially via the TRAIL-R2/DR5 Receptor. *Biochim. Biophys. Acta Mol. Cell Res.* **2018**, *1865*, 522–531. [CrossRef]
63. Shlyakhtina, Y.; Pavet, V.; Gronemeyer, H. Dual Role of DR5 in Death and Survival Signaling Leads to TRAIL Resistance in Cancer Cells. *Cell Death Dis.* **2017**, *8*, e3025. [CrossRef] [PubMed]
64. Micheau, O.; Tschopp, J. Induction of TNF Receptor I-Mediated Apoptosis via Two Sequential Signaling Complexes. *Cell* **2003**, *114*, 181–190. [CrossRef]
65. Dhuriya, Y.K.; Sharma, D. Necroptosis: A Regulated Inflammatory Mode of Cell Death. *J. Neuroinflamm.* **2018**, *15*, 199. [CrossRef] [PubMed]
66. Park, M.Y.; Ha, S.E.; Vetrivel, P.; Kim, H.H.; Bhosale, P.B.; Abusaliya, A.; Kim, G.S. Differences of Key Proteins between Apoptosis and Necroptosis. *Biomed. Res. Int.* **2021**, *2021*, 3420168. [CrossRef]
67. Zargarian, S.; Shlomovitz, I.; Erlich, Z.; Hourizadeh, A.; Ofir-Birin, Y.; Croker, B.A.; Regev-Rudzki, N.; Edry-Botzer, L.; Gerlic, M. Phosphatidylserine Externalization, "Necroptotic Bodies" Release, and Phagocytosis during Necroptosis. *PLoS Biol.* **2017**, *15*, e2002711. [CrossRef]
68. Shlomovitz, I.; Speir, M.; Gerlic, M. Flipping the Dogma—Phosphatidylserine in Non-Apoptotic Cell Death. *Cell Commun. Signal* **2019**, *17*, 139. [CrossRef]
69. Li, K.; Qiu, J.; Pan, J.; Pan, J.-P. Pyroptosis and Its Role in Cervical Cancer. *Cancers* **2022**, *14*, 5764. [CrossRef]
70. Tamura, R.E.; de Vasconcellos, J.F.; Sarkar, D.; Libermann, T.A.; Fisher, P.B.; Zerbini, L.F. GADD45 Proteins: Central Players in Tumorigenesis. *Curr. Mol. Med.* **2012**, *12*, 634–651. [CrossRef] [PubMed]
71. Jin, S.; Mazzacurati, L.; Zhu, X.; Tong, T.; Song, Y.; Shujuan, S.; Petrik, K.L.; Rajasekaran, B.; Wu, M.; Zhan, Q. Gadd45a Contributes to P53 Stabilization in Response to DNA Damage. *Oncogene* **2003**, *22*, 8536–8540. [CrossRef] [PubMed]
72. Carrier, F.; Smith, M.L.; Bae, I.; Kilpatrick, K.E.; Lansing, T.J.; Chen, C.Y.; Engelstein, M.; Friend, S.H.; Henner, W.D.; Gilmer, T.M. Characterization of Human Gadd45, a P53-Regulated Protein. *J. Biol. Chem.* **1994**, *269*, 32672–32677. [CrossRef]
73. Zhan, Q.; Fan, S.; Smith, M.L.; Bae, I.; Yu, K.; Alamo, I.; O'Connor, P.M.; Fornace, A.J. Abrogation of P53 Function Affects Gadd Gene Responses to DNA Base-Damaging Agents and Starvation. *DNA Cell Biol.* **1996**, *15*, 805–815. [CrossRef]
74. Nakayama, K.; Hara, T.; Hibi, M.; Hirano, T.; Miyajima, A. A Novel Oncostatin M-Inducible Gene OIG37 Forms a Gene Family with MyD118 and GADD45 and Negatively Regulates Cell Growth. *J. Biol. Chem.* **1999**, *274*, 24766–24772. [CrossRef]
75. Jin, S.; Tong, T.; Fan, W.; Fan, F.; Antinore, M.J.; Zhu, X.; Mazzacurati, L.; Li, X.; Petrik, K.L.; Rajasekaran, B.; et al. GADD45-Induced Cell Cycle G2-M Arrest Associates with Altered Subcellular Distribution of Cyclin B1 and Is Independent of P38 Kinase Activity. *Oncogene* **2002**, *21*, 8696–8704. [CrossRef]

76. Zhan, Q.; Antinore, M.J.; Wang, X.W.; Carrier, F.; Smith, M.L.; Harris, C.C.; Fornace, A.J. Association with Cdc2 and Inhibition of Cdc2/Cyclin B1 Kinase Activity by the P53-Regulated Protein Gadd45. *Oncogene* **1999**, *18*, 2892–2900. [CrossRef] [PubMed]
77. Vairapandi, M.; Balliet, A.G.; Hoffman, B.; Liebermann, D.A. GADD45b and GADD45g Are Cdc2/CyclinB1 Kinase Inhibitors with a Role in S and G2/M Cell Cycle Checkpoints Induced by Genotoxic Stress. *J. Cell Physiol.* **2002**, *192*, 327–338. [CrossRef] [PubMed]
78. Zhu, Q.-S.; Ren, W.; Korchin, B.; Lahat, G.; Dicker, A.; Lu, Y.; Mills, G.; Pollock, R.E.; Lev, D. Soft Tissue Sarcoma Are Highly Sensitive to AKT Blockade: A Role for P53 Independent Up-Regulation of GADD45α. *Cancer Res.* **2008**, *68*, 2895–2903. [CrossRef]
79. Da Violante, G.; Zerrouk, N.; Richard, I.; Provot, G.; Chaumeil, J.C.; Arnaud, P. Evaluation of the Cytotoxicity Effect of Dimethyl Sulfoxide (DMSO) on Caco2/TC7 Colon Tumor Cell Cultures. *Biol. Pharm. Bull* **2002**, *25*, 1600–1603. [CrossRef]
80. Repetto, G.; del Peso, A.; Zurita, J.L. Neutral Red Uptake Assay for the Estimation of Cell Viability/Cytotoxicity. *Nat. Protoc.* **2008**, *3*, 1125–1131. [CrossRef]
81. Abraham, M.J.; Murtola, T.; Schulz, R.; Páll, S.; Smith, J.C.; Hess, B.; Lindahl, E. GROMACS: High Performance Molecular Simulations through Multi-Level Parallelism from Laptops to Supercomputers. *SoftwareX* **2015**, *1*, 19–25. [CrossRef]
82. Jo, S.; Kim, T.; Iyer, V.G.; Im, W. CHARMM-GUI: A Web-Based Graphical User Interface for CHARMM. *J. Comput. Chem.* **2008**, *29*, 1859–1865. [CrossRef] [PubMed]
83. Tian, C.; Kasavajhala, K.; Belfon, K.A.A.; Raguette, L.; Huang, H.; Migues, A.N.; Bickel, J.; Wang, Y.; Pincay, J.; Wu, Q.; et al. Ff19SB: Amino-Acid-Specific Protein Backbone Parameters Trained against Quantum Mechanics Energy Surfaces in Solution. *J. Chem. Theory Comput.* **2020**, *16*, 528–552. [CrossRef] [PubMed]
84. Mukhtar, M.; Bilal, M.; Rahdar, A.; Barani, M.; Arshad, R.; Behl, T.; Brisc, C.; Banica, F.; Bungau, S. Nanomaterials for Diagnosis and Treatment of Brain Cancer: Recent Updates. *Chemosensors.* **2020**, *8*, 117. [CrossRef]
85. Patra, P.K.; Bhattacharya, B. Nonergodicity of the Nose-Hoover Chain Thermostat in Computationally Achievable Time. *Phys. Rev. E Stat Nonlin. Soft Matter Phys.* **2014**, *90*, 043304. [CrossRef] [PubMed]
86. Sidler, D.; Riniker, S. Fast Nosé-Hoover Thermostat: Molecular Dynamics in Quasi-Thermodynamic Equilibrium. *Phys. Chem. Chem. Phys.* **2019**, *21*, 6059–6070. [CrossRef]
87. Parrinello, M.; Rahman, A. Polymorphic Transitions in Single Crystals: A New Molecular Dynamics Method. *J. Appl. Phys.* **1981**, *52*, 7182–7190. [CrossRef]
88. Kumari, R.; Kumar, R.; Open Source Drug Discovery Consortium; Lynn, A. G_mmpbsa—A GROMACS Tool for High-Throughput MM-PBSA Calculations. *J. Chem. Inf. Model* **2014**, *54*, 1951–1962. [CrossRef]

International Journal of Molecular Sciences

MDPI

Supplementary Information

Pyrazolo[4,3-*e*]tetrazolo[1,5-*b*][1,2,4]triazine Sulfonamides as an Important Scaffold for Anticancer Drug Discovery—In Vitro and In Silico Evaluation

Mateusz Kciuk [1,2], Beata Marciniak [1], Ismail Celik [3], Enfale Zerroug [4], Amit Dubey [5,6], Rajamanikandan Sundaraj [7], Somdutt Mujwar [8], Karol Bukowski [1], Mariusz Mojzych [9] and Renata Kontek [1,*]

[1] Department of Molecular Biotechnology and Genetics, University of Lodz, Banacha 12/16, 90-237 Lodz, Poland; mateusz.kciuk@edu.uni.lodz.pl (M.K.); beata.marciniak@biol.uni.lodz.pl (B.M.); karol.bukowski@edu.uni.lodz.pl (K.B.)
[2] Doctoral School of Exact and Natural Sciences, University of Lodz, Banacha Street 12/16, 90-237 Lodz, Poland
[3] Department of Pharmaceutical Chemistry, Faculty of Pharmacy, Erciyes University, Kayseri 38280, Turkey; ismailcelik@erciyes.edu.tr
[4] Group of Computational and Pharmaceutical Chemistry, LMCE Laboratory, University of Biskra, BP 145, Biskra 07000, Algeria; anfelzerroug220@gmail.com
[5] Computational Chemistry and Drug Discovery Division, Quanta Calculus, Greater Noida 274203, Uttar Prades, India; ameetbioinfo@gmail.com
[6] Department of Pharmacology, Saveetha Dental College and Hospital, Saveetha Institute of Medical and Technical Sciences, Chennai 602105, Tamil Nadu, India
[7] Centre for Drug Discovery, Department of Biochemistry, Karpagam Academy of Higher Education, Coimbatore 641021, Tamil Nadu, India; mani.bioinfor@gmail.com
[8] Chitkara College of Pharmacy, Chitkara University, Rajpura 140401, Punjab, India; somduttmujwar@gmail.com
[9] Department of Chemistry, Siedlce University of Natural Sciences and Humanities, 3 Maja 54, 08-110 Siedlce, Poland; mariusz.mojzych@uph.edu.pl
* Correspondence: renata.kontek@biol.uni.lodz.pl

Table S1. 24-h IC_{50} values [μM] obtained from two independent experiments (1,2) with corresponding coefficients of determination (R^2) and calculated mean IC_{50} values ± SD.

MM-compounds	IC_{50} (1)	R^2(1)	IC_{50} (2)	R^2(2)	Mean IC_{50} value ± SD [μM]
		BxPC-3 cells			
MM134	**0.36**	0.93	**0.35**	0.97	**0.35 ± 0.007**
MM136	**0.24**	0.99	**0.3**	0.99	**0.27 ± 0.04**
MM137	**0.17**	0.95	**0.19**	0.94	**0.18 ± 0.014**
MM139	**0.27**	0.99	**0.3**	0.98	**0.28 ± 0.02**
		PC-3 cells			
MM134	**0.07**	0.89	**0.13**	0.97	**0.1 ± 0.04**
MM136	**0.12**	0.99	**0.14**	0.98	**0.13 ± 0.014**
MM137	**0.06**	0.99	**0.06**	0.99	**0.06**
MM139	**0.21**	0.99	**0.14**	0.99	**0.17 ± 0.05**

Table S2. Effect of 24-h incubation of PC-3 cells with IC_{50} and $2xIC_{50}$ concentrations of **MM**-compounds.

Compound	Concentration	% of proliferating cells
MM134	IC_{50}	72.6 ± 1.48
	$2xIC_{50}$	62.2 ± 4.45
MM136	IC_{50}	68.4 ± 1.27
	$2xIC_{50}$	56.7 ± 10.1
MM137	$IC_{50}/2xIC_{50}$	65.6 ± 5.79
MM139	IC_{50}	68 ± 12.7
	$2xIC_{50}$	46.8 ± 0.78

Table S3. MTT assay results of **MM**-compounds described in the literature and obtained from the non-published source. Cytotoxic/cytostatic effects of compounds were described for multiple cancer cell lines: BxPC-3 (pancreas adenocarcinoma), PC-3 (prostate cancer), cervical cancer (HeLa), colorectal adenocarcinoma (DLD1/HCT116/HT29) and normal cells: human lung fibroblasts (WI-38) and human peripheral blood mononuclear cells (PBMCs). The results were obtained for the 72-h incubation of the compounds with cells (or 24-h as indicated by pound sign; #). Yellow marking – cell lines investigated in this manuscript, green marking – normal cell lines.

Compound	Cell line							
	IC_{50} value							
	BxPC-3	**PC-3**	**HeLa**	**DLD-1**	**HCT116**	**HT-29**	**WI-28**	**PBMCs**
MM129	0.26	0.36	0.9	3.1#	0.6	3.1#	N/D	1.11
MM130	0.17	0.22	0.59	N/D	0.44	N/D	N/D	0.77
MM131	0.13	0.17	0.41	3.4#	0.39	3.9#	N/D	0.62
MM134	0.32	0.16	N/D	0.27*	0.38	0.2*	0.65	N/D
MM136	0.25	0.13	N/D	0.13*	0.25	0.12*	0.48	N/D
MM137	0.16	0.11	N/D	0.08*	0.14	0.08*	0.27	N/D
MM139	0.33	0.17	N/D	0.12*	0.35	0.09*	0.64	N/D

N/D – non determined; * - non published data; #- 24-h incubation.

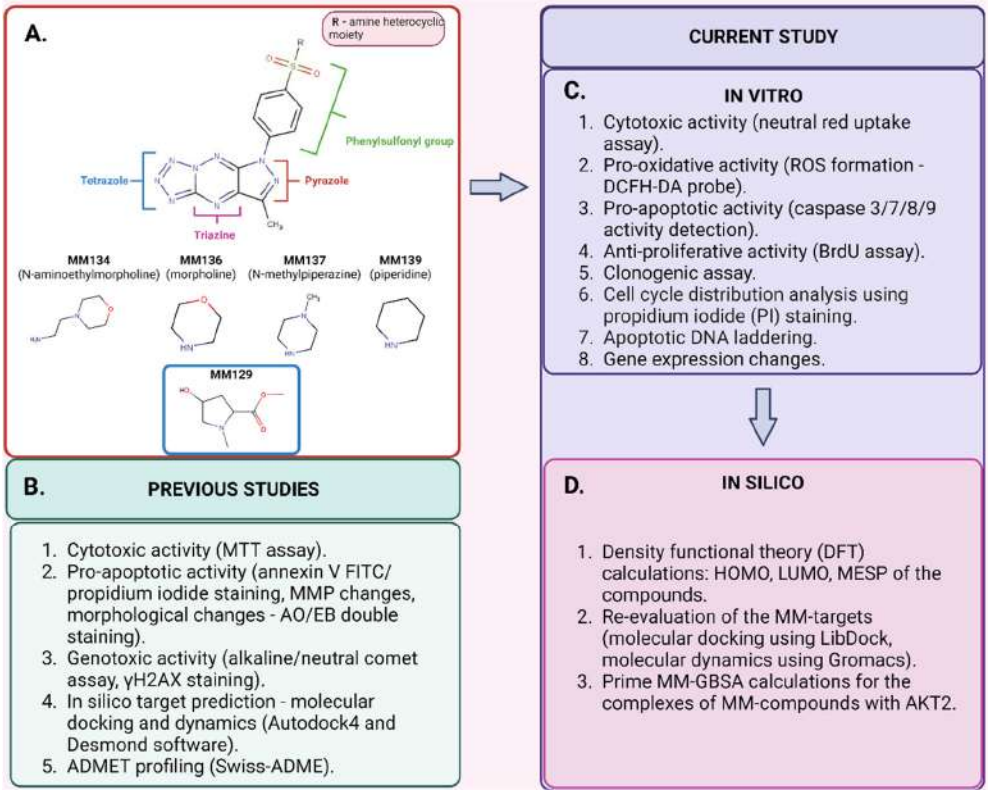

Figure S1. The study workflow. A) Four pyrazolo[4,3-*e*]tetrazolo[1,5-*b*][1,2,4]triazine sulphonamides (**MM**-compounds) were investigated in the current study. These compounds differ in the amine heterocyclic moiety which constitutes N-aminoethylmorpholine (**MM134**), morpholine (**MM136**), N-methylpiperazine (**MM137**), and piperidine (**MM139**). The compounds are close analogues of methyl 4-hydroxy-1-[4-(7-methyl-5H-pyrazolo[4,3-*e*]tetrazolo[1,5-*b*][1,2,4]triazin-5-yl)phenylsulfo-nyl]pyrrolidine-2-carboxylate (**MM129)** compound which efficiently limits cell viability via inhibition of Bruton's tyrosine kinase (BTK) [10] and exhibits antitumor activity in colon cancer xenograft mice as a result of a decrease in serine/threonine-protein kinase AKT (AKT), cyclin-dependent kinase 2 (CDK2), mammalian target of rapamycin kinase (mTOR), and programmed death-ligand 1 (PD-L1) expression [18]. B) In the previous studies [11] **MM34**, **-6**, **-7** and **-9** compounds used in micromolar concentrations showed cytotoxic, genotoxic, and pro-apoptotic properties. Additionally, compounds exhibited favorable ADMET properties and were predicted to act through the AKT-mTOR pathway or BTK and CHK1 kinase inhibition and were indicated to disrupt the PD-1/PD-L1 interaction in the in silico investigation. C) In the current study, cytotoxic and pro-apoptotic properties of the compounds were investigated, together with their anti-clonogenic, anti-proliferative, and pro-oxidative properties. Furthermore, we explored gene expression changes in BxPC-3 cells following treatment with the most pro-apoptotic **MM134** compound D) The in vitro studies were complemented with detailed in silico investigation including the re-evaluation of the interaction between the compounds and predicted targets to select the most promising hits for further investigations. The compounds' properties were investigated with HOMO, LUMO and MESP calculations. Abbreviations: ADMET—absorption, distribution, metabolism, excretion, and toxicity; AKT—serine/threonine-protein kinase AKT; BTK—Bruton's tyrosine kinase; CHK1—serine/threonine-protein kinase CHK1; HOMO—highest occupied molecular orbital; MESP— molecular electrostatic potential; mTOR—mammalian target of rapamycin kinase; LUMO—lowest occupied molecular orbital; PD-1—programmed cell death protein 1; PD-L1—programmed death-ligand 1. Created with BioRender.com accessed on 24 April 2023.

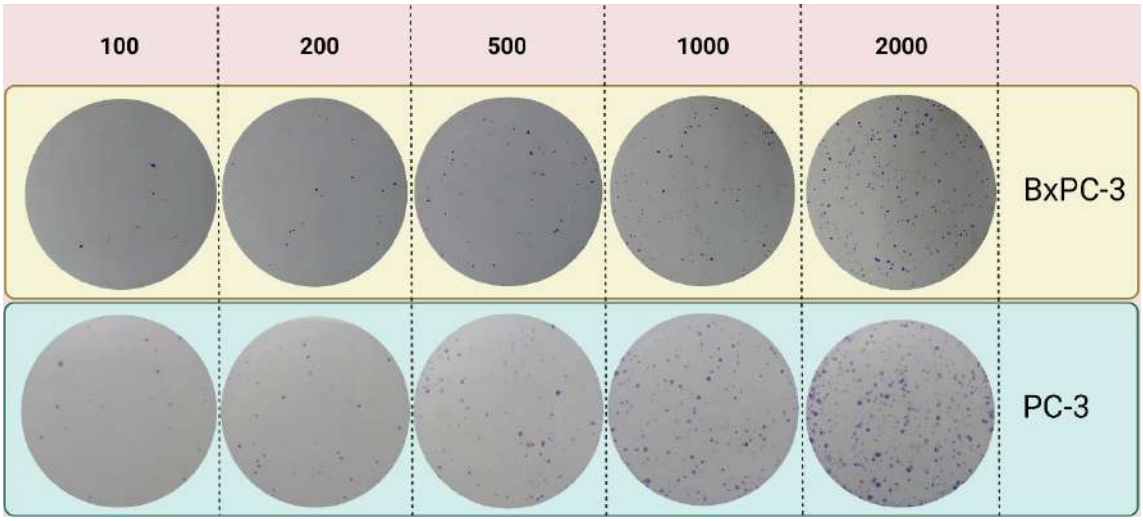

Figure S2. Examples of images obtained after seeding 100, 200, 500, 1000, and 2000 of BxPC-3 or PC-3 cells. Created with BioRender.com accessed on 24 April 2023.

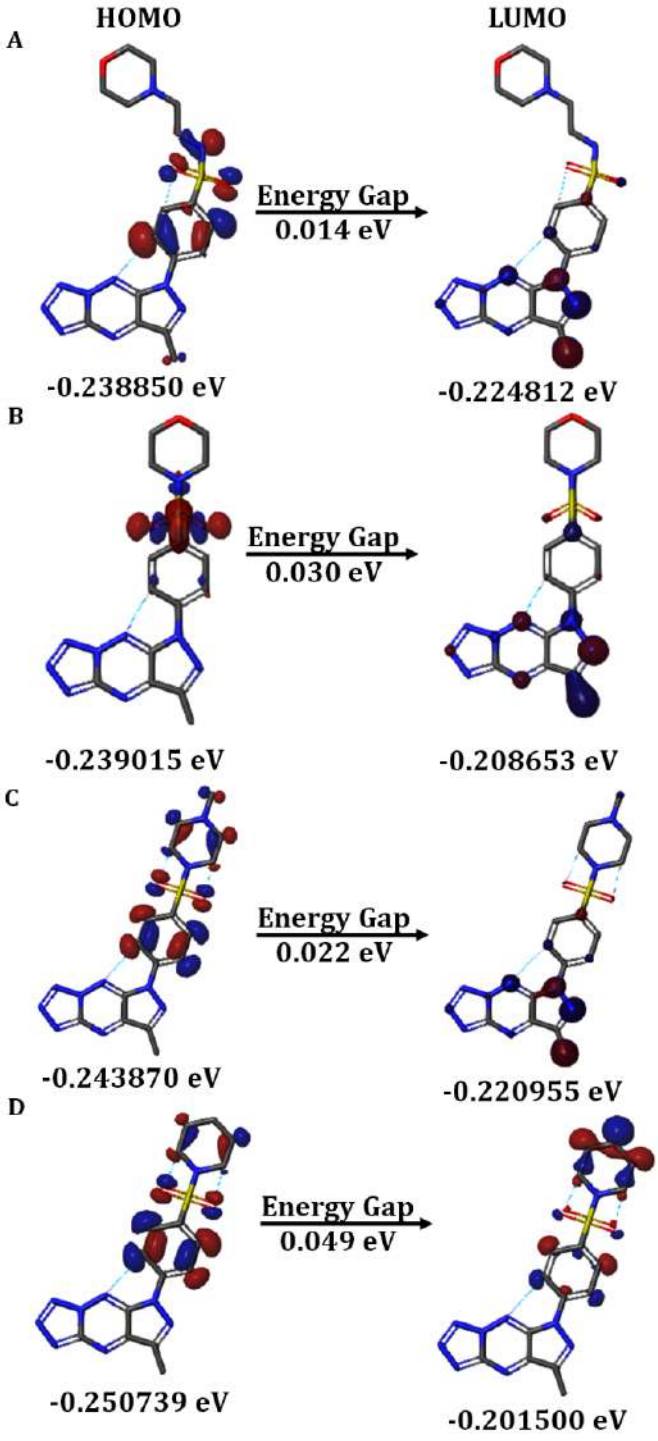

Figure S3. HOMO and LUMO distribution profile of the compounds. A) **MM134**, B) **MM136**, C) **MM137**, and D) **MM139**.

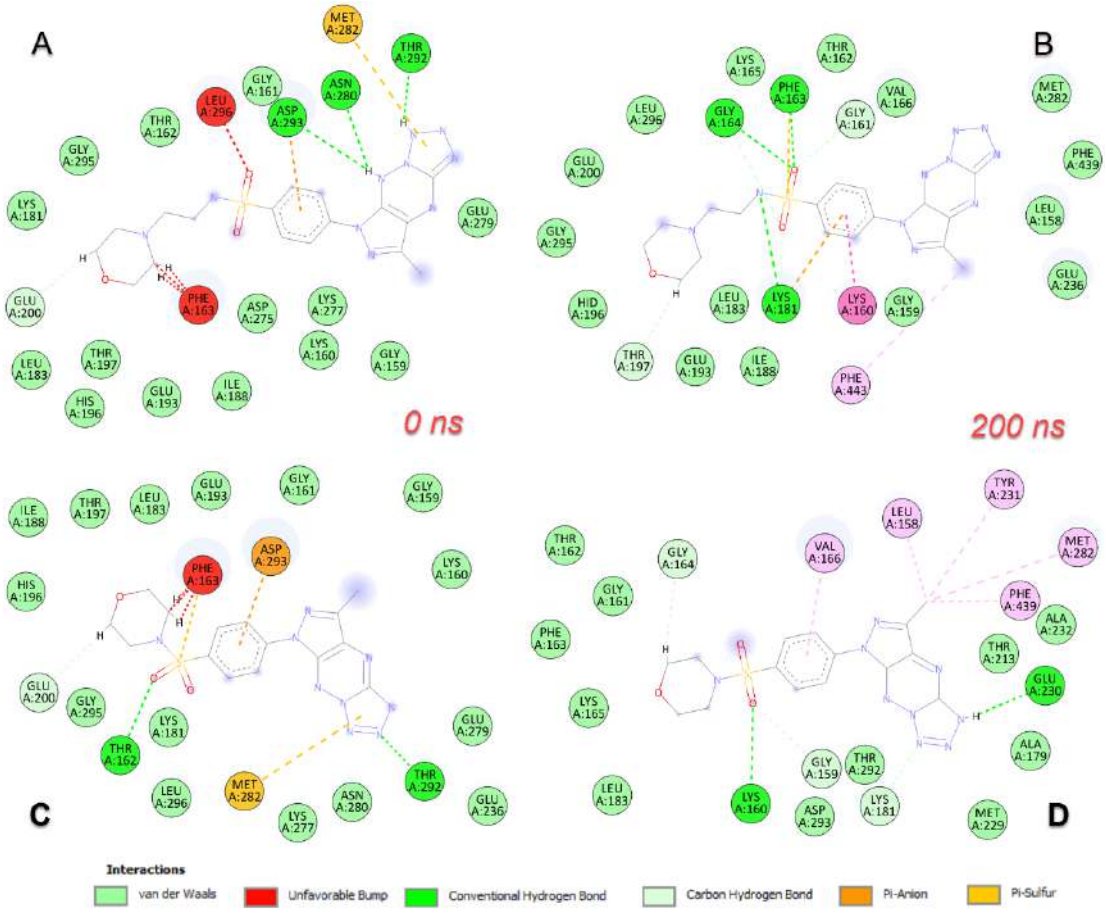

Figure S4. Diagrams of protein-ligand interactions of **AKT2** & **MM134** and **AKT2** & **MM136** complexes at the middle and end of 200 ns time simulation. (**A**) 0 ns interactions in **AKT2** & **MM134** complex, (**B**) 2D interactions at 200 ns, and (**C**) Schematic protein-ligand interaction diagrams of the **AKT2** & **MM136** complex at 0 ns and (**D**) at 200 ns of MD simulation.

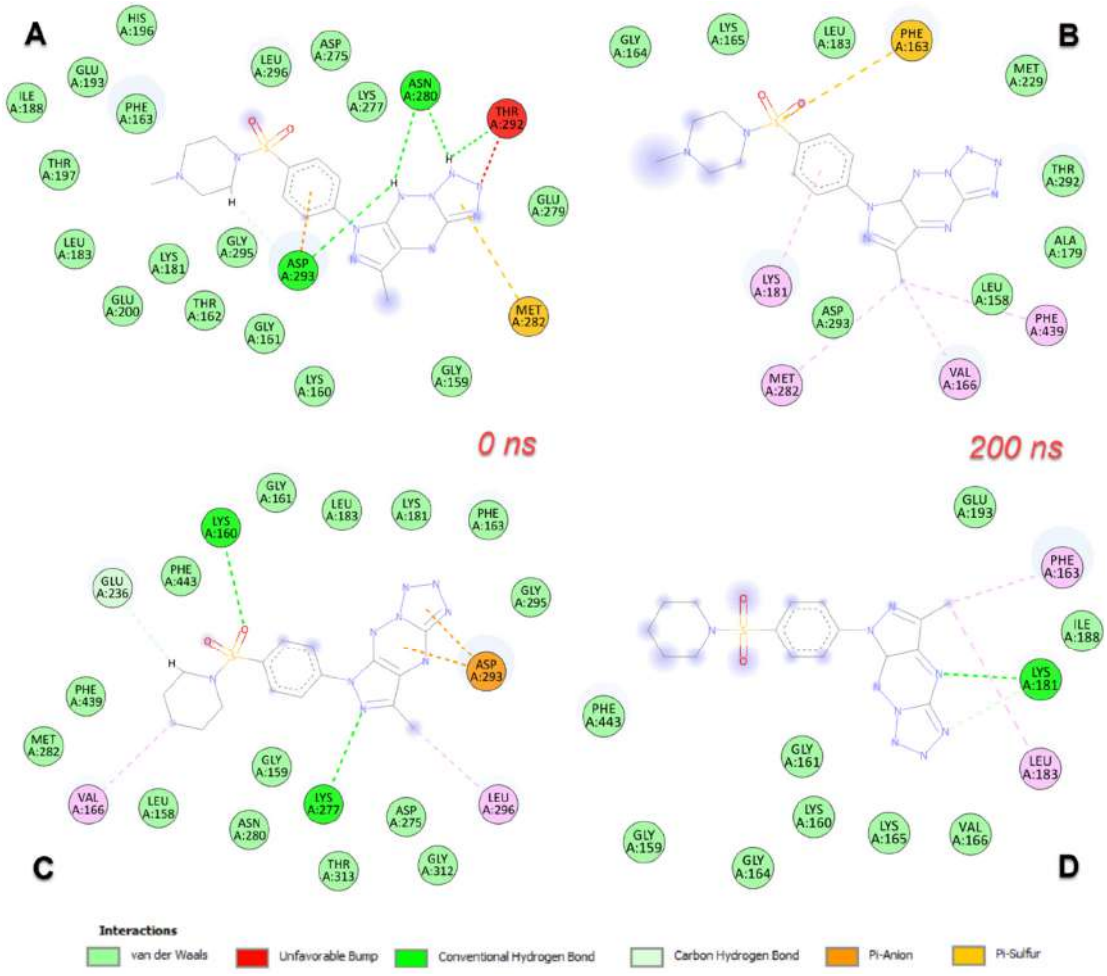

Figure S5. Diagrams of protein-ligand interactions of AKT2 & **MM137** and AKT2 & **MM139** complexes at the middle and end of 200 ns time simulation. (**A**) 0 ns interactions in AKT2 & **MM137** complex, (**B**) 2D interactions at 200 ns, and (**C**) Schematic protein-ligand interaction diagrams of the AKT2 & **MM139** complex at 0 ns and (**D**) at 200 ns of MD simulation.

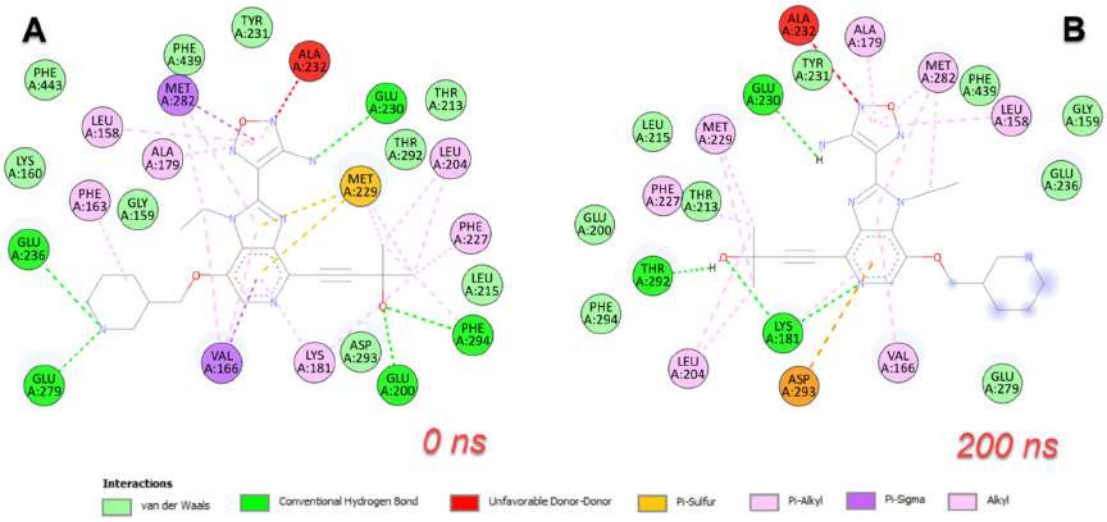

Figure S6. Diagrams of protein-ligand interactions of AKT2 & G39 complexes at the 0 ns and end of 200 ns time simulation. (**A**) 0 ns interactions in AKT2 & G39 complex, (**B**) 2D interactions at 200 ns, and of MD simulation.

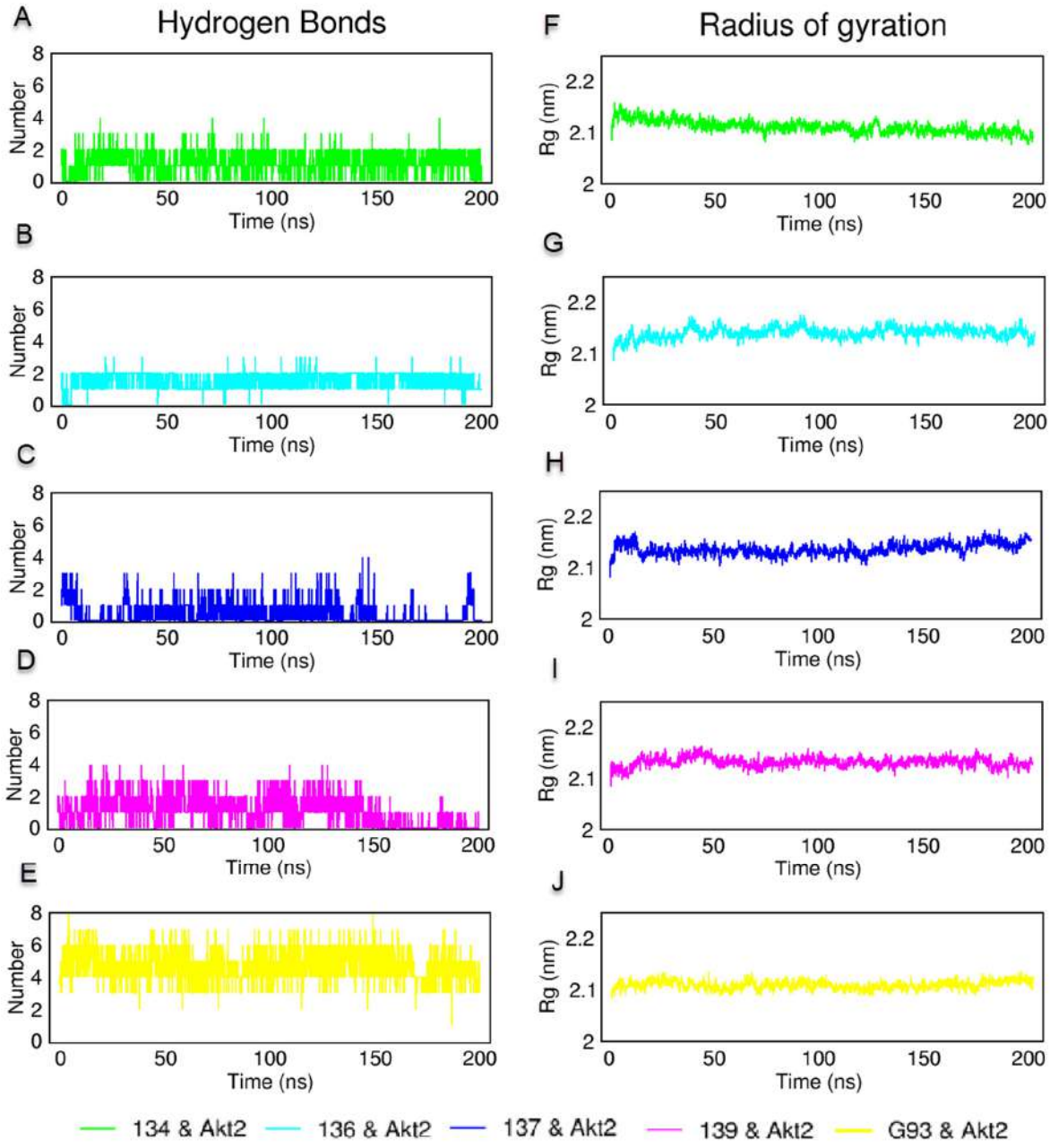

Figure S7. Hydrogen bonding and compactness analysis from molecular dynamics simulation: (A-E) H bond number and exchange between **MM134** & AKT2, **MM136** & AKT2, **MM137** & AKT2, **MM139** & AKT2, and G39 & AKT2, and (F-J) radius of gyration (Rg) measurement of these protein-ligand complexes for 200 ns.

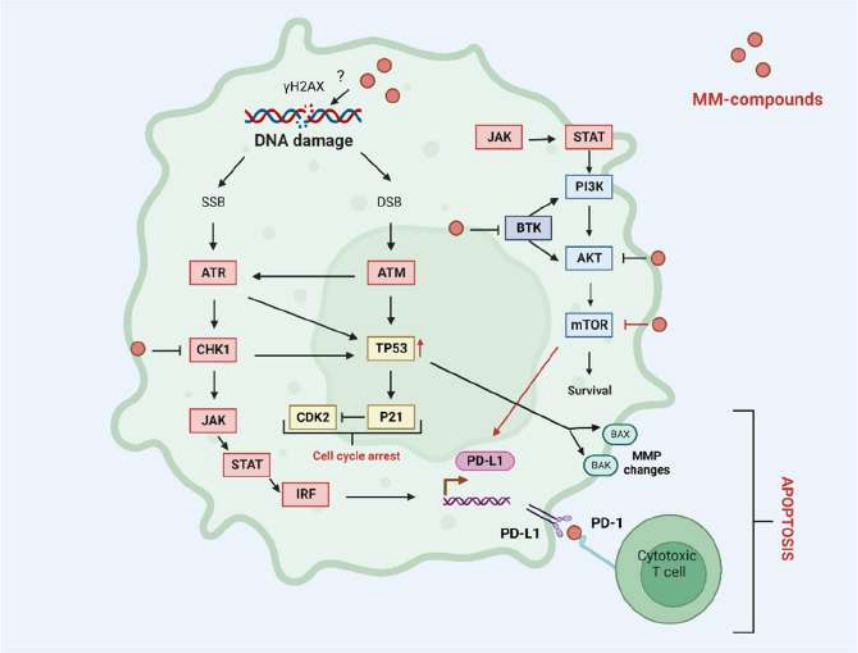

Figure S8. Possible molecular mechanism of biological activity of the **MM**-compounds. Adapted from [8] and modified. Based on [7,10,18,38,81]. Created with BioRender.com accessed on 24 April 2023.

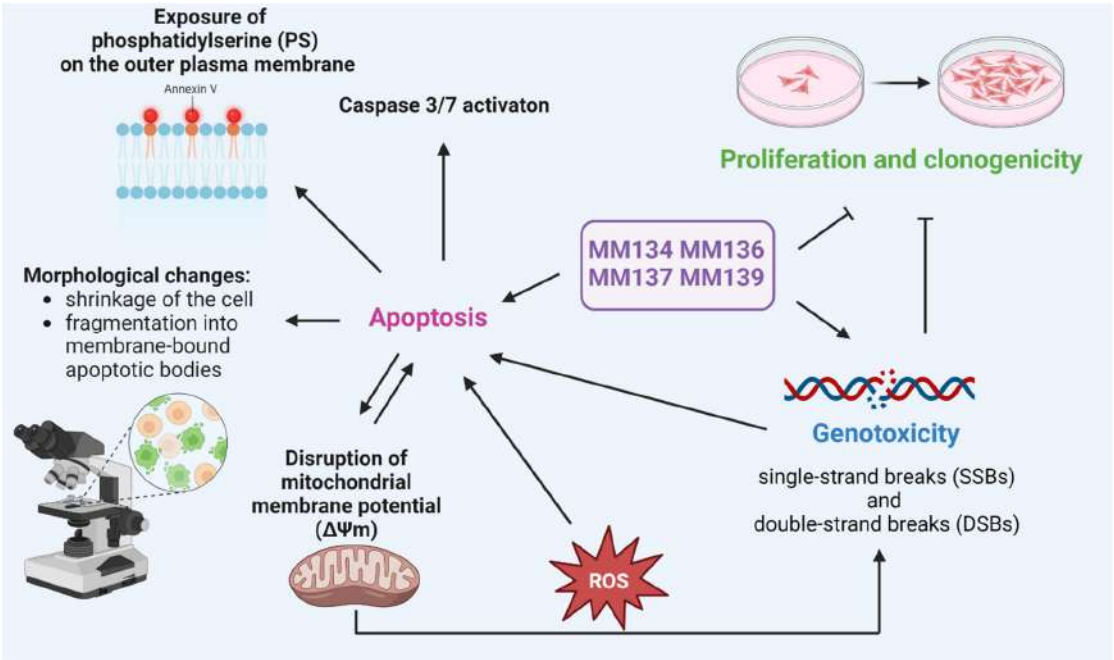

Figure S9. Summary of biological activity of **MM134**, **-6**, **-7,** and **-9** compounds reported in the literature. Based on [8,11]. Created with BioRender.com accessed on 24 April 2023.

13. Oświadczenia współautorów publikacji

Lublin dn. 30.06. 2023 r.

mgr Zofia Bernat

POMIAR – GIG

Przedstawiciel Głównego Instytutu Górnictwa Spółka z o.o.

ul. Bursaki 18, 20-150 Lublin

Oświadczenie współautora

Dotyczy publikacji

Zofia Bernat, Anna Szymanowska, Mateusz Kciuk, Katarzyna Kotwica-Mojzych and Mariusz Mojzych, ***Review of the Synthesis and Anticancer Properties of Pyrazolo[4,3-e][1,2,4]triazine Derivatives*** *Molecules* **2020**, 25(17), 3948; https://doi.org/10.3390/molecules25173948

Oświadczam, że mój udział w publikacji polegał na współudziale w powstaniu koncepcji pracy i pisaniu manuskryptu. Mój udział oceniam na 35 %.

Zofia Bernat

.....

mgr Zofia Bernat

Houston, Texas, USA, dn. 30.06. 2023 r.

Dr Anna Szymanowska

Department of Experimental Therapeutics

MDAnderson Cancer Center

Oświadczenie współautora

Dotyczy publikacji

Zofia Bernat, Anna Szymanowska, Mateusz Kciuk, Katarzyna Kotwica-Mojzych and Mariusz Mojzych, ***Review of the Synthesis and Anticancer Properties of Pyrazolo[4,3-e][1,2,4]triazine Derivatives*** *Molecules* **2020**, 25(17), 3948; https://doi.org/10.3390/molecules25173948

Oświadczam, że mój udział w publikacji polegał na współudziale w pisaniu manuskryptu. Mój udział oceniam na 10 %.

Anna Szymanowska

dr Anna Szymanowska

Łódź, 21.08.2023

mgr Mateusz Kciuk

Katedra Biotechnologii Molekularnej i Genetyki,

Uniwersytet Łódzki

Oświadczenie współautora

Dotyczy publikacji:

Bernat Z.; Szymanowska A.; **Kciuk M.**; Kotwica-Mojzych K.; Mojzych M. ***Review of the Synthesis and Anticancer Properties of Pyrazolo[4,3-e][1,2,4]Triazine Derivatives.*** Molecules 2020, 25, 3948 (IF: 4,412; punkty MEiN: 140 pkt).

Oświadczam, że mój udział w publikacji polegał na współudziale w powstawaniu koncepcji pracy i pisaniu manuskryptu. Mój udział oceniam na 25%.

Mateusz Kciuk

mgr Mateusz Kciuk

dr n. med. Katarzyna Kotwica-Mojzych
profesor uczelni

Pracownia Cytologii Doświadczalnej

ul. Radziwiłłowska 11 (Collegium Medicum)
20-080 Lublin

Telefon: (+48) 814485020 lub kom.: 606327441 e-mail: katarzynakotwicamojzych@umlub.pl

Lublin, dnia 04/07/2023

Oświadczenie współautora

Dotyczy publikacji

Zofia Bernat, Anna Szymanowska, Mateusz Kciuk, Katarzyna Kotwica-Mojzych and Mariusz Mojzych, ***Review of the Synthesis and Anticancer Properties of Pyrazolo[4,3-e][1,2,4]triazine Derivatives*** *Molecules* **2020**, 25(17), 3948; https://doi.org/10.3390/molecules25173948

Oświadczam, że mój udział w publikacji polegał na współudziale w powstaniu koncepcji pracy i pisaniu manuskryptu. Mój udział oceniam na 25 %.

Katarzyna Kotwica-Mojzych

Uniwersytet Przyrodniczo-Humanistyczny w Siedlcach

prof. dr hab. n. med. Mariusz Mojzych

Instytut Nauk Chemicznych

08-110 Siedlce, ul. 3 Maja 54, 25 643 11 13, kom. 666-037-451, e-mail: mariusz.mojzych@uph.edu.pl

Oświadczenie współautora

Dotyczy publikacji:

Zofia Bernat, Anna Szymanowska, Mateusz Kciuk, Katarzyna Kotwica-Mojzych and Mariusz Mojzych, ***Review of the Synthesis and Anticancer Properties of Pyrazolo[4,3-e][1,2,4]triazine Derivatives*** *Molecules* **2020**, 25(17), 3948; https://doi.org/10.3390/molecules25173948

Oświadczam, że mój udział w publikacji obejmował sprawdzenie i korektę manuskryptu.

Mój udział oceniam na 5 %.

Łódź, 21.08.2023

mgr Mateusz Kciuk

Katedra Biotechnologii Molekularnej i Genetyki,

Uniwersytet Łódzki

Oświadczenie współautora

Dotyczy publikacji:

Kciuk, M.; Mujwar, S.; Szymanowska, A.; Marciniak, B.; Bukowski, K.; Mojzych, M.; Kontek, R. Preparation of Novel Pyrazolo[4,3-e]Tetrazolo[1,5-b][1,2,4]Triazine Sulfonamides and Their Experimental and Computational Biological Studies. *Int. J. Mol. Sci.* **2022**, *23*, doi:10.3390/ijms23115892. (MEiN = 140 pkt, IF = 5,6).

Oświadczam, że mój udział w publikacji polegał na współudziale w powstawaniu koncepcji pracy, zaplanowaniu eksperymentów oraz ich wykonaniu. Przeprowadziłem analizę cytotoksyczność (*test MTT*) oraz właściwości proapoptotycznych (*analiza cytometryczna poprzez identyfikację fosfatydyloseryny eksponowanej na powierzchni badanych komórek przy pomocy jodku propidyny oraz aneksyny V sprzężonej z izotiocyjanianem fluoresceiny (ang. flow cytometry analysis with annexin V-FITC staining), mikroskopowa ocena zmian w morfologii komórek przy zastosowaniu mieszaniny barwników fluorescencyjnych - oranżu akrydyny oraz bromku etydyny (ang. dual acridine orange/ethidium bromide (AO/EB) fluorescent staining) oraz ocena zmian potencjału błony mitochondrialnej (ΔΨm) za pomocą barwnika fluorescencyjnego MitoTracker Red (ang. changes in transmembrane mitochondrial potential – MitoTracker Red*) związków MM. Ponadto, uczestniczyłem w syntezie oraz analizie *in silico* badanych związków (*analiza właściwości ADMET oraz dokowanie molekularne*). Dokonałem analizy statystycznej, wizualizacji danych oraz ich interpretacji. Opracowałem manuskrypt. Mój udział oceniam na 70%.

Mateusz Kciuk

mgr Mateusz Kciuk

India, 21.08.2023

dr Somdutt Mujwar

Chitkara College of Pharmacy,

Chitkara University

Contributor's Statement

Publication:

Kciuk, M.; Mujwar, S.; Szymanowska, A.; Marciniak, B.; Bukowski, K.; Mojzych, M.; Kontek, R. Preparation of Novel Pyrazolo[4,3-e]Tetrazolo[1,5-b][1,2,4]Triazine Sulfonamides and Their Experimental and Computational Biological Studies. *Int. J. Mol. Sci.* **2022**, *23*, doi:10.3390/ijms23115892. (MEiN = 140 pkt, IF = 5,6).

I declare that my participation in the publication was associated with *in silico* studies (molecular docking and molecular dynamics simulations). I rate my participation as 5%.

.....

dr Somdutt Mujwar

Houston, Texas, USA, dn. 30.08.2023

Dr Anna Szymanowska

Department of Experimental Therapeutics

MD Anderson Cancer Center

Houston, Texas, USA

Oświadczenie współautora

Dotyczy publikacji:

Kciuk, M.; Mujwar, S.; Szymanowska, A.; Marciniak, B.; Bukowski, K.; Mojzych, M.; Kontek, R. Preparation of Novel Pyrazolo[4,3-e]Tetrazolo[1,5-b][1,2,4]Triazine Sulfonamides and Their Experimental and Computational Biological Studies. *Int. J. Mol. Sci.* **2022**, *23*, doi:10.3390/ijms23115892. (MEiN = 140 pkt, IF = 5,6).

Oświadczam, że mój udział w publikacji polegał na opracowaniu wyników badań spektroskopowych. Mój udział oceniam na 5%

Anna Szymanowska

Dr Anna Szymanowska

Łódź, 21.08.2023

Beata Marciniak

Katedra Biotechnologii Molekularnej i Genetyki,

Uniwersytet Łódzki

Oświadczenie współautora

Dotyczy publikacji:

Kciuk, M.; Mujwar, S.; Szymanowska, A.; Marciniak, B.; Bukowski, K.; Mojzych, M.; Kontek, R. Preparation of Novel Pyrazolo[4,3-e]Tetrazolo[1,5-b][1,2,4]Triazine Sulfonamides and Their Experimental and Computational Biological Studies. *Int. J. Mol. Sci.* **2022**, *23*, doi:10.3390/ijms23115892. (MEiN = 140 pkt, IF = 5,6).

Oświadczam, że mój udział w publikacji polegał na współudziale w powstawaniu koncepcji pracy oraz przeglądzie literaturowym niezbędnym do jej powstania. Mój udział oceniam na 5%.

Beata Marciniak

dr Beata Marciniak

Łódź, 21.08.2023

mgr Karol Bukowski

Katedra Biotechnologii Molekularnej i Genetyki,

Uniwersytet Łódzki

Oświadczenie współautora

Dotyczy publikacji:

Kciuk, M.; Mujwar, S.; Szymanowska, A.; Marciniak, B.; Bukowski, K.; Mojzych, M.; Kontek, R. Preparation of Novel Pyrazolo[4,3-e]Tetrazolo[1,5-b][1,2,4]Triazine Sulfonamides and Their Experimental and Computational Biological Studies. *Int. J. Mol. Sci.* **2022**, *23*, doi:10.3390/ijms23115892. (MEiN = 140 pkt, IF = 5,6).

Oświadczam, że mój udział w publikacji polegał na pomocy w pisaniu manuskryptu. Mój udział oceniam na 5%.

Karol Bukowski

mgr Karol Bukowski

Uniwersytet
Przyrodniczo-
-Humanistyczny
w Siedlcach

Prof. dr hab. n. med. Mariusz Mojzych

Instytut Nauk Chemicznych

08-110 Siedlce, ul. 3 Maja 54, 25 643 11 13, kom. 666-037-451, e-mail: mariusz.mojzych@uph.edu.pl

Siedlce, 30.08.2023 r.

Oświadczenie współautora

Dotyczy publikacji:

Kciuk, M.; Mujwar, S.; Szymanowska, A.; Marciniak, B.; Bukowski, K.; Mojzych, M.; Kontek, R. *Preparation of Novel Pyrazolo[4,3-e]Tetrazolo[1,5-b][1,2,4]Triazine Sulfonamides and Their Experimental and Computational Biological Studies*.

Int. J. Mol. Sci. **2022**, 23, doi:10.3390/ijms23115892. (MEiN = 140 pkt, IF = 5,6).

Oświadczam, że mój udział w publikacji obejmował koncepcję pracy, sprawdzenie i korektę manuskryptu.

Mój udział oceniam na 5 %.

Łódź, 21.08.2023

dr hab. Renata Kontek, prof. UŁ

Katedra Biotechnologii Molekularnej i Genetyki,

Uniwersytet Łódzki

Oświadczenie współautora

Dotyczy publikacji:

Kciuk, M.; Mujwar, S.; Szymanowska, A.; Marciniak, B.; Bukowski, K.; Mojzych, M.; Kontek, R. Preparation of Novel Pyrazolo[4,3-e]Tetrazolo[1,5-b][1,2,4]Triazine Sulfonamides and Their Experimental and Computational Biological Studies. *Int. J. Mol. Sci.* **2022**, *23*, doi:10.3390/ijms23115892. (MEiN = 140 pkt, IF = 5,6).

Oświadczam, że mój udział w publikacji polegał na współudziale w powstawaniu koncepcji pracy, przeglądzie literaturowym niezbędnym do jej powstania oraz nadzorze nad pracami eksperymentalnymi. Mój udział oceniam na 5%.

R. Kontek

.....

dr hab. Renata Kontek

Łódź, 21.08.2023

mgr Mateusz Kciuk

Katedra Biotechnologii Molekularnej i Genetyki,

Uniwersytet Łódzki

Oświadczenie współautora

Dotyczy publikacji:

Kciuk M.; Mujwar S.; Marciniak B.; Gielecińska A.; Bukowski K.; Mojzych M.; Kontek R. Genotoxicity of Novel Pyrazolo[4,3-e]Tetrazolo[1,5-b][1,2,4]Triazine Sulfonamides in Normal and Cancer Cells In Vitro. Int. J. Mol. Sci. 2023, 24, 4053. (MEiN = 140 pkt, IF = 5,6).

Oświadczam, że mój udział w publikacji polegał na współudziale w powstawaniu koncepcji pracy, zaplanowaniu eksperymentów oraz ich wykonaniu. Przeprowadziłem analizy żywotności komórek (*barwienie komórek przy pomocy błękitu trypanu (ang. trypan blue staining), test Alamar Blue (ang. Alamar Blue assay)*) oraz właściwości genotoksycznych (*elektroforeza pojedynczych komórek, czyli test kometowy (ang. comet assay/single cell gel electrophoresis assay)) w wersji alkalicznej oraz neutralnej immunofluorescencyjna detekcja ufosforylowanego histonu H2AX (γH2AX) (ang. γH2AX staining*) związków MM. Ponadto, uczestniczyłem w badaniach *in silico* związków MM (*dokowanie molekularne*). Dokonałem analizy statystycznej, wizualizacji danych oraz ich interpretacji. Opracowałem manuskrypt. Mój udział oceniam na 70%.

Mateusz Kciuk

mgr Mateusz Kciuk

India, 21.08.2023

dr Somdutt Mujwar

Chitkara College of Pharmacy,

Chitkara University

Contributor's Statement

Publication:

Kciuk M.; Mujwar S.; Marciniak B.; Gielecińska A.; Bukowski K.; Mojzych M.; Kontek R. Genotoxicity of Novel Pyrazolo[4,3-e]Tetrazolo[1,5-b][1,2,4]Triazine Sulfonamides in Normal and Cancer Cells In Vitro. Int. J. Mol. Sci. 2023, 24, 4053. (MEiN = 140 pkt, IF = 5,6).

I declare that my participation in the publication was associated with *in silico* studies (molecular docking and molecular dynamics simulations). I rate my participation as 5%.

dr Somdutt Mujwar

Łódź, 21.08.2023

Beata Marciniak

Katedra Biotechnologii Molekularnej i Genetyki,

Uniwersytet Łódzki

Oświadczenie współautora

Dotyczy publikacji:

Kciuk M.; Mujwar S.; Marciniak B.; Gielecińska A.; Bukowski K.; Mojzych M.; Kontek R. Genotoxicity of Novel Pyrazolo[4,3-e]Tetrazolo[1,5-b][1,2,4]Triazine Sulfonamides in Normal and Cancer Cells In Vitro. Int. J. Mol. Sci. 2023, 24, 4053. (MEiN = 140 pkt, IF = 5,6).

Oświadczam, że mój udział w publikacji polegał na współudziale w powstawaniu koncepcji pracy, nadzorowaniu prawidłowego przebiegu eksperymentów oraz edycji ostatecznej wersji manuskryptu. Mój udział oceniam na 5%.

Beata Marciniak

dr Beata Marciniak

Łódź, 21.08.2023

mgr Adrianna Gielecińska

Katedra Biotechnologii Molekularnej i Genetyki,

Uniwersytet Łódzki

Oświadczenie współautora

Dotyczy publikacji:

Kciuk M.; Mujwar S.; Marciniak B.; Gielecińska A.; Bukowski K.; Mojzych M.; Kontek R. Genotoxicity of Novel Pyrazolo[4,3-e]Tetrazolo[1,5-b][1,2,4]Triazine Sulfonamides in Normal and Cancer Cells In Vitro. Int. J. Mol. Sci. 2023, 24, 4053. (MEiN = 140 pkt, IF = 5,6).

Oświadczam, że mój udział w publikacji polegał na pomocy w przygotowaniu koncepcji pracy oraz pisaniu manuskryptu. Mój udział oceniam na 5%.

Gielecińska Adrianna

mgr Adrianna Gielecińska

Łódź, 21.08.2023

mgr Karol Bukowski

Katedra Biotechnologii Molekularnej i Genetyki,

Uniwersytet Łódzki

Oświadczenie współautora

Dotyczy publikacji:

Kciuk M.; Mujwar S.; Marciniak B.; Gielecińska A.; Bukowski K.; Mojzych M.; Kontek R. Genotoxicity of Novel Pyrazolo[4,3-e]Tetrazolo[1,5-b][1,2,4]Triazine Sulfonamides in Normal and Cancer Cells In Vitro. Int. J. Mol. Sci. 2023, 24, 4053. (MEiN = 140 pkt, IF = 5,6).

Oświadczam, że mój udział w publikacji polegał na pomocy w pisaniu manuskryptu. Mój udział oceniam na 5%.

Karol Bukowski

.....

mgr Karol Bukowski

Uniwersytet Przyrodniczo-Humanistyczny w Siedlcach

Prof. dr hab. n. med. Mariusz Mojzych

Instytut Nauk Chemicznych

08-110 Siedlce, ul. 3 Maja 54, 25 643 11 13, kom. 666-037-451, e-mail: mariusz.mojzych@uph.edu.pl

Siedlce, 30.08.2023 r.

Oświadczenie współautora

Dotyczy publikacji:

Kciuk M.; Mujwar S.; Marciniak B.; Gielecińska A.; Bukowski K.; Mojzych M.; Kontek R. *Genotoxicity of Novel Pyrazolo[4,3-e]Tetrazolo[1,5-b][1,2,4]Triazine Sulfonamides in Normal and Cancer Cells In Vitro*.

Int. J. Mol. Sci. **2023**, 24, 4053. (MEiN = 140 pkt, IF = 5,6).

Oświadczam, że mój udział w publikacji obejmował sprawdzenie i korektę manuskryptu.

Mój udział oceniam na 5 %.

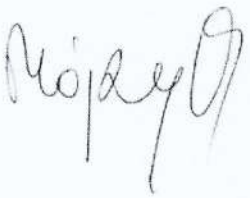

Łódź, 21.08.2023

dr hab. Renata Kontek, prof. UŁ

Katedra Biotechnologii Molekularnej i Genetyki,

Uniwersytet Łódzki

Oświadczenie współautora

Dotyczy publikacji:

Kciuk M.; Mujwar S.; Marciniak B.; Gielecińska A.; Bukowski K.; Mojzych M.; Kontek R. Genotoxicity of Novel Pyrazolo[4,3-e]Tetrazolo[1,5-b][1,2,4]Triazine Sulfonamides in Normal and Cancer Cells In Vitro. Int. J. Mol. Sci. 2023, 24, 4053. (MEiN = 140 pkt, IF = 5,6).

Oświadczam, że mój udział w publikacji polegał na współudziale w powstawaniu koncepcji pracy, opracowaniu metodologii oraz nadzorze nad pracami eksperymentalnymi. Mój udział oceniam na 5%.

R. Kontek

.....

dr hab. Renata Kontek

Łódź, 21.08.2023

mgr Mateusz Kciuk

Katedra Biotechnologii Molekularnej i Genetyki,

Uniwersytet Łódzki

Oświadczenie współautora

Dotyczy publikacji:

Kciuk M.; Marciniak B.; Celik I.; Zerroug E.; Dubey A.; Sundaraj R.; Mujwar S.; Bukowski K.; Mojzych M.; Kontek R. Pyrazolo[4,3-e]Tetrazolo[1,5-b][1,2,4]Triazine Sulfonamides as an Important Scaffold for Anticancer Drug Discovery—In Vitro and In Silico Evaluation. Int. J. Mol. Sci. 2023, 24, 10959, (MEiN = 140 pkt, IF = 5,6).

Oświadczam, że mój udział w publikacji polegał na współudziale w powstawaniu koncepcji pracy, zaplanowaniu eksperymentów oraz ich wykonaniu. Przeprowadziłem analizy cytotoksyczności/właściwości antyproliferacyjnych (*test wychwytu czerwieni obojętnej (ang. neutral red uptake assay, test włączenia bromodeoksyurydyny (BrdU) (ang. bromodeoxyuridine/5-bromo-2'-deoxyuridine incorporation assay*), właściwości proapoptotycznych (*oznaczenie aktywności kaspaz 3/7/8/9 przy pomocy sond fluorescencyjnych (ang. caspase 3/7/8/9 detection), analiza apoptotycznej fragmentacji DNA komórek (ang. DNA laddering*), przebiegu cyklu komórkowego oraz jego poszczególnych faz po inkubacji komórek linii nowotworowych z badanymi związkami, analizy zmian profilu ekspresji genów związanych z apoptozą oraz zdolności prooksydacyjnych badanych związków w komórkach linii nowotworowych człowieka. Oceniłem również wpływ badanych związków na klonogenność komórek nowotworowych. Dokonałem analizy statystycznej, wizualizacji danych oraz ich interpretacji. Opracowałem manuskrypt. Mój udział oceniam na 55%.

Mateusz Kciuk

mgr Mateusz Kciuk

Łódź, 21.08.2023

Beata Marciniak

Katedra Biotechnologii Molekularnej i Genetyki,

Uniwersytet Łódzki

Oświadczenie współautora

Dotyczy publikacji:

Kciuk M.; Marciniak B.; Celik I.; Zerroug E.; Dubey A.; Sundaraj R.; Mujwar S.; Bukowski K.; Mojzych M.; Kontek R. Pyrazolo[4,3-e]Tetrazolo[1,5-b][1,2,4]Triazine Sulfonamides as an Important Scaffold for Anticancer Drug Discovery—In Vitro and In Silico Evaluation. Int. J. Mol. Sci. 2023, 24, 10959, (MEiN = 140 pkt, IF = 5,6).

Oświadczam, że mój udział w publikacji polegał na współudziale w powstawaniu koncepcji pracy, nadzorowaniu prawidłowego przebiegu eksperymentów oraz edycji ostatecznej wersji manuskryptu. Mój udział oceniam na 5%.

Beata Marciniak

dr Beata Marciniak

Turkey, 21.08.2023

dr Ismail Celik

Department of Pharmaceutical Chemistry,

Faculty of Pharmacy,

Erciyes University, Kayseri 38280, Turkey

Contributor's Statement

Publication:

Kciuk M.; Marciniak B.; Celik I.; Zerroug E.; Dubey A.; Sundaraj R.; Mujwar S.; Bukowski K.; Mojzych M.; Kontek R. Pyrazolo[4,3-e]Tetrazolo[1,5-b][1,2,4]Triazine Sulfonamides as an Important Scaffold for Anticancer Drug Discovery—In Vitro and In Silico Evaluation. Int. J. Mol. Sci. 2023, 24, 10959, (MEiN = 140 pkt, IF = 5,6).

I declare that my participation in the publication was associated with *in silico* studies (molecular dynamics simulations). I rate my participation as 5%.

dr Ismail Celik

Algeria, 21.08.2023

dr Enfale Zerroug

Group of Computational and Pharmaceutical Chemistry,

University of Biskra,

Biskra, Algeria

Contributor's Statement

Publication:

Kciuk M.; Marciniak B.; Celik I.; Zerroug E.; Dubey A.; Sundaraj R.; Mujwar S.; Bukowski K.; Mojzych M.; Kontek R. Pyrazolo[4,3-e]Tetrazolo[1,5-b][1,2,4]Triazine Sulfonamides as an Important Scaffold for Anticancer Drug Discovery—In Vitro and In Silico Evaluation. Int. J. Mol. Sci. 2023, 24, 10959, (MEiN = 140 pkt, IF = 5,6).

I declare that my participation in the publication was associated with *in silico* studies (molecular docking). I rate my participation as 5%.

dr Enfale Zerroug

Date: 29.08.2023

Dr. Amit Dubey, Ph.D.

Quanta Calculus, Greater Noida,

India

Contributor's Statement

Publication:

Kciuk M.; Marciniak B.; Celik I.; Zerroug E.; Dubey A.; Sundaraj R.; Mujwar S.; Bukowski K.; Mojzych M.; Kontek R. Pyrazolo[4,3-e]Tetrazolo[1,5-b][1,2,4]Triazine Sulfonamides as an Important Scaffold for Anticancer Drug Discovery—In Vitro and In Silico Evaluation. Int. J. Mol. Sci. 2023, 24, 10959, (MEiN = 140 pkt, IF = 5,6).

I declare that my participation in the publication was associated with *in silico* studies. I rate my participation as 5%.

Dr. Amit Dubey

India, 21.08.2023

Dr. Rajamanikandan Sundaraj
Department of Biochemistry,
Karpagam Academy of Higher Education
Tamil Nadu, India

Contributor's Statement

Publication:

1. Kciuk M.; Marciniak B.; Celik I.; Zerroug E.; Dubey A.; Sundaraj R.; Mujwar S.; Bukowski K.; Mojzych M.; Kontek R. Pyrazolo[4,3-e]Tetrazolo[1,5-b][1,2,4]Triazine Sulfonamides as an Important Scaffold for Anticancer Drug Discovery—In Vitro and In Silico Evaluation. Int. J. Mol. Sci. 2023, 24, 10959, (MEiN = 140 pkt, IF = 5,6).

I declare that my participation in the publication was associated with *in silico* studies (Density Functional Theory calculations; DFT). I rate my participation as 5%.

21/08/2023

Dr Rajamanikandan Sundaraj

India, 21.08.2023

dr Somdutt Mujwar

Chitkara College of Pharmacy,

Chitkara University

Contributor's Statement

Publication:

Kciuk M.; Marciniak B.; Celik I.; Zerroug E.; Dubey A.; Sundaraj R.; Mujwar S.; Bukowski K.; Mojzych M.; Kontek R. Pyrazolo[4,3-e]Tetrazolo[1,5-b][1,2,4]Triazine Sulfonamides as an Important Scaffold for Anticancer Drug Discovery—In Vitro and In Silico Evaluation. Int. J. Mol. Sci. 2023, 24, 10959, (MEiN = 140 pkt, IF = 5,6).

I declare that my participation in the publication was associated with *in silico* studies. I rate my participation as 5%.

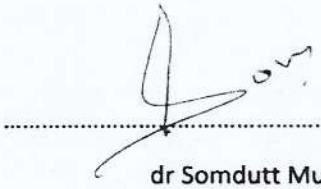

dr Somdutt Mujwar

Łódź, 21.08.2023

mgr Karol Bukowski

Katedra Biotechnologii Molekularnej i Genetyki,

Uniwersytet Łódzki

Oświadczenie współautora

Dotyczy publikacji:

Kciuk M.; Marciniak B.; Celik I.; Zerroug E.; Dubey A.; Sundaraj R.; Mujwar S.; Bukowski K.; Mojzych M.; Kontek R. Pyrazolo[4,3-e]Tetrazolo[1,5-b][1,2,4]Triazine Sulfonamides as an Important Scaffold for Anticancer Drug Discovery—In Vitro and In Silico Evaluation. Int. J. Mol. Sci. 2023, 24, 10959, (MEiN = 140 pkt, IF = 5,6).

Oświadczam, że mój udział w publikacji polegał na pomocy w pisaniu manuskryptu. Mój udział oceniam na 5%.

Karol Bukowski

.....

mgr Karol Bukowski

Uniwersytet
Przyrodniczo-
-Humanistyczny
w Siedlcach

Prof. dr hab. n. med. Mariusz Mojzych

Instytut Nauk Chemicznych

08-110 Siedlce, ul. 3 Maja 54, 25 643 11 13, kom. 666-037-451, e-mail: mariusz.mojzych@uph.edu.pl

Siedlce, 30.08.2023 r.

Oświadczenie współautora

Dotyczy publikacji:

Kciuk M.; Marciniak B.; Celik I.; Zerroug E.; Dubey A.; Sundaraj R.; Mujwar S.; Bukowski K.; Mojzych M.; Kontek R. *Pyrazolo[4,3-e]Tetrazolo[1,5-b][1,2,4]Triazine Sulfonamides as an Important Scaffold for Anticancer Drug Discovery—In Vitro and In Silico Evaluation.*

Int. J. Mol. Sci. **2023**, 24, 10959, (MEiN = 140 pkt, IF = 5,6).

Oświadczam, że mój udział w publikacji obejmował sprawdzenie i korektę manuskryptu.

Mój udział oceniam na 5 %.

Łódź, 21.08.2023

dr hab. Renata Kontek, prof. UŁ

Katedra Biotechnologii Molekularnej i Genetyki,

Uniwersytet Łódzki

Oświadczenie współautora

Dotyczy publikacji:

Kciuk M.; Marciniak B.; Celik I.; Zerroug E.; Dubey A.; Sundaraj R.; Mujwar S.; Bukowski K.; Mojzych M.; Kontek R. Pyrazolo[4,3-e]Tetrazolo[1,5-b][1,2,4]Triazine Sulfonamides as an Important Scaffold for Anticancer Drug Discovery—In Vitro and In Silico Evaluation. Int. J. Mol. Sci. 2023, 24, 10959, (MEiN = 140 pkt, IF = 5,6).

Oświadczam, że mój udział w publikacji polegał na nadzorze nad pracami eksperymentalnymi oraz powstawaniem manuskryptu. Mój udział oceniam na 5%.

R. Kontek

.....

dr hab. Renata Kontek